FACULTY OF ENGINEERING AND ARCHITECTURE

Spectroscopic Fingerprint of Electronic Excitations in Nanoporous Frameworks and Transition Metal Complexes

Liesbeth De Bruecker

Doctoral dissertation submitted to obtain the academic degree of
Doctor of Engineering Physics

Supervisor
Prof. Veronique Van Speybroeck, PhD
Department of Applied Physics
Faculty of Engineering and Architecture, Ghent University

August 2023

GHENT UNIVERSITY

ISBN 978-94-6355-739-9
NUR 928
Wettelijk depot: D/2023/10.500/71

Members of the Examination Board

Chair

Prof. Hennie De Schepper, PhD, Ghent University

Other members entitled to vote

Prof. Bartolomeo Civalleri, PhD, Università degli Studi di Torino, Italy
Jenna Mancuso, PhD, Ghent University
Samuel Neale, PhD, University of Bath, United Kingdom
Prof. Louis Vanduyfhuys, PhD, Ghent University

Supervisor

Prof. Veronique Van Speybroeck, PhD, Ghent University

This research has been conducted at the **Center for Molecular Modeling**, in collaboration with:

- The Center for Ordered Materials, Organometallics and Catalysis Research Group (COMOC), Department of Inorganic and Physical Chemistry, Faculty of Sciences, Ghent University (Prof. Van Der Voort)
- The Synthesis, Bioresources and Bioorganic Chemistry Research Group (SynBioC), Department of Green Chemistry and Technology, Faculty of Bioscience Engineering, Ghent University (Prof. Stevens)
- Inorganic Chemistry and Catalysis group, Debye Institute for Nanomaterials Science, Utrecht University (Prof. B. M. Weckhuysen, dr. M. Filez)

Voorwoord

Veel lijkt eerst moeilijk voor het gemakkelijk wordt. Deze quote vormt een uitstekende samenvatting van de voorbije vijf jaar. Al zolang ik mij kan herinneren, hangt er een poster met deze zin in mijn kinderkamer. Er is een hondje te zien dat door een verkeerde toetsencombinatie in te drukken een bom heeft gecreëerd op het computerscherm. De betekenis van deze spreuk werd voor het eerst tastbaar tijdens het middelbaar, wanneer het studeren niet meer altijd vanzelf ging en er af en toe moeite moest gedaan worden om sommige leerstof te begrijpen. Toen ik aan de opleiding toegepaste natuurkunde begon, zat ik tijdens de soms eindeloos ogende examens te studeren met uitzicht op deze poster. Ook al leek het soms onhaalbaar, de voldoening nadien was des te groter als ik weer een bepaald vak onder de knie had. Tijdens mijn doctoraat heeft deze zin echter nog meer betekenis gekregen toen het meermaals is voorgevallen dat een bepaald probleem onoplosbaar leek, maar dat er uiteindelijk, na soms wat frustraties en met het nodige doorzettingsvermogen, dan toch steeds een lampje ging branden waardoor alles vorm kreeg en ik u nu dan ook met trots dit doctoraat kan voorstellen.

Natuurlijk weten we allemaal dat een werk als dit niet tot stand kan komen door slechts één persoon en daarom wil ik dan ook deze kans grijpen om een aantal mensen te bedanken.

Eerst en vooral wil ik mijn promotor, Veronique, bedanken. Bedankt voor alle kansen die u mij heeft gegeven en om in mij te geloven als onderzoeker. Door uw boeiende lessen werd mijn interesse in de kwantummechanica aangewakkerd en volgden een thesis op het CMM en vervolgens ook een doctoraat als logische stappen. Ik ben dankbaar dat u mij met al uw ervaring en kennis door de voorbije jaren gegidsd heeft. Zonder u zou dit onderzoek er in de eerste plaats nooit geweest zijn en ook zeker niet in de huidige vorm.

Ook Michel verdient een woord van dank. Bedankt om mij bij de start wegwijs te maken in de theorie achter DFT en TDDFT en om mijn kritisch denkvermogen aan te scherpen.

Leen en Mieke, dank jullie wel voor alle hulp bij het regelen van de praktische zaken die komen kijken bij het indienen van een doctoraat. Dit heeft mij heel wat stress bespaard in de voorbije maanden.

Juul, Karen, Massimo, Ruben, Sander, Siebe en Tom, wat is de tijd voorbij gevlogen. Het voelt pas een half jaar geleden toen we startten als de CMM babies, maar ondertussen is het tijd voor mijn 'pensioen' op het CMM. Jullie hebben de afgelopen jaren zoveel aangenamer gemaakt, waarvoor dank.

Ook alle andere CMM'ers wil ik graag bedanken voor de leuke sfeer op het werk.

Daarnaast wil ik ook graag enkele mensen buiten het CMM bedanken die op de één of andere manier hebben bijgedragen tot dit werk.

Hannelore, Johanna, Klara, Hanna, en Louiza, jullie waren er altijd wanneer ik een luisterend oor nodig had of wanneer ik behoefte had aan wat afleiding. Dank jullie wel hiervoor. Charlotte en Laure, ik keek altijd uit naar onze maandelijkse dinertjes.

Arne, ik kan niet onder woorden brengen hoe hard jouw steun mij heeft geholpen bij het afronden van dit werk.

Mama, papa, Inge, meme, en pepe, bedankt om van in het begin in mij te geloven, mij alle kansen te geven en mij te steunen in al mijn keuzes.

Liesbeth De Bruecker
Gent, augustus 2023

Contents

Voorwoord iii

Contents v

Samenvatting xi

Summary xv

List of Symbols xix

List of Abbreviations xxiii

I Spectroscopic Fingerprint of Electronic Excitations in Nanoporous Frameworks and Transition Metal Complexes 1

1 Introduction 3

1.1 UV-Vis spectroscopy 4

1.2 Nanoporous materials 6

1.2.1 Covalent triazine frameworks 7

1.2.2 Zeolitic imidazolate frameworks 9

1.3 Computational chemistry 11

1.3.1 Atomic representation of system under study 12

1.3.2 Computational method 12

1.4 Goals and outline 14

2 Foundations of Density Functional Theory and Time-Dependent Density Functional Theory 17

2.1 From the Schrödinger equation to density functional theory . 17

2.1.1 Schrödinger equation for static Hamiltonians 17

2.1.2 Density functional theory 20

2.2 Time-dependent potentials in time-dependent density functional theory 23

2.2.1 Fundamental theorems behind time-dependent density functional theory 25

2.2.2 Linear response time-dependent density functional theory 28

I. Linear response theory 28

II. Linear response applied to time-dependent external potentials 30

2.2.3 Working equations of time-dependent density functional theory 33

I. Dyson equation 34

II. Excitation energies via the Casida equation 36

III. Oscillator strengths 39

IV. Assignment problem 43

2.2.4 Spin in time-dependent density functional theory . . 45

2.2.5 Approximations in time-dependent density functional theory 46

2.2.6 Shortcomings of time-dependent density functional theory 49

I. Charge-transfer excitations 49

II. Double excitations 50

3 Coordination Chemistry 55

3.1 Transition metal complexes 56

3.1.1 d-orbitals in transition metals 56

3.1.2 Ligands 58

3.2 Symmetry 60

3.2.1 Symmetry operations and elements 60

3.2.2 Point groups and character tables 63
3.3 Correlation diagrams 65
3.3.1 Weak field limit 66
3.3.2 Strong field limit 67
3.3.3 Tanabe-Sugano diagrams 69
3.4 Electronic structure theories 74
3.4.1 Crystal field theory 74
I. Qualitative effects of the ligand field 74
II. Effective Hamiltonian 76
3.4.2 Ligand field theory 83
I. Ligand field theory: a combination of crystal field theory and molecular orbital theory 83
II. Angular overlap model 85
3.4.3 Ligand field DFT 86

4 Unraveling the Photocatalytic Properties of Heterogeneous Catalysts 91

4.1 Introduction to covalent triazine framework materials and their linkers 92
4.1.1 Influence of the level of theory on the ground and excited state properties 95
4.1.2 Influence of extending the π-system and increasing the π-electron deficiency on the excited state properties. 96
4.1.3 Influence of the dihedral angle on the excited state properties 98
4.1.4 Excited state properties of all ligands 100
4.2 Photocatalytic Ru^{2+} complexes with polypyridyl ligands . . . 102
4.3 Embedding of photocatalytic Ru^{2+} complexes on the covalent triazine framework 109

5 Ground and Excited State Properties of Transition Metal Complexes Relevant for the ZIF Nucleation Process 113

5.1 Influence of symmetry on the electronic structure of Co^{2+} aqua-complexes 116

5.1.1 Qualitative d-orbital splitting: crystal field theory, ligand field theory, and angular overlap model 117
5.1.2 Quantitative d-orbital splitting: average of configuration versus unrestricted DFT 118
I. Average of configuration 119
II. Comparison of average of configuration with unrestricted DFT 123
5.2 Excited state properties 126
5.2.1 Using Tanabe-Sugano diagrams for the description of d-d excitations in TMCs 126
5.2.2 Challenges for first-row octahedral aqua-complexes . 129
I. Non-degenerate ground state but double excitations 132
II. Degenerate ground state and double excitations 133
5.2.3 Spectroscopic fingerprint for nucleation process of Co-ZIF-67 135
I. Experimental data 135
II. $[Co(2\text{-mIm})_4]^{2+}$ 137
III. $[Co(2\text{-mIm})_3(H_2O)]^{2+}$ 138
IV. $[Co(H_2O)_6]^{2+}$ 140
V. Spectroscopic fingerprint 142

6 Conclusions and Outlook 145
6.1 Conclusions 145
6.2 Outlook 149

II Published Papers 153

A Publications in International Peer–Reviewed Journals 155
Paper I: Optical Properties of Isolated and Covalent Organic Framework-Embedded Ruthenium Complexes 157
Paper II: Structural and Photophysical Properties of Various Polypyridyl Ligands: A Combined Experimental and Computational Study 173

Paper III: Influence of Number of Ligands and Point Group on the Electronic Structure of Co^{2+} Aqua-Complexes 191
Paper IV: On the Prediction of Spectroscopic Fingerprints of Co^{2+} Complexes Relevant in the ZIF Nucleation Process 207

B Appendix **255**

B.1 Proofs of the fundamental theorems and derivations of expressions encountered in the study of TDDFT 255
B.1.1 Proof of the Runge-Gross theorem 255
B.1.2 Proof of the van Leeuwen theorem 260
B.1.3 Derivation of expression for the Lehmann representation of the LR function 265
B.1.4 Derivation of expression for the Lehmann representation of the KS response function 266
B.1.5 Derivation of expression for the transition density . . 268
B.1.6 Derivation of the alternative form of the Casida equation 268
B.2 Symmetry elements of trigonal bipyramidal and square pyramidal structures 270
B.3 Character tables 271
B.4 Tanabe-Sugano diagrams 274

C List of Publications **277**

Publications in international peer–reviewed journals 277
Book chapter 278
Conference contributions 278
Oral presentation 278
Poster presentations 278
Master's thesis 279

D List of Software Packages **281**

Bibliography **283**

Acknowledgements **309**

Samenvatting

De interactie tussen elektromagnetische golven en materie wordt bestudeerd aan de hand van spectroscopie. De rol ervan in toepassingen gaande van de atomaire tot de astronomische schaal kan niet worden onderschat doordat het een brug vormt tussen theoretische/computationele studies en experimentele waarnemingen. Zo speelde het bijvoorbeeld een belangrijke rol bij de ontwikkeling van de kwantummechanica. Computationele spectroscopie is zeer belangrijk omdat het een link legt tussen de moleculaire schaal en experimenteel waargenomen spectroscopische signalen. In dit werk ligt de nadruk op overgangen van valentie-elektronen die leiden tot excitaties van de grondtoestand naar geëxciteerde toestanden en die onderzocht worden in ultraviolet en zichtbare (UV-Vis, afgeleid van de Engelstalige naamgeving ultraviolet and visible) spectroscopie. In het bijzonder bestuderen we spectroscopische vingerafdrukken van excitaties tussen elektronische energieniveaus in nanoporeuze roosters en transitie metaal complexen (TMCs, afgeleid van de Engelstalige naamgeving transition metal complexes).

Om dit te bereiken worden geavanceerde theoretische berekeningen gebruikt die gebaseerd zijn op de dichtheidsfunctionaaltheorie (DFT). Deze bieden een goed evenwicht tussen nauwkeurigheid en computationele kost. De geëxciteerde toestanden worden bereikt via adiabatische tijdsafhankelijke DFT (TDDFT, afgeleid van de Engelstalige naamgeving time-dependent DFT) in het lineair respons regime. Bovendien wordt de elektronische structuur van TMCs onderzocht via technieken die uit de tijd stammen waarin er nog geen geavanceerde kwantummechanische berekeningen mogelijk waren, maar die nog steeds zeer waardevol zijn. Zo worden kristalveldtheorie en uitbreidingen ervan behandeld. Ligand-veld DFT wordt ook gebruikt, omdat hiermee kwantitatieve resultaten verkregen kunnen worden door gebruik te maken van DFT berekeningen.

Dit proefschrift bestaat uit twee grote onderdelen. Ten eerste worden de eigenschappen van fotokatalytische complexen ingebed in covalente triazine roosters (CTFs, afgeleid van de Engelstalige naamgeving crystal triazine frameworks) onderzocht. Dit werk werd uitgevoerd in samenwerking met onze experimentele partners bij COMOC (Center for Ordered Materials, Prof. Van Der Voort) en SynBioC (Synthesis, Bioresources and Bioorganic Chemistry, Prof. Stevens). We concentreren ons op Ru^{2+} complexen ingebed in een CTF, aangezien deze heterogene katalysatoren veelbelovende, milieuvriendelijke kandidaten zijn voor fotokatalytische toepassingen. TDDFT is bij uitstek geschikt om deze TMCs met gesloten schil en de CTF-linkers te bestuderen. Bovendien kan het ingebedde complex in de CTF ook bestudeerd worden dankzij de lage computationele kost.

In een eerste stap onderzoeken we welke factoren de structurele en fotokatalytische eigenschappen van de CTF beïnvloeden. Daarom richten we ons op verschillende polypyridyl-liganden, die veelbelovende CTF-bouwstenen zijn, en bestuderen de ladingstransfer excitaties die hun UV-Vis spectra domineren. Hoe groter het π-systeem en hoe hoger de π-elektronendeficiëntie, hoe meer de belangrijkste absorptiepiek verschuift naar grotere golflengten. Grote π-systemen worden verkregen wanneer aromatische ringen aanwezig zijn en voor planaire structuren. Een grotere π-electkronendeficiëntie kan worden bekomen door het stikstofgehalte te verhogen of de linker te termineren met elektronenonttrekkende groepen. Voorts kan ook het toevoegen van functionele groepen een aanzienlijke invloed hebben op de eigenschappen van de geëxciteerde toestanden. Ten tweede onderzoeken we het fotokatalytische Ru^{2+} complex en hoe de eigenschappen ervan kunnen worden beïnvloed door het stikstofgehalte van de linkers te veranderen. Naast de singlet excitaties, worden ook triplet geëxciteerde toestanden onderzocht. Hoewel hun oscillator sterkte veel kleiner is, spelen zij een belangrijke rol in het fotokatalytische proces. Deze excitaties zijn moeilijk om experimenteel waar te nemen, maar vormen geen extra uitdaging voor TDDFT. Zowel de band gaps, verkregen uit grondtoestand-berekeningen, als de ladingstransfer excitaties, verkregen uit geëxciteerde toestand-berekeningen, blijken sterk af te hangen van het stikstofgehalte in de linkers. Ten slotte onderzoeken we ook op welke manier de heterogenisering van de Ru^{2+} complexen in een CTF invloed heeft op de energie en het karakter van de geëxciteerde toestand. Uit berekeningen volgt dat lagere energieën kunnen worden gebruikt om ladingstransfer-excitaties te bevorderen, wat gunstig is voor bijvoorbeeld nabij-infrarood fotokatalyse. Bovendien verandert de verankering van het complex het karakter van de excitaties. Het zijn metaal-ligand ladingstransfer excitaties

in het geïsoleerde complex, terwijl bij het verankerde systeem een elektron wordt overgedragen van het kristal naar de liganden van het complex. Als zodanig tonen wij aan dat het systeem in brede zin kan worden afgestemd door het complex in te bedden in een CTF en door de componenten van het rooster en die van het verankerde fotokalytisch complex te veranderen.

In het tweede deel, geïnspireerd door het experimentele werk van dr. ir. Matthias Filez van de Weckhuysen onderzoeksgroep aan de Universiteit van Utrecht, onderzoeken we TMCs die relevant zijn tijdens het nucleatieproces van Co-ZIF-67 om een spectroscopische vingerafdruk voor te stellen. We starten met een onderzoek naar de invloed van symmetrie op de d-orbitaal splitsing, gevolgd door een studie van de d-d overgangen.

We onderzoeken d-orbitaal splitsingen in Co^{2+} aqua-complexen met octahedrale, vierkant-pyramidale, trigonale bipyramidale en tetrahedrale symmetrie. Hierbij wordt zowel de invloed van de coördinatie omgeving als van de specifieke puntgroep beschouwd. Kwalitatieve technieken, zoals kristalveldtheorie, laten zien dat de d-orbitaal splitsing karakteristiek is voor het aantal liganden dat gecoördineerd is met het TM. Aangezien de partieel gevulde d-orbitalen deze TMCs computationeel zeer uitdagend maken, voeren we zowel berekeningen uit met fractionele bezettingsgetallen (AOC, afgeleid van de Engelstalige naamgeving average of configuration) als berekeningen met gehele bezetting (UDFT, afgeleid van de Engelstalige benaming unrestricted DFT) om kwantitatieve resultaten te bekomen. In tegenstelling tot AOC, is UDFT niet in staat om de kwalitatief verkregen d-orbitaal splitsingen te reproduceren omdat slechts een deel van de d-orbitalen bezet is. Het energieverschil tussen de bezette en niet-bezette orbitalen wordt overschat met één grootte-orde in vergelijking met de AOC en experimentele resultaten. Bovendien is de ordening van de d-orbitalen soms omgewisseld. De verschillen tussen beide technieken zijn te wijten aan de andere elektronenbezettingen wat resulteert in verschillende interelektron repulsies. De AOC-orbitalen komen overeen met de chemische intuïtie zoals gegeven door CFT aangezien beide technieken de elektron-elektron interacties op een sferische manier beschrijven. De d-orbital splitsing verkregen door UDFT verschilt hiervan door de gehele bezettingsgetallen die resulteren in andere elektron-elektron repulsies.

Om de performantie van beide technieken verder te testen, berekenen we de d-d overgangen, startend van zowel een AOC- als van een UDFT-referentie via respectievelijk ligand-veld DFT en TDDFT. Bijkomende moeilijkheden treden op voor de berekening van deze geëxciteerde toestanden aangezien ontaarding niet alleen voorkomt in de grondtoestand

maar ook in de geëxciteerde toestanden en dubbele excitaties aanwezig kunnen zijn. Bovendien zijn d-d overgangen Laporte-verboden in systemen met een symmetrie-centrum, en hebben ze dus lage oscillator sterktes. Daarom beginnen we bij het testen van de technieken met eerste rij octahedrale aqua-complexen om de complexiteit van de elektronische structuur te onderzoeken als functie van het aantal d-elektronen. Hoewel het energieverschil tussen bezette en onbezette orbitalen wordt overschat door UDFT, in vergelijking met AOC, is het beeld van d-d excitaties verkregen met beide technieken kwalitatief hetzelfde. Dit geldt zelfs voor moeilijke systemen met een ontaarde grondtoestand en waarbij dubbele excitaties aanwezig zijn. Bovendien geven beide technieken complementaire informatie, terwijl ligand-veld DFT dubbele excitaties kan beschrijven, levert TDDFT oscillator sterktes. Met deze kennis berekenen we de d-d-excitaties van TMCs die relevant zijn voor het nucleatieproces van Co-ZIF-67 via beide technieken en vergelijken de resultaten met de experimentele spectra van Filez *et al.* Alhoewel ligand-veld DFT niet geschikt is voor complexen met niet-compacte liganden, kunnen de octahedrale en tetrahedrale structuren worden onderscheiden op basis van TDDFT. De oscillator sterkte is veel groter en de absorptiepiek is verschoven naar kleinere energieën voor de tetrahedrale complexen in vergelijking met de octahedrale complexen. Bovendien zijn de tetrahedrale complexen, die het nucleatieproces op gang brengen, 10^7-10^8 keer minder aanwezig dan de octahedrale structuren. Tenslotte worden geëxciteerde toestanden bij zeer kleine energieën alleen waargenomen voor octahedrale systemen. Toch zijn er andere technieken nodig om de door Filez *et al.* geobserveerde toestanden die zich in het UV-Vis gebied bevinden te berekenen, aangezien ze voornamelijk bestaan uit dubbele en spin-flip-excitaties, die niet bereikbaar zijn met TDDFT.

Samenvattend is TDDFT, door de uitstekende balans tussen computationele kosten en accuraatheid, perfect geschikt om spectroscopische vingerafdrukken te bepalen voor systemen met een gesloten schil en geeft het een beter inzicht in de onderliggende moleculaire mechanismen. Bovendien kan een kwalitatief beeld worden verkregen voor de berekening van d-d transities in meer uitdagende TMCs. Als zodanig benadrukt dit werk het belang en de veelzijdigheid van theoretische UV-Vis spectroscopie voor verschillende toepassingen.

Summary

The interaction between electromagnetic waves and matter is studied by means of spectroscopy. Its significance in applications ranging from the atomic up to the astronomic scale can not be underestimated, as it builds a bridge between theoretical/computational studies and experimental observations. For example, it played an important role in the development of quantum mechanics. Computational spectroscopy is, in this regard, of utmost importance to link the molecular scale to experimentally observed spectroscopic signals. The focus of this work is on transitions of valence electrons which cause excitations from the ground state to excited states and are probed in ultraviolet and visible (UV-Vis) spectroscopy. In particular, we study spectroscopic fingerprints of excitations between electronic energy levels in nanoporous frameworks and transition metal complexes (TMCs).

In order to achieve this, advanced theoretical calculations based on density functional theory (DFT) are used in this PhD, as they provide a good balance between accuracy and computational cost. The excited states are reached via adiabatic time-dependent DFT (TDDFT) in its linear response regime. Furthermore, the electronic structure of TMCs is investigated with crystal field theory and its extensions. These techniques stem from the time before advanced quantum mechanical calculations were possible, but still have their merits today. Ligand field DFT will be employed too, as it allows one to retrieve quantitative results by making use of DFT calculations.

This thesis consists of two large components. First of all, the properties of photocatalytic complexes embedded in covalent triazine frameworks (CTFs) are investigated. This work is performed in collaboration with our experimental partners at COMOC (Center for Ordered Materials, Prof. Van Der Voort) and SynBioC (Synthesis, Bioresources and Bioorganic Chemistry, Prof. Stevens). We focus on Ru^{2+} complexes with CTF supports, as these heterogeneous catalysts are very promising, environmentally clean candidates for photocatalytic applications. TDDFT is ideally suited to study

these closed-shell TMCs as well as the CTF linkers. Furthermore, due to its low computational cost, the embedded complex in the CTF can be examined too.

In a first step, we investigate which factors influence the structural and photocatalytic properties of the CTF. Therefore, we focus on various polypyridyl ligands, being promising CTF building blocks, and study the charge-transfer excitations, which dominate their UV-Vis spectra. The larger the π-system and the higher its π-electron deficiency, the more the main absorption peak shifts to larger wavelengths. Large π-systems are obtained when aromatic rings are present and for planar systems. A larger π-electron deficiency can be acquired by increasing the nitrogen content or by terminating the linker with electron withdrawing groups. Furthermore, adding functional groups can have a significant influence on the excited state properties. Second, we examine the photocatalytic Ru^{2+} complex and how its properties can be influenced by changing the nitrogen content of the linkers. Besides the singlet excitations, triplet excited states are also investigated. Although their oscillator strength is much smaller, they play a significant role in the photocatalytic process. They are difficult to discern experimentally but pose no additional challenges for TDDFT. Both band gaps, obtained from ground state calculations, and charge-transfer states, retrieved from excited state computations, are found to be strongly adaptable by changing the nitrogen content of its linkers. Finally, we also investigate how the heterogenizaiton of the Ru^{2+} complexes on a CTF support affects the energy and character of the excited states. Calculations reveal that lower energies can be harvested to promote charge-transfer excitations, which is beneficial for near-infrared photocatalysis, for example. Furthermore, anchoring of the complex changes the character of the transitions. They are metal-ligand charge-transfer states in the isolated complex, whereas for the embedded system, an electron is transferred from the crystal to the ligands of the complex. As such, we show that the system can be tuned in a broad sense by embedding the complex in a CTF and by varying the framework components as well as these of the anchored photocalytic complex.

In the second part, inspired by the experimental work performed by dr. ir. Matthias Filez at the Weckhuysen research group in Utrecht University, we investigate TMCs relevant to the Co-ZIF-67 nucleation process in order to propose a spectroscopic fingerprint. We start with an investigation of the influence of symmetry on the d-orbital splitting, followed by a study of the d-d transitions.

We investigate the d-orbital splitting of Co^{2+} aqua-complexes with

octahedral, square pyramidal, trigonal bipyramidal, and tetrahedral symmetry. Hereby, both the influence of the coordination environment and the specific point group are considered. Qualitative techniques, such as crystal field theory, reveal that the d-orbital splitting is characteristic of the number of ligands coordinated to the TM. As the partially filled d-orbitals make these TMCs very challenging from a computational point of view, we perform both average of configuration (AOC), with fractional occupation numbers, and unrestricted DFT (UDFT) calculations, in which integer occupations are considered, in order to obtain quantitative results. In contrast to AOC, DFT is not capable of reproducing the qualitatively obtained d-orbital splittings as only part of the d-orbitals are occupied. Indeed, the gap between the occupied and unoccupied orbitals is overestimated by one order of magnitude compared to the AOC and experimental results. Furthermore, the ordering of the d-orbitals is sometimes interchanged. The discrepancies between both techniques are due to the different electron occupations resulting in different interelectron repulsions. The AOC orbitals confirm the chemical intuition as given by crystal field theory, as both techniques describe the electron repulsion in a spherical way. The d-orbital splitting obtained by UDFT is different, due to the integer occupation numbers resulting in different interelectron repulsions.

To further test the performance of both techniques, we calculate the d-d transitions, both from an AOC and UDFT reference via ligand field DFT and TDDFT, respectively. Additional challenges are encountered for the calculation of these excited states as degeneracies do not only occur in the ground state but also in the excited states and double excitations can be present. Furthermore, in systems with a center of symmetry, d-d transitions are Laporte-forbidden and hence have low oscillator strengths. Therefore, we first test these techniques for first-row octahedral aqua-complexes in order to investigate the complexity of the electronic structure as a function of the number of d-electrons. Although the gap between occupied and unoccupied orbitals is overestimated by UDFT compared to AOC, the picture of d-d excitations obtained from both techniques is qualitatively similar. This even holds for challenging systems with a degenerate GS and for which double excitations are present. Moreover, both techniques give complementary information, whereas ligand field DFT is capable of describing double excitations, TDDFT yields oscillator strengths. With this knowledge, we calculate the d-d excitations of TMCs relevant for the Co-ZIF-67 nucleation process via both techniques and compare the results with the experimental spectra of Filez *et al.* Although ligand field DFT is not suited for complexes with extended ligands, the octahedral and tetrahedral species can be distinguished based on TDDFT. The oscillator

strength is much larger and the main absorption peak is shifted toward smaller energies for the tetrahedral complexes compared to the octahedral ones. Furthermore, the tetrahedral complexes, which trigger the nucleation process, are 10^7-10^8 times less present than the octahedral structures. Finally, excited states at very small energies are only observed for octahedral systems. Nevertheless, other techniques are needed to calculate the excited states proposed by Filez *et al.* which are situated in the UV-Vis range and mainly contain double and spin-flip excitations, not reachable by TDDFT.

Summarizing, TDDFT is, due to its excellent balance between computational cost and accuracy, perfectly suited to determine spectroscopic fingerprints for closed-shell systems and provides a better understanding of the underlying mechanisms. In addition, a qualitative picture for the calculation of d-d transitions in more challenging TMCs can be obtained. As such, this work highlights the importance and versatility of theoretical UV-Vis spectroscopy for various applications.

List of Symbols

In this thesis, italicized variables indicate scalars, italicized and bold-faced variables indicate vectors or tensors, and bold-faced variables indicate matrices. The indices $\alpha, \beta, \ldots$ will be used to denote variables related to nuclei or atomic cores and the indices $i, j, \ldots$ will be used to denote variables related to the electronic degrees of freedom.

Latin symbols	
a	Occupation number
A, B, C	Racah parameters
B_q^k	Wybourne-normalized crystal field parameters
C_{4v}	Square pyramidal point group
C_n	Proper rotation over $\frac{2\pi}{n}$
D_{3h}	Trigonal bipyramidal point group
e, E	Double degenerate representation term
E	Identity operation
$\boldsymbol{E}(t)$	Time-dependent electric field
E_0	Ground-state energy
E_{corr}	Correlation energy
E_{exact}	Exact non-relativistic energy
E_{HF}	Hartree-Fock energy
E_n	Energy of state n
E_n^e	Electronic energy of state n
$E_v[n]$	Energy functional corresponding with external potential v
$E_{XC}[n]$	Exchange-correlation energy functional
$\mathcal{E}$	Electric field amplitude
f	Oscillator strength
f_{HXC}	Hartree-exchange-correlation kernel
f_{XC}	Exchange-correlation kernel
F^k, G^k	Slater-Condon parameters
$\hat{H}$	Hamiltonian

$\hat{H}_1$	Hamiltonian describing the time-dependent perturbation
$\hat{H}_e$	Electronic Hamiltonian
$\hat{H}^{\text{eff}}$	Effective Hamiltonian
$\mathcal{H}$	Heaviside step function
i	Inversion operation
$J[n]$	Direct Coulomb functional
J_{ij}	Coulomb integral
K_{ij}	Exchange integral
l	Azimuthal quantum number
$\boldsymbol{l}$	Angular momentum
L	Total angular momentum quantum number
$\mathbf{L}$	Magnetic hessian matrix
m	Magnetic quantum number
m_s	Spin quantum number
$\mathbf{M}$	Electric hessian matrix
M_α	Mass of nucleus α
n	Principle quantum number
$n(\boldsymbol{r}, t)$	Time-dependent electron density
$n_0(\boldsymbol{r})$	Ground state electron density
$n_1(\boldsymbol{r})$	Density response
$\hat{n}(\boldsymbol{r})$	Density operator
N	Number of electrons in a molecular system
N_d	Number of d-electrons in a molecular system
N_n	Number of nuclei in a molecular system
O_h	Octahedral point group
$\boldsymbol{p}$	Static electric dipole moment
$\boldsymbol{p}(t)$	Time-dependent electric dipole moment
$\boldsymbol{p}_1(t)$	Electric dipole moment response
$\boldsymbol{r}$	Position vector
$\boldsymbol{r}_i$	Position vector of electron i
$\boldsymbol{r}_l$	Position vector of ligand l
R	Radial wave function
R_{CT}	Charge-transfer distance
$\boldsymbol{R}_\alpha$	Position vector of nucleus α
$\boldsymbol{s}$	Spin
S	Total spin quantum number
S_n	rotation-reflection operation or improper rotation over $\frac{2\pi}{n}$
t	Time
t, T	Triple degenerate representation term
t_0	Initial time
$T_{\beta\alpha}$	(β,α)$^{\text{th}}$ element of momentum-stress tensor

T_d	Tetrahedral point group
$T_{e,s}[n]$	Kinetic energy of the electrons in a Kohn-Sham system
$\hat{T}_e$	Kinetic energy operator of the electrons in a molecular system
$\hat{T}_n$	Kinetic energy operator of the nuclei in a molecular system
$\hat{\mathcal{U}}(t, t_0)$	Time evolution operator
$v(\boldsymbol{r}, t)$	Time-dependent external potential
$v_0(\boldsymbol{r})$	Time-independent external potential
$v_1(\boldsymbol{r})$	External potential response
$v_s[n]$	Kohn-Sham potential
$v_{s1}(\boldsymbol{r})$	Kohn-Sham potential response
$v_{XC}[n]$	Exchange-correlation potential
$\hat{V}$	External potential operator
$\hat{V}_{ee}$	Coulomb repulsion operator between the electrons in a molecular system
$\hat{V}_{en}$	Coulomb attraction operator between the electrons and the nuclei in a molecular system
$\hat{V}_{nn}$	Coulomb repulsion operator between the nuclei in a molecular system
$\boldsymbol{x}$	Space and spin coordinates
Y	Spherical harmonic
Z_l	Charge of ligand l
Z_α	Atomic number of nucleus α

Greek symbols	
α, β	General observables
$\boldsymbol{\alpha}$	Dynamic dipole polarizability
$\bar{\alpha}$	Mean polarizability
α_{kj}	Difference between the occupation numbers of orbitals k and j
δ	Delta function
δ_{ij}	Kronecker delta
ϵ_i	Kohn-Sham single-particle energies
ζ	Spin-orbit coupling constant
θ	polar angle
σ	Reflection operation spin variable
σ_d	Reflection operation with dihedral mirror plane
σ_h	Reflection operation with mirror plane perpendicular with respect to the principle axis

σ_v	Reflection operation with mirror plane containing principle axis
τ	Time
ϕ	Azimuthal angle
ϕ_i	Kohn-Sham single-particle orbitals
Φ	Kohn-Sham Slater determinant
χ	Spin part of the wave function
χ_{nn}	Density-density response function
χ_s	Kohn-Sham response function
$\chi_{\alpha\beta}$	General response function
$\|\Psi_n\rangle$	n^{th} wave function in the Hilbert space
$\|\Psi_n^e\rangle$	n^{th} electronic wave function in the Hilbert space
$\|\Psi(t)\rangle$	Time-dependent wave function in the Hilbert state space
$\Psi(\boldsymbol{x}_1 \cdots \boldsymbol{x}_N)$	Time independent wave function in the coordinate space
$\Psi(\boldsymbol{x}_1 \cdots \boldsymbol{x}_N, t)$	Time-dependent wave function in the coordinate space
ω	Angular frequency
ω_{jk}	Excitation energy in the non-interacting system for a transition between the j^{th} and k^{th} single particle orbital
Ω_n	n^{th} excitation energy of the true interacting system

Mathematical symbols	
a_0	Ground state of a/ evaluated at t_0
a_1	Linear order response of a
a_2	Quadratic order response of a
$a^\dagger$	Hermitian adjoint of a
a^I	Interaction picture representation of α
$\mathcal{I}(a)$	The imaginary part of a
$\mathcal{R}(a)$	The real part of a
∇a	Gradient of a
Tr(**A**)	Trace of the square matrix **A**
$[A, B]$	Commutator between A and B
$A \star B$	$\int \mathrm{d}\boldsymbol{x} A(\boldsymbol{r}, \boldsymbol{x}) B(\boldsymbol{x}, \boldsymbol{r}')$

List of Abbreviations

1,2-dmIm	1,2-dimethylimidazole
2-mIm	2-methylimidazolate
AMS	Amsterdam modeling suite
AOC	Average of configuration
AOM	Angular overlap model
AQ	Antiquinoid
bipm	2,2'-bipyrimidine
bipy	Cis-2,2'-bipyridine
bipz	Cis-2,2'-bipyrazine
CCCT	Crystal-to-crystal charge-transfer
CFT	Crystal field theory
CLCT	Crystal-to-ligand charge-transfer
CMM	Center for Molecular Modeling
COF	Covalent organic framework
COMOC	Center for Ordered Materials, Organometallics and Catalysis
COSMO	Conductor-like screening model
CShM	Continuous shape measure
CT	Charge-transfer
CTF	Covalent triazine framework
DFT	Density functional theory
ES	Excited state
GGA	Generalized gradient approximation
GS	Ground state
HF	Hartree-Fock
HK	Hohenberg-Kohn
HPC	High performance computers
HOMO	Highest occupied molecular orbital
HS	High-spin
ISC	Inter-system crossing
IUPAC	International Union of Pure and Applied Chemistry
JT	Jahn-Teller
KS	Kohn-Sham

LDA	Local density approximation
LF	Ligand field
LFT	Ligand field theory
LFDFT	Ligand field density functional theory
LMCT	Ligand-to-metal charge-transfer
LR	Linear response
LUMO	Lowest unoccupied molecular orbital
LS	Low-spin
MD	Molecular dynamics
MLCT	Metal-to-ligand charge-transfer
MO	Molecular orbital
MOF	Metal-organic framework
PCM	Polarizable continuum model
PES	Potential energy surface
Q	Quinoid
RSH	Range-separated hybrid
SCF	Self-consistent field
SF	Spin-flip
SF-TDDFT	Spin-flip time-dependent density functional theory
SP	Square pyramidal
SOC	Spin-orbit coupling
SynBioC	Synthesis, Bioresources and Biooranic Chemistry
TBP	Trigonal bipyramidal
TDDFT	Time-dependent density functional theory
TD	Time-dependent
TM	Transition metal
TMC	Transition metal complex
TTET	Triplet-triplet energy transfer
UDFT	Unrestricted density functional theory
UV-Vis	Ultraviolet and visible
XC	Exchange-correlation
ZIF	Zeolitic imidazolate framework
ZORA	Zeroth order regular approximation

Part I

Spectroscopic Fingerprint of Electronic Excitations in Nanoporous Frameworks and Transition Metal Complexes

1

Introduction

Our fingerprints are different for each of us due to their unique line pattern, making them ideally suited to use as marks of human identity. In exactly the same way, molecular systems possess spectroscopic fingerprints which can be used to identify them. Their fingerprint is, however, in contrast to humans, not straightforward to reveal. This is where spectroscopy comes into play.

In spectroscopy, the interactions between electromagnetic waves and matter are studied. The early beginnings of this discipline can be situated in optics. In the 17^{th} century, Newton discovered that sunlight, although we perceive it as white light, is in fact made up of a wide range of colors. By letting sunlight pass through a prism, he discerned a rainbow of colors, which he denoted by the word "spectrum". In the 19^{th} century, spectroscopy was extended by Maxwell from visible light to cover the entire electromagnetic spectrum. The role this research field plays, can not be underestimated as it builds a bridge between theoretical/computational studies and experimental observations. This is also reflected in the considerable amount of Nobel prizes which have already been awarded to researchers who contributed to the field of spectroscopy, including optical, X-ray, laser, electron, and neutron spectroscopy.

Spectroscopy allows one to investigate the composition, physical properties, and electronic structure of matter from the atomic up to the astronomic scale. The areas of application are therefore widespread. First, we can

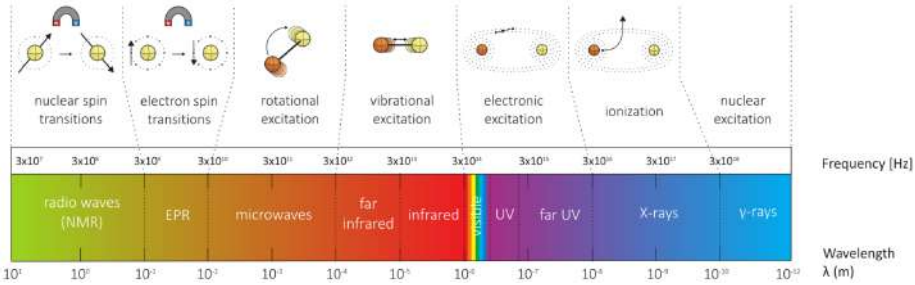

Figure 1.1: Classification of the electromagnetic radiation associated with nuclear and electronic transitions based on their frequency. Figure taken from Ref. 6

not ignore its importance in chemistry and physics.[1] Spectroscopic studies played a crucial role in the development of quantum mechanics as the first atomic models were capable of producing the spectral lines of hydrogen, hereby providing the basis for discrete jumps. Due to the quantized energy levels, only electromagnetic waves with specific frequencies are allowed to interact with the system. Besides, we would also like to mention its applications in bio-medicine, in which it has an important function in the diagnosis of diseases,[2] the analysis of tissue,[3] and medical imaging.[4] Finally, spectroscopy has become an indispensable tool in astronomy to study for example the properties of stars.[5] Not only their chemical composition, temperature, distance and luminosity can be investigated, but also their velocity by measuring the Doppler shift.

In Figure 1.1, an overview of the electromagnetic spectrum divided in several frequency ranges is given. Each nuclear and/or electronic transition is situated in a specific region of the electromagnetic spectrum and can be probed by a particular spectroscopic technique. In chemical analysis, some common methods include ultraviolet and visible (UV-Vis) spectroscopy, infrared spectroscopy, electron paramagnetic resonance, and nuclear magnetic resonance, which are used to investigate electronic excitations, vibrational excitations, electron spin transitions, and nuclear spin transitions, respectively. In this work, we exclusively focus on electronic excitations explored by UV-Vis spectroscopy.

1.1 UV-Vis spectroscopy

Spectroscopic observations located in the UV-Vis region are linked to transitions of valence electrons causing excitations and emissions between

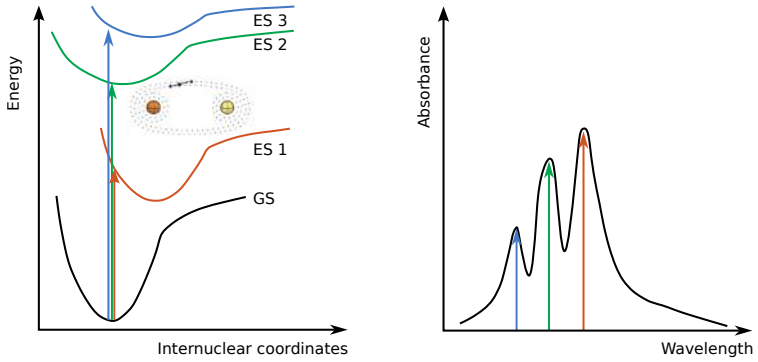

Figure 1.2: Graphical representation of the GS and ES potential energy surfaces in the left pane. Examples of vertical excitations are indicated with arrows in red, green, and blue. The corresponding absorption spectrum is plotted as a function of the photon wavelength in the right pane.

the ground state (GS) and excited states (ESs). A distinction needs to be made between absorption and emission spectroscopy.

On the one hand, absorption occurs when radiant energy is absorbed by the material, causing a transfer from the GS to an ES. Figure 1.2 shows a graphical representation of the potential energy surfaces (PESs) of the GS and several ESs. Absorption of photons then corresponds to the vertical excitations presented by red, green, and blue arrows. Vertical excitations are good approximations for the true excitations due to the Franck-Condon principle, stating that in electronic transitions the nuclear movement is much smaller than the electronic one.[7] The plot on the right in Figure 1.2 shows the amount of light absorbed by a sample as a function of the photon wavelength. The absorption in the visible range directly affects the perceived color of the sample. For example, healthy plants are green because the chlorophyll in the chloroplasts absorbs significantly more blue and red light than green light, which is reflected by plant structures like cell walls.[8] In the fall, chlorophyll breaks down causing less absorption of red and blue light, which results in leaves showing a beautiful color palette.

On the other hand, emission is the process in which radiant energy is emitted by the material, which thereby undergoes a transition from an ES back to the GS. A luminescent material spontaneously emits light without the presence of heat. Fluorescence and phosphorescence are two different types of luminescence and are depicted in Figure 1.3 with purple and yellow arrows, respectively. The electronic and vibrational energy levels are

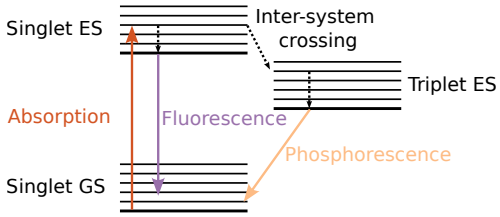

Figure 1.3: Graphical representation of a fluorescence and a phosphorescence process, two types of luminescence. The photon undergoes inter-system crossing in the latter. Electronic and vibrational energy levels are indicated by thick and thin lines, respectively.

indicated by thick and thin lines, respectively. In these processes, first a photon is absorbed, taking the material from its GS to an ES. In Figure 1.3, we assumed that the absorption is from a singlet GS to a singlet ES. The system relaxes vibrationally, after which a photon of lower energy is emitted such that it returns to the GS. As such, the emissions correspond to non-vertical or adiabatic transitions. The lifetime of the absorbed photon is notably larger in phosphorescence compared to fluorescence as it undergoes inter-system crossing (ISC) into a state with a different spin multiplicity, in this case a triplet ES. Well-known examples of phosphorescence are glow-in-the-dark stickers which continue to emit light long after the stimulating light source has been removed.

1.2 Nanoporous materials

In this work we focus on electronic excitations in nanoporous materials, which contain voids with diameters between 1 and 100 nm.[9] These structures are very interesting as due to their pores they can have specific interactions, not only at the surface, but also throughout the bulk of the material. High surface area, chemical versatility, excellent accessibility to active sites, and improved diffusion and mass transport are some of the outstanding properties typical for porous materials.[10–13] As a result, they are extensively used and explored in various application fields such as absorption, catalysis, separations, *etc.*

In this work we concentrate on two specific types of nanoporous materials, namely covalent triazine frameworks (CTFs) and zeolitic imidazolate frameworks (ZIFs). These choices are inspired by collaborations with experimental partners. The work on CTFs was part of a concerted research action (GOA) with our experimental partners at the Center for Ordered

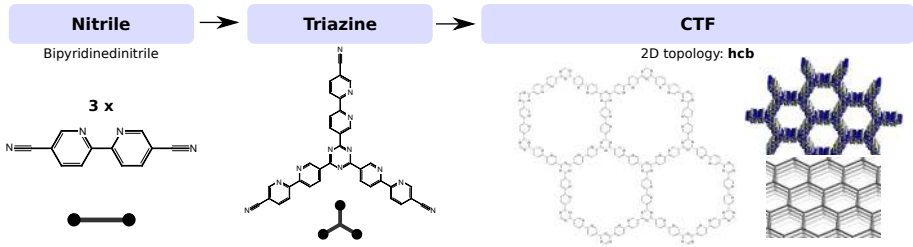

Figure 1.4: Synthesis of CTFs via trimerization of aromatic nitriles. Figure reproduced from Ref. 25 with permission of Chemistry Europe.

Materials, Organometallics and Catalysis (COMOC, Prof. Van Der Voort) and Synthesis, Bioresources and Biooranic Chemistry (SynBioC, Prof. Stevens), whereas the study on ZIFs was inspired by experimental work performed by dr. ir. Matthias Filez (CoCooN, Ghent University and Roeffaers group, KU Leuven) at the Weckhuysen Research group, Utrecht University. In what follows, these two types of materials are briefly introduced.

1.2.1 Covalent triazine frameworks

CTFs, a subclass of covalent organic frameworks (COFs), are porous 2D materials made by trimerization of aromatic nitriles as shown in Figure 1.4. Due to their high surface area,[14] chemical and thermal stability,[14–23] and tunability because of the availability of various building blocks,[24] they are very promising to use as support materials for heterogeneous catalysis. Furthermore, they are much lighter than most other porous supports and contain no toxic or environmentally unfriendly elements.

The search for new heterogeneous catalysts is a hot topic today. Indeed, one of the major challenges of our society is how to provide materials and chemicals in a more sustainable and energy efficient way. Even today most of our energy resources originate from fossil fuels.[26] Sunlight is an abundantly available energy source and may provide sustainable opportunities for activating chemical reactions based on photocatalysis.[27–34] However, most of the currently used photocatalytic homogeneous catalysts necessitate an environmentally unfriendly cycle to remove them from the products.[32, 35] In this respect, it is important to develop recyclable and reusable heterogeneous photocatalysts, which can be achieved by anchoring the photocatalytic complexes on a porous framework. The step to remove the catalyst can thus be avoided and, as such, heterogeneous photocatalysis can serve as an environmentally cleaner alternative than homogeneous catalysts.[36–39]

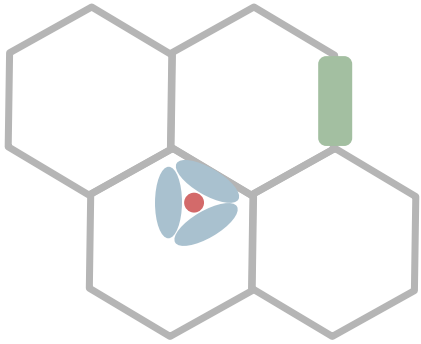

Figure 1.5: Schematic representation of a CTF (grey). The CTF linker is indicated in green, the ligands and the TM of the photocatalytic complex in blue and red, respectively.

A schematic representation of a CTF is given in gray in Figure 1.5. The CTF linker is presented in green and the photocatalytic transition metal complex (TMC) consists of a transition metal (TM) surrounded by ligands, indicated in red and blue, respectively. The photocatalytic properties depend on the energy ranges of the electromagnetic spectrum which are absorbed by the material, corresponding to the excitation energies of the system. It has been shown that CTFs display photocatalytic activity in their pristine form,[40–42] without even anchoring an active complex. Therefore, we will investigate the structural and photophysical properties of various CTF ligands. In addition, we will estimate how the photocatalytic properties can be tuned by varying the linkers of the complex. With the application as photocatalyst in mind, we are interested in excitations at small energies/large wavelengths and with large oscillator strengths, as in this way, the freely available sunlight can be exploited to the fullest. In the relevant excitations in the photocatalytic complex, an electron is transferred from the TM to the ligands or vice versa, and these processes are therefore conveniently called metal-to-ligand charge-transfer (MLCT) and ligand-to-metal charge-transfer (LMCT) excitations, respectively.

In order to further illustrate these transitions, a schematic representation of the molecular orbitals (MOs) in TMCs is shown in Figure 1.6. We distinguish the occupied and unoccupied ligand orbitals, presented in blue, and the e_g- and t_{2g}-orbitals, indicated in red. The latter are mainly located on the TM and originate from the TM d-orbitals.[43] In Chapter 3 and Chapter 5, we will show that the splitting of these orbitals is characteristic for the ligand environment. In the specific case shown in figure 1.6, we present the results

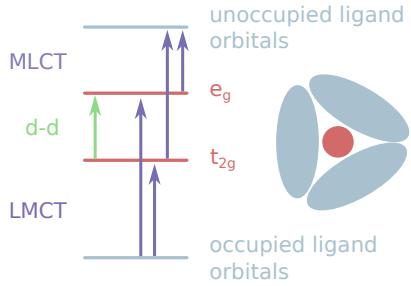

Figure 1.6: Schematic representation of the MOs and different types of excitations in an octahedral TMC.

for an octahedral complex. Other frequently encountered configurations as well as the nomenclature of the d-orbitals will be discussed in more detail in Chapter 3. The MLCT and LMCT transitions, in which an electron is transferred from the TM to the ligands or vice versa, are indicated in purple.[43] Transitions from the t_{2g}- to the e_g-orbitals, indicated in green, are generally labeled as d-d transitions and will be addressed in the next section.

1.2.2 Zeolitic imidazolate frameworks

The second type of materials investigated in this work are ZIFs. These are a sub-class of metal-organic frameworks (MOFs) in which divalent metal cations, mostly Fe^{2+}, Co^{2+}, Cu^{2+}, or Zn^{2+}, are tetrahedrally coordinated by bridging imidazolate-type linkers.[44–49] Since the cation-linker-cation angle in ZIFs is similar to the Si-O-Si angle in zeolites, they are topologically isomorphic, hence their name.[44, 50–52] We exclusively focus on Co-ZIF-67,[53–56] in which tetrahedrally coordinated Co^{2+} ions are bridged by 2-methylimidazolate (2-mIm) linkers. The crystal structure is shown in Figure 1.7. ZIFs are due to their chemical stability, robust porosity, and resistance to thermal changes very promising candidate materials for several applications. Among others, we mention the use as catalysts or carbon dioxide caption materials,[57] molecular sieves for gas separation,[58] and high-impact shock absorbers.[59]

An in-depth understanding of the formation process of these materials is indispensable for a targeted search for structures with the best properties for a specific application as, unfortunately, this is at the moment mainly done via high-throughput synthesis.[61] Although the particle nucleation step is more or less understood by now,[62, 63] the underlying molecular assembly processes in the pre-nucleation stage have been less thoroughly investigated and remain largely unknown. Only very recently, a combined experimental-

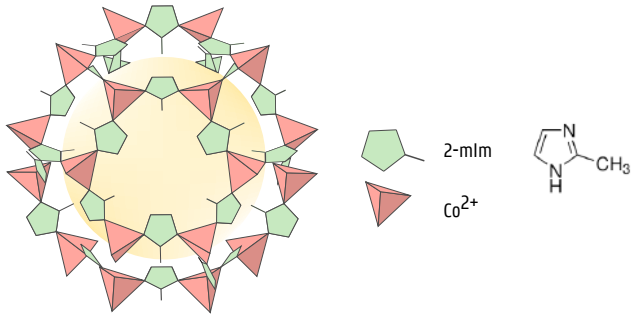

Figure 1.7: Crystal structure of Co-ZIF-67. Figure adapted from Ref. 60 with permission of Elsevier, 2015.

computational study has been conducted,[64] in which it is suggested that, during Co-ZIF-67 nucleation, a metal-organic pool with a variety of complexes is formed caused by ligand elimination and substitution reactions. This is visualized with green and blue arrows in Figure 1.8, respectively. In this way, the symmetry of the octahedral precursors with simple ligands like water, methanol, and/or NO_3^-, shown in the upper left corner, is lowered by two mechanisms during the nucleation process. On one hand, some of the ligands are substituted with 2-mIm, on the other hand, some of them are eliminated. The complex thus goes from octahedral Co^{2+} complexes with simple ligands over a five-coordinated system toward $[Co(2\text{-mIm})_4]^{2-}$, a tetrahedral complex with four 2-mIm ligands. The latter is presented in the bottom right corner of Figure 1.8 and forms the building blocks of Co-ZIF-67, visualized in Figure 1.7.

In order to fully understand this complicated mechanism, we aim to characterize the d-d excitations, indicated in green in Figure 1.6, of the TMCs observed during the nucleation process.[43, 64] Hereto, we focus on their number, intensity, and position as they change during the course of the formation process and therefore can serve as a fingerprint. As already briefly mentioned above, the d-orbital splitting is characteristic for the coordination environment as it depends on the number and type of ligands coordinated to the TM and the specific symmetry of the system. This will be explored further in Chapter 3 and Chapter 5.

Analyzing d-d spectra poses various challenges. Indeed, due to the partially filled d-orbitals, there might be degeneracies in the GS and/or ES as well as numerous ESs lying closely together, making the assignment of peaks ambiguous. Furthermore, in complexes with a center of symmetry, d-d transitions conserve the parity and are therefore Laporte-forbidden and

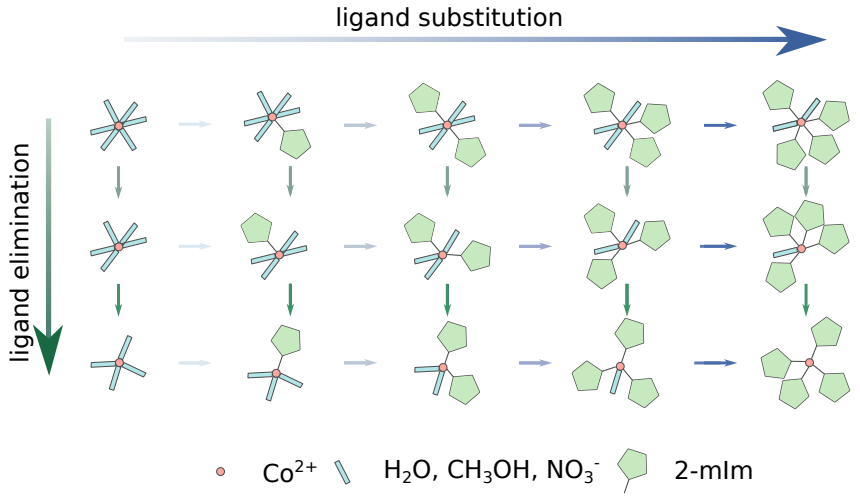

Figure 1.8: Reaction network of ligand elimination and substitution reactions leading to fast pre-equilibrium formation toward a metal-organic pool. Figure adapted from Ref. 64 with permission of Elsevier, Copyright 2021.

hence not intense.[43] This is in contrast to the MLCT and LMCT transitions encountered in Section 1.2.1, which are usually spin- and Laporte-allowed and therefore easier to discern experimentally.

1.3 Computational chemistry

Spectroscopic experiments reveal a lot of information by measuring macroscopic properties. However, it is not always possible to fully unravel the obtained spectra and to understand the underlying atomic mechanisms. For example, as will be shown in Chapter 4, triplet ESs from a singlet GS play an important role in photocatalytic processes. However, as these transitions are spin-forbidden, they have a low probability of occurrence, making it difficult to observe them experimentally. Meanwhile, computational techniques describe triplets without extra effort and provide in this way complementary information to the experimental findings. Moreover, computational studies allow one to screen a broad set of possible interesting materials for a specific application, without the need for synthesizing and experimentally characterizing them. Among the vast amount of candidates, even systems difficult to synthesize can be included. Furthermore, the character of the ESs can be investigated which can help to unravel complicated spectra. Indeed, for challenging systems such as TMCs,

experimental studies are almost routinely accompanied by theoretical calculations.[65–70] Finally, simulations can be controlled very precisely and environment effects can be avoided when desirable, as opposed to most experimental methods.

The accuracy of the computational results depends on both the atomic representation of the system under study and the computational method used to approximately solve the Schrödinger equation.

1.3.1 Atomic representation of system under study

The first step in a computational calculation consists of constructing a molecular representation that is able to represent the material or system as closely as possible. As most materials extend in three dimensions, they can be represented by constructing a unit cell and subjecting it to periodic boundary conditions or by extracting a cluster, for which a trade-off needs to be made between its size and the computational accuracy. Furthermore, experiments are often conducted in a solvent. As in computational models, it is very costly to include all solvent molecules explicitly, the continuum model, in which the system is embedded in a cavity representing the continuous environment, is widely used. Common implementations are the polarizable continuum model (PCM)[71] and conductor-like screening model (COSMO)[72]. In this way, the influence of the solvent can easily be estimated, as will be shown in Chapter 4.

1.3.2 Computational method

Once the molecular model for the system under study is determined, a series of approximations needs to be made to approximately solve the Schrödinger equation. Quantum mechanical computational techniques are, in general, divided in two groups. A distinction is made according to whether the method is based on the wave function or on the density, as visualized in the left bottom corner of Figure 1.9. Post-Hartree-Fock methods are part of the first category and are conceptually rather simple. Nevertheless, their key quantity, being the wave function, is very complicated. The tables are turned for the other group of methods, which are based on the much simpler density, but are characterized by a more complex formalism.

For the systems studied in this work, not all of these techniques are computationally feasible due to their increasing computational cost. High level wave function based techniques, for example, might yield extremely

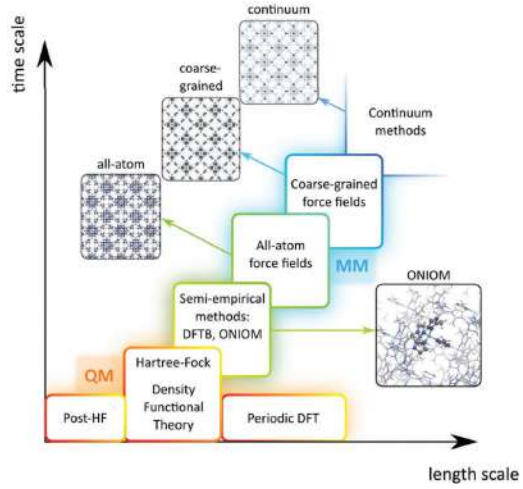

Figure 1.9: Schematic overview of length and time scales of computational methods. Reproduced from Ref. [37] with permission from the Royal Society of Chemistry.

accurate results but are only applicable for very small systems, as shown in Figure 1.9. In this regard, density functional theory (DFT) and time-dependent DFT (TDDFT), its most common extension to include excitations, offer a good balance between computational cost and accuracy.[73] These methods gained an increasing popularity in the last decades and are now widely used in diverse research fields going from biology to material science.[74] They are based on the fact that any property of the system can in principle be expressed as a functional of the density. Although these techniques are formally exact, the precise expression of the exchange correlation functional is not known and a broad range of functionals, often referred to as the functional zoo, are available to approximate it. We refer the reader to Chapter 2, in which these techniques will be introduced in more detail.

In many situations, static calculations provide sufficiently accurate results. Nevertheless, sometimes the dynamical nature of the system under study has a large influence on the properties in which one is interested. In these situations, one has to rely on dynamical techniques such as molecular dynamics (MD) simulations, which are applied in Chapter 4.[75] Furthermore, additional choices need to be made in order to set up the calculation. We mention, among others, the basis set, convergence criteria, inclusion of relativistic effects, *etc.* More details are given in Chapter 4 and Chapter 5.

Computational techniques such as DFT have become widely popular since the invention and development of high performance computers (HPC), resulting in an increase of the available computational power. Prior to this, methods such as crystal field theory (CFT) and modifications like ligand field theory (LFT) were commonly used to study TMCs. Even though experimental input data are needed to obtain quantitative results, these techniques are very important from a historical point of view. Up until today, certain concepts are used in order to gain a qualitative understanding of many properties of these challenging systems. Therefore, an introduction to these techniques should not be missing in this thesis. In this regard, ligand field density functional theory (LFDFT) will be studied too as it allows one to retrieve quantitative results in the framework of CFT via DFT calculations. We refer the reader to Chapter 3 for more theoretical background and to Chapter 5 for applications of these methods.

1.4 Goals and outline

The overall aim of this PhD thesis is to provide more fundamental insight in the spectroscopic fingerprints of electronic excitations in nanoporous frameworks and TMCs. This is very important in order to explore these materials for specific applications and to unravel their nucleation process.

On the one hand, inspired on experimental collaborations, we investigated how the photocatalytic properties of heterogeneous catalysts can be tuned. In order to do so, TDDFT, providing a good balance between cost and accuracy, has been applied to calculate the UV-Vis spectra of CTF linkers and both isolated and embedded photocatalytic complexes. As CTFs display photocatalytic activity in their pristine form,[40–42] we first investigated how the structural and photocatalytic properties of CTFs can be tuned by changing the polypyridyl ligands. Second, we studied how the optical properties of isolated Ru complexes can be adapted via changing the nitrogen content of the ligands. Finally, we examined the influence of embedding the complex in the CTF on the optical properties.

On the other hand, we investigated small TMCs, which are of interest in the formation of Co-ZIF-67. These complexes have a challenging electron structure and we examined in how far the d-d transitions can serve as a spectroscopic probe to unravel the nucleation process. In order to do this, we first investigated the d-orbital splitting of the TMCs using computational techniques based on DFT and compared the results with these from qualitative techniques such as CFT. We focus on the influence of

the number of ligands and point group on the d-orbital splitting. Second, the performance of TDDFT and LFDFT for the calculation of d-d excitations has been studied. Difficulties such as degeneracies in the GS and/or ES and the presence of double excitations are addressed and the results are analyzed along with experimental spectra.

The remainder of this PhD thesis is organized as follows:

- In Chapter 2 time-dependent density functional theory, used to investigate the electronic transitions in nanoporous materials and TMCs, is introduced. The theory behind this method is discussed in-depth as it was less commonly employed at the Center for Molecular Modeling (CMM) and very thoroughly used in this thesis.
- In Chapter 3, we focus on the aspects of coordination chemistry which are relevant in this work. In addition, the theory behind ligand field density functional theory, which will be used to study d-d excitations in challenging TMCs, is elucidated.
- In Chapter 4, the first part of the major research results obtained during this PhD is presented. Here, the work on photocatalytic ruthenium complexes and CTF supports is considered, which focuses on how the photocatalytic properties can be tuned by altering their building blocks. Furthermore, the influence of anchoring of the complex is examined. These results were published in international peer-reviewed journals, which can be found in **Part II**.
- In Chapter 5, the second part of the major research results obtained during this PhD is presented. This Chapter covers the research on the spectroscopic fingerprint of cobalt complexes relevant during the nucleation process of ZIFs. Most of these results were also published in international peer-reviewed journals or are currently under evaluation, which can be found in **Part II**.
- In Chapter 6, the main conclusions of this PhD research and an outlook to future research is given.

2

Foundations of Density Functional Theory and Time-Dependent Density Functional Theory

As discussed in Chapter 1, various techniques exist to approximately solve the Schrödinger equation. We will focus in Section 2.1 on static Hamiltonians and we will elucidate how the GS of a molecular system can be determined via DFT. In Section 2.2, time-dependent electromagnetic fields are included in the Hamiltonian in order to study ESs. TDDFT will play an important role in this thesis and therefore, the underlying theorems and working equations will be introduced in detail.

2.1 From the Schrödinger equation to density functional theory

In the first part of this Chapter, we focus on the GS of molecular systems. We start with an introduction of the Schrödinger equation, followed by a brief discussion of DFT.

2.1.1 Schrödinger equation for static Hamiltonians

Molecular systems consist of electrons and nuclei, as schematically shown in Figure 2.1, and can be described quantum mechanically by the non-

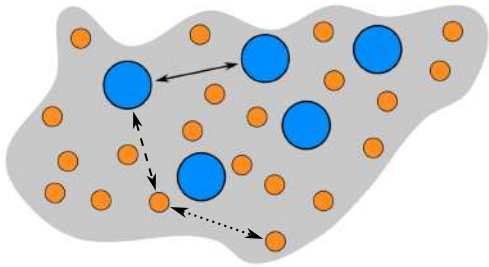

Figure 2.1: Schematic representation of the electron-electron, electron-nucleus, and nucleus-nucleus interactions in a molecular system, indicated with a dotted, dashed, and full line, respectively.

relativistic time-dependent (TD) Schrödinger equation, which has been postulated in 1925 by Erwin Schrödinger:[76]

$$i\frac{\partial}{\partial t}|\Psi(t)\rangle = \hat{H}(t)|\Psi(t)\rangle. \tag{2.1}$$

Note that we will use atomic units throughout this work. The Hamiltonian of a general molecular system contains the following contributions:

$$\hat{H} = \hat{T}_e + \hat{T}_n + \hat{V}_{ee} + \hat{V}_{en} + \hat{V}_{nn}. \tag{2.2}$$

$\hat{T}_e$ and $\hat{T}_n$ are the kinetic energy operators of the electrons and nuclei, respectively:

$$\hat{T}_e = -\frac{1}{2}\sum_{i=1}^{N}\nabla_i^2 \qquad \text{and} \qquad \hat{T}_n = -\frac{1}{2}\sum_{\alpha=1}^{N_n}\frac{\nabla_\alpha^2}{M_\alpha}, \tag{2.3}$$

with N and N_n the number of electrons and nuclei in the system and M_α the mass of nucleus α. ∇_i and ∇_α denote the gradient operator with respect to the position of electron i, $\boldsymbol{r_i}$, and the position of nucleus α, $\boldsymbol{R_\alpha}$, respectively.

$\hat{V}_{ee}$ represents the electron-electron repulsion operator, which can be described by the Coulomb interaction:

$$\hat{V}_{ee} = \frac{1}{2}\sum_{i\neq j}^{N}\frac{1}{|\boldsymbol{r}_i - \boldsymbol{r}_j|}. \tag{2.4}$$

$\hat{V}_{en}$ is the Coulomb attractive operator between the electrons and nuclei:

$$\hat{V}_{en} = -\sum_{\alpha=1}^{N_n}\sum_{i=1}^{N}\frac{Z_\alpha}{|\boldsymbol{R}_\alpha - \boldsymbol{r}_i|}, \tag{2.5}$$

where Z_α is the charge of nucleus α. This coupling term between the nuclear and electronic degrees of freedom makes the problem difficult to solve as it prohibits the separation of the wave function in a nuclear and electronic contribution.

Finally, $\hat{V}_{nn}$ designates the Coulomb repulsion operator between two nuclei:

$$\hat{V}_{nn} = \frac{1}{2}\sum_{\alpha\neq\beta}^{N_n} \frac{Z_\alpha Z_\beta}{|\boldsymbol{R}_\alpha - \boldsymbol{R}_\beta|}. \tag{2.6}$$

Because none of the terms in the Hamiltonian does explicitly depend on the time, one can find the general solution of Eq. (2.1) via the solutions of the stationary Schrödinger equation:

$$\hat{H}|\Psi_n\rangle = E_n|\Psi_n\rangle, \tag{2.7}$$

which has the general form of an eigenvalue problem. E_0 is the energy of the GS Ψ_0, E_1 the energy of the first ES Ψ_1, and so on. Using the eigenstates Ψ_n, which remain unaltered through evolution of time, one can construct the general solution of the TD Schrödinger equation given in Eq. (2.1):

$$|\Psi(t)\rangle = \sum_n c_n e^{-iE_n t}|\Psi_n\rangle, \tag{2.8}$$

where the coefficients c_n are determined by the initial conditions of the system. Hence, the behaviour of a molecular system can be completely determined via the eigenstates of the time-independent Hamiltonian given in Eq. (2.2).

In order to solve Eq. (2.7), two assumptions are invoked. First, we suppose that the nuclear mass is much larger than the electron mass. This is the so-called clamped nuclei approximation, as the nuclei are supposed to be fixed in space. Second, we assume that all ESs are much higher in energy than the GS, which is the adiabatic approximation. These two assumptions form the basis of the Born-Oppenheimer approximation,[77, 78] as a result of which the nuclear coordinates are no longer degrees of freedom, but appear as parameters in the Hamiltonian. Consequently, the wave function Ψ_n can be separated in a nuclear and electronic contribution. The latter is the solution of the Schrödinger equation with the electronic Hamiltonian $\hat{H}_e$ and describes the electronic structure of the system:

$$\hat{H}_e|\Psi_n^e\rangle = E_n^e|\Psi_n^e\rangle \tag{2.9}$$

with

$$\hat{H}_e = \hat{T}_e + \hat{V}_{ee} + \hat{V}_{en}. \tag{2.10}$$

Compared to the Hamiltonian of the full system given in Eq. (2.2), $\hat{H}_e$ does not include the kinetic energy operator of the nuclei $\hat{T}_n$. Furthermore, the potential energy operator of the nuclei $\hat{V}_{nn}$ is dropped out, as for a fixed configuration this contribution is constant and the energy is only determined up to a constant. Of course, when describing the PES in terms of the nuclear coordinates, as shown in the left pane of Figure 1.2 for example, this term is important and needs to be taken into account. However, in other cases, only the one-body operators $\hat{T}_e$ and $\hat{V}_{en}$ and two-body operator $\hat{V}_{ee}$ remain in the electronic Hamiltonian.

2.1.2 Density functional theory

Many techniques with the aim of solving the electronic structure problem start from the wave function, which completely describes each observable of the system in its GS. However, it is very complex and depends on N spin and $3N$ spatial coordinates as the position of one electron is correlated with the positions of all other electrons.

According to the Hohenberg-Kohn (HK) theorems, the GS electron density $n_0(\boldsymbol{r})$ also completely characterizes the system in its GS.[74, 79] Note that the notation $n_0(\boldsymbol{r})$ is used in this work to represent the electron density, while it is denoted by $\rho(\boldsymbol{r})$ in various textbooks. The GS electron density is defined as follows:

$$\begin{aligned} n_0(\boldsymbol{r}) &= \langle \Psi_0 | \hat{n}(\boldsymbol{r}) | \Psi_0 \rangle \\ &= \langle \Psi_0 | \sum_{i=1}^{N} \delta(\boldsymbol{r} - \boldsymbol{r}_i) | \Psi_0 \rangle, \end{aligned} \tag{2.11}$$

where Ψ_0 is the GS wave function. In order to transform to the coordinate representation, we insert a completeness relation in the spacial and spin coordinates, for which the shorthand notation $\boldsymbol{x}_i \equiv (\boldsymbol{r}_i, \sigma_i)$ is introduced. After recognizing that all terms are equal as the electrons are non-distinguishable, the following expression for the density in the coordinate representation is obtained:

$$n_0(\boldsymbol{r}) = N \sum_{\sigma} \int \mathrm{d}\boldsymbol{x}_2 \cdots \boldsymbol{x}_N |\Psi_0(\boldsymbol{r}, \boldsymbol{x}_2 \cdots \boldsymbol{x}_N)|^2, \tag{2.12}$$

where $\int \mathrm{d}\boldsymbol{x}_i = \sum_{\sigma_i} \int \mathrm{d}\boldsymbol{r}_i$. As such, the GS electron density $n_0(\boldsymbol{r})$ describes the probability of finding one of the electrons at a specific position $\boldsymbol{r}$.

Before continuing, we introduce the notation used by Hohenberg and

Kohn.[74, 79] As stated before, $\hat{V}_{en}$ describes the potential generated by the nuclei resulting in an attractive interaction with the electrons. However, this term can be generalized to include all forces acting on an electron that are not caused by other electrons. In general, this external potential operator is a sum of one-body operators and can be written as follows:

$$\hat{V}_0 = \sum_{i=1}^{N} v_0(\boldsymbol{r}_i). \tag{2.13}$$

The subscript indicates that the external potential is time-independent. In the case that we consider the attractive Coulomb potential generated by the nuclei, the external potential $v_0(\boldsymbol{r})$ is expressed as follows:

$$v_0(\boldsymbol{r}) = -\sum_{\alpha=1}^{N_n} \frac{Z_\alpha}{|\boldsymbol{R}_\alpha - \boldsymbol{r}|}. \tag{2.14}$$

With this notation, the total electronic Hamiltonian given in Eq. (2.10) can be rewritten:

$$\hat{H}_e = \hat{T}_e + \hat{V}_{ee} + \hat{V}_0. \tag{2.15}$$

The expectation value of the external potential in the GS is formulated as a functional of the density:

$$\begin{aligned} \langle \Psi_0 | \hat{V}_0 | \Psi_0 \rangle &= \int \mathrm{d}\boldsymbol{x}_1 \cdots \boldsymbol{x}_N \Psi_0^*(\boldsymbol{x}_1 \cdots \boldsymbol{x}_N) \left[\sum_{i=1}^{N} v_0(\boldsymbol{r}_i) \right] \Psi_0(\boldsymbol{x}_1 \cdots \boldsymbol{x}_N) \\ &= \int \mathrm{d}\boldsymbol{r} v_0(\boldsymbol{r}) n_0(\boldsymbol{r}). \end{aligned} \tag{2.16}$$

The first HK theorem states that there is a one-to-one correspondence between the external potential and the density in the GS. As a result, the external potential is a unique functional of the GS density. All properties of the system are thus uniquely determined by the GS density, being a much simpler quantity than the wave function, as it only depends on three spatial coordinates. By using Eq. (2.16), the energy is then expressed as a functional of the density:

$$\begin{aligned} E_{v_0}[n_0] &= \langle \psi[n_0] | \hat{T}_e | \psi[n_0] \rangle + \langle \psi[n_0] | \hat{V}_{ee} | \psi[n_0] \rangle + \langle \psi[n_0] | \hat{V}_0 | \psi[n_0] \rangle \\ &= T_e[n_0] + V_{ee}[n_0] + \int \mathrm{d}\boldsymbol{r} v_0(\boldsymbol{r}) n_0(\boldsymbol{r}). \end{aligned} \tag{2.17}$$

The electron-electron repulsion and the electronic kinetic energy terms are generic as they are independent of the nuclear configuration. Various N-electron systems thus only differ in the term generated by the external

potential.

The second HK theorem provides a procedure to find the GS density via the Rayleigh-Ritz variational principle, stating that the GS energy is minimized by the GS density:

$$E_0 = \min_{n_0} E_{v_0}[n_0]. \tag{2.18}$$

Based on these two theorems, Kohn and Sham proposed an independent particle model with the same GS density as the real system.[80] The energy expression given in Eq. (2.17), is then written as

$$E_{v_0}[n_0] = T_{e,s}[n_0] + \int \mathrm{d}\boldsymbol{r} v_0(\boldsymbol{r}) n_0(\boldsymbol{r}) + J[n_0] + E_{XC}[n_0], \tag{2.19}$$

with $T_{e,s}[n_0]$ the kinetic energy of the KS system, $J[n_0]$ the direct Coulomb contribution, and $E_{XC}[n_0]$ the exchange-correlation (XC) term which is defined as follows:

$$E_{XC}[n_0] = T_e[n_0] - T_{e,s}[n_0] + V_{ee}[n_0] - J[n_0]. \tag{2.20}$$

The Schrödinger equation is then replaced by N independent particle equations, the Kohn-Sham (KS) equations, in which the interactions with other electrons are replaced by an effective KS potential $v_s[n_0](\boldsymbol{r})$:

$$\left[-\frac{\nabla_i^2}{2} + v_s[n_0](\boldsymbol{r})\right] \phi_i(\boldsymbol{r}) = \epsilon_i \phi_i(\boldsymbol{r}), \tag{2.21}$$

with ϕ_i the KS orbitals and ϵ_i the corresponding KS single-particle energies. The KS potential is given by:

$$v_s[n_0](\boldsymbol{r}) = v_0(\boldsymbol{r}) + \int \mathrm{d}\boldsymbol{r}' \frac{n_0(\boldsymbol{r}')}{|\boldsymbol{r} - \boldsymbol{r}'|} + v_{XC}[n_0](\boldsymbol{r}), \tag{2.22}$$

where the first term is the external potential $v_0(\boldsymbol{r})$ and the second term the classical Coulomb potential. The last part is the XC potential, defined as

$$v_{XC}[n_0](\boldsymbol{r}) = \frac{\delta E_{XC}[n_0]}{\delta n_0(\boldsymbol{r})}, \tag{2.23}$$

which includes all nontrivial many-body effects. No exact expression is known for this term and approximations are needed.

The GS of the non-interacting system is then written as a Slater determinant composed of the KS orbitals ϕ_i:

$$\Phi_0(\boldsymbol{x}_1 \cdots \boldsymbol{x}_N) = \frac{1}{\sqrt{N!}} \begin{vmatrix} \phi_1(\boldsymbol{r}_1) & \phi_2(\boldsymbol{r}_1) & \dots & \phi_N(\boldsymbol{r}_1) \\ \phi_1(\boldsymbol{r}_2) & \phi_2(\boldsymbol{r}_2) & \dots & \phi_N(\boldsymbol{r}_2) \\ \vdots & \vdots & & \vdots \\ \phi_1(\boldsymbol{r}_N) & \phi_2(\boldsymbol{r}_N) & \dots & \phi_N(\boldsymbol{r}_N) \end{vmatrix}. \tag{2.24}$$

Once the KS equations are solved, the GS density can simply be calculated as follows:

$$n_0(\boldsymbol{r}) = \sum_{i=1}^{N} |\phi_i(\boldsymbol{r})|^2. \tag{2.25}$$

In practice, a basis set needs to be introduces to solve the KS equations given in Eq.(2.21). In order to reduce the computational cost, the basis set must be chosen to enable an accurate description of the system albeit with a computationally feasible number of basis functions. For molecules, which will be the subject of this work, a localized basis set is typically used. Different types are available, but the most common ones are Gaussian and Slater-type orbitals.[81]

We conclude that, on the one hand, the quantity used to describe the system is much simpler, *i.e.,* the density instead of the wave function. However, on the other hand, the methodology becomes more complicated as we have to deal with an unknown KS potential instead of the interactions given in Eq. (2.15). The price we have to pay for transforming the true interacting problem to a non-interacting one is that we have to come up with approximations for the XC potential. An enormous amount of functionals have in the course of time been developed and have been arranged on Jacob's ladder based on their complexity.[82] We will go more into details in Section 2.2.5

2.2 Time-dependent potentials in time-dependent density functional theory

The GS of molecular systems subjected to time-independent external potentials can be described by DFT, as outlined in the previous section. However, this approach cannot be applied to describe ESs reached when the system interacts with light. Indeed, when the system is exposed to a TD electromagnetic field, the external potential becomes time-dependent and DFT is no longer applicable.

In this section, we discuss how we can solve the TD Schrödinger equation in Eq. (2.1) where the Hamiltonian is given by the TD analogue of Eq. (2.15), where we dropped the subscript e to ease the notation:

$$\hat{H}(t) = \hat{T}_e + \hat{V}_{ee} + \hat{V}(t), \tag{2.26}$$

with $\hat{V}(t)$ the TD external potential:

$$\hat{V}(t) = \sum_{i=1}^{N} v(\boldsymbol{r}_i, t). \tag{2.27}$$

One might be tempted to interpret the KS single-particle energy differences as excitation energies. This interpretation, however, has no rigorous basis as KS orbital energy differences do not, in general, stand for electron addition or removal energies. Throughout the years, various techniques based on DFT have been developed to calculate ESs. One of the most straightforward techniques is Δ self-consistent field (SCF).[83–85] In this time-independent technique, separate SCF calculations are performed for the GS and the ES of interest. The latter is obtained via a non-Aufbau occupation of the KS orbitals. The excitation energy is then determined as the energy difference between both states. An advantage is that orbital relaxation is taken into account. However, when there are other states with the same symmetry as the ES of interest but lower in energy, one might converge to these states instead of to the target ES. By far, the most widely used technique is TDDFT.[86, 87] In contrast to ΔSCF, orbital relaxation is not included but configuration mixing in the ESs emerges as a natural consequence of the formalism.

The remainder of this section is organized as follows. First, we thoroughly describe the fundamental theorems behind TDDFT. This is followed by a description of linear response theory, after which the working equations of TDDFT in the linear response regime are derived. A short note on the treatment of spin in TDDFT is given afterwards and we briefly touch upon the commonly made approximations. The above can be found in standard textbooks about TDDFT, like for example in Ref. 88, but for completeness it is included in this work. Finally, we conclude with the well-known deficiencies of TDDFT and possible solutions, where the focus is on the challenges which will be encountered in Chapter 4 and Chapter 5.

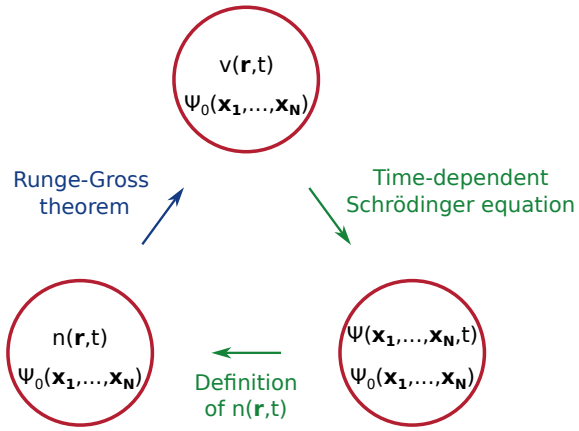

Figure 2.2: Illustration of the relations between the TD potential, wave function, and electron density. The Runge-Gross theorem closes the triangle.

2.2.1 Fundamental theorems behind time-dependent density functional theory

In the same way as for GS DFT, there are two fundamental theorems which form the basis of TDDFT. We start with a generalization of the first HK theorem to TD potentials, which is the subject of the so-called **Runge-Gross** theorem[86]. Consider an initial state $\Psi(\boldsymbol{x}_1 \cdots \boldsymbol{x}_N, t_0) \equiv \Psi_0(\boldsymbol{x}_1 \cdots \boldsymbol{x}_N)$, or in the bra-ket notation: $|\Psi(t_0)\rangle \equiv |\Psi_0\rangle$. When the TD potential $v(\boldsymbol{r}, t)$ is given, the wave function is obtained as the unique solution of the TD Schrödinger equation given in Eq. (2.1), as shown in Figure 2.2. The density can then be retrieved via its definition given in Eq. (2.12). As such, the density is a functional of the potential and the initial state. The Runge-Gross theorem closes the triangle in Figure 2.2 and is formulated as follows:

Two densities $n(\boldsymbol{r}, t)$ and $n'(\boldsymbol{r}, t)$, evolving from an initial state $\Psi_0(\boldsymbol{x}_1 \cdots \boldsymbol{x}_N)$ under the influence of two different TD potentials $v(\boldsymbol{r}, t)$ and $v'(\boldsymbol{r}, t)$ will start to differentiate infinitesimally later than t_0. Therefore, there is, for a fixed initial state, a one-to-one correspondence between densities and potentials.[86]

This is graphically shown in Figure 2.3 and the proof is given in Appendix B.1.1. As a result of the Runge-Gross theorem, both the TD external potential $v(\boldsymbol{r}, t)$ and the wave function $\Psi(\boldsymbol{x}_1 \cdots \boldsymbol{x}_N, t)$, and by extension every property of the system, are functionals of the TD density $n(\boldsymbol{r}, t)$ and the initial state $\Psi_0(\boldsymbol{x}_1 \cdots \boldsymbol{x}_N)$.

The Runge-Gross theorem only ensures that a unique potential corresponds

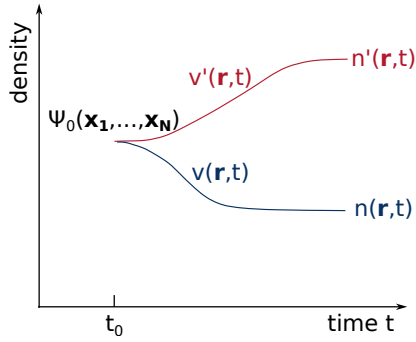

Figure 2.3: Graphical visualization of the Runge-Gross theorem: if a many-body system evolves under the influence of two different TD potentials $v(\boldsymbol{r},t)$ and $v'(\boldsymbol{r},t)$, starting from a fixed initial state $\Psi_0(\boldsymbol{x}_1,\cdots,\boldsymbol{x}_N)$, then the resulting TD densities $n(\boldsymbol{r},t)$ and $n'(\boldsymbol{r},t)$ will become different infinitesimally later than t_0. Figure adapted from Ref. 88 with permission of Oxford Publishing Limited, copyright 2012.

to a given density. When reverting to GS DFT in Section 2.1.2, it was stated that Kohn and Sham also made use of the second HK theorem, providing a variational principle to find the GS density, to prove the existence of a KS potential such that an independent particle model can be constructed with the same density. However, straightforward extension to the TD domain is not possible since the total energy is no longer conserved and therefore the variational principle is not applicable.[88] We need the **van Leeuwen** theorem[89] stating the following:

For a TD density $n(\boldsymbol{r},t)$ associated with a system with a given electron-electron interaction $\hat{V}_{ee}$, external potential $v(\boldsymbol{r},t)$, and initial state $\Psi_0(\boldsymbol{x}_1\cdots\boldsymbol{x}_N)$, a different system exists featuring an interaction $\hat{V}'_{ee}$ and a unique external potential $v'(\boldsymbol{r},t)$ which reproduces the same density. The initial state of this system $\Psi'_0(\boldsymbol{x}_1\cdots\boldsymbol{x}_N)$ must be chosen such that it correctly yields the given density and its time-derivative at t_0.[89]

The van Leeuwen theorem is visualized in Figure 2.4 and proven in Appendix B.1.2. Remark that by choosing $\hat{V}'_{ee} = \hat{V}_{ee}$ and $\Psi'_0(\boldsymbol{x}_1\cdots\boldsymbol{x}_N) = \Psi_0(\boldsymbol{x}_1\cdots\boldsymbol{x}_N)$, it follows that there exists a unique potential yielding $n(\boldsymbol{r},t)$, which is just the Runge-Gross theorem. This is the reason why the van Leeuwen theorem is also called the extended Runge-Gross theorem.

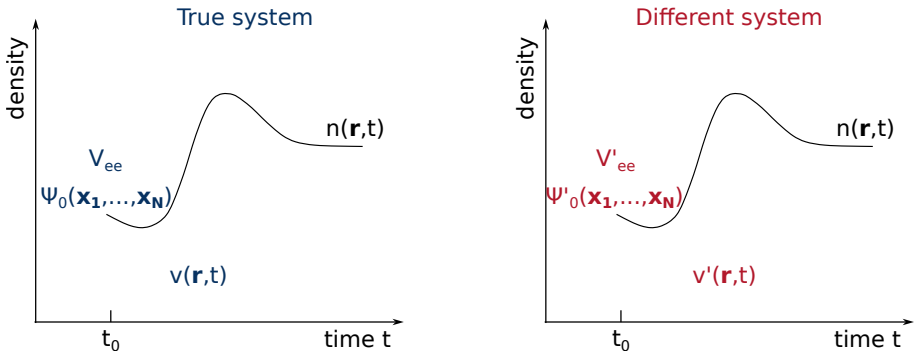

Figure 2.4: Graphical representation of the true system and a different system with the same density $n(\boldsymbol{r}, t)$. Figure adapted from Ref. 88 with permission of Oxford Publishing Limited, copyright 2012.

Now, if we choose $\hat{V}'_{ee} = 0$, the second system is a non-interacting one. When we assume that there exists a non-interacting state $\Psi'_0(\boldsymbol{x}_1 \cdots \boldsymbol{x}_N) = \Phi_0(\boldsymbol{x}_1 \cdots \boldsymbol{x}_N)$ with the correct initial density and time-derivative of the density, the van Leeuwen theorem states that each external potential $v(\boldsymbol{r}, t)$ uniquely determines a density $n(\boldsymbol{r}, t)$, which in turn uniquely determines another potential $v_s(\boldsymbol{r}, t)$ such that the density of non-interacting particles moving in $v_s(\boldsymbol{r}, t)$ is identical to the density of the true system moving in the external potential $v(\boldsymbol{r}, t)$. Whether or not the initial state can be chosen as a non-interacting GS cannot be definitely answered in general and boils down to the non-interacting v-representability problem for GS systems. We will not go into the details here but refer the reader to more specialized literature.[88, 90]

In the most general case, $v_s(\boldsymbol{r}, t)$ is a functional of the TD density and the initial wave functions of the interacting and non-interacting systems. When the system is in the GS at the initial time t_0, the functional-dependence on the initial wave functions drops out as both are functionals of the GS density $n_0(\boldsymbol{r})$ due to the HK theorem. Now, $v_s(\boldsymbol{r}, t)$ is only a functional of the TD density: $v_s[n](\boldsymbol{r}, t)$.

In this way, the van Leeuwen theorem allows for the construction of the TD KS system and we arrive at the TD analogue of the KS equations given in Eqs. (2.21), (2.22), and (2.25):

$$\left[-\frac{\nabla_i^2}{2} + v_s[n](\boldsymbol{r}, t)\right] \phi_i(\boldsymbol{r}, t) = i\frac{\partial}{\partial t}\phi_i(\boldsymbol{r}, t) \tag{2.28}$$

with

$$v_s[n](\boldsymbol{r},t) = v(\boldsymbol{r},t) + \int \mathrm{d}\boldsymbol{r}' \frac{n(\boldsymbol{r}',t)}{|\boldsymbol{r}-\boldsymbol{r}'|} + v_{XC}[n](\boldsymbol{r},t). \tag{2.29}$$

The density is then calculated as follows:

$$n(\boldsymbol{r},t) = \sum_{i=1}^{N} |\phi_i(\boldsymbol{r},t)|^2. \tag{2.30}$$

The procedure to solve the Schrödinger equation for molecular systems with TD external potentials consists of two steps. First, an initial set of KS orbitals is chosen, reproducing the exact density of the true initial state and its time-derivative. In the second step, the TD KS equations are then used to propagate the initial orbitals over time.

The TD XC potential $v_{XC}(\boldsymbol{r},t)$ is a very complex quantity. Although it is local in space, it functionally depends on the density and its history. Therefore, TDDFT is most commonly applied in the linear response (LR) regime and we investigate in the remainder of this Chapter how the properties which define the absorbance UV-Vis spectrum are retrieved from the linear response of the system.

2.2.2 Linear response time-dependent density functional theory

After a thorough discussion of the fundamental theorems laying the foundation of TDDFT, we now focus on the practical working equations. We will work in the LR regime, which can be applied when the effect of a weak perturbation is studied, and prove that the LR of a system contains all the information about its excitation spectrum.

I. Linear response theory

Consider a system, which is acted upon by a TD perturbation:

$$\hat{H}(t) = \hat{H}_0 + \hat{H}_1(t), \tag{2.31}$$

with

$$\hat{H}_1(t) = F(t)\hat{\beta}\mathcal{H}(t-t_0), \tag{2.32}$$

where $F(t)$ is an external field that couples to an observable $\hat{\beta}$ and $\mathcal{H}$ is the Heaviside step function. At t_0, the system is in its GS, determined by

$\hat{H}(t_0) = \hat{H}_0$. We consider a quantum mechanical observable $\hat{\alpha}$, for which the GS expectation value is given by

$$\alpha_0 = \langle\Psi_0|\hat{\alpha}|\Psi_0\rangle. \tag{2.33}$$

Due to the perturbation, the wave function changes and the expectation value of $\hat{\alpha}$ becomes TD:

$$\alpha(t) = \langle\Psi(t)|\hat{\alpha}|\Psi(t)\rangle. \tag{2.34}$$

In the interaction picture representation, we have:

$$\hat{\alpha} \to \hat{\alpha}^I(t-t_0) = e^{i\hat{H}_0(t-t_0)}\hat{\alpha}e^{-i\hat{H}_0(t-t_0)} \tag{2.35}$$

and similar for $\hat{\beta}$. $|\Psi(t)\rangle$ can, by using the time evolution operator $\hat{\mathfrak{U}}(t,t_0)$, be written as follows: [88]

$$\begin{aligned} |\Psi(t)\rangle &= \hat{\mathfrak{U}}(t-t_0)|\Psi_0\rangle \\ &= e^{-i\hat{H}_0(t-t_0)}\left[1 - i\int_{t_0}^{t} \mathrm{d}t'\, F(t')\hat{\beta}^I(t'-t_0)\right]|\Psi_0\rangle. \end{aligned} \tag{2.36}$$

The response of $\hat{\alpha}$ to the perturbation in Eq. (2.32) is defined as $\alpha(t) - \alpha_0$ and can be expanded in powers of the field $F(t)$

$$\alpha(t) - \alpha_0 = \alpha_1(t) + \alpha_2(t) + \cdots \tag{2.37}$$

where $\alpha_1(t)$ is the linear, $\alpha_2(t)$ the quadratic order response, and so on. When only the first order terms are taken into account, we obtain, by using Eq. (2.36), an expression for $\alpha_1(t)$:

$$\begin{aligned} \alpha_1(t) &= \alpha(t) - \alpha_0 \\ &= \langle\Psi_0|\left[1 + i\int_{t_0}^{t} \mathrm{d}t'\, F(t')\hat{\beta}^I(t'-t_0)\right]\hat{\alpha}^I(t-t_0)\times \\ &\quad \left[1 - i\int_{t_0}^{t} \mathrm{d}t'\, F(t')\hat{\beta}^I(t'-t_0)\right]|\Psi_0\rangle - \langle\Psi_0|\hat{\alpha}|\Psi_0\rangle \\ &= -i\int_{t_0}^{t} \mathrm{d}t'\, F(t')\langle\Psi_0|\left[\hat{\alpha}^I(t-t_0), \hat{\beta}^I(t'-t_0)\right]|\Psi_0\rangle \\ &= -i\int_{t_0}^{t} \mathrm{d}t'\, F(t')\langle\Psi_0|\left[\hat{\alpha}^I(t), \hat{\beta}^I(t')\right]|\Psi_0\rangle. \end{aligned} \tag{2.38}$$

Since $\hat{H}_0$ is time-independent, the commutator $\left[\hat{\alpha}^I(t), \hat{\beta}^I(t')\right]$ can be replaced by $\left[\hat{\alpha}^I(t-t'), \hat{\beta}\right]$. The LR of $\hat{\alpha}$ can then be rewritten as

$$\alpha_1(t) = \int_{-\infty}^{\infty} \mathrm{d}t'\, \chi_{\alpha\beta}(t-t')F(t'), \tag{2.39}$$

where we introduced the LR function:

$$\chi_{\alpha\beta}(t-t') = -i\mathcal{H}(t-t')\langle\Psi_0|\left[\hat{\alpha}^I(t-t'),\hat{\beta}\right]|\Psi_0\rangle. \tag{2.40}$$

The presence of the step function is a reflection of the fact that the external potential is a causal functional as it depends at time t on the density at earlier times t'.

In the next step, we transform to frequency space in order to extract the excitation energies of a system from its LR. The relations for transforming between time and frequency domain are given below:

$$\begin{aligned} F(t) &= \int_{-\infty}^{\infty} \frac{\mathrm{d}\omega}{2\pi} F(\omega) e^{-i\omega t} \\ F(\omega) &= \int_{-\infty}^{\infty} \mathrm{d}t\, F(t) e^{i\omega t}. \end{aligned} \tag{2.41}$$

The LR function given in Eq. (2.39) then becomes in frequency space:

$$\alpha_1(\omega) = \chi_{\alpha\beta}(\omega) F(\omega), \tag{2.42}$$

where we applied the convolution property.

We now introduce the Lehmann representation or spectral decomposition of the LR function. This representation is very useful because it explicitly shows the coupling between a frequency-dependent perturbation and the excitation spectrum of the system:

$$\chi_{\alpha\beta}(\omega) = \lim_{\eta\to 0^+} \sum_{n=1}^{\infty} \left\{ \frac{\langle\Psi_0|\hat{\alpha}|\Psi_n\rangle\langle\Psi_n|\hat{\beta}|\Psi_0\rangle}{\omega-\Omega_n+i\eta} - \frac{\langle\Psi_0|\hat{\beta}|\Psi_n\rangle\langle\Psi_n|\hat{\alpha}|\Psi_0\rangle}{\omega+\Omega_n+i\eta} \right\}. \tag{2.43}$$

The response function shows poles at the excitation energies $\Omega_n = E_n - E_0$ and at the negative values of the excitation energies $-\Omega_n$. The strength of the poles is determined by the matrix elements of the operators $\hat{\alpha}$ and $\hat{\beta}$ coupling the GS to the ESs. The derivation of Eq. (2.43) is given in Appendix B.1.3.

II. Linear response applied to time-dependent external potentials

After this general introduction to LR theory, we apply it to molecular systems subject to TD external potentials. We investigate how the density of a system at position $\boldsymbol{r}$ and time t is influenced by the external potential changes at position $\boldsymbol{r}'$ and earlier time t', as shown in Figure 2.5. The

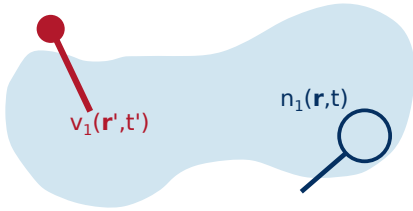

Figure 2.5: We observe how the density of a system at position $\boldsymbol{r}$ and at time t responds to all small perturbations in the external potential at position $\boldsymbol{r}'$ and earlier time t'. Figure adapted from Ref. 88 with permission of Oxford Publishing Limited, copyright 2012.

Lehmann representation of the LR function in Eq. (2.43) will prove to be very useful in this regard as it contains the exact excitation energies in its poles.

The TD external potential is given by:

$$v(\boldsymbol{r},t) = v_0(\boldsymbol{r}) + v_1(\boldsymbol{r},t)\mathcal{H}(t-t_0). \tag{2.44}$$

The system starts in its GS and at t_0 a small TD perturbation, described by the potential $v_1(\boldsymbol{r},t)$, is switched on. The external perturbation couples to the density operator according to Eq. (2.32):

$$\hat{H}_1(t) = \int \mathrm{d}\boldsymbol{r}' v_1(\boldsymbol{r}',t)\hat{n}(\boldsymbol{r}'). \tag{2.45}$$

Similarly to Eq. (2.37), the density response can be expanded in powers of the perturbation $v_1(\boldsymbol{r},t)$

$$n(\boldsymbol{r},t) - n_0(\boldsymbol{r}) = n_1(\boldsymbol{r},t) + n_2(\boldsymbol{r},t) + \ldots \tag{2.46}$$

The LR of the density is given by Eq. (2.39)

$$n_1(\boldsymbol{r},t) = \int_{-\infty}^{\infty} \mathrm{d}t' \int \mathrm{d}\boldsymbol{r}' \chi_{nn}(\boldsymbol{r},\boldsymbol{r}',t-t')v_1(\boldsymbol{r}',t'), \tag{2.47}$$

where the density-density response function, measuring the response in the density to a perturbing external potential, is defined as in Eq. (2.40)

$$\chi_{nn}(\boldsymbol{r},\boldsymbol{r}',t-t') = -i\mathcal{H}(t-t')\langle\Psi_0|\left[\hat{n}(\boldsymbol{r},t-t'),\hat{n}(\boldsymbol{r}')\right]|\Psi_0\rangle. \tag{2.48}$$

In order to find an expression for $v_1(\boldsymbol{r},t)$, we first formally write the TD density as a functional of the external potential, without any dependence on the initial wave function

$$n(\boldsymbol{r},t) = n[v](\boldsymbol{r},t). \tag{2.49}$$

Indeed, the initial GS wave function is uniquely determined by the HK theorem of GS DFT and, according to the Runge-Gross theorem, there exists a one-to-one correspondence between $v(\boldsymbol{r},t)$ and $n(\boldsymbol{r},t)$. In addition, since Eq. (2.46) represents a Taylor expansion of the density response, we obtain the following expression for the density-density response function:

$$\chi_{nn}(\boldsymbol{r},\boldsymbol{r}',t-t') = \frac{\delta n[v](\boldsymbol{r},t)}{\delta v(\boldsymbol{r}',t')}|_{v_0(\boldsymbol{r})}. \tag{2.50}$$

Via the HK theorem, the initial potential $v_0[n_0](\boldsymbol{r})$ is a functional of n_0. Eq. (2.50) thus explicitly shows that the density-density response function χ_{nn} is a functional of n_0 only.[88]

The one-to-one correspondence between TD densities and potentials implies that the perturbing potential can be calculated from the linear density response:

$$v_1(\boldsymbol{r},t) = \int_{-\infty}^{\infty} \mathrm{d}t' \int \mathrm{d}\boldsymbol{r}'\, \chi_{nn}(\boldsymbol{r},\boldsymbol{r}',t-t')^{-1} n_1(\boldsymbol{r}',t'). \tag{2.51}$$

When transforming Eq. (2.47) to the frequency domain, the frequency-dependent density response has the following form:

$$n_1(\boldsymbol{r},\omega) = \int \mathrm{d}\boldsymbol{r}' \chi_{nn}(\boldsymbol{r},\boldsymbol{r}',\omega) v_1(\boldsymbol{r}',\omega) \tag{2.52}$$

and the Lehmann representation of the density-density response function is given by Eq. (2.43):

$$\begin{aligned}\chi_{nn}(\boldsymbol{r},\boldsymbol{r}',\omega) = \lim_{\eta\to 0^+} \sum_{n=1}^{\infty} \Bigg\{ &\frac{\langle\Psi_0|\hat{n}(\boldsymbol{r})|\Psi_n\rangle\langle\Psi_n|\hat{n}(\boldsymbol{r}')|\Psi_0\rangle}{\omega-\Omega_n+i\eta} - \\ &\frac{\langle\Psi_0|\hat{n}(\boldsymbol{r}')|\Psi_n\rangle\langle\Psi_n|\hat{n}(\boldsymbol{r})|\Psi_0\rangle}{\omega+\Omega_n+i\eta} \Bigg\}.\end{aligned} \tag{2.53}$$

In Section 2.2.1, we concluded that a KS system of non-interacting particles yields the same density as the true system containing interacting particles. Following the above reasoning, the LR equation for the KS system is given by:

$$n_1(\boldsymbol{r},t) = \int_{-\infty}^{\infty} \mathrm{d}t' \int \mathrm{d}\boldsymbol{r}' \chi_s(\boldsymbol{r},\boldsymbol{r}',t-t') v_{s1}(\boldsymbol{r}',t'). \tag{2.54}$$

In analogy to Eq. (2.49):

$$n(\boldsymbol{r},t) = n[v_s](\boldsymbol{r},t) \tag{2.55}$$

and equivalently to Eq. (2.50), we obtain:

$$\chi_s(\boldsymbol{r},\boldsymbol{r}',t-t') = \frac{\delta n[v_s](\boldsymbol{r},t)}{\delta v_s(\boldsymbol{r}',t')}|_{v_s[n0](\boldsymbol{r})}. \tag{2.56}$$

Following Eq. (2.29), the linearized effective potential can be expressed as follows:

$$v_{s1}[n](\boldsymbol{r},t) = v_1(\boldsymbol{r},t) + \int \mathrm{d}\boldsymbol{r}' \frac{n_1(\boldsymbol{r}',t)}{|\boldsymbol{r}-\boldsymbol{r}'|} + v_{XC1}(\boldsymbol{r},t). \tag{2.57}$$

The last term is the linearized XC potential, and an explicit expression for it is obtained by functional Taylor expansion:[88]

$$v_{XC1}(\boldsymbol{r},t) = \int_{-\infty}^{\infty} \mathrm{d}t' \int \mathrm{d}\boldsymbol{r}' \frac{\delta v_{XC}[n](\boldsymbol{r},t)}{\delta n(\boldsymbol{r}',t')}|_{n_0(\boldsymbol{r})} n_1(\boldsymbol{r}',t'). \tag{2.58}$$

The exact linear density response $n_1(\boldsymbol{r},t)$ of an interacting system is in this way written as the linear density response of a non-interacting system subjected to the effective perturbation $v_{s1}(\boldsymbol{r},t)$. The Lehmann representation of the linear KS response function then becomes:

$$\chi_s(\boldsymbol{r},\boldsymbol{r}',\omega) = \lim_{\eta\to 0^+} \sum_{j,k=1}^{\infty} (a_k - a_j) \frac{\phi_k^*(\boldsymbol{r})\phi_k(\boldsymbol{r}')\phi_j^*(\boldsymbol{r}')\phi_j(\boldsymbol{r})}{\omega - \omega_{jk} + i\eta}, \tag{2.59}$$

where a_j and a_k are occupation numbers of the KS GS single-particle orbitals. In the double summation, only those terms contribute where one index indicates an occupied orbital, while the other refers to an unoccupied orbital. $w_{jk} = \epsilon_j - \epsilon_k$ are differences between KS orbital energies and their absolute values correspond to the excitation energies of the KS system. The non-interacting KS response function has thus poles at the excitation energies of the KS system. This expression is derived from Eq. (2.53) by replacing the wave functions with the KS Slater determinants constructed using the KS orbitals ϕ_i, as shown in Appendix B.1.4.

We can take advantage of the simple form of the LR function of a KS system with non-interacting particles, shown in Eq. (2.59), in order to determine, in principle exactly, the true density and any property which depends on the density. The only input that is required for the determination of the excitation energies are GS properties, namely occupied and virtual KS orbitals of the system in its GS.

2.2.3 Working equations of time-dependent density functional theory

The excitation energies of the KS and true system are situated at the poles of the response functions given in Eqs. (2.59) and (2.53), respectively. In the

following, we start with a derivation of a Dyson-like equation, which provides a relation between both response functions. From this, we determine expressions for the excitation energies Ω_n. Afterwards, the oscillator strengths f_n are determined. The UV-Vis absorption spectrum is now completely defined by the excitation energies and oscillator strengths. Finally, we briefly touch upon the assignment problem.

I. Dyson equation

Eq. (2.59) has poles at the excitation energies ω_{jk} of the KS system which differ from the poles of the true density-density response function given in Eq. (2.53), which are situated at the true excitation energies Ω_n. We need a shift to transform the KS excitation energies to the true ones. In order to attain this, we determine the relation between the LR functions of the true and the KS system. Therefore, we first introduce the XC kernel f_{XC} as the functional derivative of the XC potential evaluated at the GS density:

$$f_{XC}(\boldsymbol{r}, t, \boldsymbol{r}', t') = \frac{\delta v_{XC}[n](\boldsymbol{r}, t)}{\delta n(\boldsymbol{r}', t')}|_{n_0(\boldsymbol{r})}. \tag{2.60}$$

This XC kernel, which is a functional of the GS density, is the key quantity of TDDFT in the LR regime.

We rewrite Eq. (2.54) by inserting Eqs. (2.57) and (2.58), and the definition of the XC kernel given in Eq. (2.60):

$$\begin{aligned} n_1(\boldsymbol{r}, t) = \int \mathrm{d}t' \int \mathrm{d}\boldsymbol{r}' \chi_s(\boldsymbol{r}, t, \boldsymbol{r}', t') \times \\ \left[v_1(\boldsymbol{r}', t') + \int \mathrm{d}\tau \int \mathrm{d}\boldsymbol{x} \left(\frac{\delta(t' - \tau)}{|\boldsymbol{r}' - \boldsymbol{x}|} + f_{XC}(\boldsymbol{r}', t', \boldsymbol{x}, \tau) \right) n_1(\boldsymbol{x}, \tau) \right]. \end{aligned} \tag{2.61}$$

From now on, the integration boundaries are omitted to ease the notation. The density response entering in each side of the equation can be rewritten using Eq. (2.47):

$$\begin{aligned} \int \mathrm{d}t' \int \mathrm{d}\boldsymbol{r}' \chi_{nn}(\boldsymbol{r}, t, \boldsymbol{r}', t') v_1(\boldsymbol{r}', t') = \int \mathrm{d}t' \int \mathrm{d}\boldsymbol{r}' \chi_s(\boldsymbol{r}, t, \boldsymbol{r}', t') v_1(\boldsymbol{r}', t') + \\ \int \mathrm{d}\tau \int \mathrm{d}\boldsymbol{x} \chi_s(\boldsymbol{r}, t, \boldsymbol{x}, \tau) \int \mathrm{d}\tau' \int \mathrm{d}\boldsymbol{x}' \left(\frac{\delta(\tau - \tau')}{|\boldsymbol{x} - \boldsymbol{x}'|} + f_{XC}(\boldsymbol{x}, \tau, \boldsymbol{x}', \tau') \right) \times \\ \int \mathrm{d}t' \int \mathrm{d}\boldsymbol{r}' \chi_{nn}(\boldsymbol{x}', \tau', \boldsymbol{r}', t') v_1(\boldsymbol{r}', t'), \end{aligned} \tag{2.62}$$

where we changed the integration variables in the second term on the right-hand side. Since this equation holds for any perturbation of the external potential, we obtain the following relation between the interacting and non-interacting response functions:

$$\begin{aligned}&\chi_{nn}(\boldsymbol{r},t,\boldsymbol{r}',t') = \chi_s(\boldsymbol{r},t,\boldsymbol{r}',t') \\ &+ \int \mathrm{d}\tau \int \mathrm{d}\boldsymbol{x} \int \mathrm{d}\tau' \int \mathrm{d}\boldsymbol{x}' \chi_s(\boldsymbol{r},t,\boldsymbol{x},\tau) \left(\frac{\delta(\tau-\tau')}{|\boldsymbol{x}-\boldsymbol{x}'|} + f_{XC}(\boldsymbol{x},\tau,\boldsymbol{x}',\tau') \right) \times \\ &\chi_{nn}(\boldsymbol{x}',\tau',\boldsymbol{r}',t'),\end{aligned} \tag{2.63}$$

which is a Dyson-like equation. In general, Dyson-like equations express any type of Green's function for an interacting system in terms of its non-interacting counterpart and the self-energy, implicitly containing all correlation effects of the many-body system.[88] In short-hand notation, we get after a Fourier transformation:

$$\hat{\chi}_{nn}(\omega) = \hat{\chi}_s(\omega) + \hat{\chi}_s(\omega) \star \hat{f}_{HXC}(\omega) \star \hat{\chi}_{nn}(\omega), \tag{2.64}$$

where we have dropped the spatial indices and introduced the shorthand $\star$ to indicate integrals like $A \star B = \int \mathrm{d}\boldsymbol{x} A(\boldsymbol{r},\boldsymbol{x}) B(\boldsymbol{x},\boldsymbol{r}')$, thinking of χ, χ_s, and f_{HXC} as infinite-dimensional matrices depending on the frequency. Operators in $\boldsymbol{r}$-space are indicated with $\hat{}$. The Hartree-XC kernel is defined as:

$$f_{HXC}(\boldsymbol{r},\boldsymbol{r}',\omega) = \frac{1}{|\boldsymbol{r}-\boldsymbol{r}'|} + f_{XC}(\boldsymbol{r},\boldsymbol{r}',\omega), \tag{2.65}$$

where the frequency-dependent XC kernel $f_{XC}(\boldsymbol{r},\boldsymbol{r}',\omega)$ is the Fourier transform of Eq. (2.60). Eq. (2.64) expresses the true density-density response function in terms of the KS response function and a frequency-dependent Hartree-XC kernel. While this kernel is still more complex than the GS XC potential $v_{XC}(\boldsymbol{r})$, it is much more manageable than the full TD XC potential $v_{XC}(\boldsymbol{r},t)$ entering the TD KS equations in Eqs. (2.28) and (2.29). Indeed, it is only a functional of the initial GS density. The kernel is memory-dependent as it depends on the frequency. This is much simpler than for the TD XC potential which functionally depends on the density and its history. However, the spatial-dependence of the XC kernel is more complicated as it is a non-local function of $\boldsymbol{r}$ and $\boldsymbol{r}'$, whereas the TD XC potential is local in space.

Starting from the Dyson-like equation given in Eq. (2.64), we derive the Casida equation. After a unitary transformation, an eigenvalue problem is retrieved from which the excitation energies are obtained via the eigenvalues.

II. Excitation energies via the Casida equation

Integrating Eq. (2.64) against $v_1(\omega)$ yields:

$$\left[\hat{1} - \hat{\chi}_s(\omega) \star \hat{f}_{HXC}(\omega)\right] \star \boldsymbol{n_1}(\omega) = \hat{\chi}_s(\omega) \star \boldsymbol{v_1}(\omega), \tag{2.66}$$

where vectors in $\boldsymbol{r}$-space are indicated in bold. χ_{nn} and thus n_1 have poles at the true excitation energies Ω, whereas χ_s has poles at the KS excitation energies ω_{jk}. Hence, the right-hand side remains finite for $\omega = \Omega$. Therefore, the integral operator acting on n_1 on the left-hand side cannot be invertible for $\omega = \Omega$ as it must cancel out a pole in n_1 in order to create a finite right-hand side. The true excitation energies Ω are therefore precisely those frequencies for which the eigenvalues of the operator on the left vanish. This can be expressed via the following eigenvalue equation:

$$\hat{\chi}_s(\omega) \star \hat{f}_{HXC}(\omega) \star \boldsymbol{\gamma}(\omega) = \lambda(\omega)\boldsymbol{\gamma}(\omega), \tag{2.67}$$

where $\lambda(\omega)$ is a scalar which equals one for $\omega = \Omega$.

We define the difference between the GS occupation numbers of orbitals j and k and Φ_{jk} as follows:

$$\begin{aligned} \alpha_{kj} =& a_k - a_j \\ \Phi_{jk} =& \phi_j(\boldsymbol{r})\phi_k^*(\boldsymbol{r}). \end{aligned} \tag{2.68}$$

Furthermore we introduce the following quantity:

$$\xi_{jk}(\omega) = \int \mathrm{d}\boldsymbol{r'} \int \mathrm{d}\boldsymbol{r''} \Phi_{jk}^*(\boldsymbol{r'}) f_{HXC}(\boldsymbol{r'}, \boldsymbol{r''}, \omega)\gamma(\boldsymbol{r''}, \omega). \tag{2.69}$$

The eigenvalue equation in Eq. (2.67) can then, by using Eq. (2.59) for χ_s, be rewritten as follows:

$$\sum_{j,k=1}^{\infty} \frac{\alpha_{kj}\Phi_{jk}(\boldsymbol{r})}{\omega - \omega_{jk}} \xi_{jk}(\omega) = \lambda(\omega)\gamma(\boldsymbol{r}, \omega). \tag{2.70}$$

Remark that we eased the notation by dropping $\lim_{\eta \to 0^+}$ and $i\eta$ in the denominator. Next, we define the coupling matrix elements

$$M_{jkj'k'}(\omega) = \int \mathrm{d}\boldsymbol{r} \int \mathrm{d}\boldsymbol{r'} \Phi_{jk}^*(\boldsymbol{r}) f_{HXC}(\boldsymbol{r}, \boldsymbol{r'}, \omega)\Phi_{j'k'}(\boldsymbol{r'}). \tag{2.71}$$

We multiply Eq. (2.69) with $\lambda(\omega)$ and use Eq. (2.70) to rewrite the right-hand side:

$$\lambda(\omega)\xi_{jk}(\omega) = \sum_{j'k'=1}^{\infty} \frac{\alpha_{k'j'} M_{jkj'k'}(\omega)}{\omega - \omega_{j'k'}} \xi_{j'k'}(\omega). \tag{2.72}$$

Evaluating Eq. (2.72) for $\omega = \Omega$ and thus $\lambda(\Omega) = 1$ yields:

$$\beta_{jk}(\Omega - \omega_{jk}) = \sum_{j'k'=1}^{\infty} \alpha_{k'j'} M_{jkj'k'}(\Omega)\beta_{j'k'}, \tag{2.73}$$

where, in order to simplify the notation, the following quantity is introduced:

$$\beta_{jk} = \frac{\xi_{jk}(\Omega)}{\Omega - \omega_{jk}}. \tag{2.74}$$

Eq. (2.73) is an eigenvalue equation which yields the exact excitation energies Ω of the system:

$$\sum_{j'k'=1}^{\infty} \left(\alpha_{k'j'} M_{jkj'k'}(\Omega) + \omega_{j'k'}\delta_{jj'}\delta_{kk'}\right) \beta_{j'k'} = \Omega\beta_{jk} \tag{2.75}$$

A visualization of the density changes induced during a particular excitation is obtained from the eigenvectors $\beta_{j'k'}$. As proven in Appendix B.1.5, this is expressed as:

$$n_1(\boldsymbol{r}, \Omega) = \sum_{j,k=1}^{\infty} \alpha_{kj} \Phi_{jk}(\boldsymbol{r})\beta_{jk}, \tag{2.76}$$

which corresponds to the $\gamma(\omega)$ eigenvector with eigenvalue $\lambda(\omega) = 1$ in Eq. (2.67).

We cast Eq. (2.75) in a matrix equation. Reasonably, we only consider transitions between occupied and unoccupied KS states, labeled with p, p' and h, h', respectively. Eq. (2.75) can then be rewritten as two coupled equations:

$$\begin{aligned} \sum_{j'k'=1}^{\infty} \left(\alpha_{k'j'} M_{phj'k'}(\Omega) + \omega_{j'k'}\delta_{pj'}\delta_{hk'}\right) \beta_{j'k'} &= \Omega\beta_{ph} \\ \sum_{j'k'=1}^{\infty} \left(\alpha_{k'j'} M_{hpj'k'}(\Omega) + \omega_{j'k'}\delta_{hj'}\delta_{pk'}\right) \beta_{j'k'} &= \Omega\beta_{hp}, \end{aligned} \tag{2.77}$$

where $j = p$ and $k = h$ in the first line, whereas in the second line $j = h$ and $k = h$. We consider two cases. In the first term: $j' = p'$ and $k' = h'$,

whereas $j' = h'$ and $k' = p'$ in the second term:

$$\begin{aligned}\sum_{p'h'=1}^{\infty} \left\{ \left(\alpha_{h'p'} M_{php'h'}(\Omega) + \omega_{p'h'}\delta_{pp'}\delta_{hh'}\right)\beta_{p'h'} + \alpha_{p'h'} M_{phh'p'}(\Omega)\beta_{h'p'} \right\} \\ = \Omega\beta_{ph} \\ \sum_{p'h'=1}^{\infty} \left\{ \alpha_{h'p'} M_{hpp'h'}(\Omega)\beta_{p'h'} + \left(\alpha_{p'h'} M_{hph'p'}(\Omega) + \omega_{h'p'}\delta_{hh'}\delta_{pp'}\right)\beta_{h'p'} \right\} \\ = \Omega\beta_{hp}.\end{aligned} \tag{2.78}$$

Now we use that $\alpha_{p'h'} = 1$ and $\alpha_{h'p'} = -1$ and notice that $\omega_{h'p'} > 0$ and $\omega_{p'h'} = -\omega_{h'p'} < 0$. Furthermore, we define

$$X_{ph} = -\beta_{ph} \qquad\qquad Y_{ph} = \beta_{hp} \tag{2.79}$$

such that Eq. (2.78) yields:

$$\begin{aligned}\sum_{p'h'=1}^{\infty} \left\{ \left(M_{php'h'}(\Omega) + \omega_{h'p'}\delta_{pp'}\delta_{hh'}\right) X_{p'h'} + M_{phh'p'}(\Omega) Y_{p'h'} \right\} = -\Omega X_{ph} \\ \sum_{p'h'=1}^{\infty} \left\{ M_{hpp'h'}(\Omega) X_{p'h'} + \left(M_{hph'p'}(\Omega) + \omega_{h'p'}\delta_{hh'}\delta_{pp'}\right) Y_{p'h'} \right\} = \Omega Y_{ph}.\end{aligned} \tag{2.80}$$

The density given in Eq. (2.76) can, by using the definitions given in Eq. (2.79), be expressed as follows:

$$n_1(\boldsymbol{r}, \Omega) = \sum_{ph} \left[\Phi_{ph}(\boldsymbol{r}) X_{ph} + \Phi_{hp}(\boldsymbol{r}) Y_{ph}\right]. \tag{2.81}$$

Since the GS Hamiltonian has time-reversal symmetry, we assume that the KS orbitals are real.[88] In this case: $M_{abcd} = M_{bacd} = M_{abdc} = M_{badc}$. The set of coupled eigenvalue equations given in Eq. (2.80) can then be cast into the following matrix form, known as the Casida equation:

$$\begin{pmatrix} \mathbf{L} & \mathbf{M} \\ \mathbf{M} & \mathbf{L} \end{pmatrix} \begin{pmatrix} \boldsymbol{X} \\ \boldsymbol{Y} \end{pmatrix} = \Omega \begin{pmatrix} \mathbf{-1} & \mathbf{0} \\ \mathbf{0} & \mathbf{1} \end{pmatrix} \begin{pmatrix} \boldsymbol{X} \\ \boldsymbol{Y} \end{pmatrix} \tag{2.82}$$

with

$$L_{php'h'}(\Omega) = \delta_{pp'}\delta_{hh'}\omega_{h'p'} + M_{php'h'}(\Omega). \tag{2.83}$$

L and **M** are called the magnetic and electric hessian matrices [91] or orbital rotation Hessians [92, 93]. Eq. (2.82) has the structure of an infinite-dimensional anti-Hermitian eigenvalue problem, *i.e.*, taking the Hermitian conjugate

leads to the same eigenvalue equation, but with eigenvalue $-\Omega_n$ instead of Ω_n. Hence, the solutions come in pairs $(\Omega_n, -\Omega_n)$, which is also evident from the pole structure of the response function given in Eq. (2.53).

In practice, the Casida equation is often cast into the alternative form:

$$\mathbf{C}\boldsymbol{Z} = \Omega^2 \boldsymbol{Z}, \tag{2.84}$$

with

$$\begin{aligned} \mathbf{C} =& (\mathbf{L}-\mathbf{M})^{1/2}(\mathbf{L}+\mathbf{M})(\mathbf{L}-\mathbf{M})^{1/2} \\ \boldsymbol{Z} =& (\mathbf{L}-\mathbf{M})^{1/2}(\boldsymbol{X}-\boldsymbol{Y}). \end{aligned} \tag{2.85}$$

The proof is given in Appendix B.1.6. Via a 2×2 unitary transformation, given in Eq. (2.85), the anti-Hermitian eigenvalue problem in Eq. (2.82) is reformulated as an Hermitian eigenvalue problem of half the dimension. The eigenvalues of $\mathbf{C}$ are the squares of the true excitation energies.

Given the definition of $\mathbf{L}$ in Eq. (2.83), we can write the matrix element in Eq. (2.84) as follows:

$$\begin{aligned} C_{php'h'} &= \sum_{\tilde{p}\tilde{h}=1}^{\infty}\sum_{\hat{p}\hat{h}=1}^{\infty} \sqrt{\delta_{p\tilde{p}}\delta_{h\tilde{h}}\omega_{\tilde{h}\tilde{p}}}\left(2M_{\tilde{p}\tilde{h}\hat{p}\hat{h}}(\Omega) + \delta_{\tilde{p}\hat{p}}\delta_{\tilde{h}\hat{h}}\omega_{\hat{h}\hat{p}}\right)\sqrt{\delta_{\hat{p}p'}\delta_{\hat{h}h'}\omega_{h'p'}} \\ &= 2M_{php'h'}(\Omega)\sqrt{\omega_{ph}\omega_{p'h'}} + \delta_{hh'}\delta_{pp'}\omega^2_{p'h'} \end{aligned} \tag{2.86}$$

Hence, Eq. (2.84) becomes,

$$\sum_{p'h'=1}^{\infty}\left[\delta_{hh'}\delta_{pp'}\omega^2_{p'h'} + 2\sqrt{\omega_{ph}\omega_{p'h'}}M_{php'h'}(\Omega)\right]Z_{p'h'} = \Omega^2 Z_{ph}. \tag{2.87}$$

In Eq. (2.87), one clearly sees the shift applied to the excitation energy of the non-interacting KS system to transform them to the true excitation energy.

III. Oscillator strengths

The next step in the characterization of the UV-Vis spectrum is to determine the oscillator strengths. Therefore, the dynamic dipole polarizability is introduced and we show how the oscillator strengths are retrieved from a matrix equation.

Dynamic dipole polarizability

The electric dipole moment is a measure of the separation of the positive and negative electric charges in a system:

$$\boldsymbol{p}(t) = -\int \mathrm{d}\boldsymbol{r}\, \boldsymbol{r} n(\boldsymbol{r}, t), \tag{2.88}$$

where a minus-sign is introduced because we consider the charge density instead of the electron density. The electric dipole moment can be expressed as follows:

$$\boldsymbol{p}(t) = \boldsymbol{p} + \boldsymbol{p}_1(t) + \cdots \tag{2.89}$$

The first term corresponds to the permanent dipole moment of the system without the presence of external fields. The second term is the LR of the dipole moment, *i.e.,* the first-order induced electronic dipole polarization, which can be written as follows:

$$\boldsymbol{p}_1(t) = \int \mathrm{d}t'\, \boldsymbol{\alpha}(t - t')\boldsymbol{E}(t'), \tag{2.90}$$

where $\boldsymbol{E}$ is a TD but space-independent externally applied electric field and $\boldsymbol{\alpha}$, the dynamic dipole polarizability tensor, describes the dynamical response of the electric dipole moment to a TD external field. After a Fourier transformation of Eq. (2.90), we obtain:

$$\boldsymbol{p}_1(\omega) = \boldsymbol{\alpha}(\omega)\boldsymbol{E}(\omega). \tag{2.91}$$

The mean polarizability $\bar{\alpha}$ is defined as one third of the trace of the dynamic dipole polarizability tensor

$$\bar{\alpha}(\omega) = \frac{1}{3}\mathrm{Tr}\boldsymbol{\alpha}(\omega) \tag{2.92}$$

and can be written as follows:

$$\bar{\alpha}(\omega) = \sum_{n=1}^{\infty} \frac{f_n}{\omega^2 - \Omega_n^2}. \tag{2.93}$$

The poles of $\bar{\alpha}$ are the excitation energies Ω_n and the residues are the oscillator strengths f_n, which are dimensionless quantities defined as the ratio of the absorption rate of a given transition in a molecular system to the absorption rate of a classical, single-electron oscillator with frequency Ω_n.[88] It counts how much of the total oscillating potential is used for a specific transition. Furthermore, f_n satisfy the Thomas-Reiche-Kuhn sum rule or f-sum rule:[88]

$$\sum_{n=1}^{\infty} f_n = N. \tag{2.94}$$

Let us now consider the external potential associated with an electric field, assumed to be linearly polarized along the z-direction:

$$v_1(\boldsymbol{r},\omega) = zE(\omega) \tag{2.95}$$

According to Eq. (2.91), the zz element of the dynamic dipole polarizability tensor is given by:

$$\alpha_{zz}(\omega) = -\frac{1}{E(\omega)}\int \mathrm{d}\boldsymbol{r} z n_1(\boldsymbol{r},\omega), \tag{2.96}$$

where we used the Fourier transform of the z-component of the first order term in Eq. (2.88). Introducing Eqs. (2.52) and (2.95) in Eq. (2.96) results in:

$$\alpha_{zz}(\omega) = -\int \mathrm{d}\boldsymbol{r}\int \mathrm{d}\boldsymbol{r}' z z' \chi_{nn}(\boldsymbol{r},\boldsymbol{r}',\omega). \tag{2.97}$$

By inserting the spectral decomposition of χ_{nn}, given in Eq. (2.53), we obtain:

$$\begin{aligned}
\alpha_{zz}(\omega) = & \int \mathrm{d}\boldsymbol{r}\int \mathrm{d}\boldsymbol{r}' z z' \sum_{n=1}^{\infty}\left\{\frac{\langle\Psi_0|\hat{n}(\boldsymbol{r})|\Psi_n\rangle\langle\Psi_n|\hat{n}(\boldsymbol{r}')|\Psi_0\rangle}{\omega-\Omega_n} - \right. \\
& \left. \frac{\langle\Psi_0|\hat{n}(\boldsymbol{r}')|\Psi_n\rangle\langle\Psi_n|\hat{n}(\boldsymbol{r})|\Psi_0\rangle}{\omega+\Omega_n}\right\} \\
= & \sum_{n=1}^{\infty}\left\{\frac{\langle\Psi_0|\int \mathrm{d}\boldsymbol{r}\sum_{i=1}^{N} z\delta(\boldsymbol{r}-\boldsymbol{r}_i)|\Psi_n\rangle\langle\Psi_n|\int \mathrm{d}\boldsymbol{r}'\sum_{i=1}^{N} z'\delta(\boldsymbol{r}'-\boldsymbol{r}_i)|\Psi_0\rangle}{\omega-\Omega_n} - \right. \\
& \left. \frac{\langle\Psi_0|\int \mathrm{d}\boldsymbol{r}'\sum_{i=1}^{N} z'\delta(\boldsymbol{r}'-\boldsymbol{r}_i)|\Psi_n\rangle\langle\Psi_n|\int \mathrm{d}\boldsymbol{r}\sum_{i=1}^{N} z\delta(\boldsymbol{r}-\boldsymbol{r}_i)|\Psi_0\rangle}{\omega+\Omega_n}\right\} \\
= & \sum_{n=1}^{\infty}\left\{\frac{|\langle\Psi_n|\hat{z}|\Psi_0\rangle|^2}{\omega-\Omega_n} - \frac{|\langle\Psi_n|\hat{z}|\Psi_0\rangle|^2}{\omega+\Omega_n}\right\} \\
= & \sum_{n=1}^{\infty}\frac{2\Omega_n|\langle\Psi_n|\hat{z}|\Psi_0\rangle|^2}{\omega^2-\Omega_n^2},
\end{aligned} \tag{2.98}$$

where $\hat{z} = \sum_{i=1}^{N} z_i$. In a similar way, expressions are obtained for the other elements of $\boldsymbol{\alpha}$, which are inserted in Eq. (2.92). Comparing to Eq. (2.93) results in the following definition for the oscillator strengths f_n:

$$f_n = \frac{2}{3}\Omega_n\left(|\langle\Psi_0|\hat{x}|\Psi_n\rangle|^2 + |\langle\Psi_0|\hat{y}|\Psi_n\rangle|^2 + |\langle\Psi_0|\hat{z}|\Psi_n\rangle|^2\right). \tag{2.99}$$

Oscillator strengths from a matrix equation

It can be shown that, using a similar derivation and assuming that the KS orbitals are real,[94] the Fourier-transform of Eq. (2.54) can be recast into

$$\left[\begin{pmatrix}\mathbf{L} & \mathbf{M}\\ \mathbf{M} & \mathbf{L}\end{pmatrix} - \omega\begin{pmatrix}-\mathbf{1} & \mathbf{0}\\ \mathbf{0} & \mathbf{1}\end{pmatrix}\right]\begin{pmatrix}\boldsymbol{X}\\ \boldsymbol{Y}\end{pmatrix} = -\begin{pmatrix}\boldsymbol{v_1}\\ \boldsymbol{v_1^*}\end{pmatrix}, \tag{2.100}$$

where the elements of the vector v_1 are given by

$$v_{1,ph} = \int \mathrm{d}\boldsymbol{r}\Phi_{ph}(\boldsymbol{r})v_1(\boldsymbol{r},\omega). \tag{2.101}$$

This can be rewritten as follows:

$$\begin{aligned}(\mathbf{L}+\omega)(\mathcal{R}(\boldsymbol{X})+i\mathcal{I}(\boldsymbol{X})) + \mathbf{M}(\mathcal{R}(\boldsymbol{X})-i\mathcal{I}(\boldsymbol{X})) &= -(\mathcal{R}(\boldsymbol{v_1})+i\mathcal{I}(\boldsymbol{v_1}))\\ \mathbf{M}(\mathcal{R}(\boldsymbol{X})+i\mathcal{I}(\boldsymbol{X})) + (\mathbf{L}-\omega)(\mathcal{R}(\boldsymbol{X})-i\mathcal{I}(\boldsymbol{X})) &= -(\mathcal{R}(\boldsymbol{v_1})-i\mathcal{I}(\boldsymbol{v_1})),\end{aligned} \tag{2.102}$$

where we used the fact that $\boldsymbol{X} = \mathcal{R}(\boldsymbol{X}) + i\mathcal{I}(\boldsymbol{X})$ is the complex conjugate of $\boldsymbol{Y}$.[88] Subtracting and summing those equations results in:

$$\begin{aligned}-\mathcal{R}(\boldsymbol{X})(\mathbf{L}+\mathbf{M}) - i\omega\mathcal{I}(\boldsymbol{X}) &= \mathcal{R}(\boldsymbol{v_1})\\ \omega\mathcal{R}(\boldsymbol{X}) + i\mathcal{I}(\boldsymbol{X})(\mathbf{L}-\mathbf{M}) &= -i\mathcal{I}(\boldsymbol{v_1}),\end{aligned} \tag{2.103}$$

from which we obtain separate equations for the real and imaginary parts of X:

$$\begin{aligned}\left(-\mathbf{L}-\mathbf{M}+\frac{\omega^2}{\mathbf{L}-\mathbf{M}}\right)\mathcal{R}(\boldsymbol{X}) &= \mathcal{R}(\boldsymbol{v_1}) - i\mathcal{I}(\boldsymbol{v_1})\frac{\omega}{\mathbf{L}-\mathbf{M}}\\ \left(-\frac{\omega^2}{\mathbf{L}+\mathbf{M}}+\mathbf{L}-\mathbf{M}\right)i\mathcal{I}(\boldsymbol{X}) &= \mathcal{R}(\boldsymbol{v_1})\frac{\omega}{\mathbf{L}+\mathbf{M}} - i\mathcal{I}(\boldsymbol{v_1}).\end{aligned} \tag{2.104}$$

If there is only a real perturbation, Eq. (2.104) simplifies to:

$$\mathcal{R}(\boldsymbol{X}) = \mathbf{S}^{-1/2}\left(\mathbf{C}-\omega^2\right)^{-1}\mathbf{S}^{-1/2}\boldsymbol{v_1}, \tag{2.105}$$

with

$$\mathbf{S} = (\mathbf{L}-\mathbf{M})^{-1} \tag{2.106}$$

and $\mathbf{C}$ has already been defined in Eq. (2.85). Next, we use the following spectral expansion[88]

$$(\mathbf{C}-\omega^2)^{-1} = \sum_n \frac{\boldsymbol{Z_n}\boldsymbol{Z_n}^\dagger}{\Omega_n^2-\omega^2}, \tag{2.107}$$

which is implied by the completeness of the eigenvectors $\sum_n \boldsymbol{Z_n}\boldsymbol{Z_n}^T = \mathbf{1}$,[95] and insert it in Eq. (2.105), which is substituted in Eq. (2.81). The result is then introduced in Eq. (2.96):[88]

$$\alpha_{zz}(\omega) = -\sum_n 2\boldsymbol{z}\mathbf{S}^{-1/2}\frac{\boldsymbol{Z_n}\boldsymbol{Z_n}^\dagger}{(\Omega_n^2-\omega^2)}\mathbf{S}^{-1/2}\boldsymbol{z}, \tag{2.108}$$

where the elements of $\boldsymbol{z}$ are given by:

$$z_{ph} = \int \mathrm{d}\boldsymbol{r}\, \Phi_{ph}(\boldsymbol{r}) z. \tag{2.109}$$

By comparing Eq. (2.108) with Eq. (2.98), we obtain the following expression:

$$\boldsymbol{z}\mathbf{S}^{-1/2}\boldsymbol{Z_n} = \Omega_n^{1/2}\langle\Psi_0|\hat{z}|\Psi_n\rangle. \tag{2.110}$$

Expressions for the x- and y-components are similar. Using Eq. (2.99), the oscillator strength of transition n can be obtained from the eigenvectors $\boldsymbol{Z_n}$ via

$$f_n = \frac{2}{3}\left(|\boldsymbol{x}\mathbf{S}^{-1/2}\boldsymbol{Z_n}|^2 + |\boldsymbol{y}\mathbf{S}^{-1/2}\boldsymbol{Z_n}|^2 + |\boldsymbol{z}\mathbf{S}^{-1/2}\boldsymbol{Z_n}|^2\right). \tag{2.111}$$

In this way, the excitation energies Ω_n and oscillator strengths f_n of the true system are extracted from the KS system via Eqs. (2.87) and (2.111).

IV. Assignment problem

Expressions for the excitation energies as well as the oscillator strengths have now been obtained. All that remains to be done in the last step, is to determine which excited Slater determinants appear in the expressions of the ESs. This is the subject of the so-called assignment problem.[94] We work in the second quantization, in which $\hat{a}_h$ and $\hat{a}_p^\dagger$ are annihilation and creation operators for particles in orbitals ϕ_h and ϕ_p, respectively. It can be proven that the coefficients c_{ph}^n of the singly excited Slater determinants in the expansion

$$|\Psi_n\rangle = \sum_{ph}^{f_h-f_p>0} c_{ph}^n \hat{a}_p^\dagger \hat{a}_h |\Phi_0\rangle \tag{2.112}$$

are given by

$$c_{ph}^n = \sqrt{\frac{\epsilon_p-\epsilon_h}{\Omega_n}}(\boldsymbol{Z_n})_{ph}. \tag{2.113}$$

As the proof would take us too far, we do not go into the details but refer the reader to specialized books.[94] Note that only singly excited

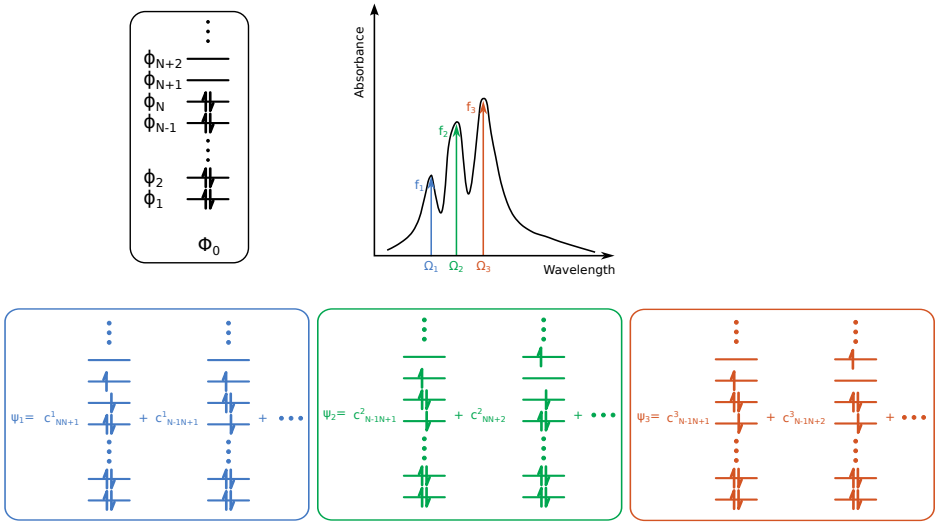

Figure 2.6: Schematic representation of the first three ESs obtained from a TDDFT calculation from the KS reference Φ_0. Each ES is characterized by the excitation energy Ω_n, oscillator strength f_n, and coefficients c_{ph}^n of the singly excited Slater determinants.

Slater determinants are taken into account. This is due to the adiabatic approximation, which will be discussed in detail in Section 2.2.6.

As such, the complete UV-Vis spectrum is defined. In Figure 2.6, an overview is given for an N-electron system. The GS of the non-interacting KS system is described by the Slater determinant Φ_0, which is constructed with single-particle orbitals ϕ_i as indicated in black. N of them are occupied, the others are virtual. In addition, three ESs, Ψ_1, Ψ_2, and Ψ_3, are shown, indicated in blue, green, and red. Each ES is characterized as follows. First of all, we have the excitation energy Ω_n, which yields the position of the peak. The excitation energies are obtained as the eigenvalues of the matrix equation given in Eq. (2.87). Second, the height of the peak is defined by the oscillator strength f_n, calculated using Eq. (2.111). To each ES, we fit a Gaussian function, positioned at the excitation energy and with a height equal to the oscillator strength. The width of the Gaussian function can be chosen arbitrarily. Finally, each ES is written as a linear combination of singly excited Slater determinants as shown in the bottom pane of Figure 2.6. The coefficients c_{ph}^n are determined using Eq. (2.113).

Efficient Davidson-type algorithms are generally used in the actual implementation of TDDFT in its LR regime to iteratively obtain a small

number of lowest excitation energies and corresponding transition vectors.[96–98] However, we will not go into the details here.

2.2.4 Spin in time-dependent density functional theory

Up until now, we did not focus on the spin of the electrons. Detailed discussions of the formal aspects of spin in GS DFT can be found in the literature.[74, 99–101] In restricted DFT, the spin-up or α and spin-down or β electrons have the same spatial orbitals, whereas in unrestricted DFT (UDFT) they are allowed to be different. LR TDDFT is most commonly applied in an explicitly spin-dependent formulation. As the generalization is for the most part straightforward, we will not go into details but only give some results.[102] The spin-dependent versions of Eqs. (2.28)-(2.30) are:

$$\left[-\frac{\nabla_i^2}{2} + v_{s\sigma}[n_\uparrow, n_\downarrow](\boldsymbol{r}, t)\right] \phi_{i\sigma}(\boldsymbol{r}, t) = i\frac{\partial}{\partial t}\phi_{i\sigma}(\boldsymbol{r}, t) \tag{2.114}$$

$$v_{s\sigma}[n_\uparrow, n_\downarrow](\boldsymbol{r}, t) = v_\sigma(\boldsymbol{r}, t) + \int \mathrm{d}\boldsymbol{r}' \frac{n(\boldsymbol{r}', t)}{|\boldsymbol{r} - \boldsymbol{r}'|} + v_{XC\sigma}[n_\uparrow, n_\downarrow](\boldsymbol{r}, t) \tag{2.115}$$

$$\begin{aligned} n(\boldsymbol{r}, t) &= \sum_{\sigma=\uparrow,\downarrow} n_\sigma(\boldsymbol{r}, t) \\ &= \sum_{\sigma=\uparrow,\downarrow} \sum_{i=1}^{N_\sigma} |\phi_{i\sigma}(\boldsymbol{r}, t)|^2. \end{aligned} \tag{2.116}$$

In a similar way, the LR equations are modified too. The details can be found in Ref. 43, but we only explicitly mention the spin-dependent XC kernel:

$$f_{XC,\sigma\sigma'}(\boldsymbol{r}, t, \boldsymbol{r}', t') = \frac{\delta v_{XC\sigma}[n_\uparrow, n_\downarrow](\boldsymbol{r}, t)}{\delta n_{\sigma'}(\boldsymbol{r}', t')}|_{n_{0\uparrow}(\boldsymbol{r}), n_{0\downarrow}(\boldsymbol{r})}. \tag{2.117}$$

Now, consider a spin-unpolarized electronic closed-shell GS, for which: $\phi_{ph\uparrow}(\boldsymbol{r}) = \phi_{ph\downarrow}(\boldsymbol{r}) = \phi_{ph}(\boldsymbol{r})$ and $\omega_{ph\uparrow} = \omega_{ph\downarrow} = \omega_{ph}$. Furthermore, with the following definitions

$$\begin{aligned} X_{ph}^{\pm} &= X_{ph\uparrow} \pm X_{ph\downarrow} \\ Y_{ph}^{\pm} &= Y_{ph\uparrow} \pm Y_{ph\downarrow} \\ L_{ph,p'h'}^{\pm} &= \delta_{pp'}\delta_{hh'}\omega_{p'h'} + M_{ph\uparrow,p'h'\uparrow} \pm M_{ph\uparrow,p'h'\downarrow} \\ M_{ph,p'h'}^{\pm} &= M_{ph\uparrow,p'h'\uparrow} \pm M_{ph\uparrow,p'h'\downarrow} \\ f_{XC}^{(1)}(\boldsymbol{r}, \boldsymbol{r}', \omega) &= \frac{1}{2}\left[f_{XC\uparrow\uparrow}(\boldsymbol{r}, \boldsymbol{r}', \omega) + f_{XC\uparrow\downarrow}(\boldsymbol{r}, \boldsymbol{r}', \omega)\right] \\ f_{XC}^{(2)}(\boldsymbol{r}, \boldsymbol{r}', \omega) &= \frac{1}{2}\left[f_{XC\uparrow\uparrow(\boldsymbol{r},\boldsymbol{r}',\omega)} - f_{XC\uparrow\downarrow(\boldsymbol{r},\boldsymbol{r}',\omega)}\right] \end{aligned} \tag{2.118}$$

and by using that $f_{XC\uparrow\uparrow} = f_{XC\downarrow\downarrow}$ and $f_{XC\uparrow\downarrow} = f_{XC\downarrow\uparrow}$ for spin-unpolarized systems, the eigenvalue equations are decoupled in two independent eigenvalue equations:

$$\begin{pmatrix} \mathbf{L^{\pm}} & \mathbf{M^{\pm}} \\ \mathbf{M^{\pm}} & \mathbf{L^{\pm}} \end{pmatrix} \begin{pmatrix} \mathbf{X^{\pm}} \\ \mathbf{Y^{\pm}} \end{pmatrix} = \Omega_{\pm} \begin{pmatrix} \mathbf{-1} & \mathbf{0} \\ \mathbf{0} & \mathbf{1} \end{pmatrix} \begin{pmatrix} \mathbf{X^{\pm}} \\ \mathbf{Y^{\pm}} \end{pmatrix}, \tag{2.119}$$

with

$$\begin{aligned} M^{+}_{ph,p'h'} &= 2 \int \mathrm{d}\boldsymbol{r}\mathrm{d}\boldsymbol{r'} \Phi^{*}_{ph}(\boldsymbol{r}) \left[\frac{1}{|\boldsymbol{r} - \boldsymbol{r'}|} + f^{(1)}_{XC}(\boldsymbol{r}, \boldsymbol{r'}, \omega) \right] \Phi_{p'h'}(\boldsymbol{r'}) \\ M^{-}_{ph,p'h'} &= 2 \int \mathrm{d}\boldsymbol{r}\mathrm{d}\boldsymbol{r'} \Phi^{*}_{ph}(\boldsymbol{r}) f^{(2)}_{XC}(\boldsymbol{r}, \boldsymbol{r'}, \omega) \Phi_{p'h'}(\boldsymbol{r'}) \end{aligned} \tag{2.120}$$

and similarly for $L^{\pm}_{ph,p'h'}$.

Two independent sets of solutions $\Omega_{\pm}$ are obtained, which correspond to the singlet and triplet excitation energies of the system. To clarify this, let us consider the two orbital two electron model, presented in Figure 2.7. The GS is indicated in blue. The single excitations from this reference form a singlet and a triplet. On the one hand, the former is obtained in TDDFT as the singlet coupled single excitation, which is indicated with the upper arrow. For this state: $n_{1\uparrow}(\boldsymbol{r}, \Omega_{+}) = -n_{1\downarrow}(\boldsymbol{r}, \Omega_{+})$, *i.e.*, the response of the system is such that the spin-up and spin-down eigenmodes are out of phase. On the other hand, the triplet consists of the triplet coupled single excitation, *i.e.,* the first configuration indicated by the lower arrow, and two other configurations which are obtained by a spin-flip (SF) and are indicated in red. SF transitions are beyond the formalism presented here but will be addressed in Section 2.2.6. For the triplet coupled single excitation: $n_{1\uparrow}(\boldsymbol{r}, \Omega_{-}) = n_{1\downarrow}(\boldsymbol{r}, \Omega_{-})$, *i.e.*, the response of the system is such that the spin-up and spin-down eigenmodes are in phase. In this way, we demonstrated how, starting from a closed-shell GS, single excitations can be coupled to singlet and triplet configurations, depending on the relative phase of the spin-up and spin-down eigenmodes. These results are used in Chapter 4 in which triplet ESs, playing an important role in photocatalytic processes, will be calculated.

2.2.5 Approximations in time-dependent density functional theory

In order to perform TDDFT calculations, various approximations are needed. As stated in Section 2.1.2, the exact expression of the GS XC potential is not known. A wide variety of approximate XC functionals has been presented

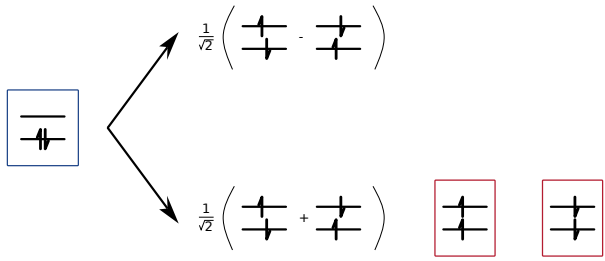

Figure 2.7: Schematic representation of the two orbital two electron model. The GS is indicated in blue. There are four single ESs from this reference, forming a singlet and a triplet. Two of the single excitations couple to the singlet coupled single excitation (upper arrow). The two single excitations can also couple to the triplet coupled single excitation (first configuration lower arrow). Together with two additional configurations which require a spin-flip and are indicated in red, they form the triplet.

throughout the years and the search for better ones is still a hot topic today. Recently, an extensive overview and benchmark has been presented in Ref. 103. Functionals are ordered in different rungs on Jacob's ladder as shown in Figure 2.8.[82] One starts at the Hartree level of theory at the bottom and climbs upwards toward chemical accuracy. The computational complexity and cost increase the higher the functional is situated on the ladder as more variables are taken into account. In principle, this should also imply a higher accuracy.

Functionals based on the local density approximation (LDA) are situated at the lowest rung of Jacob's ladder. In generalized gradient approximations (GGA) functionals, the gradient of the density is taken into account too, making them semi-local. Some examples used in this work are BLYP,[104] BP86,[105] and PBE.[106] In meta-GGA functionals, the second derivative of the density has been included as well. The performance of M06L[108] and MN15L[107] has been tested. Hybrid functionals are GGA functionals in which parts of Hartree-Fock (HF) exchange are explicitly included. Bauernschmitt and Ahlrichs have introduced hybrid functionals in TDDFT.[119] We studied O3LYP,[110], B3LYP,[104, 109] X3LYP,[111] and PBE0.[106] Similarly, meta-hybrid functionals are meta-GGA functionals in which some HF exchange is taken into account. Examples considered in this work are M06[112] TPSSh,[113, 114] and MN15.[115] Finally, also some range-separated hybrid (RSH) functionals have been assessed: CAM-B3LYP,[116] ωB97x,[117] and LC-ωHPBE.[118] They use a growing fraction of exact exchange as the interelectronic distance increases,

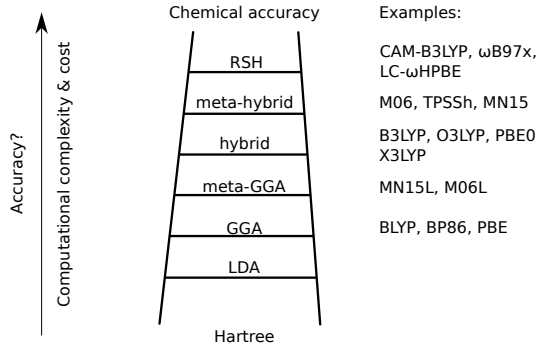

Figure 2.8: Jacob's ladder with XC functionals: the local density approximation or LDA (first rung), the generalized gradient approximation or GGA (second rung), the meta-generalized gradient approximation or meta-GGA (third rung), the hybrid (fourth rung), the meta-hybrid (fifth rung), and the range-separated hybrid or RSH (sixth rung). The XC functionals that were used in this work are indicated on the ladder: BLYP,[104] BP86,[105] PBE,[106] MN15L,[107] M06L,[108] B3LYP,[104, 109] O3LYP,[110] PBE0,[106] X3LYP,[111] M06,[112] TPSSh,[113, 114] MN15,[115] CAM-B3LYP,[116] ωB97x,[117] and LC-ωHPBE.[118]

giving a long-range correction to the original DFT scheme. The performance of the functionals listed above will be tested in Chapter 4 and Chapter 5.

In addition, when TD phenomena are studied, extra approximations need to be introduced for the XC kernel f_{XC} given in Eq. (2.60). In practice, every calculation includes the adiabatic approximation, in which we neglect the history-dependence of $v_{XC}[n](\boldsymbol{r}, t)$ and assume that it reacts instantaneously to temporal changes in the density. We take the XC potential from GS DFT and plug in the TD density $n(\boldsymbol{r}, t)$. The functional-dependence of v_{XC} at time t is only on the density at the very same time, making f_{XC} no longer frequency-dependent. In practice, all regular TDDFT calculations are performed in the adiabatic approximation, including the applications in Chapter 4 and Chapter 5.

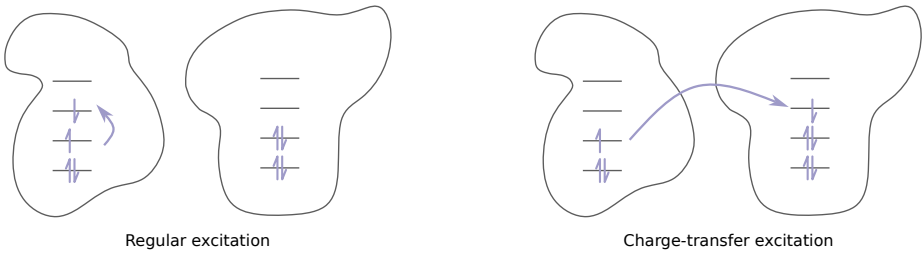

Figure 2.9: Schematic representation of a regular (left) and a charge-transfer (right) excitation. Figure adapted from Ref. 88 with permission of Oxford Publishing Limited, copyright 2012.

2.2.6 Shortcomings of time-dependent density functional theory

We conclude this Chapter with a section in which some shortcomings of adiabatic TDDFT are discussed.[120–122] Hereby, we focus on challenges which will be addressed in Chapter 4 and Chapter 5. We start with a description of charge-transfer (CT) excitations, which will be encountered in Chapter 4 when studying MLCT excitations. This is followed by a discussion of double excitations, which are frequently observed in the d-d spectra of TMCs as will be shown in Chapter 5.

I. Charge-transfer excitations

The dominant particle and hole contributions in CT excitations have probability densities situated in separated parts of the system.[43] As such, a donor and acceptor can be identified. This is schematically presented in the right pane of Figure 2.9.

In Chapter 4, we mainly focus on the appearance of CT ghost states energetically far below the real ESs,[123, 124] which could lead to a wrong interpretation of the spectroscopic behavior. Therefore, we use the Mulliken averaged configuration (M_{AC}) index of Ciofini and co-workers to spot ghost states. This diagnostic index, which discerns unrealistic CT produced by the limitations of the level of theory, is a generalization of the Mulliken estimation of transition energy for CT excitations. From this, we are ensured that our TDDFT results are reliable. Furthermore, it is also shown that for TMCs, the CT problem is more prominent for inter-ligand excitations. The transitions of our interest are between the TM and the ligands and are hence usually described well.[66]

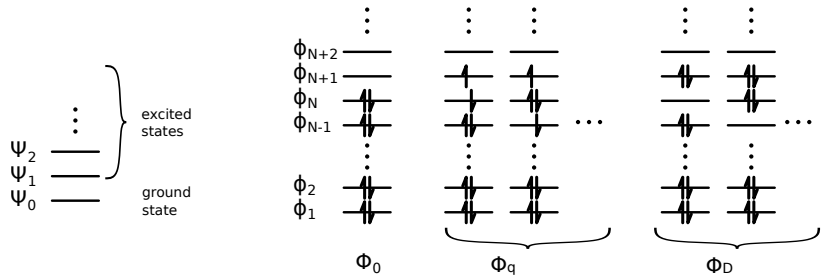

Figure 2.10: Schematic representation of the GS and ESs of an N-electron system in the many-body picture (left) and the single-particle orbital picture (right), where two examples of single and double ESs are given.

II. Double excitations

CT excitations are of minor importance when studying d-d transitions. In contrast, double excitations are encountered as will be shown in Chapter 5. Therefore, we discuss how double excitations are treated in adiabatic TDDFT and give a brief overview of techniques developed to cope with them in the remainder of this Chapter.

In order to define double excitations, let us take a look at an N-electron system with GS Ψ_0 and ESs Ψ_i, as shown in the left pane of Figure 2.10. In the KS single-particle picture, the GS of this system is described by a single Slater determinant Φ_0 built with single-particle orbitals ϕ_i of which N are occupied. In singly excited Slater determinants, one electron is transferred from an occupied orbital ϕ_i into a virtual one ϕ_a. The set of all single excitations out of Φ_0 is denoted by Φ_q, $q = i \rightarrow a$. Similarly, a doubly excited Slater determinant is characterized by two electrons which are promoted out of occupied orbitals ϕ_i and ϕ_j into virtual ones ϕ_a and ϕ_b. These are labeled with Φ_D, where $D = (i \rightarrow a, j \rightarrow b)$. Analogous definitions apply for triple ESs *etc.*

The true GS and ESs of the system can be expanded in a complete set of Slater determinants:

$$\Psi_n = c_{n0}\Phi_0 + \sum_q c_{nq}\Phi_q + \sum_D c_{nD}\Phi_D + \cdots \qquad n = 0, 1, 2, ... \quad (2.121)$$

The term single excitation is a short-hand for a state of single-excitation character and is characterized by an expansion dominated by singly excited Slater determinants. Double excitations are defined analogously.

Clearly, this classification depends on the chosen non-interacting reference, but once this is fixed, it has been shown that the labeling can be done unambiguously.[125, 126]

The fact that double excitations are not treated in adiabatic TDDFT can be made clearer by simple counting arguments.[88, 94, 120, 127–129] First, we apply Eq. (2.53) for the non-interacting KS system. The numerator involves matrix elements in which the one-body density operator is sandwiched between the ground and ES Slater determinants. As these matrix elements cannot connect states differing by more than one orbital, the numerator will only yield non-zero contributions for the singly excited Slater determinants Φ_q. This is also visible in Eq. (2.59). Indeed, a double-excitation in a non-interacting system means two excited electrons, and requires two photons. This process is quadratic in the perturbation strength, and therefore beyond LR. It was already shown in Figure 2.6 that in adiabatic TDDFT, the ESs are obtained as a linear combination of singly excited Slater determinants and no higher order ones are present. Now, we apply Eq. (2.53) to the true many-body system of which the states can be expanded via Eq. (2.121) as linear combinations of the GS, singly, doubly, and higher excited Slater determinants. The poles of the true response function are at the true excitation energies as the numerator remains finite due to the mixed nature of the states. Within the adiabatic approximation, there are clearly more poles in the interacting response function than in the KS one. Now, we derived in Section 2.2.3 that the true response function is obtained from the KS one through the Dyson-like equation given in Eq. (2.64). The only way in which extra poles can be introduced in the KS response function is when f_{XC} is frequency-dependent. As a result, excitations with mainly double excitation character are not present in the adiabatic approximation.

Double and higher excitations appear in spectra due to mixing with single excitations. Consider the situation of a KS single excitation Φ_q with excitation energy ω_q, as shown in red in the left pane of Figure 2.11. This state is close to a double excitation Φ_D with excitation energy ω_D, presented with a dashed line, and well separated from all other ESs. Let the true ESs Ψ_1 and Ψ_2 near this frequency be mixtures of the single and double ones, such that as the electron-electron interaction strength approaches zero:

$$\begin{aligned} \Psi_1 &= \sqrt{1-m^2}\Phi_D - m\Phi_q \\ \Psi_2 &= m\Phi_D + \sqrt{1-m^2}\Phi_q, \end{aligned} \tag{2.122}$$

where $0 < m < 1$ determines how much single/double excitation character the true excitations have. For $m^2 > 1/2$, we say that $\Psi_{1/2}$ is predominantly

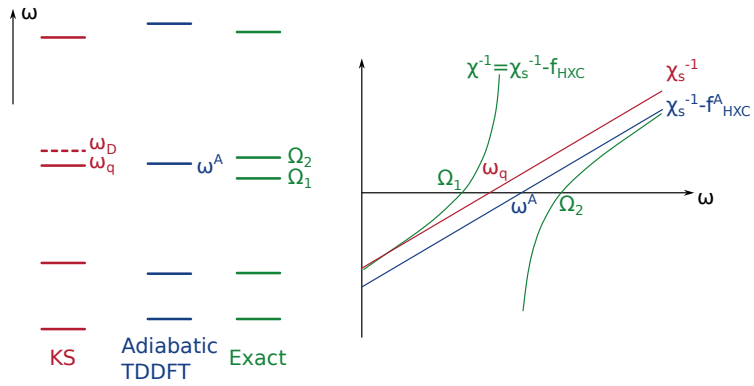

Figure 2.11: Schematic representation of how a frequency-dependent kernel generates an extra pole. Figure adapted from Ref. 128 with permission of AIP Publishing, copyright (2004).

a single/double excitation. The true excitation energies are presented in green in Figure 2.11.

The density-density response functions are plotted in the right pane of Figure 2.11. The true response function has two roots at Ω_1 and Ω_2. The KS response function has a single pole at ω_q. In adiabatic TDDFT, this root is shifted toward ω^A by the adiabatic XC kernel, indicated in blue.

An expression for the exact f_{HXC} at frequencies near ω_q when a double excitation interacts with a single excitation, has been derived in Ref. 127. For states that include only a small fraction of double excitations, adiabatic TDDFT performs well, but as the double excitation component increases, it begins to deviate. For example, if the two levels are 50:50 mixtures of single and double excitations, it gives one energy approximately halfway between the true energies. If the true energies are close, then it will appear to give a good estimate for the state which has significant double excitation character, just because it is close to the single-dominated state. However, when there is strong mixing and the levels are not close to each other, it does not give accurate results for either excitation.[128]

To conclude this section, some methods designed to cope with double ESs are mentioned. For a complete overview, the reader is referred to Ref. 127.

TDDFT is, in general, based on a closed-shell singlet GS, indicated in blue in Figure 2.12. The double ES, shown in yellow, can not be reached in

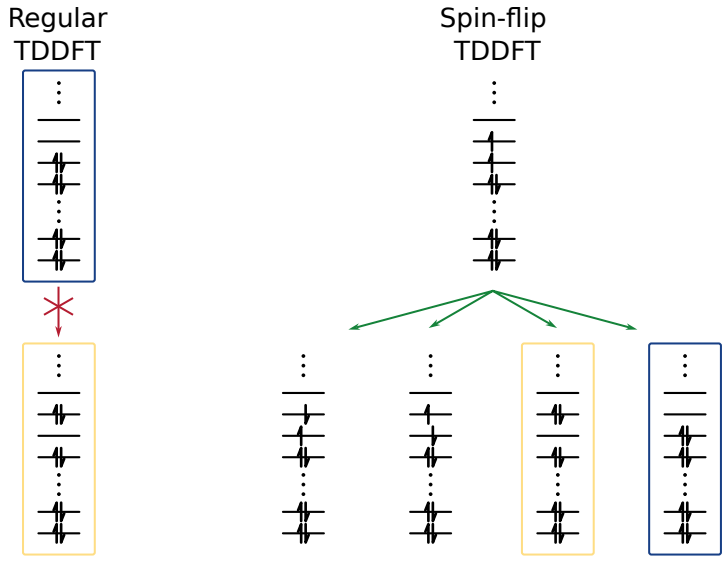

Figure 2.12: In regular TDDFT, the double ES indicated in yellow cannot be reached starting from the GS reference. In SF-TDDFT, the triplet ES with maximal spin is taken as a reference, from which the double ES is calculated via a single spin-flip excitation.

adiabatic TDDFT. In contrast, spin-flip TDDFT (SF-TDDFT) starts from an unrestricted KS calculation of a triplet state in which both unpaired electrons are spin-up.[130, 130–134] From this reference, excitations and de-excitations are determined in which an electron is transferred from an α-orbital to a β-orbital. As such, the singlet GS is retrieved as well as the double ES, which was not reachable in regular TDDFT. Two additional states are observed, which are neither pure singlets, nor pure triplets, as shown in the right pane of Figure 2.12. SF-TDDFT has already been used to for example determine spin-forbidden d-d excitations in TMCs.[135]

Some other promising methods to treat double excitations are constrained variational DFT[136, 137] and dressed TDDFT, in which *ad hoc* many-body corrections are applied to TDDFT.[128] However, these techniques are not widely used yet.

In Chapter 5, LFDFT will be used to calculate double excitations. This technique has a completely different origin than TDDFT and will be discussed in Chapter 3.

3

Coordination Chemistry

As stated in Chapter 1, transition metal complexes (TMCs), in which a number of ligands is attached to one or multiple TMs, will play a major role in Chapter 4 and Chapter 5. Coordination chemistry is the study of these TMCs or coordination clusters. The foundation for modern coordination chemistry has been laid by Werner, the first inorganic chemist to win the Nobel Prize in Chemistry in 1913 for proposing the octahedral configuration of TMCs.[138]

We start with an introduction of the building blocks of TMCs. This is followed by a section devoted to symmetry, a concept which is indispensable in coordination chemistry and will be very useful in Chapter 5. A short introduction to symmetry operations and elements, point groups, and character tables is given. Afterwards, the influence of the ligands on the TM is studied and we will explain how to construct Tanabe-Sugano diagrams, in which the ES energies are plotted as a function of the ligand field splitting. Furthermore, we also show why these diagrams are so helpful for the description of ESs in TMCs. We end this Chapter with a discussion of different electronic structure theories used to describe TMCs, starting with historically important techniques, such as CFT and LFT, and concluding with the more recently proposed LFDFT. These methods are applied in Chapter 5 to study the TMCs relevant for the nucleation process of ZIFs.

3.1 Transition metal complexes

In this section, the building blocks of TMCs, namely TMs and ligands, are presented.

3.1.1 d-orbitals in transition metals

TMs are characterized by their partially filled d-orbitals. These complex orbitals are solutions to the Schrödinger equation and can be represented pictorially by fixing the radial part and by plotting the angular-dependence of the wave function, as shown in Figure 3.1.[139, 140] More information about the spherical harmonics describing the angular part of the wave function is given in Section 3.4.1. The plots show regions of space with a high probability of finding the electron and the signs of different lobes, indicated by a difference in color intensity, reveal the relative phases of the wave functions. All orbitals have axial symmetry around the z-axis. d_0 is concentrated along this axis and the pairs $d_{\pm 1/2}$ form rings around it, where $\pm$ indicates that the two members of the pair only differ in the clockwise/counter-clockwise rotation of the electron. The $d_{\pm 2}$-orbitals are located in the xy-plane.

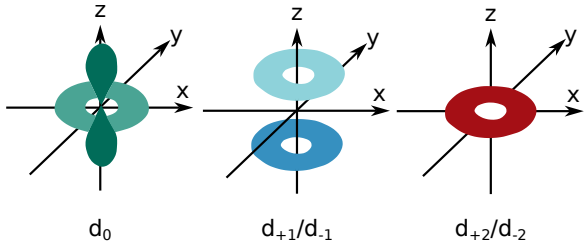

Figure 3.1: Angular dependence of the electron density distribution corresponding to the complex d-orbitals. Figure adapted from Ref. 139 with permission of Wiley, copyright (1999).

These complex d-orbitals are usually employed for actual calculations. However, in order to visualize the relationships among the different orbitals, it is more convenient to express them explicitly in terms of Cartesian coordinates. The real d-orbitals are then obtained as linear combinations of the complex

d-orbitals:

$$\begin{aligned} d_{z^2} &= d_0 \\ d_{x^2-y^2} &= \frac{1}{\sqrt{2}}\left[d_2 + d_{-2}\right] \\ d_{yz} &= -\frac{i}{\sqrt{2}}\left[d_1 + d_{-1}\right] \\ d_{xz} &= \frac{1}{\sqrt{2}}\left[d_1 - d_{-1}\right] \\ d_{xy} &= -\frac{i}{\sqrt{2}}\left[d_2 - d_{-2}\right]. \end{aligned} \tag{3.1}$$

They are shown in Figure 3.2. Two of them, $d_{x^2-y^2}$ and d_{z^2}, have lobes along the coordinate axes, whereas the others, d_{xy}, d_{xz}, and d_{yz}, have lobes oriented in between the axes. As will be shown later, the orientation of these lobes will play an important role when considering the bonding with ligands to form TMCs.

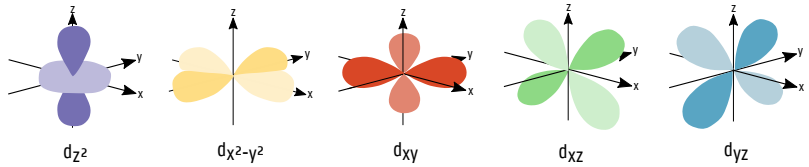

Figure 3.2: Angular dependence of the electron density distribution corresponding to the real d-orbitals. Figure adapted from Ref. 139 with permission of Wiley, copyright (1999).

Due to the partial occupation of the d-orbitals, there might be degeneracies in the GS and/or ESs of TMCs. In these cases, not only dynamic, but also non-dynamic correlation effects become important. Before specifying these two types of correlation, we first introduce the following definition for the total correlation energy E_{corr}:

$$E_{corr} = E_{exact} - E_{HF}, \tag{3.2}$$

with E_{exact} the exact non-relativistic energy and E_{HF} the HF energy calculated in a complete basis.[141] The correlation energy refers to all the deficiencies of the HF approach and can be divided into two contributions. First, we consider the dynamic or weak correlation. It has its origin in the fact that an electron does not instantaneously interact with the other electrons, but rather via the mean field created by them. Classically speaking, the movement of an electron is such that locations close to the instantaneous positions of the other electrons are avoided. These are

short-range, instantaneous effects.[142, 143] Besides this, there is also static or strong correlation due to the fact that the wave function is approximated as a single Slater determinant in HF. These are long-range effects.[142, 143]

Both types of correlation can be taken into account by adding additional excited Slater determinants ϕ_i with weight c_i to the HF Slater determinant ϕ_{HF}:

$$\Psi = c_{HF}\phi_{HF} + \sum_i c_i\phi_i, \tag{3.3}$$

where c_{HF} is assumed to be close to one. On the one hand, systems with significant dynamic correlation can be described by taking into account a large number of ϕ_i, each having only a limited contribution. On the other hand, the description of systems containing static correlation can be improved by adding only a few excited determinants ϕ_i with weights close to c_{HF}.

3.1.2 Ligands

A ligand is an atom, ion, or molecule that binds to one or multiple TM(s) to form a TMC. The bond is called a coordination or dative bond and is a special kind of covalent bond in which two electrons derived from the same atom are shared. In general, these electrons originate from the ligand.

Ligands can occupy one or more coordination sites and are called mono- and polydentate respectively. In Chapter 4, we will encounter examples of both mono- and bidentate ligands, schematically shown in Figure 3.3.

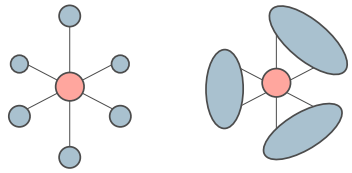

Figure 3.3: Schematic representation of mono- (left) and bidentate (right) ligands in an octahedral TMC.

Later in this Chapter, we will demonstrate that the ligands generate a so-called ligand field (LF) when they approach and bond to the TM, resulting in a splitting of the degenerate d-orbitals. Some of the d-orbitals gain energy and others lose energy. The appearance of the splitting depends on the coordination symmetry and the extent to which the d-orbitals separate is influenced by both the TM and the ligands. The spectrochemical series orders the ligands according to their ligand strength and thus to their ability to split

the d-orbitals, as shown in Figure 3.4.[144] This classification was first proposed in 1938 based on the results of absorption spectra of cobalt complexes.[145] Negatively charged atomic ligands such as I^-, Br^-, Cl^-, and F^- possess a smaller LF splitting than neutral molecules like H_2O, NH_3, pyridine, and 2,2'-bipyridine, which on their turn are weaker than CN^- and CO, being the strongest ligands.

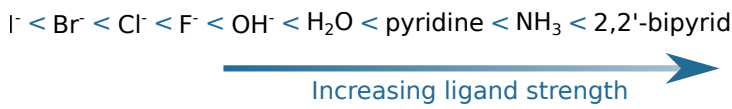

Figure 3.4: Visualization of the spectrochemical series.

The order of the spectrochemical series is linked to the donor or acceptor character of the ligands. Some ligands, like for example NH_3, are σ-donors only and have no orbitals of appropriate symmetry for π-interactions. On the one hand, ligands with vacant p-orbitals can be π-acceptors. When the TM possesses d-orbitals of suitable energy, electron density can be transferred back from the TM to the ligands. This is also called π back-bonding and results in a stronger bond and increased LF splitting. Examples include CN^- and CO. On the other hand, ligands containing occupied p-orbitals are potentially π-donors. Along with the σ-electrons, π-electrons are carried from the ligand to the TM. Examples are the halide ligands, H_2O, and OH^-, which are characterized by a smaller LF splitting. As such, ligands are arranged in the spectroscopic series according to their strong/weak field character which corresponds to π-acceptors/π-donors, respectively. We will further elaborate on the different types of bonding in Section 3.4.2.

Different spin-states are possible in TMCs with four up to seven d-electrons due to the (partial) lifting of the degeneracy of the d-orbitals. In TMCs with weak field ligands, the d-orbital splitting is smaller than the pairing energy, making it more advantageous to place an electron in the higher lying orbital set and forming a high-spin (HS) complex. However, when the d-orbital splitting is larger than the pairing energy, usually the case in TMCs with strong field ligands, low-spin (LS) complexes are more stable. The relative energies of HS and LS complexes are typically small, making it, even today, a non-trivial task to calculate the spin-state energies accurately.[146, 147]

While the variable spin, oxidation state, and coordination environment make TMCs very tunable for achieving target properties, it makes them also very challenging to describe and model.[148] The specific symmetry of

the complex has a large influence on its electronic properties. Therefore, an introduction to symmetry concepts relevant for the study of TMCs is given in the next section.

3.2 Symmetry

Symmetry is not only omnipresent at the macroscopic scale, just think of flowers, snowflakes, or leaves, but it also shows up at the molecular level. Some examples of highly symmetric molecules include buckminsterfullerene or buckyball, which is composed of 60 carbon atoms and resembles a soccer ball, cubane, containing eight hydrogen-bonded carbon atoms situated at the corners of a cube, and keplerates,[149] in which some of the metals lie on the vertices of a Platonic solid and others on the vertices of an Archimedian solid.

The underlying mathematical theory of symmetry is group theory.[150] Its introduction in chemical models is extremely useful as it makes the mathematical procedure less complicated. Analyzing the symmetry of molecules allows one for example to predict vibrational spectra, understand chemical bonding, interpret electronic excitation spectra, and determine the optical activity in a very efficient way.[43]

In this work, symmetry will be a valuable tool in the construction of MO diagrams and the interpretation of electronic spectra of TMCs. First, we discuss the symmetry operations and elements. We then describe how molecular systems can be classified on the basis of the number and kind of symmetry elements they possess. The symmetry of molecules is described via point groups, which are mathematical groups of symmetry operations with a fixed point in common. Space groups are used to describe solids and are generated by combining a Bravais lattice with each of the crystallographic point groups corresponding to it.[150] We will not go further into the details of space groups, as in this work only complexes are considered. Finally, the character tables of different point groups will be studied.

3.2.1 Symmetry operations and elements

Symmetry is defined in terms of symmetry operations. For molecules, point symmetry operations are used, for which at least one point remains stationary. The five fundamental operations include the identity operation, rotation, reflection, inversion, and improper rotation. It is common to denote

the symmetry operations with Schönflies symbols.[150] With every symmetry operation, a symmetry element is associated. This is a point, line or plane around which the symmetry operation is carried out. The five fundamental symmetry operations are listed below.

1. The identity operation E causes no change in the molecule but must be included for mathematical completeness. It is characteristic of every molecule, even if there is no other symmetry.

2. C_n represents a proper rotation of $\frac{2\pi}{n}$ radians about a rotation axis, which is the associated symmetry element. In molecules with more than one rotation axis, the C_n axis with the largest value of n is the principal axis. Multiple principal axes are distinguished by primes. An additional rule is that an axis in the same position as the principal axis gets the least number of primes. An example of a C_6 rotation is given in the first pane of Figure 3.5.

3. The reflection operation σ moves each point perpendicularly through a mirror plane to an equal distance at the other side. When the mirror plane is perpendicular with respect to an axis of highest symmetry, it is labeled with the subscript h. The subscript v states that the mirror plane contains the principal axis. The special case when the mirror plane bisects the angle between a pair of twofold rotational axes, is called a dihedral mirror plane and is denoted by σ_d. Convention dictates that the subscript h takes precedence over d whenever both are applicable. The effect of a reflection operation σ is shown in the second pane of Figure 3.5.

4. During the inversion i, each point moves through the center of the molecule to a place opposite to the original position and as far from the central point as where it started. In the third pane of Figure 3.5, an inversion i is shown.

5. The rotation-reflection operation or improper rotation S_n requires a rotation of $\frac{2\pi}{n}$ radians followed by a reflection through a plane perpendicular to the rotation axis. An improper S_6 rotation is visualized in the last pane of Figure 3.5.

In order to contain a given symmetry element, the molecule obtained after the symmetry operation must be indistinguishable from the initial configuration. In the following, we will investigate the symmetry elements for octahedral and tetrahedral structures which will play a substantial role in Chapter 5. Also trigonal bipyramids and square pyramids will be important

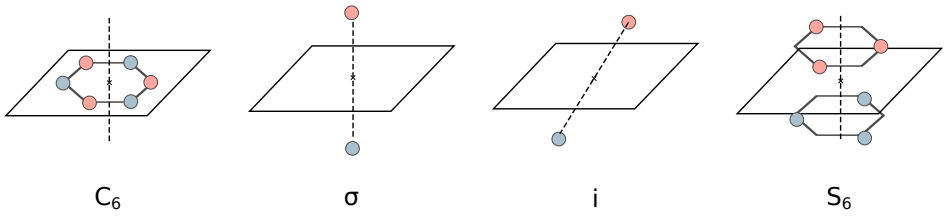

Figure 3.5: Visualization of a proper C_6 rotation, reflection operation σ, inversion i, and improper S_6 rotation. The structures before and after the operation are indicated in pink and blue, respectively.

for which the symmetry elements are visualized in Appendix B.2.

The symmetry elements of octahedrons are shown in Figure 3.6. An octahedron contains 4 C_3 axes, coinciding with the body diagonals as they go through the center of two opposite triangular faces. The structure remains unaltered when rotated over plus or minus 120° around one of these axes. This yields thus in 8 C_3 symmetry elements. Furthermore, there are 3 C_4 axes, piercing opposite vertices. A rotation around one of these axes over plus or minus 90° yields an unaltered structure. Moreover, a rotation over 180° also results in the same system. Therefore the 3 C_4 axes coincide with 3 C_2 axes. This brings forth 6 C_4 and 3 C_2 symmetry elements. Additionally, 6 C_2' axes occur, which go through two opposite edges and generate 6 C_2' symmetry elements. There are 8 S_6, 3 σ_h, 6 S_4, 6 σ_d symmetry elements too, as well as the inversion operation i. The S_6 axes coincide with the C_3 axes. The structure remains unaltered after a rotation over 60° followed by a reflection in a perpendicular plane. The axes of the S_4 operation, which consists of a rotation over 90° followed by a reflection in a mirror plane perpendicular to the rotation axis, coincide with the C_4 axes. For the S_4 operations, both the 90° rotation and reflection exist independently as C_4 and σ_h, respectively. However, this is not the case for the S_6 operations.

The symmetry elements of a tetrahedron are shown in Figure 3.7. It has 4 C_3 axes which pass through a vertex and the opposite triangular face. A rotation over plus or minus 120° leaves the system unaltered, giving rise to 8 C_3 symmetry elements. There are 3 C_2 axes coinciding with the S_4 axes and going through the middle of two opposite edges. This results in 3 C_2 and 6 S_4 symmetry elements. Furthermore, there are 3 σ_d mirror planes, which contain one edge, thereby bisecting the tetrahedron. This yields 6 σ_d symmetry elements.

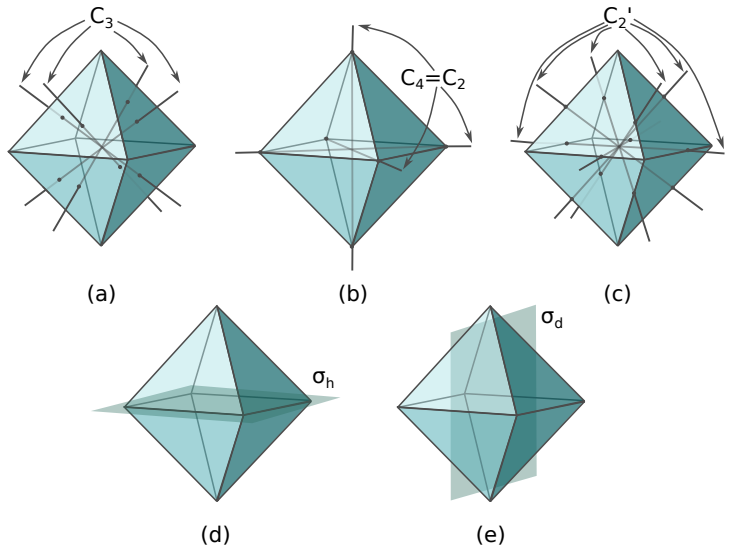

Figure 3.6: Visualization of the symmetry elements of an octahedron. The first line contains the rotational symmetry elements (a): 4 C_3 axes. (b): 3 C_4 axes coinciding with 3 C_2 axes. (c): 6 C_2' axes. The mirror planes are visualized in the second line (d): One of three σ_h mirror planes. (e): One of six σ_d mirror planes.

3.2.2 Point groups and character tables

The complete set of symmetry elements possessed by an object defines its point group. A group is an algebraic structure formed by a set and a binary operation, which need to fulfill the following conditions: the operation must be closed and associative, the set must contain an identity element, and every element of the set needs to have an inverse. Point groups are groups of symmetry operations endowed with the group operation of composition. The total number of symmetry operations in a group is called the order of the group.

First, we have the high-symmetry point groups derived from Platonic solids, being the tetrahedron, with tetrahedral T_d symmetry, octahedron and cube, belonging to the octahedral O_h point group, and dodecahedron and icosahedron, with icosahedral I_h symmetry. In view of the systems studied in Chapter 5, the following point groups are also very important. Dihedral point groups D_{nh} and D_{nd} have n C_2 axes perpendicular to a principal axis. The main difference between both is that the former contains a σ_h plane. The rotational point group C_{nv} possesses, in addition to vertical mirror planes, a principal axis but no perpendicular C_2 axes. The S_{2n} point

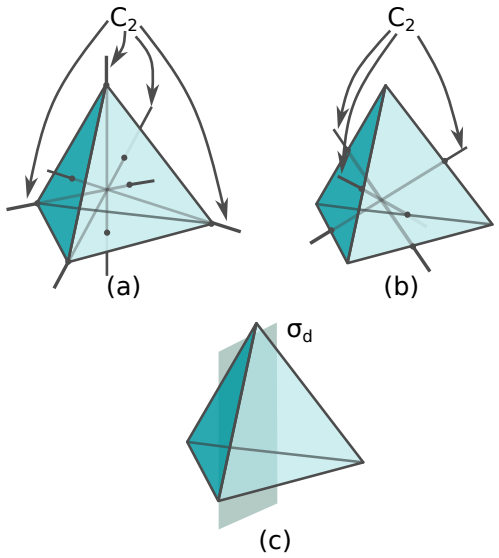

Figure 3.7: Visualization of the symmetry elements of a tetrahedron. The first line contains the rotational symmetry elements (a): 8 C_3 axes. (b): 3 C_2 axes. The mirror planes are visualized in the second line (c): One of six σ_d mirror planes.

group contains a principal axis and a S_{2n} axis, but no perpendicular C_2 axes and no mirror planes. In contrast to O_h, the T_h point group does not have C_4 and C_2' axes and the corresponding improper symmetry elements.

Hereafter some concepts to represent groups via character tables are summarized. Especially those important for this work are highlighted and illustrated for the O_h and T_d point groups, which are frequently encountered for TMCs. More general explanations on symmetry and point groups can be found in dedicated textbooks. [43, 150, 151]

Information about the symmetry aspects of point groups is summarized in character tables, which are presented in Tables 3.1 and 3.2 for O_h and T_d symmetry, respectively. The main part of the table consists of characters, showing how an object or mathematical function responds to the symmetry operation. Each character can adopt a positive or negative value, depending on the symmetric or anti-symmetric behavior of the system with respect to the specific symmetry operation. Symmetry operations with identical characters are grouped in classes, forming the columns of the character table. Each row corresponds to a particular irreducible representation, which is, broadly speaking, a fundamental type of symmetry in the group.

The label in the first column is the symmetry species of that irreducible representation, which is identified as follows. First of all, A, E, and T designate the degeneracy or the dimension of the representation, indicating singly, doubly, and triply degenerate states, respectively. Next, the subscripts g and u reveal whether the system is symmetric (*gerade*) or anti-symmetric (*ungerade*) with respect to the inversion operator. Finally, symmetry or anti-symmetry with respect to a rotation around the C_4/S_4 axis for the O_h/T_d point group is specified by the subscripts 1 and 2.

Besides octahedral and tetrahedral complexes, square pyramidal and trigonal bipyramidal structures with C_{4v} and D_{3h} symmetry, respectively, will be studied in Chapter 5 too. Their character tables are shown in Appendix B.3.

We would also like to mention that deviations from the ideal symmetry can occur due to for example Jahn-Teller distortions, extended ligands, *etc.* Therefore, additional tables for the T_h, D_{3d}, D_{2d}, D_{2h}, C_{2v}, and S_6 point groups are listed in Appendix B.3, for which extra labels are encountered. Similar to A, B indicates single degenerate states, the difference being in the symmetry with respect to a rotation around the principal axis: A is symmetric, whereas B is anti-symmetric. Finally, prime and double prime indicate symmetry and anti-symmetry with respect to a reflection in the σ_h plane. For complexes possessing little symmetry, we can determine whether the structure is closer to one symmetry or another by calculating the continuous shape measures (CShMs) via the program SHAPE.[152, 153] CShMs are defined as the distances to ideal reference polyhedra, independent of the size and orientation. The coordinates of the TM along with these of the atoms with which the ligands are anchored to it are provided to SHAPE, which then evaluates the CShMs based on the algorithm described by Pinsky and Avnir.[154] The smaller the CShM, the closer the complex is to that symmetry. Examples are given in Section 5.1.2 for five-coordinated complexes, for which the reference structures can be found in Ref. 155.

3.3 Correlation diagrams

As we now have encountered the most important point groups relevant for the study of TMCs, we focus our attention on the influence exerted by the

O_h	E	$8C_3$	$3C_2$	$6C_4$	$6C_2'$	i	$8S_6$	$3\sigma_h$	$6S_4$	$6\sigma_d$
A_{1g}	1	1	1	1	1	1	1	1	1	1
A_{2g}	1	1	1	-1	-1	1	1	1	-1	-1
E_g	2	-1	2	0	0	2	-1	2	0	0
T_{1g}	3	0	-1	1	-1	3	0	-1	1	-1
T_{2g}	3	0	-1	-1	1	3	0	-1	-1	1
A_{1u}	1	1	1	1	1	-1	-1	-1	-1	-1
A_{2u}	1	1	1	-1	-1	-1	-1	-1	1	1
E_u	2	-1	2	0	0	-2	1	-2	0	0
T_{1u}	3	0	-1	1	-1	-3	0	1	-1	1
T_{2u}	3	0	-1	-1	1	-3	0	1	1	-1

Table 3.1: Character table of O_h.[43]

T_d	E	$8C_3$	$3C_2$	$6S_4$	$6\sigma_d$
A_1	1	1	1	1	1
A_2	1	1	1	-1	-1
E	2	-1	2	0	0
T_1	3	0	-1	1	-1
T_2	3	0	-1	-1	1

Table 3.2: Character table of T_d.[43]

ligands on the TM. Therefore, two extreme regimes are considered, called the weak and strong field limit.[140, 156] In the former, it is assumed that the field created by the ligands is much weaker than the electron-electron repulsion interactions, whereas it is supposed to be much stronger in the latter.

3.3.1 Weak field limit

In the extreme limit of a weak field, free ions are encountered without the presence of ligands. The atomic terms can be classified by the total momentum L and total spin quantum number S according to the Russel-Saunders coupling scheme, employing the complex d-orbitals d_0, $d_{\pm1}$, and $d_{\pm2}$.

For example, for d^7 TMs, which will play a major role in Chapter 5, the possible LS term symbols are ${}^4F$, ${}^4P$, ${}^2H$, ${}^2G$, ${}^2F$, $2\times{}^2D$, and ${}^2P$. As will be shown in Section 3.4.1, the energies of the term symbols can be fully

described by the Racah parameters A, B, and C[157] and are given by:[158]

$$\begin{aligned} E(^4F) =& 3A - 15B \\ E(^4P) =& 3A \\ E(^2H) =& E(^2P) = 3A - 6B + 3C \\ E(^2G) =& 3A - 11B + 3C \\ E(^2F) =& 3A + 9B + 3C \\ E(^2D) =& 3A + 5B + 5C \pm \left(193B^2 + 8BC + 4C^2\right)^{1/2}. \end{aligned} \tag{3.4}$$

A is usually roughly the same for every TM and B is the so-called interelectronic repulsion parameter.[159] The energy differences between states of the same spin multiplicity are, in general, multiples of B only. The differences between states of different multiplicity are expressed via both B and C. In accordance to Hund's rules, ^4F is the GS. Based on these expressions and experimental energies, values for B and C can be estimated.

3.3.2 Strong field limit

In the strong field limit, the d-electrons are much more influenced by the LF than by the interactions with other electrons. Therefore, it no longer makes sense to label them with atomic term symbols. In order to determine the states in this case, only the interactions with the LF are considered, whereas the electron-electron repulsion is neglected. The real d-orbitals d_{z^2}, $d_{x^2-y^2}$, d_{xy}, d_{yz}, and d_{xz}, which are eigenfunctions of the LF operator $\hat{H}_{LF}$, are utilized. This operator will be addressed in more detail in Section 3.4.1.

Before proceeding, we introduce some of the results which will be derived in Section 3.4.1. Figure 3.8 shows the d-orbital splitting of TMCs with a spherical and octahedral LF. Whereas the five d-orbitals are degenerate for the former, they split in a low-lying triply degenerate t_{2g} set and a higher lying doubly degenerate e_g set in octahedral complexes. The orbital sets are separated by an energy gap Δ_o, where the subscript stands for octahedral. Compared to the situation of a spherical LF, the e_g-orbitals are pushed up in energy by $3/5\Delta_0$ and the t_{2g}-orbitals are pushed down by $2/5\Delta_0$. For now, we will only use these results and refer the reader to Section 3.4.1 for more information.

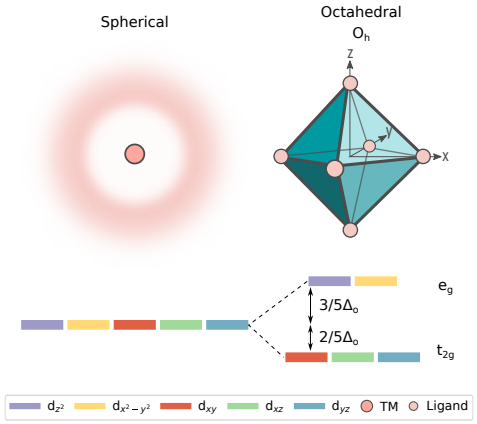

Figure 3.8: Schematic representation of the d-orbital splitting in a spherical and octahedral LF. For the latter, the d-orbitals split in a lower t_{2g} and higher e_g set.

Reverting to the example of octahedral d^7 complexes, the possible electron configurations are: $t_{2g}^6 e_g^1$, $t_{2g}^5 e_g^2$, $t_{2g}^4 e_g^3$, and $t_{2g}^3 e_g^4$, for which possible micro-state are shown in Figure 3.9. The energies of these states are completely described by Δ_o:

$$\begin{aligned} E(t_{2g}^6 e_g^1) &= -\frac{9}{5}\Delta_0 \\ E(t_{2g}^5 e_g^2) &= -\frac{4}{5}\Delta_0 \\ E(t_{2g}^4 e_g^3) &= \frac{1}{5}\Delta_0 \\ E(t_{2g}^3 e_g^4) &= \frac{6}{5}\Delta_0. \end{aligned} \tag{3.5}$$

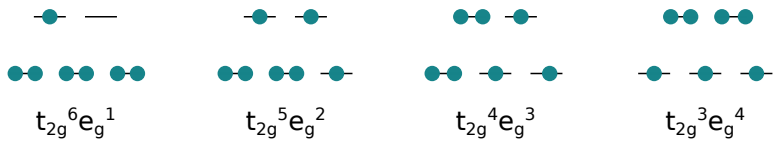

Figure 3.9: Schematic representation of a possible micro-state for the electron configurations in octahedral d^7 complexes.

Of course, in actual TMCs, the situation lies in between these two extreme limits. In the following section, we investigate how the states in the two regimes are altered for intermediate values of the LF strength and how this is visualized in correlation diagrams.

3.3.3 Tanabe-Sugano diagrams

Let us again consider a d^7 TM in an octahedral LF. In order for this explanation to be valid for tetrahedral complexes too, we drop the subscripts g and u in this section. The term symbols defined in the weak field limit and given in Eq. (3.4) will split when the influence of the field increases. If the LF is not very strong, the influence of the ligands can be taken as a perturbation.[160] As terms in a LF behave in a similar way as orbitals, the various LS states of a configuration split in the same way as the orbitals. The wave functions for the S, P, D, F, G, and H states have the same symmetry as the s-, p-, d-, f-, g-, and h-orbitals and give thus also the same splitting pattern, as shown in Table 3.3.

State of free ion	States in octahedral/tetrahedral LF
S	A_1
P	T_1
D	$E + T_2$
F	$A_2 + T_1 + T_2$
G	$A_1 + E + T_1 + T_2$
H	$E + T_1 + T_1 + T_2$

Table 3.3: Splitting of free ion LS term symbols in an octahedral or tetrahedral field.[151]

Analogously, we determine how the electron configurations in the strong field limit given in Eq. (3.5) alter and split in substates when electron-electron interactions are taken into account. We start with the simplest example in which electron-electron repulsion is present, *i.e.,* d^2 systems. There are three possible electron configurations, namely t_2^2, $t_2^1e^1$, and e^2, for which possible micro-states are presented in Figure 3.10. For the first configuration, there are 15 possibilities in which two electrons, being spin up or spin down, can occupy the t_2-orbitals. In a similar way, we obtain the degeneracies of the other configurations, 24 and 6, respectively, resulting in a total degeneracy of 45. For the $t_2^1e^1$ configuration, we have to perform the following multiplication:

$$T_2 \times E = T_1 + T_2. \tag{3.6}$$

The fact that the two electrons can have the same or a different spin, results in the following substates: ${}^1T_1 + {}^1T_2 + {}^3T_1 + {}^3T_2$, with indeed a total degeneracy

of 24. For the t_2^2 state, the substates are obtained as

$$T_2 \times T_2 = A_1 + E + [T_1] + T_2, \tag{3.7}$$

where square brackets indicate that the term is anti-symmetric with respect to particle permutation. Thus, in order for the total wave function to be anti-symmetric, T_1 requires a symmetric spin part, resulting in a spin multiplicity of three. Besides, A_1, E, and T_2 need an anti-symmetric spin part and thus a spin multiplicity equal to one. As such, t_2^2 splits in the following substates: ${}^1A_1 + {}^1E + {}^1T_2 + {}^3T_1$, which results in a total degeneracy of 15. In a similar way, the substates of e^2 are obtained: ${}^3A_2 + {}^1A_1 + {}^1E$, with a total degeneracy of 6.

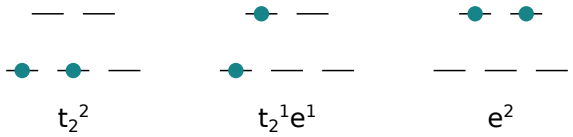

Figure 3.10: Schematic representation of a possible micro-state for the electron configurations in octahedral d^2 complexes.

It becomes a bit more complicated when three electrons are present. d^3 TMs have the following possible electron configurations: t_2^3, $t_2^2e^1$, $t_2^1e^2$, and e^3, for which possible micro-states are shown in Figure 3.11. The last one is the easiest as it corresponds to ${}^2E$. For the second and third configuration, we start from the results of the t_2^2 and e^2 electron configurations obtained above for the d^2 TM and multiply this with ${}^2E$ and ${}^2T_2$, respectively. The resulting substates are $2 \times {}^2E + {}^2A_1 + {}^2A_2 + 2 \times {}^2T_1 + 2 \times {}^2T_2 + {}^4T_1 + {}^4T_2$ and $2 \times {}^2T_2 + 2 \times {}^2T_1 + {}^4T_1$ for $t_2^2e^1$ and $t_2^1e^2$, respectively. For the t_2^3 configuration, things get even more complex. When one multiplies the results obtained for t_2^2 with ${}^2T_2$, more states than the total degeneracy are obtained. Based on symmetry arguments, it can be shown that some of the states vanish and only ${}^2E + {}^2T_1 + {}^2T_2 + {}^4A_2$ remains.[140] One can check that with these states a total degeneracy of 120 is obtained, as expected for d^3 TMs.

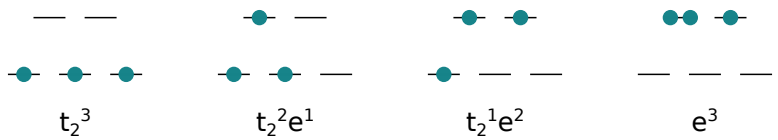

Figure 3.11: Schematic representation of a possible micro-state for the electron configurations in octahedral d^3 complexes.

Once we have studied the d^1, d^2, and d^3 configurations, we are able to determine the substates for every configuration. The possible states of t_2^n are

identical to these of t_2^{6-n} and, similarly, e^n and e^{4-n} yield the same states. Indeed, according to the particle-hole formalism, n holes may be treated like n positrons. Therefore, their behavior in a LF is the same, except for changes in the signs of energy terms. As a result, also the substates of the d^n and d^{10-n} configurations are the same. The substates for all electron configurations can be found in Ref. 161 and are shown in Table 3.4 for d^7 systems.

Electron configuration	States in octahedral/tetrahedral field
$t_2^6e^1$	^2E
$t_2^5e^2$	$2\times^2 T_1 + 2\times^2 T_2 +^4 T_1$
$t_2^4e^3$	$^2A_1 +^2 A_2 + 2\times^2 E + 2\times^2 T_1$
	$+^4T_1 + 2\times^2 T_2 +^4 T_2$
$t_2^3e^4$	$^4A_2 +^2 E +^2 T_1 +^2 T_2$

Table 3.4: Splitting of the electron configurations of d^7 TMs in an octahedral or tetrahedral field.[161]

As now the weak and strong field limits as well as their intermediate regions are understood, we can construct the correlation diagram shown in Figure 3.12 for d^7 systems. Hereby, we take into account that lines connect states of the same symmetry and can therefore not cross due to the von Neumann-Wigner non-crossing rule.[162, 163] In Figure 3.12, the first excitation from the $^4T_1$ GS to each irreducible representation is given. Spin-allowed transitions are drawn in solid lines, whereas spin-forbidden excitations are indicated with dashed lines. This diagram illustrates how the energies of electronic states change between the weak and strong field limits as a function of the LF strength.

Correlation diagrams form the basis of Tanabe-Sugano diagrams, published by Yukito Tanabe and Satoru Sugano with the aim of explaining the absorption spectra of complex ions in a more quantitative way.[140, 164] They predict the character and number of ESs and can also be used to approximate the value of the LF splitting. In Figure 3.13, the Tanabe-Sugano diagram for octahedral d^7 complexes is shown, with inclusion of the subscripts g and u. The energy E is presented as a function of the LF splitting Δ, where both quantities are scaled by the Racah parameter B, already encountered in Section 3.3.1. The lowest energy state is plotted along the horizontal axis. As a consequence, the vertical distance above this axis is a measure of

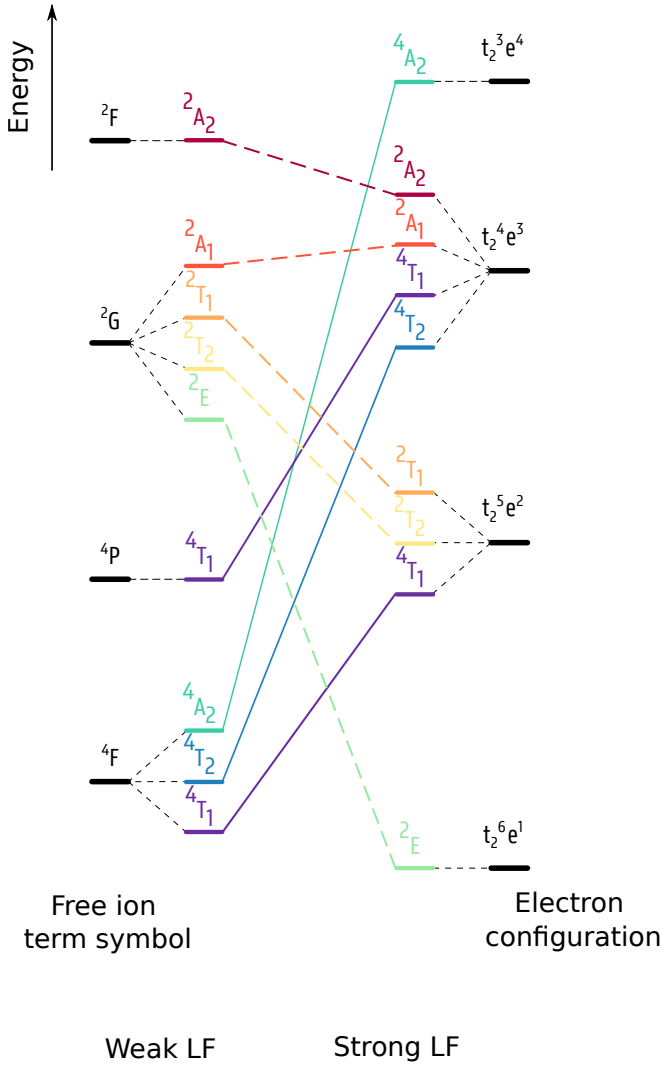

Figure 3.12: Correlation diagram for octahedral d^7 TMCs. Quartet and doublet states are indicated with full and dashed lines, respectively.

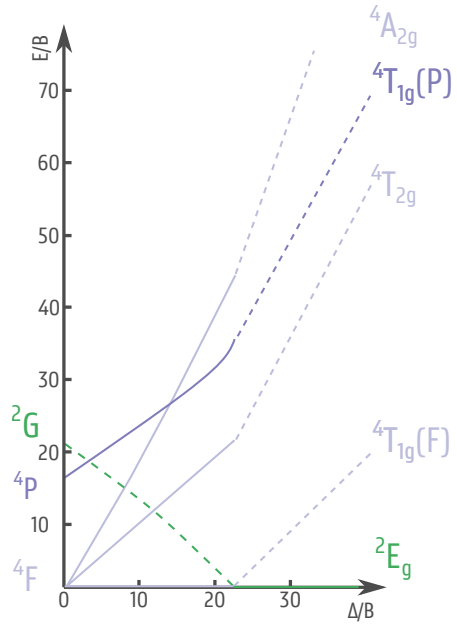

Figure 3.13: Tanabe-Sugano diagram for octahedral d^7 TMCs. Spin-allowed and spin-forbidden transitions are indicated with full and dashed lines, respectively. Figure adapted from Ref. 165 with permission of Oxford Publishing Limited, copyright 2010.

the energy of the ES above the GS. In analogy to orbitals, terms with the same symmetry and which are close in energy can interact with each other, resulting in curved lines.

The other Tanabe-Sugano diagrams are presented in Appendix B.4. As already mentioned, the substates of d^n and d^{10-n} configurations are the same. Therefore, it is not surprising that their Tanabe-Sugano diagrams are very similar too, with inverted d-level splittings for d^{10-n} and d^n systems.

As will be shown in Section 3.4.1, the splitting pattern for the d-orbitals in a tetrahedral field is the inverse of that in an octahedral field. The energy level diagrams in both fields are each other's inverse too. As a result, the Tanabe-Sugano diagrams for octahedral d^n complexes are identical to those of tetrahedral d^{10-n} systems.

Tanabe-Sugano diagrams will be extensively employed in Chapter 5. For example, they will be useful in determining which ESs are double excitations and for which states degeneracies are expected.

3.4 Electronic structure theories

In the remainder of this Chapter, a brief overview is given of some of the earlier theories used to describe TMCs, which stem from the times when no advanced quantum mechanical calculations were possible. Although today, very accurate computational techniques are available, some of these earlier methods still have their merits to interpret the results, as will be shown in Chapter 5. We start this section with an introduction of CFT, in which only electrostatic interactions are taken into account. This approach is extended in LFT, which is described next. Finally, LFDFT is explained, in which concepts from LFT are incorporated in DFT.

3.4.1 Crystal field theory

CFT was originally introduced for the description of metal ions in crystals, hence the name. In the 1930's, Bethe and van Vleck applied this technique to isolated TMCs.[139, 166–168] The key feature is that the ligands are represented as point charges and the interactions between them and the TM are treated as purely electrostatic.[151] This description is thus purely ionic and the electron transfer between the TM and the ligands is completely ignored.

First, the qualitative effects of the LF are discussed for octahedral and tetrahedral complexes, which will be studied in detail in Chapter 5. Afterwards, the effective Hamiltonian is introduced and expressions are derived for the various terms. Some of these results were already used in Section 3.3.1, but their derivations were postponed to this section.

I. Qualitative effects of the ligand field

The ligand electrons responsible for the formation of the bonds in TMCs repel the electrons of the TM, resulting in an increase of the average energy of the five d-orbitals. Remark that only the energy of the d-orbitals is considered and not the absolute binding energies. Indeed, the total energy of the system can decrease when the attraction between the often positively charged TM and the ligands is larger than the destabilization energies of the TM electrons. However, for many purposes we are more interested in the effect of the LF on the degeneracy of the d-orbitals.[160] The electron-electron repulsion is greater the more the d-orbitals are directed toward the ligands and therefore different d-orbitals will be affected in different ways.

First, we look at octahedral complexes with O_h symmetry. Six ligands,

approximated as point charges, are positioned along the coordinate axes at the corners of an octahedron with the TM in the center, as shown in Figure 3.14. The degeneracy of the d-orbitals is partially raised as they split in two orbital sets: t_{2g} and e_g. d_{z^2} and $d_{x^2-y^2}$, with lobes directed toward the ligands, are raised in energy by the electrostatic repulsion between the ligands and the TM and form the e_g set. The t_{2g} set contains d_{xy}, d_{xz}, and d_{yz}, having lobes oriented in between the ligands. Therefore, their energies remain relatively unaffected. The energy gap between these two sets is indicated by Δ_o, which was already introduced in Section 3.3.2.

In TMCs with tetrahedral T_d symmetry, the ligands are situated in between the coordinate axes and at the origin as shown in Figure 3.14. In contrast to octahedral complexes, d_{xy}, d_{xz}, and d_{yz}, grouped in the t_2 set, now point toward the ligands, whereas $d_{x^2-y^2}$ and d_{z^2}, forming the e set, are situated in between the ligands. Therefore, the e set is more stable in comparison with the t_2 set. Furthermore, it can be shown that the d-orbital splitting is reduced to $4/9\Delta_o$ when all other factors such as the metal-ligand distance are the same.

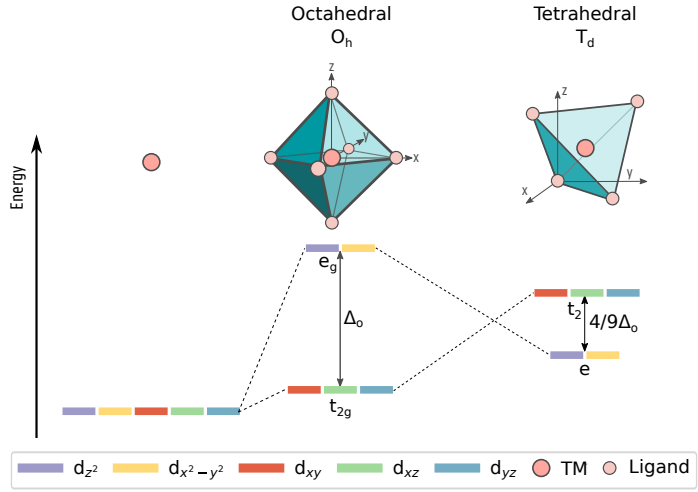

Figure 3.14: Splitting of the d-orbitals of a TM in various environments. For an isolated TM, all d-orbitals are degenerate, whereas for complexes with octahedral and tetrahedral symmetry, the degeneracy is (partially) lifted. The splitting between the two orbital sets in octahedral and tetrahedral complexes is denoted by Δ_o and $\frac{4}{9}\Delta_o$, respectively. The labeling of the d-orbitals in the various point groups is also indicated.

After this qualitative description of the influence of the LF on the d-orbital

splitting in octahedral and tetrahedral complexes, an expression for the effective Hamiltonian is now provided. It does not only form the foundation of CFT but is also used in LFDFT.

II. Effective Hamiltonian

As discussed in Chapter 2, the molecular system consisting of a TM surrounded by ligands can be described by the eigenvalue equation shown in Eq. (2.9), where the electronic Hamiltonian is defined in Eq. (2.10). In CFT, we use an effective Hamiltonian, which acts in a reduced space of Slater determinants Φ_μ^d composed of d-orbitals:[169]

$$\hat{H}^{\text{eff}}|\Phi_\mu^d\rangle = E_\mu^d|\Phi_\mu^d\rangle, \tag{3.8}$$

with $\mu = 1, ..., \binom{10}{N_d}$, where N_d is the number of d-electrons. The eigenvalues E_μ^d, also known as the multiplet energy levels, are ideally equal to those of the true Hamiltonian. This approach is valid when the metal-ligand bond is mainly ionic, resulting in a well-defined d^{N_d} electron configuration and d-d excitations well separated from the other ESs.

In CFT, the effective Hamiltonian is given by:

$$\begin{aligned}\hat{H}^{\text{eff}} &= \hat{T}_e^{\text{eff}} + \hat{V}_{en}^{\text{eff}} + \hat{V}_{ee}^{\text{eff}} + \hat{H}_{LF}^{\text{eff}} + \hat{H}_{SOC}^{\text{eff}} \\ &= \hat{H}_0^{\text{eff}} + \hat{V}_{ee}^{\text{eff}} + \hat{H}_{LF}^{\text{eff}} + \hat{H}_{SOC}^{\text{eff}},\end{aligned} \tag{3.9}$$

where in the second line the one-body operators $\hat{T}_e^{\text{eff}}$ and $\hat{V}_{en}^{\text{eff}}$ are grouped as $\hat{H}_0^{\text{eff}}$. From now on, we neglect this term as it only results in a general shift. $\hat{V}_{ee}^{\text{eff}}$ includes the electron-electron repulsion within the d-electrons and $\hat{H}_{LF}^{\text{eff}}$ takes into account the presence of the surrounding ligands, approximated as point charges in CFT. The spin-orbit coupling (SOC) term $\hat{H}_{SOC}^{\text{eff}}$ represents the coupling between the spin and the angular momenta of the d-electrons. For atoms in the first- and second-transition series, the contribution of the SOC term is smaller than that of the LF and electron-electron interactions.[139] Therefore, $\hat{H}_{SOC}^{\text{eff}}$ is, at first instance, not accounted for. Note that, as stated previously, the interaction between the ligands and the TM nuclei are generally not included in CFT.

The effective Hamiltonian is parameterized in such a way that it is almost as precise as the full Hamiltonian. Expressions for the LF multiplet energies can be obtained as a function of the parameters, which can then be used to construct the Tanabe-Sugano diagrams. Quantitative results are obtained when these parameters are derived from experimental input

data.[169] In the following, the electron-electron interaction and LF terms are analyzed in detail.

$\hat{V}_{ee}^{\text{eff}}$ is the two-body Coulomb operator introduced in Eq. (2.4). However, now the summation runs only over the d-electrons and describes the electron-electron interactions between them. This term is treated like in the free atom and thus preserves the spherical symmetry.

As the wave function is a Slater determinant composed of d-orbitals, we can use the Slater-Condon rules to write the electron-electron repulsion energy as follows:[158]

$$\begin{aligned}\langle \Phi^d | \hat{V}_{ee}^{\text{eff}} | \Phi^d \rangle &= \frac{1}{2} \sum_{i \neq j}^{N_d} \left(\langle d_i d_j | \hat{v}_{ee} | d_i d_j \rangle - \langle d_i d_j | \hat{v}_{ee} | d_j d_i \rangle \right) \\ &\equiv \frac{1}{2} \sum_{i \neq j}^{N_d} \left(J_{ij} - K_{ij} \right),\end{aligned} \tag{3.10}$$

where d_i are the one-particle d-orbitals and $\hat{v}_{ee}$ is for a general matrix element written as follows:

$$\langle d_a d_b | \hat{v}_{ee} | d_c d_d \rangle = \int \mathrm{d}\boldsymbol{x}_1 \, \mathrm{d}\boldsymbol{x}_2 \, \frac{d_a^*(\boldsymbol{x}_1) d_b^*(\boldsymbol{x}_2) d_c(\boldsymbol{x}_1) d_d(\boldsymbol{x}_2)}{|\boldsymbol{r}_1 - \boldsymbol{r}_2|}. \tag{3.11}$$

In the second line of Eq. (3.10), the Coulomb J_{ij} and exchange K_{ij} integrals have been introduced. The first term corresponds to the classical Coulomb repulsion between two charge distributions due to the electrons in d_i and d_j. This integral does not depend on the spin. In contrast, the exchange term is zero unless the i^{th} and j^{th} electron have the same spin. This interaction term has a fully quantum mechanical nature and lies at the origin of Hund's first rule, which states that the configuration with the highest multiplicity is the most stable one. This term is attractive and diminishes the Coulomb repulsion between orbitals having the same spin. Finally, we note that both integrals are symmetric.

We will now express the Coulomb and exchange contributions in terms of Slater-Condon parameters.[170] We first derive an expression for the general matrix element given in Eq. (3.11). Therefore, we consider the following multipole decomposition:

$$\begin{aligned}\frac{1}{|\boldsymbol{r}_1 - \boldsymbol{r}_2|} &= \frac{1}{\left(r_1^2 + r_2^2 - 2 r_1 r_2 \cos(\omega) \right)^{1/2}} \\ &= \sum_{k=0}^{\infty} \frac{r_<^k}{r_>^{k+1}} P_k(\cos(\omega)),\end{aligned} \tag{3.12}$$

with ω the angle between $\boldsymbol{r_1}$ and $\boldsymbol{r_2}$ and $r_<$ and $r_>$ the smallest and largest of the distances r_1 and r_2, respectively. $P_k(cos(\omega))$ are the Legendre polynomials. Furthermore, we use the fact that a general d-orbital can be separated in a radial, angular, and spin part:

$$d(\boldsymbol{x}) = R_{nl}(r)Y_{lm}(\theta,\phi)\chi_{m_s}(\sigma), \tag{3.13}$$

with R_{nl} the radial wave function, Y_{lm} the spherical harmonic and χ_{m_s} the spin part. n, l, m, and m_s are the principal, orbital momentum, magnetic, and spin quantum number, respectively. Note that in our case $l = 2$ as we are dealing with d-orbitals, but the following derivation is conducted for a general orbital momentum quantum number.

Eq. (3.11) can then be reformulated as a product of an angular and a radial integral:

$$\begin{aligned}\langle d_a d_b|\hat{v}_{ee}|d_c d_d\rangle =& \sum_{k=0}^{\infty}\langle R_{n_a l_a}R_{n_b l_b}|\frac{r_<^k}{r_>^{k+1}}|R_{n_c l_c}R_{n_d l_d}\rangle\times \\ & \langle Y_{l_a m_a}Y_{l_b m_b}|P_k(\cos(\omega))|Y_{l_c m_c}Y_{l_d m_d}\rangle\delta_{\sigma_a\sigma_c}\delta_{\sigma_b\sigma_d} \\ \equiv& \sum_{k=0}^{\infty} R^k(n_a l_a, n_b l_b, n_c l_c, n_d l_d)A_k\delta_{\sigma_a\sigma_c}\delta_{\sigma_b\sigma_d}.\end{aligned} \tag{3.14}$$

In the second line, we introduced the notation R^k for the radial part and A_k for the angular part. The latter can be simplified with the help of the addition theorem for spherical harmonics:

$$P_k(cos(\omega)) = \frac{4\pi}{2k+1}\sum_{m=-k}^{k} Y_{km}(\theta_1,\phi_1)Y_{km}^*(\theta_2,\phi_2), \tag{3.15}$$

yielding

$$A_k = \frac{4\pi}{2k+1}\sum_{m=-k}^{k}\langle Y_{l_a m_a}Y_{l_b m_b}|Y_{km}(\theta_1,\phi_1)Y_{km}^*(\theta_2,\phi_2)|Y_{l_c m_c}Y_{l_d m_d}\rangle. \tag{3.16}$$

By using the following identity[171]

$$\langle Y_{lm}|Y_{l_1 m_1}|Y_{l_2 m_2}\rangle = \sqrt{\frac{(2l_1+1)(2l_2+1)}{4\pi(2l+1)}}\langle l_1 0 l_2 0|l0\rangle\langle l_1 m_1 l_2 m_2|lm\rangle \tag{3.17}$$

we obtain that $\langle Y_{l_a m_a}|Y_{km}|Y_{l_c m_c}\rangle$ is zero unless $m_a = m + m_c$. Similarly, $\langle Y_{l_b m_b}|Y_{km}^*|Y_{l_d m_d}\rangle$ is zero unless $m_b + m = m_d$. Therefore, A_k vanishes

unless $m_a + m_b = m_c + m_d$. The sum in Eq. (3.16) then reduces to a single term:

$$\begin{aligned} A_k =& \frac{4\pi}{2k+1} \langle Y_{l_a m_a} | Y_{k m_a - m_c} | Y_{l_c m_c} \rangle \langle Y_{l_b m_b} | Y_{k m_d - m_b} | Y_{l_d m_d} \rangle \times \\ & \delta_{m_a + m_b, m_c + m_d} \\ =& c^k(l_a m_a, l_c m_c) c^{k*}(l_d m_d, l_b m_b) \delta_{m_a + m_b, m_c + m_d}, \end{aligned} \tag{3.18}$$

where we introduced the following definition of c^k

$$c^k(lm, l'm') \equiv \left(\frac{4\pi}{2k+1} \right)^{1/2} \langle Y_{lm} | Y_{km-m'} | Y_{l'm'} \rangle. \tag{3.19}$$

Substituting this back into Eq. (3.14), we get:

$$\begin{aligned} \langle d_a d_b | \hat{v}_{ee} | d_c d_d \rangle =& \delta_{\sigma_a \sigma_c} \delta_{\sigma_b \sigma_d} \delta_{m_a + m_b, m_c + m_d} \times \\ & \sum_{k=0}^{\infty} R^k(n_a l_a, n_b l_b, n_c l_c, n_d l_d) c^k(l_a m_a, l_c m_c) c^{k*}(l_d m_d, l_b m_b). \end{aligned} \tag{3.20}$$

Now that we have obtained expressions for the general matrix element given in Eq. (3.11), we look for expressions for the Coulomb and exchange integrals introduced in Eq. (3.10). Therefore, we define the Slater-Condon parameters:

$$\begin{aligned} F^k(n_i l_i, n_j l_j) \equiv& R^k(n_i l_i, n_j l_j, n_i l_i, n_j l_j) \\ G^k(n_i l_i, n_j l_j) \equiv& R^k(n_i l_i, n_j l_j, n_j l_j, n_i l_i) \end{aligned} \tag{3.21}$$

and introduce

$$\begin{aligned} A^k(l_i m_i, l_j m_j) \equiv& c^k(l_i m_i, l_i m_i) c^{k*}(l_j m_j, l_j m_j) \\ B^k(l_i m_i, l_j m_j) \equiv& c^k(l_i m_i, l_j m_j) c^{k*}(l_i m_i, l_j m_j). \end{aligned} \tag{3.22}$$

The Coulomb and exchange terms are then written as follows:

$$J_{ij} = \langle d_i d_j | \hat{v}_{ee} | d_i d_j \rangle \tag{3.23}$$

$$= \sum_{k=0}^{\infty} A^k(l_i m_i, l_j m_j) F^k(n_i l_i, n_j l_j) \tag{3.24}$$

$$K_{ij} = \langle d_i d_j | \hat{v}_{ee} | d_j d_i \rangle \tag{3.25}$$

$$= \delta_{\sigma_i \sigma_j} \sum_{k=0}^{\infty} B^k(l_i m_i, l_j m_j) G^k(n_i l_i, n_j l_j). \tag{3.26}$$

A general formula for c^k has been worked out by Gaunt,[172] but is very complicated and hence tabulated values are used in practice. However, we

can still simplify the expressions in Eqs. (3.24) and (3.26) by using the fact that c^k is zero unless k, l, and l' satisfy the conditions:[158]

$$\begin{aligned} &k + l + l' \text{ is even} \\ &|l - l'| \leq k \leq l + l'. \end{aligned} \tag{3.27}$$

The expressions for J_{ij} and K_{ij} are then simplified for equivalent electrons for which we can drop the arguments:

$$\begin{aligned} J_{ij} =& \sum_{k=0}^{2l} A^k F^k \\ K_{ij} =& \delta_{\sigma_i \sigma_j} \sum_{k=0}^{2l} B^k F^k. \end{aligned} \tag{3.28}$$

We are now able to express the multiplet energies of any configuration as functions of the parameter F^k. Since the radial parts of the wave functions are in general not well known, these parameters are determined by fitting to experimental electronic spectra.

Alternatively, the electron-electron repulsion energy can be expressed as a function of the Racah parameters A, B and C.[157] The relations between the Racah and Slater-Condon parameters are given by:

$$\begin{aligned} A &= F^0 - \frac{49}{441} F^4 \\ B &= \frac{1}{49} F^2 - \frac{5}{441} F^4 \\ C &= \frac{35}{441} F^4, \end{aligned} \tag{3.29}$$

where A is sometimes ignored because it is roughly the same for every TM, as stated before. The electron-electron repulsion energy is then in general written as follows:

$$\beta B + \gamma C, \tag{3.30}$$

with β and γ coefficients, which are obtained by substituting the expression for J_{ij} and K_{ij}.

To conclude, the term symbols of a given electron configuration are in the weak-field limit completely determined by the electron-electron interactions, as stated in Section 3.3.1. Expressions for their energies can be determined as follows. Via the diagonal sum-rule,[173] and Eq. (3.10), we can write the energies as a function of the Coulomb and exchange integrals J_{ij}

and K_{ij}, which in turn can be expressed as a function of F^k via Eq. (3.28), where the coefficients A^k and B^k are tabulated.[161] This can also be written as a function of the Racah parameters (A), B, and C by means of Eq. (3.29). An example was already given in Eq. (3.4) for d^7 complexes.

The electrostatic interaction between the ligands, approximated as point charges with charge Z_l and coordinates $\boldsymbol{r}_l$, and the d-electrons is included in $\hat{H}_{LF}$. This one-body interaction is given by:

$$\hat{H}_{LF}^{\text{eff}} = -\sum_{i=1}^{N_d}\sum_{l=1}^{N_l}\frac{Z_l}{|\boldsymbol{r}_i - \boldsymbol{r}_l|}. \tag{3.31}$$

If Z_l is negative, the electron-ligand interaction destabilizes the TM d-electrons. Nevertheless, the complex is stable due to the attractive interaction between the negatively charged ligands and the TM nuclei. However, these interactions are independent of the electron coordinates, and therefore rarely considered in CFT, in which the main interest goes to the relative d-orbital energies, as already mentioned previously. Unlike the electron-electron interactions, full account is taken for the lowering of the symmetry when a spherical TM is introduced in a LF environment. Therefore, it is only this term which carries information about the symmetry in the TMC. Hence, no general expression exists for this contribution.

In Section 3.3.2, the influence of an octahedral LF environment on the d-orbitals was already shown in Figure 3.8. The proof is given here. If we take a look at the potential generated by the ligands and consider it as a perturbation on the other interactions present in the system, the following secular equation needs to be solved in order to find the effect of the ligands on the d-orbitals:[139, 160]

$$|V_{mm'} - E\delta_{mm'}| = 0 \qquad m, m' = -2, -1, 0, 1, 2, \tag{3.32}$$

with $V_{mm'} = -\langle d|\sum_{l=1}^{N_l}\frac{Z_l}{|\boldsymbol{r}-\boldsymbol{r}_l|}|d'\rangle$. A general expression for Eq. (3.32) is given by[160]:

$$V_{mm'} = \sum_{l=1}^{N_l} Z_l[A_{mm'}F_4(r_l)Y_{4m-m'}(\theta_l,\phi_l) + B_{mm'}F_2(r_l)Y_{2m-m'}(\theta_l,\phi_l) + D_{mm'}F_0(r_l)Y_{0m-m'}(\theta_l,\phi_l)], \tag{3.33}$$

where $A_{mm'}$, $B_{mm'}$, and $D_{mm'}$ are tabulated constants[160] and $F_k(R)$ is defined as:

$$F_k(R) = R^{-(k+1)}\int_0^R \mathrm{d}r\, r^k R_{nl}^2(r)r^2 + R^k\int_R^\infty \mathrm{d}r\, R_{nl}^2(r)r^2. \tag{3.34}$$

For octahedral complexes with $Z_l = q$ and in which the distance between the TM and the ligands is denoted with a, we have: $\theta_1 = 0$, $\theta_2 = \theta_3 = \theta_5 = \theta_6 = \pi/2$, $\theta_4 = \pi$, $\phi_2 = 0$, $\phi_3 = \pi/2$, $\phi_5 = \pi$, and $\phi_6 = 3\pi/2$. The only non-zero matrix elements are then

$$\begin{aligned} V_{22} = V_{-2-2} =& q\left[6F_0(a) + \frac{1}{6}F_4(a)\right] \\ V_{11} = V_{-1-1} =& q\left[6F_0(a) - \frac{2}{3}F_4(a)\right] \\ V_{00} =& q\left[6F_0(a) + F_4(a)\right] \\ V_{-22} = V_{2-2} =& q\frac{5}{6}F_4(a). \end{aligned} \tag{3.35}$$

The roots of the secular equation given in Eq. (3.32), *i.e.,* the perturbation corrections to the atomic energy levels, are then given by:

$$\begin{aligned} E_1 = E_2 &= q[6F_0(a) + F_4(a)] \\ E_3 = E_4 = E_5 &= q[6F_0(a) - \frac{2}{3}F_4(a)]. \end{aligned} \tag{3.36}$$

Hence, the d-orbitals split by an octahedral LF into a doubly degenerate e_g and a triply degenerate t_{2g} set. We label the energy gap between both sets as Δ_o, as introduced in Section 3.3.2, and obtain:

$$\begin{aligned} E_{e_g} &= q6F_0(a) + \frac{3}{5}\Delta_0 \\ E_{t_{2g}} &= q6F_0(a) - \frac{2}{5}\Delta_o, \end{aligned} \tag{3.37}$$

where the first term equals the average repulsion energy from six negative charges q uniformly distributed over a sphere with radius a. Furthermore, this equation reveals that the e_g-orbitals are pushed up in energy by $3/5\Delta_o$, while the t_{2g}-orbitals are pushed down by $2/5\Delta_o$, as previously shown in Figure 3.8. In general, Δ_o is treated as a semi-empirical parameter and is obtained from experimental data.[174]

In conclusion, the effective Hamiltonian is now parameterized via the Slater-Condon or Racah parameters for the electron-electron interactions and Δ_o for the effect of the ligands for the specific case of octahedral TMCs. These parameters are determined based on experimental data and allow one to obtain the multiplet energy levels associated with a given electron configuration.

In the next section, we extend CFT to include interactions other than electrostatic ones. Based on this, we will construct MO diagrams for different types of ligands.

3.4.2 Ligand field theory

In CFT, many aspects of the electronic structure of TMCs can be treated in a conceptually simple way. Nevertheless, this technique is not capable of describing the bonding in TMCs, as the interaction between the TM and ligands is approximated as purely electrostatic, thereby neglecting its partially covalent nature.[43] Furthermore, under this approximation, electrons occupy pure d-orbitals. Therefore, all d-d transitions in complexes with a center of symmetry would be spectroscopically dark as they are completely Laporte-forbidden. Nevertheless, such transitions are observed in experiments, albeit weakly. Therefore, we can conclude that the general assumption of CFT is sometimes too crude.

LFT covers all techniques in which one goes beyond electrostatic metal-ligand interactions. CFT can then be seen as a limiting special case.[139] The most straightforward way in which the simple CFT can be modified, is by taking the Slater-Condon or Racah parameters in the effective Hamiltonian as variables, which can be adjusted empirically for each TMC, rather than taking them equal to the values found for free ions. This technique is the so-called adapted CFT. In this way, the effects of covalency are introduced implicitly in CFT. The decrease of the value of the Racah parameter B in the TMC compared to the one in the free ion is due to the nephelauxetic effect,[43] a term originating from the Greek word for cloud-expanding. The electron-electron repulsion is reduced as the d-electron cloud expands due to the presence of the ligands, resulting in a decrease of B.

I. Ligand field theory: a combination of crystal field theory and molecular orbital theory

Griffith and Orgel introduced a combination of CFT and molecular orbital theory, named LFT .[173] Before continuing, we add a small note about the nomenclature. In the literature, it is common to denote not only this method with LFT, but all techniques which extend the metal-ligand interactions beyond the electrostatic approach employed in CFT, as stated before.

In molecular orbital theory,[139] the bonding electrons of the TM and ligands are not entirely associated with either of them, but rather, to some extent, with both of them. Bonds are achieved when the ligand and TM orbitals overlap which results in the formation of MOs.

Interactions between the TM and the ligands can be of the σ- or π-type. In the former, the overlap between the atomic orbitals is axial, whereas

it is lateral in the latter. We first consider the interactions in octahedral TMCs with σ-donor ligands, visualized in the MO diagram presented in Figure 3.15. The reduced representation of the six ligand donor orbitals is as follows:[43]

$$A_{1g} + T_{1u} + E_g. \tag{3.38}$$

The E_g ligand orbitals match with the E_g d-orbitals of the TM. Therefore, both can interact and a pair of bonding e_g and anti-bonding e_g^* MOs is formed. Indeed, the lobes of the $d_{x^2-y^2}$- and d_{z^2}-orbitals are oriented along the σ-donor orbitals, making interactions possible, whereas this is not the case for the d_{xy}-, d_{xz}-, and d_{yz}-orbitals with lobes pointing in between the ligands. Therefore the t_{2g}-orbitals remain non-bonding and their energies are unaffected by the presence of the ligands. The splitting between the t_{2g}-and e_g^*-orbitals is, similar to that in CFT, indicated with Δ_0 and is a measure of the magnitude of metal-ligand interactions. The bonding and anti-bonding MOs carry large contributions from the ligands and TM, respectively. Also the valence s- and p-orbitals of the TM, with A_{1g} and T_{1u} symmetry, can interact with the ligands. As a result, four bonding MOs, a_{1g} and t_{1u}, are formed along with four anti-bonding MOs, a_{1g}^* and t_{1u}^*.

The six electron pairs originating from the ligands and the d-electrons from the TM occupy more bonding MOs than anti-bonding ones in the TMC. The resulting stabilization is an important factor in the driving force for the formation of the TMC, an aspect which is not considered in CFT.

Now, we examine the case in which the ligands can additionally engage in π-interactions. The reduced representation of the π-ligand orbitals is given by:[43]

$$T_{1g} + T_{2g} + T_{1u} + T_{2u}. \tag{3.39}$$

Now, there is also a match for the T_{2g} set of the TM d-orbitals d_{xy}, d_{xz}, and d_{yz}. If on the one hand, the ligands have low-lying occupied π-orbitals, they can act as π-donors. This results in a decrease of the gap between the t_{2g}^* and e_g^* sets compared to the case in which only σ-interactions are present. This is presented in Figure 3.16. If, on the other hand, the ligands have high-lying unoccupied π-orbitals, they can act as π-acceptors. The gap between the t_{2g}-orbitals and the e_g^*-orbitals is now increased, as visualized in Figure 3.17. In both cases, the T_{1g}- and T_{2u}-orbitals have no matching metal orbitals and are therefore non-bonding. Furthermore, as we assumed that the overlap between the T_{1u} ligand orbitals and the TM p-orbitals is smaller than that in the T_{1u} σ-interactions, the T_{1u} set remains non-bonding. The difference between weak π-donor ligands and strong π-acceptor ligands will be important for the study of Co^{2+} complexes in Chapter 5.

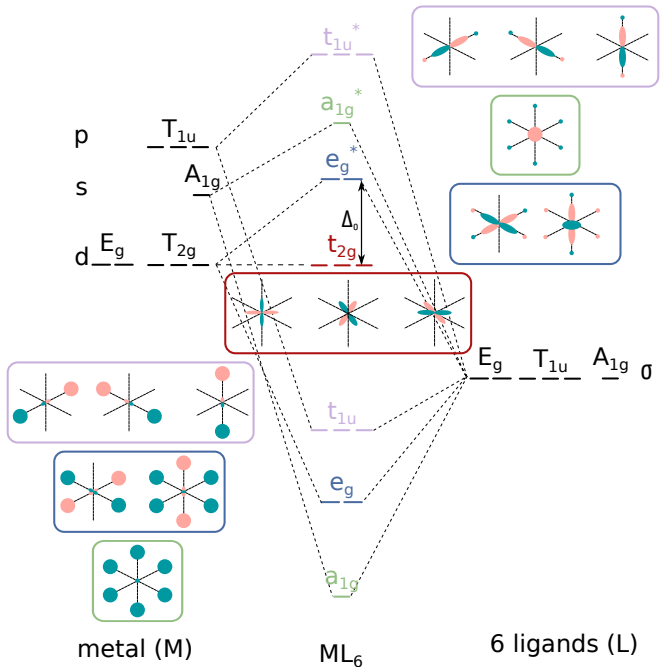

Figure 3.15: MO diagram for octahedral complexes with σ-donor ligands.

II. Angular overlap model

A different approach is used in the angular overlap model (AOM) in which local contributions to the LF potential are defined in contrast to the global, symmetry-adapted parameters encountered previously. Parameters are introduced which represent the strength of the σ- and π-interactions between the TM d-orbitals and the ligand orbitals and are based on their mutual overlap.[156, 175] The amount of overlap strongly depends on the angular position of the ligand with respect to the TM, hence the name AOM.[43] Contributions from all ligands are added to yield a 5×5 LF matrix. One of the main advantages is that a variety of coordination numbers, geometries, and ligands can be studied, where even heteroleptic complexes containing different ligands are possible. A disadvantage is that the focus is exclusively on the d-orbitals and the role of the s and p TM valence orbitals is completely omitted. This technique will be shortly addressed in the next section which concludes this Chapter with a short introduction on LFDFT.

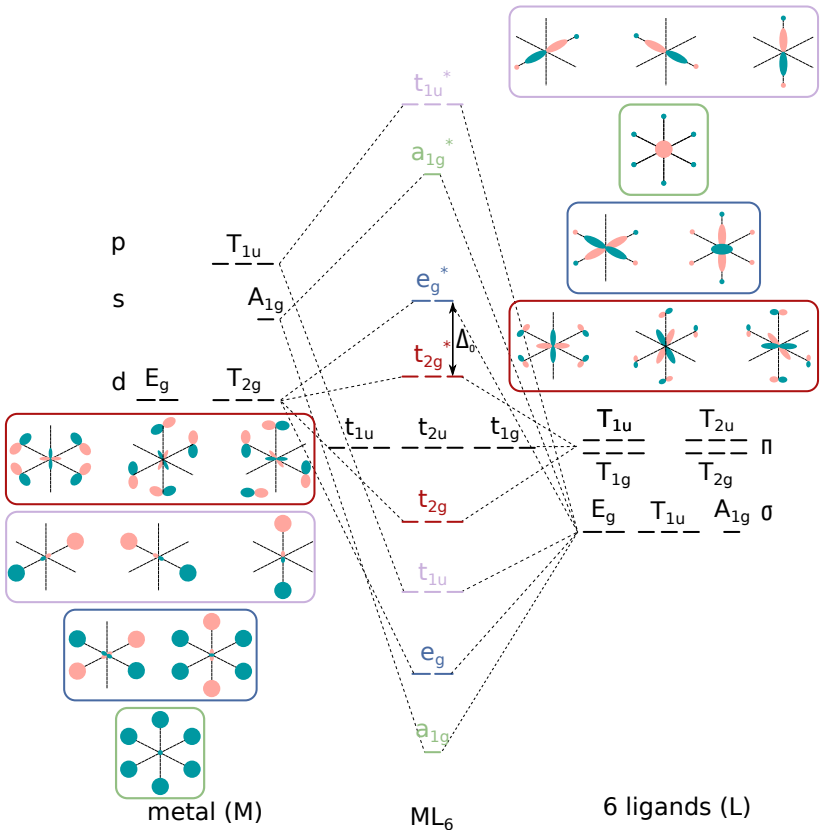

Figure 3.16: MO diagram for octahedral complexes with σ-donor and π-donor ligands.

3.4.3 Ligand field DFT

As stated at the end of Section 3.4.1, the multiplet energies are calculated in CFT by estimating the parameters in the effective Hamiltonian based on experimental data. Such calculations are especially useful for the description of trends in the d-orbital splitting due to differences in coordination number and geometry.[176] However, as experimental input data is required, they rather serve as a tool for interpreting than for predicting electronic phenomena in TMCs.

The most straightforward approach to obtain multiplet energies without experimental input data is by calculating the energies of suitable determinants.[83] Although this method has been extended by Daul,[177] it remains limited as mixing between states is not included. Furthermore, for highly symmetric TMCs, deviations are observed from the imposed

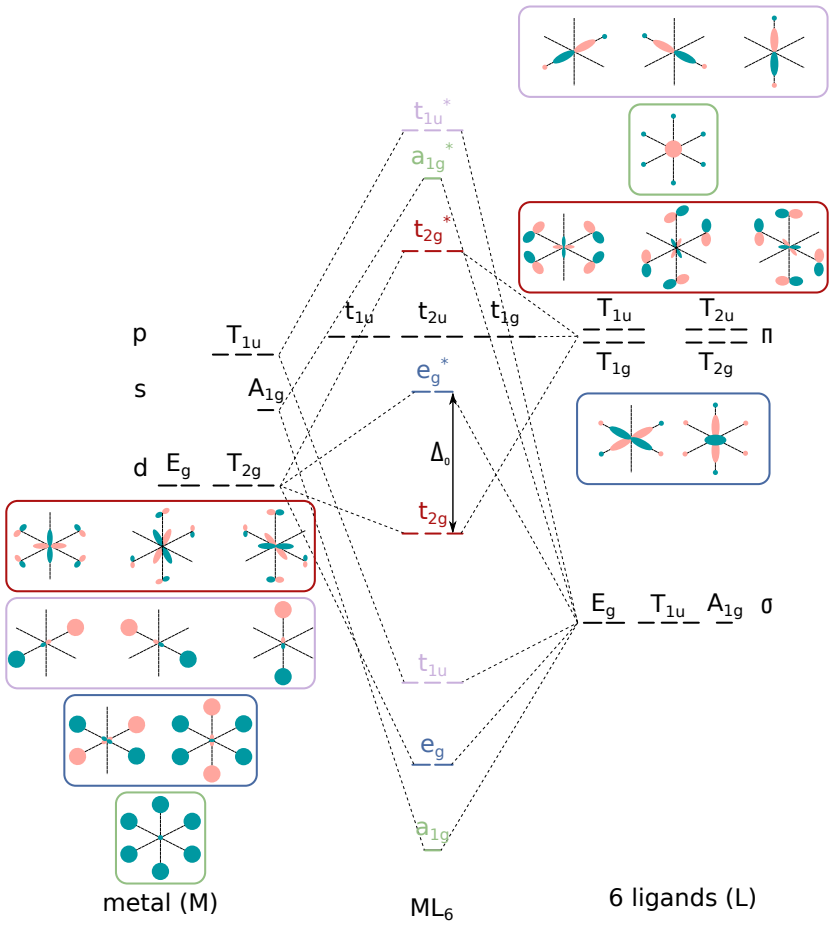

Figure 3.17: MO diagram for octahedral complexes with σ-donor and π-acceptor ligands.

symmetry conditions. Therefore, in this section, we will investigate LFDFT, which will be employed for the calculation of d-d excitations in TMCs relevant for the ZIF nucleation process in Chapter 5.

In LFDFT, the determination of the parameters entering the effective Hamiltonian is not based on experimental input data, but on DFT calculations. The method has been introduced by Atanasov *et al.* and consists of three steps, where we assume that the molecular geometry is known, either from a previously performed geometry optimization or from X-ray data.[178–181]

First, the electronic structure is determined via a spin-restricted DFT

calculation in which the KS orbitals with dominant d-character are equally occupied. This technique is called average of configuration (AOC). One of the great advantages of DFT is, as it is based on the electron density, that there is no formal constraint that orbitals must have integer occupations.[182] The constructed KS orbitals are ideally suited for a treatment in which electron-electron repulsion is treated within full spherical symmetry.

Secondly, we construct the active space of KS orbitals with dominant d-character, also called the LF manifold, and determine the energy of the Slater determinants. In order to do so, the orbitals are kept frozen in spin-unrestricted calculations. For example, the energy of the Slater determinant Φ_μ^d can be written as follows for octahedral TMCs:

$$E_\mu^d = E_0 + \frac{3m_\mu - 2n_\mu}{5}\Delta_o + \beta_\mu B + \gamma_\mu C. \tag{3.40}$$

E_0 represents the gauge origin of energy. The second term corresponds to the LF contributions described by Eq. (3.36), where m_μ and n_μ specify the electron configuration $t_{2g}^{n_\mu} e_g^{m_\mu}$. The electron-electron interactions are included in the last two terms and are obtained from Eq. (3.30), where β_μ and γ_μ are coefficients obtained by substituting the expressions of the Coulomb J_{ij} and exchange K_{ij} integrals.

Having obtained an expression for the energy of each Slater determinant by determining m_μ, n_μ, β_μ, and γ_μ, an over-determined system of linear equations is obtained from which the unknown parameters B, C, Δ_o, and E_0 can be estimated using a least-squares fit procedure. As such, the effective Hamiltonian in Eq. (3.8) is completely determined. Finally, the multiplet splitting E_μ^d of the d^{N_d} electron configuration is then calculated by diagonalizing the effective Hamiltonian with the Slater determinants as basis. In this way, CI within the LF manifold is included. The key feature of this approach is that both dynamical and non-dynamical correlation are taken into account, the former via the DFT exchange-correlation functional and the latter via CI of the valence electrons in the d-orbitals.[180]

For complexes with lower symmetry, the procedure is similar, but as the orbitals in the Slater determinant are not purely d-orbitals, the technical details are a bit more complicated. We refer the reader to detailed explanations in Ref.180. The LF part of the effective Hamiltonian is then parameterized within the Wybourne formalism:[139]

$$\hat{H}_{LF}^{\text{eff}} = \sum_{k=0,2,4} \sum_{q=-k}^{k} B_q^k(3d,3d) C_q^{(k)}, \tag{3.41}$$

with B_q^k the Wybourne-normalized CF parameters and

$$C_q^{(k)} = \sqrt{\frac{4\pi}{2k+1}} Y_{kq}. \tag{3.42}$$

However, this elegant representation does not provide any chemical insight. To circumvent this problem, the LF potential can be represented using the 5×5 LF matrix introduced in the AOM in Section 3.4.2.

We end this discussion with a short note about the inclusion of SOC in LFDFT,[183] which had not been considered yet. SOC is represented by a sum of one-electron spin-orbit contributions.

$$\hat{H}_{SOC}^{\text{eff}} = \sum_{i=1}^{N_d} \zeta(\hat{\boldsymbol{l}}_i \cdot \hat{\boldsymbol{s}}_i), \tag{3.43}$$

with ζ the SOC constant, which can be evaluated analytically using the radial part of the d-orbitals or from a zeroth order regular approximation (ZORA) calculation. $\boldsymbol{l}_i$ and $\boldsymbol{s}_i$ are the angular momentum and spin of the i^{th} electron, respectively.

LFDFT has already been applied to Co(acacen),[184] TM dimers,[185] rare earth haxachloro complexes,[186] and Co(II) and Cu(II) porphyrins.[187] Additionally, the ^{59}Co shielding tensor[188, 189] and the zero field splitting[190] have been calculated. Furthermore, applications on Cr(III) complexes have been reported.[191] LFDFT has also already been used to study the $2p$ core electron excitations in 3d TMs,[192] and for $f \rightarrow d$ transitions in for example actinides and lanthanides [193–200]. Other applications are included in Refs. 201–204.

Finally, we also note that the parameters in the effective Hamiltonian can be obtained via *ab initio* LFT too.[205] However, as this technique is based on the wavefunction rather than on the density it is not studied in this work.

In summary, in this Chapter we gave an overview of the most important theories to describe the metal-ligand interactions, determine d-orbital splittings, and characterize ESs, both using effective Hamiltonians and more complicated methods. Empirical parameters are used in CFT, whereas these are derived from DFT in LFDFT. The interactions between the TM and the ligands is assumed to be purely electrostatic in CFT, whereas in other techniques the covalent part is accounted for too. In Chapter 5, the qualitative results obtained from CFT and LFT will be used to unravel the nucleation process of ZIFs as well as quantitative results obtained via LFDFT.

4

Unraveling the Photocatalytic Properties of Heterogeneous Catalysts

As stated in Chapter 1, CTFs are promising candidates to serve as support materials for photocatalytic complexes. In this PhD thesis, we would like to make a contribution to the rational design of such heterogeneous catalysts. Indeed, the photocatalytic properties can, to a certain extent, be tuned in order to match specific activation energies required for a certain application or such that the portion of radiation which can be used to activate the complex increases. First of all, as CTFs also display photocatalytic activity in their pristine form,[40–42] we investigate which factors governed by the ligands influence the photophysical properties of the CTF and more specifically the position of the main absorption peak. Therefore, structural and photophysical properties of various polypyridyl linkers, which can be used to build CTFs, have been investigated in **Paper II**. Subsequently, the mechanisms responsible for the photoactivation of octahedral ruthenium complexes are studied. We show that triplet ESs play an important role in this process. In **Paper I**, we studied the influence of varying the ligands of the complex on its optical properties and examined the effect of embedding the complex in the CTF.

Both investigations were part of a concerted research action (GOA) and were performed in collaboration with the experimental groups of

Prof. Christian V. Stevens (SynBioC, Ghent University) and Prof. Pascal Van Der Voort (COMOC, Ghent University), who were responsible for the experiments conducted in **Paper I** and **Paper II**.

4.1 Introduction to covalent triazine framework materials and their linkers

A guidance to design CTFs, shown in Figure 1.4, is given in **Paper II**, in which we applied the principle of orthogonal electronic structure engineering, stating that, within a COF scaffold, the overall electronic structure can be tuned by varying the electronic structure of the constituents.[206] This combined computational/experimental study provides detailed insights in how varying the CTF ligands influences the structural and optical properties in order to select interesting building blocks for CTFs. We focused on a special branch of CTFs that contain polypyridyl ligands as they allow for a stable anchoring of photocatalytic complexes.[206] A large variety of ligands can be used, creating a versatile platform to engineer support materials for anchoring various complexes. Therefore, a fundamental study of their structural and photophysical properties is needed. The polypyridyl ligands studied in this work are presented in the left column of Table 4.1 and vary in their ring topology, nitrogen content, termination, and the presence of additional functional groups. Most of the linkers are terminated by cyano groups to mimic the experimental conditions in which CTF are synthesized by trimerization of linkers terminated by such groups, as shown in Figure 1.4.[207] The pristine pyridine (1) and bipyridine (3) linkers, which are terminated by hydrogen atoms, are included to make a proper comparison with literature data. For the bipyridine linker, we also included linker (5), terminated with triazine groups, to investigate the influence of the termination group in more detail. Complementary to the computational study, linkers (1)-(4) and (6) have also been characterized experimentally in this work.

The experimental and theoretical UV-Vis spectra of linkers (1)-(6) are shown in Figures 4.1 and 4.2 and illustrate that the photocatalytic properties of the linkers are mainly characterized by the position of the main absorption peak, *i.e.,* the first ES with a significant oscillator strength. As this electronic excitation corresponds to a $\pi \rightarrow \pi^*$ transition, the size of the π-system and the π-electron deficiency will play an important role. The same holds for the other linkers in Table 4.1.

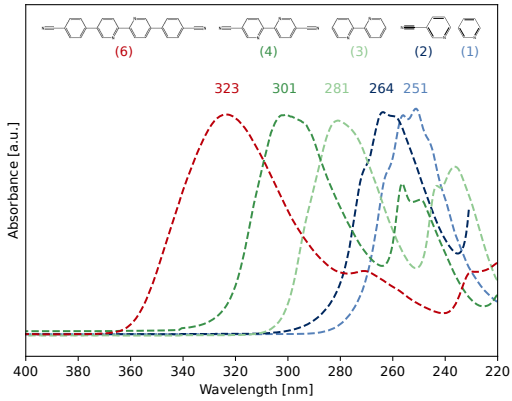

Figure 4.1: Experimental UV-Vis spectra of ligands (1)–(4) and (6) in acetonitrile as solvent. The energies of the main absorption peaks are indicated. Figure reproduced from Ref. 25 with permission of Chemistry Europe, 2020.

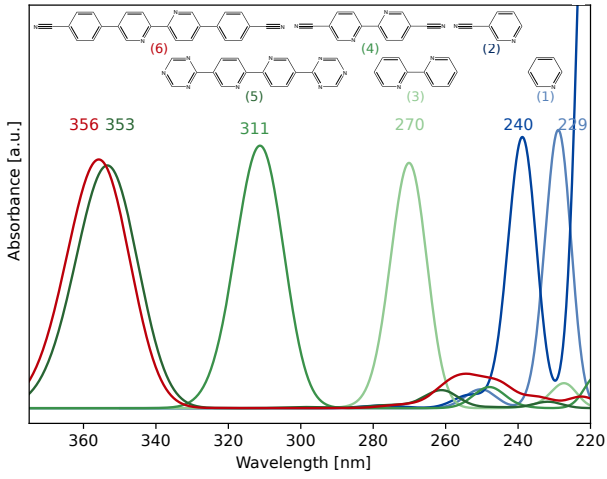

Figure 4.2: Theoretical UV-Vis spectra of ligands (1)–(6). The energies of the main absorption peak are indicated. Calculations carried out at the B3LYP/6-31++G** level of theory and with acetonitrile as solvent. Figure reproduced from Ref. 25 with permission of Chemistry Europe, 2020.

Linker	E_{trans}	E_{cis}	Cis dihedral angle	E	Dihedral angle	E_{exp}
 (1)				229(5.41)	/	251(4.94)
 (2)				240(5.17)	/	264(4.70)
 (3)	270(4.59)	257(4.82)	34.2			281(4.41)
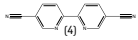 (4)	311(3.99)	298(4.16)	32.4			301(4.12)
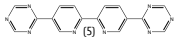 (5)	353(3.51)	338(3.67)	33.3			
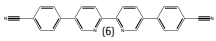 (6)	356(3.48)	340(3.65)	32.8			323(3.84)
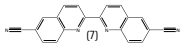 (7)	377(3.29)	345(3.59) 266(4.66)	34.2			
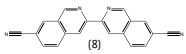 (8)	377(3.29)	363(3.42) 275(4.51)-270(4.59)	36.4			
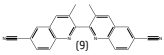 (9)				310(4.00) 252(4.92)	112	
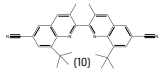 (10)				305(4.07) 258(4.81)	106	
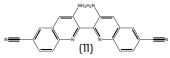 (11)				500(2.48) 351(3.53) 296(4.19)-285(4.35)	158	
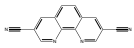 (12)				311(3.99) 289(4.29)	180	
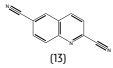 (13)				326(3.80) 301(4.12) 255(4.86)	180	

Table 4.1: Dihedral angle [°] and energy of the main absorption peak [nm] and [eV] between brackets for all linkers. Linkers (3)-(8) have both a cis and trans structure and E_{trans}, E_{cis}, and the cis dihedral angle are reported whereas the other linkers only have one optimized structure for which E and the dihedral angle are given. For linkers (1)-(4) and (6), the experimental results are displayed in the last column. Calculations carried out at the B3LYP/6-31++G** level of theory and with acetonitrile as solvent. (1): pyridine (2): pyridine-3-carbonitrile (nicotinonitrile) (3): 2,2'-bipyridine (4): 2,2'-bipyridine-5,5'-dicarbonitrile (5): 5,5'-bis(4-cyanophenyl)-2,2'-bipyridine (6): 5,5'-bis(4-cyanophenyl)-2,2'-bipyridine (7): [2,2'-biquinoline]-6,6'-dicarbonitrile (8): [3,3'-biisoquino-line]-7,7'-dicarbonitrile (9): 3,3'-dimethyl-[2,2'-biquinoline]-6,6'-dicarbonitrile (10): 8,8'-di-tert-butyl-3,3'-dimethyl-[2,2'-biquinoline]-6,6'-dicarbonitrile (11): 3,3'-diamino-[2,2'-biquinoline]-6,6'-dicarbonitrile (12): phenantroline-5,5'-dicarbonitrile (13): quinoline-2,6-dicarbonitrile.

This Chapter is further organized as follows. After a short note on the chosen level of theory, we examine the influence of the size of the π-system and the π-electron deficiency on the main absorption band. This is followed by a study of the dependence of the ES properties on the dihedral angle, as some of the linkers have an extra degree of freedom, namely a rotation around the central carbon-carbon bond. In this regard, computational techniques are extremely useful as they allow one to easily estimate the influence of the dihedral angle, whereas this is not the case for experimental investigations. We conclude this section with an overview of the relative shifts between all ligands studied in this work and a summary of the main factors influencing the ES properties. In this way, insight is gained in how the optical properties of the CTF linkers are influenced and how they can be tuned by varying their topology, making it possible to engineer the most suited candidate for specific applications.

4.1.1 Influence of the level of theory on the ground and excited state properties

First of all, a benchmark study has been performed for the UV-Vis spectrum of the trans conformer of linker (4), as shown in Figure 4.3. We observed that functionals lacking the inclusion of Hartree-Fock exchange need a significant blue-shift to match the experimental data. Contrarily, long-range corrected functionals require a large red-shift. The best performance was obtained for B3LYP and M06 and we chose to continue with the former. We tested several basis sets too, but observed only slight changes in the UV-Vis spectra. Furthermore, the influence of the level of theory on the geometrical parameters was found to be negligibly small. Finally, we investigated the influence of the acetonitrile solvent and discovered that the barrier for going from the trans to the cis conformer, where the nitrogen atoms are either on opposite or on the same side of the two pyridine rings, decreases with at least 10 kJ/mol, resulting in an increase of the probability of finding the ligand in its cis conformation.

The theoretical calculations in this work are not only based on static approaches. Besides the geometry optimizations and ESs calculations, we also performed MD simulations at the BLYP level of theory with the inclusion of Grimme D3 dispersion.[208] We refer the reader to **Paper II** for a complete overview of the computational details.

Once the level of theory is fixed, we note that the position of the main absorption peak strongly differs for the various linkers, as shown in

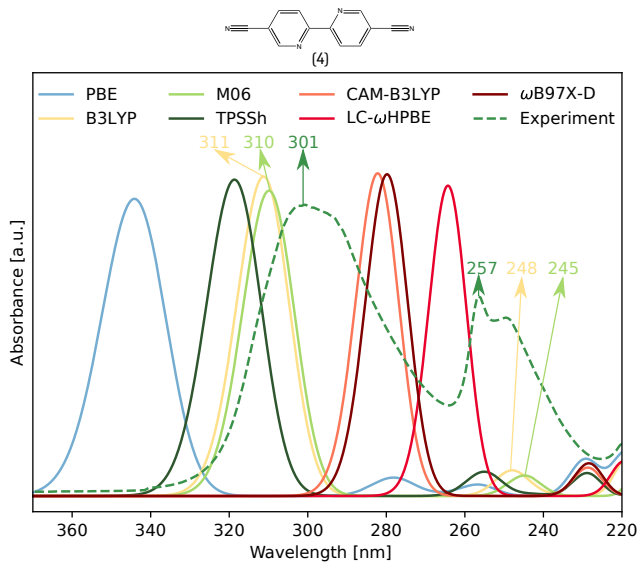

Figure 4.3: UV-Vis spectra of ligand (4) for several functionals (full lines) together with the experimental spectrum (dashed line). The energies of the first and second absorption peak are indicated for B3LYP, M06, and experiment. Calculations carried out with the 6-31++G** basis set and with acetonitrile as solvent. Figure reproduced from Ref. 25 with permission of Chemistry Europe, 2020.

Figures 4.1 and 4.2. In the next section, we investigate which factors have an influence on the position of the main absorption peak.

4.1.2 Influence of extending the π-system and increasing the π-electron deficiency on the excited state properties.

The position of the main absorption peak is strongly affected by the size of the π-system, which can be enlarged by adding more aromatic rings, and by the π-electron deficiency of the system. Polypyridyl linkers are π-electron deficient due to the presence of nitrogen atoms. Indeed, their free electron pairs are not part of the aromatic system and as a result, the linker will accept electrons more easily. The π-electron deficiency can be increased by adding electron-withdrawing groups such as the cyano group CN^- or termination groups containing nitrogen atoms.

For linkers (1)-(6), the influence of both properties on the position of

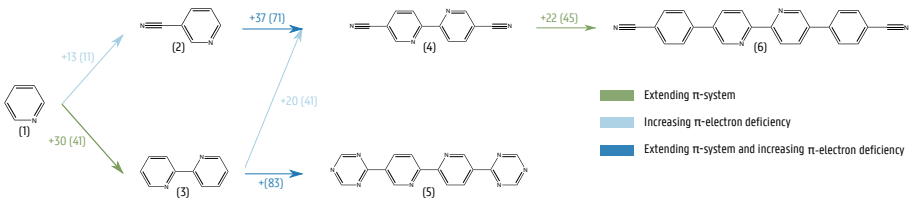

Figure 4.4: Influence of extending the π-system and increasing the π-electron deficiency of the linkers on the position of the main absorption peak. Shifts are given in nm. We report experimental results along with the computational findings between parentheses. Figure reproduced from Ref. 25 with permission of Chemistry Europe, 2020.

the main absorption peak is visualized in Figure 4.4. Experimental results are presented along with the computational findings between parentheses. We notice a shift toward larger wavelengths, both when the π-system increases as when the linker becomes more π-electron deficient. This is indicated in green and light blue, respectively. On the one hand, the influence of extending the π-system is studied by comparing linkers (3) and (6) to linkers (1) and (4), respectively. On the other hand, the π-electron deficiency is increased when going from linkers (1) and (3) to linkers (2) and (4). For the combined effect of increasing the size of the π-system and the π-electron deficiency, a large shift toward larger wavelengths is observed, as indicated with dark blue. In this regard, linkers (2) and (4) and linkers (3) and (5) are studied. Note that, in general, the experimentally observed shift is smaller than the one obtained from TDDFT calculations.

As an example, the most important orbitals for the trans conformer of linker (4) are shown in Figure 4.5, where the first bright excitation is indicated in green. The subscript indicates whether the orbital is quinoid (Q) or antiquinoid (AQ), respectively. This nomenclature is borrowed from the Jahn-Teller (JT) distorted benzene radical anion.[209] We will elaborate on the JT effect in TMCs in Chapter 5. Placing an electron in a π^*_Q-orbital causes a shortening of the lateral bonds, while placing it in a π^*_{AQ}-orbital results in an elongation of those bonds. The most intense transition is of the type $\pi_Q \rightarrow \pi^*_Q$, a conclusion which applies for the other linkers too.

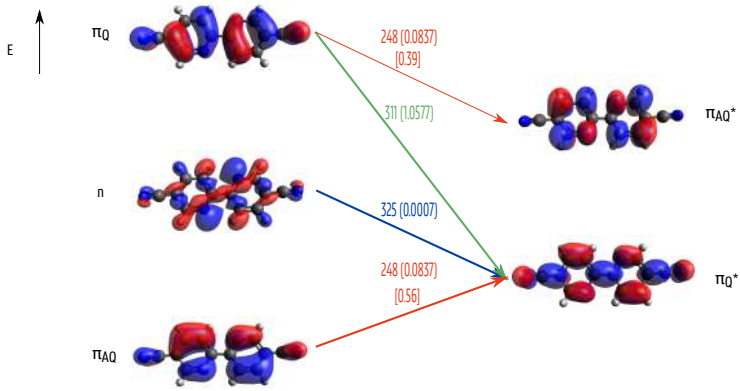

Figure 4.5: Visualization of the important orbitals of the trans conformer of linker (4). The arrows indicate the most dominant contributions of the first non-dark (blue) and two bright (green and red) excitations, characterized by the excitation energy in nm, oscillator strength, f, between parentheses, and amplitude in square brackets if more contributions are reported for a specific excitation. The occupied MOs in the left represent respectively the HOMO, HOMO-1 and HOMO-5 in descending order. The unoccupied MOs in the right represent respectively the LUMO + 3 and LUMO. Calculations carried out at the B3LYP/6-31++G** level of theory and with acetonitrile as solvent. Figure reproduced from Ref. 25 with permission of Chemistry Europe, 2020.

4.1.3 Influence of the dihedral angle on the excited state properties

Until now, we neglected for linkers (3)-(8) the rotational degree of freedom about the central carbon-carbon bond, as schematically shown in Figure 4.6. We limited the study to static calculations by assuming that the linkers are in the energetically most favorable trans configuration corresponding to a dihedral angle of $180°$. The nitrogen atoms are then on opposite sides of the two pyridine rings. However, some polypyridyl ligands favor the cis conformation, in which the nitrogen atoms are on the same side, in some specific environments, as for example for the anchoring of photocatalytic complexes. Therefore, we extend this study by investigating the influence of the dihedral angle for linkers (3)-(8). In order to study the dynamic behaviour of these systems, MD simulations were performed starting from the trans and cis conformer of linker (4). The MD calculations were carried out at the BLYP level of theory and in gas phase. However, the overall qualitative picture is expected to remain unaltered when solvent is taken into account.

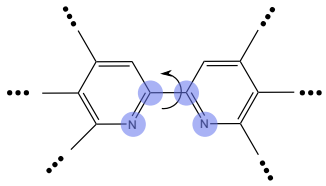

Figure 4.6: Schematic representation of the dihedral angle in a polypyridyl ligand. Figure reproduced from Ref. 25 with permission of Chemistry Europe, 2020.

The histograms of the dihedral angle are presented in the left and right pane of Figure 4.7, respectively. On the one hand, for the simulation starting from the cis structure, a transition to the trans conformer is observed after 48 ps, after which the linker remained in the trans conformer and no transition back to the cis structure has been observed after 100 ps. On the other hand, no transitions are detected after 53 ps when one starts from the trans structure. These results are expected as the barrier to go from the trans to the cis conformer is rather high, *i.e.,* 35.25 kJ/mol, as shown in **Paper II**. Furthermore, as shown in the inset in the left pane of Figure 4.7, it was found that the trans conformer is not completely planar, which is in agreement with experiment.[210] Remark that for this observation the dynamic behavior of the system plays a crucial role as the structures obtained from geometry optimizations are completely planar.

In order to investigate the influence of the dihedral angle on the UV-Vis spectrum, we performed a rotational scan, in which we started with the optimized cis conformer of linker (4), possessing a dihedral angle of circa 32°, after which we varied the dihedral angle with a step size of 10°. At every step, the structure was fully optimized except for the frozen dihedral. The UV-Vis spectrum was calculated for each point of the rotational scan and shown for some specific values of the dihedral angle in Figure 4.8. When the dihedral angle decreases, the peak shifts to smaller wavelengths and thus the excitation energy increases. Meanwhile, the size of the conjugated π-system decreases when the structure becomes less and less planar as the π-interactions along the bond get weaker. Furthermore, the oscillator strength decreases. The lowest wavelength is observed for structures with a dihedral angle of 92°. Then, the spectrum closely resembles that of linker (2), as shown by the dotted black line. Indeed, the orbitals in the two rings are only slightly connected and the spectrum of linker (4) is just the sum of its components, *i.e.,* linker (2). When the dihedral angle decreases further, the peak shifts to larger wavelengths again. This is accompanied by an increase

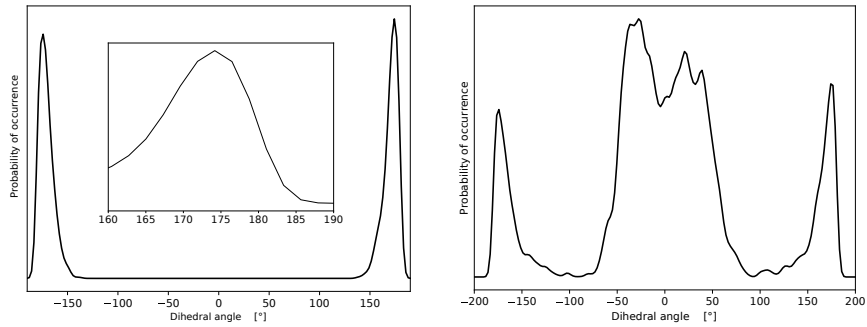

Figure 4.7: Histogram of the dihedral angle for the MD simulations starting from the trans conformer (left) and cis conformer (right) of linker (4). In the left pane, we zoomed in on the range between 160° and 190°. Calculations carried out at the BLYP-D3 level of theory. The time step for integrating the equations of motion was set at 0.5 fs and the simulations were performed in the NVT ensemble at a temperature of 300 K. Figure reproduced from Ref. 25 with permission of Chemistry Europe, 2020.

of the oscillator strength as the conjugated π-system increases again when the structure becomes more planar. As such, the largest conjugated system has the smallest excitation energy, which is in agreement with Ref. 211. As the main absorption peak mainly consists of a HOMO→LUMO transition for all dihedral angles, these observations are in agreement with the well known fact that the HOMO-LUMO gap decreases when the conjugated system increases.

The shift of the brightest transition observed between the cis and trans conformers is 13 nm and amounts to circa 50 nm between structures with a dihedral angle of 2° and 92°. Finally, we also note that for most values of the dihedral angle, a second peak is observed around 250-260 nm. However, no second peak is found for dihedral angles around 90°. This has been detected earlier: the presence of two bands is an indication that the structure is not twisted, whereas only one band is visible in this region for a large twist.[211]

4.1.4 Excited state properties of all ligands

Lastly, we extend this study by including linkers (7)-(13), which might be interesting CTF building blocks too. Table 4.1 gives an overview of the energy of the main absorption peak, along with the dihedral angle of the optimized structure. For linkers (3)-(8), both the cis and trans conformers

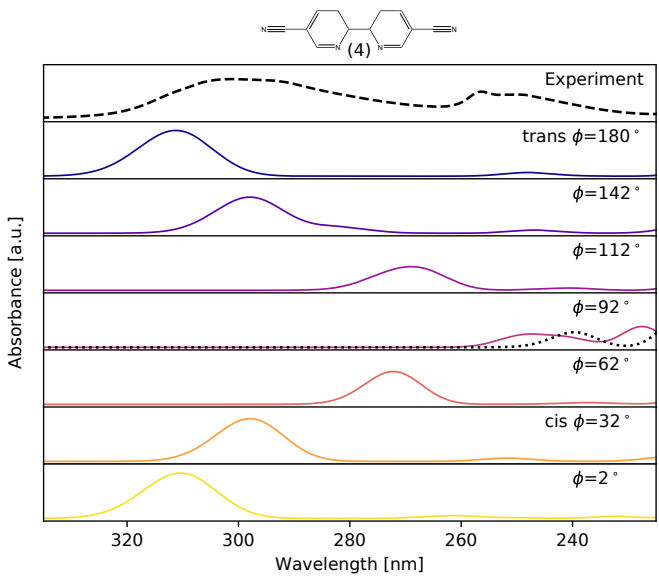

Figure 4.8: Influence of the dihedral angle on the UV-Vis spectrum of ligand (4). The experimental spectrum is indicated with a dashed line and the dotted line represents the spectrum of linker (2). Figure reproduced from Ref. 25 with permission of Chemistry Europe, 2020.

are studied. Experimental values, measured by Jonas Everaert (SynBioC, Ghent University), are given in the last column. As stated before, the larger the π-system and the higher the π-electron deficiency, the more the main absorption peak shifts to larger wavelengths. This can be achieved by adding more aromatic rings, electron-withdrawing groups, or termination groups containing nitrogen atoms. Furthermore, as described in the previous section, the dihedral angle has a significant influence on the size of the π-system too. The position of the main absorption peak can be explained based on the above arguments for almost all linkers as shown in **Paper II**. There is only one exception, namely the relatively large difference observed between the trans conformers of linkers (7) and (8), which can be understood as follows. Both the HOMO and LUMO of ligand (7) have a large contribution from the nitrogen atoms, whereas this is only the case for the LUMO of ligand (8). The inclusion of nitrogen into the orbital results in a lowering of the orbital energy due to the larger electron negativity of nitrogen compared to carbon. As such, both the HOMO and LUMO decrease in energy for ligand (7), whereas only the LUMO of linker (8) gets stabilized, resulting in a smaller HOMO-LUMO gap and thus also lower excitation

energies for the latter.

Finally, it is worth mentioning that the maximal shift of the main absorption peak is observed for linker (11) and amounts to 271 nm with respect to pyridine. This is due to the presence of the electron-donating NH_2 functional groups. Indeed, this linker has an extra occupied orbital situated on the NH_2 group, which is higher in energy than the occupied orbitals which are not situated on these groups. Therefore, we observe an extra transition for linker (11) at very high wavelengths.

We conclude that the position of the main absorption peak can be tuned as follows. First of all, one can alter the size of the conjugated π-system, which depends on the number of aromatic rings and the dihedral angle. Second, the amount of π-electron deficiency can be increased by terminating the linker with groups containing nitrogen atoms or adding electron withdrawing structures such as CN^-. Finally, also the addition of functional groups can have a significant influence on the ES properties. The broad range of shifts of the main absorption peak gives perspective in the modulation of the electronic structure by varying the ligands and can help in the rational design of efficient photocatalysts.

4.2 Photocatalytic Ru^{2+} complexes with polypyridyl ligands

In the previous section, we studied how the properties of the CTF can be tuned by altering the ligands. Now, we revert our attention to the photocatalytic complex which is anchored to the CTF to form a heterogeneous catalyst. In this work, we focus on Ru^{2+} complexes. First, we study the mechanisms relevant for the photocatalytic behavior of these complexes. Afterwards, we investigate how their optical properties can be tuned by varying the nitrogen content of the linkers.

When the Ru^{2+} complexes, of which an example with three cis-2,2'-bipyridine ligands is shown in Figure 4.9, are exposed to light, the ESs have two possible relaxation mechanisms, resulting in a reduction or oxidation of the substrate molecules. This is schematically shown in Figure 4.10, in which the orbital occupancy of the frontier electron states is sketched for the different steps in the process. As discussed in Chapter 3, the d-orbitals of octahedral TMCs split in a t_{2g}- and e_g-orbital set, indicated in red. Ligand orbitals, shown in blue, are situated in between these two sets. In the GS,

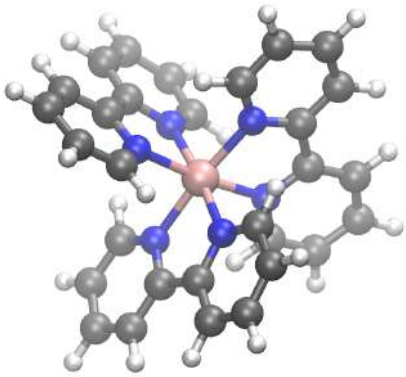

Figure 4.9: Visualization of the geometrical structure of [Ru(cis-2,2'-bipyridine)$_3$]$^{2+}$. Carbon, hydrogen, nitrogen, and ruthenium are indicated in gray, light gray, blue, and pink, respectively.

the six d-electrons of Ru^{2+} fully occupy the t_{2g} set, depicted in the left box. By absorption of a photon in the visible region, a singlet $\rightarrow$ singlet MLCT excitation occurs, leaving an electron hole in the t_{2g}-orbitals. Consequently, the oxidation number of ruthenium increases by one. The singlet ES quickly converts to a lower-energy triplet ES via non-radiative means. This mechanism is called inter-system crossing (ISC) and the resulting state, shown in the second box in Figure 4.10, is long-lived as the decay to the singlet GS is spin-forbidden. The ES can relax via two mechanisms. On the one hand, the electron in the ligand orbitals can be transferred to the organic substrate. Hence, the latter is reduced and the Ru^{3+} cation is maintained as indicated with the upper arrow in Figure 4.10. On the other hand, an electron can be transferred from the substrate to the vacant t_{2g}-orbital, resulting in a reduction of the complex, as presented by the lower arrow in Figure 4.10. Consequently, Ru^{3+} reverts to Ru^{2+} and the substrate is oxidized.

Besides these electron-transfer processes, the decay of the complex from a triplet ES can also involve the excitation of the substrate to a triplet ES. This mechanism is called triplet-triplet energy transfer (TTET) and has been the subject of both theoretical[212] and application-oriented investigations.[213]

The research community's enduring interest in these Ru-complexes and analogues dates back to the 1970s in the efforts to apply these TMCs to water-splitting technologies.[214] From 2008 onward, more sophisticated organic synthetic applications have been targeted too.[215]

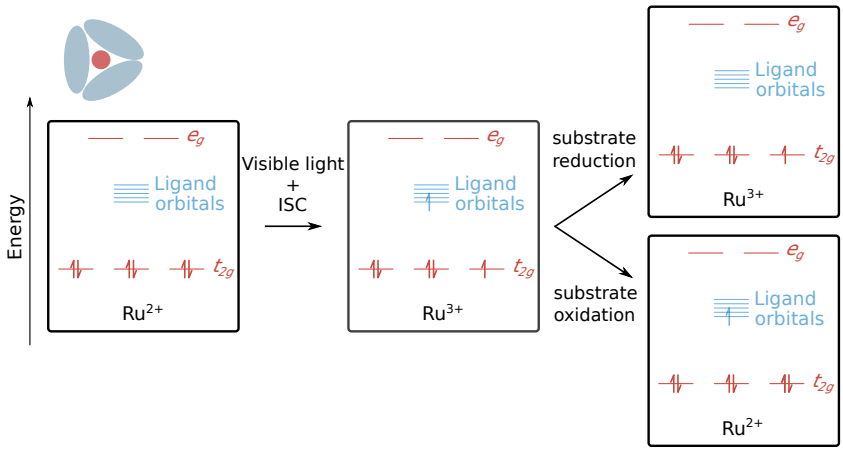

Figure 4.10: Photoactivation of an octahedral ruthenium complex from the GS (left box) to a triplet ES (second box) under the influence of visible light, exciting an electron toward a state localized on the ligands, followed by ISC. The ES relaxes by reduction (upper arrow) or oxidation (lower arrow) of the substrate. Figure reproduced from Ref. 32 with permission of American Chemical Society, 2013.

In the remainder of this section, we will not only focus on the main absorption peak of the complex, corresponding to a singlet ES, but also on triplet ESs since they play an important role in the photocatalytic process. As these transitions are spin-forbidden for systems with a singlet GS, they are difficult to discern in experimental spectra. Nevertheless, they are easily retrieved via computational techniques such as TDDFT, as shown in Section 2.2.4.

In this work, the influence of the nitrogen content on the photocatalytic properties is studied for $[RuL_3]^{2+}$ complexes, where L can be 2,2'-bipyrimidine (bipm), cis-2,2'-bipyridine (bipy), or cis-2,2'-bipyrazine (bipz). The ten possible photocatalytic complexes are shown in Figure 4.11. We assume that the LS singlet state of the Ru^{2+} complexes is the most stable spin-state. Indeed, the orbitals of $4d$ TMs are more diffuse than their $3d$ counterparts,[216] resulting in stronger metal-ligand bonds and a larger LF splitting. In Ref. 217, it was also shown that properties, like for example spin-state energetics, which strongly depend on the amount of HF exchange included in the functional for $3d$ TMs, are considerably less sensitive for $4d$ metals. Hence, in this work, we will only focus on the properties of singlet Ru^{2+} complexes.

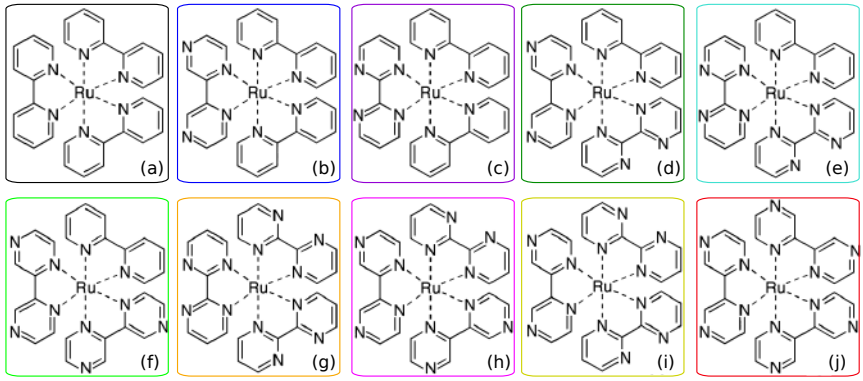

Figure 4.11: Ten $[RuL_3]^{2+}$ complexes investigated here. (a) L = bipy × 3; (b) L = bipy × 2, bipz × 1; (c) L = bipy × 2, bipm × 1; (d) L = bipy × 1, bipz × 1, bipm × 1; (e) L = bipy × 1, bipm × 2; (f) L = bipy × 1, bipz × 2; (g) L = bipm × 3; (h) L = bipz × 2, bipm × 1; (i) L = bipz × 1, bipm × 2; (j) L = bipz × 3. Figure reproduced from Ref. 218 with permission of American Chemical Society, 2019, available from https://pubs.acs.org/doi/full/10.1021/acs.jpca.9b05216.

The performance of PBE, B3LYP, CAM-B3LYP, and M06 has been investigated for the calculation of the ESs of $[Ru(bipy)_3]^{2+}$. Similarly as for the CTF linkers studied in Section 4.1, functionals lacking HF contributions need a significant blue-shift, whereas long-range corrected functionals require a red-shift to match experimental data. Although both B3LYP and M06 are in good agreement with experimental results, we chose to continue with M06 as it produces a better shape of the absorption bands. The reader is referred to **Paper I** for a summary of the computational details.

The vertical excitation spectra of $[Ru(bipy)_3]^{2+}$ obtained by TDDFT are shown in Figure 4.12. Theoretical calculations were carried out both in the gas phase and with water and acetonitrile solvents modeled with the PCM. The simulated spectra are compared with the experimental UV-Vis absorption profiles in water[219] and acetonitrile solvents, which were generated within this work. The very good agreement between theory and experiment strengthens our confidence to apply this level of theory for the embedded complex too.

As discussed in Section 2.2.6, it is known that TDDFT might fail to correctly describe CT excitations. Therefore, it is important to corroborate

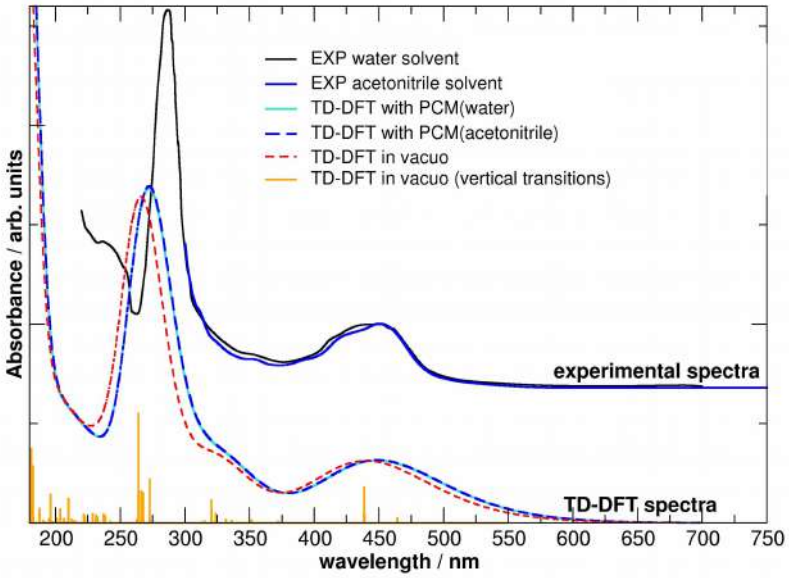

Figure 4.12: Experimental UV-Vis absorption (top, Ref. 219 and **Paper I**) and TDDFT with the M06 functional spectra (bottom) of $[Ru(bipy)_3]^{2+}$. Vertical excitations for the in vacuo TDDFT spectrum are indicated as orange spikes. Computed spectra have been smoothed using Gaussian functions of half-width at half-height of 0.333 eV. The computed spectra have not been rescaled nor shifted. Figure reproduced from Ref. 218 with permission of American Chemical Society, 2019, available from https://pubs.acs.org/doi/full/10.1021/acs.jpca.9b05216.

the ES observations with GS considerations. Moreover, we have employed CAM-B3LYP, which is often considered better suited to describe CT phenomena,[220] to compute KS gaps in the isolated and CTF-embedded complexes. The results are in qualitative agreement with those for the M06 functional, but are significantly blue-shifted. To further investigate the nature of the transitions, we have also used the M_{AC} index, introduced in Section 2.2.6, from which we could certify the CT character of the transition and confirm the reliability of the TDDFT results.

A side note is warranted on how to compare the theoretical and experimental data. The optical gap can be extrapolated from UV-Vis absorption measurements as the energy of the first divergence of the spectrum from its baseline and is approximated as the energy of the first allowed transition in TDDFT. It is defined by a neutral excitation and equals

the difference between the energies of the lowest allowed ES and the GS.[221] As the optical gap accounts for the electron-hole recombination energy or exciton binding energy, it is systematically lower than the fundamental gap, which is defined by charged excitations, namely as the difference between the first ionization potential and the first electron affinity.[221]

The influence of the nitrogen content on the optical gap, *i.e.,* the energy of the first singlet ES with a non-zero oscillator strength, is presented in the top pane of Figure 4.13. The corresponding transitions are of the MLCT type. We conclude that the optical gap can to a certain extent be tuned by varying the nitrogen content of the ligands. Interestingly, the lowest value is observed for complex (b), *i.e.,* $[Ru(bipy)_2(bipz)]^{2+}$, which contains eight nitrogen atoms and is composed of one bipz and two bipy ligands. A similar distribution of values, albeit with different magnitudes, is observed for the most intense transitions, occurring in the UV and blue visible region between 3 and 2.7 eV, as can be seen in Figure 4.16.

Triplet ESs are nested between the singlet ESs and are also MLCT transitions. Although the contributions of these spin-forbidden ESs to the absorption spectra are negligible, they play an important role in TTET and can still be encountered during non-radiative processes and decays which require a relaxation of the geometry. Therefore, they have to be taken into account to describe photocatalytic complexes.[222, 223] The adiabatic transition energies of the first triplet states closely follow the same trend for an increasing nitrogen content as the non-forbidden singlet ESs, as shown in the bottom pane of Figure 4.13. Although the ESs are situated at lower energies and have a smaller overall variation, complex (b) is still pinpointed as the complex with the smallest transition energy.

The results are also in agreement with these obtained from GS calculations on $[Ru(L)_3]^{2+}$ complexes. Indeed, we observe that the HOMO-LUMO gap, approximately describing the MLCT, attains its minimal value for complex (b). The variation as a function of the nitrogen content is much smaller than the one of the HOMO-3-LUMO gap, which approximates the ligand-ligand gap and decreases as a function of an increasing nitrogen content.

As such, we conclude that the $[Ru(bipy)_2(bipz)]^{2+}$ complex is very promising as calculations of the GS, first singlet, most intense, and adiabatic first triplet ESs reveal that it has the lowest excitation energy, allowing for a larger portion of radiation to be used for its activation.

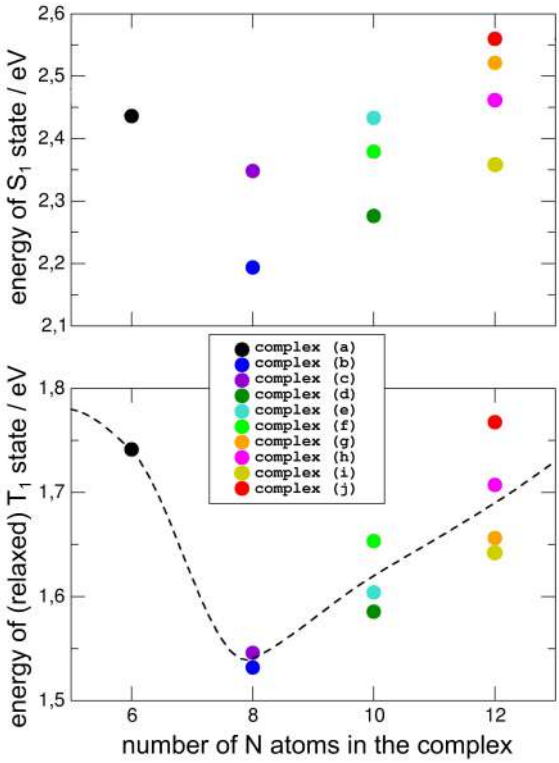

Figure 4.13: Vertical TD-M06 energies of the first non-forbidden singlet states (upper panel) and of the first optimized triplet states (lower panel) for the ten complexes introduced in Figure 4.11. Figure reproduced from Ref. 218 with permission of American Chemical Society, 2019, available from https://pubs.acs.org/doi/full/10.1021/acs.jpca.9b05216.

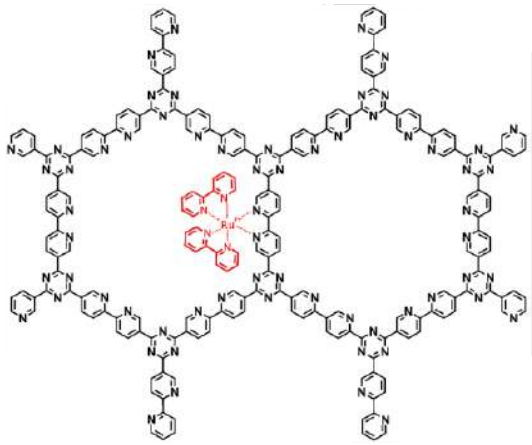

Figure 4.14: Model of the $[Ru_2]^{2+}$@CTF system for the specific case of $[Ru(bipy)_2]^{2+}$@CTF. Figure reproduced from Ref. 218 with permission of American Chemical Society, 2019, available from https://pubs.acs.org/doi/full/10.1021/acs.jpca.9b05216.

4.3 Embedding of photocatalytic Ru^{2+} complexes on the covalent triazine framework

In the attempt to design new green catalysts, there is a high interest in developing recyclable and reusable heterogeneous photocatalytic systems.[36–39] Therefore, we investigate in the last part of this Chapter how the electronic properties of Ru^{2+} complexes are affected when they are embedded in an extensive CTF structure model.[207] We studied a CTF composed of triazine nodes interlinked with bipy linkers which can naturally act as ligands for the $[RuL_3]^{2+}$ complexes, giving rise to a $[RuL_2]^{2+}$@CTF compound, as shown in Figure 4.14. Due to the fact that the ligand embedded in the CTF is bipy, the number of possible ligand combinations in the $[RuL_2]^{2+}$@CTF complex is reduced with respect to the isolated complexes from ten to six as only complexes (a)-(f) remain. The investigated model consists of two full CTF pores to minimize edge effects as a consequence of the sudden truncation of our cluster model. The cluster was terminated by completing the coordination of carbon atoms with hydrogen atoms.

In the $[RuL_2]^{2+}$@CTF system, occupied framework states are situated between the occupied t_{2g}- and virtual ligand orbitals, as schematically shown in Figure 4.15. This results in a substantial lowering of the HOMO-LUMO gaps by about 2.5-2.8 eV compared to the isolated complexes.

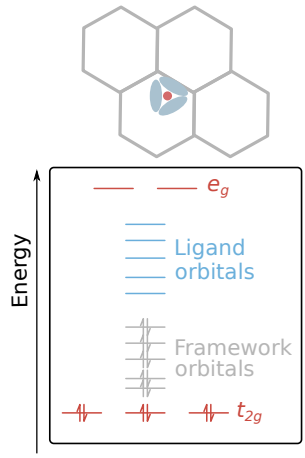

Figure 4.15: Schematic representation of the orbital energies for the GS of $[RuL_2]^{2+}$@CTF. Figure reproduced from Ref. 218 with permission of American Chemical Society, 2019, available from https://pubs.acs.org/doi/full/10.1021/acs.jpca.9b05216.

Furthermore, we observe that the HOMO-LUMO gap decreases with an increasing nitrogen content in the linkers of the complex. When the number of nitrogen atoms increases from six to ten, the energy of the t_{2g} and e_g sets reduces by about 1 eV with respect to $[Ru(bipy)_2]^{2+}$@CTF. Moreover, the energy of the framework orbitals remains rather unaffected and the virtual ligand orbitals decrease with about 0.5 eV, resulting in a reduction of the HOMO-LUMO gap.

The first ES with non-vanishing oscillator strength is no longer mainly of the MLCT type as was the case for isolated complexes. Instead, we observe a CT from states localized on the CTF toward states situated on the ligands of the complex. The target orbital can be localized on the bipy ligand of the CTF or on the ligands exposed inside the pore. The first non-forbidden transition in $[RuL_2]^{2+}$@CTF is thus of the crystal-to-crystal charge-transfer (CCCT) or crystal-to-ligand charge-transfer (CLCT) type.

The energy of the strongest excitation of the embedded complexes, which is also a CCCT or CLCT, is shown in the bottom pane of Figure 4.16. The excitation energies fall into the orange-near-infrared region. This is expected, as the HOMO-LUMO gap is much smaller for the embedded complexes than for the isolated ones. Furthermore, as the excitation occurs from an occupied orbital which is no longer situated on the metal, changing the nitrogen content of the ligands induces a significant drop in the vertical

excitation energy of the most intense transition, down to values as low as 1.6 eV. This is also in agreement with the observed trends in the GS orbital energies as described previously.

As such, we conclude that embedding of the complex has a significant effect on the nature and energy of the ESs. First of all, the transition energies are significantly red-shifted toward the near IR. Furthermore, while in isolated complexes the change of the energy of the strongest ES with the number of nitrogen atoms of the ligands is small and non-monotonous, a clear decrease is observed in the embedded complexes. This is due to the fact that the transition occurs from an occupied orbital which is no longer localized on the TM but on the CTF, whereas the target orbital remains situated on the ligands of the Ru^{2+} complex. By tuning the nitrogen content of the linkers of the complex, the optical gap can be reduced by about 0.5 eV. For example, near-infrared photocatalysis could greatly benefit from the nanoporous environment and thus make better use of the near-infrared solar irradiation, making up 44% of the solar spectrum.[224, 225]

In this Chapter, we provided a route toward rational design of green heterogeneous catalysts by showing how the photocatalytic properties can be tuned by varying the ligands, both of the CTF and the photocatalytic complex. In this regard, some of our computational results have been verified experimentally. Furthermore, it has been demonstrated how anchoring of the Ru^{2+} complex on a support allows one to increase the range of wavelengths that may be exploited for photocatalysis.

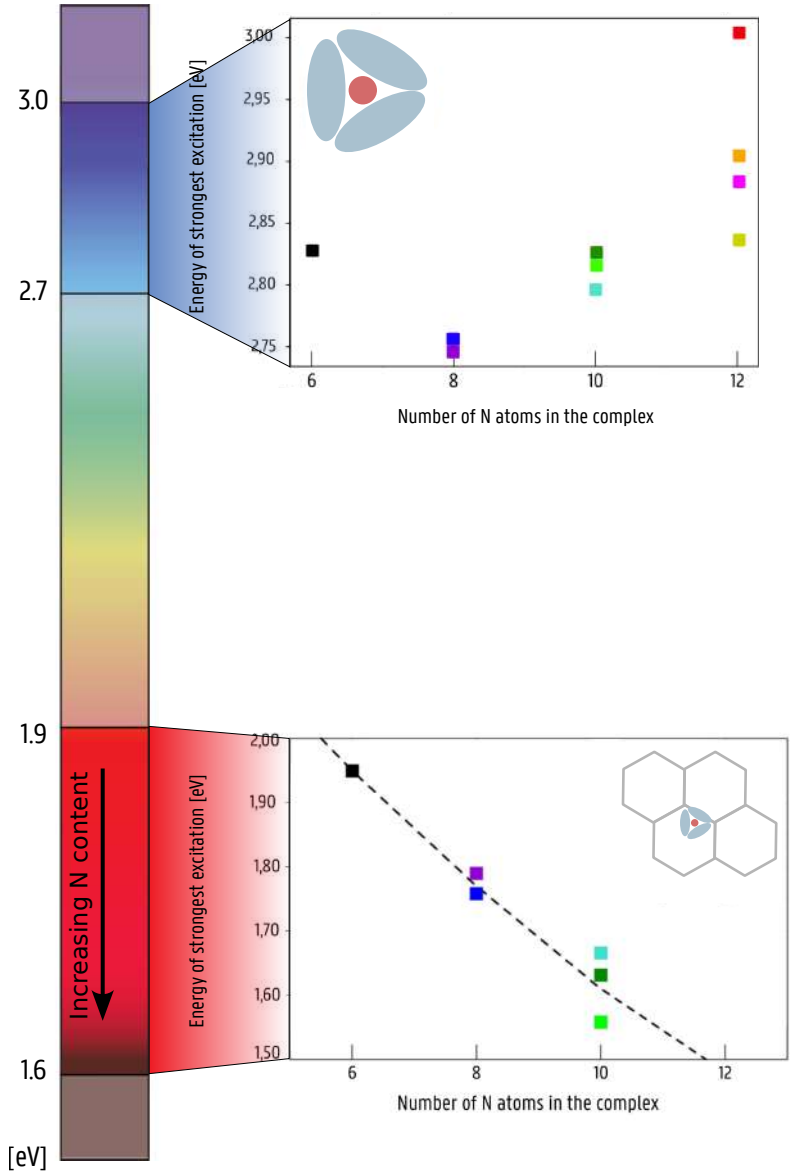

Figure 4.16: Energy of the strongest excitation for the isolated and embedded complexes. The colors for the various structures are defined in Figure 4.11. Figure reproduced from Ref. 218 with permission of American Chemical Society, 2019, available from https://pubs.acs.org/doi/full/10.1021/acs.jpca.9b05216.

5

Ground and Excited State Properties of Transition Metal Complexes Relevant for the ZIF Nucleation Process

It was already mentioned in Chapter 1 that an in-depth understanding of the formation process of ZIFs is crucial to enable a more targeted search for materials for specific applications. Although the particle nucleation step is more or less understood by now,[62, 63] the elementary molecular processes in the pre-nucleation stage have been less thoroughly investigated and remain largely unknown. Only very recently, a combined experimental-computational study has been conducted by Matthias Filez (CoCooN, Ghent University and Roeffaers group, KU Leuven) at the Weckhuysen Research group, Utrecht University, in collaboration with the CMM.[64] By using *in situ* UV-Vis spectroscopy, they revealed that during Co-ZIF-67 formation, mixing of the pink $Co(NO_3)_2 \cdot 6H_2O$ and the transparent 2-mIm methanolic solutions induces a rapid color change to purple, as schematically shown in Figure 5.1. A metal-organic pool with a variety of complexes is formed caused by ligand elimination and substitution reactions. As a result, the octahedral Co^{2+} precursors are transformed, over five-coordinated systems, into tetrahedral $[Co(2\text{-mIm})_4]^{2+}$ complexes, which are the building blocks of Co-ZIF-67, as shown in Figure 1.7. The experimental study was accompanied by DFT and MD simulations in order to unravel the molecular driving forces behind pre-nucleation.

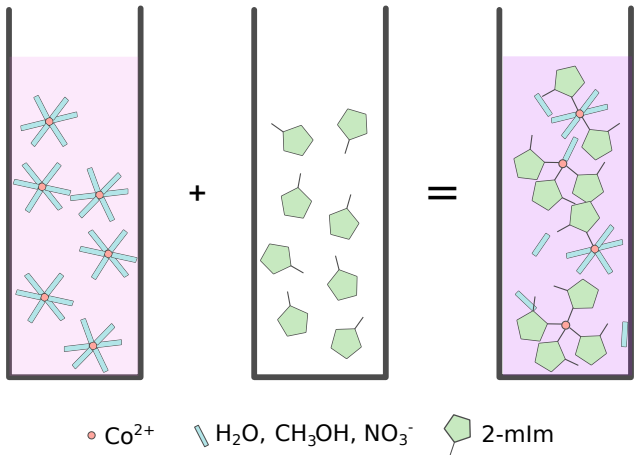

Figure 5.1: Mixing of $Co(NO_3)_2 \cdot 6H_2O$ (pink) and 2-mIm (transparent) methanolic solutions induces rapid color change (purple) due to ligand substitution/elimination reactions and coordination changes of $[Co(OR)_6]^{2+}$ (OR = methanol, H_2O, NO_3^-) to $Co(2\text{-mIm})_x(OR)_{y-x}$. Figure adapted from Ref. 64 with permission of Elsevier, 2021.

To fully understand the complicated underlying mechanisms, we aim to characterize the d-d transitions of the TMCs and focus on their number, intensity, and position which change during the course of the formation process and can therefore serve as a spectroscopic fingerprint. As ES calculations are based on a GS reference, we start with an investigation of the GS properties of the TMCs and concentrate on the d-orbital splitting, which is decisive for the d-d transitions. This is the subject of **Paper III**, in which the influence of the symmetry on the position of the d-orbital energy levels is assessed. Two phenomena underlie the variations in symmetry. First of all, large effects are expected when the number of ligands is changed, resulting in various coordination environments, *i.e.*, six-coordinated octahedral, five-coordinated square pyramidal (SP) or trigonal bipyramidal (TBP), and four-coordinated tetrahedral complexes. Furthermore, additional effects are caused by the various point groups encountered for each coordination environment. Indeed, as will be shown later in this Chapter, deviations from the perfect symmetry are observed. Hereby, special attention is devoted to the JT effect, stating that non-linear molecules with a degenerate electronic GS undergo a geometrical distortion in order to lower the energy.[226] We test the performance of AOC and UDFT, presented in Chapter 3 and Chapter 2, respectively, by comparing their

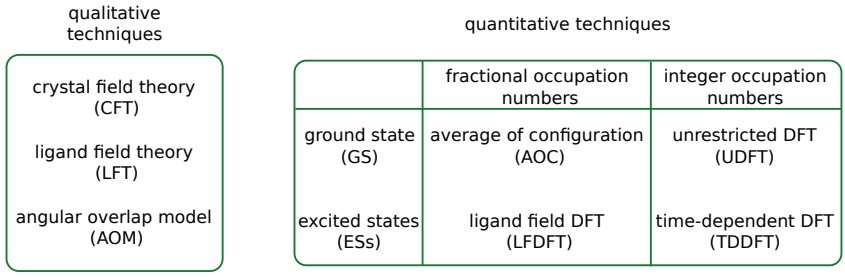

Figure 5.2: Overview of the techniques used in this Chapter. For the quantitative techniques, a distinction is made between methods employing fractional and integer occupation numbers as well as between techniques used to determine the GS and ES properties.

results with qualitative techniques such as CFT, LFT, and AOM, introduced in Chapter 3. After studying the GS properties, transitions between the d-orbitals are investigated in **Paper IV**. As TMCs pose various challenges on computational techniques, we first examine the performance of TDDFT and LFDFT, introduced in Chapter 2 and Chapter 3, respectively, for first-row octahedral aqua-complexes. They are categorized according to the degeneracy of their GS and the presence of double excitations. With this knowledge, we then calculate the d-d transitions for the TMCs relevant in the nucleation process of Co-ZIF-67. An overview of the techniques used in this Chapter is given in Figure 5.2. Our computational data are complemented with experimental data of Ref 64.

The workflow followed in this work is shown in Figure 5.3. First, an UDFT geometry optimization is performed using gaussian or ADF. As an additional pre-processing step, the input can be constrained to a certain point group via gaussview. The same program can be used to determine the point group of the optimized geometry. In addition, when the structure is not highly symmetric, SHAPE can be employed to determine the continuous shape measures, as discussed in Section 3.2. This step is followed by a single point calculation. When integer occupation numbers are used, this corresponds to the final step of the geometry optimization. However, when fractional occupation numbers are desired, an extra AOC calculation needs to be performed by ADF. Moreover, if one is interested in the ESs, additional calculations are needed. On the one hand, when considering integer occupation numbers, a TDDFT calculation is conducted via gaussian or ADF. The results can be investigated via gaussview. On the other hand, when fractional occupation numbers are used, a LFDFT calculation is performed by ADF.

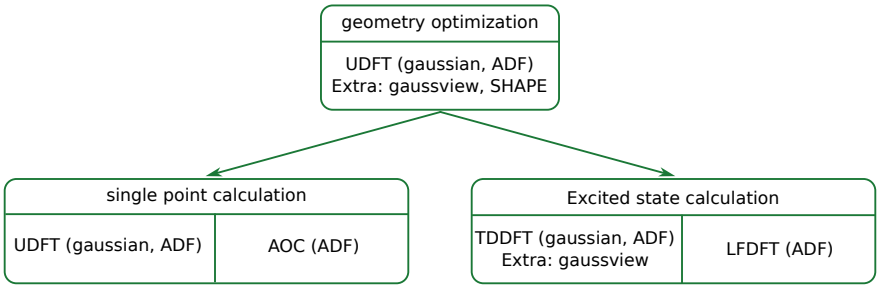

Figure 5.3: Overview of the workflow used in this work.

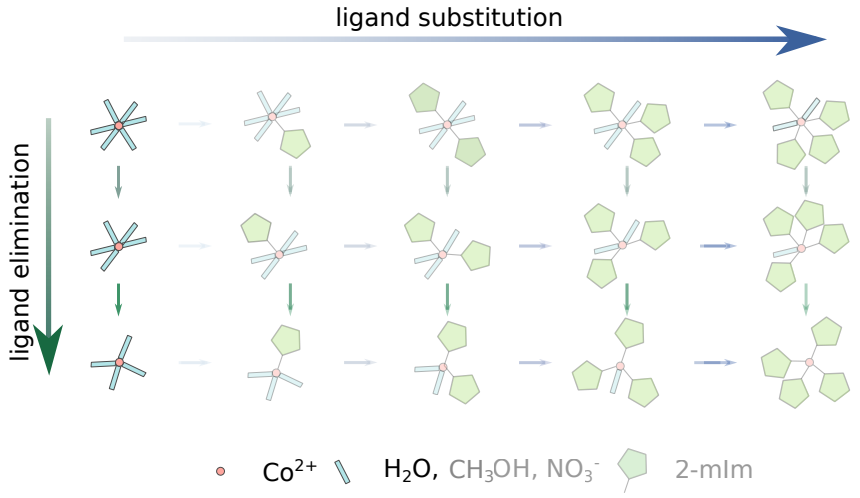

Figure 5.4: Reaction network of ligand elimination and substitution reactions leading to fast preequilibrium formation toward a metal-organic pool. The GS properties of Co^{2+} complexes with six, five, and four aqua ligands are studied in this work and are indicated. Figure adapted from Ref. 64 with permission of Elsevier, 2021.

5.1 Influence of symmetry on the electronic structure of Co^{2+} aqua-complexes

In the first part of this Chapter, we study the GS properties of octahedral, SP, TBP, and tetrahedral Co^{2+} complexes, shown in Figure 5.4. We restrict ourselves to aqua ligands as, in particular for hexa-aqua Co^{2+} complexes, the results can be compared to previous studies. We start with an overview of the results obtained from qualitative techniques, after which the d-orbital splitting is calculated via AOC and UDFT.

5.1.1 Qualitative d-orbital splitting: crystal field theory, ligand field theory, and angular overlap model

As discussed in Section 3.4, several theoretical models, such as CFT, LFT, and AOM, have been introduced in the past century to describe the electronic structure of TMCs and are still extensively used today. All these models have their advantages and disadvantages, but in general, give the same qualitative results. Although quantitative results can be obtained by determining the parameters from experimental absorption spectra, we will not focus on this and only give a qualitative explanation of the d-orbital splittings for complexes with various symmetries as shown in Figure 5.5. The labeling of the orbital sets in the various point groups is indicated too.

For an isolated TM, all five d-orbitals are degenerate. As described in Section 3.4.1, the average energy of the d-orbitals is above that of the free ion orbitals when the TM is surrounded by ligands. Furthermore, the degeneracy of the d-orbitals is (partially) lifted. This will be studied in the subsequent paragraph for six-, five-, and four-coordinated complexes.

Octahedral TMCs with O_h symmetry have already been discussed in Section 3.4.1. When removing one ligand, a five-coordinated structure is obtained. On the one hand, a SP structure belonging to the C_{4v} point group can be retrieved; d_{z^2}, d_{xz} , and d_{yz} are stabilized compared to the octahedral case, as there is less repulsive interaction along the z-direction. On the other hand, a TBP structure with D_{3h} symmetry can be obtained. As opposed to the octahedral complex, d_{xy} and $d_{x^2-y^2}$ are increased/decreased in energy, respectively, because they point more/less toward the ligands. When another ligand is taken out, we obtain a tetrahedral structure with T_d symmetry, which has already been encountered in Section 3.4.1. As such, qualitative techniques reveal that the d-orbital splitting is characteristic for the number of ligands coordinated to the TM.

When no experimental input data is used, these techniques serve as tools for interpreting rather than for predicting phenomena in TMCs. Therefore, we perform computational studies based on DFT to acquire quantitative d-orbital splittings for Co^{2+} aqua-complexes. These *ab initio* results can then be compared to the theoretical predictions shown in Figure 5.5 and to the available experimental information.

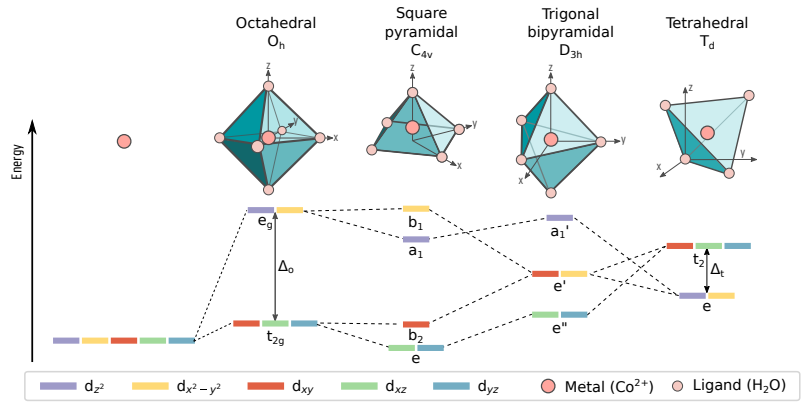

Figure 5.5: Splitting of the d-orbitals for a TM in various environments. For an isolated TM, all d-orbitals are degenerate, whereas for complexes with octahedral, SP, TBP, and tetrahedral symmetry, the degeneracy is (partially) lifted. The splitting between the two orbital sets in octahedral and tetrahedral complexes is denoted by Δ_o and Δ_t, respectively. The labeling of the d-orbitals in the various point groups is also indicated. A graphical visualization of the d-orbitals is shown in Figure 3.2. Figure reproduced from Ref. 227 with permission of American Chemical Society, 2022.

5.1.2 Quantitative d-orbital splitting: average of configuration versus unrestricted DFT

As stated in Section 3.1, different spin-states are possible for some TMCs. For the Co^{2+}-ion with seven d-electrons, there are two possible spin multiplicities, four and two, forming the HS and LS configuration, respectively. According to the spectrochemical series, water is a weak π-donor ligand.[228] Therefore, the LF splitting in octahedral complexes is rather small and the energy needed to pair two electrons is larger than the energy required to place an electron in the higher-lying e_g set. Hence, the HS state of $[Co(H_2O)_6]^{2+}$ is more stable. [229] Moreover, since the LF splitting is in general smaller in tetrahedral complexes, we conclude that their HS state is more stable too. Finally, it has also been observed that, in five-coordinated complexes, ligands with oxygen donor atoms usually result in HS configurations.[230, 231]

Two types of calculations based on DFT have been performed, *i.e.,* AOC and UDFT. In the former, introduced in Chapter 3, a spin-restricted DFT calculation is performed, in which the d-electrons are distributed evenly among the five MOs dominated by d-orbitals. This results in an average occupation of 1.4 electrons for d^7 complexes. Meanwhile, in UDFT, the spin

multiplicity is specified and all of the five α-orbitals are filled, whereas only two β-orbitals are occupied. Geometry optimizations have been performed using UDFT. Using the single-reference UDFT method for these challenging systems may at first instance appear to be unsatisfactory as configuration averaging, necessary to treat the degenerate micro-states of the GS equally, is lacking. However, Shee *et. al.* have recently put forward that in most TMCs, static correlation is rarely found in the GS.[232] Indeed, the degeneracy is mostly elevated by JT effects. Furthermore, it has been shown that good structures and energies are often obtained from DFT calculations at a moderate computational cost.[233] These arguments justify our choice for using UDFT to describe the GS properties of these systems. Nevertheless, as there are complex interactions present, including ligand-to-metal σ- and π-donation, a proper treatment of the dynamic correlation becomes extremely important.

We assessed the following functionals: BLYP[104] and BP86[105] based on the GGA, M06L[108] and MN15L[107] built on the meta-GGA, O3LYP,[110] B3LYP,[104, 109] X3LYP,[111] and PBE0[106] as hybrid GGA, with 12, 20, 21.8, and 25 % of Hartree-Fock exchange, the hybrid mGGA MN15[115] and TPSSh[113, 114] with 44% and 10% Hartree-Fock exchange, respectively, and the long-range corrected CAM-B3LYP[116] and ωB97x[117]. As shown in **Paper III**, our results immediately indicate that not enough Hartree-Fock exchange is included in O3LYP, for which the splitting between the e_g and t_{2g} set is too large. All other functionals provide similar results and we have chosen to continue with B3LYP-D3. We refer the reader to **Paper III** for a complete overview of the computational details.

In the following, the AOC results are discussed in detail for $[Co(H_2O)_6]^{2+}$, $[Co(H_2O)_5]^{2+}$, and $[Co(H_2O)_4]^{2+}$. We systematically investigate how the lowering of the number of ligands affects the symmetry and thus the geometry and the electronic structure of these Co^{2+} complexes. This is followed by a comparison between the performance of AOC and UDFT.

I. Average of configuration

We start with $[Co(H_2O)_6]^{2+}$, of which the geometrical structure has already been investigated thoroughly in literature.[229, 234] These complexes have O_h symmetry when the ligands are assumed to be spherical symmetric. However, when we take into account the structure of the aqua ligands, the highest possible symmetry becomes T_h. In contrast to the results of Varadwaj[234] and Schmiedekamp,[229] we did not find a stable minimum with

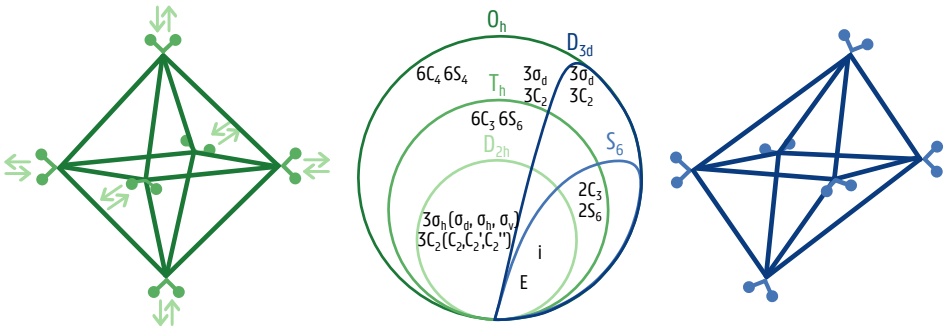

Figure 5.6: Graphical visualization of the point groups encountered for the six-coordinated complexes, *i.e.*, O_h, T_h, D_{2h}, D_{3d}, and S_6. In the middle pane, all symmetry elements enclosed belong to the corresponding point group. Perfect octahedral symmetry, O_h, is indicated in dark green. The presence of hydrogen atoms reduces the symmetry to T_h and is indicated in middle green. Elongation or contraction of the metal-ligand bonds results in D_{2h} symmetry and is shown in light green. An increase or decrease of the ligand-metal-ligand angles leads to a tilted structure with D_{3d} symmetry and is presented in dark blue. When the hydrogen atoms are taken into account in the tilted structure, the S_6 symmetry is obtained as shown in light blue. Figure reproduced from Ref. 227 with permission of American Chemical Society, 2022.

T_h symmetry. This is in agreement with the JT effect. Despite the fact that only weak JT effects are expected for unevenly occupied t_{2g}-orbitals, we did observe them. We obtained a stable structure with D_{2h} symmetry in which the rhombic JT distortions are clearly visible as unequal amounts of elongation or compression occur along the fourfold axes of rotation. As such, the structure remains orthogonal, but the bond distances are no longer equal. Besides this, we also found a structure with S_6 symmetry, acquired via a trigonal distortion of the complex, *i.e.,* an elongation/compression along one of the four threefold symmetry axes. All ligand bond distances are equal, but the structure is no longer orthogonal. A graphical visualization of the symmetry elements present in the point groups encountered for $[Co(H_2O)_6]^{2+}$ is presented in Figure 5.6.

The d-orbital splittings along with their atomic contributions are shown in Figure 5.7 and are very similar to the theoretical predictions presented in Figure 5.5. In general, each MO has a dominant contribution from a specific

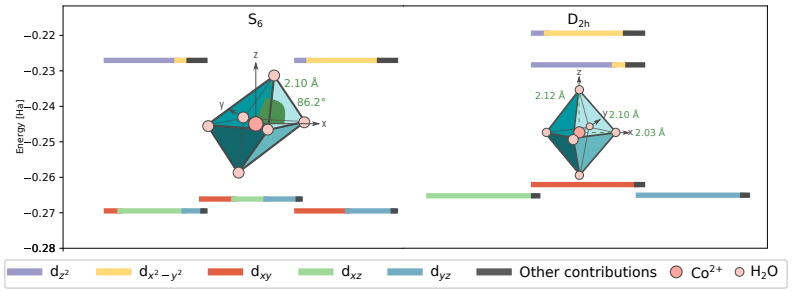

Figure 5.7: Splitting of the d-orbitals along with their atomic contributions for the optimized $[Co(H_2O)_6]^{2+}$ complexes with S_6 (left) and D_{2h} (right) symmetry. Figure reproduced from Ref. 227 with permission of American Chemical Society, 2022.

d-orbital, which can be used to label the MOs. The orbitals in the t_{2g} set are no longer completely degenerate. This is in agreement with CFT, which reveals that a trigonal distortion splits the t_{2g}, but not the e_g-orbitals in octahedral complexes.[139] For the D_{2h}-complex, the degeneracy in the e_g set is lifted too. The reason for this is that the bonds between the ligands and the TM along the x-axis are compressed, resulting in a stronger repulsion between the $d_{x^2-y^2}$-orbital and the metal compared to the d_{z^2}-orbital. Finally, we note that the value of Δ_o, which can be calculated as the difference between the average energy of the e_g and t_{2g} orbitals, being 9065 and 8836 cm^{-1} for the S_6 and D_{2h} structures, respectively, is in close agreement with experimentally obtained splitting of 8400 cm^{-1}.[235]

For the five-coordinated complexes two stable structures have been obtained with C_{2v} and C_1 symmetry, respectively. We determined the CShMs via the program SHAPE, which has been introduced in Section 3.2.2 and evaluates the magnitude of distortion around the TM,[152, 153] in order to determine whether the complexes are closer to SP or TBP symmetry. From this, we conclude that the structure with C_{2v} symmetry is closer to SP, whereas the C_1 structure is closer to TBP. In general, the resulting d-orbital splitting shown in Figure 5.8 agrees with the theoretical predictions shown in Figure 5.5, but some differences should be mentioned. The gap between the $d_{x^2-y^2}$- and d_{z^2}-orbitals is rather large for the SP complex and d_{xz} and d_{yz} are not completely degenerate. This is not surprising since the complex only has C_{2v} symmetry, in contrast to the results shown in Figure 3.4.2 for C_{4v} structures. The degeneracy is also lifted for the TBP complex as d_{xz}/d_{yz} and $d_{x^2-y^2}/d_{xy}$ are no longer degenerate.

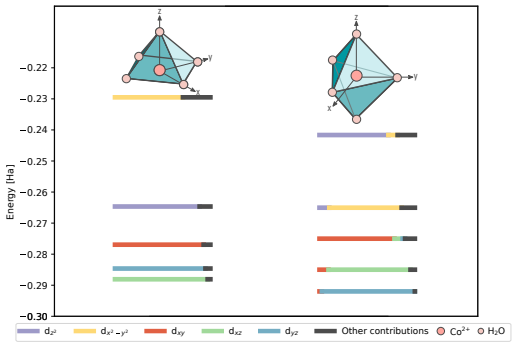

Figure 5.8: Splitting of the d-orbitals along with their atomic contributions for the optimized $[Co(H_2O)_5]^{2+}$ complexes with C_{2v} symmetry (left) and no symmetry (right). Figure reproduced from Ref. 227 with permission of American Chemical Society, 2022.

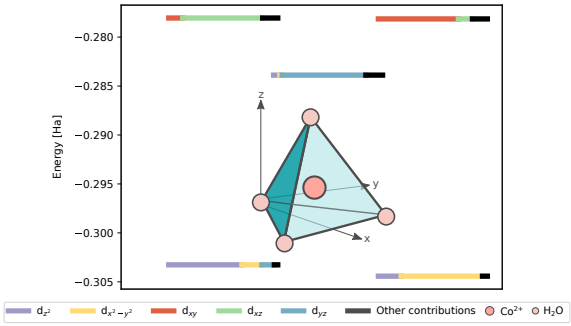

Figure 5.9: Splitting of the d-orbitals along with their atomic contributions for the optimized $[Co(H_2O)_4]^{2+}$ complex. Figure reproduced from Ref. 227 with permission of American Chemical Society, 2022.

The optimized $[Co(H_2O)_4]^{2+}$ structure does not possess any symmetry. The results presented in Figure 5.9 are in good agreement with those obtained in Figure 5.5: two orbital sets can be distinguished, t_2 and e, where the former is lower in energy. Due to the fact that the complex is not purely tetrahedral, the degeneracy in the t_2 set is lifted slightly. Furthermore, the computed value of the LF splitting is much smaller than the one in the octahedral complex, as we expected from AOM.

From the above observations, we conclude that the AOC method is capable of reproducing the theoretical d-orbital splittings for octahedral, SP, TBP, and tetrahedral complexes.

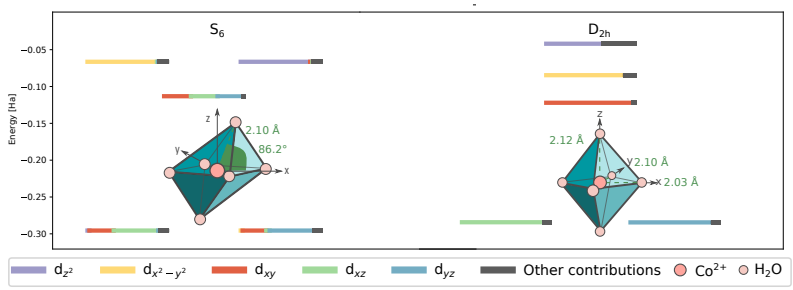

Figure 5.10: Splitting of the β d-orbitals for the optimized $[Co(H_2O)_6]^{2+}$ complexes with S_6 (left) and D_{2h} (right) symmetry calculated by UDFT. Figure reproduced from Ref. 227 with permission of American Chemical Society, 2022.

II. Comparison of average of configuration with unrestricted DFT

In the next step, we compare the AOC results with these from UDFT calculations. The energies of the β d-orbitals obtained from UDFT are shown in Figure 5.10 for $[Co(H_2O)_6]^{2+}$. Some major distinctions compared to the AOC results need to be highlighted. First of all, remark that the splitting of the d-orbitals is one order of magnitude larger than for the AOC results and the experimentally found splitting. Secondly, the t_{2g} set is divided into two low-lying orbitals and one orbital with higher energy. This is because only two of the β d-orbitals are occupied.

Additionally, in the UDFT results of the D_{2h} complex, d_{z^2} is higher in energy than $d_{x^2-y^2}$, which is in contrast to the AOC results. This can be explained by the fact that UDFT and LFT treat the interelectron repulsion differently, as argued by Deeth *et al.* for square planar d^8 Pd-complexes.[236] The interelectron repulsion effects are included within a central field approximation in LFT, whereas in UDFT the calculations are performed using the true molecular symmetry of the complex.[236] Consequently, the AOC orbitals confirm the chemical intuition as given by LFT as both techniques describe the electron repulsion in a spherical way, whereas, in UDFT, only d_{yz} and d_{xz} are occupied, resulting in more interelectron repulsion along the z-axis than along the x- or y-axis, leading to a higher-lying d_{z^2}-orbital compared to $d_{x^2-y^2}$.

Inspired by the work of Deeth *et al.,* we verified this by systematically moving some portion of the electrons from d_{xz} and d_{yz} to d_{xy}. Therefore, single point UDFT calculations, in which the d-orbital occupation is specified, were performed and shown in Figure 5.11. Two observations

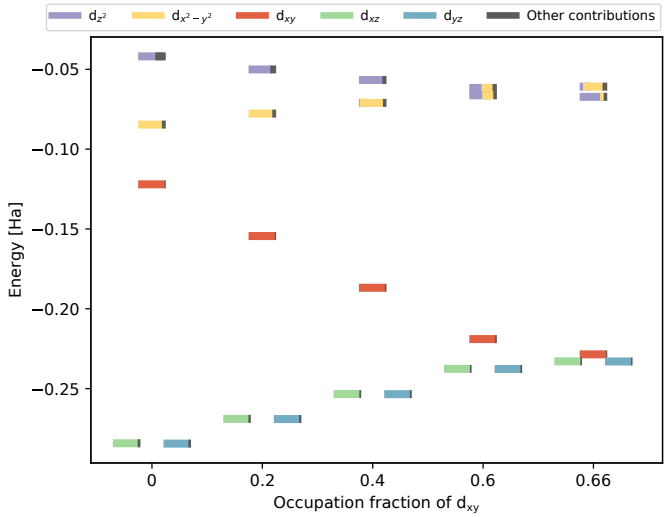

Figure 5.11: Variation of the splitting of the d-orbitals as a function of the electron occupation fraction of d_{xy} which is transferred equally from d_{xz} and d_{yz} for the $[Co(H_2O)_6]^{2+}$ complex with D_{2h} symmetry. Figure reproduced from Ref. 227 with permission of American Chemical Society, 2022.

can be made as more and more of the electrons initially on d_{xz} and d_{yz} are transferred to d_{xy}. First of all, the orbitals become closer in energy and are almost degenerate when 0.66 of an electron is placed at d_{xy}. The reason for this is that the two β electrons are now almost equally divided among the three orbitals, resulting in a similar interelectron repulsion along the x-, y-, and z-axes. Secondly, d_{z^2} and $d_{x^2-y^2}$ decrease and increase in energy, respectively. At an occupation of 0.6 electrons for d_{xy}, the two most energetic orbitals presented in Figure 5.11 have similar d_{z^2} and $d_{x^2-y^2}$ contributions and are almost degenerate. When d_{xy} is populated even more, $d_{x^2-y^2}$ becomes higher in energy than d_{z^2}.

In the UDFT results for the S_6 complex, the $d_{x^2-y^2}$- and d_{z^2}-orbitals are degenerate in accordance with the AOC results. Indeed, the effect of the difference in interelectron repulsion is smaller as the two occupied d-orbitals do not only have contributions from d_{yz} and d_{xz}, but also from d_{xy}. Similar observations have been made for the five-coordinated complexes.

For the four-coordinated complexes, the two e-orbitals are occupied, and therefore, the splitting is in accordance with the AOC and theoretical results. Nevertheless, the energy gap between the e and t_2 set is still one

order of magnitude too large.

To further test the validity of UDFT, additional calculations have been performed on $[V(H_2O)_6]^{2+}$, $[Mn(H_2O)_6]^{2+}$, and $[Ni(H_2O)_6]^{2+}$, having three, five, and eight d-electrons, respectively, as shown in Figure 5.12. These TMs have been selected as no JT effects are expected, since the t_{2g} set is completely filled with α electrons for V^{2+} and Mn^{2+} or α and β electrons for Ni^{2+}. This is also observed from the calculations for the V^{2+} and Ni^{2+} complexes, for which stable structures with T_h symmetry are retrieved. However, the most symmetric stable Mn^{2+} complexes have S_6 and D_{2h} symmetries. First, remark that, for all systems, both AOC and UDFT predict a splitting of the d-orbitals into a t_{2g} and e_g set, in agreement with CFT. This is due to the fact that the t_{2g}-orbitals are either completely filled with α-electrons, as is the case for Mn^{2+} and V^{2+}, or with both α- and β-electrons, as is the case for the Ni^{2+} complex. Second, for $[Mn(H_2O)_6]^{2+}$, all α d-orbitals are occupied, resulting in a correct prediction of the magnitude of the d-orbital splitting by both techniques. This result is not surprising since the only differences between the AOC and UDFT calculations are due to the spin polarization which is absent in the former. Nevertheless, as with the Co^{2+} complex, the splitting is severely overestimated by UDFT for $[V(H_2O)_6]^{2+}$ and $[Ni(H_2O)_6]^{2+}$. The observations are in agreement with Ref. 236, in which it was argued that DFT is expected to yield the same d-orbitals sequence as LFT in those cases where a suitable spherical configuration is constructed corresponding to equal populations of the d-orbitals as for d^{10} or HS d^5 complexes. Here, this observation is confirmed and extended to octahedral d^3 , d^5, and d^8 HS systems.

Summarizing, based on qualitative techniques, we conclude that the d-orbital splitting is characteristic for the number of ligands. This can be reproduced by the AOC method, but UDFT calculations do not succeed in this when only part of the d-orbitals are occupied. Indeed, for example for octahedral d^7 complexes, the energy gap between the e_g and t_{2g} sets is overestimated and there is a gap between the occupied and unoccupied t_{2g}-orbitals. Based on the work of Deeth *et al.*,[236] we demonstrated that the discrepancies between UDFT and AOC are due to the different electron occupations resulting in different interelectron repulsions.

As stated in Ref. 236, the observation that UDFT and AOC result in different d-orbital splittings does not necessarily mean that one of these techniques is right whereas the other is wrong. Orbitals themselves are not experimentally observable, and therefore, additional properties need to be calculated, like for example ESs.[236] This is the subject of **Paper IV** and will

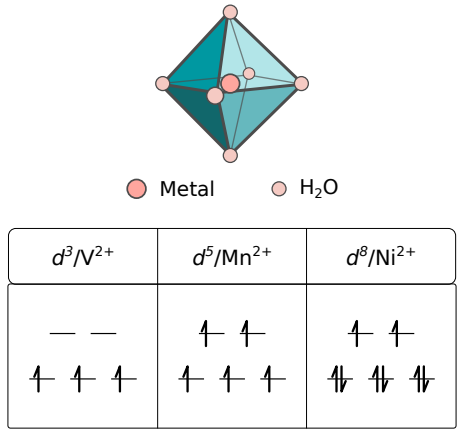

Figure 5.12: Overview of the electron configurations of $[V(H_2O)_6]^{2+}$, $[Mn(H_2O)_6]^{2+}$, and $[Ni(H_2O)_6]^{2+}$.

be discussed in the next section.

5.2 Excited state properties

It was shown in Ref. 64 that the metal-organic pool formed in the Co-ZIF-67 nucleation process contains a diversity of TMCs showing fingerprints of octahedral and tetrahedral Co^{2+} complexes with simple ligands such as water, methanol, and NO_3^-, as well as 2-mIm ligands. The experimental spectra reveal mainly the presence of the complexes highlighted in Figure 5.13.[64] Our goal is to characterize the d-d excitations of these TMCs and propose a spectroscopic fingerprint. Therefore, we first discuss how the Tanabe-Sugano diagrams, introduced in Section 3.3, can be used to describe the d-d excitations in TMCs. In a next step, the challenges encountered for first-row octahedral aqua-complexes are discussed and the performance of TDDFT and LFDFT is investigated. With this knowledge, we finally examine the d-d excitations in the relevant TMCs, shown in Figure 5.13, where we again only consider water and not methanol nor NO_3^-, in order to put forward a spectroscopic fingerprint.

5.2.1 Using Tanabe-Sugano diagrams for the description of d-d excitations in TMCs

Tanabe-Sugano diagrams were introduced in Chapter 3 and are shown in Figures B.3, B.4, B.5, B.6, 3.13, and B.7 for octahedral d^2, d^3, d^4, d^6, d^7,

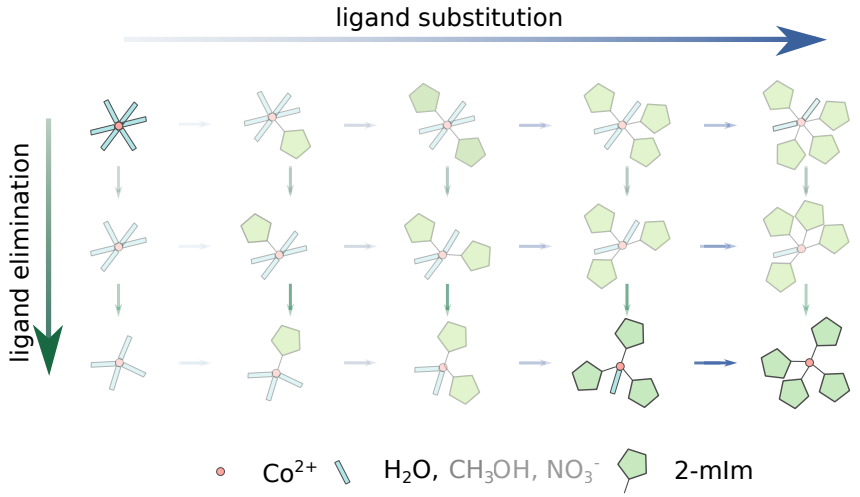

Figure 5.13: Reaction network of ligand elimination and substitution reactions leading to fast preequilibrium formation toward a metal-organic pool. The excitation spectra of $[Co(H_2O)_6]^{2+}$, $[Co(2\text{-mIm})_3(H_2O)]^{2+}$, and $[Co(2\text{-mIm})_4]^{2+}$ are studied in this work and are indicated. Figure adapted from Ref. 64 with permission of Elsevier, 2021.

and d^8 complexes. As octahedral and tetrahedral d^7 complexes will play a major role in the remainder of this Chapter, their diagrams are repeated for convenience in Figures 5.14 and 5.15. In addition, some micro-states are included in the right panes which will now be discussed.

For octahedral d^7 complexes in the weak field limit situated at the left of the diagram, the lowest energy terms ^4F, ^4P, and ^2G are indicated in light purple, dark purple and green, respectively. Under the influence of an increasing LF, these terms split in several states. As stated in Section 5.1.2, the GS electron configuration of $[Co(H_2O)_6]^{2+}$ is $t_{2g}^5e_g^2$, which corresponds to the $^4T_{1g}(F)$ state. The three micro-states with maximal spin projection associated with this configuration are shown in the bottom row on the right and are labeled (a)-(c). The meaning of the line style of the boxes will be explained later. The Tanabe-Sugano diagram shows that there are three spin-allowed and one spin-forbidden transitions in the low-energy range. First of all, one t_{2g}-electron can excite to an e_g-orbital, resulting in the $t_{2g}^4e_g^3$ electron configuration, indicated by the $^4T_{2g}$ and $^4T_{1g}(P)$ states in light and dark purple, respectively. These states are reached via a single excitation and are therefore indicated with a dashed line. Six possible micro-states with maximal spin projection can be drawn, (d)-(i).

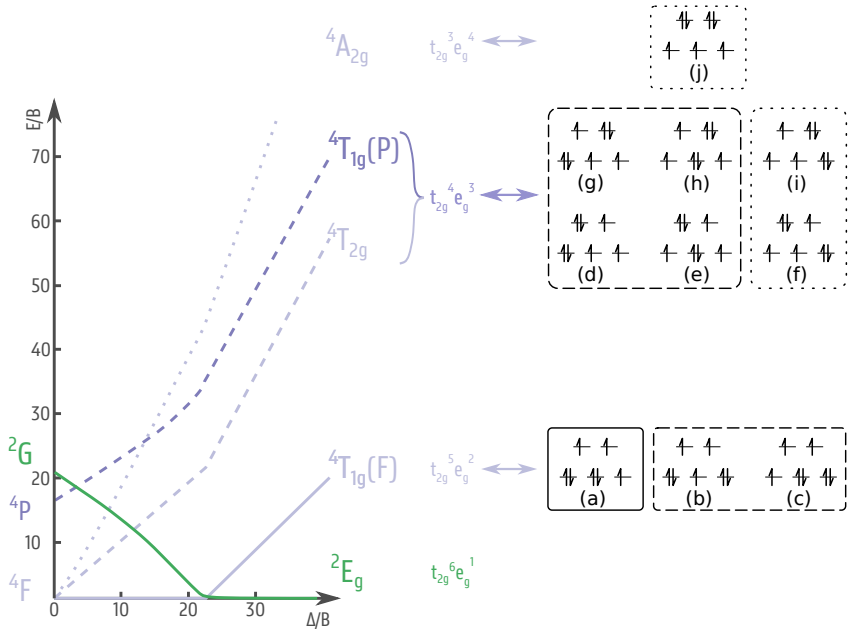

Figure 5.14: Tanabe-Sugano diagram for octahedral d^7 complexes in which the energy E is plotted as a function of the ligand field splitting Δ, both scaled by the Racah parameter B. Quartet and doublet states are indicated with purple and green lines, respectively. Dashed and dotted lines represent single and double excitations. On the right, the corresponding micro-states with maximal spin projection are indicated for the quartet states and are labeled (a)-(j). In DFT, one micro-state is chosen as the GS reference, of which the box is denoted with a solid line. Single excitations from this GS reference are characterized with dashed lines and double ESs with dotted lines.

When another t_{2g}-electron is transferred to an e_g-orbital, $t_{2g}^3e_g^4$ is obtained, corresponding to the $^4A_{2g}$ term. This is a double excitation as now two electrons are excited, which is indicated in the TS diagram with a dotted line. There is only one micro-state with maximal spin projection, namely (j). The lowest spin-forbidden excitation is obtained when an e_g-electron is transferred toward a t_{2g}-orbital followed by a spin flip, resulting in the ^2E_g state with $t_{2g}^6e_g^1$ configuration as presented in green.

It is important to note that these d-d transitions are Laporte-forbidden in complexes with a center of symmetry,[43] as mentioned in Chapter 1. Therefore, d-d absorption bands are expected to be weak for octahedral

complexes. As spin-forbidden transitions are presumed to be even less intense, we will only focus on spin-allowed excitations. Furthermore, one must keep in mind that this description applies for TMCs with perfect octahedral symmetry. When geometrical distortions occur, some of the states split into substates, leading to more peaks in the spectra, as will be observed.

As mentioned above, tetrahedral d^7 complexes will play a significant role in this work too. Hence, we also discuss the diagram presented in Figure 5.15. The GS is $^4A_2$, corresponding to the $t_2^3\mathrm{e}^4$ electron configuration. Again three spin-allowed transitions with low energy occur. When an e-electron gets excited toward a t_2-orbital, the $^4T_2$ and $^4T_1(F)$ terms are obtained, indicated in light purple with dashed lines. When another e-electron is transferred to a t_2-orbital, we arrive at the $t_2^5e^2$ configuration, labeled with $^4T_1(P)$. This double excitation is again indicated with a dotted line. The micro-states with maximal spin projection are also drawn for each electron configuration. In contrast to the octahedral complexes, tetrahedral systems lack a center of symmetry, and therefore, they have more intense absorption bands.

5.2.2 Challenges for first-row octahedral aqua-complexes

The GS has been studied in Section 5.1 via AOC and UDFT calculations. Now, we discuss how ESs can be determined from this GS reference. The most used technique to calculate ESs when starting from an AOC reference is LFDFT,[178–181] discussed in Section 3.4.3. When the GS is obtained via UDFT, TDDFT, introduced in Chapter 2, is the most popular technique to determine ESs. However, we have to pay attention when analyzing the results for TMCs. Sometimes, the fact that the GS is not described correctly in DFT can be reflected in a wrong characterization of the ESs. For example, Deeth *et al.* discovered that in tetrahedral Pd complexes, the d-orbital splitting is predicted incorrectly by DFT, which is reflected in the ESs.[236] In **Paper III**, we found that for the six-coordinated complexes the order of d-orbitals within the t_{2g} or e_g set are sometimes interchanged in UDFT calculations compared to AOC due to the different electron occupations, resulting in different interelectron repulsions. However, no mixing between the two orbital sets occurs. Furthermore, we observed that the gap between the occupied and unoccupied orbitals is overestimated by UDFT. Before we examine in how far these discrepancies are reflected in the ESs, we first address the main challenges encountered for the calculation of ESs in TMCs.

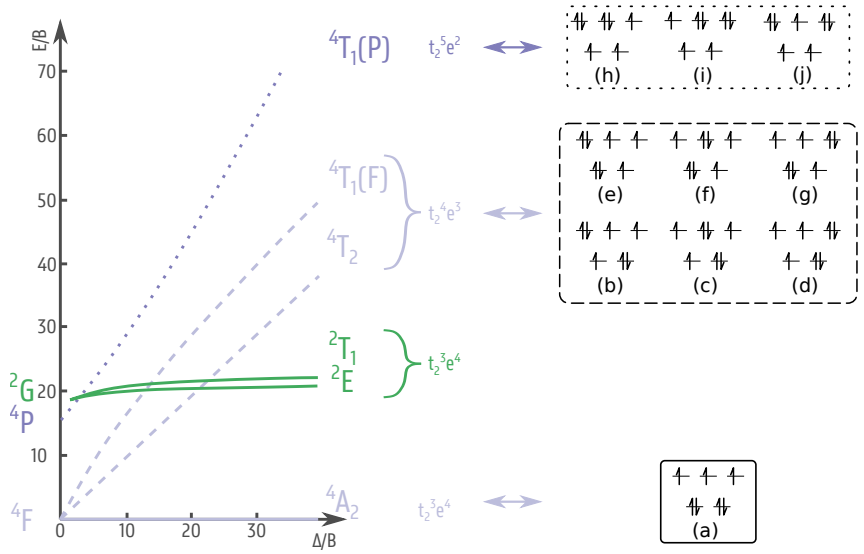

Figure 5.15: Tanabe-Sugano diagram for octahedral d^3 and tetrahedral d^7 complexes in which the energy E is plotted as a function of the ligand field splitting Δ, both scaled by the Racah parameter B. Quartet and doublet states are indicated with purple and green lines, respectively. Dashed and dotted lines represent single and double excitations. On the right, the corresponding micro-states with maximal spin projection are indicated for the quartet states and are labeled (a)-(j). In DFT, one micro-state is chosen as the GS reference, of which the box is denoted with a solid line. Single excitations from this GS reference are characterized with dashed lines and double ESs with dotted lines.

To set the scene, Figure 5.16 gives an overview of the most important difficulties for the calculation of ESs in octahedral first-row aqua-complexes, being the presence of a degenerate GS and/or double excitations. The electron configuration is shown too, where we assumed that for all complexes the HS state is the most stable one. Remark that Mn^{2+} with the d^5 configuration has been omitted as this complex has no spin-allowed d-d transitions.

First of all, whether the GS is degenerate or not, is indicated in red or green, respectively. Most of the octahedral TMCs have a degenerate GS, except for V^{2+} and Ni^{2+}. In Figures 5.14 and B.4, this micro-state is indicated with a solid line. For the octahedral d^7 TMC, we arbitrarily chose one of the

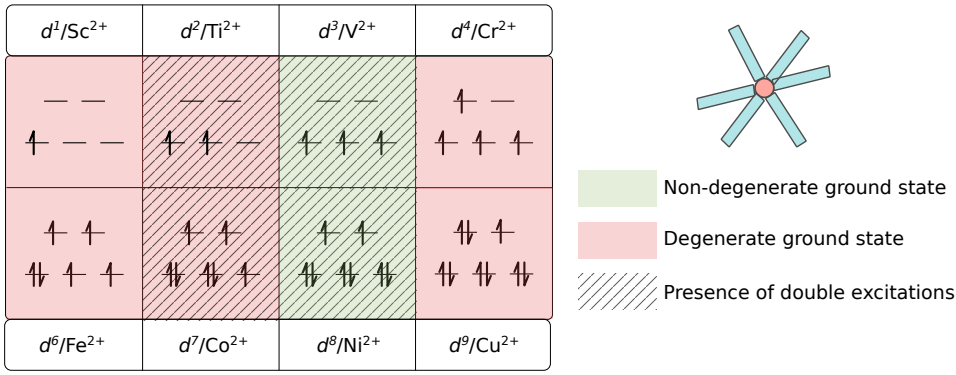

Figure 5.16: Overview of the challenges encountered for the calculation of ESs in octahedral first-row TMCs. The electron configuration of the high-spin GS is shown. Green/red indicates that the GS is non-degenerate/degenerate and diagonal stripes denote the presence of double excitations.

three micro-states corresponding to $^4T_{1g}(F)$ as the GS reference, namely (a). The fact that TDDFT, being a single reference technique, selects a specific micro-state from which excitations are determined, has two consequences. First of all, the other two micro-states belonging to $^4T_{1g}(F)$, (b) and (c), are reached via single excitations, indicated with dashed lines. Second, only four of the six micro-states corresponding to $^4T_{1g}(P)$ and $^4T_{2g}$ are reached via an excitation of a single electron. These are (d), (e), (g), and (h), and are indicated with a dashed line. (f) and (i) can only be reached when two electrons are excited from the GS reference. These double excitations are indicated with a dotted line. Micro-state (j) corresponding to $^4A_{2g}$ is also a double ES. The behaviour of the tetrahedral d^7 complexes shown in Figure B.4 is different. All micro-states corresponding to $^4T_2$ and $^4T_1(F)$, *i.e.,* (b)-(g), are single ESs and all micro-states corresponding to $^4T_1(P)$, *i.e.,* (h)-(j), are double ESs. They are indicated with dashed and dotted lines, respectively.

As discussed in Section 2.2.6, TDDFT within the adiabatic approximation is not capable of treating ESs with mainly double excitation character.[127] Let us consider the two previous cases. In the situation of a non-degenerate GS in Figure 5.15, there are three double excitations, as stated before. They correspond to a transfer of two e_g-electrons to t_{2g}-orbitals, leading to the $^4T_1(P)$ state. Interactions can occur between the single $^4T_1(F)$ and double $^4T_1$(P) ESs, visualized by the bending of both lines in the Tanabe-Sugano diagram. However, TDDFT is not capable of reproducing the double excitations and will only generate single ESs too high in energy, as

the interaction with the double ESs is lacking.[127] Now, consider the case of a degenerate GS presented in Figure 5.14. According to the Tanabe-Sugano diagram, there is only one double ES state, $^4A_{2g}$, which does not have any ESs with matching symmetry with which it can interact. However, due to the fact that TDDFT selects a specific GS, also micro-states (f) and (i) become double ESs. They have symmetry $^4T_{1g}$ or $^4T_{2g}$ and therefore, interactions with $^4T_{1g}(F)$ can occur.

We can now divide the first-row octahedral aqua-complexes shown in Figure 5.16 in three categories, based on the degeneracy of the GS and the presence of double ESs, and compare the performance of LFDFT and TDDFT. The first category contains octahedral V^{2+} and Ni^{2+} TMCs with non-degenerate GSs. Tetrahedral d^7 complexes belong to this group too and will be investigated as they play a central role in the ZIF nucleation process. After this, we distinguish TMCs with a degenerate GS, but for which no double excitations are present, examples include octahedral Sc^{2+}, Cr^{2+}, Fe^{2+}, and Cu^{2+} complexes. We conclude with the most difficult systems to which octahedral Ti^{2+} and Co^{2+} structures belong, both having a degenerate GS and double excitations. A proper description of the latter is also indispensable in order to unravel the nucleation process. We refer the reader to **Paper IV** for the computational details.

I. Non-degenerate ground state but double excitations

First of all, we study the most simple TMCs with a non-degenerate GS. We show the results for $[Co(H_2O)_4]^{2+}$, of which the GS has been studied in Section 5.1.2, in Figure 5.17, as tetrahedral Co^{2+} complexes play a major role in the ZIF nucleation process. The same conclusions apply for $[V(H_2O)_6]^{2+}$ and $[Ni(H_2O)_6]^{2+}$.

First, we take a look at the LFDFT spectrum in the top pane. The micro-states are plotted as vertical bars, of which the colors represent their contributions, the quartet states are shown in purple and the doublet states in green. The labeling of the micro-states according to the TS diagrams is based on their contributions and degeneracy. Remark that in Amsterdam Modeling Suite (AMS), LFDFT intensities can only be calculated between different electron configurations. We can clearly distinguish the $^4A_2$ GS and $^4T_2$ and $^4T_1(F)$ single excitations, which all have almost exclusively ^4F contributions. The $^4T_1(P)$ band corresponding to a double excitation is rather broad. Moreover, there is very little mixing between the $^4T_1(F)$ single and $^4T_1(P)$ double excitations.

Now, let's inspect the TDDFT results in the bottom pane of Figure 5.17. The black curve represents the convoluted absorption spectrum, whereas the vertical bars positioned at the excitation energies are hatched according to the main contributions present in the ES. The different hatch styles are introduced in the inset showing the d-orbital splitting obtained by UDFT. There are six ESs in which an electron is transferred from an e-orbital to a t_2-orbital and which correspond to transitions to the micro-states (b)-(g) in Figure 5.15. These single ESs are grouped in two clusters and are labeled as $^4T_2$ and $^4T_1$. As there is a significant shift between the LFDFT and TDDFT results, we also tested the performance of PBE0 and ωB97, for which the spectra are shifted toward larger and smaller wavelengths with respect to B3LYP, respectively. The excitation energies strongly depend on the chosen functional as shifts up to 3700 cm^{-1} are observed.

Similar results are obtained for the second category with a degenerate GS but no double excitations. Therefore, we continue with the most difficult group, namely the TMCs with a degenerate ground state and double excitations.

II. Degenerate ground state and double excitations

We focus on $[Co(H_2O)_6]^{2+}$, of which the GS has been studied in Section 5.1.2, as this complex will be important when defining a spectroscopic fingerprint for the nucleation process. We start with the structure with D_{2h} symmetry, for which the spectra are presented in Figure 5.18. In order of increasing energy, we can clearly discern the $^4T_{1g}(F)$ GS, single excited $^4T_{2g}$, double excited $^4A_{2g}$, and single excited $^4T_{1g}(P)$ in the LFDFT spectrum. Remark that mixing between the single and double excitations is limited. When investigating the TDDFT spectrum, we first of all remark the much smaller oscillator strengths compared to the non centro-symmetric tetrahedral complex in Figure 5.17. This information can not be obtained from LFDFT calculations. For the TDDFT spectrum, six ESs occur, which correspond to transitions from the GS to the micro-states (b)-(e), (g), and (h), as shown in Figure 5.14. They are grouped in three clusters of two ESs each. The first two are excitations in between the t_{2g}-orbital set, corresponding to the micro-states (b) and (c), reached via a single excitation from the GS reference (a). These two ESs can thus be labeled as $^4T_{1g}(F)$. For the other four excitations, an electron is excited from a t_{2g}- to an e_g-orbital, which are thus labeled as $^4T_{2g}$ and $^4T_{1g}(P)$. We also tested the performance of the PBE0 and ωB97 functionals for this complex. The position of

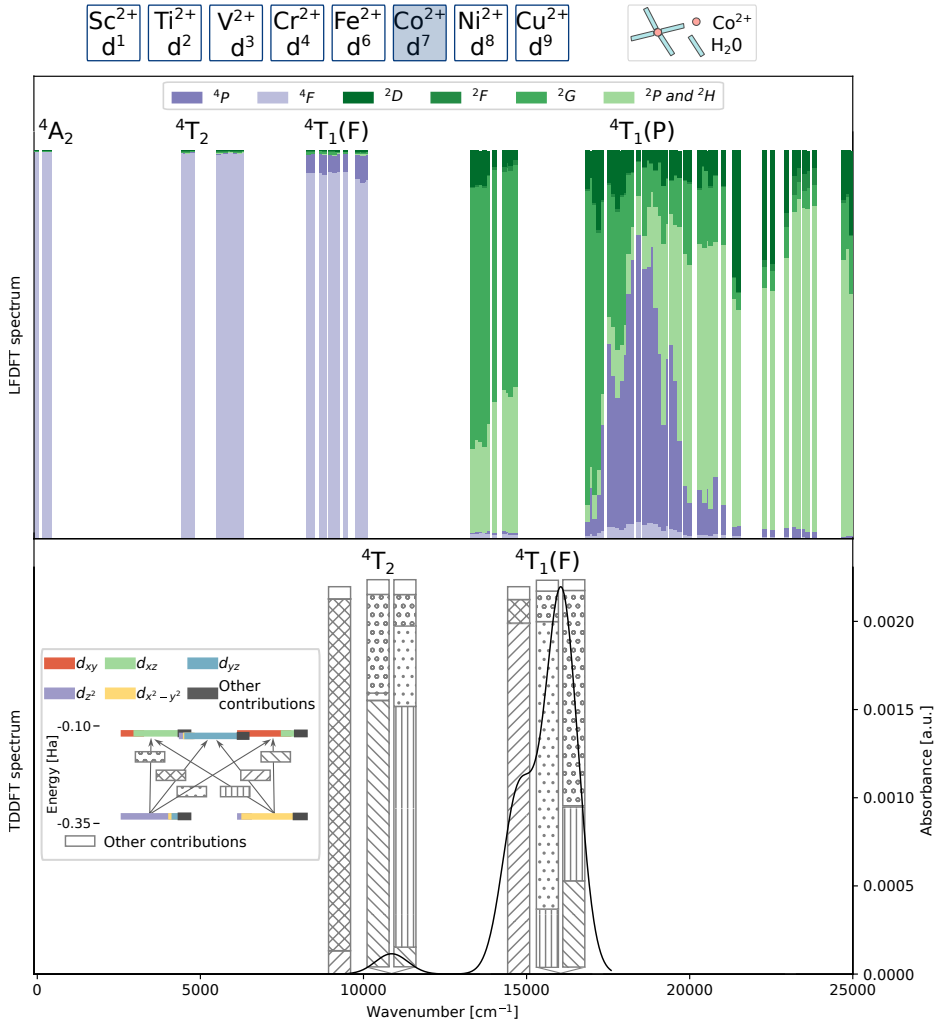

Figure 5.17: LFDFT and TDDFT spectrum of $[Co(H_2O)_4]^{2+}$. In the LFDFT spectrum, the contributions of each micro-state are indicated. The degeneracy is not displayed. In the TDDFT spectrum, the excitations with mainly d-d character are shown, whereby the largest contributions are denoted. The legend for the different hatch types is given in the inset in which the β d-orbital splitting obtained via UDFT is presented.

$^4T_{1g}(P)$ is shifted to larger/smaller wavelengths compared to the B3LYP results for PBE0 and ωB97, respectively. The functional dependence is less pronounced than for $[Co(H_2O)_4]^{2+}$, but shifts up to 1900 cm^{-1} are still observed. A comparison with the experimental results of Filez *et al.* and other literature data is given later. We observed a good agreement with the LFDFT spectrum of the S_6 structure, but discrepancies in the TDDFT spectra. Therefore, we only continue with the structure with D_{2h} symmetry.

As such, we conclude that, although the gap between occupied and unoccupied orbitals is overestimated by UDFT compared to AOC, the picture of d-d excitations obtained from both techniques is qualitatively similar. This holds for both octahedral and tetrahedral complexes and even for challenging systems with a degenerate GS and double excitations. Moreover, both techniques give complementary information, whereas LFDFT is capable of describing double excitations, oscillator strengths can be obtained via TDDFT. However, care must be taken for TMCs with a degenerate GS and S_6 symmetry, for which only LFDFT gives reliable results. Nevertheless, there are some shifts between the ESs obtained from TDDFT and LFDFT, especially for tetrahedral complexes. As the TDDFT results strongly depend on the functional, further investigation is needed.

In the next section, we revert our attention to the complexes which are relevant in the ZIF nucleation process.

5.2.3 Spectroscopic fingerprint for nucleation process of Co-ZIF-67

I. Experimental data

The experimental UV-Vis spectrum of the metal-organic pool formed after mixing is shown in blue in Figure 5.19 and is deconvoluted by a linear combination fit presented with a dashed line in three main contributions. Note that excitations below 14000 cm^{-1} are not measured as this region is situated in the near infra-red and lies outside the scope of the work presented in Ref. 64. The yellow curve corresponds to $[Co(OR)_6]^{2+}$ complexes, whereby OR can be water, methanol, or NO_3^-. Red indicates $[Co(2\text{-mIm})_3(OR)]^{2+}$ and the green curve has been identified as $[Co(2\text{-mIm})_4]^{2+}$. In the following, we will investigate each structure separately.

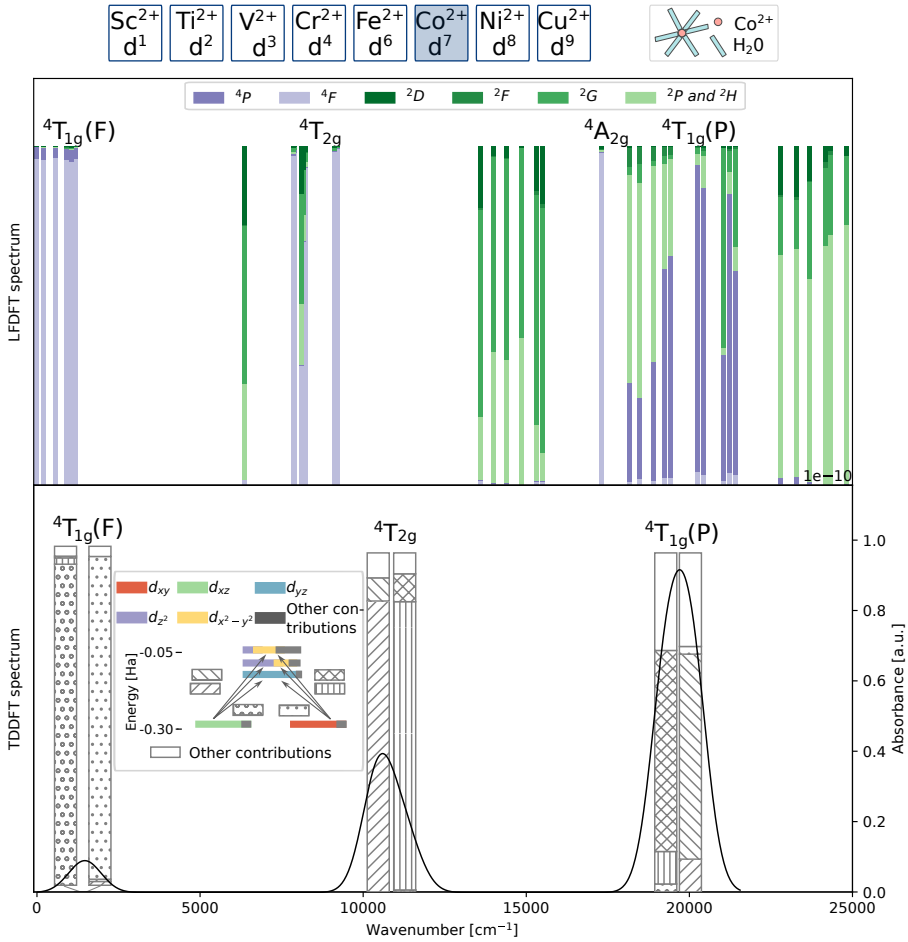

Figure 5.18: LFDFT and TDDFT spectrum of $[Co(H_2O)_6]^{2+}$ with D_{2h} symmetry. In the LFDFT spectrum, the contributions of each microstate are indicated. The degeneracy is not displayed. In the TDDFT spectrum, the excitations with mainly d-d character are shown, whereby the largest contributions are denoted. The legend for the different hatch types is given in the inset in which the β d-orbital splitting obtained via UDFT is presented.

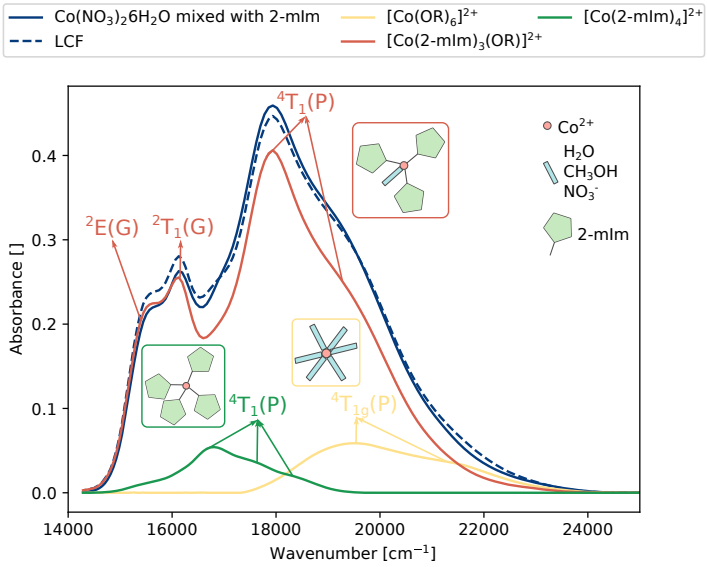

Figure 5.19: Experimental absorption spectra in the visible range of the electromagnetic spectrum after $Co(NO_3)_2 \cdot 6H_2O$-2-mIm mixing (blue). A LCF (blue, dotted) deconvolutes the spectrum in $Co(OR)_6$ (yellow), $Co(2\text{-mIm})_3(OR)$ (red), and $Co(2\text{-mIm})_4$ (green) constituents. Figure adapted from Ref. 64 with permission of Elsevier, 2021.

II. $[Co(2\text{-mIm})_4]^{2+}$

The $[Co(2\text{-mIm})_4]^{2+}$ complex indicated in green in Figure 5.19 is characterized by the $^4T_1(P)$ state of which three spin-orbit split sub-peaks are situated at 16667, 17637, and 18315 cm^{-1}. This is in agreement with Banci *et al.*, who used AOM to state that, for general tetrahedral Co^{2+} complexes, the $^4T_1(P)$ state is situated in the region between 13500 and 19500 cm^{-1}.[237] Furthermore, she showed that there are two additional ESs at lower energies, namely $^4T_2$ and $^4T_1(F)$. The latter lies in the region between 5000 and 11000 cm^{-1}, whereas the former is situated below 5000 cm^{-1}.[237] As these states are not situated in the the UV-Vis range, they are not observed in Figure 5.19.

Note that in our calculations we used 1,2-dimethylimidazole (1,2-dmIm) instead of 2-mIm to prevent dimerization and to exclusively study the initial change in the symmetry and coordination of Co^{2+}. In Figure 5.21, we show the LFDFT and TDDFT spectra of $[Co(1,2\text{-dmIm})_4]^{2+}$, of which the geometrical structure is presented in the left pane of Figure 5.20 and

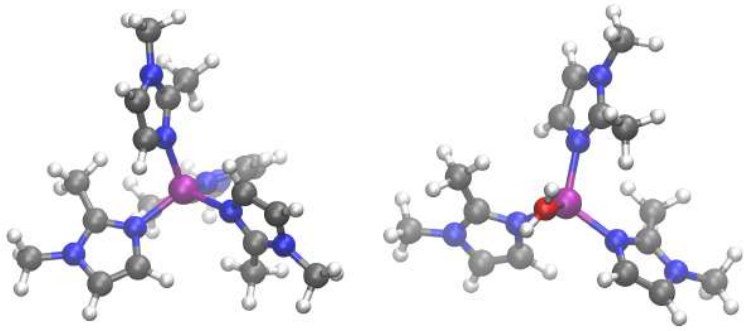

Figure 5.20: Visualization of the geometrical structure of $[Co(1,2\text{-dmIm})_4]^{2+}$ (left) and $[Co(1,2\text{-dmIm})_3H_2O]^{2+}$ (right). Carbon, cobalt, hydrogen, nitrogen, and oxygen are indicated in gray, purple, light gray, blue, and red, respectively.

compare them with these of $[Co(H_2O)_4]^{2+}$ in Figure 5.17 in order to estimate the influence of changing the ligands from aqua to 1,2-dmIm. Except for larger oscillator strengths for the former and some minor shifts in the ESs, the overall picture remains unaltered. $^4T_2$ is situated around 10000 cm^{-1}, whereas $^4T_1(F)$ is located around 15000 cm^{-1}. Compared to the results of Banci *et al.*, the spectra are strongly blue-shifted over around 5000 cm^{-1}. This is maybe due to our choice of functional. Indeed, as stated previously, the specific position of the peak is strongly functional-dependent. As $^4T_1(P)$ is a double excitation, it is not reachable by TDDFT. The micro-states in the LFDFT spectra are no longer present in clusters, but they are more spread-out, making it difficult to determine the energies of the states. This is due to the fact that the 1,2-dmIm ligands are less compact than the aqua ligands resulting in a reduction of the symmetry. We can roughly say that $^4T_2$ is located between 5000 and 8000 cm^{-1} and the $^4T_1(F)$ state lies between 9000 and 12000 cm^{-1}, which is in agreement with the results of Banci *et al.*. The double excited $^4T_1(P)$ state is located at around 17500 cm^{-1}, in accordance with the results of Filez *et al.*. However, as the bands are rather spread-out, very specific conclusions can not be drawn.

III. $[Co(2\text{-mIm})_3(H_2O)]^{2+}$

The following d-d excitations are discerned in the spectrum of $[Co(2\text{-mIm})_3(OR)]^{2+}$, indicated in red in Figure 5.19. First, two doublet ESs are observed: $^2E(G)$ at 15408 cm^{-1} and $^2T_1(G)$ at 16155 cm^{-1}. At 17825 and 19268 cm^{-1}, the double excited $^4T_1(P)$ state is situated. This spectrum is

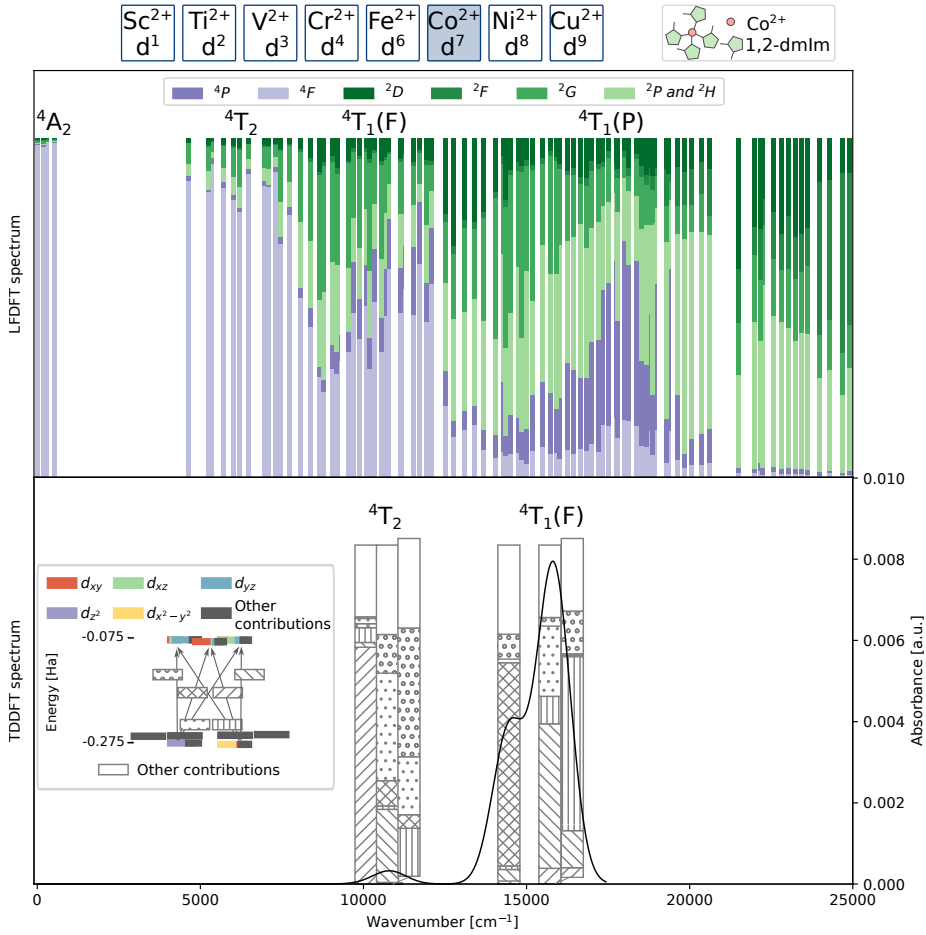

Figure 5.21: LFDFT and TDDFT spectrum of $[Co(1,2\text{-dmIm})_4]^{2+}$ symmetry. In the LFDFT spectrum, the contributions of each micro-state are indicated. The degeneracy is not displayed. In the TDDFT spectrum, the excitations with mainly d-d character are shown, whereby the largest contributions are denoted. The legend for the different hatch types is given in the inset in which the β d-orbital splitting obtained via UDFT is presented.

clearly different from that of $[Co(2\text{-mIm})_4]^{2+}$.

The geometrical structure of $[Co(1,2\text{-dmIm})_3(OR)]^{2+}$ is shown in the right pane of Figure 5.20 and the LFDFT and TDDFT spectra in Figure 5.22. The LFDFT spectrum is even more diffuse than for $[Co(1,2\text{-dmIm})_4]^{2+}$, making it impossible to draw conclusions from it. In contrast to Filez *et al.*, we do not observe large differences in the TDDFT spectra between $[Co(1,2\text{-dmIm})_3(OR)]^{2+}$ and $[Co(1,2\text{-dmIm})_4]^{2+}$. The four ESs identified in the experimental spectrum are not reachable by TDDFT as they are SF or double excitations. In order to examine the large differences between the tetrahedral Co^{2+} complexes found by Filez *et al.*, more advanced techniques are needed, which are more precise and capable of determining d-d transitions corresponding with double and SF excitations.

IV. $[Co(H_2O)_6]^{2+}$

As indicated with yellow in Figure 5.19, $[Co(OR)_6]^{2+}$ complexes are characterized by their band maximum at 19531 cm^{-1} along with a shoulder at 21277 cm^{-1}, both corresponding to the ${}^4T_{1g}(P)$ state. This is in agreement with the results of Banci *et al.*, who concluded that, in general, ${}^4T_{1g}(P)$ is situated in between 15500 and 22000 cm^{-1} for octahedral Co^{2+} complexes.[237] Furthermore, he observed that ${}^4T_{2g}$ is situated in the band 6500-10500 cm^{-1}, but this ES is located below the experimentally measured range in Figure 5.19. Finally, octahedral Co^{2+} complexes have a double excited ${}^4A_{2g}$ state with a lower intensity which is therefore often hidden by ${}^4T_{1g}(P)$. The ${}^4A_{2g}$ state is experimentally observed as a small peak around 15400 cm^{-1} in the raw experimental absorption spectrum of Filez *et al.*

Good agreement is also found between the spectrum shown in Figure 5.19 and experimental data of $[Co(H_2O)_6]^{2+}$ complexes in aqueous solution.[238] Indeed, in Ref. 238, the spin-allowed single excitations to ${}^4T_{2g}$ and ${}^4T_{1g}(P)$ are situated at 8100 cm^{-1} and at 19400 and 21550 cm^{-1}, respectively and the spin-allowed double excitation to ${}^4A_{2g}$ is located at 16000 cm^{-1}. Finally, the lowest energy doublet state, *i.e.,* ${}^2E_g$, is situated at 11300 cm^{-1}.

We now compare the experimental spectrum shown in yellow in Figure 5.19 with the LFDFT and TDDFT results presented in Figure 5.18. There is a good correspondence with the LFDFT spectrum in which ${}^4T_{2g}$ and ${}^4T_{1g}(P)$ are situated at 8100-9400 cm^{-1} and 18400-21900 cm^{-1}, respectively. ${}^4A_{2g}$ is located at 17500 cm^{-1}. It is more difficult to determine the specific excitation energy of ${}^2E_g$ as contributions from doublet states are observed

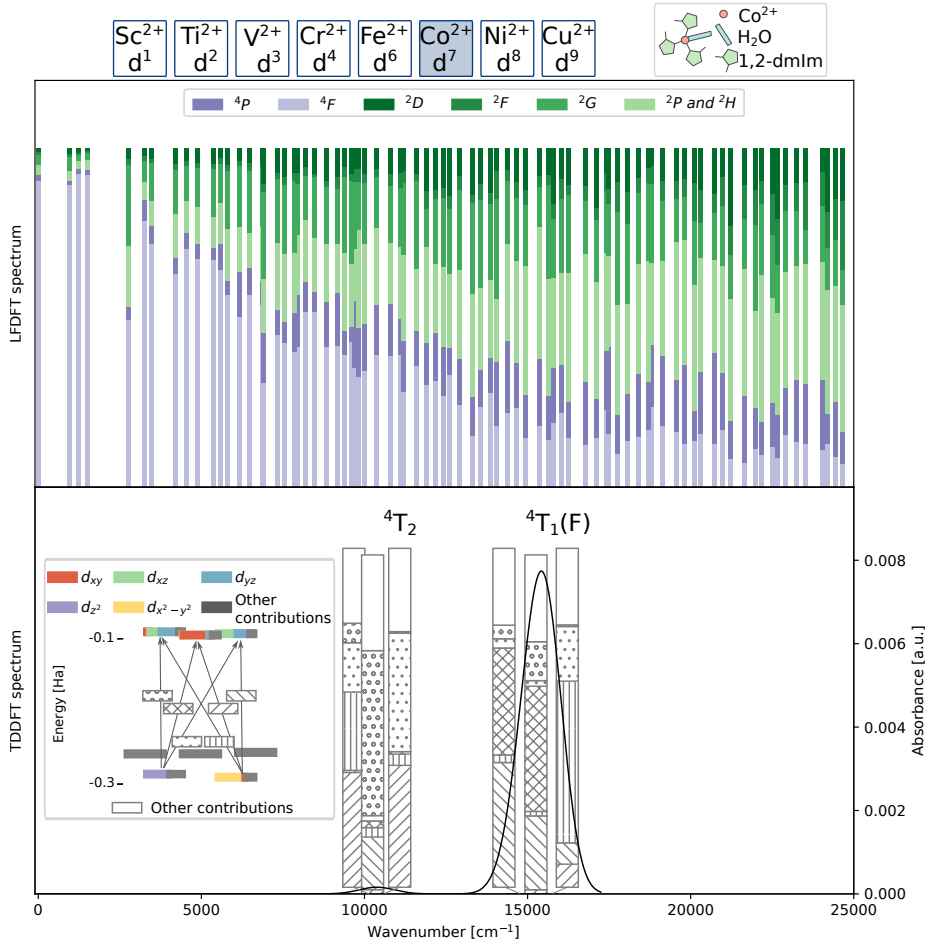

Figure 5.22: LFDFT and TDDFT spectrum of $[Co(1,2\text{-dmIm})_3(OR)]^{2+}$ symmetry. In the LFDFT spectrum, the contributions of each microstate are indicated. The degeneracy is not displayed. In the TDDFT spectrum, the excitations with mainly d-d character are shown, whereby the largest contributions are denoted. The legend for the different hatch types is given in the inset in which the β d-orbital splitting obtained via UDFT is presented.

at 6600, 8400, and 13600-15700 cm^{-1}. The TDDFT results are also in good agreement: ${}^4T_{1g}(P)$ is located around 20000 cm^{-1}, whereas there is a slight shift observed for ${}^4T_{2g}$, which is located at 10000-11300 cm^{-1}.

V. Spectroscopic fingerprint

In order to propose a spectrosocpic fingerprint, we compare the TDDFT spectra, shown in Figures 5.18, 5.21, and 5.22 and summarized in Figure 5.23. Remark that the absorbance is shown on the right axis for $[Co(H_2O)_6]^{2+}$, whereas it is on the left axis for the other complexes. The LFDFT spectra are not considered, as no conclusions can be drawn when the TMC possesses the extended 1,2-dmIm ligands. The species can be distinguished via the following features. First of all, the oscillator strength is much larger for the tetrahedral complexes than for the octahedral ones, because the latter have a center of symmetry. A comparison of the calculated oscillator strength with the experimental data shows that the tetrahedral complexes triggering the nucleation process are 10^7-10^8 times less present in the solution. Moreover, there is a significant difference in the position of the main absorption peak, which is situated at 20000 cm^{-1} and 15000 cm^{-1} for octahedral and tetrahedral systems, respectively. Both observations are in agreement with experimental and CFT results. Lastly, we observe some excitations at very small energies below 2000 cm^{-1} for the octahedral complex, which arise due to the degeneracy of the GS. Nevertheless, we are not able to extensively compare our computational results with the experimental UV-Vis spectra of Filez *et al.*, in which mainly SF and double excitations are situated which are not reachable by TDDFT. Furthermore, as LFDFT is not suited for systems with extended ligands, other techniques are needed to investigate the substantial differences observed between the two types of tetrahedral complexes by Filez *et al.*

To conclude, the octahedral and tetrahedral species can be distinguished based on TDDFT via their oscillator strength and the position of the main absorption peak. Furthermore, ESs at very small energies are only observed for octahedral systems. However, alternative techniques are needed to calculate the ESs proposed by Filez *et al.* Interesting candidates might be tensor-networks for example, which will be discussed in more detail in Chapter 6.

The studies in this Chapter reveal that the d-orbital splitting is characteristic for the number of ligands coordinated to the TM. Furthermore, although discrepancies are observed between the d-orbital splitting obtained from

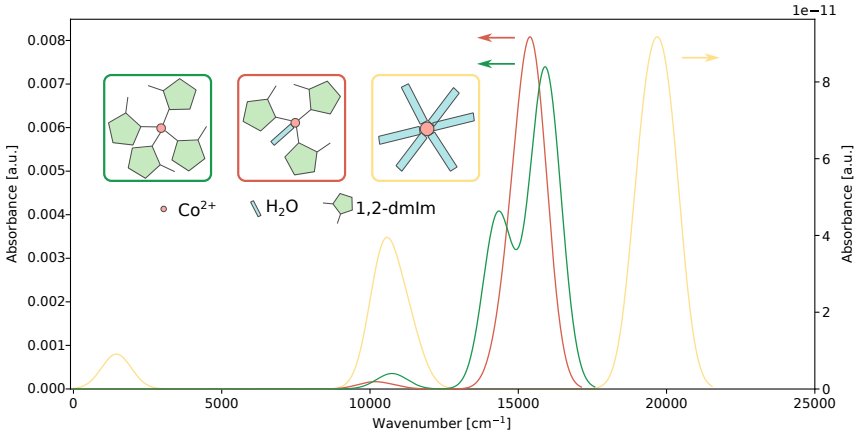

Figure 5.23: TDDFT spectra of $[Co(H_2O)_6]^{2+}$ (yellow), $[Co(1,2\text{-dmIm})_3(OR)]^{2+}$ (red), and $[Co(1,2\text{-dmIm})_4]^{2+}$ (green). The absorbance is on the right for $[Co(H_2O)_6]^{2+}$, whereas it is on the left for $[Co(1,2\text{-dmIm})_3(OR)]^{2+}$ and $[Co(1,2\text{-dmIm})_4]^{2+}$.

AOC and UDFT, both techniques are able to provide reference states from which electronic excitations can be determined. Moreover, additional information is provided: oscillator strengths can be obtained from TDDFT, whereas double excitations can be studied via LFDFT. Nevertheless, the latter is not suited when the TMCs without symmetry are studied.

6

Conclusions and Outlook

6.1 Conclusions

Computational spectroscopy is of utmost importance to link the molecular scale with experimentally observed spectroscopic signals. By computationally obtaining energy levels of the molecular scale system, we can directly reconstruct the unique spectroscopic fingerprint arising from their transitions. More specifically, UV-vis spectroscopy studies electronic excitations during which the system undergoes a transition from its GS to an ES. In this work, we focused on the UV-Vis spectra of the building blocks of nanoporous materials. Using spectra, we were able to provide insights in how the photocatalytic properties of heterogeneous catalysts can be tuned in order to help in their rational design. At the same time, studying the GS and ESs of TMCs helped us unravel the nucleation process of ZIFs.

As outlined in Chapter 4, our study of photocatalytic complexes consists of three parts. Firstly, we studied, in collaboration with our experimental partners, which factors influence the structural and photocatalytic properties of the CTF in **Paper II**. We investigated various polypyridyl ligands which are promising to use as CTF building blocks. We observed that the larger the π-system and the higher the π-electron deficiency, the more the main absorption peak shifts to larger wavelengths. Systems with aromatic rings and a dihedral angle close to 0 or 180° are characterized by a large π-system. More π-electron deficient systems can be acquired by increasing the nitrogen content or terminating the linker with electron

withdrawing CN^- groups. Furthermore, adding functional groups can have a significant influence on the ES properties. Indeed, among the linkers studied in this work, the maximum shift obtained by tuning the ESs amounts to 271 nm with respect to pyridine. This broad range of shifts of the main absorption peak gives a new perspective in the modulation of the optical properties of the CTF scaffold by varying the ligands.

Second, we investigated how the photocatalytic properties are influenced by varying the nitrogen content of the linkers in the complex. Both the GS and ESs of $[RuL_3]^{2+}$ complexes, which can be exploited either as oxidant or as reductant agents in reactions via triplet-triplet energy transfer (TTET), are the subject of **Paper I**. As triplet states, playing an important role in this process, are difficult to investigate experimentally, computational techniques provide a valuable alternative. For the various complexes, the first non-forbidden singlet excitation is found between 2.2 and 2.6 eV, whereas the strongest excitation is situated in the 2.7-3.0 eV range. Both are of the metal-to-ligand charge-transfer (MLCT) type and show a minimum for $[Ru(bipy)_2(bipz)]^{2+}$. The same trend is observed for the first adiabatic triplet MLCT excitation located between 1.5 and 1.8 eV. This particular complex is thus an interesting candidate for processes induced by visible light as it shows a red-shift of both singlet and triplet MLCT ESs. These results are in agreement with those obtained from GS calculations. The HOMO-LUMO gap, which is an approximation of the MLCT ES energy, attains its minimal value for the same complex.

In the last part, we examined how the heterogenization of the Ru complexes on a CTF support consisting of bipyridine ligands affects the energy and character of the ESs. For the resulting $[RuL_2]^{2+}$@CFT system, we observed a significant red-shift to the 1.5-2.0 eV range for the strongest excitation. The CTF environment thus allows harvesting these lower energies to promote charge-transfer (CT) excitations, which is beneficial for near-infrared photocatalysis.[224, 225] The smaller excitation energies are reflected in the GS results. Occupied framework states are situated between the occupied TM and virtual ligand orbitals, resulting in a reduction of the HOMO-LUMO gap. Furthermore, both the HOMO-LUMO gap and the energy of the strongest ES decrease with an increasing nitrogen content. Finally, we note that the character of these transitions changes. They are no longer MLCT states, but result from CT between orbitals localized on the framework toward orbitals mainly localized on the Ru complex and are thus of the CCCT or CLCT type.

This investigation indicates how optoelectronic properties of Ru complexes

can be changed and, eventually, tuned for specific applications by varying the ligands and heterogenization within a CTF environment. As such, this contribution aids in making thoughtful choices for the most appropriate compound for the specific task at hand. On the one hand, the system can be engineered such that a larger spectrum of radiation can be harvested for activation of the photocatalytic complex. On the other hand, the photocatalytic properties of the system can, to a certain extent, be tuned to match a specific activation energies absorption band. In this regard, TDDFT is ideally suited to study excitations, both for closed-shell TMCs as well as for CTF linkers. Furthermore, due to its low computational cost, it is also applicable for larger systems such as the embedded complex in the CTF.

Inspired by experimental findings on the nucleation process of ZIFs,[64] we investigated in Chapter 5 whether it is possible to propose a spectroscopic fingerprint of Co^{2+} complexes which are part of this formation procedure. In order to achieve this, the GS and ESs of relevant TMCs are studied.

First, we investigated the GS properties of Co^{2+} aqua-complexes with six, five, and four ligands in **Paper III**. The focus is on the d-orbital splitting and how it depends on the symmetry, where both the influence of the coordination environment and the specific point group were considered. Qualitative techniques such as CFT and LFT reveal that the d-orbital splitting is characteristic of the number of ligands coordinated to the TM. To obtain quantitative results, both AOC and UDFT, with fractional and integer electron occupations respectively, have been performed.

For the six-coordinated TMCs, we obtained a stable structure with D_{2h} symmetry in which JT distortions are clearly visible. Besides this, we also found a structure with S_6 symmetry. Moreover, we have shown that AOC is capable of reproducing the theoretical d-orbital splittings obtained from CFT. However, UDFT calculations do not succeed in this when only part of the d-orbitals are occupied. Indeed, the HOMO-LUMO gap is overestimated by one order of magnitude, resulting in non-degenerate t_{2g}-orbitals. Based on the work of Deeth *et al.*,[236] we demonstrated that the discrepancies between UDFT and AOC are due to the different electron occupations resulting in different interelectron repulsions. In agreement with Ref. [236], we observed that the AOC orbitals confirm the chemical intuition as given by LFT, as both techniques describe the electron repulsion in a spherical way. The d-orbital splitting obtained by UDFT is different due to the integer occupation numbers resulting in different interelectron repulsions. This has been confirmed by calculation on TMs for which the t_{2g} set is evenly occupied.

The above conclusions also apply for the four-coordinated and five-coordinated TBP and SP Co^{2+} aqua-complexes. For the former, the two e orbitals are completely occupied, resulting in a splitting in accordance with the AOC and theoretical results. Nevertheless, the energy gap between the e and t_2 set is still one order of magnitude too large.

After having obtained a thorough understanding of the GS properties, we examined the ESs in **Paper IV**. Before we investigated the spectroscopic fingerprint of complexes relevant for the nucleation of ZIFs, we first tested the performance of TDDFT and LFDFT for the calculation of d-d excitations in first-row octahedral aqua-complexes. This sequence is put forward to investigate the variations in complexity of the electronic structure of the TMs caused by their different number of d-electrons. Although the gap between occupied and unoccupied orbitals is overestimated by UDFT compared to AOC, the picture of d-d excitations obtained from both techniques is qualitatively similar. This holds for both octahedral and tetrahedral complexes and even for challenging systems with a degenerate GS and for which double excitations are present. Moreover, both techniques give complementary information: whereas LFDFT is capable of describing double excitations, TDDFT yields oscillator strengths. However, care must be taken for TMCs with a degenerate GS and S_6 symmetry, for which only LFDFT gives reliable results. Nevertheless, there are some shifts between the excitation energies obtained from TDDFT and LFDFT, especially for tetrahedral complexes. Furthermore, they also strongly depend on the functional for the former.

With this knowledge, we calculate the d-d excitations of TMCs which are relevant for the ZIF nucleation process via TDDFT and LFDFT and compare the results with the experimental spectra of Filez *et al.*. We found that, although LFDFT is not suited for complexes which are not symmetric, the octahedral and tetrahedral species can be distinguished based on TDDFT. The oscillator strength is much larger for the tetrahedral complexes and the main absorption peak is shifted toward smaller energies compared to the octahedral ones. Furthermore, we were able to show that the tetrahedral complexes, which trigger the nucleation process, are 10^7-10^8 times less present than the octahedral structures. Finally, ESs at very small energies are only observed for octahedral systems. Nevertheless, other techniques are needed to calculate the ESs proposed by Filez *et al.* which are situated in the UV-Vis range and mainly contain double and SF excitations, not reachable by TDDFT.

6.2 Outlook

It would be interesting to extend the presented study by exploring photocatalytic complexes with other TMs than Ru. The terrestrial abundance of TMs spans a wide range as shown by the bar height on a log scale in Figure 6.1. First-row, as well as early second-row and third-row TMs, are relatively abundant, whereas the other TMs have substantially lower earth abundance, which are therefore also called precious metals. The values range from 5.6% for Fe to ∼0.001 ppm for Rh and Ir. As the former is up to 10^4 times more abundant, its cost can be reduced significantly. The black bar shows on a log scale the relative amount of CO_2 production through mining and purification for each TM. The smaller the bar, the lower the amount of CO_2 produced during the production process, resulting in a reduced environmental footprint.[239]

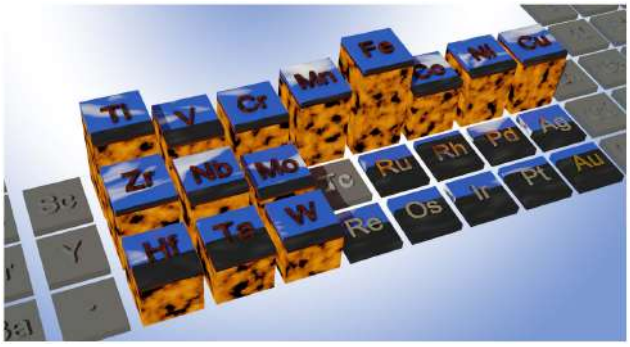

Figure 6.1: Visualization of the earth abundance and relative production of CO_2 for the TMs. The height of the pillar for each metal indicates its crustal abundance on a log scale. The black bar on each metal shows, also on a log scale, the relative amount of CO_2 produced through mining and purification for each metal.[240] Tc is shown but is radioactive and unstable. From Ref. [239]. Reprinted with permission from AAAS.

In the search for alternatives with a reduced cost and environmental footprint, Fe complexes appear to be very promising, as shown in an excellent review in Ref. [241]. However, the shift from Ru to Fe complexes causes additional challenges. Indeed, as discussed in Chapter 4, $3d$-orbitals extend to a lower degree beyond the $3s$- and $3p$-orbitals compared to their $4d$ and $5d$ counterparts.[216] This leads to less overlap with bonding partners and thus weaker metal-ligand bonds and a reduced LF splitting. The electronic structure is considerably impacted as the MLCT states, active in

the TTET mechanism, are now higher in energy than some metal-centered states. So, while the lowest ESs of Ru complexes are MLCT states, these transitions can decay in Fe complexes to inactive metal-centered states, leading to much shorter ES lifetimes. Therefore, additional research is required on how to change the ordering of the MLCT and metal-centered states in order to be able to make the transition to more ecologic alternatives.

Furthermore, it would be instructive to test the effectiveness of the orthogonal electronic structure engineering principle employed in **Paper II**. On the one hand, we found in **Paper I** that the strongest absorption band is situated around 3.32 eV for the pristine CTF constructed with bipy linkers. On the other hand, values between 3.51 and 4.82 eV, depending on the termination of the linker and whether it has a trans or cis configuration, are obtained in **Paper II**. Further research needs to be conducted to unravel the influence of building a full CTF structure starting from an isolated linker.

Due to the fact that open-shell systems require spin-unrestricted calculations,[242] spin contamination arises in their GSs. Indeed, there is artificial mixing of spin-states, resulting in wave functions which are not pure eigenfunctions of the total spin operator. Ipatov *et al.* studied the spin contamination in ESs of open-shell molecules and showed that large amounts of spin contamination can result in incorrect or missing states.[243] Equations are presented for calculating spin contamination in TDDFT ESs in order to help identify non-physical solutions. The absence of double and higher excitations was found to be the main origin of spin contamination. However, as these equations are not routinely implemented in standard DFT software packages, additional investigations are required as it would be interesting to test this for the challenging Co^{2+} complexes encountered during the ZIF nucleation process, for example.

Nowadays, we cannot deny the prominent role machine learning is playing in various branches of science. This research field has matured by offering a greater accuracy and efficiency and has made its entrance in computational chemistry, including coordination chemistry.[244] These new techniques complement, extend, and sometimes even completely replace the traditional ones.[245] As stated in the introduction of Chapter 3, determining the spin-state energies of TMCs is a demanding task and the complicated nature of the metal-ligand bonds poses various challenges on computational techniques. In recent years, machine learning has proven to be very helpful in this regard. For example, the GS spin-state of TMCs has been determined by only making use of structural information in Ref. [246]. Furthermore, promising ligands for the design of new phosphors are determined by

predicting the ES properties of Ir complexes with an accuracy competitive or superseding that of TDDFT in Ref. [247]. In addition, progress is made for the high-throughput computational screening for materials discovery in Refs. [248–250]. Two recent overviews are given in Refs. [148, 245]. We believe that machine learning could also contribute significantly in this work as it can be applied to perform a high throughput screening to select the most promising linkers for CTFs and photocatalytic complexes, to aid in unraveling the electronic structure of challenging systems, and to assess the main sources of errors in DFT.

Despite these emerging techniques, there is still a need to investigate on a fundamental level how the electronic structure of strongly correlated systems can be solved in an accurate way. In this respect, a fundamentally different approach to treat many-body systems has been proposed in literature and is based on tensor-network states, which have risen over the past two decades as extremely versatile and powerful trial wave functions for interacting quantum lattice systems.[251] They do not involve corrections on top of a non-interacting reference configuration, but take into account the spatial distribution of quantum correlations. Tensor-network states may be very promising for isolated systems too, as shown for example for Mn complexes.[252] However, as Mn is one of the more easier elements in the $3d$ TM series having a non-degenerate GS, it would be very interesting to extend the tensor-network formalism to the calculation of ESs for more challenging TMCs by using variational optimization schemes for the tensor-network wave function.[253, 254]

Summarizing, TDDFT has evolved to be a standard technique for the determination of spectroscopic fingerprints in the UV-Vis region for systems not prone to strong correlation or complicated spin structures. If we manage to combine this technique with efficient machine learning schemes, we will be able to provide accurate feedback to experiments orders of magnitude faster than what is possible today, which could greatly accelerate the development of efficient heterogeneous photocatalysts. For TMCs having more complicated electronic structures, playing a major role in the nucleation process of ZIFs for example, there is still the need to develop advanced many-body techniques and to apply techniques such as tensor-networks to new chemical systems. For this to be successful, a strong synergy between various communities is necessary, namely fundamental many-body physicists, chemists, and the experimental community.

Part II

Published Papers

A

Publications in International Peer–Reviewed Journals

Paper I **Optical Properties of Isolated and Covalent Organic Framework-Embedded Ruthenium Complexes**
F. Muniz-Miranda†, L. De Bruecker†, A. De Vos, F. Vanden Bussche, C. V. Stevens, P. Van Der Voort, K. Lejaeghere, and V. Van Speybroeck
J. Chem. Phys. A, **2019**, *123* (6854-6867)

Paper II **Structural and Photophysical Properties of Various Polypyridyl Ligands: A Combined Experimental and Computational Study**
L. De Bruecker, J. Everaert, P. Van Der Voort, C. V. Stevens, M. Waroquier, and V. Van Speybroeck
ChemPhysChem, **2020**, *21* (2489-2505)

Paper III **Influence of Number of Ligands and Point Group on the Electronic Structure of Co^{2+} Aqua-Complexes**
L. De Bruecker and V. Van Speybroeck
Inorg. Chem., **2022**, *61* (20743-20756)

Paper IV **Using DFT to examine the spectroscopic fingerprint of Co^{2+} complexes relevant for ZIF nucleation processes**
L. De Bruecker and V. Van Speybroeck
Inorg. Chem., **2023**, *Submitted*

† Authors contributed equally to this work.

Paper I

Optical Properties of Isolated and Covalent Organic Framework-Embedded Ruthenium Complexes

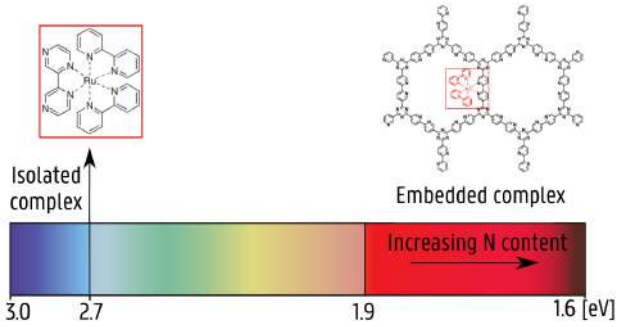

F. Muniz-Miranda†, L. De Bruecker†, A. De Vos, F. Vanden Bussche, C. V. Stevens, P. Van Der Voort, K. Lejaeghere, and V. Van Speybroeck

The Journal of Physical Chemistry A, **2019**, *123* (6854-6867)

† Authors contributed equally to this work.
L. De Bruecker interpreted the data and wrote the initial draft of the manuscript in collaboration with F. Muniz-Miranda.

THE JOURNAL OF PHYSICAL CHEMISTRY A

Article

Cite This: J. Phys. Chem. A 2019, 123, 6854−6867

pubs.acs.org/JPCA

Optical Properties of Isolated and Covalent Organic Framework-Embedded Ruthenium Complexes

Published as part of The Journal of Physical Chemistry virtual special issue "Leo Radom Festschrift".

Francesco Muniz-Miranda,[†,⊥,∥] Liesbeth De Bruecker,[†,∥] Arthur De Vos,[†] Flore Vanden Bussche,[‡,§] Christian V. Stevens,[‡] Pascal Van Der Voort,[§] Kurt Lejaeghere,*[,†] and Veronique Van Speybroeck*[,†]

[†]Center for Molecular Modeling (CMM), Ghent University, Technologiepark 46, 9052 Zwijnaarde, Belgium

[‡]Research Group SynBioC, Department of Green Chemistry and Technology, Faculty of Bioscience Engineering, Ghent University, Campus Coupure, Coupure Links 653 bl. B, 9000 Gent, Belgium

[§]Center for Ordered Materials, Organometallics and Catalysis (COMOC), Department of Inorganic and Physical Chemistry, Ghent University, Krijgslaan 281 (S3), 9000 Gent, Belgium

Supporting Information

ABSTRACT: Heterogenization of RuL_3 complexes on a support with proper anchor points provides a route toward design of green catalysts. In this paper, Ru(II) polypyridyl complexes are investigated with the aim to unravel the influence on the photocatalytic properties of varying nitrogen content in the ligands and of embedding the complex in a triazine-based covalent organic framework. To provide fundamental insight into the electronic mechanisms underlying this behavior, a computational study is performed. Both the ground and excited state properties of isolated and anchored ruthenium complexes are theoretically investigated by means of density functional theory and time-dependent density functional theory. Varying the ligands among 2,2′-bipyridine, 2,2′-bipyrimidine, and 2,2′-bipyrazine allows us to tune to a certain extent the optical gaps and the metal to ligand charge transfer excitations. Heterogenization of the complex within a CTF support has a significant effect on the nature and energy of the electronic transitions. The allowed transitions are significantly red-shifted toward the near IR region and involve transitions from states localized on the CTF toward ligands attached to the ruthenium. The study shows how variations in ligands and anchoring on proper supports allows us to increase the range of wavelengths that may be exploited for photocatalysis.

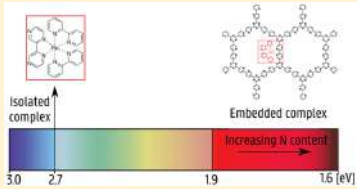

1. INTRODUCTION

Catalysis is of paramount relevance to many chemical reactions that could not occur within a reasonable time otherwise, thus disrupting either their industrial use[1] or biological functionality.[2] In the case of photocatalysis, the activation is effected by visible photons. This enables the synthesis of chemical products exploiting an easily available source of energy in mild reaction conditions, as often even the light emitted by a household bulb can be enough. Furthermore, control of the light exposure allows photocatalysis to be fine-tuned and even stopped at will, creating the ability to obtain a high degree of chemoselectivity.[3,4] However, in the attempt to design new green catalytic routes, there is a high interest in developing recyclable and reusable heterogeneous photocatalytic systems.[5−8] One way to achieve this goal is the anchoring of homogeneous complexes with photocatalytic properties on a heterogeneous stable support. This procedure is applicable in case the photocatalytic properties of the pristine complex are retained or improved in the heterogenized system. To this end, a deep knowledge is required of both electronic and excited state properties of the pristine homogeneous and anchored complex within the support. Such investigation is presented in this paper for $Ru(II)L_3$ complexes, which are commonly applied visible light photocatalysts consisting of a Ru^{2+} ion that is octahedrally chelated by three bidentate polypyridyl ligands as shown in Figure 1, parts a and b. Herein the electronic properties of such isolated and anchored ruthenium polypyridyl complexes onto a stable heterogeneous support are investigated.

Complexes of the type $Ru(2,2'\text{-bipyrdine})_3^{2+}$ are among the most interesting photoredox catalyzers. They show no catalytic properties in their ground state, but when exposed to light, their excited electronic states are able to oxidize or reduce substrate molecules through single-electron transfer (SET) processes.[10] They have proven their usefulness allowing very different reactions such as carbon dioxide reduction,[11,12] solar

Received: May 31, 2019
Revised: July 19, 2019
Published: July 19, 2019

DOI: 10.1021/acs.jpca.9b05216
J. Phys. Chem. A 2019, 123, 6854−6867

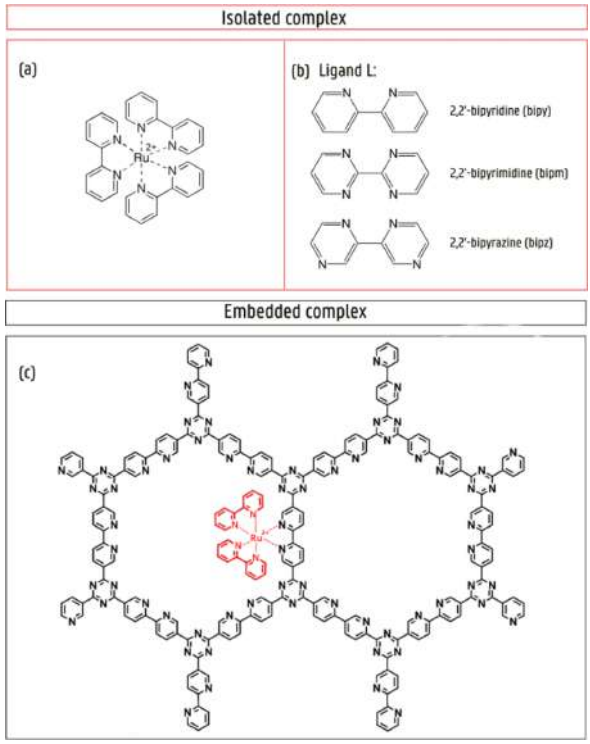

Figure 1. (a): Schematic representation of the isolated $Ru(bipy)_3^{2+}$ complex. (b): Polypyridyl ligands: *cis*-2,2′-bipyridine (bipy), 2,2′-bipyrimidine (bipm), and *cis*-2,2′-bipyrazine (bipz) considered in this study. (c) Part of the CTF synthesized in ref 9 and used as computational model here, in black. The anchored RuL_2^{2+} fragment inside one pore is shown in red.

cells development,[13,14] water splitting,[15−17] as well as Diels−Alder cycloadditions,[18,19] and can be used as a photosensitizer,[20] thus spanning both inorganic and organic reactions and acting as either reducing or oxidizing agents.[3,21−25]

The two possible relaxation mechanisms of the excited states of the Ru(II) cation are schematically shown in Scheme 1, which sketches the orbital occupancy of the frontier electron states of the ruthenium complex. The t_{2g} and e_g states originate from the octahedrally surrounded Ru(II) cation, while orbitals from the ligands are situated in between. In the ground state, depicted on the left, only the t_{2g} states are filled and ruthenium is in the Ru(II) state. By absorption of a photon in the visible region a singlet → singlet metal-to-ligand charge transfer (MLCT) excitation occurs, leaving an electron hole in the metal states. As such, the oxidation number of ruthenium increases by one. The singlet excited state can quickly convert to a lower-energy triplet excited state via nonradiative means. This mechanism is called intersystem crossing (ISC). In a recent theoretical study the decay from the singlet to triplet states was shown to occur with a time constant of 26 ± 3 fs, which was in very good agreement with experimental data. To this end a newly implemented combination of linear response time-dependent density functional theory (TD-DFT) with surface-hopping including arbitrary couplings (SHARC) was employed for the first time to model the relaxation dynamics of $Ru(bipyridine)_3^{2+}$ after light irradiation with explicit nonadiabatic and spin−orbit couplings.[26] The resulting excited state, shown in the red box in Scheme 1, is long-lived, as the decay to the singlet ground state is spin-forbidden.

The photoexcited state can then relax either by reduction of an organic substrate, maintaining an oxidized Ru(III) cation (upper arrow in Scheme 1), or by reduction of the complex via transfer of an electron from the substrate to the now vacant t_{2g} orbital of the Ru(III) cation, which then reverts to Ru(II) (lower arrow in Scheme 1).

The triplet excited state of $Ru(2,2'\text{-bipyridine})_3^{2+}$ may thus be engaged in an electron transfer process, but it may also be involved in a process called triplet−triplet energy transfer (TTET), in which the decay from the excited $Ru(2,2'\text{-bipyridine})_3^{2+}$ from its triplet to ground state involves the excitation of another molecule from its ground singlet state to its lowest triplet state. This mechanism requires the excitation of both the catalyst and substrate to a spin-triplet state and has been the subject of both theoretical[27] and application-oriented investigations.[28] The $Ru(2,2'\text{-bipyridine})_3^{2+}$ has been exploited in a number of C−C making and breaking transformations, such as trans/cis stilbene isomerization,[29] anthracene dimeri-

DOI: 10.1021/acs.jpca.9b05216
J. Phys. Chem. A 2019, 123, 6854−6867

Scheme 1. Photoactivation of an Octahedral Ruthenium Complex from the Ground State (Left Black Box) to an Excited State (Red Box) under the Influence of Visible Light, Exciting an Electron toward a State Localized on the Ligands, followed by ISC[a]

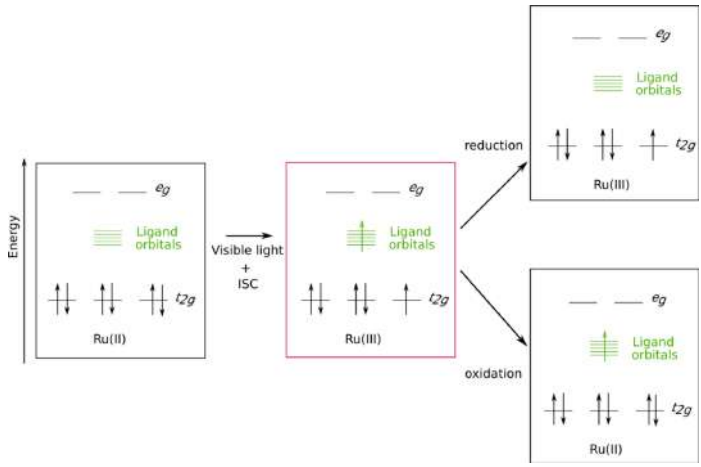

[a]The excited state relaxes by reduction (upper arrow) or oxidation (lower arrow) of the substrate. Schematic adapted from ref 3. Copyright 2013 American Chemical Society.

zation,[30] cycloadditions,[31] and trifluoromethylations of styrene substrates[32] via the TTET mechanism.

Herein we investigate the photocatalytic properties of $Ru(II)L_3$ type complexes, where the ligands may either be *cis*-2,2′-bipyridine (bipy), 2,2′-bipyrimidine (bipm), or *cis*-2,2′-bipyrazine (bipz) as schematically shown in Figure 1b. Complexes with a varying number of nitrogen containing aromatic rings have been synthesized both in the literature[33−35] and in this work. In the first instance, we investigate to what extent the nitrogen content affects the photocatalytic properties. Second, the impact of heterogenizing the $Ru(II)L_3$ complexes on covalent triazine frameworks (CTFs) (see Figure 1c), which are a subclass of the broader family of covalent organic frameworks (COFs), are assessed.[36] Unfunctionalized COFs have been explored within catalysis to some extent,[6,37−39] but additional functionalization of the materials with metal complexes may open additional perspectives for their usage within catalysis by merging some of the most important features of both the organic, i.e., stability, and the inorganic, i.e., catalytic properties, worlds.

CTFs are potentially interesting supports since they are chemically and thermally stable.[40−46] Furthermore, they are much lighter than most other porous supports and contain no toxic or environmentally unfriendly elements. These porous 2D materials are made by ionothermal trimerization of aromatic nitriles and when fabricated with bidentate nitrogen containing ligands—similar to the chelating ligands in the ruthenium homogeneous complex—they may serve as ideal anchoring materials for the latter complexes.[47] The first reports on COFs containing (bi)pyridine have appeared recently, showing great promise for applications in catalysis and gas sorption.[9,48−54] In a similar way, this has already been applied for metal organic frameworks (MOFs),[55] where photocatalytic complexes were successfully anchored to both linkers[56,57] and nodes.[58] However, MOFs are in general less stable, making it interesting to explore other heterogeneous supports.[59−61]

To optimize the photocatalytic system, a thorough understanding of the ground- and excited-state properties of the tethered RuL_3^{2+} complexes is mandatory.[62] Ground state properties of the heterogeneous system have been studied in detail in our previous work,[63] whereas in this work, we focus on the calculation of excited states. The investigation of the distribution of most singlet states can be performed experimentally by UV−vis absorption spectroscopy. Contrarily, triplet states are more difficult to characterize without a computational investigation due to electronic selection rules preventing singlet → triplet excitations to achieve a significant oscillator strength, i.e., probability of occurrence. In order to understand how the CTF support impacts the photocatalytic properties of the ruthenium complexes, a stepwise computational analysis is adopted. The ground- and excited-state electronic properties of both the isolated ruthenium complexes and the anchored systems are investigated by means of density functional theory (DFT) and time-dependent density functional theory (TD-DFT).

To this end, we embed RuL_2^{2+} (represented in red in Figure 1c) into an extensive CTF structure model (represented in black in Figure 1c).[9] This CTF organic scaffold contains bipyridine groups belonging to the CTF exposed inside the pores, which are suitable to act as linkers for the ruthenium complex, thus giving rise to a RuL_2^{2+}@CTF compound. The results are analyzed to obtain insight into the electronic charge rearrangement and optical gap tuning induced by the ligands. For the isolated ruthenium complexes, we are able to compare and validate the calculated optical properties with experimentally measured UV−vis absorption data. However, specifically investigating the excitations of COFs by means of UV−vis absorption spectroscopy is cumbersome as these

DOI: 10.1021/acs.jpca.9b05216
J. Phys. Chem. A 2019, 123, 6854−6867

compounds often absorb light in a wide wavelength region, in part due their high flexibility. In addition, photoemission spectroscopy may yield results difficult to interpret without some theoretical understanding. In this light the current computational approach gives new insights into the excited state properties of the RuL_2^{2+}@CTF system, which in turn affect its photocatalytic properties. While TD-DFT calculations have been performed on COFs before,[64] to our knowledge this is one of the first applications on a COF model to which a photoactive complex has been anchored.

2. COMPUTATIONAL DETAILS

All calculations were performed with the Gaussian 16 software.[65] Ground state information was extracted at the DFT level. Excited states were investigated adopting the TD-DFT scheme,[66] within the linear-response approach due to Casida.[67]

2.1. Assessment of the Level of Theory for the Ground States. Four different exchange-correlation functionals coming from different rungs on Jacob's ladder[68] were tested on isolated RuL_3^{2+} complexes to compare their relaxed structures: the generalized gradient approximation PBE,[69] hybrid B3LYP,[70,71] long-range corrected CAM-B3LYP,[72] and metahybrid M06.[73] All computed internal normal modes of the relaxed structures show positive frequencies, ensuring that the optimized geometries represent minima of the ground state potential energy surface.

The average differences in bond lengths calculated with the various functionals and basis sets are below the 0.05 Å threshold. The optimized structures for $Ru(bipy)_3^{2+}$ are included in section S4 of the Supporting Information. All levels of theory employed here predict a positive partial Hirshfeld charge on the Ru(II) cations, with differences between the same complexes of about 0.02 $|e|$, with e the electron charge (see Table S1 of the Supporting Information).

2.2. Assessment of the Level of Theory for the Excited States. The vertical excitation spectra from the ground state geometry of $Ru(bipy)_3^{2+}$, obtained by TD-DFT,[67,74] are shown in Figure 2. Theoretical calculations were carried out both in the gas phase, i.e., without solvent, and with water and acetonitrile solvents modeled with the polarizable continuum method (PCM) to take into account the effect of the environment on the excitation energies.[75] The simulated UV−vis absorption spectra at the TD-DFT level of theory are compared with the experimental optical profiles for $Ru(bipy)_3^{2+}$ complexes in water[76] and acetonitrile solvents. The latter experimental data were generated within the framework of this work (vide infra for details on the experimental part). A side note is warranted on how to compare the theoretical and experimental data. The TD-DFT energy of the first allowed transition is an approximation of the optical gap, which is defined by a neutral excitation and as the difference between the energies of the lowest dipole-allowed excited state and the ground state.[77] As it accounts for the electron−hole recombination energy or exciton binding energy, the optical gap is systematically lower than the fundamental gap,[78] defined by a charged excitation and as the difference between the first ionization potential and the first electron affinity.[77] From UV−vis absorption measurements, optical gaps can be extrapolated as the energy of the first divergence of the spectrum from its baseline.

The spectrum calculated with the M06 functional yields the best agreement with experimental data with respect to those

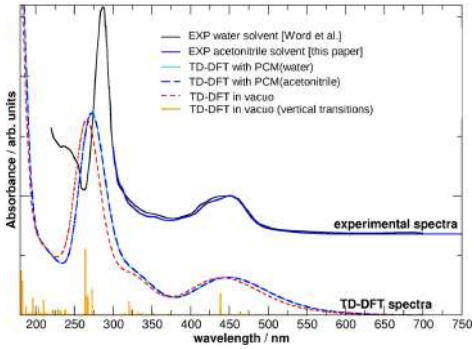

Figure 2. Experimental UV−vis absorption (top, Word et al.[76] and this paper) and TD M06 spectra (bottom) of $Ru(bipy)_3^{2+}$. Vertical excitations for the in vacuo TD M06 spectrum are reported as orange spikes. Computed spectra have been smoothed using Gaussian functions of half-width at half-height of 0.333 eV (default value of Gaussview). The computed spectra have not been rescaled nor shifted.

computed with PBE, B3LYP, and CAM-B3LYP (see Figure S1 of the Supporting Information) in terms of both shapes and positions of the bands, and no further rescaling of energies nor of wavelengths—as often employed for similar comparisons when pseudopotentials are used to simulate core electrons in metal atoms—were necessary.[79] As expected,[80,81] TD PBE spectra obtained by using a semilocal functional without Hartree−Fock exchange necessitated significant blueshifts to match the experimental data. Contrarily, TD CAM-B3LYP spectra required a significant redshift, in agreement with earlier studies on compounds ranging from metal−organic frameworks (MOFs)[82] to noble metal nanoclusters.[80] TD B3LYP spectra are rather similar to TD M06 spectra in frequencies, but the agreement regarding the shape of the absorption bands is better when using the M06 functional. As the M06/LanL2DZ level of theory correctly reproduces the optical features of the studied complexes, we have consistently used this level of theory unless otherwise stated. Errors between the various tested functionals are always smaller than 20 nm (see Figure S1 of the Supporting Information). We used the LanL2DZ[83] basis as it has been shown that the choice of basis set has a minimal influence on excitation energies, oscillator strengths, and assignments for transition metal complexes.[84] Tests with the Def2TZVPP basis set reveal a difference for the energy of the strongest transition of only 11 nm. Overall, M06 performs particularly well in systematic reviews of both organic and inorganic molecules,[85,86] yielding accurate transition energies.

Our conclusions are in agreement with ref[87] in which several functionals were tested for a few ruthenium complexes, including $Ru(bipy)_3^{2+}$. Besides the excitation energies, for which hybrid functionals and their range-separated and meta counterparts are the most accurate, Atkins et al. focused on the energy gaps between excited states, which tend to be best described by the pure generalized gradient approximation exchange-correlation functionals.[87] Since we are in this work interested in excitation energies, this confirms our choice for the M06 functional.

DOI: 10.1021/acs.jpca.9b05216
J. Phys. Chem. A 2019, 123, 6854−6867

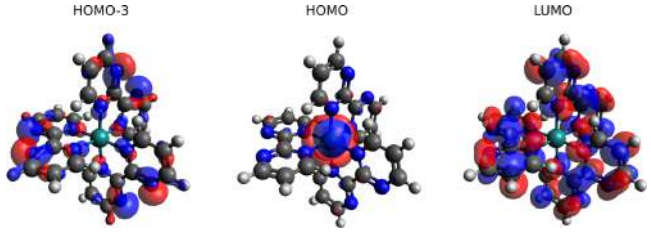

Figure 3. Isosurfaces of the HOMO−3, HOMO, and LUMO of the $Ru(bipm)_3^{2+}$ compound (complex g in Figure 4). Calculation carried out at the M06/LanL2DZ level of theory.

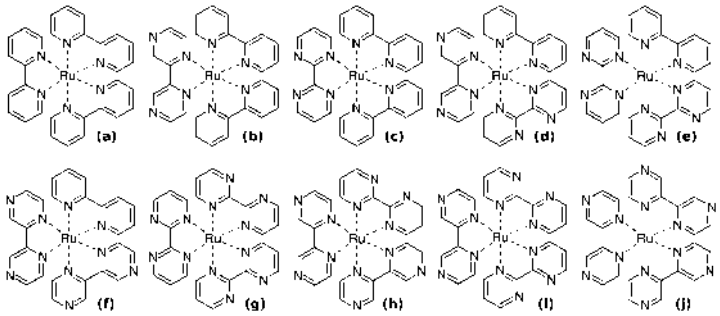

Figure 4. Ten RuL_3^{2+} complexes investigated here. (a) L = bipy × 3; (b) L = bipy × 2, bipz × 1; (c) L = bipy × 2, bipm × 1; (d) L = bipy × 1, bipz × 1, bipm × 1; (e) L = bipy × 1, bipm × 2; (f) L = bipy × 1, bipz × 2; (g) L = bipm × 3; (h) L = bipz × 2, bipm × 1; (i) L = bipz × 1, bipm × 2; (j) L = bipz × 3.

The overall shape of the spectrum is due to the many transitions from the singlet ground state to singlet excited states ($S_0 \rightarrow S_n$; n = 1, ...), which are spin-allowed. The effect of the solvent seems very modest, both from an experimental and a computational point of view. In addition, the effect of PCM with respect to the calculation in vacuo (dashed red line in Figure 2) is negligible for the first strong absorption band centered at about ∼450 nm (∼2.75 eV) and is rather small for the second peak located between 300 and 200 nm, i.e., in the UV region, with discrepancies smaller than 10 nm.

2.3. Optimization of the Ru(II)@CTF Models. To investigate the influence of embedding the ruthenium complexes within a CTF support, a Ru(II)@CTF model was constructed as schematically shown in Figure 1c. A CTF composed of triazine nodes interlinked with bipy linkers was considered. The bipy residues embedded into the CTF can naturally act as ligands for the ruthenium complexes, together with two other ligands that remain exposed inside the pore of the CTF.

The investigated model consists of two full CTF pores to minimize "edge effects" due to the sudden truncation of our cluster model (see Figure 1c). The cluster was terminated by completing the coordination of carbon atoms with hydrogen atoms. During the geometry optimization, the structures were allowed to relax freely and they converged to approximately planar structures, with small differences due to the different types of ligands.

Because the models including the COFs are very large (10 triazine and 34 pyridine rings, see Figure 1c), geometry optimizations of the models including the COFs were carried out with a step-by-step approach. First, the COFs were optimized using a small basis set (e.g., LanL1DZ). Second, the system was reoptimized with the addition of the Ru(II) cation and the two other ligands at the same level of theory. Finally, the total system was reoptimized at the M06/LanL2DZ level of theory within Gaussian 16 standard convergence criteria.

3. EXPERIMENTAL DETAILS

The UV−Vis absorption spectrum was collected using a Shimadzu UV1800 UV−vis spectrometer. The sample was prepared by dissolving 1 mg of $Ru(bipy)_3(PF_6)_2$ (Sigma-Aldrich) in 1.5 mL acetonitrile (Sigma-Aldrich, used without further purification). The solution was filtered through a 0.45 μm Whatman syringe filter and placed in a 1 cm × 1 cm cuvette. Further dilution of the sample was performed to obtain the desired absorbance range.

4. RESULTS AND DISCUSSION

4.1. Ground State Properties of Isolated Complexes. The three ligands investigated here all maintain a largely planar geometry when coordinating with a Ru(II) cation; the dihedral angles linking the two aromatic subunits are less than 1.5°. However, they contain a different number of nitrogen atoms (2 in bipy and 4 in bipm and bipz as shown in Figure 1b). Frontier orbitals of the ruthenium complexes may be sensitive to the nitrogen content of the ligands and their different aromaticity. In Figure 3, the HOMO and LUMO of $Ru(bipm)_3^{2+}$ are displayed, showing a general trend for this class of complexes. The HOMO, which is a nonbonding (n)

DOI: 10.1021/acs.jpca.9b05216
J. Phys. Chem. A 2019, 123, 6854−6867

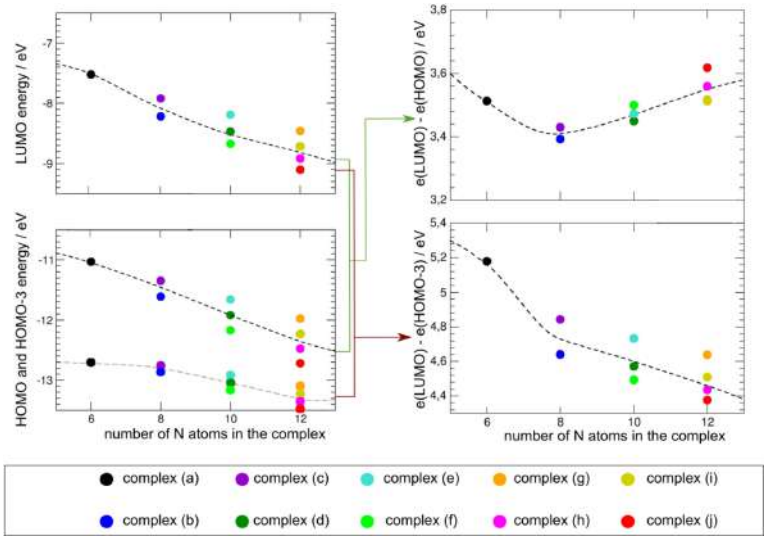

Figure 5. Energies of LUMOs (top left panel), HOMOs and HOMOs-3 (bottom left panel). Energy differences between HOMOs and LUMOs (top right panel) and HOMOs-3 and LUMOs (bottom right panel). The ten RuL_3^{2+} complexes are (a) L = bipy × 3; (b) L = bipy × 2, bipz × 1; (c) L = bipy × 2, bipm × 1; (d) L = bipy × 1, bipz × 1, bipm × 1; (e) L = bipy × 1, bipm × 2; (f) L = bipy × 1, bipz × 2; (g) L = bipm × 3; (h) L = bipz × 2, bipm × 1; (i) L = bipz × 1, bipm × 2; and (j) L = bipz × 3. Calculation carried out at the M06/LanL2DZ level of theory.

orbital, is mainly localized on the central Ru(II) cation, thus largely coinciding with a t_{2g} orbital, whereas the LUMO, which is a π^* orbital, is localized on the ligands. In addition, also the HOMO−3 orbital is visualized as it is the first occupied orbital below the HOMO, which is mainly localized on the ligands. In contrast, the HOMO−1 and HOMO−2 orbitals are mainly of the t_{2g} type (see Figure S2 of the Supporting Information).

It is now interesting to investigate to what extent the nitrogen content in the ligands affects their orbital energies. Various complexes were considered as schematically shown in Figure 4. For each of these complexes the energies of the HOMO, LUMO, and HOMO−3 in terms of the number of nitrogen atoms are plotted in Figure 5. The energies of both frontier orbitals decrease by ∼1 eV by going from the $Ru(bipy)_3^{2+}$ complex, containing only 6 nitrogen atoms (black circles), to complexes with only bipz and bipm ligands (red, pink, yellow, and orange circles), which contain 12 nitrogen atoms instead. The simultaneous decrease in energy for both types of orbitals results in a rather flat profile by about 0.2 eV for the HOMO−LUMO gaps. Nevertheless, a small minimum at N = 8 atoms can be discerned, a recurring feature in many energy gap profiles of these complexes as will be shown later.

While the HOMO−LUMO gap seems largely unaffected by the ligands, the energy gap between orbitals mainly localized on the ligands shows a different behavior. The contribution of the nitrogen atoms is small in the HOMO−3 orbital, as can be seen in the expansion in atomic contributions of the wave function (Table S2 in Supporting Information). As a result, the energy of the HOMO−3 is only slightly affected by the increase in number of nitrogen atoms from 6 to 12 (Figure 5 bottom left panel). Then, as expected, the energy gap between the LUMO and HOMO−3, which is indicative for ligand−ligand transitions, decreases with the number of nitrogen atoms in the complexes, as shown in the bottom right panel of Figure 4. These conclusions are in agreement with our previous work on the ground state properties of RuL_3^{2+}.[62] Thus, the energy difference between the HOMO−3 and LUMO can be considered as a sort of effective "ligand gap", i.e., an energy gap between states mainly localized on the organic rings. Even if this gap shows significant internal variations for a fixed number of nitrogen atoms in the complex, it seems to be more clearly dependent on the nitrogen content than the HOMO−LUMO gap, as it spans a full 1 eV range (see Figure 5, right panels).

Further clarification for the previous findings can be found by inspecting the electronic density of states (eDoS) for $Ru(bipy)_3^{2+}$ (see Figure 6). It confirms that the major contributions of ruthenium around the band gap are found on the HOMO, HOMO−1, and HOMO−2.

Such an analysis was also performed for the different complexes having a varying degree of nitrogen content. The eDoSs are superimposed in the left pane of Figure 7, showing that the nitrogen content actually affects all the eigenvalues of the systems. With an increasing number of nitrogen atoms in the ligands we observe decreasing energies; i.e., the distribution is shifted to the left side of the plot, as indicated by the colored arrow. The contributions of the eDoS originating from ruthenium, while mainly localized on the HOMOs and on virtual states which are about 5 eV higher in energy than the LUMOs (see Figure 6), are still affected by the number of nitrogen atoms in the complexes, as shown in the right pane of Figure 7.

The organic ligands investigated here are all heteroaromatic compounds and the degree of aromaticity might play a role to

DOI: 10.1021/acs.jpca.9b05216
J. Phys. Chem. A 2019, 123, 6854−6867

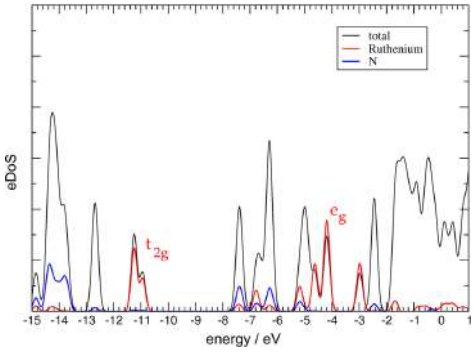

Figure 6. eDoS of $Ru(bipy)_3^{2+}$ complex, with contributions due to the Ru(II) cation and the N atoms colored in red and blue, respectively. Calculation carried out at the M06/LanL2DZ level of theory. The zero is set at the calculated ionization energy.

elucidate the observed trends for the energy levels in terms of the nitrogen content. Aromaticity is usually considered as a particular stabilization of the occupied states localized on aromatic rings with respect to the virtual states. This property can be quantified using a number of different scales and indexes. Herein we used the aromaticity index of Bird,[88,89] which is based on the resonance stabilization energy. The latter property is smaller for pyrimidine (40.6 kcal/mol) and pyrazine (40.9 kcal/mol) than for pyridine (43.3 kcal/mol).[88] This fact can be qualitatively understood in terms of electron content because adding more nitrogen atoms, with additional electron pairs that do not participate in delocalized π orbitals, decreases the overall stabilization. We notice that the energy difference between the HOMO−3 and LUMO has some correlation with Bird's aromatic stabilization energy, as shown in Figure S3 of the Supporting Information. However, we have not found any clear correlation between the HOMO−LUMO gap and the aromaticity index of Bird.[88,89] This is reasonable since this gap is strongly affected by ruthenium, which is not taken into account by this aromaticity descriptor. We also investigated the correlation with some other aromaticity indices. More information can be found in section S2.1 and Figure S4 of the Supporting Information.

In order to effectively catalyze redox reactions, ruthenium has to possess a net charge. The partial charges obtained with both the Hirshfeld and Mulliken partition schemes of the ten complexes are reported in Table S3 of the Supporting Information. As can be seen, the Ru(II) cation is consistently positive, but a correlation with the number of nitrogen atoms or aromatic descriptors is not evident, because the differences are rather small, being of the order of 0.02 lel. As expected, the Hirshfeld charges are in absolute values smaller than the Mulliken charges.[90]

In conclusion from the ground state properties of the isolated $Ru(L)_3^{2+}$, it is observed that the HOMO−LUMO gap—approximately describing the MLCT—remains nearly unaffected by the number of nitrogen atoms, whereas the HOMO−3-LUMO gap—approximately describing the ligand−ligand gap—is reduced for a higher number of nitrogen atoms.

4.2. Excited States Properties of Isolated Complexes.

The photoredox and charge-transfer properties are strongly affected by the optical properties of the complexes, in particular by their absorption and emission of UV−vis radiation. First, we discuss the singlet and triplet excitations in the visible-light range which are mainly of the MLCT type, as stated before. Afterward, we focus on the triplet metal-centered states. The triplet excitations are spin-forbidden but play an important role in TTET. The energy of the first spin-allowed transition, i.e., the energy of the first singlet state (S_1), approximates the optical gap, as discussed previously. From our TD-DFT calculations we determine how it changes with the nitrogen content of the complexes. The results are shown in the upper panel of Figure 8.

The complex showing the lowest S_1 energy contains eight nitrogen atoms and is composed of two bipy ligands and one bipz (blue dot, complex b), whereas the complex with the highest energy is $Ru(bipz)_3^{2+}$ (red dot, complex j), with a difference of about 0.4 eV. A similar distribution of values,

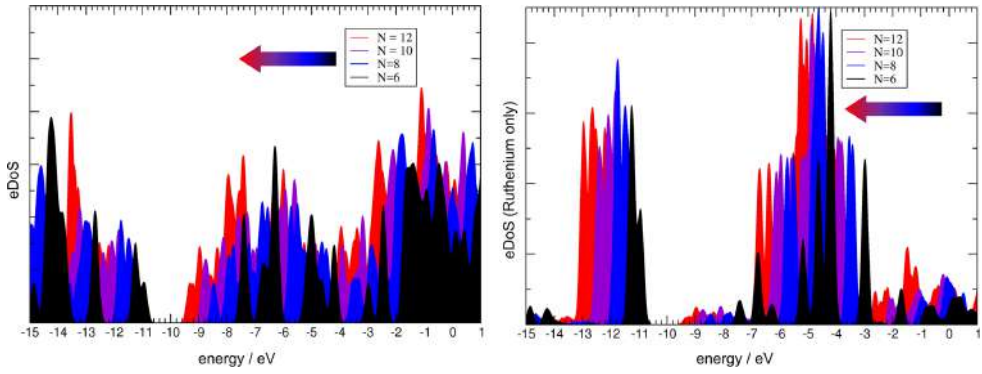

Figure 7. Total eDoS (left) and contribution localized on ruthenium (right) of the ten complexes investigated here, sorted by color according to the number of N atoms in the ligands (N = 6, 8, 10, and 12). The eDoS are superimposed. Calculations have been carried out at the M06/LanL2DZ level of theory.

DOI: 10.1021/acs.jpca.9b05216
J. Phys. Chem. A 2019, 123, 6854−6867

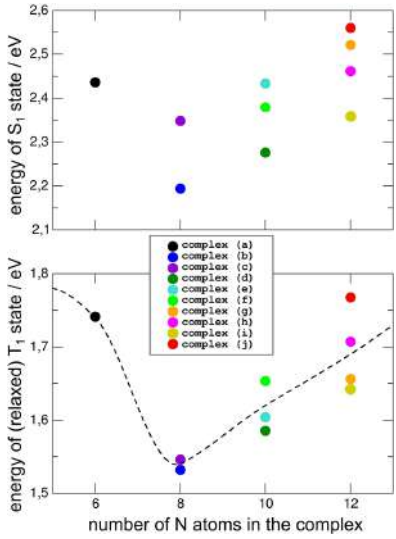

Figure 8. Vertical TD-M06 energies of the S_1 states (upper panel) and of the optimized T_1 states (lower panel). The ten RuL_3^{2+} complexes are (a) L = bipy × 3; (b) L = bipy × 2, bipz × 1; (c) L = bipy × 2, bipm × 1; (d) L = bipy × 1, bipz × 1, bipm × 1; (e) L = bipy × 1, bipm × 2; (f) L = bipy × 1, bipz × 2; (g) L = bipm × 3; (h) L = bipz × 2, bipm × 1; (i) L = bipz × 1, bipm × 2; and (j) L = bipz × 3 according to the nomclature introduced in Figure 4. Calculation carried out at the M06/LanL2DZ level of theory.

albeit with different magnitudes, can be observed for the most intense transitions of the visible spectra, occurring between 3 and 2.7 eV, at ∼430 nm as can be seen in Figure S5 of the Supporting Information. All excitation energies and their corresponding oscillator strengths are given in Table S4 of the Supporting Information.

Although the experimental absorption spectrum is mainly due to vertical excitations, adhering to the Franck−Condon principle, we also examined to which extent the geometries of the excited MLCT S_1 and S_2 states change when we optimize them. These states correspond to adiabatic, i.e., nonvertical, excitations and may be observed in fluorescence measurements. We find that their relaxed excited-state geometries are very similar to those of their respective ground states (see Figure S6 (left pane) Supporting Information). Moreover, the overall effect of geometry optimization on the excitation energies is a shift toward lower values, which is rather constant, i.e., between 0.43 and 0.66 eV for the ten RuL_3^{2+} complexes (Table S4 and S5 of the Supporting Information). For $Ru(bipy)_3^{2+}$ the S_1 energy for the relaxed geometry becomes 2.00 eV (compared with 2.45 eV when the geometry of the excited state is not optimized), corresponding to a wavelength of 618.7 nm. This is in good agreement with a fluorescence emission occurring at 615 nm.[91,92]

Nested between the $S_0 \rightarrow S_n$ transitions, there are spin-forbidden MLCT transitions to triplet states (T_n), whose contributions to the absorption spectra are negligible. However, these T_n states play a role in TTET and can still be encountered during nonradiative processes and decays which require a relaxation of the geometry. They therefore have to be taken into account to describe the electronic structures of complexes with emerging catalytic properties.[93,94] The adiabatic transition energies of the first triplet states closely follow the trend of the S_1 ones (Figure 8, bottom panel), albeit with a smaller overall variation (∼0.3 eV instead of 0.4 eV) and at lower energies. However, they still pinpoint $Ru(bipy)_2(bipz)^{2+}$ as the complex with the smallest transition energy (N = 8). As expected, the distributions of T_1 and S_1 excitation energies versus the number of nitrogen atoms also follow a pattern very similar to that of the HOMO−LUMO gaps (see Figure 5).

Transitions toward T_1, T_2, and T_3 states are all of the MLCT type. In the case of the $Ru(bipy)_3^{2+}$, $Ru(bipz)_3^{2+}$, and $Ru(bipm)_3^{2+}$ complexes, i.e., those with three equal ligands, the corresponding vertical transitions are basically degenerate as the energy difference is below the 0.02 eV threshold. This degeneracy is removed when a ligand is substituted with one of a different type, as shown in Figure S7 of the Supporting Information for the case of $Ru(bipy)_3^{2+}$. By a subsequent exchange of ligands, the $T_1-T_2-T_3$ energy separation increases from less than 0.02 eV to more than 0.2 eV. In addition, the triplet transitions whose degeneracy is broken by passing from RuL_3^{2+} to a $Ru(L)_2L'^{2+}$ complex (with L and L′ two different ligands), do not involve charge transfer to both L′ and L, but to only one ligand, either L′ or L.[63]

At energies higher than the triplet MLCT states, triplet states centered on ruthenium can be found, which are called metal-centered states (^{3}MC).[95] These states are found at ∼3.3 eV in the vertical excitations, which qualitatively agrees with what has been observed for the ground state eDoS (see Figure 7), showing contributions due to Ru(II) cations at energies higher than 3 eV above the LUMO.

While singlet and triplet MLCT states have a relaxed geometry close to that of the ground state, relaxed ^{3}MC states show more significant distortions: there is a loss of coplanarity between the two rings of the ligands, with dihedral angles between the two aromatic subunits of more than 7° (see Figure S6 (right pane) of the Supporting Information). This suggests that intersections with nearby excited states may occur, potentially leading to ISC phenomena.

Even if these triplet states are centered on the metal, they involve an increase in the positive Hirshfeld partial charge on the Ru(II) ion with respect to the ground state, as shown in Figure S8 of the Supporting Information. This can be explained as ^{3}MC states are thought to be predissociation states,[91,96−98] thus leaving a higher excess positive charge on the Ru(II) cation. While this latter increment is small in absolute value, in cases with a high content of nitrogen atoms, it represents an increase of about 40% in the overall positive charge on the cation, potentially changing the energetics of intermediate and transition states during catalytic processes going via the TTET mechanism.

4.3. Ground State Properties of Complexes Embedded into a COF. In second instance we investigate how the electronic properties of the ruthenium complexes are affected by embedding them into a CTF support. The CTF is composed of triazine nodes interlinked with bipy linkers and the bipy residues embedded into the CTF can naturally act as ligands for the ruthenium complexes. The fact that the ligand embedded into the CTF is bipy has also the effect of reducing the number of possible ligand combinations in the RuL_2^{2+}@

DOI: 10.1021/acs.jpca.9b05216
J. Phys. Chem. A 2019, 123, 6854−6867

Scheme 2. Schematic Representation of Orbital Energies for the Ground State of $Ru(bipy)_2^{2+}$@CTF (Left Pane) and $Ru(L)_2^{2+}$@CTF with 10 Nitrogen Atoms (Right Pane), Indicating the Proposed Change of Orbital Energies Due to an Increase of Nitrogen Content from 6 to 10 Atoms in the Ligands[a]

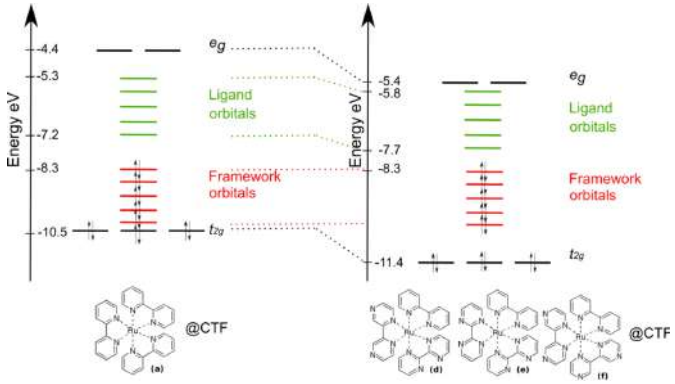

[a]The energy levels in the right pane correspond to $Ru(bipz)_2^{2+}$@CTF and $Ru(bipzbipm)^{2+}$@CTF. Calculations are at the M06 level of theory.

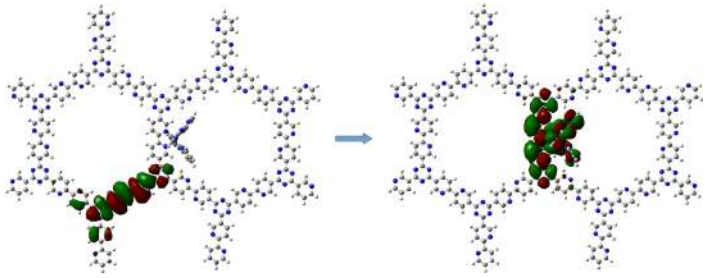

Figure 9. Orbitals involved in the first allowed transition in $Ru(bipy)_2^{2+}$@CTF complex. Calculation carried out at the M06/LanL2DZ level of theory.

CTF complex with respect to the isolated complexes from 10 to 6, i.e., complexes a–f in Figure 4.

We observe some significant electronic changes with respect to the isolated ruthenium complexes discussed before. In particular, occupied framework states are found between the states localized on the metal and on the ligands, as schematically shown in Scheme 2. This conclusion is in agreement with previous ground state calculations of RuL_2^{2+}@CTF.[63] According to the molecular orbital composition, the occupied t_{2g} and virtual e_g d orbitals of the Ru(II) cation remain separated in energy by ~6 eV for the $Ru(bipy)_2^{2+}$@CTF, which is close to the energy separation observed in the eDOS of the isolated complex (see Figure 6). However, in the Ru@CTF system, there are occupied framework states between the occupied orbitals of ruthenium and the virtual orbitals on the ligands, lowering the HOMO–LUMO gaps substantially by about 2.5–2.8 eV compared to the isolated complexes.

Furthermore, we also investigate the influence of the nitrogen content on the electronic states of the system. The nitrogen content has a clear influence on the electronic states of the system, as schematically shown in the right pane of Scheme 2. An increased nitrogen content from 6 to 10 atoms reduces the energy of t_{2g} and e_g orbitals by about 1 eV with respect to $Ru(bipy)_2^{2+}$@CTF, the shift for $Ru(bipm)_2^{2+}$@CTF is somewhat smaller, i.e. 0.6 eV. Instead the energy of the framework orbitals (~8.3 eV) is rather unaffected. The virtual orbitals of the ligands are decreasing with about 0.5 eV, thus bringing the energy gap between HOMO and LUMO to values of the order of 0.6–0.8 eV for nitrogen rich compounds such as $Ru(bipz)_2^{2+}$@CTF, $Ru(bipm)_2^{2+}$@CTF, and $Ru(bipzbipm)^{2+}$@CTF. The exact numerical values for the HOMO–LUMO gaps of the CTF-embedded complexes are reported in Table S6 of the Supporting Information.

4.4. Excited States Properties of Complexes Embedded into a COF. In CTF-embedded complexes, we notice that the orbital character of the first allowed TD M06 excitation, i.e., the first excitation with nonvanishing oscillator strength, is no longer mainly of the MLCT type as was the case for isolated complexes. Instead, we observe a charge transfer from states localized on the organic framework toward states localized on the complex, as shown in Figure 9. The target orbital is mainly localized on the bipyridine ligand of the CTF and only marginally on the ligands exposed inside the pore.

DOI: 10.1021/acs.jpca.9b05216
J. Phys. Chem. A 2019, 123, 6854–6867

These orbitals are the LUMOs in case of $Ru(bipy)_2^{2+}$@CTF. It may be possible that if the pore ligands should have a higher nitrogen content, the target orbital would be situated on them instead, as ground state calculations on similar periodic systems suggest.[63]

The first allowed transition in RuL_2^{2+}@CTF is thus of the crystal to crystal charge transfer (CCCT) or crystal to ligand charge transfer (CLCT) type. In the work of De Vos et al., where periodic ground state electronic structures were performed on the ruthenium complexes in CTF frameworks, it was indeed suggested that excitations of the highest occupied crystal orbital to the linkers or ligands attached to the ruthenium ion might be interesting, but it could not be deduced whether those states would be realistic as they are spatially relatively far separated. Here we find based on excited state calculations that these transitions are indeed realistic as they have a nonvanishing oscillator strength. A list of all excitation energies and their corresponding oscillator strengths is given in Table S7 in the Supporting Information.

Changing the nitrogen content of the ligands connected to ruthenium and pointing into the pores of the material, induces a significant drop in the vertical excitation energy of the most intense transition, with values as low as 1.6 eV for an increasing number of nitrogen atoms in the ligands around ruthenium (see Figure 10). So, while in isolated complexes the excitation energy of the strongest transition is in the UV/blue visible region, the gap falls into the orange-near-infrared (NIR) region when the complex is included into the CTF (see Figure 11). Furthermore, it has to be emphasized that this effect is specific to this metal complex@CTF adduct, as the optical gap of the CTF model alone (i.e., without any anchored ruthenium complex) is ~3.32 eV, which is close to the near-UV range of energies instead.

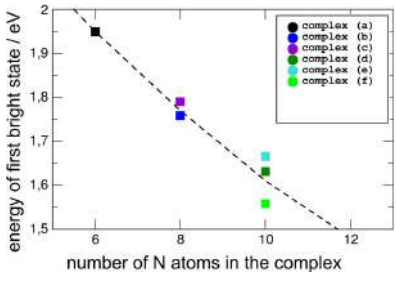

Figure 10. Change of the strongest excitation energy with the number of N atoms in the ligands around the Ru(II) cation in RuL_2^{2+}@CTF. The six RuL_2^{2+}@CTF complexes are (a) L = bipy × 2; (b) L = bipy × 1, bipz × 1; (c) L = bipy × 1, bipm × 1; (d) L = bipz × 1, bipm × 1; (e) L = bipm × 2; (f) L = bipz × 2. Calculation carried out at the M06/LanL2DZ level of theory.

While in isolated complexes the change of the excitation energy of the strongest transition with the number of nitrogen atoms of the ligands was small and nonmonotonous, a clear decrease of the excitation energy with the nitrogen content is observed in the embedded complexes (see Figure 10). This is due to the fact that the HOMO is no longer localized on the ruthenium but on the CTF, whereas the target virtual orbital is mainly localized on the ligands of the ruthenium complex.

These results show that the hybrid RuL_2^{2+}@CTF system offers an extra degree of versatility in tuning the electronic response of the photocatalyst. By tuning the nitrogen content of the anchoring linkers pointing into the pore of the RuL_2^{2+}@CTF system, the optical gap can be reduced by about 0.5 eV and the direction of the charge transfer can be designed. A schematic representation of the excitation energies corresponding to the strongest transition in both isolated, embedded ruthenium complex and isolated CTF is shown in Figure 11 together with an indication on how these excitations would be influenced by the nitrogen content.

As it is known that TD-DFT might fail to correctly reproduce charge-transfer excitations,[99] it is important to corroborate the above interpretation with ground state considerations. We notice here that the predicted TD M06 optical gaps shown in Figure 10 are in qualitative agreement with those of the occupied framework orbitals/virtual ligand orbitals described in Scheme 2 calculated with ground state M06 calculations. Furthermore, the trend with the nitrogen content is similar. Moreover, to further assess the reliability of the previous M06 ground state considerations, we have employed the range-separated CAM-B3LYP exchange correlation functional (which is often considered better suited to describe charge-transfer phenomena[100]) to compute Kohn–Sham gaps in the isolated and CTF-embedded complexes. In this case, the gap between the occupied framework orbitals and virtual ligand orbitals calculated at the CAM-B3LYP level of theory is about 1.9–1.7 eV smaller than the HOMO–LUMO gap in isolated complexes, which is in qualitative agreement with the aforementioned M06 results. With CAM-B3LYP, however, all the absolute energies are significantly blueshifted. This seems reasonable, as range-separated hybrid functionals are outperformed by global hybrid functionals for n → π^* transitions.[64] To further investigate the nature of this transition, we have used the Mulliken averaged configuration (M_{AC}) index of Ciofini and co-workers that is able to spot ghost states which appear by significantly underestimating the energy.[101] This diagnostic index, which discerns unrealistic charge transfer produced by the limitations of the level of theory, is a generalization of the Mulliken estimation of

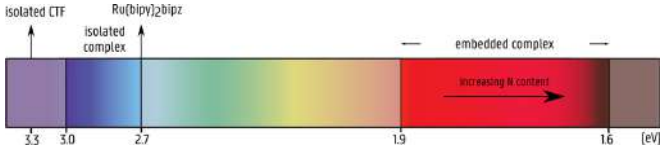

Figure 11. Schematic representation of the strongest singlet excitation energies of the isolated and embedded complexes. The lowest excitation energy for the isolated complex is found for $Ru(bipy)_2bipz$ at ~2.7 eV. For the embedded complexes the excitation energy decreases for an increasing number of nitrogen atoms. The energy of the first transition with nonzero oscillator strength of the empty CTF is also indicated.

DOI: 10.1021/acs.jpca.9b05216
J. Phys. Chem. A 2019, 123, 6854–6867

transition energy for charge transfer excitations. With it we were able to confirm the charge transfer character of the transition; it is not a ghost state as the transition energy is larger than the M_{AC} index. From this, we are ensured that our TD-DFT results are reliable.

5. CONCLUSIONS

In this work, we have investigated how polypyridyl ligands, characterized by a varying nitrogen content and aromaticity, can affect the photocatalytic properties of ruthenium-based complexes of the type RuL_3^{2+} in both the ground and the excited states. As those complexes can be exploited either as oxidant or reductant agents in photochemical reactions, this overall insight into their energetics allows a choice for the most appropriate compound for the specific task at hand. Studying triplet states with computational approaches is necessary to optimize catalytic conditions for reactions going through triplet−triplet energy transfer (TTET), since investigating nonsinglet states by means of UV−vis absorption is often unpractical.

In second instance, we studied how the heterogenization of the ruthenium complexes on a CTF support consisting of bipyridine ligands affects the electronic ground and excited state properties of the RuL_2^{2+}@CFT system.

For the isolated RuL_3^{2+}, an increase in the number of nitrogen atoms in the ligands redshifts the overall energetics of the compound, albeit without significantly altering the HOMO−LUMO gap. The energy gaps between linker−linker states, on the other hand, are significantly affected by both aromaticity and nitrogen content of the ligands. Singlet metal-to-ligand charge transfer (MLCT) excitations are found between 2.2 and 2.6 eV for complexes within varying nitrogen content. They are only slightly affected by changing the ligands. Triplet metal-to-ligand charge transfer (MLCT) excitations are situated in the 1.5−1.8 eV range and can to a certain extent be tuned for a range of applications that require specific activation energies. One particular complex, $Ru(bipy)_2(bipz)^{2+}$, shows a redshift of both singlet and ^{3}MLCT triplet excited states, making it an interesting candidate for processes induced by visible light. Changes induced in higher-energy triplet metal-centered (MC) states moreover deplete the electronic density around the Ru(II) cation, increasing its positive charge and, thus, its oxidant power.

For the complex embedded into a bipyridine-composed CTF, we observe a significant redshift of the allowed excitations to energies bordering the near IR region of the spectrum. This allows harvesting these lower energies to promote charge-transfer excitations. For example, near-infrared photocatalysis[102,103] could greatly benefit from the nanoporous environment and thus make better use of the near-infrared solar irradiation (making up 44% of solar irradiation spectrum) to reduce the ruthenium active site. Furthermore, the first allowed transition occurs from orbitals localized on the framework toward orbitals mainly localized on the ruthenium complex.

Overall, this investigation indicates how optoelectronic properties of ruthenium complexes can be changed and, possibly, tuned by the ligands and heterogenization within a CTF environment. Furthermore, this means that, potentially, a larger spectrum of radiation can be harvested to activate the complex. In the future, this kind of investigation could also be extended to other nitrogen containing aromatic ligands and transition metals, e.g., iridium, to further develop these promising platforms for heterogeneous photocatalysis.

■ ASSOCIATED CONTENT

Supporting Information

The Supporting Information is available free of charge on the ACS Publications website at DOI: 10.1021/acs.jpca.9b05216.

Charges, spectra and optimized structures of $Ru(bipy)_3^{2+}$ across different functionals; ground state orbital isosurfaces of $Ru(bipm)_3^{2+}$; atomic contributions and energies of $Ru(bipy)_3^{2+}$; influence of polypyridyl aromaticity on the electronic levels; comparison of charge schemes; excitation energies and oscillator strengths of isolated and embedded Ru(II) polypyridyl complexes; influence of excited-state optimization; removal of triplet state degeneracy; and Ru charge in metal-centered states (PDF)

■ AUTHOR INFORMATION

Corresponding Authors

*(K.L.) E-mail: kurt.lejaeghere@ugent.be.
*(V.V.S.) E-mail: Veronique.VanSpeybroeck@UGent.be.

ORCID

Arthur De Vos: 0000-0002-4916-6066
Christian V. Stevens: 0000-0003-4393-5327
Pascal Van Der Voort: 0000-0002-4874-0943
Kurt Lejaeghere: 0000-0002-4462-8209
Veronique Van Speybroeck: 0000-0003-2206-178X

Present Address

⊥Chimie ParisTech, PSL Research University, CNRS, Institute of Chemistry for Life and Health Sciences (i-CLeHS), FRE 2027, F-75005 Paris, France

Author Contributions

∥These authors contributed equally

Notes

The authors declare no competing financial interest.

■ ACKNOWLEDGMENTS

The authors acknowledge the Fund for Scientific Research Flanders (FWO) and the Research Board of Ghent University (BOF) through a Concerted Research Action (GOA) for funding. V.V.S. and L.D.B. acknowledge funding from the European Union's Horizon 2020 research and innovation program (consolidator ERC Grant Agreement No. 647755 − DYNPOR (2015-2020)). The computational resources and services used in this work were provided by VSC (Flemish Supercomputer Center), funded by Ghent University, FWO, and the Flemish Government Department EWI.

■ REFERENCES

(1) Armor, J. N. A History of Industrial Catalysis. *Catal. Today* **2011**, *163*, 3−9.
(2) Editorial. Closing in on Catalysis. *Nat. Chem. Biol.* **2009**, *5*, 515−515.
(3) Prier, C. K.; Rankic, D. A.; MacMillan, D. W. C. Visible Light Photoredox Catalysis with Transition Metal Complexes: Applications in Organic Synthesis. *Chem. Rev.* **2013**, *113*, 5322−5363.
(4) Kärkäs, M. D.; Porco, J. A.; Stephenson, C. R. J. Photochemical Approaches to Complex Chemotypes: Applications in Natural Product Synthesis. *Chem. Rev.* **2016**, *116*, 9683−9747.
(5) Slater, A. G.; Cooper, A. I. Porous Materials. Function-Led Design of New Porous Materials. *Science* **2015**, *348*, aaa8075.

DOI: 10.1021/acs.jpca.9b05216
J. Phys. Chem. A 2019, 123, 6854−6867

(6) Rogge, S. M. J.; Bavykina, A.; Hajek, J.; Garcia, H.; Olivos-Suarez, A. I.; Sepúlveda-Escribano, A.; Vimont, A.; Clet, G.; Bazin, P.; Kapteijn, F.; et al. Metal−Organic and Covalent Organic Frameworks as Single-Site Catalysts. *Chem. Soc. Rev.* **2017**, *46*, 3134−3184.
(7) Takeda, H.; Ohashi, M.; Goto, Y.; Ohsuna, T.; Tani, T.; Inagaki, S. A Versatile Solid Photosensitizer: Periodic Mesoporous Organosilicas with Ruthenium Tris(Bipyridine) Complexes Embedded in the Pore Walls. *Adv. Funct. Mater.* **2016**, *26*, 5068−5077.
(8) Tu, W.; Xu, Y.; Yin, S.; Xu, R. Rational Design of Catalytic Centers in Crystalline Frameworks. *Adv. Mater.* **2018**, *30*, 1707582.
(9) Hug, S.; Tauchert, M. E.; Li, S.; Pachmayr, U. E.; Lotsch, B. V. A Functional Triazine Framework Based on N-Heterocyclic Building Blocks. *J. Mater. Chem.* **2012**, *22*, 13956−13964.
(10) Hedstrand, D.; Kruizinga, W.; Kellogg, R. Light-Induced and Dye Accelerated Reductions of Phenacyl Onium Salts by 1,4-Dihydropyridines. *Tetrahedron Lett.* **1978**, *19*, 1255−1258.
(11) Takeda, H.; Ishitani, O. Development of Efficient Photocatalytic Systems for CO_2 Reduction Using Mononuclear and Multinuclear Metal Complexes Based on Mechanistic Studies. *Coord. Chem. Rev.* **2010**, *254*, 346−354.
(12) Sekizawa, K.; Sato, S.; Arai, T.; Morikawa, T. Solar-Driven Photocatalytic CO_2 Reduction in Water Utilizing a Ruthenium Complex Catalyst on p-Type Fe_2O_3 with a Multiheterojunction. *ACS Catal.* **2018**, *8*, 1405−1416.
(13) Gao, F.; Wang, Y.; Zhang, J.; Shi, D.; Wang, M.; Humphry-Baker, R.; Wang, P.; Zakeeruddin, S. M.; Grätzel, M. A New Heteroleptic Ruthenium Sensitizer Enhances the Absorptivity of Mesoporous Titania Film for a High Efficiency Dye-Sensitized Solar Cell. *Chem. Commun.* **2008**, 2635−2637.
(14) Kamata, R.; Kumagai, H.; Yamazaki, Y.; Sahara, G.; Ishitani, O. Photoelectrochemical CO_2 Reduction Using a Ru(II)-Re(I) Supramolecular Photocatalyst Connected to a Vinyl Polymer on a NiO Electrode. *ACS Appl. Mater. Interfaces* **2019**, *11*, 5632−5641.
(15) Concepcion, J. J.; Jurss, J. W.; Templeton, J. L.; Meyer, T. J. One Site Is Enough. Catalytic Water Oxidation by $[Ru(Tpy)(Bpm)(OH_2)]^{2+}$ and $[Ru(Tpy)(Bpz)(OH_2)]^{2+}$. *J. Am. Chem. Soc.* **2008**, *130*, 16462−16463.
(16) Kaveevivitchai, N.; Chitta, R.; Zong, R.; El Ojaimi, M.; Thummel, R. P. A Molecular Light-Driven Water Oxidation Catalyst. *J. Am. Chem. Soc.* **2012**, *134*, 10721−10724.
(17) Gil-Sepulcre, M.; Böhler, M.; Schilling, M.; Bozoglian, F.; Bachmann, C.; Scherrer, D.; Fox, T.; Spingler, B.; Gimbert-Suriñach, C.; Alberto, R.; et al. Ruthenium Water Oxidation Catalysts Based on Pentapyridyl Ligands. *ChemSusChem* **2017**, *10*, 4517−4525.
(18) Lin, S.; Ischay, M. A.; Fry, C. G.; Yoon, T. P. Radical Cation Diels−Alder Cycloadditions by Visible Light Photocatalysis. *J. Am. Chem. Soc.* **2011**, *133*, 19350−19353.
(19) Matsui, K.; Shibuya, M.; Yamamoto, Y. Synthesis of Pyrroles via Ruthenium-Catalyzed Nitrogen-Transfer [2 + 2 + 1] Cycloaddition of α,ω-Diynes Using Sulfoximines as Nitrene Surrogates. *Commun. Chem.* **2018**, *1*, 21.
(20) Karges, J.; Heinemann, F.; Maschietto, F.; Patra, M.; Blacque, O.; Ciofini, I.; Spingler, B.; Gasser, G. A Ru(II) Polypyridyl Complex Bearing Aldehyde Functions as a Versatile Synthetic Precursor for Long-Wavelength Absorbing Photodynamic Therapy Photosensitizers. *Bioorg. Med. Chem.* **2019**, *27*, 2666−2675.
(21) Ghizdavu, L.; Pierard, F.; Rickling, S.; Aury, S.; Surin, M.; Beljonne, D.; Lazzaroni, R.; Murat, P.; Defrancq, E.; Moucheron, C.; et al. Oxidizing Ru(II) Complexes as Irreversible and Specific Photo-Cross-Linking Agents of Oligonucleotide Duplexes. *Inorg. Chem.* **2009**, *48*, 10988−10994.
(22) Kalyanasundaram, K. Photophysics, Photochemistry and Solar Energy Conversion with Tris(Bipyridyl)Ruthenium(II) and Its Analogues. *Coord. Chem. Rev.* **1982**, *46*, 159−244.
(23) Estalayo-Adrián, S.; Garnir, K.; Moucheron, C. Perspectives of Ruthenium(Ii) Polyazaaromatic Photo-Oxidizing Complexes Photoreactive towards Tryptophan-Containing Peptides and Derivatives. *Chem. Commun.* **2018**, *54*, 322−337.
(24) Kulkarni, M. S.; Kumbhar, A. S.; Mohan, H.; Rao, B. S. M. Synthesis, Characterization and Redox Chemistry of Ru(II) Complexes of N-Methyl Pyridyl Quinoxaline. *Dalton Trans.* **2009**, 6185−6191.
(25) Nakada, A.; Koike, K.; Nakashima, T.; Morimoto, T.; Ishitani, O. Photocatalytic CO_2 Reduction to Formic Acid Using a Ru(II)−Re(I) Supramolecular Complex in an Aqueous Solution. *Inorg. Chem.* **2015**, *54*, 1800−1807.
(26) Atkins, A. J.; González, L. Trajectory Surface-Hopping Dynamics Including Intersystem Crossing in $[Ru(Bpy)_3]^{2+}$. *J. Phys. Chem. Lett.* **2017**, *8*, 3840−3845.
(27) Olivares-Amaya, R.; Hu, W.; Nakatani, N.; Sharma, S.; Yang, J.; Chan, G. K.-L. The Ab-Initio Density Matrix Renormalization Group in Practice. *J. Chem. Phys.* **2015**, *142*, 034102.
(28) Ho, J.; Kish, E.; Méndez-Hernández, D. D.; WongCarter, K.; Pillai, S.; Kodis, G.; Niklas, J.; Poluektov, O. G.; Gust, D.; Moore, T. A.; et al. Triplet-Triplet Energy Transfer in Artificial and Natural Photosynthetic Antennas. *Proc. Natl. Acad. Sci. U. S. A.* **2017**, *114*, E5513−E5521.
(29) Wrighton, M.; Markham, J. Quenching of the Luminescent State of Tris(2,2′-Bipyridine)Ruthenium(II) by Electronic Energy Transfer. *J. Phys. Chem.* **1973**, *77*, 3042−3044.
(30) Islangulov, R. R.; Castellano, F. N. Photochemical Upconversion: Anthracene Dimerization Sensitized to Visible Light by a Ru^{II} Chromophore. *Angew. Chem., Int. Ed.* **2006**, *45*, 5957−5959.
(31) Lu, Z.; Yoon, T. P. Visible Light Photocatalysis of [2 + 2] Styrene Cycloadditions via Energy Transfer. *Angew. Chem., Int. Ed.* **2012**, *51*, 10329−10332.
(32) Lin, Q.-Y.; Xu, X.-H.; Qing, F.-L. Chemo-, Regio-, and Stereoselective Trifluoromethylation of Styrenes via Visible Light-Driven Single-Electron Transfer (SET) and Triplet-Triplet Energy Transfer (TTET) Processes. *J. Org. Chem.* **2014**, *79*, 10434−10446.
(33) Strouse, G. F.; Anderson, P. A.; Schoonover, J. R.; Meyer, T. J.; Keene, F. R. Synthesis of Polypyridyl Complexes of Ruthenium(II) Containing Three Different Bidentate Ligands. *Inorg. Chem.* **1992**, *31*, 3004−3006.
(34) Kubeil, M.; Vernooij, R. R.; Kubeil, C.; Wood, B. R.; Graham, B.; Stephan, H.; Spiccia, L. Studies of Carbon Monoxide Release from Ruthenium(II) Bipyridine Carbonyl Complexes upon UV-Light Exposure. *Inorg. Chem.* **2017**, *56*, 5941−5952.
(35) Myahkostupov, M.; Castellano, F. N. Synthesis and Characterization of Tris(Heteroleptic) Ru(II) Complexes Bearing Styryl Subunits. *Inorg. Chem.* **2011**, *50*, 9714−9727.
(36) Gonçalves, R. S. B.; de Oliveira, A. B. V.; Sindra, H. C.; Archanjo, B. S.; Mendoza, M. E.; Carneiro, L. S. A.; Buarque, C. D.; Esteves, P. M. Heterogeneous Catalysis by Covalent Organic Frameworks (COF): Pd(OAc)2@COF-300 in Cross-Coupling Reactions. *ChemCatChem* **2016**, *8*, 743−750.
(37) Vyas, V. S.; Haase, F.; Stegbauer, L.; Savasci, G.; Podjaski, F.; Ochsenfeld, C.; Lotsch, B. V. A Tunable Azine Covalent Organic Framework Platform for Visible Light-Induced Hydrogen Generation. *Nat. Commun.* **2015**, *6*, 8508.
(38) Stegbauer, L.; Schwinghammer, K.; Lotsch, B. V. A Hydrazone-Based Covalent Organic Framework for Photocatalytic Hydrogen Production. *Chem. Sci.* **2014**, *5*, 2789−2793.
(39) Banerjee, T.; Lotsch, B. V. The Wetter the Better. *Nat. Chem.* **2018**, *10*, 1175−1177.
(40) Ding, S.-Y.; Wang, W. Covalent Organic Frameworks (COFs): From Design to Applications. *Chem. Soc. Rev.* **2013**, *42*, 548−568.
(41) Kuhn, P.; Antonietti, M.; Thomas, A. Porous, Covalent Triazine-Based Frameworks Prepared by Ionothermal Synthesis. *Angew. Chem., Int. Ed.* **2008**, *47*, 3450−3453.
(42) Feng, X.; Ding, X.; Jiang, D. Covalent Organic Frameworks. *Chem. Soc. Rev.* **2012**, *41*, 6010−6022.
(43) Stewart, D.; Antypov, D.; Dyer, M. S.; Pitcher, M. J.; Katsoulidis, A. P.; Chater, P. A.; Blanc, F.; Rosseinsky, M. J. Stable and Ordered Amide Frameworks Synthesised under Reversible Conditions Which Facilitate Error Checking. *Nat. Commun.* **2017**, *8*, 1102.

DOI: 10.1021/acs.jpca.9b05216
J. Phys. Chem. A 2019, 123, 6854−6867

(44) Halder, A.; Karak, S.; Addicoat, M.; Bera, S.; Chakraborty, A.; Kunjattu, S. H.; Pachfule, P.; Heine, T.; Banerjee, R. Ultrastable Imine-Based Covalent Organic Frameworks for Sulfuric Acid Recovery: An Effect of Interlayer Hydrogen Bonding. *Angew. Chem., Int. Ed.* **2018**, *57*, 5797−5802.
(45) Ding, S.-Y.; Gao, J.; Wang, Q.; Zhang, Y.; Song, W.-G.; Su, C.-Y.; Wang, W. Construction of Covalent Organic Framework for Catalysis: Pd/COF-LZU1 in Suzuki-Miyaura Coupling Reaction. *J. Am. Chem. Soc.* **2011**, *133*, 19816−19822.
(46) Waller, P. J.; Gándara, F.; Yaghi, O. M. Chemistry of Covalent Organic Frameworks. *Acc. Chem. Res.* **2015**, *48*, 3053−3063.
(47) Liu, M.; Guo, L.; Jin, S.; Tan, B. Covalent Triazine Frameworks: Synthesis and Applications. *J. Mater. Chem. A* **2019**, *7*, 5153−5172.
(48) Hug, S.; Stegbauer, L.; Oh, H.; Hirscher, M.; Lotsch, B. V. Nitrogen-Rich Covalent Triazine Frameworks as High-Performance Platforms for Selective Carbon Capture and Storage. *Chem. Mater.* **2015**, *27*, 8001−8010.
(49) Park, K.; Gunasekar, G. H.; Prakash, N.; Jung, K.-D.; Yoon, S. A Highly Efficient Heterogenized Iridium Complex for the Catalytic Hydrogenation of Carbon Dioxide to Formate. *ChemSusChem* **2015**, *8*, 3410−3413.
(50) Tahir, N.; Muniz-Miranda, F.; Everaert, J.; Tack, P.; Heugebaert, T.; Leus, K.; Vincze, L.; Stevens, C.; Van Speybroeck, V.; Van Der Voort, P. Immobilization of Ir(I) Complex on Covalent Triazine Frameworks for CAH Borylation Reactions: A Combined Experimental and Computational Study. *J. Catal.* **2019**, *371*, 135−143.
(51) Johnson, E. M.; Haiges, R.; Marinescu, S. C. Covalent-Organic Frameworks Composed of Rhenium Bipyridine and Metal Porphyrins: Designing Heterobimetallic Frameworks with Two Distinct Metal Sites. *ACS Appl. Mater. Interfaces* **2018**, *10*, 37919−37927.
(52) Aiyappa, H. B.; Thote, J.; Shinde, D. B.; Banerjee, R.; Kurungot, S. Cobalt-Modified Covalent Organic Framework as a Robust Water Oxidation Electrocatalyst. *Chem. Mater.* **2016**, *28*, 4375−4379.
(53) Popov, D. A.; Luna, J. M.; Orchanian, N. M.; Haiges, R.; Downes, C. A.; Marinescu, S. C. A 2,2′-Bipyridine-Containing Covalent Organic Framework Bearing Rhenium(i) Tricarbonyl Moieties for CO_2 Reduction. *Dalton Trans. Camb. Engl. 2003* **2018**, *47*, 17450−17460.
(54) Gunasekar, G. H.; Park, K.; Jeong, H.; Jung, K.-D.; Park, K.; Yoon, S. Molecular Rh(III) and Ir(III) Catalysts Immobilized on Bipyridine-Based Covalent Triazine Frameworks for the Hydrogenation of CO_2 to Formate. *Catalysts* **2018**, *8*, 295.
(55) Hendon, C. H.; Bonnefoy, J.; Quadrelli, E. A.; Canivet, J.; Chambers, M. B.; Rousse, G.; Walsh, A.; Fontecave, M.; Mellot-Draznieks, C. A Simple and Non-Destructive Method for Assessing the Incorporation of Bipyridine Dicarboxylates as Linkers within Metal-Organic Frameworks. *Chem. - Eur. J.* **2016**, *22*, 3713−3718.
(56) Maza, W. A.; Morris, A. J. Photophysical Characterization of a Ruthenium(II) Tris(2,2′-Bipyridine)-Doped Zirconium UiO-67 Metal−Organic Framework. *J. Phys. Chem. C* **2014**, *118*, 8803−8817.
(57) Hou, C.-C.; Li, T.-T.; Cao, S.; Chen, Y.; Fu, W.-F. Incorporation of a $[Ru(Dcbpy)(Bpy)_2]^{2+}$ Photosensitizer and a $Pt(Dcbpy)Cl_2$ Catalyst into Metal−Organic Frameworks for Photocatalytic Hydrogen Evolution from Aqueous Solution. *J. Mater. Chem. A* **2015**, *3*, 10386−10394.
(58) Yang, D.; Odoh, S. O.; Wang, T. C.; Farha, O. K.; Hupp, J. T.; Cramer, C. J.; Gagliardi, L.; Gates, B. C. Metal-Organic Framework Nodes as Nearly Ideal Supports for Molecular Catalysts: NU-1000- and UiO-66-Supported Iridium Complexes. *J. Am. Chem. Soc.* **2015**, *137*, 7391−7396.
(59) Wang, C.; Xie, Z.; deKrafft, K. E.; Lin, W. Doping Metal−Organic Frameworks for Water Oxidation, Carbon Dioxide Reduction, and Organic Photocatalysis. *J. Am. Chem. Soc.* **2011**, *133*, 13445−13454.
(60) Burtch, N. C.; Jasuja, H.; Walton, K. S. Water Stability and Adsorption in Metal-Organic Frameworks. *Chem. Rev.* **2014**, *114*, 10575−10612.
(61) Leus, K.; Bogaerts, T.; De Decker, J.; Depauw, H.; Hendrickx, K.; Vrielinck, H.; Van Speybroeck, V.; Van Der Voort, P. Systematic Study of the Chemical and Hydrothermal Stability of Selected "Stable" Metal Organic Frameworks. *Microporous Mesoporous Mater.* **2016**, *226*, 110−116.
(62) Daniel, C. Photochemistry and Photophysics of Transition Metal Complexes: Quantum Chemistry. *Coord. Chem. Rev.* **2015**, *282*−*283*, 19−32.
(63) De Vos, A.; Lejaeghere, K.; Muniz-Miranda, F.; Stevens, C. V.; Van der Voort, P.; Van Speybroeck, V. Electronic Properties of Heterogenized Ru(II) Polypyridyl Photoredox Complexes on Covalent Triazine Frameworks. *J. Mater. Chem. A* **2019**, *7*, 8433−8442.
(64) Jacquemin, D.; Perpète, E. A.; Vydrov, O. A.; Scuseria, G. E.; Adamo, C. Assessment of Long-Range Corrected Functionals Performance for n→pi* Transitions in Organic Dyes. *J. Chem. Phys.* **2007**, *127*, 094102.
(65) Frisch, M. J.; Trucks, G. W.; Schlegel, H. B.; Scuseria, G. E.; Robb, M. A.; Cheeseman, J. R.; Scalmani, G.; Barone, V.; Petersson, G. A.; Nakatsuj, H.; et al. *Gaussian 16*, Revision B.01; Gaussian, Inc.: Wallingford, CT, 2016.
(66) Runge, E.; Gross, E. K. U. Density-Functional Theory for Time-Dependent Systems. *Phys. Rev. Lett.* **1984**, *52*, 997−1000.
(67) Casida, M. E.; Jamorski, C.; Casida, K. C.; Salahub, D. R. Molecular Excitation Energies to High-Lying Bound States from Time-Dependent Density-Functional Response Theory: Characterization and Correction of the Time-Dependent Local Density Approximation Ionization Threshold. *J. Chem. Phys.* **1998**, *108*, 4439−4449.
(68) Perdew, J. P.; Ruzsinszky, A.; Tao, J.; Staroverov, V. N.; Scuseria, G. E.; Csonka, G. I. Prescription for the Design and Selection of Density Functional Approximations: More Constraint Satisfaction with Fewer Fits. *J. Chem. Phys.* **2005**, *123*, 062201.
(69) Perdew, J. P.; Burke, K.; Ernzerhof, M. Generalized Gradient Approximation Made Simple. *Phys. Rev. Lett.* **1996**, *77*, 3865−3868.
(70) Lee, C.; Yang, W.; Parr, R. G. Development of the Colle-Salvetti Correlation-Energy Formula into a Functional of the Electron Density. *Phys. Rev. B: Condens. Matter Mater. Phys.* **1988**, *37*, 785−789.
(71) Becke, A. D. Density-functional Thermochemistry. III. The Role of Exact Exchange. *J. Chem. Phys.* **1993**, *98*, 5648−5652.
(72) Yanai, T.; Tew, D. P.; Handy, N. C. A New Hybrid Exchange−Correlation Functional Using the Coulomb-Attenuating Method (CAM-B3LYP). *Chem. Phys. Lett.* **2004**, *393*, 51−57.
(73) Zhao, Y.; Truhlar, D. G. The M06 Suite of Density Functionals for Main Group Thermochemistry, Thermochemical Kinetics, Noncovalent Interactions, Excited States, and Transition Elements: Two New Functionals and Systematic Testing of Four M06-Class Functionals and 12 Other Functionals. *Theor. Chem. Acc.* **2008**, *120*, 215−241.
(74) Adamo, C.; Jacquemin, D. The Calculations of Excited-State Properties with Time-Dependent Density Functional Theory. *Chem. Soc. Rev.* **2013**, *42*, 845−856.
(75) Tomasi, J.; Mennucci, B.; Cammi, R. Quantum Mechanical Continuum Solvation Models. *Chem. Rev.* **2005**, *105*, 2999−3094.
(76) Word, T. A.; Whittington, C. L.; Karolak, A.; Kemp, M. T.; Woodcock, H. L.; van der Vaart, A.; Larsen, R. W. Photoacoustic Calorimetry Study of Ligand Photorelease from the Ru(II)Bis(2,2′-Bipyridine)(6,6′-Dimethyl-2,2′-Bipyridine) Complex in Aqueous Solution. *Chem. Phys. Lett.* **2015**, *619*, 214−218.
(77) Baerends, E. J.; Gritsenko, O. V.; van Meer, R. The Kohn−Sham Gap, the Fundamental Gap and the Optical Gap: The Physical Meaning of Occupied and Virtual Kohn−Sham Orbital Energies. *Phys. Chem. Chem. Phys.* **2013**, *15*, 16408−16425.
(78) Kronik, L.; Stein, T.; Refaely-Abramson, S.; Baer, R. Excitation Gaps of Finite-Sized Systems from Optimally Tuned Range-Separated Hybrid Functionals. *J. Chem. Theory Comput.* **2012**, *8*, 1515−1531.
(79) Muniz-Miranda, F.; Menziani, M. C.; Pedone, A. DFT and TD-DFT Assessment of the Structural and Optoelectronic Properties of

DOI: 10.1021/acs.jpca.9b05216
J. Phys. Chem. A 2019, 123, 6854−6867

an Organic−Ag_{14} Nanocluster. *J. Phys. Chem. A* **2015**, *119*, 5088−5098.
(80) Muniz-Miranda, F.; Menziani, M. C.; Pedone, A. Assessment of Exchange-Correlation Functionals in Reproducing the Structure and Optical Gap of Organic-Protected Gold Nanoclusters. *J. Phys. Chem. C* **2014**, *118*, 7532−7544.
(81) De Meyer, T.; Steyaert, I.; Hemelsoet, K.; Hoogenboom, R.; Van Speybroeck, V.; De Clerck, K. Halochromic Properties of Sulfonphthaleine Dyes in a Textile Environment: The Influence of Substituents. *Dyes Pigm.* **2016**, *124*, 249−257.
(82) Hendrickx, K.; Vanpoucke, D. E. P.; Leus, K.; Lejaeghere, K.; Van Yperen-De Deyne, A.; Van Speybroeck, V.; Van Der Voort, P.; Hemelsoet, K. Understanding Intrinsic Light Absorption Properties of UiO-66 Frameworks: A Combined Theoretical and Experimental Study. *Inorg. Chem.* **2015**, *54*, 10701−10710.
(83) Hay, P. J.; Wadt, W. R. *Ab Initio* Effective Core Potentials for Molecular Calculations. Potentials for the Transition Metal Atoms Sc to Hg. *J. Chem. Phys.* **1985**, *82*, 270−283.
(84) Petit, L.; Maldivi, P.; Adamo, C. Predictions of Optical Excitations in Transition-Metal Complexes with Time Dependent-Density Functional Theory: Influence of Basis Sets. *J. Chem. Theory Comput.* **2005**, *1*, 953−962.
(85) Laurent, A. D.; Jacquemin, D. TD-DFT Benchmarks: A Review. *Int. J. Quantum Chem.* **2013**, *113*, 2019−2039.
(86) Jacquemin, D.; Perpète, E. A.; Ciofini, I.; Adamo, C.; Valero, R.; Zhao, Y.; Truhlar, D. G. On the Performances of the M06 Family of Density Functionals for Electronic Excitation Energies. *J. Chem. Theory Comput.* **2010**, *6*, 2071−2085.
(87) Atkins, A. J.; Talotta, F.; Freitag, L.; Boggio-Pasqua, M.; González, L. Assessing Excited State Energy Gaps with Time-Dependent Density Functional Theory on Ru(II) Complexes. *J. Chem. Theory Comput.* **2017**, *13*, 4123−4145.
(88) Bird, C. W. Heteroaromaticity, 5, a Unified Aromaticity Index. *Tetrahedron* **1992**, *48*, 335−340.
(89) Bird, C. W. The Relationship of Classical and Magnetic Criteria of Aromaticity. *Tetrahedron* **1996**, *52*, 9945−9952.
(90) Wiberg, K. B.; Rablen, P. R. Comparison of Atomic Charges Derived via Different Procedures. *J. Comput. Chem.* **1993**, *14*, 1504−1518.
(91) Innocenzi, P.; Kozuka, H.; Yoko, T. Fluorescence Properties of the $Ru(Bpy)_3^{2+}$ Complex Incorporated in Sol−Gel-Derived Silica Coating Films. *J. Phys. Chem. B* **1997**, *101*, 2285−2291.
(92) Juris, A.; Balzani, V.; Belser, P.; von Zelewsky, A. Characterization of the Excited State Properties of Some New Photosensitizers of the Ruthenium (Polypyridine) Family. *Helv. Chim. Acta* **1981**, *64*, 2175−2182.
(93) Alary, F.; Boggio-Pasqua, M.; Heully, J. L.; Marsden, C. J.; Vicendo, P. Theoretical Characterization of the Lowest Triplet Excited States of the Tris-(1,4,5,8-Tetraazaphenanthrene) Ruthenium Dication Complex. *Inorg. Chem.* **2008**, *47*, 5259−5266.
(94) Alary, F.; Heully, J.-L.; Bijeire, L.; Vicendo, P. Is the ^{3}MLCT the Only Photoreactive State of Polypyridyl Complexes? *Inorg. Chem.* **2007**, *46*, 3154−3165.
(95) Mukuta, T.; Tanaka, S.; Inagaki, A.; Koshihara, S. Y.; Onda, K. Direct Observation of the Triplet Metal-Centered State in $[Ru(bpy)_3]^{2+}$ Using Time-Resolved Infrared Spectroscopy. *ChemistrySelect* **2016**, *1*, 2802−2807.
(96) Alcover-Fortuny, G.; Wu, J.; Caballol, R.; de Graaf, C. Quantum Chemical Study of the Interligand Electron Transfer in Ru Polypyridyl Complexes. *J. Phys. Chem. A* **2018**, *122*, 1114−1123.
(97) Lord, R. L.; Allard, M. M.; Thomas, R. A.; Odongo, O. S.; Schlegel, H. B.; Chen, Y.-J.; Endicott, J. F. Computational Modeling of the Triplet Metal-to-Ligand Charge-Transfer Excited-State Structures of Mono-Bipyridine−Ruthenium(II) Complexes and Comparisons to Their 77 K Emission Band Shapes. *Inorg. Chem.* **2013**, *52*, 1185−1198.
(98) Österman, T.; Abrahamsson, M.; Becker, H.-C.; Hammarström, L.; Persson, P. Influence of Triplet State Multidimensionality on Excited State Lifetimes of Bis-Tridentate RuII Complexes: A Computational Study. *J. Phys. Chem. A* **2012**, *116*, 1041−1050.
(99) Dreuw, A.; Head-Gordon, M. Failure of Time-Dependent Density Functional Theory for Long-Range Charge-Transfer Excited States: The Zincbacteriochlorin−Bacteriochlorin and Bacteriochlorophyll−Spheroidene Complexes. *J. Am. Chem. Soc.* **2004**, *126*, 4007−4016.
(100) Kobayashi, R.; Amos, R. Erratum to 'The Application of CAM-B3LYP to the Charge-Transfer Band Problem of the Zincbacteriochlorin−Bacteriochlorin Complex' [Chem. Phys. Lett. 420 (2006) 106−109]. *Chem. Phys. Lett.* **2006**, *424*, 225.
(101) Campetella, M.; Maschietto, F.; Frisch, M. J.; Scalmani, G.; Ciofini, I.; Adamo, C. Charge Transfer Excitations in TDDFT: A Ghost-Hunter Index. *J. Comput. Chem.* **2017**, *38*, 2151−2156.
(102) Zhang, L.; Wang, W.; Sun, S.; Jiang, D. Near-Infrared Light Photocatalysis with Metallic/Semiconducting H_xWO_3/WO_3 Nanoheterostructure in Situ Formed in Mesoporous Template. *Appl. Catal., B* **2015**, *168*, 9−13.
(103) Liu, W.-X.; Zhu, X.-L.; Liu, S.-Q.; Gu, Q.-Q.; Meng, Z.-D. Near-Infrared-Driven Selective Photocatalytic Removal of Ammonia Based on Valence Band Recognition of an α-MnO_2 /N-Doped Graphene Hybrid Catalyst. *ACS Omega* **2018**, *3*, 5537−5546.

DOI: 10.1021/acs.jpca.9b05216
J. Phys. Chem. A 2019, 123, 6854−6867

Paper II

Structural and Photophysical Properties of Various Polypyridyl Ligands: A Combined Experimental and Computational Study

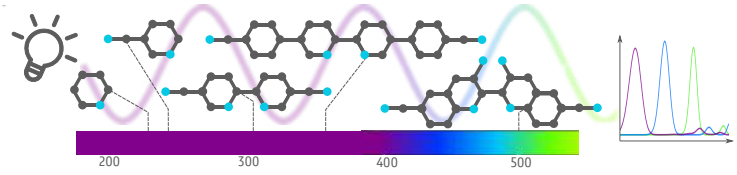

L. De Bruecker, J. Everaert, P. Van Der Voort, C. V. Stevens, M. Waroquier, and V. Van Speybroeck

ChemPhysChem, **2020**, *21* (2489-2505)

L. De Bruecker performed the research and wrote the initial draft of the manuscript.

Chemistry Europe
European Chemical Societies Publishing

Structural and Photophysical Properties of Various Polypyridyl Ligands: A Combined Experimental and Computational Study

Liesbeth De Bruecker,[a] Jonas Everaert,[b] Pascal Van Der Voort,[c] Christian V. Stevens,[b] Michel Waroquier,[a] and Veronique Van Speybroeck*[a]

Covalent triazine frameworks (CTFs) with polypyridyl ligands are very promising supports to anchor photocatalytic complexes. Herein, we investigate the photophysical properties of a series of ligands which vary by the extent of the aromatic system, the nitrogen content and their topologies to aid in selecting interesting building blocks for CTFs. Interestingly, some linkers have a rotational degree of freedom, allowing both a trans and cis structure, where only the latter allows anchoring. Therefore, the influence of the dihedral angle on the UV-Vis spectrum is studied. The photophysical properties are investigated by a combined computational and experimental study. Theoretically, both static and molecular dynamics simulations are performed to deduce ground- and excited state properties based on density functional theory (DFT) and time-dependent DFT. The position of the main absorption peak shifts towards higher wavelengths for an increased size of the π-system and a higher π-electron deficiency. We found that the position of the main absorption peak among the different ligands studied in this work can amount to 271 nm; which has a significant impact on the photophysical properties of the ligands. This broad range of shifts allows modulation of the electronic structure by varying the ligands and may help in a rational design of efficient photocatalysts.

1. Introduction

One of the major challenges of today's society is how to provide materials and chemicals in a more sustainable and energy efficient way. Still today most of our energy resources originate from fossil fuels.[3] Sunlight is an abundantly available energy source and may provide sustainable opportunities for activating chemical reactions based on photocatalysis.[6,70,94,41,84,69,47,75] However, most of the currently used active photocatalytic homogeneous catalysts[69,61] necessitate an environmentally unfriendly cycle to remove the catalyst from the products. In this respect, it is important to develop recyclable and reusable heterogeneous photocatalysts, which can be achieved by anchoring the photocatalytic complexes on a porous framework. The step to remove the catalyst can be avoided in this way and, as such, heterogeneous photocatalysis can serve as an environmentally cleaner alternative.[76,71,85,88]

Covalent organic frameworks (COFs) and covalent triazine frameworks (CTFs) are a relatively new class of materials with a large potential to be used as support materials for heterogeneous catalysis due to their high surface area[21] and tunability because of the availability of various building blocks.[53] Compared to other supports which have been explored for anchoring photocatalytic complexes such as metal organic frameworks,[35,38] they are more stable.[54,37,96] Interestingly, they also display (photo)catalytic activity in their pristine form[91,78,5] without even anchoring an active complex, and in this sense it is important to understand the electronic properties of the various building blocks of the CTF framework. A special branch of COFs and CTFs are those that contain polypyridyl ligands (Figure 1), as they allow for a stable secured anchoring of active complexes to the solid support.[90,58] In principle, a large variety of ligands can be used, creating a versatile platform to engineer supports for anchoring various active complexes. For the CTF-type materials, several N-heterocyclic systems have been synthesized, including (bi)pyridine,[65,40,39,66,82,44,4,68,32] luditine[39] and pyrimidine[39] systems. We recently studied the anchoring of a Ru^{2+}, octahedrally chelated by three bidentate polypyridyl ligands, on a biphenyl-based CTF where some of the biphenyl linkers are replaced with polypyridyl ones.[58,90] Furthermore, the anchoring of Ir(I) on a CTF containing bipyridine has been shown to be very promising for C–H borylation[82] and the post-metalated hexaazatrinaphthylene based CTF with a $Cu(OAc)_2$ complex can be utilized as an efficient heterogeneous catalyst

[a] L. De Bruecker, Prof. M. Waroquier, Prof. V. Van Speybroeck
Center for Molecular Modeling (CMM), Ghent University, Technologiepark 46, 9052 Zwijnaarde, Belgium
E-mail: Veronique.VanSpeybroeck@UGent.be
[b] J. Everaert, Prof. C. V. Stevens
Research Group SynBioC, Department of Green Chemistry and Technology, Faculty of Bioscience Engineering, Ghent University, Coupure Links 653, 9000 Ghent, Belgium
[c] Prof. P. Van Der Voort
Center for Ordered Materials, Organometallics and Catalysis (COMOC), Department of Inorganic and Physical Chemistry, Ghent University, Krijgslaan 281 (S3), 9000 Gent, Belgium

Supporting information for this article is available on the WWW under https://doi.org/10.1002/cphc.202000592

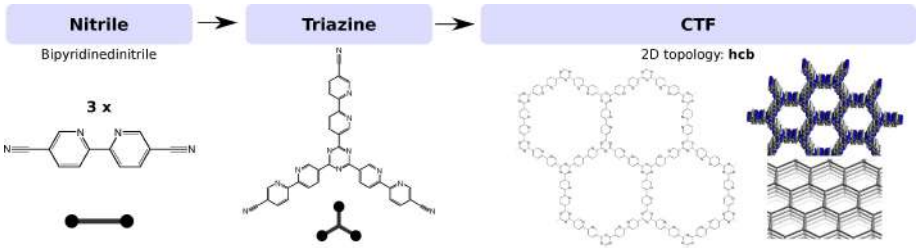

Figure 1. Synthesis of CTFs via cyclic trimerization of aromatic polypyridyls.

for the Henry reaction.[83] A review on this topic can be found in Ref. [81].

Driven by this application oriented goal, we ought it necessary to perform an in-depth investigation of the fundamental structural and photophysical properties of a series of polypyridyl ligands, which can eventually be used in a CTF scaffold. The considered nitrogen containing ligands are shown in Figure 2. The box indicates the linkers which are experimentally characterized in this work. Note that most of the linkers are terminated by cyano groups to mimic the experimental conditions in which a CTF is synthesized by trimerization of linkers terminated by such groups as shown in Figure 1.[40] To make a proper comparison with literature data we also examined the pristine pyridine and bipyridine linker, which are

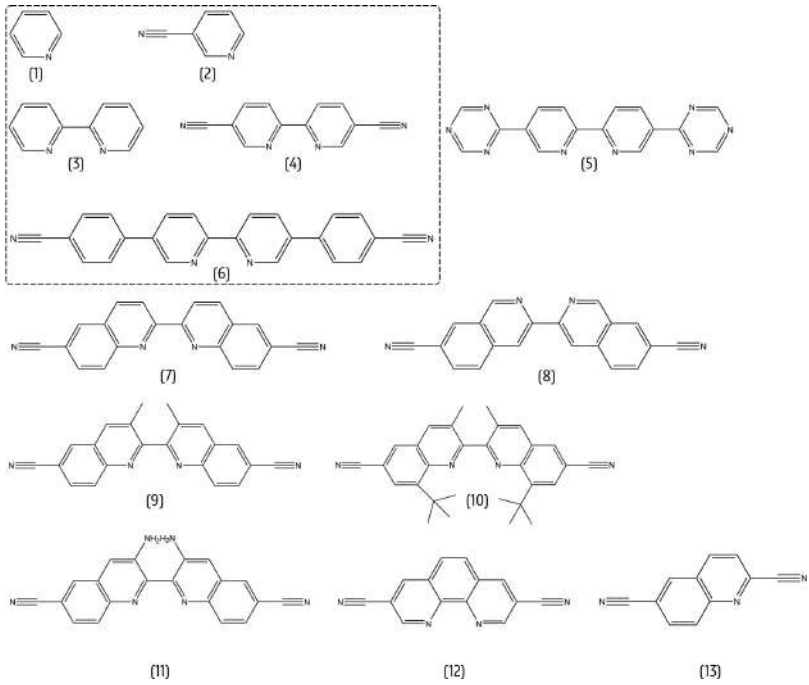

Figure 2. Polypyridyl ligands studied in this work: (1): pyridine (2): pyridine-3-carbonitrile (nicotinonitrile) (3): 2,2′-bipyridine (4): 2,2′-bipyridine-5,5′-dicarbonitrile (5): 5,5′-bis(4-cyanophenyl)-2,2′-bipyridine (6): 5,5′-bis(4-cyanophenyl)-2,2′-bipyridine (7): [2,2′-biquinoline]-6,6′-dicarbonitrile (8): [3,3′-biisoquinoline]-7,7′-dicarbonitrile (9): 3,3′-dimethyl-[2,2′-biquinoline]-6,6′-dicarbonitrile (10): 8,8′-di-tert-butyl-3,3′-dimethyl-[2,2′-biquinoline]-6,6′-dicarbonitrile (11): 3,3′-diamino-[2,2′-biquinoline]-6,6′-dicarbonitrile (12): phenantroline-5,5′-dicarbonitrile (13): quinoline-2,6-dicarbonitrile. The box indicates the linkers which are experimentally characterized in this work.

terminated by hydrogen atoms. For the bipyridine linker, we also investigated the influence of the termination group, which is the reason why we also included linker (5) terminated with triazine groups. We performed a combined theoretical and experimental study. Ligands (4), (6) and (13) were synthesized and together with ligands (1)–(3), their photophysical properties were characterized by means of UV-Vis spectroscopy. From a theoretical point of view, the structural and photophysical properties of all ligands were studied using both static and molecular dynamics (MD) based density functional theory (DFT) methods. We especially focused on the possible occurrence of both cis- and trans conformers, where the nitrogen atoms are either on the same or on opposite sides of two pyridine rings. The trans structure is energetically the most stable, but for anchoring of metal containing complexes the cis structure is preferred.[16,22,46] Furthermore we studied the influence of the dihedral angle on the UV-Vis spectrum calculated by means of time-dependent density functional theory (TDDFT) and performed a fundamental analysis of the most important electronic excitations. This theoretical study provides insight in the characterization of the excited states of the linkers and can in this way complement the experimental results. Earlier work showed that within a COF scaffold, the principle of orthogonal electronic structure engineering is valid, *i.e.*, the overall electronic structure can be tuned by independently varying the constituents.[90] This has been shown for the catalytic complex, but also extends to the combined complex-CTF catalyst. In this sense, a detailed insight is provided into how the electronic structure can be modulated by varying the ligands. Overall this study should give a guidance to design nitrogen containing CTFs and more in particular how the specific linker topology influences the optical properties.

Computational details

In this work, the theoretical approach is based on both static and molecular dynamics simulations. All static calculations were performed with the Gaussian 16 software.[24] Geometrical optimizations and rotational scans were calculated using density functional theory (DFT). We checked that all computed internal normal modes of the optimized structures show positive frequencies, ensuring that the geometries represent minima of the ground state potential energy surface. Excited states were investigated adopting the time-dependent density functional theory (TDDFT) scheme,[72] within the linear-response approach as developed by Casida.[14] Electronic excitations are characterized by both the energies and oscillator strengths,[2] which correspond to peak positions and intensities of the transitions respectively. We convoluted the simulated spectra with a Gaussian envelope with a half-width at half height of 0.1 eV to simulate the Franck-Condon width of spectra. Solvent effects have been taken into account in the static and TDDFT calculations using a polarizable continuum model (PCM).[87] For the pyridine molecule, expressed by ligand (1), different functionals and basis sets have already been tested in literature,[23,64] revealing that B3LYP/6-31 + G* yields good results. In all our calculations, we used the larger 6–31 + +G** basis set. In accordance with what has been reported in literature, there is still a discrepancy between theory and experiment. No DFT level of theory is able to predict a correct state ordering of the low-energy excited states of pyridine, as observed in experiment.[8,92,30] Besides, we have used several functionals coming from different rungs on Jacob's ladder[67] to test their performance in reproducing the structural properties of ligand (4): PBE[1] and BLYP[50,57] based on Generalized Gradient Approximation (GGA), B3LYP[7,51] as hybrid functional, the long-range corrected CAM-B3LYP,[95] ωB97X-D,[15] LC-ωHPBE,[34] and the metahybrid M06[98] and TPSSh.[77,86] These functionals will also be used to compute the electronic excitations of bipyridine. Furthermore, we also studied the dependence on the choice of basis set for the calculation of the excited states.

The ab initio molecular dynamics (MD) simulations have been carried out with the CP2K software package (CP2K 3.0)[89] at the BLYP level of theory. The time step for integrating the equations of motion was set at 0.5 fs and the simulations were performed in the NVT ensemble at a temperature of 300 K. Grimme D3 dispersion corrections were included.[31]

Explicit information about the experimental details can be found in the Supporting Information.

2. Results and Discussion

We start with analyzing the experimental UV-Vis spectra of linkers (1)–(4) and (6) and explore the influence of extending the π-system and increasing the π-electron deficiency. After this we proceed with a computational study. As all linkers shown in Figure 2 are composed of one or more pyridine rings, we first investigate the ground and excited state properties of a pyridine molecule alone (ligand (1)), before exploring the more complex linkers. By comparing linkers (1) and (2), we examine the effect of adding a cyano group. Subsequently, we investigate the structural properties of linkers (3)–(8) which possess an additional rotational degree of freedom around the central axis. Biphenyl, being the most simple poly-cyclic aromatic hydrocarbon with this internal rotation, has been extensively studied in literature.[26,29,80] As the lone electron pairs of the nitrogen atoms will have a significant effect on the rotational profile of the energy, we preferred to take ligand (4) as study case for a thorough analysis as this compound is more representative for the polypyridyl linkers (3)–(10). At the same time, the influence of the internal rotation on the photophysical properties is investigated.

Complementary to a static approach, the sensitivity of the UV-Vis spectra to structural deformations has also been explored via a series of molecular dynamics (MD) calculations. This multi-step procedure has been introduced earlier by some of us.[36,20] Finally, we investigate the UV-Vis spectra of the other ligands which contain a varying amount of nitrogen atoms and which show different topologies of the aromatic rings in order to select the most promising structure for the construction of CTF scaffolds.

2.1. Experimental UV-Vis Spectra

The experimental spectra of linkers (1)–(4) and (6) are shown in Figure 3 along with the energies of the main absorption peaks. Two effects are studied. First, we analyze the influence of extending the π-system, which is achieved when more aromatic

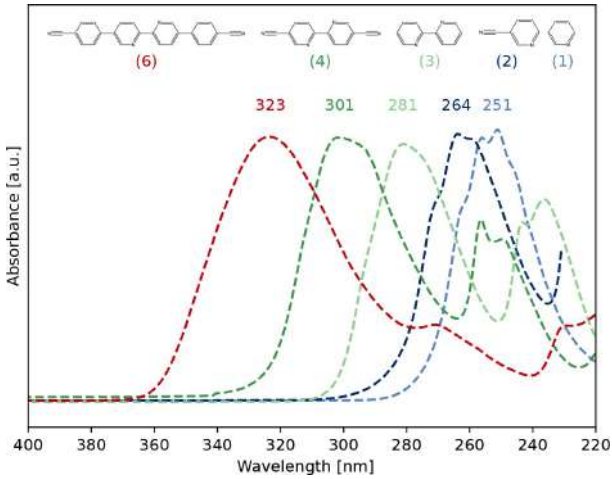

Figure 3. Experimental UV-Vis spectra of ligands (1)–(4) and (6) in acetonitrile as solvent. The energies of the main absorption peaks are indicated.

rings are added. Therefore, we compare linkers (1) and (3) on the one hand, and linkers (4) and (6) on the other hand. In both cases, the experiment predicts a shift towards larger wavelengths of 30 and 22 nm, respectively. This is indicated with green arrows in Figure 4. The experimental values are shown along with the computational results between parentheses, which will be discussed in Sections 3.2 and 3.4. The system is π-electron deficient due to the presence of nitrogen atoms as their free electron pairs are not part of the aromatic system and as a result, the linker will accept electrons more easily. Therefore, we also investigate the effect of increasing the π-electron deficiency. This can be done by adding electron-withdrawing groups such as the cyano group, CN^-. Its influence can be quantified by comparing the spectra of linkers (1) and (3) with those of linkers (2) and (4) respectively. In both cases, we observe a shift towards larger wavelengths: 13 nm and 20 nm, respectively, as shown in light blue in Figure 4. These shifts are in agreement with Ref. [90], in which it has been shown that the band gap decreases when the nitrogen content of the CTF increases. Finally, by comparing linkers (2) and (4), we study the combined effect of increasing the size of the π-system and π-electron deficiency. We observe a large shift of 37 nm towards larger wavelengths. This is indicated in dark blue in Figure 4. The computational results will be discussed later.

3.2. Ground State and Excited State Properties of Pyridine and Nicotinonitrile

We will now proceed with the theoretical study. We start with pyridine as the smallest species of the N-hetero-aromatic family (ligand (1)) and which is regarded as reference system to tackle the more complex linkers. Several experimental studies[92,30,8] are devoted to pyridine and due to its small size and C_{2v} symmetry very accurate methods can be used to investigate this system computationally.[92,62,11,93,74,73,43,13,23] An extended benchmark study of the excitation energies in the pyridine ring has been done by Egidi et al..[23] This computational study uses a large set

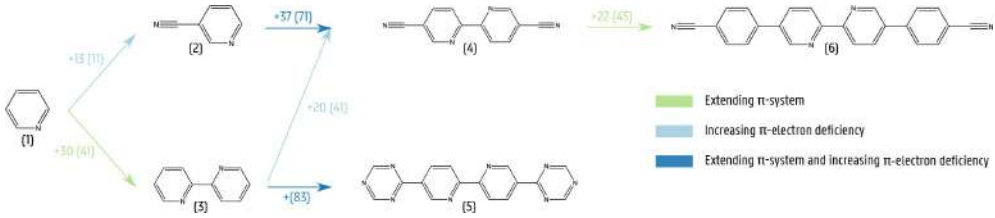

Figure 4. Influence of extending the π-system and increasing the π-electron deficiency of the linkers on the position of the main absorption peak. Shifts are given in nm. We report experimental results along with the computational findings between parentheses. The computational results are obtained at the B3LYP/6-31++G** level of theory with acetonitrile as solvent and are discussed in Sections 3.2 and 3.4.

of multi-reference, coupled cluster singles and doubles (CCSD), and DFT methods. Contrary to the wave function based methodologies, TDDFT fails to reproduce the excited state ordering as observed in experiment,[92,30,8] for all tested functionals (B3LYP, CAM-B3LYP and M06-2X). The same failure of TDDFT has also been noticed for biphenyl.[26] It was found that PBE1PBE calculations significantly underestimated the excitation energy of the 1^1B_1 state because the dynamical and non-dynamical correlations are not considered appropriately. Indeed, it is known that TDDFT sometimes underestimates the energy differences of low-lying excited states of conjugated systems with several degenerate states such as porphyrines and fullerenes.[25,27,28]

In the following, we focus on the first three singlet excitations in pyridine, resulting from B3LYP/6-31++G** calculations. As the ground state is a singlet, only singlet excitations can have a non-zero oscillator strength. This is due to the spin selection rule, which states that no change in the spin quantum number can occur.[33] This rule is strongly obeyed and can only be relaxed by effects that make the spin a poor quantum number like spin-orbit coupling. The molecular orbitals (MOs) involved in the first three singlet transitions are shown in Figure 5. The three highest occupied MOs (HOMO, HOMO-1, and HOMO-2) are displayed on the left in descending order and the unoccupied orbitals (LUMO and LUMO+1) are displayed on the right. As their ordering can easily be switched by changing the level of theory or by extending the π-system, we therefore prefer to specify the levels with their true nature, being n, π_{AQ} or π_Q. The HOMO is a non-bonding orbital, n, whereas all others are π-orbitals, of which two quinoid (Q) and two antiquinoid (AQ) structures. This nomenclature is borrowed from the Jahn-Teller distorted benzene radical anion.[18] Placing an electron in a π_Q* orbital causes a shortening of the lateral bonds, while placing it in a π_{AQ}* orbital results in an elongation of those bonds. The transition with the lowest excitation energy involves an electron transfer from the n-orbital to π_Q* and is indicated with a blue arrow in Figure 5. For the second transition, presented in black, an n$\rightarrow\pi_{AQ}$* excitation takes place. This transition is dark, *i.e.*, the oscillator strength, f, = 0. The third transition, indicated in green, is the brightest one with f = 0.0382 and corresponds to the highest peak in the UV-Vis spectrum. It has two contributions, namely $\pi_{AQ} \rightarrow \pi_{AQ}$* and $\pi_Q \rightarrow \pi_Q$*. In the case when the transition has multiple non-negligible contributions, the strongest components are taken up in the figure accompanied by their corresponding amplitude in square brackets. It implies that the 229 nm peak mainly consists of a strong $\pi_Q \rightarrow \pi_Q$* transition with an amplitude of 0.64 and a less significant $\pi_{AQ} \rightarrow \pi_{AQ}$* transition with an amplitude of 0.29. This mix of local transitions in the dominant excitation peak is also reported by Egidi et al.[23] The darkness of the second transition at 234 nm can be explained based on symmetry rules. As shown in the Supporting Information, the symmetry of the excited state must equal the symmetry of one of the components of the dipole moment operator. Pyridine belongs to the C_{2v} symmetry point group and the orbitals shown in Figure 5 have B_1, A_2, A_1, B_1, and A_2 symmetry in order

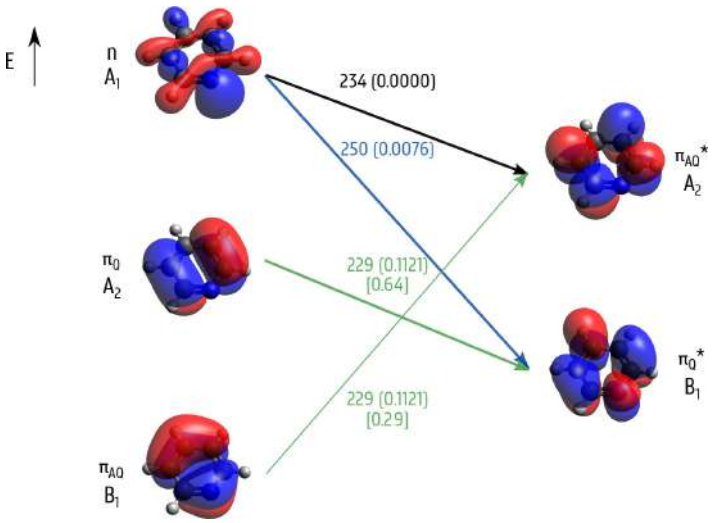

Figure 5. Visualization of the important orbitals of pyridine (1) along with their symmetry labels. The arrows indicate the most dominant contributions of the first three singlet excitations, characterized by the excitation energy in nm, oscillator strength, *f*, between brackets, and amplitude in square brackets if more contributions are reported for a specific excitation. The occupied MOs in the left represent respectively the HOMO, HOMO-1 and HOMO-2 in descending order. The unoccupied MOs in the right represent respectively the LUMO+1 and LUMO. This labeling is conform the binding energies taken up in Table S1. The transition with the lowest excitation energy is indicated with a blue arrow, the dark transition is presented in black and the brightest transition is indicated in green. Calculations carried out at the B3LYP/6-31++G** level of theory and with acetonitrile as solvent.

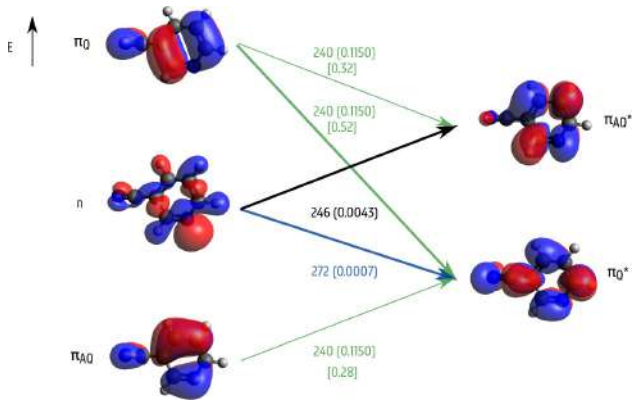

Figure 6. Visualization of the important orbitals of linker (2). The arrows indicate the most dominant contributions of the first three singlet excitations, characterized by the excitation energy in nm, oscillator strength, *f*, between parentheses, and amplitude in square brackets if more contributions are reported for a specific excitation. The occupied MOs in the left represent respectively the HOMO, HOMO-1 and HOMO-2 in descending order. The unoccupied MOs in the right represent respectively the LUMO + 1 and LUMO. This labeling is conform the binding energies taken up in Table S1. The transition with the lowest excitation energy is indicated with a blue arrow, the dark transition is presented in black and the brightest transition is indicated in green. Calculations carried out at the B3LYP/6-31 + + G** level of theory and with acetonitrile as solvent.

of ascending energy. The dipole moment operator components have the B_1, B_2, and A_1 symmetries.[33] Therefore, the second transition is forbidden as the product of A_1 and A_2 is A_2. Relaxation of this rule is possible by vibronic coupling, which we will not study in this paper.

The binding energies of some relevant MOs are reported for the series of ligands (1)–(6) in Table S1 of the Supporting Information. The nature of these orbitals is also given, and it is indicated how the binding energy of these orbitals with a certain nature changes in terms of the specific structure of the ligands. We can now easily investigate the effect of adding a cyano group and thus increasing the π-electron deficiency of the system, by comparing the UV-Vis spectra of ligands (1) and (2). The isosurfaces of the orbitals involved in the most dominant contributions of the first three singlet excitations of linker (2) are shown in Figure 6 and can be compared to those of linker (1) shown in Figure 5. We notice that the n-orbital is now lower in energy than π_Q, although the difference is very small (see Table S1), and that it is no longer figuring as HOMO. Furthermore, the orbitals of $\pi_Q{}^*$ and $\pi_{AQ}{}^*$ are rotated clockwise over one atom when CN^- is added. Based on the nature of the orbitals, we notice that the characteristics of the first three excitations of ligand (2) are the same as in pyridine. The only difference is the smaller contribution of the main absorption peak at 240 nm, but the largest contribution is identical. Furthermore, the second peak at 246 nm is not dark, in contrary to what has been observed in pyridine. This is because the symmetry group is reduced, namely from C_{2v} to C_s, and therefore there are no symmetry forbidden transitions. Indeed, in the C_s symmetry group, the dipole moment operator components have *A′* and *A″* symmetry, and thus every transition is electric-dipole allowed.

The theoretical and experimental UV-Vis spectra of linkers (1) and (2) are shown in Figure 7. Although there is a significant

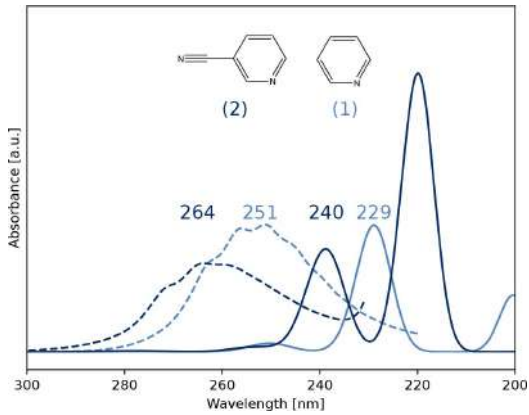

Figure 7. Theoretical (full lines) and experimental (dashed lines) UV-Vis absorbance spectra of ligands (1) and (2). Calculations carried out at the B3LYP/6-31 + + G** level of theory and with acetonitrile as solvent.

shift between theory and experiment, which has also been observed in Ref. [23], the calculations confirm the experimentally observed shift towards higher wavelengths when CN^- is added. The calculated shift is 11 nm for the bright excited state, which is in excellent agreement with the experimental shift of 13 nm as shown in Figure 4.

Our calculations on these reference systems show that the addition of a cyano group results in a shift of the main absorption peak towards larger wavelengths and confirm our experimental results.

3.3. Structural Properties of Polypyridyl Ligands

After analyzing the photophysical properties of the reference systems (1) and (2), we study several polypyridyl ligands which are promising for the construction of CTF scaffolds as shown in Figure 1. Before we investigate the excited state properties, we perform an in-depth analysis of the structure of the ligands exhibiting a rotational degree of freedom around the central bond, *i.e.*, linkers (3)–(8). This rotation is characterized by the dihedral angle shown in Figure 8. In order to perform a rotational scan, we start with an optimized cis conformer, after which we vary the dihedral angle with a step size of 10 . At every step, the structure is fully optimized except for the frozen dihedral. A schematic representation of the rotational profile, relative to the trans configuration, is shown in Figure 9. Two minima are observed as the ligands have two (meta)stable conformers, namely trans and cis. In the trans conformation, characterized by a dihedral angle of 180 , the nitrogen atoms are at opposite sides of the bond between the two pyridine rings, while in cis the nitrogen atoms are at the same side of the bond, corresponding to a dihedral angle ϕ_{cis}. The conformational equilibrium is determined by conjugation of the two $\pi-$systems, steric hindrance by the hydrogen atoms and electrostatic interactions.[29,45] The trans conformer is predicted to be lower in energy than the cis conformer. The reason for this is that the repulsive interaction between the lone-pair electrons of the nitrogen atoms is smaller than the attractive interactions between a nitrogen and a hydrogen atom situated on different rings.

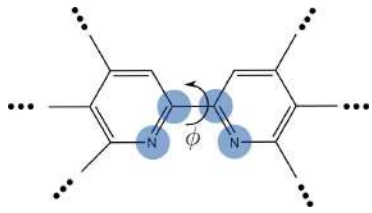

Figure 8. Schematic representation of the dihedral angle ϕ in a polypyridyl ligand.

Now we focus on linker (4), for which we discuss the rotational profile in detail and test the performance of various levels of theory. The trans conformer is the most stable structure, both in the gas phase as with acetonitrile as solvent. This is in agreement with literature data found for bipyridine where it has been reported that the trans conformer is also present in organic solvents and in basic or very strong acidic environment.[60] Furthermore, results of X-ray analysis indicate that the molecule has a trans configuration in the crystalline state.[55] The trans configuration is found to be planar in our theoretical calculation, which is in agreement with Ref. [55]. However, dipole moment measurements in organic solvents and in basic solutions indicate a non-planar trans configuration, with a dihedral angle of 20 .[17] This discrepancy has been studied before. As the non-planarity was not due to the lack of electron correlation during the optimization,[63] it has been shown that the solvent-solute interactions lie on the basis for this deviation. However, we observe a planar trans conformation in our static calculations in which solvent is included using PCM.

On the other hand, the cis form has not yet been observed in its isolated form. Only in some specific environments it appears that the cis conformation indeed exists and even prevails. So are metal-chelate compounds[22,46,16] and monocation structures of bipyridine favoring the cis-form.[60,19] Also compounds forming an adduct with typical Lewis acceptors such as $SbCl_3$, $AsCl_3$, $BiCl_3$[52,12,9] or embedded in phosphinic centers[10] appear as stable structures with the bipyridine in a cis conformation. The cis structure is not planar, which is caused by the steric hindering between the extended non-bonding orbitals of the nitrogen atoms. However, when embedded in a transition metal complex, the linker is planar.[58] The large difference in the permanent dipole moment between the cis and trans conformers means that not only chelating and protonation effects, but that also pure electrostatic interactions contribute to the stabilization of the cis structure.

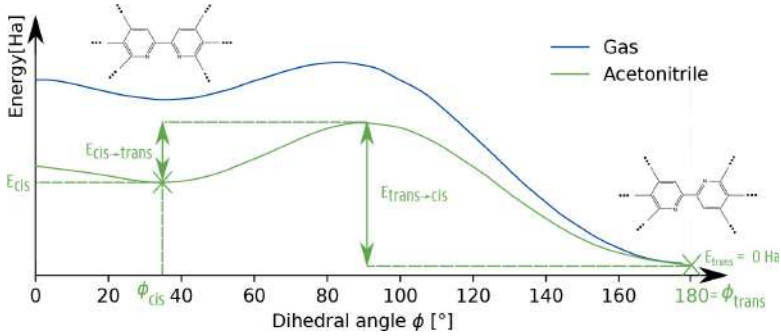

Figure 9. Schematic representation of the torsional potential energy curve for the relaxed ground state, both in the gas phase and in solvent. The two (meta) stable conformers are indicated.

We now examine the dependence of ϕ_{cis} on the selected DFT method. This structural parameter may vary in a relatively wide window (30 −43) as shown in Table 1. The long-range corrected functionals, CAM-B3LYP, ωB97X–D and LC-ωHPBE, yield significant larger ϕ_{cis} values compared to the other functionals. Furthermore, it is not surprising that the dihedral angle is strongly correlated with the energy difference between the trans and cis structures, E_{cis}, and with the barrier $E_{trans\rightarrow cis}$, which has to be overcome to go from the trans to the cis configuration (Figure 9). These energies are also tabulated in Table 1. Values of E_{cis} are not varying much with the choice of functional. Larger deviations are observed for the barrier $E_{trans\rightarrow cis}$ and obviously for $E_{cis\rightarrow trans} = E_{trans\rightarrow cis} - E_{cis}$ too, *i.e.*, the barrier which has to be overcome to go from the cis to trans structure. The smallest barriers are noticed for the long-range corrected functionals. Other structural parameters of the geometry of the trans structure of ligand (4) are tabulated in Table S2 of the Supporting Information. Only results for B3LYP and M06 are shown as the other functionals are inferior for the description of the excited states as will be shown in Section 3.4. Both for organic and inorganic molecules, M06 performs particularly well.[42,49] We may generally conclude that the influence of the level of theory on the geometrical parameters of the trans configuration is negligibly small.

The influence of solvent on the energetics is large as can be seen in Figure 9 and Table 1. The results reported in Table 1 are obtained with acetonitrile, which has a relative permittivity of ε_r =37.5. The barrier $E_{trans\rightarrow cis}$ decreases with at least 10 kJ/mol, resulting in an increase of the probability of finding the ligand in the cis conformation. This is in agreement with the findings of Ref. [45] where the authors report an increase of the dipole moment when ε_r increases. The larger dipole moment is attributed to a higher population of the dipolar cis structure.

To support these findings, we performed a series of molecular dynamics (MD) simulations at 300 K and checked if a transition from the trans to cis structure or vice versa takes place. In Figure 10, the histograms are shown for the dihedral angles encountered in the MD simulations from the trans to cis conformer (left) and vice versa (right). When starting in the trans conformer, we do not observe any transition after 53 ps. In the inset of the left pane of Figure 10, it is shown that the peak of the trans conformer is situated at 175 instead of at 180 as we would expect from the geometry optimizations. This confirms the non-planar trans configuration with a dihedral angle of 20 observed in experiments.[17] When starting from the cis conformer, we see a transition to the trans conformer after 48 ps. After this, the linker remains in the trans conformer and no transition back to the cis structure has been observed

Table 1. ϕ_{cis}, E_{cis}, $E_{trans\rightarrow cis}$, and $E_{cis\rightarrow trans}$ for ligand (4), both with and without acetonitrile as solvent. Energies are given in kJ/mol and angles in . Calculations carried out at the B3LYP/6-31++G** level of theory.

Functional	Without solvent				With solvent			
	ϕ_{cis}	E_{cis}	$E_{trans\rightarrow cis}$	$E_{cis\rightarrow trans}$	ϕ_{cis}	E_{cis}	$E_{trans\rightarrow cis}$	$E_{cis\rightarrow trans}$
PBE	32.6	28.31	37.16	8.85	29.7	14.48	27.13	12.65
BLYP	34.0	27.71	35.25	7.54	30.8	13.85	25.23	11.38
B3LYP	35.7	28.69	35.58	6.89	32.4	14.33	25.14	10.81
M06	34.7	28.67	37.32	8.65	31.8	14.49	27.05	12.56
TPSSh	33.0	29.18	37.49	8.31	29.9	14.95	27.18	12.23
CAM-B3LYP	39.5	28.92	33.92	5.00	36.1	14.04	22.69	8.65
ωB97X-D	40.9	27.48	33.31	5.83	38.1	12.81	21.05	8.24
LC-ωHPBE	42.5	27.76	33.92	6.16	39.2	13.02	20.63	7.61

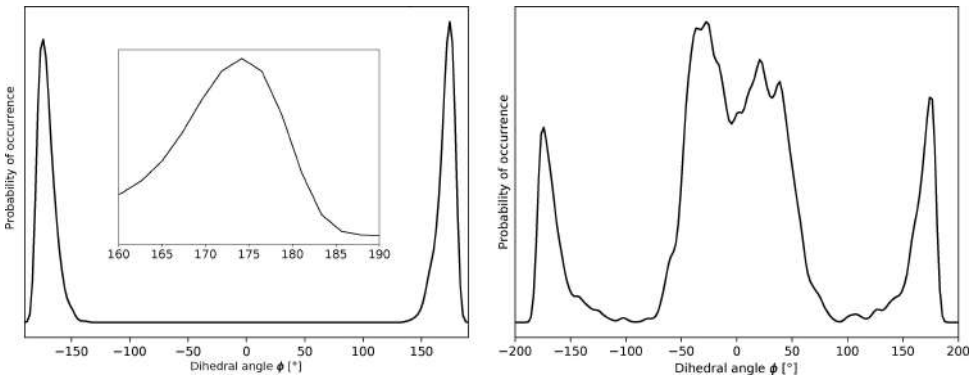

Figure 10. Histogram of the dihedral angle for the MD simulations starting from the trans conformer (left) and cis conformer (right) of linker (4). In the left pane, we zoomed in on the range between 160 and 190 . Calculations carried out at the BLYP level of theory.

after 100 ps. These results are expected, considering the rather high values for E_{cis} and $E_{trans\rightarrow cis}$ reported in Table 1. The MD calculations were performed at the BLYP level of theory and in gas phase, however, the overall qualitative picture is expected to remain unaltered when solvent is taken into account.

Next, we study the influence of various terminations of the bipyridine linker on the energy profile, inspired by the synthesis conditions of the CTF scaffold. The results are shown in Table 2. Therefore we examine linkers (3)–(5) with H, CN^-, and triazine as termination group respectively. Compared to the pristine bipyridine linker, E_{cis} and $E_{trans\rightarrow cis}$ are slightly increased for a cyano- or triazine group termination. In addition, ϕ_{cis} is larger. Bipyridine (linker (3)) has been studied extensively in literature and we find a good correspondence between our values and literature data (see Table S3). Table 2 also reports E_{cis}, ϕ_{cis}, $E_{trans\rightarrow cis}$, and $E_{cis\rightarrow trans}$ for the other ligands with a rotational degree of freedom and we do not observe large differences between them. We mention the presence of an extra rotational degree of freedom of linker (6), *i.e.*, the rotation between the pyridine and benzene ring. However, this angle changes with less than 2 when a rotational scan is performed for ϕ, the dihedral angle between the two pyridine rings.

3.4. Excited State Properties of Polypyridyl Ligands

3.4.1. Influence of Level of Theory on Excited State Properties

After studying the ground state properties, we investigate the electronic excitation spectra. First of all, we study the influence of the chosen functional on the UV-Vis spectrum of the trans conformer of linker (4). The resulting calculated spectra are compared with experiment in Figure 11. As expected, the lack of including Hartree-Fock exchange in PBE results in a spectrum which needs a significant blue-shift to match the experimental data.[56,59] Contrarily, the long-range corrected functionals, shown in red, require a large red-shift, which is in agreement with earlier studies on compounds ranging from MOFs[36] to noble metal nanoclusters.[59] The best correspondence between theory and experiment is found for B3LYP and M06, for which the excitation energies of the two absorption peaks are indicated in Figure 11 along with the experimental values. Also the dependence on the choice of the basis set has been studied (see Figure S10): the UV-Vis spectrum varies only slightly. As no reference data has been found in literature for linker (4), we compare the calculated spectrum of the extensively studied linker (3) with experimental and computational literature data in order to test the chosen level of theory. Table S4 of the Supporting Information shows the structural parameters of the trans conformer of linker (3) from literature data and our calculations. In Table 3, the energies for the visible absorption peaks for the trans conformer of linker (3) are reported. Experimental studies reveal two absorption bands at 279 and 232 nm.[60] In Ref. [79] an overview is given of other experimental results. The gas phase UV-Vis spectrum has been calculated at the PBE1PBE/6-31++G** level of theory in Ref. [48], in which two intense transitions at 265 and 227 nm are observed. We conclude that B3LYP and M06 perform equally well and in the remainder of this paper we will systematically employ B3LYP as functional. Remark that those calculations were performed in the gas phase in contrast to the previous simulations in order to be comparable with the literature.

Table 2. ϕ_{cis}, E_{cis}, $E_{trans\rightarrow cis}$, and $E_{cis\rightarrow trans}$ for linkers (3)–(8). Energies are given in kJ/mol and angles in . Calculations carried out at the B3LYP/6-31++G** level of theory and with acetonitrile as solvent.

Ligand	ϕ_{cis}	E_{cis}	$E_{trans\rightarrow cis}$	$E_{cis\rightarrow trans}$
 (3)	34.2	11.97	20.86	8.89
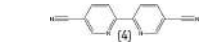 (4)	32.4	14.33	25.14	10.81
 (5)	33.3	13.77	24.46	10.69
 (6)	32.8	13.19	24.09	10.90
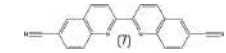 (7)	34.2	14.94	24.11	9.17
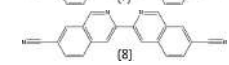 (8)	36.4	14.20	25.74	11.54

Table 3. Energies of the visible absorption peaks [nm] and oscillator strength, *f*, between parentheses of the trans conformer of linker (3). Own calculations and literature data, both computational and experimental, are compared. Calculations are performed in the gas phase.

Level of theory	Electronic excitations		
B3LYP/6-31++G**	272 (0.465)	233 (0.061)	209 (0.065)
M06/6-311++G**	273 (0.456)	233 (0.0366)	210 (0.051)
PBE1PBE/6-31+G**[98]	265 (0.485)	227 (0.057)	201 (0.080)
Experiment[83]	279	232	

Before continuing with the analysis of the UV-Vis spectrum, we briefly discuss the influence of the solvent on the excitation spectra. The results of linker (4) are shown in Table S5 of the Supporting Information. When solvent is included, we observe a shift of 5–9 nm towards larger wavelengths compared to the gas phase results.

We now examine the UV-Vis spectrum of linker (4) in detail. Figure 12 visualizes the orbitals involved in the most dominant contributions of the first non-dark and two bright excitations. They have the same character as the orbitals of ligand (2) shown in Figure 6. The first non-dark and first bright excitation are identical to these of linker (2) involving an n$\rightarrow \pi_Q^*$ and $\pi_Q \rightarrow \pi_Q^*$ excitation, respectively. The second bright excitation appears at a smaller wavelength (248 nm), has a much lower oscillator strength ($f=0.0837$) and involves the following transitions: $\pi_{AQ} \rightarrow \pi_Q^*$ and $\pi_Q \rightarrow \pi_{AQ}^*$. Furthermore, we studied the differences in geometry between the ground and relaxed excited state structures as shown in Table S6 of the Supporting Information. We remark that for the excited states the distance between the two rings decreases.

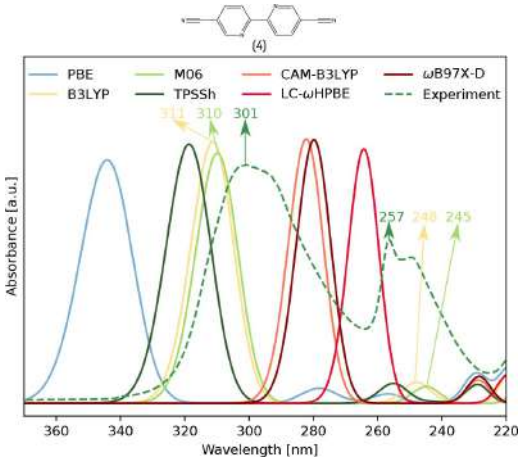

Figure 11. UV-Vis spectra of ligand (4) for several functionals (full lines) together with the experimental spectrum (dashed line). The energies of the first and second absorption peak are indicated for B3LYP, M06, and experiment. Calculations carried out with the 6-31++G** basis set and with acetonitrile as solvent.

3.4.2. Influence of Extending π-system and Increasing π-electron Deficiency

The ligands in the series (1)–(6) show an increasing π-electron deficiency by adding a cyano group, CN^-, or an aromatic ring containing nitrogen atoms as termination group as demonstrated in Figure 4. Addition of aromatic rings to the chain extends the π-system. The theoretical UV-Vis spectra for this series of linkers are displayed in Figure 13. We observe that the larger the termination group, going from linker (3) over (4) to (5), the larger the shift of the highest peak towards longer wavelengths. This confirms the experimental results of Section 3.1. The MOs involved in the important excitations of linker (4), (3) and (5) are shown in Figure 12 and Figures S11 and S12 of the Supporting Information respectively. The character of all orbitals is identical and the contributing transitions to the first and two bright excitations are the same. Compared to linkers (3) and (4), the state ordering is interchanged for linker (5): for the former, the brightest transition is the second one, whereas it is the first for linker (5). However, we note that the excitation energies of the first two transitions lie very close to each other for linker (5). The energy shift of the bright excitation between linker (3) to (4) is circa 41 nm, where a shift of 20 nm has been observed experimentally as shown in Figure 4.

The influence of extending the π-system is best studied by comparing linkers (1) and (3) on the one hand and (4) and (6) on the other hand. The main absorption peak for linkers (1) and (3) shifts 41 nm (see Figure 11), which is larger than the experimental shift of 30 nm. A similar shift is noticed between ligands (4) and (6) (45 nm), which again is an overestimation with respect to experiment (shift of 22 nm).

By comparing the shifts between ligands (2) and (4), and between (3) and (5), we can study the combined effect of an extended π-system which is also more π-electron deficient. For both cases, we observe a large shift of 71 and 83 nm respectively as can be extracted from Figure 11. For completeness, the orbitals involved in the main absorption peak of linker (6) are shown in Figure S13 of the Supporting Information. The characters of the HOMO and LUMO are identical to these of the previously described linkers.

3.4.3. Influence of Dihedral Angle on Excited State Properties

In the previous subsections, we limited the excited state calculations by assuming that the system is in the energetically most favorable trans configuration corresponding with a dihedral angle of $\phi = 180$. As some polypyridyl ligands favor the cis conformation in some specific environments, we extend this study by investigating the influence of the dihedral angle on the UV-Vis spectrum. As reference compound we consider ligand (4) for which experimental data are available in the literature. Structural properties have also been investigated theoretically in this study and have been discussed in Section 3.3. At the B3LYP/6-31++G** level, a metastable cis conformation is found at $\phi_{cis} = 35.7$. The UV-Vis spectrum is calculated for each point of the rotational scan and displayed in Figure 14 for some specific values of the dihedral angle.

We start the analysis from the planar trans conformer with a dihedral angle of 180 . The brightest transition is situated at high wavelengths, corresponding to a low excitation energy. When ϕ decreases, the peak shifts to smaller wavelengths and thus the excitation energy increases. Meanwhile the conjugated π-system decreases when the structure becomes less and less planar as the π-interactions along the bond get weaker. Furthermore, the oscillator strength decreases. The lowest

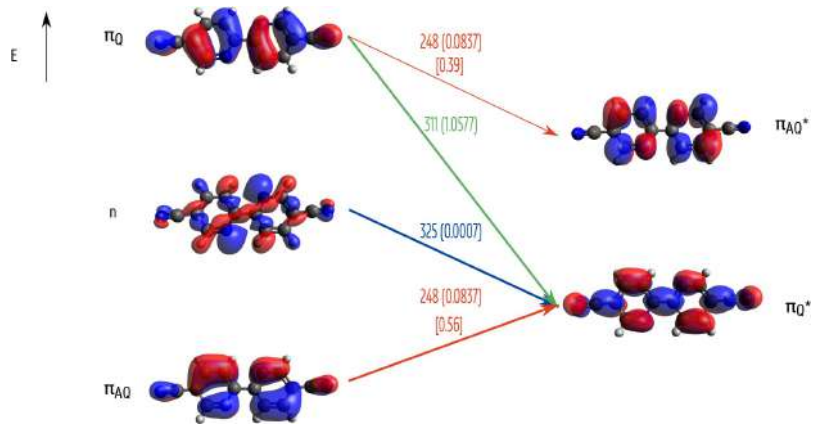

Figure 12. Visualization of the important orbitals of linker (4). The arrows indicate the most dominant contributions of the first non-dark and two bright excitations, characterized by the excitation energy in nm, oscillator strength, f, between parentheses, and amplitude in square brackets if more contributions are reported for a specific excitation. The occupied MOs in the left represent respectively the HOMO, HOMO-1 and HOMO-5 in descending order. The unoccupied MOs in the right represent respectively the LUMO + 3 and LUMO. This labeling is conform the binding energies taken up in Table S1. The transition with the lowest excitation energy is indicated with a blue arrow and the first and second bright transitions are represented with green and red respectively. Calculations carried out at the B3LYP/6-31 + + G** level of theory and with acetonitrile as solvent.

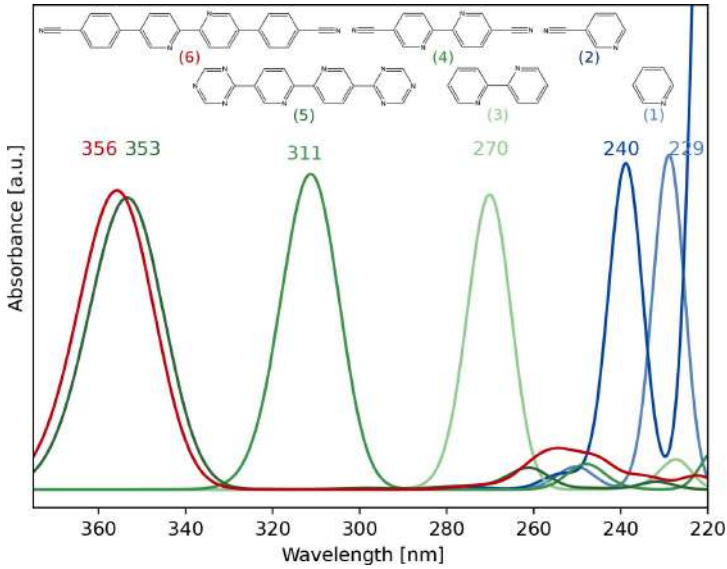

Figure 13. Theoretical UV-Vis spectra of ligands (1)–(6). The energies of the main absorption peak are indicated. Calculations carried out at the B3LYP/6-31 + + G** level of theory and with acetonitrile as solvent.

wavelength is observed for structures with a dihedral angle of 92 . Then the spectrum closely resembles that of linker (2) as shown by the dotted black line. Indeed, the orbitals in the two rings are only slightly connected and the spectrum of linker (4) is just the sum of its components, *i.e.*, linker (2). The dominant absorption peak of ligand (4) comes from a $\pi_Q \rightarrow \pi_Q{}^*$ transition, which, in this compound, corresponds with a HOMO→LUMO excitation as demonstrated in Figure 12 for the

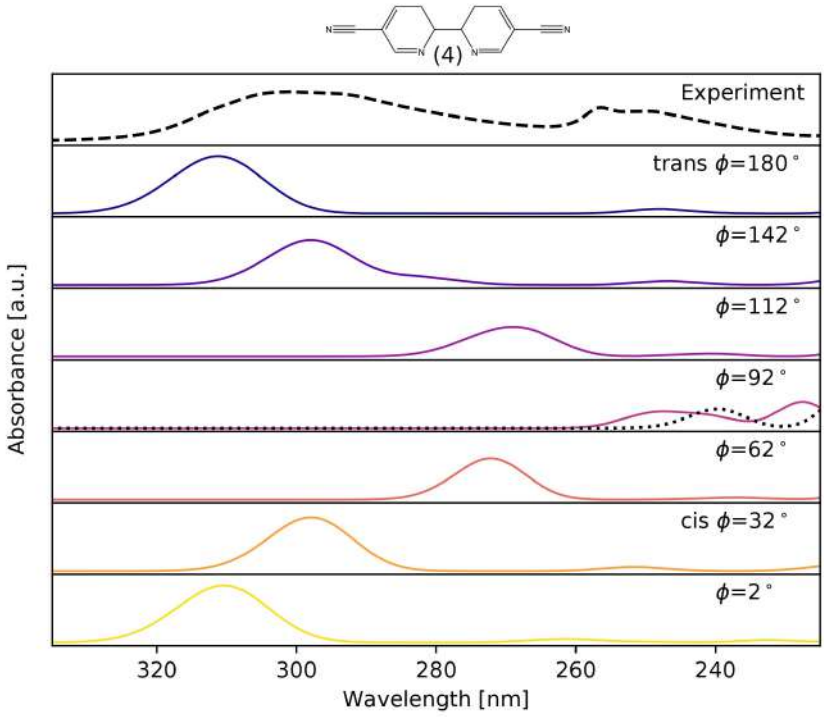

Figure 14. Influence of the dihedral angle on the UV-Vis spectrum of ligand (4). The experimental spectrum is indicated with a dashed line and the dotted line represents the spectrum of linker (2). Calculations carried out at the B3LYP/6-31++G** level of theory and with acetonitrile as solvent.

trans structure. For a dihedral angle of 92 , the MOs are shown in Figure S14 of the Supporting Information. When ϕ decreases further, the peak shifts to larger wavelengths again. This is accompanied by an increase of f as the conjugated $\pi-$system increases again when the structure becomes more planar. So the largest conjugated system has the smallest excitation energy, which is in agreement with Ref. [80]. The observed shift between planar and non-planar structures is 50 nm. Special attention is devoted to the cis conformer which is shown in orange. The orbitals involved in the most important transitions of the cis conformer are shown in Figure S15 of the Supporting Information and are compared to the orbitals of the trans structure. The brightest transition of the cis conformer is shifted 13 nm towards smaller wavelengths compared to the trans structure. Just as for the trans conformer, we compare the geometries of the optimized ground and excited states as shown in Table S7 of the Supporting Information. It is interesting to note that, whereas the ground cis structure has a dihedral angle of circa 32 , the excited states become planar. Finally, we also note that for most values of ϕ, a second peak is observed around 250–260 nm. However, no second peak is found for dihedral angles around 90 . This has been observed earlier: the presence of two bands is an indication that the structure is not twisted, whereas only one band is visible in this region for a large twist.[80]

As already stated above, the main absorption peak mainly consists of a HOMO→LUMO transition for all dihedral angles. Therefore, these observations are in agreement with the well known fact that the HOMO-LUMO gap decreases when the conjugated system increases as shown in Figure S16 of the Supporting Information.

The same rotational analysis has been performed for linkers (3), (5)–(8) and their UV-Vis spectra are taken up in Figures S17, S18, S19, S20 and S21 respectively. All these spectra show the same qualitative behaviour, the main absorption peak fluctuates over a relatively large wavelength range up to 80 nm, but for some linkers, the global pattern can be different at some specific values of the dihedral angle.

We also performed some MD simulations from which snapshots are extracted which are used as input structures for TDDFT calculations.[20,36] The small spread in the dihedral angles results in a broadening of the main absorption peak as shown in Figure S22.

3.4.4. Other Ligands

Finally, we extend the study by a series of linkers (7)–(13) which might be interesting building blocks for CTF structures. Table 4 gives an overview of the energy of the main absorption peaks along with the dihedral angle of the optimized structure. For linkers (3)-(8), both the cis and trans conformers are studied. Experimental values are given in the last column.

First, we compare linkers (7) and (8) with the cis conformer of linker (4). They have similar dihedral angles, nevertheless, the shift of the position of the main absorption peak is rather large, *i.e.*, 47 nm and 65 nm respectively. This is because the conjugated π-system of linkers (7) and (8) is larger with respect to linker (4) which results in a shift towards larger wavelengths. However, it is remarkable that although linkers (7) and (8) have a similar value of ϕ_{cis} and only differ in the position of the two nitrogen atoms, their UV-Vis spectra reveal some specific discrepancies (Figure S30 in the Supporting Information). Both spectra exhibit three dominant peaks, but the position of the main absorption peak at the smallest excitation energy is shifted by 18 nm. They represent HOMO→LUMO excitations and their MOs are shown in Figures S23 and S24 of the Supporting Information. These orbitals are similar to those of naphthalene as predicted by Hückel's theory.[97] The contribution of the nitrogen atoms on the ring to the molecular orbital coefficients are reported in Table S8. The largest contributions

Table 4. Dihedral angle [ ] and energy of the main absorption peak [nm] and [eV] between brackets for all linkers. Linkers (3)-(8) have both a cis and trans structure and E_{trans}, E_{cis}, and ϕ_{cis} are reported whereas the other linkers only have one optimized structure for which E and ϕ are given. Largest shift of the main absorption peak with respect to pyridine amounts to 271 nm and belongs to ligand 11. In the last column the experimental results are displayed. Calculations carried out at the B3LYP/6-31++G** level of theory and with acetonitrile as solvent.

Linker	E_{trans}	E_{cis}	ϕ_{cis}	E	ϕ	E_{exp}
 (1)				229(5.41)	/	251(4.94)
 (2)				240(5.17)	/	264(4.70)
 (3)	270(4.59)	257(4.82)	34.2			281(4.41)
 (4)	311(3.99)	298(4.16)	32.4			301(4.12)
 (5)	353(3.51)	338(3.67)	33.3			
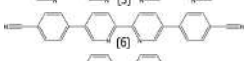 (6)	356(3.48)	340(3.65)	32.8			323(3.84)
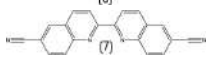 (7)	377(3.29)	345(3.59) 266(4.66)	34.2			
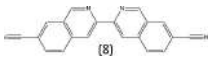 (8)	377(3.29)	363(3.42) 275(4.51)-270(4.59)	36.4			
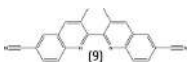 (9)				310(4.00) 252(4.92)	112	
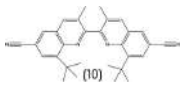 (10)				305(4.07) 258(4.81)	106	
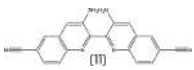 (11)				500(2.48) 351(3.53) 296(4.19)-285(4.35)	158	
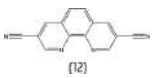 (12)				311(3.99) 289(4.29)	180	
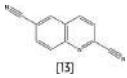 (13)				326(3.80) 301(4.12) 255(4.86)	180	

are indicated in green and show that both the HOMO and LUMO of ligand (7) have a large contribution from the nitrogen atoms, whereas only the LUMO of ligand (8) has a significant contribution. The inclusion of nitrogen into the orbital results in a lowering of the orbital energy due to the larger electron negativity of nitrogen compared to carbon. For ligand (7), both the HOMO and LUMO decrease in energy, whereas for ligand (8), only the LUMO gets stabilized. Therefore, the HOMO-LUMO gap is smaller for ligand (8), *i.e.* 3.905 eV, than for ligand (7), *i.e.* 4.085 eV. This explains the observed shift in the main absorption peak for these linkers.

Second, we focus on linkers (7) and (9)–(11) which have more or less the same ring topology but differ in the number of side groups. The UV-Vis spectra are displayed in Figure 15. We can explain the position of the main absorption peak by accounting for the size of the conjugated π-system which is correlated to the dihedral angle. We observe that the more planar the structure is, *i.e.*, ϕ is close to 0 or 180 , the more the peak shifts towards larger wavelengths. Ligands (9) and (10) show an optimized structure with a dihedral angle equal to 112 and 106 respectively, and are thus far from planar. Their main absorption peaks are clearly positioned at lower wavelengths than those in ligands (7) and (11). We found in Section 3.4.3 a shift of around 50 nm between planar and dihedral angles of 90 for linker (4). The shifts observed between linkers (7), (9) and (10) are of the same order of magnitude. However, for linker (11), we notice an absorption peak at 500 nm, isolated from the peaks of the other linkers which are situated in the range of 350 nm–200 nm. This significant shift toward larger wavelengths cannot be explained by considering only the size of the π-system which is correlated to the dihedral angle, but can be explained by the presence of the electron-donating NH_2 groups. Indeed, this linker has an extra occupied orbital situated on the NH_2 group, which is higher in energy than occupied orbitals which are not situated on these groups. Therefore, we observe an extra transition for linker (11) at very high wavelengths. Compared to linker (1), the main absorption peak is shifted 271 nm towards larger wavelengths for linker (11).

Furthermore, it is also interesting to compare the cis structure of linker (4) and linker (12) shown in Figure S31 of the Supporting Information. As the latter has a larger conjugated π-system, we expect the peak to be situated at larger wavelengths. Indeed, we observe a shift between the peaks corresponding with a $\pi_Q \rightarrow \pi_Q^*$ transition of 13 nm towards longer wavelengths. Remark that ligand (12) has a transition with higher oscillator strength at 289 nm.

Finally we also compare linkers (2) and (13) of which the UV-Vis spectra are shown in Figure 16. The shift of the main absorption peak, which is a $\pi_Q \rightarrow \pi_Q^*$ transition for both linkers, amounts to 86 nm. Indeed, linker (13) is more π-electron deficient and has a larger π-system than linker (2). Furthermore, we notice that both linkers have a stronger excitation, at 221 nm and 255 nm respectively.

This shows that the position of the main absorption peak can be explained, and even tuned, by changing the size of the conjugated π-system, the amount of π-electron deficiency and by adding functional groups.

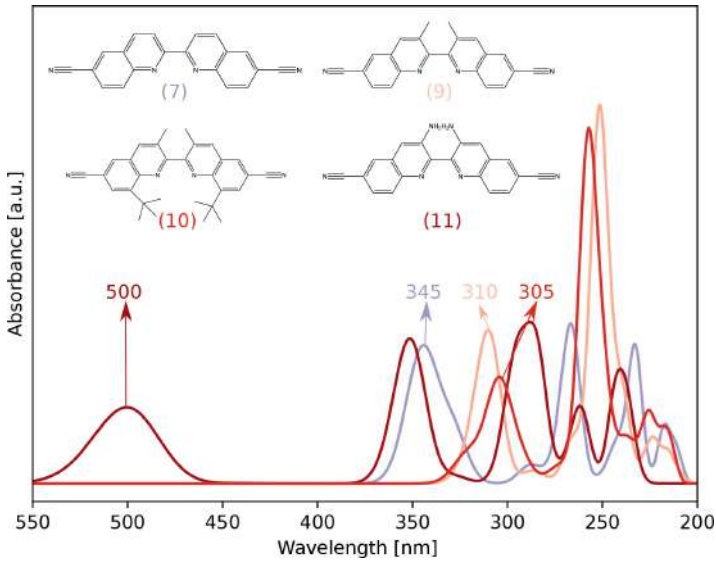

Figure 15. Theoretical UV-Vis spectra of ligands (7),(9), (10), and (11). Calculations carried out at the B3LYP/6-31++G** level of theory and with acetonitrile as solvent.

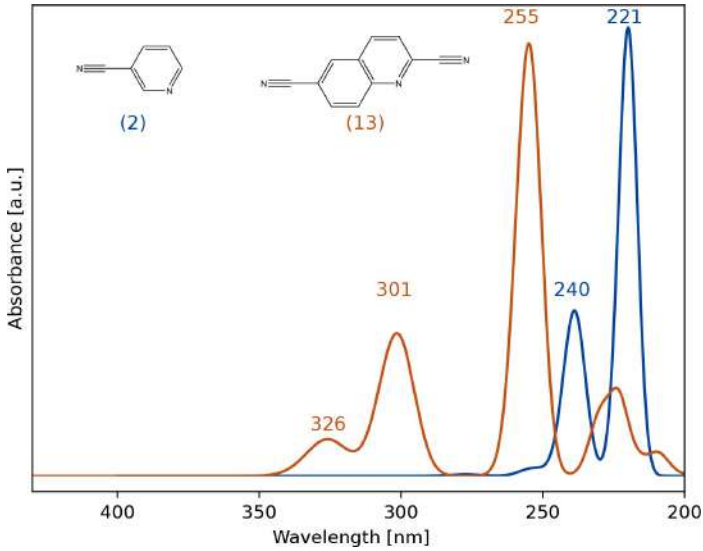

Figure 16. Theoretical UV-Vis spectra of ligands (2) and (13). Calculations carried out at the B3LYP/6-31++G** level of theory and with acetonitrile as solvent.

For completeness, the orbitals contributing to the most important excitations of linkers (7)-(12) are shown in Figures S23, S24, S25, S26, S27, S28 and S29 of the Supporting Information. The UV-Vis spectra are shown in Figures 15 and 16 and Figures S30 and S31 of the Supporting Information. Furthermore, all singlet excitation energies along with the oscillator strength are listed in Table S9 of the Supporting Information for all linkers studied in this work.

4. Conclusions

We investigated, both experimentally and computationally, the structural and photophysical properties of various polypyridyl ligands which can be used to build CTFs. Therefore, we performed TDDFT calculations at the B3LYP/6-31++G** level of theory and investigated the shift of the main absorption peak. We found that the larger the π -system and the higher its π -electron deficiency, the more the main absorption peak shifts to larger wavelengths. This can be achieved by adding aromatic rings, increasing the nitrogen content, or terminating the linker with electron withdrawing CN^- groups. Furthermore, we studied the influence of the dihedral angle, determined by the rotation about the central C–C bond, which is characteristic for all polypyridyl ligands under study in this work, on the UV-Vis spectrum. We found that the main absorption peak shifts to smaller wavelengths when the π-system decreases, which occurs when the dihedral angle is close to 90 . Furthermore, we showed that the position of the main absorption peak can be further shifted to larger wavelengths by increasing the nitrogen content of the linker. The maximum shift can amount to 271 nm with respect to pyridine, which is sufficiently large to have a significant impact on the photophysical properties of the polypyridyl ligands. This broad range of shifts of the main absorption peak gives perspective in the modulation of the electronic structure by varying the ligands. Therefore, this study reveals how the optical properties of the CTF scaffold can be tuned by choosing the linkers.

Acknowledgements

The authors acknowledge the Fund for Scientific Research Flanders (FWO) and the Research Board of Ghent University (BOF) through a Concerted Research Action (GOA) for funding. V.V.S. and L.D.B. acknowledge funding from the European Union's Horizon 2020 research and innovation program (consolidator ERC Grant Agreement No. 647755-DYNPOR (2015-2020)). The computational resources and services used in this work were provided by VSC (Flemish Supercomputer Center), funded by Ghent University, FWO, and the Flemish Government Department EWI.

Conflict of Interest

The authors declare no conflict of interest.

Keywords: covalent triazine framework · photocatalysis · polypyridyl ligand · time-dependent functional theory · UV-Vis spectroscopy

[1] C. Adamo, V. Barone, *J. Chem. Phys.* **1999**, *110*, 6158.
[2] C. Adamo, D. Jacquemin, *Chem. Soc. Rev.* **2013**, *42*, 845–856.
[3] U. I. E. Agency *International Energy Outlook* **2016**.
[4] H. B. Aiyappa, J. Thote, D. B. Shinde, R. Banerjee, S. Kurungot, *Chem. Mater.* **2016**, *28*, 4375–4379.
[5] T. Banerjee, B. V. Lotsch, *Nat. Chem.* **2018**, *10*, 1175–1177.
[6] A. M. Beale, S. D. M. Jacques, B. M. Weckhuysen, *Chem. Soc. Rev.* **2010**, *39*, 4656–4672.
[7] A. D. Becke, *J. Chem. Phys.* **1993**, *98*, 5648.
[8] A. Bolovinos, P. Tsekeris, J. Philis, E. Pantos, G. Andritsopoulos, *J. Mol. Spectrosc.* **1984**, *103*, 240–256.
[9] G. A. Bowmaker, F. M. M. Hannaway, P. C. Junk, A. M. Lee, B. W. Skelton, A. H. White, *Austr. J. Chem.* **1988**, *51*, 331–336.
[10] N. Burford, T. S. Cameron, K. N. Robertson, A. D. Phillips, H. A. Jenkins, *Chem. Commun.* **2000**, 2087–2088.
[11] Z. L. Cai, J. R. Reimers, *J. Phys. Chem. A* **2000**, *104*, 8389.
[12] J. U. Cameron, R. C. G. Killean, *Cryst. Struct. Commun.* **1972**, *1*, 31–45.
[13] M. Caricato, G. W. Trucks, M. J. Frisch, K. B. Wiber, *J. Chem. Theory Comput.* **2010**, *6*, 370.
[14] M. E. Casida, C. Jamorski, K. C. Casida, D. R. Salahub, *J. Chem. Phys.* **1998**, *108*, 4439–4449.
[15] J. D. Chai, M. Head-Gordon, *Phys. Chem. Chem. Phys.* **2008**, *10*, 6615–6620.
[16] G. Chelucci, R. P. Thummel, *Chem. Rev.* **2002**, *102*, 3129–3170.
[17] C. L. Cheng, D. S. N. Murthy, G. L. Ritchie, *J. Chem. Soc. Faraday Trans. 2* **1972**, *68*, 1679–1690.
[18] S. Cogan, S. Zilberg, Y. Haase, *J. Am. Chem. Soc.* **2006**, *128*, 3335.
[19] Z. Dega-Szafran, *Rocz. Chem.* **1976**, *50*, 423.
[20] A. Van Yperen-De Deyne, K. Hendrickx, L. Vanduyfhuys, G. Sastre, P. Van Der Voort, V. Van Speybroeck, K. Hemelsoet, *Theor. Chem. Acc.* **2016**, *135*.
[21] S. Y. Ding, W. Wang, *Chem. Soc. Rev.* **2013**, *42*, 548–568.
[22] E. V. Dose, L. J. Wilson, *Inorg. Chem.* **1978**, *17*, 2660–2666.
[23] F. Egidi, M. Segado, H. Koch, C. Cappelli, V. Barone, *J. Chem. Phys.* **2014**, *141*, 224114.
[24] M. J. Frisch, G. W. Trucks, H. B. Schlegel, G. E. Scuseria, M. A. Robb, J. R. Cheeseman, G. Scalmani, V. Barone, G. A. Petersson, H. Nakatsuji, X. Li, M. Caricato, A. V. Marenich, J. Bloino, B. G. Janesko, R. Gomperts, B. Mennucci, H. P. Hratchian, J. V. Ortiz, A. F. Izmaylov, J. L. Sonnenberg, D. Williams-Young, F. Ding, F. Lipparini, F. Egidi, J. Goings, B. Peng, A. Petrone, T. Henderson, D. Ranasinghe, V. G. Zakrzewski, J. Gao, N. Rega, G. Zheng, W. Liang, M. Hada, M. Ehara, K. Toyota, R. Fukuda, J. Hasegawa, M. Ishida, T. Nakajima, Y. Honda, O. Kitao, H. Nakai, T. Vreven, K. Throssell, Montgomery Jr., J. A., J. E. Peralta, F. Ogliaro, M. J. Bearpark, J. J. Heyd, E. N. Brothers, K. N. Kudin, V. N. Staroverov, T. A. Keith, R. Kobayashi, J. Normand, K. Raghavachari, A. P. Rendell, J. C. Burant, S. S. Iyengar, J. Tomasi, M. Cossi, J. M. Millam, M. Klene, C. Adamo, R. Cammi, J. W. Ochterski, R. L. Martin, K. Morokuma, O. Farkas, J. B. Foresman, D. J. Fox, **2016**, Gaussian 16 Revision B.01; Gaussian Inc. Wallingford CT.
[25] R. Fukuda, M. Ehara, *J. Chem. Phys.* **2012**, *137*, 134304.
[26] R. Fukuda, M. Ehara, *Phys. Chem. Chem. Phys.* **2013**, *15*, 17426–17434.
[27] R. Fukuda, M. Ehara, *J. Chem. Theory Comput.* **2013**, *9*, 470–480.
[28] R. Fukuda, M. Ehara, H. Nakatsuji, *J. Chem. Phys.* **2010**, *133*, 144316.
[29] A. Göller, U. W. Grummt, **2000**, *321*, 399–405.
[30] L. Goodman, *J. Mol. Spectrosc.* **1961**, *6*, 109.
[31] S. Grimme, J. Antony, S. Ehrlich, H. Krieg, *J. Chem. Phys.* **2010**, *132*, 154104.
[32] G. H. Gunasekar, K. Park, H. H. Jeong, K. D. Jung, K. Park, S. Yoon, *Catalysts.* **2018**, *8*, 295.
[33] D. C. Harris, M. D. Bertolucci, *Symmetry and spectroscopy : an introduction to vibrational and electronic spectroscopy*. Oxford University Press, **1978**.
[34] T. M. Henderson, A. F. Izmaylov, G. Scalmani, G. E. Scuseria, *J. Chem. Phys.* **2009**, *131*, 044108.
[35] C. H. Hendon, J. Bonnefoy, E. A. Quadrelli, J. Canivet, M. B. Chambers, G. Rousse, A. Walsh, M. Fontecave, C. Mellot-Draznieks, *Chem. Eur. J.* **2016**, *22*, 3713–3718.
[36] K. Hendrickx, D. E. P. Vanpoucke, K. Leus, K. Lejaeghere, A. Van Yperen-De Deyne, V. Van Speybroeck, P. Van Der Voort, K. Hemelsoet, *Inorg. Chem.* **2015**, *54*, 10701–10710.
[37] C. C. Hou, T. T. Li, S. Cao, Y. Chen, W. F. Fu, *J. Mater. Chem. A* **2015**, *3*, 10386–10394.
[38] S. Hug, M. B. Mesch, H. Oh, N. Popp, M. Hirscher, J. Senker, B. V. Lotsch, *2* **2014**, *J. Mater. Chem. A*, 5928–5936.
[39] S. Hug, L. Stegbauer, H. Oh, M. Hirscher, B. V. Lotsch, *Chem. Mater.* **2015**, *27*, 8001–8010.
[40] S. Hug, M. E. Tauchert, S. Li, U. E. Pachmayr, B. V. A. Lotsch, *J. Mater. Chem.* **2012**, *22*, 13956–13964.
[41] P. A. Jacobs, M. Dusselier, B. F. Sels, *Angew. Chem. Int. Ed.* **2014**, *53*, 8621–8626; *Angew. Chem.* **2014**, *126*, 8765–8770.
[42] D. Jacquemin, E. A. Perpete, I. Ciofini, C. Adamo, R. Valero, Y. Zhao, D. G. Truhlar, *J. Chem. Theory Comput.* **2010**, *6*, 2071–2085.
[43] D. Jacquemin, V. Wathelet, E. A. Perpète, C. Adamo, *J. Chem. Theory* **2009**, *5*, 2420–2435.
[44] E. M. Johnson, R. Haiges, S. C. Marinescu, *ACS Appl. Mater. Interfaces* **2018**, *10*, 37919–3792.
[45] J. Kalenik, Z. Pawelka, *J. Mol. Liq.* **2005**, *121*, 63–68.
[46] K. Kalyanasundaram, *Coord. Chem. Rev.* **1982**, *46*, 159–244.
[47] M. D. Kärkäs, J. A. J. Porco, C. R. Stephenson, *Chem. Rev.* **2016**, *116*, 9683–9747.
[48] F. Labat, P. P. Laine, I. Ciofini, C. Adamo, *Chem. Phys. Lett.* **2006**, *417*, 445–451.
[49] A. D. Laurent, D. Jacquemin, *Int. J. Quantum Chem.* **2013**, *113*, 2019–2039.
[50] C. Lee, W. Yang, R. G. Parr, *Phys. Rev. B* **1988**, *37*, 785–789.
[51] C. Lee, W. Yang, R. G. Parr, *Phys. Rev. B* **1988**, *37*, 785.
[52] A. Lipka, H. Wunderlich, *Z. Naturforsch. B* **1980**, *35*, 1548.
[53] M. S. Lohse, T. Bein, *Adv. Funct. Mater.* **2018**, *28*, 1705553.
[54] W. A. Maza, A. J. Morris, *J. Phys. Chem. C* **2014**, *118*, 8803–8817.
[55] L. L. Merritt, E. D. Schroeder, *Acta Crystallogr.* **1956**, *9*, 801–804.
[56] T. D. Meyer, I. Steyaert, K. Hemelsoet, R. Hoogenboom, V. Van Speybroeck, K. De Clerck, *Dyes Pigm.* **2016**, *124*, 249–257.
[57] B. Miehlich, A. Savin, H. Stoll, H. Preuss, *Chem. Phys. Lett.* **1989**, *157*, 200–206.
[58] F. Muniz-Miranda, L. De Bruecker, A. De Vos, F. Vanden Bussche, C. V. Stevens, P. Van Der Voort, K. Lejaeghere, V. Van Speybroeck, *J. Phys. Chem. A* **2019**, *123*, 6854–6867.
[59] F. Muniz-Miranda, M. C. Menziani, A. Pedone, *J. Phys. Chem. C* **2014**, *118*, 7532–7544.
[60] K. Nakamoto, *J. Phys. Chem.* **1960**, *64*, 1420–1425.
[61] J. M. R. Narayanam, C. R. J. Stephenson, *Chem. Soc. Rev.* **2011**, *40*, 102–113.
[62] M. Nooijen, R. J. Bartlett, *J. Chem. Phys.* **1997**, *106*, 6441.
[63] L. Oresmaa, M. Haukka, P. Vainiotalo, T. A. Pakkanen, *J. Org. Chem.* **2002**, *67*, 8216–8219.
[64] M. Pagliai, G. Mancini, I. Carnimeo, N. D. Mitri, V. Barone, *J. Comb. Chem.* **2017**, *38*, 319–335.
[65] R. Palkovits, M. Antonietti, A. T. P. Kuhn, F. Schüth, *Angew. Chem. Int. Ed.*. **2009**, *48*, 6909–6912.
[66] K. Park, G. H. Gunasekar, N. Prakash, K. D. Jung, S. A. Yoon, *ChemSusChem* **2015**, *8*, 3410–3413.
[67] J. P. Perdew, A. Ruzsinszky, J. Tao, V. N. Staroverov, G. E. Scuseria, G. I. Csonka, *J. Chem. Phys.* **2005**, *123*, 062201.
[68] D. A. Popov, J. M. Luna, N. M. Orchanian, R. Haiges, C. A. Downes, S. C. Marinescu, *Dalton Trans.* **2018**, *47*, 17450–17460.
[69] C. K. Prier, D. A. Rankic, D. W. MacMillan, *Chem. Rev.* **2013**, *113*, 5322–5363.
[70] A. Primo, H. Garcia, *Chem. Soc. Rev.* **2014**, *43*, 7548–7561.
[71] S. M. J. Rogge, A. Bavykina, J. Hajek, H. Garcia, A. I. Olivos-Suarez, A. Sepúlveda-Escribano, A. Vimont, G. Clet, P. Bazin, F. Kapteijn, M. Daturi, E. V. Ramos-Fernandez, F. X. L. I. Xamena, V. Van Speybroeck, J. Gascon, *Chem. Soc. Rev.* **2017**, *46*, 3134–3184.
[72] E. Runge, E. K. U. Gross, *Phys. Rev. Lett.* **1984**, *52*, 997–1000.
[73] S. P. A. Sauer, M. Schreiber, M. R. Silva-Junior, W. Thiel, *J. Chem. Theory Comput.* **2009**, *5*, 555–564.
[74] M. Schreiber, M. R. Silva-Junior, S. P. A. Sauer, W. Thiel, *J. Chem. Phys.* **2008**, *128*, 134110.
[75] D. M. Schultz, T. P. Yoon, *Science* **2014**, *343*, 1239176.
[76] A. G. Slater, A. I. Cooper, *Science* **2015**, *348*, aaa8075.
[77] V. N. Staroverov, G. E. Scuseria, J. Tao, J. P. Perdew, *J. Chem. Phys.* **2003**, *119*, 12129.

[78] L. Stegbauer, K. Schwinghammer, B. V. Lotsch, *Chem. Sci.* **2014**, *5*, 2789–2793.
[79] L. A. Summers, *Adv. Heterocycl. Chem.* **1984**, *35*, 281.
[80] H. Suzuki, *Bull. Chem. Soc. Jpn.* **1959**, *32*, 1340–1350.
[81] N. Tahir, C. Krishnaraj, K. Leus, P. Van Der Voort, *Polymer* **2019**, *11*.
[82] N. Tahir, F. Muniz-Miranda, J. Everaert, P. Tack, T. Heugebaert, K. Leus, L. Vincze, C. V. Stevens, V. Van Speybroeck, P. Van Der Voort, *J. Catal.* **2019**, *371*, 135–143.
[83] N. Tahir, G. Wang, Y. Onyshchenko, N. D. Geyter, K. Leus, R. Morent, P. Van Der Voort, *J. Catal.* **2019**, *375*, 242–248.
[84] K. Takanabe, *ACS Catal.* **2017**, *7*, 8006–8022.
[85] H. Takeda, M. Ohashi, Y. Goto, T. Ohsuna, T. Tani, S. Inagaki *Adv. Funct. Mater.*, **2016**, *26*, 5068–5077.
[86] J. Tao, J. P. Perdew, V. N. Staroverov, G. E. Scuseria, *Phys. Rev. Lett.* **2003**, *91*, 146401.
[87] J. Tomasi, B. Mennucci, R. Cammi, *Chem. Rev.* **2005**, *105*, 2999–3094.
[88] W. Tu, Y. Xu, S. Yin, R. Xu, *Adv. Mater.* **2018**, *30*, 1707582.
[89] J. VandeVondele, M. Krack, F. Mohamed, M. Parrinello, T. Chassaing, J. Hutter, *Comput. Phys. Commun.* **2005**, *167*, 103–128.
[90] A. De Vos, K. Lejaeghere, F. Muniz-Miranda, C. V. Stevens, P. Van Der Voort, V. Van Speybroeck, *J. Mater. Chem. A* **2019**, *7*, 8433–8442.
[91] V. S. Vyas, F. Haase, L. Stegbauer, G. Savasci, F. Podjaski, C. Ochsenfeld, B. V. Lotsch, *Nat. Commun.* **2015**, *6*, 8508.
[92] I. C. Walker, M. H. Palmer, A. Hopkirk, *Chem. Phys.* **1990**, *141*, 365.
[93] J. Wan, M. E. M. Hada, H. Nakatsuji, *J. Chem. Phys.* **2001**, *114*, 5117.
[94] B. M. Weckhuysen, *ChemSusChem* **2013**, *6*, 1559–1563.
[95] T. Yanai, D. P. Tew, N. C. Handy, *Chem. Phys. Lett.* **2004**, *393*, 51–57.
[96] D. Yang, S. O. Odoh, T. C. Wang, O. K. Farha, J. T. Hupp, C. J. Cramer, L. Gagliardi, B. C. Gates, *J. Am. Chem. Soc.* **2015**, *5*, 7391–7396.
[97] K. Yoshizawa, T. Tada, A. Staykov, *JACS* **2008**, *130*, 9406–9413.
[98] Y. Zhao, D. G. Truhlar, *Theor. Chem. Acc.* **2008**, *120*, 215–241.

Manuscript received: July 10, 2020
Revised manuscript received: September 7, 2020
Accepted manuscript online: September 11, 2020
Version of record online: October 28, 2020

Paper III

Influence of Number of Ligands and Point Group on the Electronic Structure of Co^{2+} Aqua-Complexes

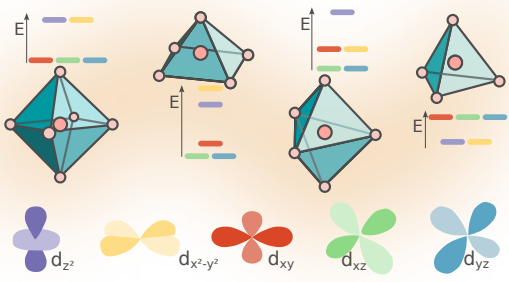

L. De Bruecker and V. Van Speybroeck

Inorganic Chemistry, **2022**, *61* (20743-20756)

L. De Bruecker performed the research and wrote the initial draft of the manuscript.

Inorganic Chemistry

pubs.acs.org/IC Article

Influence of Number of Ligands and Point Group on the Electronic Structure of Co^{2+} Aqua-Complexes

Liesbeth De Bruecker and Veronique Van Speybroeck*

Cite This: *Inorg. Chem.* 2022, 61, 20743−20756 Read Online

ACCESS | Metrics & More | Article Recommendations | Supporting Information

ABSTRACT: The nucleation process of zeolitic imidazolate frameworks (ZIFs) is, to date, not yet completely understood, making the search for tailored materials very difficult. Recently, it has been shown that, during the formation process, the symmetry of the precursors is reduced by ligand elimination and substitution reactions. The octahedral precursors with simple ligands, such as water, methanol, and/or NO_3^-, are transformed to five- and finally four-coordinated complexes with imidazole ligands. This reduction of symmetry, caused both by the changing coordination environment and distortions from the perfect symmetry leading to another point group, will have a large influence on the electronic structure and more specifically on the d-orbital splitting. This, in turn, will affect the d−d electronic excitations, which can be followed using UV−vis spectroscopy and which can help to unravel the formation process. In this work, we systematically investigate how the lowering of the number of ligands affects the symmetry and thus the geometry and electronic structure of Co^{2+} complexes with six, five, and four aqua ligands. Therefore, we first resort to qualitative techniques, such as crystal field theory (CFT) and ligand field theory (LFT), which reveal that the orbital splitting is characteristic for the number of ligands. However, as these techniques are not capable of providing quantitative results without the use of experimental data as input, we perform various computational calculations. Both average of configuration (AOC) and unrestricted density functional theory (UDFT) are thoroughly investigated, and we will determine which technique is the best suited to properly describe the ground state of these systems. To investigate the dependency on the d-orbital occupation, we also investigated V^{2+}, Mn^{2+}, and Ni^{2+} hexa-aqua-complexes and compared them to the Co systems.

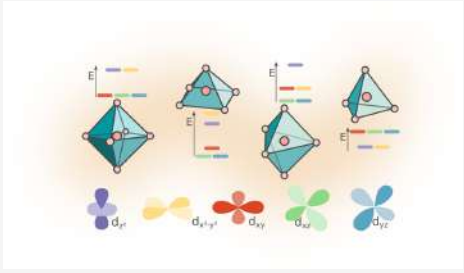

1. INTRODUCTION

Zeolitic imidazolate frameworks (ZIFs) are a subclass of metal−organic frameworks (MOFs) in which divalent metal cations, mostly Fe^{2+}, Co^{2+}, Cu^{2+}, or Zn^{2+}, are tetrahedrally coordinated by bridging imidazolate-type linkers.[1−6] Since the cation-linker-cation angle in ZIFs is similar to the Si−O−Si angle in zeolites, they are topologically isomorphic, hence their name.[1,7−9] ZIFs are due to their chemical stability, robust porosity, and resistance to thermal changes very promising candidate materials for several applications. Among others, we mention the use as catalysts or carbon dioxide caption materials,[10] molecular sieves for gas separation,[11] and high-impact shock absorbers.[12] Zn-ZIF-8 is a typical model system, consisting of tetrahedrally coordinated Zn^{2+} ions bridged by 2-methylimidazolate (2-mIm).[1,3,5,13−15] By replacing the Zn^{2+} cations with Co^{2+}, the iso-structural Co-ZIF-67 is obtained,[16−19] which has a sodalite topology and $Co(2\text{-mIm})_4^{2-}$ tetrahedral secondary building units (SBUs), as shown in Figure 1.

An in-depth understanding of the formation process of these materials is indispensable for a targeted search for structures with the best properties for a specific application, as this is at the moment mainly done *via* high-throughput synthesis.[21] Although the particle nucleation step is more or less understood by now,[22,23] the underlying molecular assembly processes in the pre-nucleation stage have been less thoroughly investigated and remain largely unknown. Only very recently, a combined experimental−computational study has been conducted,[24] in which it is suggested that, during Co-ZIF-67 nucleation, a metal−organic pool with a variety of complexes is formed caused by ligand elimination and substitution reactions. This is visualized with green and blue arrows, respectively, in Figure 2. In this way, the symmetry of the octahedral precursors in methanol solution, $[CoL_6]^{2+}$, with L simple ligands like aqua, methanol, and/or NO_3^-, is lowered by two mechanisms during the nucleation process. On the one hand, some of the ligands are substituted with imidazole; on the other hand, some of them are eliminated. The complex

Received: July 7, 2022
Published: December 15, 2022

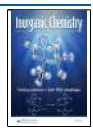

https://doi.org/10.1021/acs.inorgchem.2c02358
Inorg. Chem. 2022, 61, 20743−20756

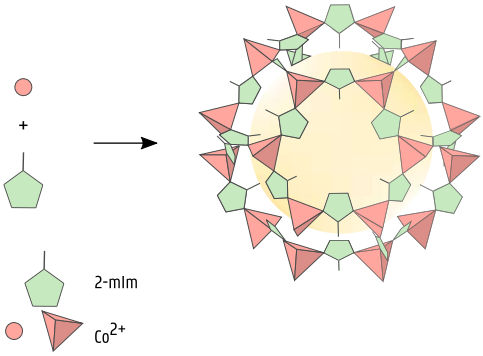

Figure 1. Crystal structure of Co-ZIF-67. Co^{2+} is indicated with a circle when it is isolated and with a tetrahedron when coordinated with the 2-mIm linkers. Figure adapted from ref 20 with permission of Elsevier, 2015.

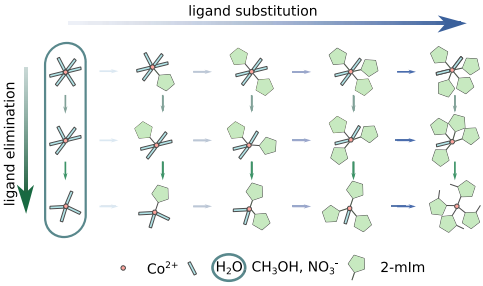

Figure 2. Reaction network of ligand elimination and substitution reactions leading to fast preequilibrium formation toward a metal−organic pool. Co^{2+} complexes with six, five, and four aqua ligands are studied in this work and are indicated. Figure adapted from ref 24 with permission of Elsevier, 2021.

thus goes from $[CoL_6]^{2+}$, an octahedral system with six simple ligands, over a five-coordinated system, toward $Co(2\text{-mIm})_4^{2-}$, a tetrahedral complex with four 2-mIm ligands, which are the building blocks of Co-ZIF-67. To fully understand this complicated mechanism, we would like to follow the evolution of the UV−vis spectrum, and more specifically, of the d−d transitions, as the number of them and the intensity with which they occur change during the course of the formation process and can therefore serve as a fingerprint for the crystal formation process. An excellent recent review on computational molecular spectroscopy can be found in ref 25.

In this work, we investigate six-coordinated octahedral, five-coordinated square pyramidal (SP), five-coordinated trigonal bipyramidal (TBP), and four-coordinated tetrahedral Co^{2+} complexes, as shown in Figure 2. We restrict ourselves to aqua ligands as, in particular for hexa-aqua Co^{2+} complexes, we can compare our results to previous studies. We will concentrate on the ground-state properties as they need to be described correctly and understood completely before an investigation of the excited states can be started. The ground-state properties of TMCs still pose various challenges as for example recently shown in refs 26 and 27 for the calculation of spin-state energetics.

As stated before, octahedral Co^{2+} aqua-complexes have already been extensively studied in the literature. Structural properties and excitation energies have been obtained from experimental studies.[28−33] Besides this, $[Co(H_2O)_6]^{2+}$ has also been the subject of many computational investigations as it can serve as a model system for much more complicated Co^{2+} complexes, and, due to its small size, direct comparisons to highly correlated *ab initio* calculations are feasible.[34] A detailed review of the ground-state properties using a wide variety of computational methods has been given in ref 35. More recent works also investigate the excited states but this lies outside the scope of this work.[36−39] These complexes have also already been investigated using multireference *ab initio* calculations where solvent effects have been included.[40]

In the present study, we will extend the computational results by examining the electronic structure of these complexes, and more specifically, we will focus on the influence of symmetry on the position of the energy levels of the d-orbitals as this is decisive for the d−d transitions. There are two origins for the changes in symmetry. First of all, large influences are expected when the number of ligands is changed, resulting in various coordination environments, *i.e.*, octahedral,

Table 1. Overview of the Complexes Studied in This Work, Ordered Based on Their Number of Aqua Ligands[a]

Number of aqua ligands	Symmetry	Visualisation of geometry	Elements studied
6	Octahedral		Co^{2+}, V^{2+}, Mn^{2+}, Ni^{2+}
5	Square pyramidal (SP)		Co^{2+}
	Trigonal bipyramidal (TBP)		Co^{2+}
4	Tetrahedral		Co^{2+}

[a]For every system, both AOC and UDFT calculations are performed. Experimental data are available for the six-coordinated complexes.

https://doi.org/10.1021/acs.inorgchem.2c02358
Inorg. Chem. 2022, 61, 20743−20756

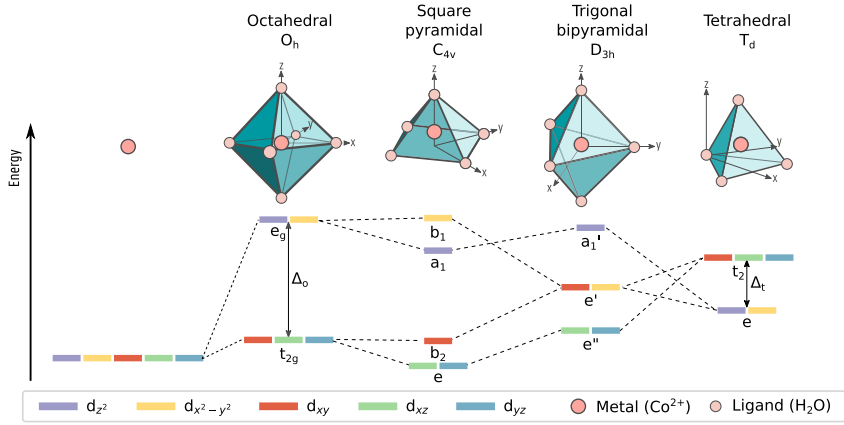

Figure 3. Splitting of the d-orbitals for a TM in various environments. For an isolated TM, all d-orbitals are degenerate, whereas for complexes with octahedral, SP, TBP, and tetrahedral symmetry, the degeneracy is (partially) lifted. The splitting between the two orbital sets in octahedral and tetrahedral complexes is denoted by Δ_o and Δ_t, respectively. The labeling of the d-orbitals in the various point groups is also indicated.

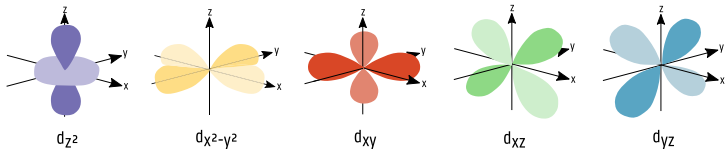

Figure 4. Graphical visualization of the five d-orbitals: d_{z^2}, $d_{x^2-y^2}$, d_{xy}, d_{xz}, and d_{yz}.

SP, TBP, and tetrahedral. Furthermore, additional effects will be studied for the various point groups encountered for each coordination environment as we will note that deviations from the perfect symmetry are present. We will search for, and find, stable structures which are capable of reproducing the experimental data. Furthermore, we will explore how the properties of these complexes change when one and two of the aqua ligands are removed and how this reduction in symmetry is translated in alternations of the d-orbital splitting. To validate our results, we will make comparisons with experimental data where possible.

The remainder of this work is organized as follows. First, we focus on the qualitative predictions for the d-orbital splitting in various coordination symmetries obtained from theoretical techniques such as crystal field theory (CFT), ligand field theory (LFT), and the angular overlap method (AOM). In the next section, the results from density functional theory (DFT) calculations, both average of configuration (AOC) and unrestricted density functional theory (UDFT), are discussed. The molecular orbitals (MOs) with large contributions from d-orbitals will be studied in-depth and more particular, we will concentrate on the influence of symmetry on the splitting of these orbitals. We will determine which technique is suited to correctly describe the ground-state properties of these transitions metal complexes (TMCs). Besides Co^{2+}, we will also investigate other transition metals, V^{2+}, Mn^{2+}, and Ni^{2+}, the d-orbital splitting of which poses less challenges, as will be explained in Section 3.6. In the final section, we conclude with the main outcomes obtained in this study. An overview of the systems studied in this work is given in Table 1.

2. QUALITATIVE INSIGHTS INTO THE D-ORBITAL SPLITTING *VIA* CFT, LFT, AND AOM

In the past century, several theoretical models have been introduced to describe the electronic structure of TMCs, which are still extensively used. First, Becke and Van Vleck applied the CFT, which already existed for the description of metal ions in crystals, to isolated TMCs.[41−43] In this electrostatic approach, ligands are approximated by point charges. The metal d-orbitals pointing toward the ligands will raise in energy due to electrostatic repulsion, whereas the d-orbitals directed between the ligands remain relatively unaffected. As such, this approach predicts the d-orbital splittings in coordination complexes with various symmetries. However, as this method does not describe metal−ligand bonding, LFT, combining CFT and molecular orbital theory (MOT), has been introduced by Griffith and Orgel.[44] It describes the interactions between metal and ligand frontier orbitals which are responsible for the formation of MOs. Additionally, the AOM takes into account the angular geometry of the complex and estimates the strength of interaction between individual ligand orbitals and metal d-orbitals based on their mutual overlap.[45,46] The benefit of this technique is that it is capable of treating systems with little or no symmetry. This comes at the cost of the large number of parameters to be determined from experiment.[47] These models present different approaches to solve the electronic structure of TMCs and all have their advantages and disadvantages, but in general, they give the same qualitative results. These methods can be made quantitative by determining the parameters from

https://doi.org/10.1021/acs.inorgchem.2c02358
Inorg. Chem. 2022, 61, 20743−20756

experimental absorption spectra. However, we will not focus on this and only give a qualitative explanation of the results as shown in Figure 3 for complexes with various symmetries.

For an isolated TM ion, all five d-orbitals are degenerate, *i.e.*, d_{z^2}, $d_{x^2-y^2}$, d_{xy}, d_{xz}, and d_{yz}, indicated in purple, yellow, red, green, and blue, respectively, and have the same energy. A graphical visualization of these orbitals is shown in Figure 4. Two of them, *i.e.*, d_{z^2} and $d_{x^2-y^2}$, have lobes that are oriented along the coordinate axes, whereas the lobes of the other orbitals are situated in between the coordinate axes. As will be discussed later, the orientation plays an important role when coordinating with ligands. When the TM atom is surrounded by ligands, the average energy of the five d-orbitals is above that of the free ion orbitals because of the electrostatic field generated by the ligands. Furthermore, the degeneracy of the d-orbitals is (partially) lifted. This will be studied in the subsequent paragraphs for six-, five-, and four-coordinated complexes.

Octahedral complexes have six ligands positioned along the coordinate axes and situated at the corners of an octahedron with the TM in the center, as shown in Figure 3. The degeneracy of the d-orbitals is raised partially as they split in two degenerate orbital sets: t_{2g} and e_g; d_{z^2} and $d_{x^2-y^2}$ with lobes directed toward the ligands are raised in energy by the electrostatic repulsion between the electrons of the TM and the ligands and form the e_g set. The t_{2g} set contains d_{xy}, d_{xz}, and d_{yz}, with lobes oriented in between the ligands, and therefore, they remain relatively unaffected. The energy gap between these two sets is indicated in Figure 3 by Δ_o, where the subscript o denotes that this is the splitting for octahedral complexes. When we assume that the ligands are spherical symmetric, the corresponding symmetry is octahedral, O_h. However, as will be seen later, the symmetry will be lowered for aqua ligands.

When removing one ligand, a distinction needs to be made between the removal of a ligand oriented along the *z*-direction or one lying in the *xy*-plane. When one of the ligands along the *z*-direction is eliminated, the SP structure, which belongs to the C_{4v} point group, is obtained; d_{z^2}, d_{xz}, and d_{yz} are stabilized, compared to the octahedral case, as the repulsive interaction between the orbitals and one of the ligands on the *z*-axis is now no longer present. When one of the ligands in the *xy*-plane is removed, the TBP structure, belonging to D_{3h}, is retrieved. As opposed to the octahedral complex, d_{xy} and $d_{x^2-y^2}$ are increased/decreased in energy, respectively, because they point more/less toward the ligands. The application of the AOM shows that the overall splitting of the *d*-orbitals is smaller in D_{3h} than in C_{4v} symmetry.[48] The labeling of the orbital sets in these point groups is indicated in Figure 3.

When, starting from the TBP structure, another ligand is taken out along the *z*-axis, we obtain a tetrahedral structure with T_d symmetry, in which the ligands are situated in between the coordinate axes and at the origin. In contrast to the octahedral complex, d_{xy}, d_{xz}, and d_{yz}, grouped in t_2, now point toward the ligands, whereas $d_{x^2-y^2}$ and d_{z^2}, forming the *e* set, are situated in between the ligands. Therefore, the *e* set is more stable in comparison with the t_2 set. In a similar way as for the octahedral complexes, we can define Δ_t, the splitting between the t_{2g} and e_g orbitals. Δ_t is smaller compared to the octahedral case since the ligands are not oriented directly toward the d-orbitals and therefore the effects will be smaller. This is in agreement with AOM calculations, which show that $\Delta_t \approx \frac{4}{9}\Delta_o$.[49]

These d-orbital splittings are in accordance with the LFT results of Solomon et al.,[50] who studied six-, five-, and four-coordinated Fe^{2+} complexes with oxygen-type ligands.

As stated before, quantitative d-orbital splittings can be obtained from techniques such as LFT using experimental input data. However herein, we will perform computational calculations based on DFT to acquire quantitative d-orbital splittings for Co^{2+} aqua-complexes, as will be discussed in Section 3. As a consequence, we will perform computational calculations to obtain qualitative results for Co^{2+} aqua-complexes, as will be discussed in Section 3. These *ab initio* results can then be compared to the theoretical predictions shown in Figure 3 and to the available experimental information.

3. QUANTITATIVE *AB INITIO* CALCULATIONS: AOC AND UDFT

In this section, the computational techniques used to study Co^{2+} complexes with six, five, and four aqua ligands are explained. The results are analyzed and compared to the qualitative outcomes shown in Figure 3. Before diving into this, attention is paid to the different spin multiplicities Co^{2+} ions can possess.

The Co^{2+} ion has seven d-electrons, which can be placed in five d-orbitals. There are two possible spin multiplicities, 4 and 2, forming the high-spin (HS) and low-spin (LS) configurations, respectively. In the former, as much as possible electrons are unpaired, whereas in the latter, only 1 unpaired electron is present. According to the spectrochemical series, water is a weak ligand.[51] Therefore, Δ_o in octahedral complexes is rather small and the energy needed to pair two electrons is larger than the energy required to place an electron in the higher-lying e_g set. Hence, the HS state of $[Co(H_2O)_6]^{2+}$ is more stable, resulting in five α- and two β-electrons. This is also in agreement with the DFT study on relative stabilities reported in ref 52. Moreover, since $\Delta_t < \Delta_o$, we can conclude that the HS configuration of the tetrahedral complex will also be more stable than the LS state. Finally, it has also been observed that, in five-coordinated complexes, ligands with oxygen donor atoms usually result in HS configurations.[53,54]

In this work, two types of calculations have been performed, AOC and UDFT, both based on DFT. In AOC, a spin-restricted self-consistent field (SCF) DFT calculation of the d^7 configuration is performed, in which the d-electrons are distributed evenly among the five MOs dominated by d-orbitals. This results in an average occupation of 1.4 electrons. One thus allows systems with fractional occupation numbers. Indeed, one of the great advantages of DFT is, as it is based on the electron density, that there is no formal constraint that orbitals must have integer occupations.[55] Remark that the spin multiplicity is not imposed in these calculations. Meanwhile, in UDFT, the spin multiplicity is specified and all of the five α-orbitals are filled, whereas only two β-orbitals are occupied.

In the following, the AOC results are discussed in detail for $[Co(H_2O)_6]^{2+}$, $[Co(H_2O)_5]^{2+}$, and $[Co(H_2O)_4]^{2+}$. We systematically investigate how the lowering of the number of ligands affects the symmetry and thus the geometry and electronic structure of these Co^{2+} complexes. This is followed by a comparison between AOC and UDFT. As outlined in the

https://doi.org/10.1021/acs.inorgchem.2c02358
Inorg. Chem. 2022, 61, 20743−20756

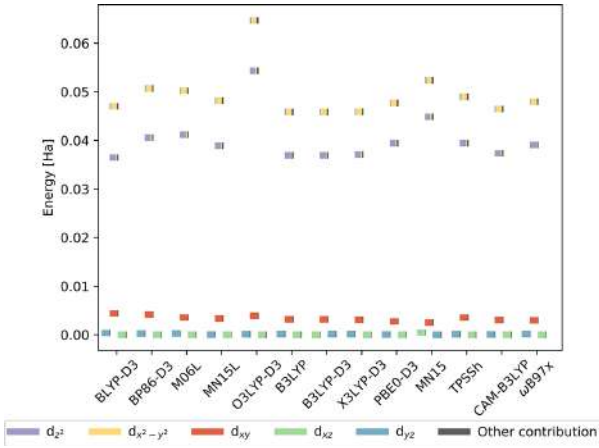

Figure 5. Splitting of the d-orbitals along with their atomic contributions for $[Co(H_2O)_6]^{2+}$ with D_{2h} symmetry obtained from AOC calculations. Different functionals have been used for the geometry optimizations as displayed on the horizontal axis. For the AOC calculations, Grimme D3 dispersion corrections have not been included since they only affect the geometry but not the orbital energies. Energies are shifted with respect to the lowest d-orbital.

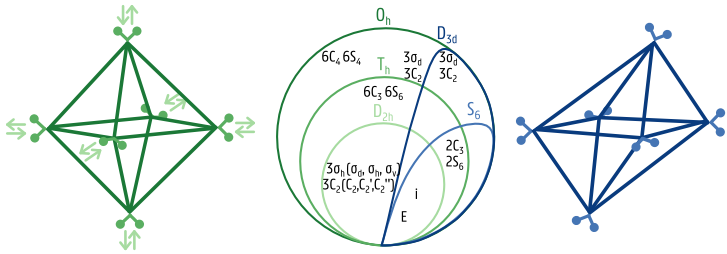

Figure 6. Graphical visualization of the point groups encountered for the six-coordinated complexes, *i.e.*, O_h, T_h, D_{2h}, D_{3d}, and S_6. In the middle pane, all symmetry elements enclosed belong to the corresponding point group. Perfect octahedral symmetry, O_h is indicated in dark green. The presence of hydrogen atoms reduces the symmetry to T_h and is indicated in middle green. Elongation or contraction of the metal−ligand bonds results in D_{2h} symmetry and is shown in light green. An increase or decrease of the ligand−metal−ligand angles leads to a tilted structure with D_{3d} symmetry and is presented in dark blue. When the hydrogen atoms are taken into account in the tilted structure, the S_6 symmetry is obtained as shown in light blue.

Section 3.1, optimized structures have been obtained using UDFT.

3.1. Computational Details. The calculations, both AOC and UDFT, were performed with the Amsterdam modeling suite (AMS).[56] The TZ2P+ basis set, with extra d-Slater type orbitals (STO), has been applied for the transition metals, and the TZ2P basis set has been used for the other elements. Methanol has been included as a solvent using COSMO.[57] Radoń et al. recently revealed that the inclusion of the second solvation shell is important to properly determine the exited states of octahedral aqua-complexes.[40] However, for the aqua-complexes studied in this work, the environment is more complex and consists of both water and methanol to mimic the experimental conditions valid in the formation of ZIFs. A full study of the influence of the complex solvation environment on the chemical and electronic properties of the aqua-complexes is beyond the scope of this article since here we focus on the influence of reducing the number of aqua ligands directly coordinated to the transition metal. Scalar relativistic effects were taken into account using the ZORA formalism.[58−60] Grimme D3 dispersion corrections, which affect the geometry but not the orbital energies, have also been added.[61] We have made use of several functionals coming from different rungs on Jacob's ladder to test their performance in reproducing the d-orbital splitting of $[Co(H_2O)_6]^{2+}$ with D_{2h} symmetry, which will be explained in Section 3.2, using AOC calculations. We assessed the following functionals: BLYP[62] and BP86[63] based on the generalized gradient approximation (GGA), M06L[64] and MN15L[65] built on the meta GGA (mGGA), O3LYP,[66] B3LYP,[62,67] X3LYP,[68] PBE0,[69] and MN15[70] as hybrid GGA, with 12, 20, 21.8, 25, and 44% of Hartree−Fock exchange, the hybrid mGGA TPSSh[71,72] with 10% Hartree−Fock exchange, and the long-range corrected CAM-B3LYP[73] and ωB97x.[74] The results are shown in Figure 5. It stands immediately out that not enough Hartree−Fock exchange is included in O3LYP, for which the splitting between the e_g and t_{2g} set is too large. All other functionals have similar results. We have chosen to continue with B3LYP-D3.

https://doi.org/10.1021/acs.inorgchem.2c02358
Inorg. Chem. 2022, 61, 20743−20756

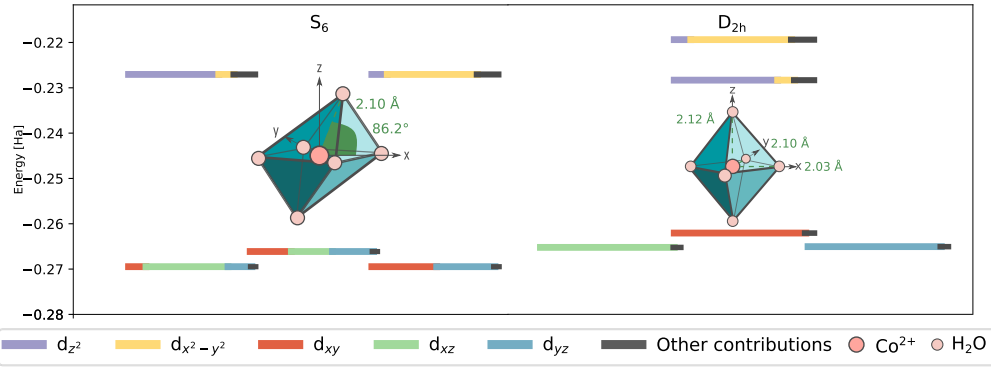

Figure 7. Splitting of the d-orbitals along with their atomic contributions for the optimized $[Co(H_2O)_6]^{2+}$ complexes with S_6 (left) and D_{2h} (right) symmetry. Some bond lengths [Å] and bond angles [deg] are also indicated.

Geometry optimizations have been performed using UDFT. We checked that all computed internal normal modes of the optimized structures show positive frequencies, ensuring that the geometries represent minima of the ground-state potential energy surface. The optimized coordinates of all complexes studied in this work are shown in Table S6. The spin contamination is negligible for all systems as shown in Table S1. The symmetry of the complexes has been determined by GaussView 5.0.[75]

Using the single-reference UDFT method for these challenging electronic structure systems may at first instance appear to be unsatisfactory. However, Shee et al. have recently put forward that in most transition-metal complexes, static correlation is rarely found in the ground states of mono-TMCs.[76] Furthermore, it has been shown that often good structures and energies are obtained from DFT calculations at a moderate computational cost.[77] Hence, we chose DFT to describe the ground-state properties of these systems. Nevertheless, as there are complex interactions present, including ligand-to-metal σ-donation and metal-to-ligand π-backdonation, proper treatment of the dynamic correlation becomes extremely important.

3.2. AOC: $[Co(H_2O)_6]^{2+}$. Octahedral TMCs belong to the O_h point group when the ligands have spherical symmetry. However, when we take into account the structure of the aqua ligands, the highest possible symmetry becomes T_h, with six equivalent ligand bond distances and all O−Co−O angles equal to 90 or 180°. A graphical visualization of the symmetry elements present in the point groups encountered for $[Co(H_2O)_6]^{2+}$ is presented in Figure 6. The geometrical structure of $[Co(H_2O)_6]^{2+}$ has already been investigated thoroughly in the literature. DFT studies have been performed by both Varadwaj et al.[35] and Schmiedekamp et al.[52] Calculations have been performed at the following levels of theory, respectively: UX3LYP and UB3LYP with a 6-311++G** full core basis set and B3LYP with LACVP** effective core potential basis set for Co and 6-31G** basis for all other atoms. Varadwaj et al. compared their results with 163 structures containing the $[Co(H_2O)_6]^{2+}$ ion found in the Cambridge structural database (CSD).[78] Most of the structures, 122 out of the 163 found in the CSD, have three different pairs of bond lengths, the shortest, intermediate, and longest bonds are 2.06 ± 0.02, 2.09 ± 0.02, and 2.11 ± 0.02 Å, respectively. Overall, a mean Co−O bond length of 2.09 ± 0.03 Å is found, with the shortest and longest values equal to 1.975 and 2.204 Å, respectively. Based on the computational results of Varadwaj[35] and Schmiedekamp,[52] three main conclusions can be made. First, the calculations overestimate the Co−O bond lengths by 0.04[35] and 0.06 Å,[52] respectively. Second, unless the geometry is specifically constrained, the distortions in the Co−O bond lengths present in most crystallographically determined structures are not reproduced. Varadwaj et al. have observed a structure with distorted bond lengths; however, it is a fourth-order saddle point. Third, the structure is slightly tilted. This effect is also observed in the solid-state structures: 74% of the structures found in the CSD have complementary angles that differ by more than 4° and nearly 12% have complementary angles differing by more than 10°. Note that Varadwaj[35] performed gas-phase calculations, whereas Schmiedekamp[52] also studied the influence of water as a solvent.

In contrast to the results of Varadwaj and Schmiedekamp, we did not find a stable minimum near to T_h symmetry as negative vibrational frequencies were observed. This is in agreement with the Jahn−Teller (JT) effect, which states that nonlinear molecules with a spatially degenerate electronic ground state undergo a geometrical distortion to lower the energy of the system.[79] Despite the fact that only weak JT effects are expected since the t_{2g} orbitals are unevenly occupied, we observed them in the geometry optimizations. We could identify an optimized structure with D_{2h} symmetry, in which the experimentally observed JT distorted bond lengths are clearly retrieved. The observed bond lengths of the complex with D_{2h} symmetry are 2.03, 2.10, and 2.13 Å. The resulting geometric structure along with the *d*-orbital splitting and atomic contributions is shown in Figure 7(right). This deformed structure is obtained *via* a rhombic distortion, *i.e.*, an unequal amount of elongation or compression along a fourfold axis of rotation. As such, the structure remains orthogonal, but the bond distances are no longer equal. Such JT distorted $[Co(H_2O)_6]^{2+}$ complexes have already been observed by Vlahovic et al.[39] Following the methodology of Zlatar et al., we calculated the JT parameters.[80,81] The results are shown in Table S2. Besides this, we also discovered a structure with S_6 symmetry, acquired *via* a trigonal distortion of the complex, *i.e.*, an elongation/compression along one of the four threefold

https://doi.org/10.1021/acs.inorgchem.2c02358
Inorg. Chem. 2022, 61, 20743−20756

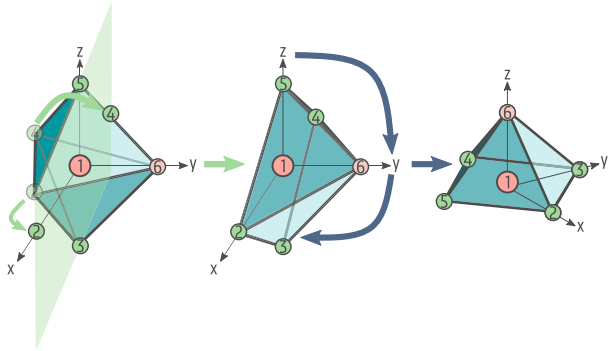

Figure 8. Transformation from a TBP to an SP complex. Ligand positions 2 and 4 are moved until they are situated along the *x*-axis and from together with 3 and 5 a square in the *xz*-plane indicated in green. This is indicated with green arrows. The SP structure is then obtained after a reorientation of the coordinate axes, indicated with blue arrows.

symmetry axes. All ligand bond distances are equal, but the structure is no longer orthogonal. Such distorted complexes have D_{3d} symmetry when the hydrogen atoms are not taken into account. For the complex with S_6 symmetry, all bond lengths are 2.10 Å and the system is tilted at 3.8°. This is shown in Figure 7 (left). This complex is slightly more stable than the complex with D_{2h} symmetry (−10 328 kJ/mol in contrast to −10 311 kJ/mol). The observed point groups along with their symmetry elements are displayed in Figure 6. The coexistence of two different distorted octahedral complexes has already been observed in $K_3[MnF_6]$.[82]

The splitting of the d-orbitals is very similar to the theoretical predictions shown in Figure 3. Some mixing with other contributions different from d-orbitals occurs, which is indicated by dark gray. In general, each MO has a dominant contribution from a specific d-orbital. This can then be used to label the MOs. This is especially the case for the complex with D_{2h} symmetry. The resulting orbitals are shown in Figure S1 and closely resemble those in Figure 4. However, there is more mixing within the t_{2g} and e_g set for the S_6 complex, for which the orbitals are shown in Figure S2. For example, the highest-lying t_{2g} orbital, which contains equal contributions from d_{xy}, d_{xz}, and d_{yz}, differs from the orbitals shown in Figure 4, but the lobes are still oriented in between the coordinated axis. Therefore, the more general label t_{2g} is more convenient. The orbitals in the t_{2g} set are no longer completely degenerate. This is probably due to the presence of contributions different from d-orbitals. This is in agreement with CFT, which reveal that a trigonal distortion splits the t_{2g} but not the e_g orbitals in octahedral complexes.[83] For the D_{2h} complex, also the degeneracy in the e_g set is lifted. The reason for this is that the bonds between the ligands and the metal along the *x*-axis are compressed, resulting in a stronger repulsion between the $d_{x^2-y^2}$ orbital and the metal compared to the d_{z^2} orbital.

The energy difference between the e_g and t_{2g} orbital sets, Δ_o, can be calculated as the difference between the average energy of the e_g and t_{2g} orbitals, being 9065 and 8836 cm^{-1} for the S_6 and D_{2h} structures, respectively. This value is in close agreement with experimental results. Johnson et al.[84] obtained a value of 8400 cm^{-1} starting from experimental absorption spectra *via* the procedure outlined in ref 85. When comparing this value to the mean pairing energy of Co^{2+}, 22 500 cm^{-1}, we indeed see that the HS state is more stable than the LS state.[49,84]

3.3. AOC: $[Co(H_2O)_5]^{2+}$. As discussed in Section 2, five-coordinated complexes can be TBP or SP, with D_{3h} and C_{4v} symmetry, respectively. For the former, two ligands are oriented along the *z*-axis and the other ligands lie in the *xy*-plane. This configuration can be converted into an SP structure by simple angular distortions, as shown by the green arrows in Figure 8. When the angle between the ligand positions 2 and 4 and the metal center is increased until the ligands lie along the *x*-axis, they form together with 3 and 5 a square in the *xz*-plane indicated with green. As such, the SP structure is obtained, which can easily be recognized after a reorientation of the coordinate axes, indicated with blue arrows in Figure 8. Now, four ligands lie in the *xy*-plane and the remaining ligand is situated along the *z*-axis. The metal center can, but does not have to be in the *xy*-plane. It has been observed that most of the five-coordinated complexes are neither perfectly TBP, nor perfectly SP, but are situated somewhere in between.[53]

When the intrinsic structure of the aqua ligands is taken into account, the most symmetric $[Co(H_2O)_5]^{2+}$ complexes have C_{2v} symmetry, both for the TBP and SP structures. Optimized geometries have been found with C_{2v} and C_1 symmetries, for which the latter is slightly more stable (−8600 kJ/mol in contrast to −8614 kJ/mol). A graphical representation of the symmetry elements and point groups encountered for $[Co(H_2O)_5]^{2+}$ is shown in Figure 9. Structural parameters of the two optimized complexes are listed in Table 2.

We performed continuous shape measurements (CShMs), which evaluate the magnitude of distortion around the metal ion in various complexes,[86,87] to determine whether the complexes are closer to the SP or TBP symmetry. The resulting continuous shape measures (CShMs) for all five possible geometries for five-coordinated structures are given in Table S4, both for the C_{2v} and C_1 complexes. From this, we concluded that the C_{2v} structure is closer to SP, whereas the C_1 structure is closer to TBP. Thus, the TBP complex is a little bit more stable than the SP one. This is in agreement with the literature, where it has been shown that the TBP structure is more stable as there is less ligand−ligand repulsion.[88] However, it has been noted that a distorted SP structure may be only slightly less stable.[88]

https://doi.org/10.1021/acs.inorgchem.2c02358
Inorg. Chem. 2022, 61, 20743−20756

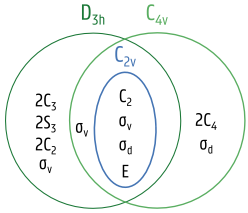

Figure 9. Graphical visualization of the point groups encountered for the five-coordinated complexes, *i.e.*, D_{3h}, C_{4v}, and C_{2v}. All symmetry elements enclosed belong to the corresponding point group.

Table 2. *d*-Orbital Splitting of $[V(H_2O)_6]^{2+}$, $[Mn(H_2O)_6]^{2+}$, and $[Ni(H_2O)_6]^{2+}$ Calculated Using AOC and UDFT[a]

	$[V(H_2O)_6]^{2+}$	$[Mn(H_2O)_6]^{2+}$	$[Ni(H_2O)_6]^{2+}$
AOC	11 883	8104	10 092
UDFT	43 359	8868	52 155
experiment[49]	12 300	7850[b]	8600

[a]The experimental value is also included. [b]Estimated value.

The splitting of the d-orbitals along with the atomic contributions is presented in Figure 10, both for the SP and TBP complexes. Again, each MO has a dominant contribution from a specific d-orbital, which will be used to label the MOs. The orbitals are shown in Figures S3 and S4. In general, the results are in agreement with the theoretical predictions shown in Figure 3, but some differences should be mentioned. The gap between the $d_{x^2-y^2}$ and d_{z^2} orbitals is rather large for the SP complex. Furthermore, d_{xz} and d_{yz} are not completely degenerate. This is not surprising since the complex only has C_{2v} symmetry and not C_{4v}, for which the results are shown in Figure 3. The degeneracy is also lifted for the TBP complex as d_{xz}/d_{yz} and $d_{x^2-y^2}/d_{xy}$ are no longer degenerate.

3.4. AOC: $[Co(H_2O)_4]^{2+}$. When another ligand is removed, $[Co(H_2O)_4]^{2+}$ complexes are obtained, in which the aqua ligands are situated at the corners of a tetrahedron. When the intrinsic structure of the aqua ligands is taken into account, the most symmetric complexes have D_{2d} symmetry, unlike the T_d symmetry which is found for point-like ligands. In our calculations, the optimized structure does not possess any symmetry. The symmetry elements and point groups encountered for $[Co(H_2O)_4]^{2+}$ are represented graphically in Figure 11. Structural parameters are listed in Table S5.

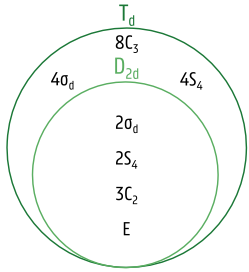

Figure 11. Graphical visualization of the point groups encountered for the four-coordinated complexes, *i.e.*, T_d and D_{2d}. All symmetry elements enclosed belong to the corresponding point group.

The splitting of the d-orbitals and the atomic contributions are shown in Figure 12, and the orbitals are presented in Figure

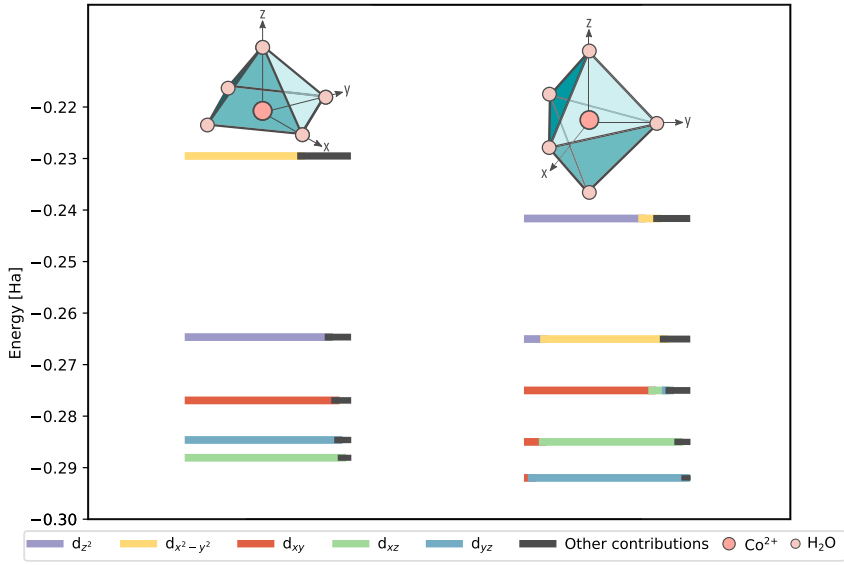

Figure 10. Splitting of the d-orbitals along with their atomic contributions for the optimized $[Co(H_2O)_5]^{2+}$ complexes with C_{2v} symmetry (left) and no symmetry (right).

https://doi.org/10.1021/acs.inorgchem.2c02358
Inorg. Chem. 2022, 61, 20743−20756

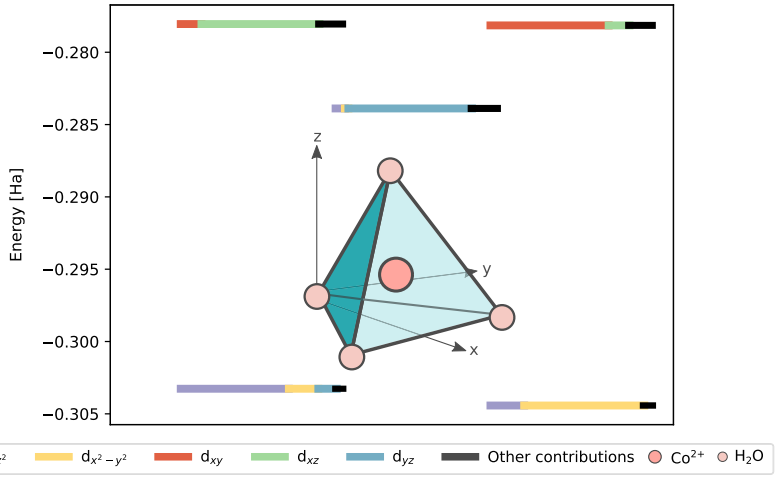

Figure 12. Splitting of the d-orbitals along with their atomic contributions for the optimized $[Co(H_2O)_4]^{2+}$ complex.

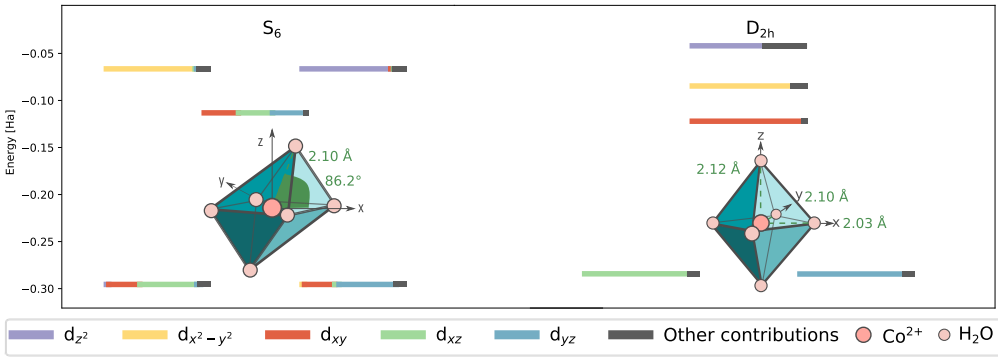

Figure 13. Splitting of the d-orbitals for the optimized $[Co(H_2O)_6]^{2+}$ complexes with S_6 (left) and D_{2h} (right) symmetry calculated by UDFT. Some bond lengths [Å] and bond angles [deg] are also indicated.

S5. The results are in good agreement with these obtained in Figure 3: two orbital sets can be distinguished, t_{2g} and e_g, where the former is less stable than the latter. Due to the fact that the complex is not purely tetrahedral, the degeneracy in the t_{2g} set is lifted slightly. Furthermore, the computed value of Δ_t is 5161 cm^{-1}, which is much smaller than Δ_o, as we expected from AOM.

3.5. Comparison of AOC with UDFT. We compared the AOC results with those from UDFT calculations. The β d-orbital energy levels along with their atomic contributions are shown in Figure 13 for $[Co(H_2O)_6]^{2+}$, as calculated with UDFT. The orbitals are presented in Figures S6 and S7 for completeness. Some major distinctions in comparison with the AOC results need to be highlighted. First of all, we remark that the splitting of the d-orbitals, 50 288 and 53 232 cm^{-1} for S_6 and D_{2h}, respectively, is 1 order of magnitude larger than that for the AOC results and the experimentally found splitting presented in Section 3.2. Second, the t_{2g} set is divided into two low-lying orbitals and one orbital, which is higher in energy. The reason for this is that only two of the β d-orbitals are occupied, resulting in a gap between the highest occupied MO (HOMO) and the lowest unoccupied MO (LUMO).

Additionally, in the UDFT results of the D_{2h} complex, d_{z^2} is higher in energy than $d_{x^2-y^2}$, compared to the AOC results. An explanation for this observation is that UDFT and LFT treat the interelectron repulsion differently, as argued by Deeth et al. for square-planar d^8 Pd complexes.[89] The interelectron repulsion effects are included within a central field approximation in LFT, whereas in UDFT, no central field is assumed and the calculations are performed using the true molecular symmetry of the complex.[89] Therefore, on the one hand, the LFT predictions are in agreement with the AOC results, in which approximate spherical states are constructed by imposing equal fractional occupations. On the other hand, as in the UDFT approach only d_{yz} and d_{xz} are occupied, there is more interelectron repulsion along the z-axis than along the x- or y-axis. Therefore, d_{z^2} will be higher in energy than $d_{x^2-y^2}$. Inspired by the work of Deeth et al., we verified this by

https://doi.org/10.1021/acs.inorgchem.2c02358
Inorg. Chem. 2022, 61, 20743−20756

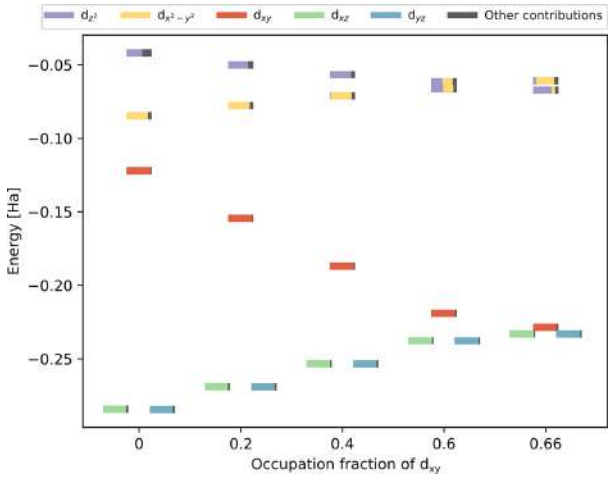

Figure 14. Variation of the splitting of the d-orbitals as a function of the electron occupation fraction of d_{xy} which is transferred equally from d_{xz} and d_{yz} for the $[Co(H_2O)_6]^{2+}$ complex with D_{2h} symmetry.

systematically removing some portion of the electrons from d_{xz} and d_{yz} and placing it on d_{xy}. Therefore, single-point UDFT calculations in which the occupation of the d-orbitals is specified are performed. The results are shown in Figure 14. Two observations can be made as more and more of the electrons initially on d_{xz} and d_{yz} are transferred to d_{xy}. First of all, the orbitals become closer in energy and are almost degenerate when 0.66 of an electron is placed at d_{xy}. The reason for this is that the two β electrons are now almost equally divided among the three orbitals, resulting in a similar interelectron repulsion along the *x*-, *y*-, and *z*-axes. Second, as more of the electrons is transferred, d_{z^2} and $d_{x^2-y^2}$ increase and decrease in energy, respectively. At an occupation of 0.6 electrons for d_{xy}, the two most energetic orbitals presented in Figure 14 have similar contributions of d_{z^2} and $d_{x^2-y^2}$ and are almost degenerate. When d_{xy} is populated even more, $d_{x^2-y^2}$ becomes higher in energy than d_{z^2}.

In the UDFT results for the S_6 complex, the $d_{x^2-y^2}$ and d_{z^2} orbitals are degenerate just like in the AOC results. Indeed, the effect of the difference in interelectron repulsion is smaller as the two occupied d-orbitals do not only have contributions from d_{yz} and d_{xz} but also from d_{xy}. This is shown in Figure S8. As the population of the initially nonoccupied orbital increases, the orbitals with contributions from d_{xy}, d_{xz}, and d_{yz} become more and more degenerate. However, the energy and contribution of the $d_{x^2-y^2}$ and d_{z^2} orbitals remain similar.

Deviations from the theoretically predicted *d*-orbital splittings are also observed in the five-coordinated complexes as shown in Figure S9. For both SP and TBP, the energy splitting is 1 order of magnitude larger compared to the AOC calculations. Furthermore, in the SP complex, $d_{x^2-y^2}$ and d_{z^2} are interchanged and are almost degenerate. Again, this is due to the different treatment of interelectron repulsion in LFT and UDFT. In the latter, only d_{xz} and d_{yz} are occupied, resulting in more interelectron repulsion along the *z*-axis, therefore d_{z^2} being higher in energy than $d_{x^2-y^2}$. Figure S10 justifies this statement: when d_{xy} is occupied by more than 0.2 electron, $d_{x^2-y^2}$ is higher in energy than d_{z^2}. The order of d_{z^2} and $d_{x^2-y^2}$ in the TBP complex is in accordance with the AOC results. Just like for the $[Co(H_2)O_6]^{2+}$ complex with S_6 symmetry, this is due to the mixed d-orbital contributions of the two lowest occupied MOs. Figure S11 indeed reveals that the orbital energies of the d_{z^2} and $d_{x^2-y^2}$ vary only slightly with the orbital population of d_{xy}.

For the four-coordinated complexes, presented in Figure S12, the two lowest β e-orbitals are occupied, and therefore, the splitting is in accordance with the AOC and theoretical results. Nevertheless, the energy gap between the e- and t_2-set is still 1 order of magnitude too large.

As stated in ref 89, the observation that UDFT and AOC result in different d-orbitals does not necessarily mean that one of these techniques is right, whereas the other is wrong. Orbitals themselves are not experimentally observable, and therefore, additional properties need to be calculated, like, for example, excited states.[89] The excitations of six-coordinated Co^{2+} aqua-complexes have already been the subject of much research.[36−40] However, to the best of our knowledge, similar studies for five- and four-coordinated complexes are not presented yet.

3.6. $[V(H_2O)_6]^{2+}$, $[Mn(H_2O)_6]^{2+}$, and $[Ni(H_2O)_6]^{2+}$. To further test the validity of the UDFT calculations, additional calculations have been performed on $[V(H_2O)_6]^{2+}$, $[Mn(H_2O)_6]^{2+}$, and $[Ni(H_2O)_6]^{2+}$, having three, five, and eight d-electrons, respectively. These transition metals have been selected as the t_{2g} set is now completely filled with α electrons for V^{2+} and Mn^{2+} or β electrons for Ni^{2+}. This is in contrast to the partially filled t_{2g} set in $[Co(H_2O)_6]^{2+}$ containing two β electrons. As such, no JT effects are expected for these systems since the e_g and t_{2g} sets are each evenly occupied. This is also observed from the calculations for the V^{2+} and Ni^{2+} complexes as stable complexes with T_h symmetry are retrieved. However, this is not the case for the Mn^{2+} complex, for which the most symmetric stable complexes have S_6 and D_{2h} symmetries. Systems with S_6 and D_{2h} symmetries have also been obtained for V^{2+} and Ni^{2+}. All structures have, within 3 kJ/mol, the same energy and we will show and discuss the results for the

https://doi.org/10.1021/acs.inorgchem.2c02358
Inorg. Chem. 2022, 61, 20743−20756

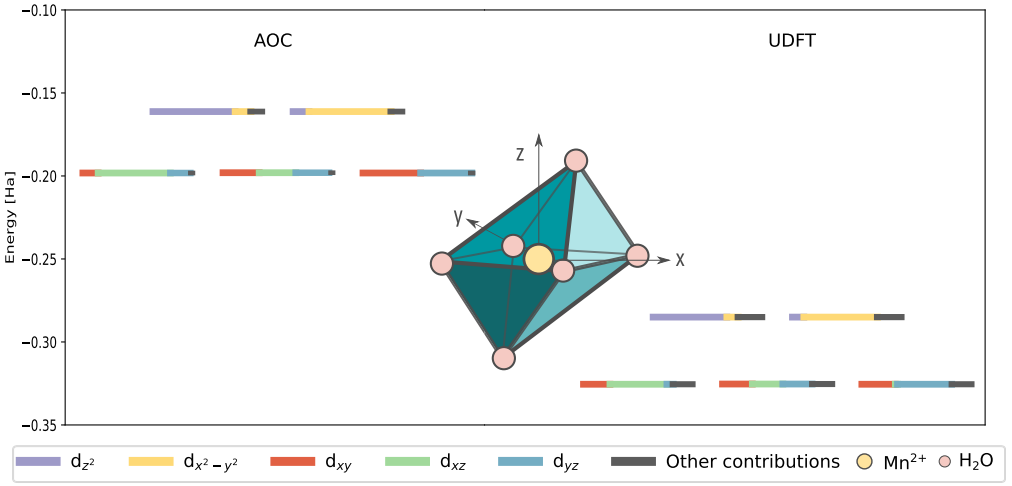

Figure 15. Splitting of the d-orbitals for the optimized $[Mn(H_2O)_6]^{2+}$ complexes with S_6 symmetry using AOC (left) and UDFT (right).

complexes with S_6 symmetry. The d-orbital splittings along with the atomic contributions are shown in Figures 15, S13, and S14 for $[Mn(H_2O)_6]^{2+}$, $[V(H_2O)_6]^{2+}$, and $[Ni(H_2O)_6]^{2+}$, respectively. For Mn^{2+} and V^{2+}, the α-electrons are shown for the UDFT calculations, whereas the β-electrons are presented for Ni^{2+}. The reason for this is that the spin-allowed d−d transitions will be within α/β-electrons for V^{2+}/Ni^{2+}, respectively. For Mn^{2+}, there are no spin-allowed d−d transitions. First, remark that, for all of the systems, both AOC and UDFT correctly predict the splitting into a t_{2g} and e_g set, which is in agreement with the qualitative LFT results. This is due to the fact that for these systems, the t_{2g} orbitals are either completely filled with α-electrons, as is the case for Mn^{2+} and V^{2+}, or with both α- and β-electrons, as is the case for the Ni^{2+} complex. Second, for $[Mn(H_2O)_6]^{2+}$, all α-d-orbitals are occupied, which results in a correct prediction of the magnitude of the d-orbital splitting by both AOC and UDFT. This result is not surprising since the only differences between the AOC and UDFT calculations are due to the spin polarization which is absent in the former. However, as is the case for the Co^{2+} complex, the splitting is severely overestimated by UDFT for $[V(H_2O)_6]^{2+}$ and $[Ni(H_2O)_6]^{2+}$. This is also shown in Table 2 in which the d-orbital splitting obtained from experiment,[49] AOC, and UDFT calculations is presented for the various complexes. This observation is in agreement with ref 89, in which it was argued that DFT is expected to yield the same *d*-orbitals sequence as LFT in those cases where a suitable spherical configuration is constructed corresponding to equal populations of the d-orbitals as for d^{10} or HS d^5 complexes. Here, this observation is confirmed and extended to octahedral d^3, d^5, and d^8 systems.

4. CONCLUSIONS

In this work, we investigated Co^{2+} aqua-complexes with six, five, and four ligands. The ground-state properties have been examined, and a lot of attention has been paid to the electronic structure. More specifically, we focused on the energy splitting of the d-electrons and how this depends on the symmetry, where both the influence on the coordination environment and the specific point group are considered. Qualitative techniques such as CFT and LFT reveal that the d-orbital splitting is characteristic of the number of ligands coordinated to the TM. To obtain quantitative results, DFT calculations have been performed, both AOC and UDFT. Stable Co^{2+} aqua-complexes with six, five, and four ligands have been obtained from UDFT optimizations. We have observed a stable structure containing six aqua ligands with D_{2h} symmetry in which JT distortions are clearly visible. Besides this, we also found a structure with S_6 symmetry. Moreover, we have shown that the AOC method is capable of reproducing the d-orbital splittings obtained from the qualitative techniques. UDFT calculations do not succeed in this when only part of the d-orbitals are occupied. Indeed, the energy gap between the d-orbitals and the energy difference between the HOMO and LUMO are overestimated by UDFT for six-coordinated aqua-complexes. As such, the t_{2g} orbitals are far from degenerate as we would expect based on qualitative techniques. Based on the work of Deeth et al., we demonstrated that the discrepancies between UDFT and AOC are due to the different electron occupations resulting in different interelectron repulsions. The AOC orbitals confirm the chemical intuition as given by LFT as both techniques describe the electron repulsion in a spherical way, which was also shown by Daul et al.[47] The d-orbital splitting obtained by UDFT will be different due to the integer occupation numbers resulting in different interelectron repulsions. To further test the performance of UDFT, other TMs have been investigated. We selected TMs for which the t_{2g} set is occupied evenly. The results for these systems are qualitatively in agreement with for example LFT. Furthermore, for $[Mn(H_2O)_6]^{2+}$, for which all α d-orbitals are occupied, even the d-orbital splitting is described correctly and in agreement with the AOC calculations and experimental results. The proper understanding of the electronic structure and symmetry of TMCs is a key element for obtaining insights into the formation process of MOFs and potentially also their defect structures.

https://doi.org/10.1021/acs.inorgchem.2c02358
Inorg. Chem. 2022, 61, 20743−20756

■ ASSOCIATED CONTENT

Supporting Information

The Supporting Information is available free of charge at https://pubs.acs.org/doi/10.1021/acs.inorgchem.2c02358.

Extra computational details, visualization of the orbitals, structural information, CShMs for the $[Co(H_2O)_6]^{2+}$ complexes, additional splittings of the d-orbitals, and geometries of optimized structures (PDF)

■ AUTHOR INFORMATION

Corresponding Author

Veronique Van Speybroeck − *Center for Molecular Modeling (CMM), Ghent University, 9052 Zwijnaarde, Belgium;* orcid.org/0000-0003-2206-178X; Email: Veronique.VanSpeybroeck@UGent.be

Author

Liesbeth De Bruecker − *Center for Molecular Modeling (CMM), Ghent University, 9052 Zwijnaarde, Belgium;* orcid.org/0000-0001-7844-6932

Complete contact information is available at: https://pubs.acs.org/10.1021/acs.inorgchem.2c02358

Notes

The authors declare no competing financial interest.

■ ACKNOWLEDGMENTS

The authors acknowledge the Research Board of Ghent University (BOF) for funding. The computational resources and services used in this work were provided by VSC (Flemish Supercomputer Center), funded by Ghent University, FWO, and the Flemish Government Department EWI.

■ REFERENCES

(1) Park, K. S.; Ni, Z.; Côté, A. P.; Choi, J. Y.; Huang, R.; Uribe-Romo, F. J.; Chae, H. K.; O'Keeffe, M.; Yaghi, O. M. Exceptional Chemical and Thermal Stability of Zeolitic Imidazolate Frameworks. *Proc. Natl. Acad. Sci. U.S.A.* **2006**, *103*, 10186−10191.

(2) Öztürk, Z.; Hofmann, J. P.; Lutz, M.; Mazaj, M.; Logar, N. Z.; Weckhuysen, B. M. Controlled Synthesis of Phase-Pure Zeolitic Imidazolate Framework Co-ZIF-9. *Eur. J. Inorg. Chem.* **2015**, *2015*, 1625−1630.

(3) Cravillon, J.; Schröder, C. A.; Bux, H.; Rothkirch, A.; Caro, J.; Wiebcke, M. Formate Modulated Solvothermal Synthesis of ZIF-8 Investigated using Time-Resolved in Situ X-Ray Diffraction and Scanning Electron Microscopy. *CrystEngComm* **2012**, *14*, 492−498.

(4) Cravillon, J.; Nayuk, R.; Springer, S.; Feldhoff, A.; Huber, K.; Wiebcke, M. Controlling Zeolitic Imidazolate Framework Nano- and Microcrystal Formation: Insight into Crystal Growth by Time-Resolved In Situ Static Light Scattering. *Chem. Mater.* **2011**, *23*, 2130−2141.

(5) Cravillon, J.; Menzer, S.; Lohmeier, S.-J.; Feldhoff, A.; Huber, K.; Wiebcke, M. Rapid Room-Temperature Synthesis and Characterization of Nanocrystals of a Prototypical Zeolitic Imidazolate Framework. *Chem. Mater.* **2009**, *21*, 1410−1412.

(6) Cravillon, J.; Schröder, C. A.; Nayuk, R.; Gummel, J.; Huber, K.; Wiebcke, M. Fast Nucleation and Growth of ZIF-8 Nanocrystals Monitored by Time-Resolved In Situ Small-Angle and Wide-Angle X-Ray Scattering. *Angew. Chem.* **2011**, *123*, 8217−8221.

(7) Venna, S. R.; Jasinski, J. B.; Carreon, M. A. Structural Evolution of Zeolitic Imidazolate Framework-8. *J. Am. Chem. Soc.* **2010**, *132*, 18030−18033.

(8) Phan, A.; Doonan, C. J.; Uribe-Romo, F. J.; Knobler, C. B.; O'Keeffe, M.; Yaghi, O. M. Synthesis, Structure, and Carbon Dioxide Capture Properties of Zeolitic Imidazolate Frameworks. *Acc. Chem. Res.* **2010**, *43*, 58−67.

(9) Hayashi, H.; Côté, A. P.; Furukawa, H.; O'Keeffe, M.; Yaghi, O. M. Zeolite A Imidazolate Frameworks. *Nat. Mater.* **2007**, *6*, 501−506.

(10) Fedorchuk, C.; Swaddle, T. W. Comment on Reinterpretation of the Spectra of Hydrated Co^{++}: An ab Initio Study (J. Phys. Chem. A 1998, 102, 6525). *J. Phys. Chem. A* **2000**, *104*, 5651−5652.

(11) Yao, J.; Wang, H. Zeolitic Imidazolate Framework Composite Membranes and Thin Films: Synthesis and Applications. *Chem. Soc. Rev.* **2014**, *43*, 4470−4493.

(12) Sun, Y.; Rogge, S. M. J.; Lamaire, A.; Vandenbrande, S.; Wieme, J.; Siviour, C. R.; Speybroeck, V. V.; Tan, J.-C. High-Rate Nanofluidic Energy Absorption in Porous Zeolitic Frameworks. *Nat. Mater.* **2021**, *20*, 1015−1023.

(13) Hu, Y.; Kazemian, H.; Rohani, S.; Huang, Y.; Song, Y. In Situ High Pressure Study of ZIF-8 by FTIR Spectroscopy. *Chem. Commun.* **2011**, *47*, 12694−12696.

(14) Sun, C.-Y.; Qin, C.; Wang, X.-L.; Yang, G.-S.; Shao, K.-Z.; Lan, Y.-Q.; Su, Z.-M.; Huang, P.; Wang, C.-G.; Wang, E.-B. Zeolitic Imidazolate Framework-8 as Efficient pH-Sensitive Drug Delivery Vehicle. *Dalton Trans.* **2012**, *41*, 6906−6909.

(15) Moggach, S. A.; Bennett, T. D.; Cheetham, A. K. The Effect of Pressure on ZIF-8: Increasing Pore Size with Pressure and the Formation of a High-Pressure Phase at 1.47GPa. *Angew. Chem., Int. Ed.* **2009**, *48*, 7087−7089.

(16) Kaur, G.; Rai, R. K.; Tyagi, D.; Yao, X.; Li, P.-Z.; Yang, X.-C.; Zhao, Y.; Xu, Q.; Singh, S. K. Room-Temperature Synthesis of Bimetallic CoZn Based Zeolitic Imidazolate Frameworks in Water for Enhanced CO_2 and H_2 Uptakes. *J. Mater. Chem. A* **2016**, *4*, 14932−14938.

(17) Kwon, H. T.; Jeong, H.-K.; Lee, A. S.; An, H. S.; Lee, J. S. Heteroepitaxially Grown Zeolitic Imidazolate Framework Membranes with Unprecedented Propylene/Propane Separation Performances. *J. Am. Chem. Soc.* **2015**, *137*, 12304−12311.

(18) Wang, C.; Yang, F.; Sheng, L.; Yu, J.; Yao, K.; Zhang, L.; Pan, Y. Synthesis of Isoalkanes over a Core (FeZnZr)Shell (Zeolite) Catalyst by CO_2 Hydrogenation. *Chem. Commun.* **2016**, *52*, 12578−12581.

(19) Yang, H.; He, X.-W.; Wang, F.; Kang, Y.; Zhang, J. Doping Copper into ZIF-67 for Enhancing Gas Uptake Capacity and Visible-Light-Driven Photocatalytic Degradation of Organic Dye. *J. Mater. Chem.* **2012**, *22*, 21849−21851.

(20) Lee, Y.-R.; Jang, M.-S.; Cho, H.-Y.; Kwon, H.-J.; Kim, S.; Ahn, W.-S. ZIF-8: AComparison of Synthesis Methods. *Chem. Eng. J.* **2015**, *271*, 276−280.

(21) Banerjee, R.; Phan, A.; Wang, B.; Knobler, C.; Furkawa, H.; O'Keeffe, M.; Yaghi, O. M. High-Throughput Synthesis of Zeolitic Imidazolate Frameworks and Application to CO2 Capture. *Science* **2008**, *319*, 939−943.

(22) Van Vleet, M. J.; Weng, T.; Li, X.; Schmidt, J. R. In Situ, Time-Resolved, and Mechanistic Studies of Metal-Organic Framework Nucleation and Growth. *Chem. Rev.* **2018**, *118*, 3681−3721.

(23) Rimer, J. D.; Tsapatsis, M. Nucleation of Open Framework Materials: Navigating the Voids. *MRS Bull.* **2016**, *41*, 393−398.

(24) Filez, M.; Caratelli, C.; Rivera-Torrente, M.; Muniz-Miranda, F.; Hoek, M.; Altelaar, M.; Heck, A. J. R.; Speybroeck, V. V.; Weckhuysen, B. M. Elucidation of the Pre-Nucleation Phase Directing Metal-Organic Framework Formation. *Cell Rep. Phys. Sci.* **2021**, *2*, No. 100680.

(25) Barone, V.; Alessandrini, S.; Biczysko, M.; Cheeseman, J. R.; Clary, D. C.; McCoy, A. B.; DiRisio, R. J.; Neese, F.; Melosso, M.; Puzzarini, C. Computational Molecular Spectroscopy. *Nat. Rev. Methods Primers* **2021**, *1*, No. 38.

(26) Stepanović, S.; Zlatar, M.; Swart, M.; Gruden, M. The Irony of Manganocene: An Interplay between the JahnTeller Effect and Close-Lying Electronic and Spin States. *J. Chem. Inf. Model.* **2019**, *59*, 1806−1810.

(27) Flöser, B. M.; Guo, Y.; Riplinger, C.; Tuczek, F.; Neese, F. Detailed Pair Natural Orbital-Based Coupled Cluster Studies of Spin Crossover Energetics. *J. Chem. Theory Comput.* **2020**, *16*, 2224−2235.

(28) Stavila, V.; Bulimestru, I.; Gulea, A.; Colson, A. C.; Whitmire, K. H. Hexaaquacobalt(II) and Hexaaquanickel(II) bis(μ-pyridine-2,6-dicarboxylato)bis[(pyridine-2,6-dicarboxyl- ato)bismuthate(III)] dihydrate. *Acta Crystallogr., Sect. C: Cryst. Struct. Commun.* **2011**, *67*, m65−m68.
(29) Jørgensen, C. K.; de Verdier, C. H.; Glomset, J.; et al. Studies of Absorption Spectra. IV. Some New Transition Group BAnds of Low Intensity. *Acta Chem. Scand.* **1954**, *8*, 1502−1512.
(30) Holmes, O. G.; McClure, D. S. Optical Spectra of Hydrated Ions of the Transition Metals. *J. Chem. Phys.* **1957**, *26*, 1686.
(31) Jörgensen, C. K.*Spectroscopy of Transition-Group Complexes in Advances in Chemical Physics*; John Wiley and Sons, Inc., 1963.
(32) Jörgensen, C. K.*Absorption Spectra and Chemical Bonding in Complexes*; Pergamon Press, 1962.
(33) Griffith, J. S.*The Theory of Transition-Metal Ions*; Cambridge University Press, 1964.
(34) Spezia, R.; Tournois, G.; Tortajada, J.; Cartailler, T.; Gaigeot, M.-P. Toward a DFT-Based Molecular Dynamics Description of Co(II) Binding in Sulfur-Rich Peptide. *Phys. Chem. Chem. Phys.* **2006**, *8*, 2040−2050.
(35) Varadwaj, P. R.; Marques, H. M. The Physical Chemistry of Coordinated Aqua-, Ammine-, and Mixed-Ligand Co^{2+} Complexes: DFT Studies on the Structure, Energetics, and Topological Properties of the Electron Density. *Phys. Chem. Chem. Phys.* **2010**, *12*, 2126−2138.
(36) Neese, F.; Petrenko, T.; Ganyushin, D.; Olbrich, G. Advanced Aspects of Ab Initio Theoretical Optical Spectroscopy of Transition Metal Complexes: Multiplets, Spin-Orbit Coupling and Resonance Raman Intensities. *Coord. Chem. Rev.* **2007**, *251*, 288−327.
(37) Boeyens, J. C. A.; Ogilvie, J. F.*Models, Mysteries and Magic of Molecules*; Springer, 2008.
(38) Yang, Y.; Ratner, M. A.; Schatz, G. C. Multireference Ab Initio Study of Ligand Field dd Transitions in Octahedral Transition-Metal Oxide Clusters. *J. Phys. Chem. C* **2014**, *118*, 29196−29208.
(39) Vlahović, F.; Peric, M.; Gruden-Pavlović, M.; Zlatar, M. Assessment of TD-DFT and LF-DFT for Study of d-d Transitions in First Row Transition Metal Hexaaqua Complexes. *J. Chem. Phys.* **2015**, *142*, No. 214111.
(40) Radoń, M.; Drabik, G. Spin States and Other Ligand-Field States of Aqua Complexes Revisited with Multireference ab Initio Calculations Including Solvation Effects. *J. Chem. Theory Comput.* **2018**, *14*, 4010−4027.
(41) Bethe, H. Termaufspaltung in Kristallen. *Ann. Phys.* **1929**, *395*, 133−208.
(42) Van Vleck, J. H. Theory of the Variations in Paramagnetic Anisotropy Among Different Salts of the Iron Group. *Phys. Rev.* **1932**, *41*, 208−215.
(43) Van Vleck, J. H. Valence Strength and the Magnetism of Complex Salts. *J. Chem. Phys.* **1935**, *3*, 807−813.
(44) Griffith, J. S.; Orgel, L. E. Ligand-Field Theory. *Q. Rev. Chem. Soc.* **1957**, *11*, 381−393.
(45) Larsen, E.; La Mar, G. N. The Angular Overlap Model: How to use it and why. *J. Chem. Educ.* **1974**, *51*, 633−640.
(46) Burdett, J. K.*Molecular Shapes*; John Wiley & Sons, Inc., 1980.
(47) Atanasov, M.; Daul, C. A.; Rauzy, C. A DFT Based Ligand Field Theory. *Struct. Bonding* **2004**, *106*, 97−125.
(48) Ciampolini, M.*Spectra of 3d Five-Coordinate Complexes*; Springer, 1969.
(49) Miessler, G. L.; Fischer, P. J.; Tarr, D. A.*Inorganic Chemistry*; Pearson, 2014.
(50) Solomon, E. I.; Pavel, E. G.; Loeb, K. E.; Campochiaro, C. Magnetic Circular Dichroism Spectroscopy as a Probe of the Geometric and Electronic Structure of Non-Heine Ferrous Enzymes. *Coord. Chem. Rev.* **1995**, *114*, 369−460.
(51) Shriver, D. F.; Langford, C. H.; Atkins, P. W.*Inorganic Chemistry*; H. Freeman and Co., 1994.
(52) Schmiedekamp, A. M.; Ryan, M. D.; Deeth, R. J. Six-Coordinate Co^{2+} with H_2O and NH_3 Ligands: Which Spin State Is More Stable? *Inorg. Chem.* **2002**, *41*, 5733−5743.
(53) Sacconi, L. Five-Coordination in 3d Complexes. *Pure Appl. Chem.* **1968**, *17*, 95−128.
(54) Sacconi, L. Some Factors Governing the Spin-Multiplicity of 5-Coordinate Complexes of Cobalt(II) and Nickel(II). *J. Chem. Soc. A* **1970**, 248−256.
(55) Slater, J. C.*The Self-Consistent Field for Molecules and Solids*; McGraw-Hill: New York, 1974.
(56) te Velde, G.; Bickelhaupt, F. M.; Baerends, E.; Guerra, C. F.; van Gisbergen, S.; Snijders, J.; Ziegler, T. Chemistry with ADF. *J. Comput. Chem.* **2001**, *22*, 931−967.
(57) Pye, C. C.; Ziegler, T. An Implementation of the Conductor-Like Screening Model of Solvation Within the Amsterdam Density Functional Package. *Ther. Chem. Acc.* **1999**, *101*, 396−408.
(58) Lenthe, E. v.; Baerends, E. J.; Snijders, J. G. Relativistic Regular Two-Component Hamiltonians. *J. Chem. Phys.* **1993**, *99*, 4597.
(59) van Lenthe, E.; Baerends, E. J.; Snijders, J. G. Relativistic total energy using regular approximations. *J. Chem. Phys.* **1994**, *101*, 9783−9792.
(60) van Lenthe, E.; Ehlers, A.; Baerends, E. J. Geometry Optimization in the Zero Order Regular Approximation for Relativistic Effects. *J. Chem. Phys.* **1999**, *110*, 8943−8953.
(61) Grimme, S.; Antony, J.; Ehrlich, S.; Krieg, H. A Consistent and Accurate Ab Initio Parametrization of Density Functional Dispersion Correction (DFT-D) for the 94 Elements H-Pu. *J. Chem. Phys.* **2010**, *132*, No. 154104.
(62) Lee, C.; Yang, W.; Parr, R. G. Development of the Colle-Salvetti Correlation-Energy Formula into a Functional of the Electron Density. *Phys. Rev. B* **1988**, *37*, 785.
(63) Becke, A. D. Density-functional exchange-energy approximation with correct asymptotic behavior. *Phys. Rev. A* **1988**, *38*, 3098−3100.
(64) Zhao, Y.; Truhlar, D. G. A New Local Density Functional for Main-Group Thermochemistry, Transition Metal Bonding, Thermochemical Kinetics, and Noncovalent Interactions. *J. Chem. Phys.* **2006**, *125*, No. 194101.
(65) Yu, H. S.; He, X.; Truhlar, D. G. MN15-L: ANew Local Exchange-Correlation Functional for KohnSham Density Functional Theory with Broad Accuracy for Atoms, Molecules, and Solids. *J. Chem. Theory Comput.* **2016**, *12*, 1280−1293.
(66) Cohen, A. J.; Handy, N. C. Dynamic Correlation. *Mol. Phys.* **2001**, *99*, 607−615.
(67) Becke, A. D. DensityFunctional Thermochemistry. III. The Role of Exact Exchange. *J. Chem. Phys.* **1993**, *98*, 5648.
(68) Xu, X.; Goddard, W. A., III. The X3LYP Extended Density Functional for Accurate Descriptions of Nonbond Interactions, Spin States, and Thermochemical Properties. *Proc. Natl. Acad. Sci. U.S.A.* **2004**, *101*, 2673−2677.
(69) Adamo, C.; Barone, V. Toward Reliable Density Functional Methods Without Adjustable Parameters: The PBE0 Model. *J. Chem. Phys.* **1999**, *110*, 6158−6169.
(70) Yu, H. S.; He, X.; Li, S. L.; Truhlar, D. G. MN15: A Kohn-Sham Global-Hybrid Exchange-Correlation Density Functional with Broad Accuracy for Multi-Reference and Single-Reference Systems and Noncovalent Interactions. *Chem. Sci.* **2016**, *7*, 5032−5051.
(71) Staroverov, V. N.; Scuseria, G. E.; Tao, J.; Perdew, J. P. Comparative Assessment of a New Nonempirical Density Functional: Molecules and Hydrogen-Bonded Complexes. *J. Chem. Phys.* **2003**, *119*, 12129−12137.
(72) Tao, J.; Perdew, J. P.; Staroverov, V. N.; Scuseria, G. E. Climbing the Density Functional Ladder: Nonempirical Meta-Generalized Gradient Approximation Designed for Molecules and Solids. *Phys. Rev. Lett.* **2003**, *91*, No. 146401.
(73) Yanai, T.; Tew, D. P.; Handy, N. C. A New Hybrid Exchange-Correlation Functional using the Coulomb-Attenuating Method (CAM-B3LYP). *Chem. Phys. Lett.* **2004**, *393*, 51−57.
(74) Chai, J.-D.; Head-Gordon, M. Long-Range Corrected Hybrid Density Functionals with Damped AtomAtom Dispersion Corrections. *Phys. Chem. Chem. Phys.* **2008**, *10*, 6615−6620.

https://doi.org/10.1021/acs.inorgchem.2c02358
Inorg. Chem. 2022, 61, 20743−20756

(75) Dennington, R.; Keith, T. A.; Millam, J. M.*GaussView*, version 5; Semichem Inc.: Shawnee Mission, KS, 2019.
(76) Shee, J.; Loipersberger, M.; Hait, D.; Lee, J.; Head-Gordon, M. Revealing the Nature of Electron Correlation in Transition Metal Complexes with Symmetry-Breaking and Chemical Intuition. *J. Chem. Phys.* **2021**, *154*, No. 194109.
(77) Neese, F.; Ames, W.; Christian, G.; Kampa, M.; Liakos, D. G.; Pantazis, D. A.; Roemelt, M.; Surawatanawong, P.; Ye, S.Dealing with Complexity in Open-shell Transition Metal Chemistry from a Theoretical Perspective: Rection Pathways, Bonding, Spectroscopy, and Magnetic Properties. *Advances in Inorganic Chemistry*; Elsevier Inc., 2010.
(78) CSD Cambridge UK. *Cambridge Structural Database*, v.5.30; CSD Cambridge, 2008 (updated to Sept 2009).
(79) Jahn, H. A.; Teller, E. Stability of Polyatomic Molecules in Degenerate Electronic States. I. Orbital Degeneracy. *Proc. R. Soc. London, Ser. A* **1937**, *161*, 220−235.
(80) Zlatar, M.; Schläpfer, C.-W.; Daul, C.*A New Method to Describe the Multimode Jahn−Teller Effect Using Density Functional Theory*; Springer, 2009.
(81) Kundu, T. K.; Bruyndonckx, R.; Daul, C.; Manoharan, P. T. A Density Functional Approach to the Jahn-Teller Effect of $[Cu(en)_3]^{2+}$ as a Model for a Macrobicyclic Cage Complex of Copper(ii). *Inorg. Chem.* **1999**, *38*, 3931−3934.
(82) Stoll, C.; Atanasov, M.; Bandemehr, J.; Neese, F.; Pietzonka, C.; Kraus, F.; Karttunen, A. J.; Heymann, G.; Seibald, M.; Huppertz, H. Coexistence of Two Different Distorted Octahedral $[MnF_6]^{3-}$ Sites in $K_3[MnF_6]$: Manifestation in Spectroscopy and Magnetism. *Chem.—Eur. J.* **2021**, *27*, 9801−9813.
(83) Figgis, B. N.; Hitchman, M. A.*Ligand Fielt Theory and Its Applications*; Wiley, 2000.
(84) Johnson, D. A.; Nelson, P. G. Factors Determining the Ligand Field Stabilization Energies of the Hexaaqua 2+ Complexes of the First Transition Series and the Irving-Williams Order. *Inorg. Chem.* **1995**, *34*, 5666−5671.
(85) Reedijk, J.; Driessen, W. L.; Groeneveld, W. L. A Semi-Empirical Energy-Level Diagram for Octahedral Cobalt(II) Complexes. *Recl. Trav. Chim. Pays-Bas* **2010**, *88*, 1095−1109.
(86) Hargittai, I. Book Review: Fuzzy Definitions: Concepts in Chemistry—A Contemporary Challenge. Edited by D. H. Rouvray. *Angew. Chem., Int. Ed.* **1997**, *36*, 2525.
(87) Zabrodsky, H.; Peleg, S.; Avnir, D. Continuous Symmetry Measures. *J. Am. Chem. Soc.* **1992**, *114*, 7843−7851.
(88) Zemann, J. Elektrostatische Energien von AB_5-Komplexen. *Z. Anorg. Allg. Chem.* **1963**, *324*, 241−249.
(89) Deeth, R. J. Ligand Field and Density Functional Descriptions of the d-States and Bonding in Transition Metal Complexes. *Faraday Discuss.* **2003**, *124*, 379−391.

https://doi.org/10.1021/acs.inorgchem.2c02358
Inorg. Chem. 2022, 61, 20743−20756

Paper IV

On the Prediction of Spectroscopic Fingerprints of Co^{2+} Complexes Relevant in the ZIF Nucleation Process

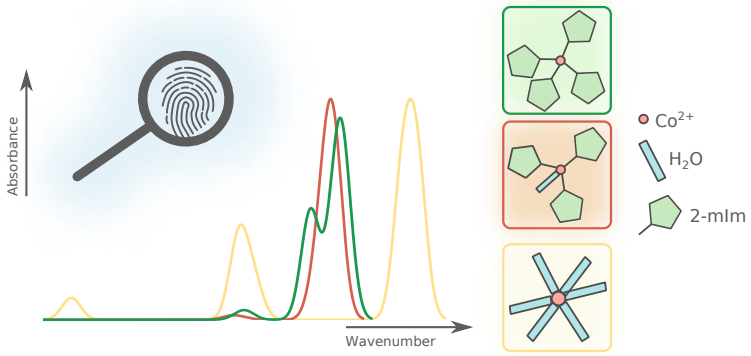

L. De Bruecker, M. Filez, and V. Van Speybroeck

Inorganic Chemistry, **2023**, *Submitted*

L. De Bruecker performed the research and wrote the initial draft of the manuscript.

On the prediction of spectroscopic fingerprints of Co^{2+} complexes relevant for the ZIF nucleation process

Liesbeth De Bruecker[a], Matthias Filez[b], and Veronique Van Speybroeck*,[a]

[a] Center for Molecular Modeling(CMM), Ghent University, Technologiepark 46, 9052 Zwijnaarde, Belgium

[b] Conformal Coating of Nanomaterials (CoCooN), Ghent University, Krijgslaan 281/S1, 9000 Gent, Belgium

* (V.V.S.) E-mail: Veronique.VanSpeybroeck@UGent.be

Abstract

The nucleation process of zeolitic imidazolate frameworks (ZIFs) is, to date, not completely understood. Recently, it has been found that, during the formation of Co-ZIF-67, after mixing imidazole-type ligands with octahedral precursors containing oxygen-coordinated ligands, a metal-organic pool with a diversity of transition metal complexes (TMCs) is formed showing fingerprints of octahedral and tetrahedral Co^{2+} complexes with both types of ligands [M. Filez *et al.* Cell Rep. Phys. Sci., 2:100680, 2021]. In order to further unravel this process, we aim to characterize the d-d transitions of the TMCs and focus on their number, intensity, and position which change during the process and can thus serve as a fingerprint for the formed species. It was previously shown that the number of ligands and symmetry has a detrimental influence on the ground state properties of Co^{2+} TMCs. Herein, we investigate in how far excited state properties of TMCs relevant during nano-porous formation processes can be predicted by time-dependent density functional theory (TDDFT) and ligand field density functional theory (LFDFT). As TMCs are known to be challenging systems with possibly degenerate ground states and double excitations, we first investigate the performance of both techniques on first-row octahedral aqua-complexes. With this knowledge, we then focus on tetrahedral

Co^{2+} complexes with aqua and imidazole-type ligands in order to investigate in how far we can propose a spectroscopic fingerprint that allows us to follow the Co^{2+} complexes during the formation of Co-ZIF-67. The results of TDDFT and LFDFT are qualitatively in agreement and provide complementary information. We found that various features can be used to distinguish between the species. However, as LFDFT is not suited for TMCs possessing the extended imidazole-type ligands and double and spin-flip states are not included in TDDFT, both techniques need to be complemented with more advanced methods to obtain a complete insight in the d-d excitations of TMCs with imidazole ligands. Therefore, we particularly explored ab initio ligand field theory, which is capable of describing double excitations and is, in contrast to LFDFT, suited for TMCs with extended ligands.

1 Introduction

The nucleation process of zeolitic imidazolate frameworks (ZIFs) is, up to now, not yet completely understood. This makes the exploration for materials tailored for specific applications in various domains very burdensome[71,62,34]. Recently, a combined experimental-computational study[27] investigated the nucleation of Co-ZIF-67, formed by mixing $Co(NO_3)_2{\cdot}6H_2O$ and 2-methylimidazole (2-mIm). The former contains predominantly octahedral transition metal complexes (TMCs) with aqua ligands. It has been revealed that after mixing a pool with a variety of TMCs is formed because of ligand elimination and substitution reactions as shown in Figure 1. The transformation of octahedral precursors to five- and finally four-coordinated complexes is accompanied by an exchange and elimination of aqua ligands with 2-mIm ligands. For the sake of fully understanding this intricate process, we would like to study the changes in the UV-Vis spectrum as this was also experimentally measured in the paper of Filez *et al.* to identify the various species in the nucleation process. More specifically, we will concentrate on the number, intensity, and position of the d-d transitions as they alter during the nucleation and can therefore act as a fingerprint. Previously, we studied the ground state (GS) properties of six-, five-, and four-coordinated Co^{2+} aqua-complexes[16] and concluded that the d-orbital splitting is characteristic for the number of ligands coordinated to the transition metal (TM) and for the symmetry of the complex. We also investigated the performance of different techniques based on density functional theory (DFT) to calculate the d-orbital splitting quantitatively. In this work, we complement our investigation toward the d-d excitations of six- and four-coordinated Co^{2+} complexes as Filez *et al.* found that after mixing $Co(NO_3)_2{\cdot}6H_2O$ and

2-mIm, the system mainly consists of $[Co(OR)_6]^{2+}$, $[Co(2\text{-mIm})_3(OR)]^{2+}$, and $[Co(2\text{-mIm})_4]^{2+}$ complexes.[27] Remark that here not only aqua ligands are considered but also other ligands coordinating with oxygen to the TM, like methanol or NO_3^-. Note that it is less probable for the latter to directly coordinate to the TM as it will likely be replaced by the stronger aqua ligand. However, NO_3^- can appear in the second solvation shell and as such counterbalance the positive charge of the complex. In this work, we only consider aqua ligands in order to minimize the complexity of the system and to be able to compare the results to literature data.[51,70,68,38] Nevertheless, we thereby neglect the possible symmetry breaking caused by for example methanol compared to water. The studied complexes are indicated with gray in Figure 1. The excited states (ESs) are calculated via time-dependent DFT (TDDFT) and ligand field (LFDFT). The computational spectra can then be compared to experimental data in order to put forward a fingerprint for the nucleation process of ZIFs.

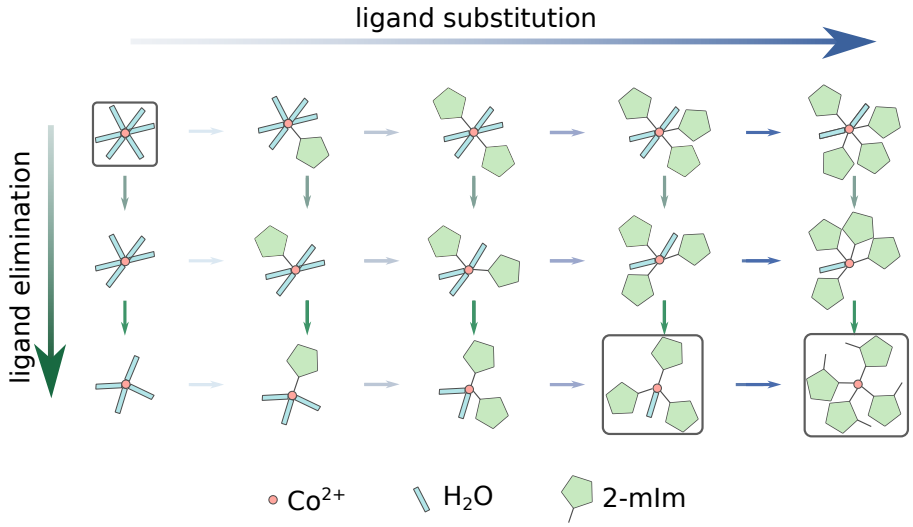

Figure 1: Reaction network of ligand elimination and substitution reactions leading to fast pre-equilibrium formation toward a metal-organic pool. The complexes which are mainly present after mixing according to Ref.[27] are indicated in gray. These include octahedral Co^{2+} complexes with six aqua ligands and two types of tetrahedral structures, one with three 2-mIm and one aqua ligand and the other with four 2-mIm ligands. Note that in practice, also methanol and to a lesser extent NO_3^- can act as ligands. Figure adapted from Ref.[27] with permission of Elsevier, Copyright 2021.

It is generally known that the calculation of ESs in TMCs is not a trivial task and poses various challenges for current computational techniques[74,23,22,2]. Indeed, there might be numerous ESs lying closely together, some of which are double excitations. Furthermore, degeneracies

in the ground and/or excited states may occur. A large body of literature is available on the usage of various electronic structure methods, including computationally very expensive techniques, for the calculations of ESs in small octahedral complexes[51,70,68,54]. As within this work, we ar not only interested in aqua-complexes but also in more complex ligands relevant for the nucleation process, not all techniques proposed thus far are computationally feasible. Therefore, within the first part of this paper, we give more fundamental insights by unraveling the difficulties for the calculation of ESs in octahedral TMCs with aqua ligands and first-row divalent TMs in a methanol environment. Furthermore, the advantages and disadvantages of two computational techniques based on DFT, *i.e.,* time-dependent DFT (TDDFT) and ligand field DFT (LFDFT), are discussed. In the second part, we return our focus to the nucleation process of Co-ZIF-67 and compare our computational results for octahedral Co^{2+} aqua-complexes and tetrahedral Co^{2+} complexes containing 2-mIm and aqua ligands with the experimental work of Filez *et al.*[27] in order to come up with a spectroscopic fingerprint. In addition, as will become clear in Section 3, the LFDFT results are difficult to interpret for complexes with extended imidazole-type ligands. Therefore, some ab initio LFT (AILFT) calculations have been performed too.

2 Challenges of d-d excitations in aqua-complexes for TDDFT and LFDFT

2.1 Using Tanabe-Sugano diagrams for the description of d-d excitations in TMCs

As octahedral and tetrahedral systems will play a major role in this work, the d-orbital splitting as predicted by crystal field theory (CFT) is shown in Figure 2, in which we also introduced the labeling of the orbital sets. In an octahedral ligand field, the d-orbitals of a TM split in a t_{2g} and e_g set. Tetrahedral complexes bear a lot of similarities with octahedral complexes since both point groups are cubic. However, as the ligands are now situated in between the coordinate axes compared to at the coordinate axes as in octahedral complexes, the d-orbital splitting pattern is reversed.

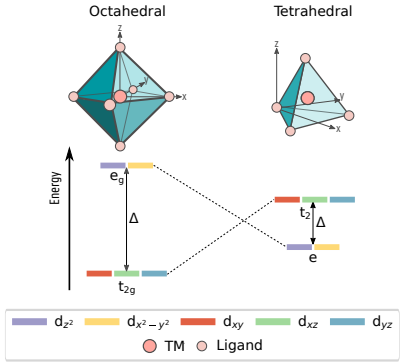

Figure 2: d-orbital splitting in complexes with octahedral and tetrahedral symmetry. The splitting between the two orbital sets is denoted by Δ. The labeling of the d-orbitals is also indicated.

Tanabe-Sugano (TS) diagrams are very helpful to predict and label the transitions between the d-orbitals in octahedral and tetrahedral TMCs[63]. They show the excitation energy E as a function of the ligand field splitting Δ, where both are scaled by the Racah parameter B. The TS diagram for octahedral Co^{2+} complexes with d^7 electron configuration is shown in the left side of Figure 3, where only the lowest energy states are included which are relevant in the remainder of this work. In the weak field limit situated at the left of the diagram, the lowest energy terms ^4F, ^4P, and ^2G are indicated in light purple, dark purple and green, respectively. Under the influence of an increasing ligand field, these terms split in several states. The GS for $[Co(H_2O)_6]^{2+}$ is the high spin (HS) $^4T_{1g}(F)$ state corresponding to the $t_{2g}^5 e_g^2$ electron configuration. The three micro-states with maximal spin projection associated with this configuration are shown in the bottom row on the right and are labeled (a)-(c). The meaning of the line style of the boxes will be explained later. From this GS, there are three spin-allowed and one spin-forbidden transitions in the low-energy range. First of all, one t_{2g}-electron can excite to an e_g-orbital, resulting in the $t_{2g}^4 e_g^3$ electron configuration, indicated by the $^4T_{2g}$ and $^4T_{1g}(P)$ states in light and dark purple, respectively. These states are reached via a single excitation and are therefore indicated with a dashed line. Six possible micro-states with maximal spin projection can be drawn, (d)-(i). When another t_{2g}-electron is transferred to an e_g-orbital, $t_{2g}^3 e_g^4$ is obtained, corresponding to the $^4A_{2g}$ term. This is a double excitation as now two electrons are excited, which is indicated in the TS diagram with a dotted line. There is only one micro-state with maximal spin projection, namely (j). The lowest spin-forbidden excitation is obtained when an e_g-electron is transferred toward a t_{2g}-orbital followed by a spin flip, resulting in the ^2E_g state with $t_{2g}^6 e_g^1$ configuration as presented in green.

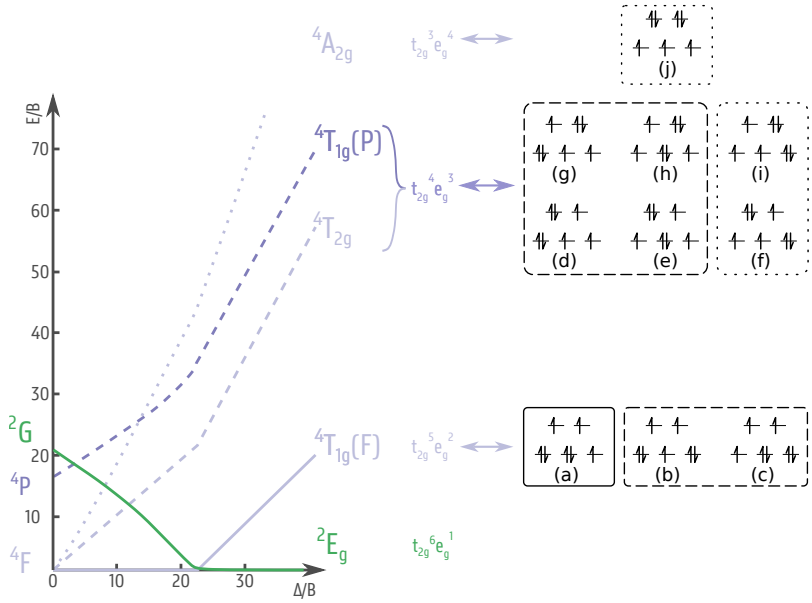

Figure 3: TS diagram for octahedral d^7 complexes in which the energy E is plotted as a function of the ligand field splitting Δ, both scaled by the Racah parameter B. Quartet and doublet states are indicated with purple and green lines, respectively. Dashed and dotted lines represent single and double excitations. On the right, the corresponding micro-states with maximal spin projection are indicated for the quartet states and are labeled (a)-(j). In DFT, one micro-state is chosen as the GS reference, of which the box is denoted with a solid line. Single excitations from this GS reference are characterized with dashed lines and double ESs with dotted lines. Left pane of Figure adapted from Ref.[7].

It is important to note that all of these transitions are Laporte forbidden since they conserve the parity in a complex with a center of symmetry[46]. Therefore, d-d absorption bands are expected to be weak for octahedral complexes. As spin-forbidden transitions are presumed to be even less intense, we will only focus on spin-allowed excitations. Furthermore, one must keep in mind that this description applies for TMCs with perfect octahedral symmetry. When geometrical distortions occur in the complex, some of the states split into substates, leading to more peaks in the spectra, as will be observed in the remainder of the manuscript.

The diagrams for d^2, d^3, d^4, d^6, and d^8 complexes are presented in Figures S1, 4, 5, 6, and S2, respectively. Note that the TS diagrams for octahedral d^n complexes are identical to those of tetrahedral d^{10-n} systems. Indeed, as stated before, the splitting pattern for the d-orbitals in a tetrahedral field is the inverse of that in an octahedral field. As such, the occupation of the t_2 and e orbital sets are similar for octahedral d^n and tetrahedral d^{10-n} complexes, resulting in

analogous TS diagrams. The only difference is in the labeling of the states. As octahedral complexes have a center of symmetry, the subscript g or u, indicating the symmetry with respect to an inversion, is included, whereas this is not the case for tetrahedral systems.

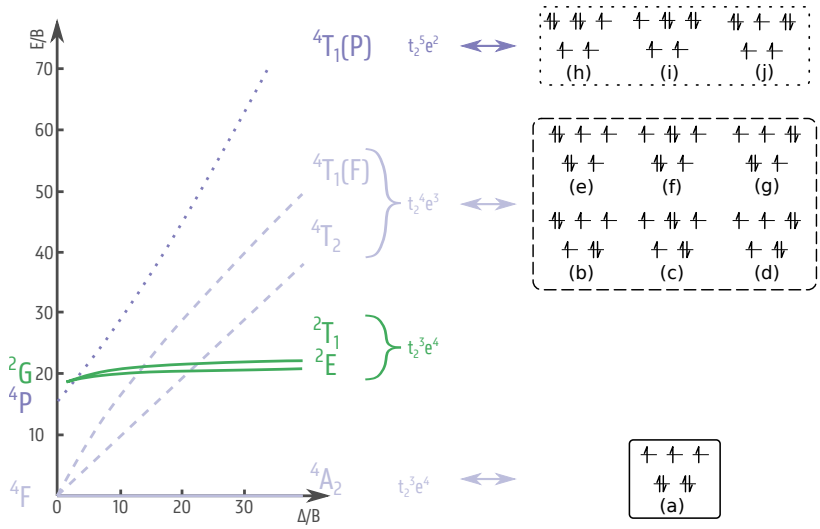

Figure 4: TS diagram for octahedral d^3 and tetrahedral d^7 complexes in which the energy E is plotted as a function of the ligand field splitting Δ, both scaled by the Racah parameter B. Quartet and doublet states are indicated with purple and green lines, respectively. Dashed and dotted lines represent single and double excitations. On the right, the corresponding micro-states with maximal spin projection are indicated for the quartet states and are labeled (a)-(j). In DFT, one micro-state is chosen as the GS reference, of which the box is denoted with a solid line. Single excitations from this GS reference are characterized with dashed lines and double ESs with dotted lines. Left pane of Figure adapted from Ref.[7].

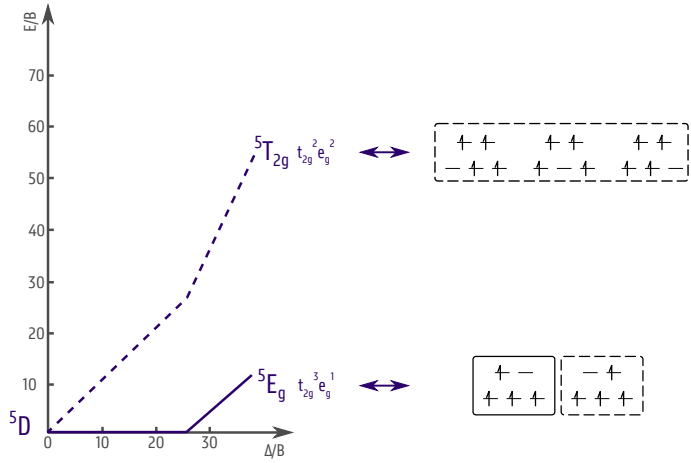

Figure 5: TS diagram for octahedral d^4 complexes in which the energy E is plotted as a function of the ligand field splitting Δ, both scaled by the Racah parameter B. Quintet states are indicated with purple lines. The dashed line represents a single excitation. On the right, the corresponding micro-states with maximal spin projection are indicated. In DFT, one micro-state is chosen as the GS reference, of which the box is denoted with a solid line. Single excitations from this GS reference are characterized with dashed lines. Left pane of Figure adapted from Ref.[7].

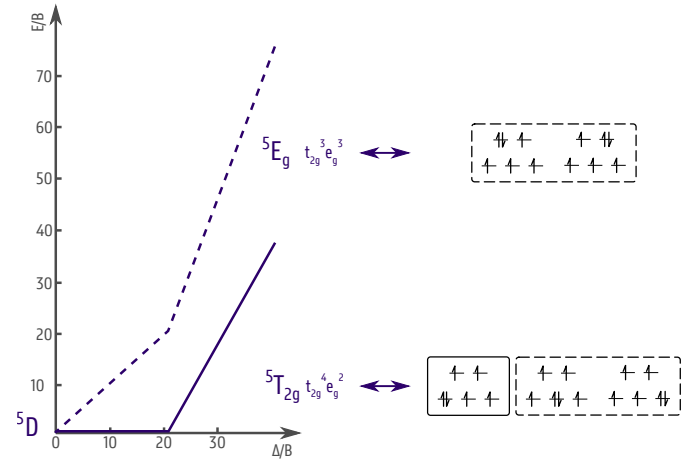

Figure 6: TS diagram for octahedral d^6 complexes in which the energy E is plotted as a function of the ligand field splitting Δ, both scaled by the Racah parameter B. Quintet states are indicated with purple lines. The dashed line represents a single excitation. On the right, the corresponding micro-states with maximal spin projection are indicated. In DFT, one micro-state is chosen as the GS reference, of which the box is denoted with a solid line. Single excitations from this GS reference are characterized with dashed lines. Left pane of Figure adapted from Ref.[7].

As mentioned above, tetrahedral d^7 complexes will play a major role in this work. Hence, we also discuss its TS diagram presented in Figure 4. The GS is now $^4A_2$, corresponding to the $t_2^3e^4$ electron configuration. Again three spin-allowed transitions with low energy occur. When an e-electron gets excited toward a t_2-orbital, the $^4T_2$ and $^4T_1(F)$ terms are obtained, indicated in light purple with dashed lines. When another e-electron is transferred to a t_2-orbital, we arrive at the $t_2^5e^2$ configuration, labeled with $^4T_1(P)$. This double excitation is again indicated with a dotted line. The micro-states with maximal spin projection are also drawn for each electron configuration. In contrast to the octahedral complexes, tetrahedral systems lack a center of symmetry, and therefore, they have much more intense absorption bands.

These TS diagrams are helpful for the study of d-d excitations in TMCs as they show for each electron configuration the number of ESs and provide a way to label them. Furthermore, the link with the corresponding electron configurations will also be of use to interpret the results obtained from TDDFT and understand its deficiencies.

2.2 TDDFT versus LFDFT

An extensive body of literature on octahedral aqua-complexes with first-row TMs is already available[51,70,68,54]. Therefore, it is important to give some positioning of this work with respect to the literature. Neese *et al.* tested complete active space self-consistent field (CASSCF) and spectroscopy oriented configuration interaction (SORCI) on these challenging systems and concluded that the SORCI method on top of state-averaged CASSCF calculations yields good results[51]. Multireference ab initio techniques such as CASSCF, complete active space second-order perturbation theory (CASPT2), and multireference configuration interaction (MRCI) have been employed by Yang *et al.*[70]. This study was followed by the work of Vlahovic *et al.*, who compared TDDFT and LFDFT results[68]. They reported LFDFT to be the preferred method as TDDFT only yields acceptable results for d^2 and d^4 TMCs. The rather poor performance of TDDFT was linked to the fact that double excitations are not covered and that orbital relaxation, which plays an important role when the ES only depends on the ligand field splitting, is neglected. Finally, Radoń *et al.* performed high-level multireference CASPT2 and second order n-electron valence state perturbation theory (NEVPT2)[54]. They retrieved excellent results by explicitly including the second solvation shell and by adequately choosing the active space and extrapolating the energetics to the complete basis set limit. In the previous works, the compu-

tational techniques were quantitatively tested against experimental results and high-level ab initio calculations[30,33,37,38].

With this work, we would like to make a contribution to the previous studies by performing a comparison between results obtained from TDDFT and LFDFT calculations. Another DFT-based technique, which is, in contrast to TDDFT, capable to describe double excitations is constricted n^{th} order variational DFT (CV(n)-DFT)[21,72,39,58]. Nevertheless, to the best of our knowledge, its current implementation does not support unrestricted calculations and can therefore only be used for closed shell systems. Hereby, we want to emphasize that our goal is to find trends which can be helpful to unravel the nucleation process of ZIFs. Hence, we will also calculate spectra of Co^{2+} complexes with more complex ligands than water. In this sense, it is not possible to perform some of the very expensive levels of theory used in previous studies. First, we will critically evaluate in how far computationally cheaper methods are able to give a qualitative correct picture for the series of first-row octahedral aqua-complexes. At second instance, we will use this knowledge to acquire some insights into the UV-Vis spectra of Co^{2+} complexes observed during the nucleation process. Theretofore, we will apply techniques based on DFT to calculate the ESs of octahedral and tetrahedral Co^{2+} complexes. These methods give a good balance between accuracy and computational cost, at least for typical, simple systems[43]. However, care must be taken when considering more challenging systems like TMCs. In addition, we will also briefly investigate the performance of AILFT for these TMCs.[47,61]

The GS reference, from which ESs are determined, can be obtained from average of configuration (AOC) or unrestricted DFT (UDFT) calculations as studied in our previous work[16]. In the former, the d-electrons are distributed evenly among the five molecular orbitals dominated by d-orbitals, resulting in a spin-restricted self-consistent field DFT calculation with fractional occupation numbers. In the latter, a spin-unrestricted calculation is performed with integer occupation numbers. In the following, we discuss how ESs can be determined via both techniques.

When starting from an AOC reference, multiplet energies can be obtained by calculating the energies of suitable determinants[73]. Although this method has been extended by Daul[24], it remains limited as mixing between states is not included. Therefore, we will examine LFDFT,

which has been introduced by Atanasov *et al.*[5,6,4,3]. Indeed, the Kohn-Sham (KS)-orbitals obtained from an AOC calculation are ideally suited for techniques in which electron-electron repulsion is treated within full spherical symmetry, like for example in CFT. In LFDFT, the LF parameters are not determined by making use of experimental input, as is usually done in CFT, but they are obtained solely based on DFT calculations. In this way, the multiplet energy levels of a given electron configuration can be determined. The key feature of this technique is that both dynamical correlation, via the DFT exchange-correlation potential, and non-dynamical correlation, via configuration interaction within the active space of KS orbitals with dominant d-character, are taken into account. LFDFT can only calculate oscillator strengths between states coming from different electron configurations. The d-d transitions studied in this work come from the same electron configuration and are hence assumed to be Laporte forbidden. Nevertheless, we will show by using TDDFT that the oscillator strengths for the d-d transitions in TMCs which are not perfectly octahedral are different from zero as they are not completely Laporte forbidden.

When the GS reference is obtained from UDFT, the most popular technique to determine ESs is TDDFT[57] within the linear-response approach as developed by Casida[18]. Usually, the adiabatic approximation is applied in which the time-dependent exchange correlation potential is approximated by a GS one[13,8]. This black box technique has already been widely used for a broad area of systems, ranging from organic[41,40] and inorganic[29,20,9,48,56] molecules[17,13,12,36,28] to the very challenging TMCs[28,49,15]. However, we have to pay attention when analyzing the results for TMCs. Sometimes, the fact that the GS is not described correctly in DFT can be reflected in a wrong characterization of the ESs. For example, Deeth *et al.* found that in tetrahedral Pd complexes, the d-orbital splitting is predicted incorrectly by DFT, which is reflected in the ESs[25]. In our previous paper, we found that for the six-coordinated complexes the order of d-orbitals within the t_{2g} or e_g set are sometimes interchanged in the AOC and UDFT calculations due to the different electron occupations, resulting in different interelectron repulsions. However, no mixing between the two orbital sets occurs. Furthermore, we observed that the gap between the occupied and unoccupied orbitals is overestimated by UDFT. We will study in this work in how far these discrepancies are reflected in the ESs.

To set the scene, Figure 7 gives an overview of the most important challenges for the calcu-

lation of ESs in octahedral first-row aqua-complexes, being the presence of a degenerate GS and/or double excitations. The electron configuration is shown too, where we assumed that for all complexes the high-spin state is the most stable one. Remark that Mn^{2+} with the d^5 configuration has been omitted as this complex has no spin-allowed d-d transitions.

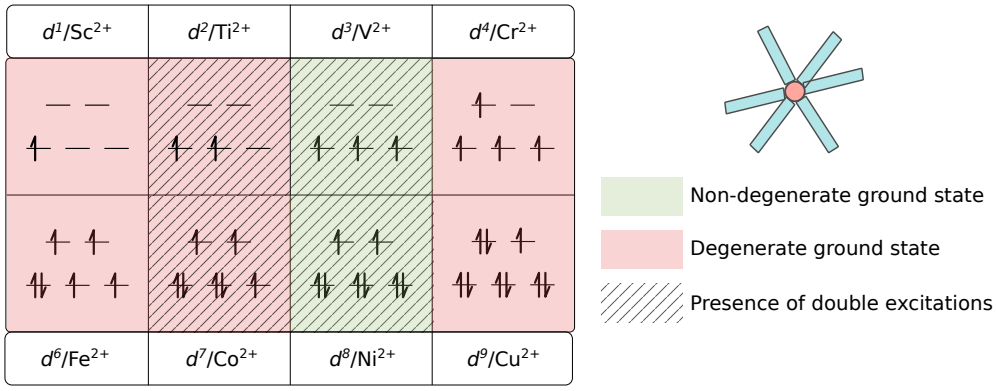

Figure 7: Overview of the challenges encountered for the calculation of ESs in octahedral first-row TMCs. The electron configuration of the high-spin GS is shown. Green/red indicates that the GS is non-degenerate/degenerate and diagonal stripes denote the presence of double excitations.

First of all, whether the GS is degenerate or not, is indicated in red or green, respectively. As can be seen, most of the octahedral TMCs have a degenerate GS, the only exceptions are V^{2+} and Ni^{2+}. On the one hand, configuration averaging, as is done in AOC, is, in principle, necessary to treat the degenerate micro-states of the GS equally. On the other hand, the degeneracy is mostly elevated by Jahn-Teller (JT) effects[35], which has been investigated for some of the complexes in our previous work[16]. This is in agreement with the results of Shee et al. who have recently put forward that in most TMCs, static correlation is rarely found in the GS[60]. Therefore, we also performed UDFT calculations, in which one of the degenerate micro-states in the GS is selected. TDDFT, being a single reference technique, calculates the ESs based on this GS reference. In Figures 3 and 4, this micro-state is indicated with a solid line. For the octahedral d^7 TMC, we arbitrarily chose one of the three micro-states with maximal spin-projection corresponding to ${}^4T_{1g}(F)$ as the GS reference, namely (a). The fact that TDDFT selects a specific micro-state as reference from which excitations are determined has two consequences. First of all, the other two micro-states belonging to ${}^4T_{1g}(F)$, (b) and (c), are reached via single excitations. These single excitations are indicated with dashed lines. Second, only four of the six micro-states corresponding to ${}^4T_{1g}(P)$ and ${}^4T_{2g}$ are reached via an excitation of a single elec-

tron. These are (d), (e), (g), and (h), and are indicated with a dashed line. (f) and (i) can only be reached when two electrons are excited from the GS reference. These double excitations are indicated with a dotted line. This has been addressed in Ref.[74] as well. Micro-state (j) corresponding to $^4A_{2g}$ is also a double ES. The behaviour of the tetrahedral d^7 complexes shown in Figure 4 is different. All micro-states corresponding to $^4T_2$ and $^4T_1(F)$, *i.e.,* (b)-(g), are single ESs, and all micro-states corresponding to $^4T_1(P)$, *i.e.,* (h)-(j), are double ESs. Therefore, they are indicated with dashed and dotted lines, respectively.

It is widely known that, due to the adiabatic approximation, TDDFT is not capable of treating ESs with mainly double excitation character[45]. Let us consider the two situations studied before. In the case of a non-degenerate GS, as for example in Figure 4, there are three double excitations, as stated before. They correspond to a transfer of two e_g electrons to t_{2g} orbitals, leading to the $^4T_1(P)$ state. Interactions can occur between the single $^4T_1(F)$ and double $^4T_1$(P) ESs, visualized by the bending of both lines in the TS diagram. However, TDDFT is not capable of reproducing the double excitations and will only generate single ESs too high in energy as the interaction with the double ESs is lacking[45]. Now, consider the case of a degenerate GS as presented in Figure 3. According to the TS diagram, there is only one double ES state, $^4A_{2g}$, which does not have any ESs with matching symmetry with which it can interact. However, due to the fact that TDDFT selects a specific GS, also micro-states (f) and (i) become double ESs. They have symmetry $^4T_{1g}$ or $^4T_{2g}$ and therefore, interactions with $^4T_{1g}(F)$ can occur.

In the following, we will divide the TMCs shown in Figure 7 in three categories, based on the degeneracy of the GS and the presence of double ESs, and compare the performance of LFDFT and TDDFT. We start with V^{2+} and Ni^{2+} with non-degenerate GSs. In this category, we will also consider tetrahedral d^7 complexes as they play a central role in the search for a possible fingerprint for the ZIF nucleation process. After this, we study Sc^{2+}, Cr^{2+}, Fe^{2+}, and Cu^{2+}, which have a degenerate GS, but for which no double excitations are present. We conclude with the most difficult systems, Ti^{2+} and Co^{2+}, which have both a degenerate GS and the presence of double excitations. A proper description of the latter is also indispensable in order to unravel the nucleation process. Before we dive into this, we first discuss the computational details.

2.2.1 Computational details

The AOC, UDFT, LFDFT, and unrestricted TDDFT calculations were performed with Amsterdam Density Functional (ADF)[64]. As in this work we only focus on isolated complexes and not on the Co-ZIF-67 material, nor on the metal-organic pool, we only performed cluster calculations. The TZ2P+ basis set, with extra d-Slater type orbitals (STO), has been applied for the TMs, and the TZ2P basis set has been used for the other elements. In analogy to our previous work[16], we have chosen to apply the B3LYP-D3 functional[14,42]. Grimme D3 dispersion corrections have also been added[31]. The calculations performed in this work use this level of theory, unless explicitly stated otherwise. As it is well-known that TDDFT results can strongly depend on the used functional[68], two other functionals have also been tested for $[Co(H_2O)_6]^{2+}$, namely PBE0[1] and ωB97[32] as they are known to perform good for the description of TMCs and are available in ADF[19,69]. Methanol has been included as a solvent using COSMO[53]. Recently, Radoń *et al*. stated that the inclusion of the second solvation shell is essential to correctly determine the ESs of octahedral aqua-complexes[54]. However, in this work, the situation is more complicated as the complexes are situated in a methanol environment to mimic the experimental conditions valid in the formation of ZIFs. A full study of the influence of the solvation environment on the ESs of the TMCs is beyond the scope of this work as our focus is on the development of a qualitative fingerprint to follow the nucleation process of ZIFs. Scalar relativistic effects were taken into account using the ZORA formalism[65,66,67]. Geometry optimizations have been performed using UDFT. We checked that all computed internal normal modes of the optimized structures show positive frequencies, ensuring that the geometries represent minima of the GS potential energy surface. The optimized coordinates of all complexes studied in this work are given in Table S2. The symmetry of the complexes has been determined by GaussView 5.0[26]. Although they do not have perfect octahedral and tetrahedral symmetry, we will, for simplicity, use the O_h and T_d symmetry labels to designate the states. In the TDDFT calculations, the lowest 30 excitations have been determined. We convoluted the simulated TDDFT spectra with a Gaussian envelope with a standard deviation of 500 cm^{-1} to simulate the Franck-Condon width of spectra. TDDFT can be performed with or without the symmetry keyword. The main advantage of adding the keyword is that it allows one to determine the symmetry of the ESs, which, in addition to their main contributions, can be helpful for labeling. The biggest disadvantage is that, when symmetry is invoked, the oscillator strength is, per definition, zero. Spin-forbidden ESs can in principle be calculated using Spin-flip (SF)-

TDDFT[59,55,68]. However, these transitions are composed of a lot of small contributions, making it difficult to label them. Furthermore, as they are spin-forbidden, they are much less intense than the excitations calculated via regular TDDFT. Therefore, we will not further discuss spin-forbidden excitations. Spin orbit coupling (SOC) has been included in the LFDFT calculations. Although the degeneracy of the states in the subsequent LFDFT spectra is not shown, this information has been used to group the micro-states and to characterize them with labels according to the TS diagrams.

The AILFT calculations are parameterized via N-electron valence perturbation theory (NEVPT2) using ORCA.[50,52] In order to estimate the effect of dynamical correlation, we compared the results with AILFT calculations starting from a CASSCF(7,5) reference, which does not capture these correlation effects. These calculations are computationally more expensive than the DFT-based techniques and have been performed using a minimal active space as it was found in Ref.[51] and Ref.[70] that this is sufficient for SORCI and multireference calculations, respectively. Although it is expected that the effect of increasing the d-orbital space is small for TMCs with an oxidation state of +2, additional investigations are needed to further test the influence of the active space size. The def2-TZVP basis set has been used and the methanol solvent has been included via the conductor-like polarizable continuum model (C-PCM)[11].

We note that the complexes studied in this work are positively charged. This charge can be counterbalanced by NO_3^- ligands surrounding the TMCs. In addition, it is possible that some of the ligands get deprotonated. However, this depends on the pH of the solution. Setting up models that account for these complexities of the molecular environment would be very complex and is beyond the scope of this study.

2.2.2 Non-degenerate GS but double excitations

$[V(H_2O)_6]^{2+}$ and $[Ni(H_2O)_6]^{2+}$

$[V(H_2O)_6]^{2+}$ and $[Ni(H_2O)_6]^{2+}$ complexes have a d^3 and d^8 configuration, respectively, and thus non-degenerate GSs. Stable structures with D_{2h}, T_h, and S_6 symmetry were obtained. For the V^{2+} complexes, the d-orbital splitting is shown in Figure S3. The LFDFT and TDDFT spectra are shown in Figures 8, S4, and S5. Ni^{2+} complexes have similar results, presented in Figures S6, S7, S8, and S9. As equivalent conclusions can be drawn for the different symmetries,

we only discuss the complexes with D_{2h} symmetry in detail. The only difference with the other complexes is that the peaks in the LFDFT spectra are much broader for the S_6 complex. Also, as the S_6 complexes have the least symmetry, the oscillator strengths calculated by TDDFT are a little bit larger, although they remain very small.

First, we take a look at $[V(H_2O)_6]^{2+}$ and examine the LFDFT results in the top pane of Figure 8. The micro-states are plotted as vertical bars, of which the colors represent their contributions, the quartet states are shown in purple and the doublet states in green. As stated in Section 2.2.1, the labeling of the micro-states according to the TS diagrams is based on their contributions and degeneracy. First of all, at around 0 cm^{-1}, the non-degenerate $^4A_{2g}$ GS is situated, which is purely ^4F. Furthermore, the second region with quartet states is situated around 11750 cm^{-1}, contains large portions of ^4F and corresponds to the $^4T_{2g}$ state. Remark that some contributions of doublet states occur to. The third quartet region at 17600 cm^{-1} contains significant parts from both ^4F and ^4P. The same holds for the band at around 27250 cm^{-1}. They are labeled as $^4T_{1g}(F)$ and $^4T_{1g}(P)$, respectively. As can be seen in the TS diagram shown in Figure 4, $^4T_{1g}(F)$ and $^4T_{1g}(P)$ correspond to a single and double excitation, respectively. They have the same symmetry and mixing is observed in the LFDFT spectrum. In between the previously stated bands doublet contributions are present which will not be analyzed further.

Now, let's inspect the TDDFT results in the bottom pane of Figure 8. The black curve represents the convoluted absorption spectrum, whereas the vertical bars positioned at the excitation energies are hatched according to the main contributions present in the ES. The different hatch styles are introduced in the inset showing the d-orbital splitting obtained by UDFT. There are six excitations with mainly d-d character, grouped in two clusters of three states each. Every ES accords to a transition from a t_{2g} to an e_g orbital. They correspond to the micro-states (b)-(g) in Figure 4 and the clusters can be labeled as $^4T_{2g}$ and $^4T_{1g}(F)$, respectively. Note the presence of an ES in the region where the double excited state $^4T_{1g}(P)$ in the LFDFT spectrum occurs. As it has no d-d character, it does not correspond to $^4T_{1g}(P)$. Indeed, TDDFT is not capable of determining double excitations. Finally remark the very small oscillator strengths for all the ESs.

In our previous work, we observed that the gap between occupied and unoccupied orbitals

is overestimated in UDFT compared to AOC[16]. Although the gap is circa 43000 cm^{-1} versus 11000 cm^{-1} for $[V(H_2O)_6]^{2+}$, the qualitative pictures of the ESs computed by LFDFT and TDDFT agree rather well apart from a shift to higher energies of only 3000-4700 cm^{-1}. The overestimation of the excitation energy of $^4T_{1g}(F)$ can be explained by the fact that the double excited $^4T_{1g}(P)$ is missing in TDDFT as explained in Section 2.2.

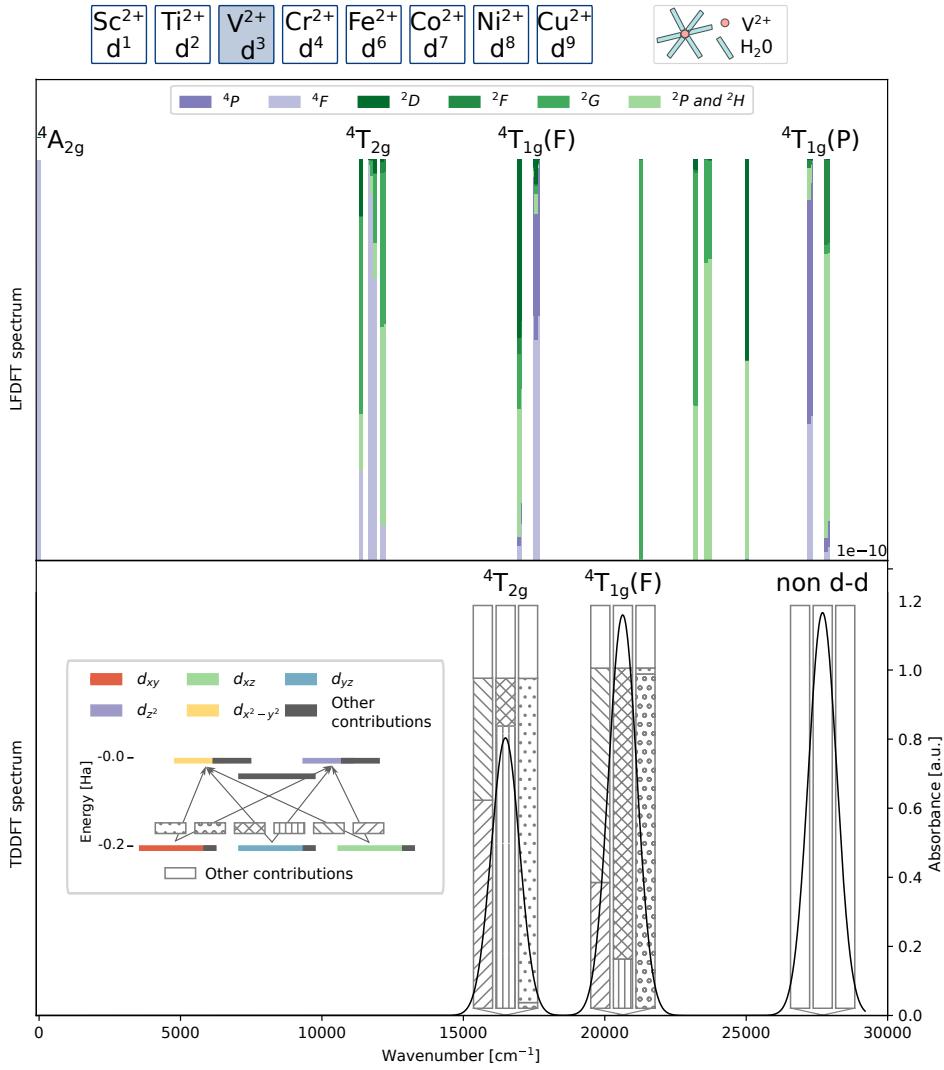

Figure 8: LFDFT (top) and TDDFT (bottom) spectrum of $[V(H_2O)_6]^{2+}$ with D_{2h} symmetry. The vertical bars in the LFDFT spectrum indicate the contribution of each micro-state. The degeneracy is not displayed. In the TDDFT spectrum, the vertical bars show the excitations with mainly d-d character, whereby the largest contributions are denoted. The legend for the different hatch types is given in the inset in which the α d-orbital splitting obtained via UDFT is presented. The black curve represents the convoluted absorption spectrum, for which the axis is presented on the right.

The results are very similar for the Ni^{2+} complexes. Triplet and singlet states are indicated with shades of red and blue, respectively. We observe that there is little mixing between the single and double excited $^3T_{1g}$ states. In the TDDFT spectrum, there are again six d-d ESs, grouped in

two peaks, $^4T_{2g}$ and $^4T_{1g}(F)$, respectively.

Based on the results of these complexes with non-degenerate GSs, we can provisionally conclude that, even though the excitation spectrum contains double ESs and the d-orbital splitting between the occupied and unoccupied orbitals is overestimated by UDFT compared to AOC, TDDFT and LFDFT yield qualitatively similar results for the d-d excitations. However, one must keep in mind that double excitations are not retrieved by TDDFT and one must verify the character of the ES to confirm whether it is a d-d transition or not.

Tetrahedral $[Co(H_2O)_4]^{2+}$ complex

Before investigating the performance of LFDFT and TDDFT for systems with degenerate GSs, we first consider tetrahedral $[Co(H_2O)_4]^{2+}$, as similar four-coordinated complexes with aqua and/or 2-mIm ligands will play an important role in the second part of this work. As can be seen in the TS diagram shown in Figure 4, these complexes have, as $[V(H_2O)_6]^{2+}$ and $[Ni(H_2O)_6]^{2+}$, a non-degenerate GS and contain double excitations. $[Co(H_2O)_4]^{2+}$ has been subject of our preceding work, in which an optimal structure has been obtained[16]. The d-orbital splitting is shown in Figure S10 and the LFDFT and TDDFT spectra in Figure 9. In the LFDFT spectrum, we can clearly distinguish the $^4A_2$ GS and $^4T_2$ and $^4T_1(F)$ single excitations, which all have almost exclusively ^4F contributions. The $^4T_1(P)$ band corresponding to a double excitation is rather broad. Moreover, there is very little mixing between the $^4T_1(F)$ single and $^4T_1(P)$ double excitations. When investigating the TDDFT spectrum, we first of all remark the much larger oscillator strengths observed in the TDDFT results, which is in agreement with our expectations for these non centrosymmetric tetrahedral complexes. This information can not be obtained from LFDFT calculations. Furthermore, there are again six ESs in which an electron is transferred from an e orbital to a t_2 orbital and which correspond to transitions to the micro-states (b)-(g) in Figure 4. These single ESs are grouped in two clusters and are labeled as $^4T_2$ and $^4T_1$. As there is a significant shift between the LFDFT and TDDFT results, we also tested the performance of PBE0 and ωB97, for which the spectra are shifted toward larger and smaller wavelengths with respect to B3LYP, respectively as shown in Figures S11, S12, and S13. The excitation energies strongly depend on the chosen functional as shifts up to 3700 cm^{-1} are observed.

As such, we conclude that also for tetrahedral complexes with non-degenerate GSs, the picture of d-d excitations obtained from LFDFT and TDDFT is qualitatively similar. Moreover, both techniques give supplemental information, whereas LFDFT is capable of describing double excitations, TDDFT yields oscillator strengths. Nevertheless, the exact position of the ESs obtained from TDDFT strongly depend on the functional and differ from the LFDFT results. Therefore, a quantitative comparison with experimental data will be given for the complexes studied in the second part of this work.

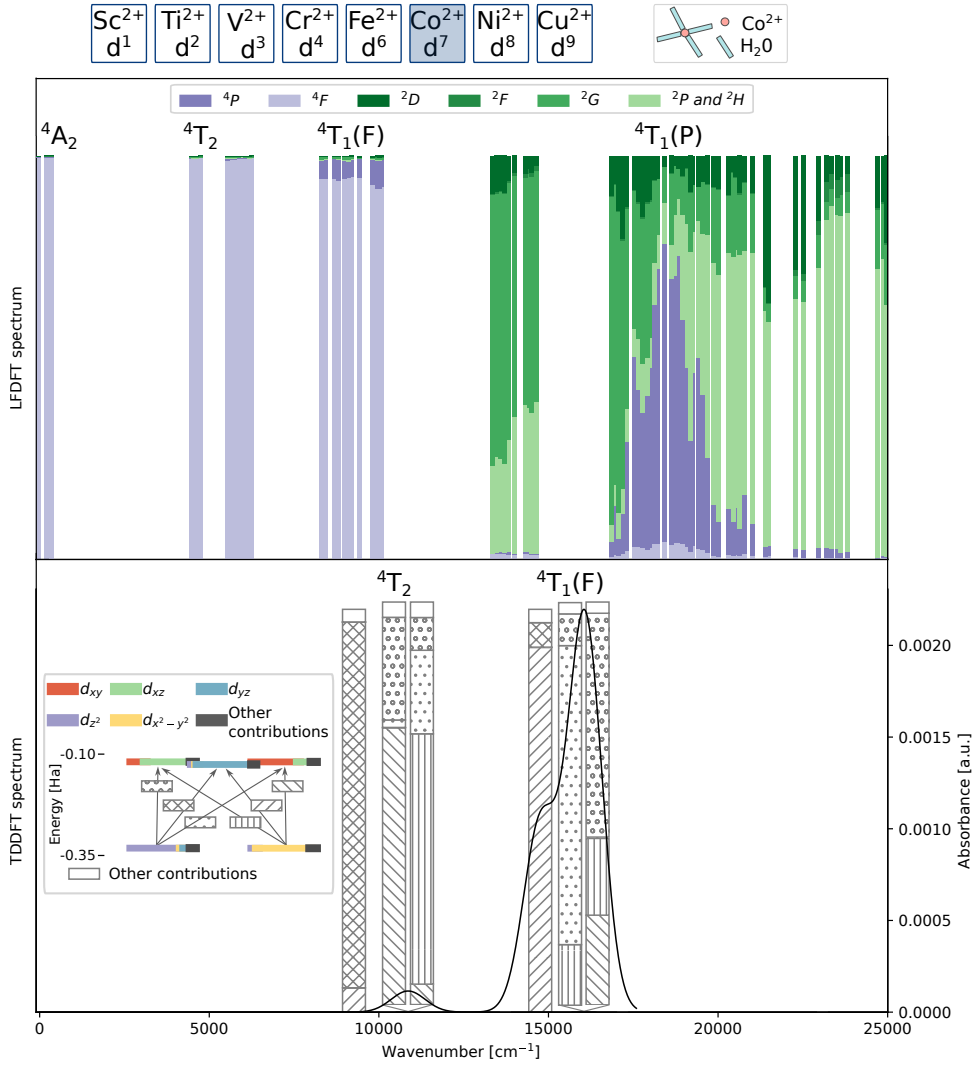

Figure 9: LFDFT (top) and TDDFT (bottom) spectrum of $[Co(H_2O)_4]^{2+}$. The vertical bars in the LFDFT spectrum indicate the contribution of each micro-state. The degeneracy is not displayed. In the TDDFT spectrum, the vertical bars show the excitations with mainly d-d character, whereby the largest contributions are denoted. The legend for the different hatch types is given in the inset in which the β d-orbital splitting obtained via UDFT is presented. The black curve represents the convoluted absorption spectrum, for which the axis is presented on the right.

2.2.3 Degenerate GS but no double excitations: $[Sc(H_2O)_6]^{2+}$, $[Cr(H_2O)_6]^{2+}$ ($[Fe(H_2O)_6]^{2+}$ and $[Cu(H_2O)_6]^{2+}$)

Now, we look into the more complicated complexes which have a degenerate GS, but do not contain double excitations. We found stable $[Cr(H_2O)_6]^{2+}$ and $[Fe(H_2O)_6]^{2+}$ complexes with D_{2h} symmetry. This is the highest possible symmetry as the GS is degenerate. The d-orbital splitting is shown in Figures S14 and S15, respectively and the LFDFT and TDDFT spectra in Figures 10 and 11. A large difference between the Cr^{2+} and Fe^{2+} complexes is that the e_g set is degenerate for the former whereas it is the t_{2g} set for the latter, which corresponds to strong and weak JT distortions, respectively. This is also reflected in the LFDFT spectra as the spread in the GS term, being ${}^5E_g$ and ${}^5T_{2g}$, is much larger for the former than for the latter. The same observation is made for the TDDFT spectra. The first peak is located at larger energies for $[Cr(H_2O)_6]^{2+}$ than for $[Fe(H_2O)_6]^{2+}$ and corresponds to an $e_g \rightarrow e_g$ and two $t_{2g} \rightarrow t_{2g}$ transitions, respectively. The other quintet states, ${}^5T_{2g}$ for Cr^{2+} and ${}^5E_g$ for Fe^{2+}, are situated at higher energies. There are respectively three and two peaks in the LFDFT spectrum which clearly agree with the three $t_{2g} \rightarrow e_g$ and two $e_g \rightarrow t_{2g}$ excitations in the TDDFT spectrum. Finally, we note that there is no mixing between the triplet or singlet contributions and the quintet states. From these case studies, we can conclude that the degeneracy of the GS poses no extra challenges for the calculation of d-d excitations via LFDFT and TDDFT.

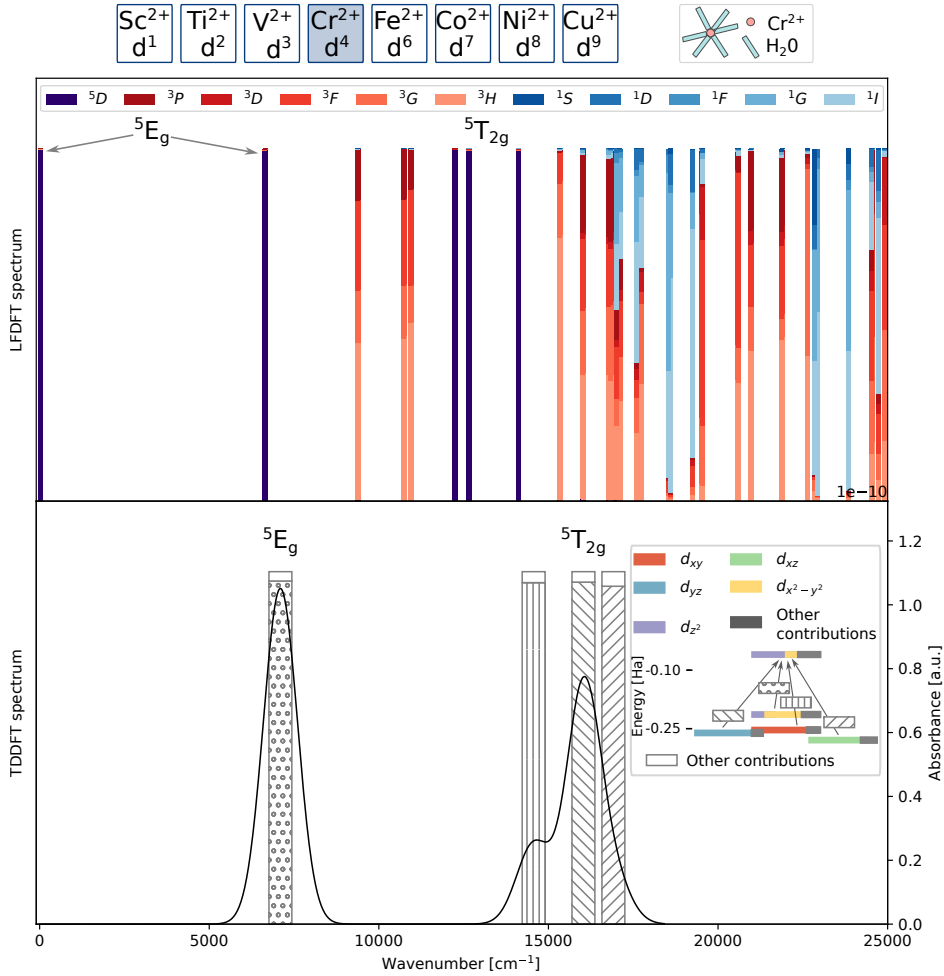

Figure 10: LFDFT (top) and TDDFT (bottom) spectrum of $[Cr(H_2O)_6]^{2+}$ with D_{2h} symmetry. The vertical bars in the LFDFT spectrum indicate the contribution of each micro-state. The degeneracy is not displayed. In the TDDFT spectrum, the vertical bars show the excitations with mainly d-d character, whereby the largest contributions are denoted. The legend for the different hatch types is given in the inset in which the α d-orbital splitting obtained via UDFT is presented. The black curve represents the convoluted absorption spectrum, for which the axis is presented on the right.

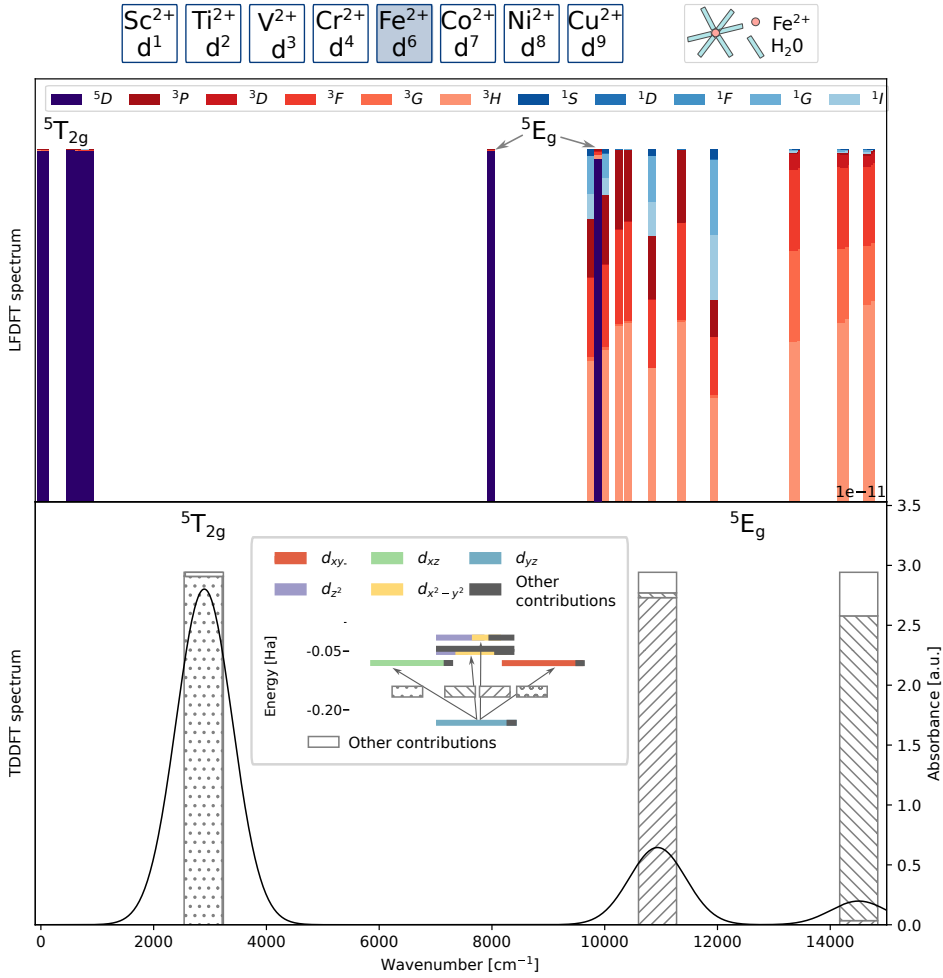

Figure 11: LFDFT (top) and TDDFT (bottom) spectrum of $[Fe(H_2O)_6]^{2+}$ with D_{2h} symmetry. The vertical bars in the LFDFT spectrum indicate the contribution of each micro-state. The degeneracy is not displayed. In the TDDFT spectrum, the vertical bars show the excitations with mainly d-d character, whereby the largest contributions are denoted. The legend for the different hatch types is given in the inset in which the β d-orbital splitting obtained via UDFT is presented. The black curve represents the convoluted absorption spectrum, for which the axis is presented on the right.

As for $[Sc(H_2O)_6]^{2+}$ some other orbitals are situated in between the d-orbitals in the AOC results shown in Figure S16, LFDFT can not be applied. Furthermore, the most common oxidation state of Sc^{2+} is +3. For $[Cu(H_2O)_6]^{2+}$ too, some problems have been encountered as no stable structures have been found in the methanol solvent environment. Therefore, we will not elaborate further on these complexes.

2.2.4 Degenerate GS and double excitations $[Ti(H_2O)_6]^{2+}$ and $[Co(H_2O)_6]^{2+}$

A stable $[Co(H_2O)_6]^{2+}$ structure with D_{2h} symmetry has been obtained previously, but is reoriented such that the smallest metal-bond distance is directed along the z-direction[16]. For completeness, the d-orbital splitting, extensively discussed in Ref.[16], is shown in the left pane of Figure S17. The spectra are presented in Figure 12. In order of increasing energy, we can clearly discern the ${}^4T_{1g}(F)$ GS, single excited ${}^4T_{2g}$, double excited ${}^4A_{2g}$, and single excited ${}^4T_{1g}(P)$ in the LFDFT spectrum. Remark that mixing between the single and double excitations is limited. For the TDDFT spectrum, six ESs occur, which correspond to transitions from the GS to the micro-states (b)-(e), (g), and (h), as shown in Figure 3. They are grouped in three clusters of two ESs each. The first two are excitations in between the t_{2g} orbital set, corresponding to the micro-states (b) and (c), reached via a single excitation from the GS reference (a). These two ESs can thus be labeled as ${}^4T_{1g}(F)$. For the other four excitations, an electron is excited from a t_{2g} to an e_g orbital, which are thus labeled as ${}^4T_{2g}$ and ${}^4T_{1g}(P)$. We also tested the performance of the PBE0 and ωB97 functionals for this complex as shown in Figures S18, S19, and S20. The position of ${}^4T_{1g}(P)$ is shifted to larger/smaller wavelengths compared to the B3LYP results for PBE0 and ωB97, respectively. The functional dependence is less pronounced than for $[Co(H_2O)_4]^{2+}$, but shifts up to 1900 cm^{-1} are still observed. A comparison with the experimental results of Filez *et al.* and other literature data is given in the next section.

In Ref.[16], we also found a stable structure with S_6 symmetry, which has been reoriented such that the ligands are oriented as much as possible toward the coordinate axes. The results are shown in the right pane of Figure S17 and S21. The LFDFT spectra for the D_{2h} and S_6 complexes are in good agreement. However, discrepancies are observed between the TDDFT spectra. Only one ES is corresponding to ${}^4T_{1g}$, which is at much larger energies in the S_6 complex than in the D_{2h} system. Furthermore, one can not distinguish the ${}^4T_{2g}$ and ${}^4T_{1g}(P)$ states. An identical behaviour has been observed for d^2 $[V(H_2O)_6]^{3+}$ complexes presented in Figures S22, S23, and S24.

Unfortunately, the AOC results show that other orbitals are situated in between the d-orbitals for $[Ti(H_2O)_6]^{2+}$ as shown in Figure S25. Hence, this complex will not be studied further.

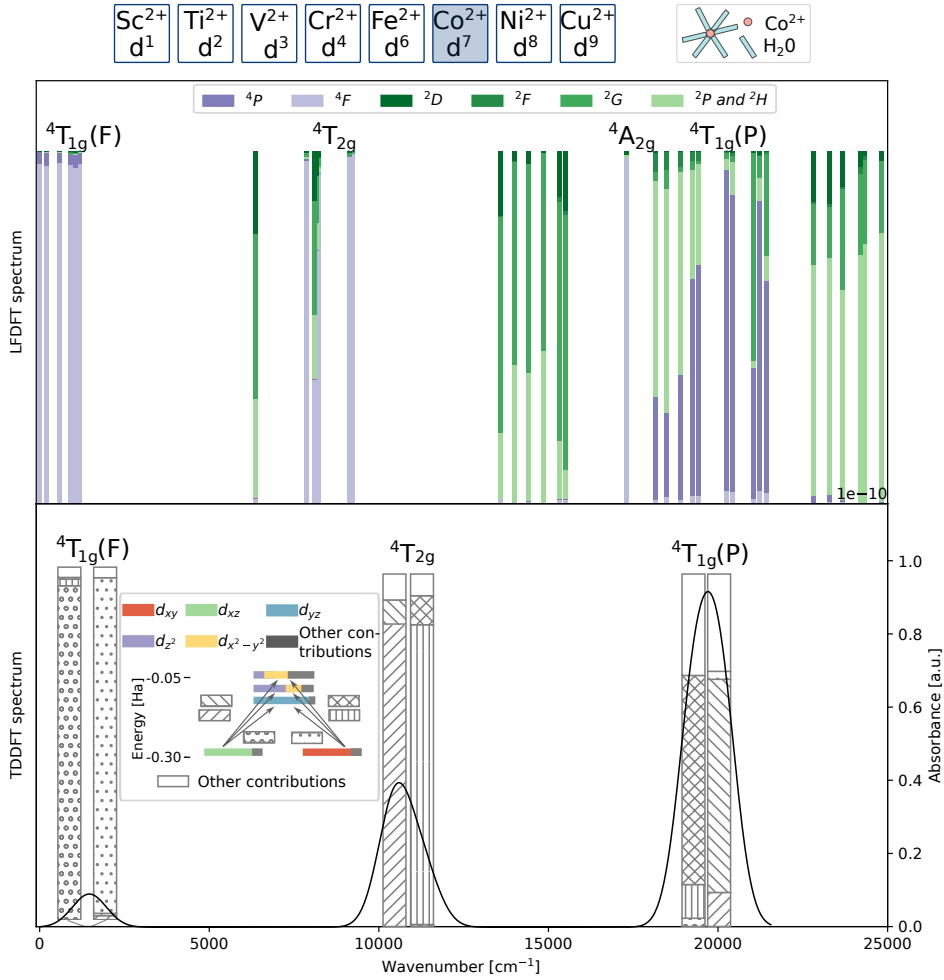

Figure 12: LFDFT (top) and TDDFT (bottom) spectrum of $[Co(H_2O)_6]^{2+}$ with D_{2h} symmetry. The vertical bars in the LFDFT spectrum indicate the contribution of each micro-state. The degeneracy is not displayed. In the TDDFT spectrum, the vertical bars show the excitations with mainly d-d character, whereby the largest contributions are denoted. The legend for the different hatch types is given in the inset in which the β d-orbital splitting obtained via UDFT is presented. The black curve represents the convoluted absorption spectrum, for which the axis is presented on the right.

From this case study of octahedral TMCs with first-row TMs and aqua ligands, extended with tetrahedral Co^{2+} aqua-complexes, we can conclude that LFDFT and TDDFT yield qualitative similar results, which are complementary to each other. Whereas LFDFT is capable of describing double excitations, TDDFT allows one to determine oscillator strengths. The overestimation of the gap between the occupied and unoccupied orbitals by UDFT compared to AOC is

not reflected in the excitation spectra. Even the d-d excitations in challenging systems, with a degenerate GS and double excitations, can be described qualitatively correctly by both techniques. However, care must be taken for complexes with degenerate GSs and double excitations possessing S_6 symmetry, for which only LFDFT yields reasonable results. Furthermore, as for some ESs, the excitation energy is different for the TDDFT and LFDFT results, a comparison with experimental data is necessary. This will be addressed in the next Section, in which we apply both LFDFT and TDDFT to TMCs relevant for the nucleation of ZIFs. The results of the octahedral Co^{2+}complexes with aqua ligands presented in this section are complemented with spectra of tetrahedral Co^{2+} complexes with aqua and/or 2-mIm ligands as indicated in Figure 1. Furthermore, we will compare our computational results for these systems with experimental data and we will briefly investigate the performance of AILFT.

3 Spectroscopic fingerprint for the nucleation of Co-ZIF-67

As stated in the Introduction, the mixture obtained after mixing $Co(NO_3)_2{\cdot}6H_2O$ and 2-mIm mainly consists of the complexes indicated in gray in Figure 1 according to Ref.[27]. The experimental UV-Vis spectrum of the mixture is shown in blue in Figure 13. A linear combination fit (LCF) presented with a dashed line deconvolutes the spectrum in three main contributions. The yellow curve corresponds to $[Co(OR)_6]^{2+}$ complexes, whereby OR can be water, methanol, or NO_3^-. Red indicates $[Co(2\text{-}mIm)_3(OR)]^{2+}$ and the green curve has been identified as $[Co(2\text{-}mIm)_4]^{2+}$. In the following, we will investigate each structure separately. Note that excitations below 14000 cm^{-1} are not measured as this region is situated in the near infra-red lying outside the scope of the work presented in Ref.[27].

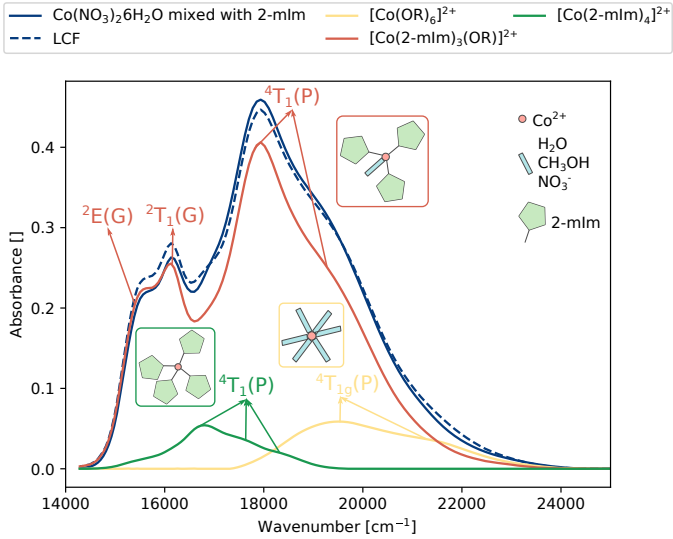

Figure 13: Experimental absorption spectra in the visible range of the electromagnetic spectrum after $Co(NO_3)_2{\cdot}6H_2O$-2-mIm mixing (blue). A LCF (blue, dotted) deconvolutes the spectrum in $[Co(OR)_6]^{2+}$ (yellow), $[Co(2\text{-mIm})_3(OR)]^{2+}$ (red), and $[Co(2\text{-mIm})_4]^{2+}$ (green) constituents. Figure adapted from Ref.[27] with permission of Elsevier, Copyright 2021.

3.1 $[Co(2\text{-mIm})_4]^{2+}$

The $[Co(2\text{-mIm})_4]^{2+}$ complex indicated in green in Figure 13 is characterized by the $^4T_1(P)$ state observed as the three spin-orbit split sub-peaks situated at 16667, 17637, and 18315 cm $^{-1}$. This is in agreement with Banci *et al.*, who used the angular overlap method to state that, for general tetrahedral Co^{2+} complexes, the $^4T_1(P)$ state is situated in the region between 13500 and 19500 cm^{-1} [10]. Furthermore, he showed that these complexes have two additional ESs at lower energies, namely $^4T_2$ and $^4T_1(F)$. The latter lies in the region between 5000 and 11000 cm^{-1}, whereas the former is situated below 5000 cm^{-1} and is therefore difficult to detect[10]. As these states are not situated in the the range of UV-Vis, they are not observed in Figure 13. An overview of ESs in tetrahedral Co^{2+} complexes can be found in Ref.[44].

We performed LFDFT and TDDFT calculations for this complex. Note that in our calculations we used 1,2-dimethylimidazole (1,2-dmIm) instead of 2-mIm to prevent dimerization and to exclusively study the initial change in the symmetry and coordination of Co^{2+}. The geometrical structure is shown in the left pane of Figure 14. The d-orbital splitting is shown in Figure S26.

We compare the LFDFT and TDDFT spectra presented in Figure 15 with these of $[Co(H_2O)_4]^{2+}$ in Figure 9 in order to estimate the influence of changing the ligands from aqua to 2-mIm. First of all, we note that the oscillator strengths in the TDDFT results are four times larger than those of $[Co(H_2O)_4]^{2+}$. Furthermore, there are some minor shifts in the ESs, resulting in a more pronounced left shoulder of the second band, but the overall picture remains unaltered. $^4T_2$ is situated around 10000 cm^{-1}, whereas $^4T_1(F)$ is located around 15000 cm^{-1}. Compared to the results of Banci *et al.*, we must conclude that the spectra are strongly blue-shifted over around 5000 cm^{-1}. This is maybe due to our choice of functional. Indeed, as stated previously, the specific position of the peak as calculated by TDDFT strongly depends on the used functional. As $^4T_1(P)$ is a double excitation, it is not reachable by TDDFT. The micro-states in the LFDFT spectra are no longer present in clusters, but they are more spread-out, making it difficult to determine the energies of the states. This is due to the fact that the imidazole ligands are less compact than the aqua ligands. We can roughly say that the $^4T_2$ state is located between 5000 and 8000 cm^{-1} and the $^4T_1(F)$ state lies between 9000 and 12000 cm^{-1}, which is in agreement with the results of Banci *et al.*. The double excited $^4T_1(P)$ state is located at around 17500 cm^{-1}, in accordance with the results of Filez *et al.*. However, as the bands are rather spread-out, very specific conclusions can not be drawn.

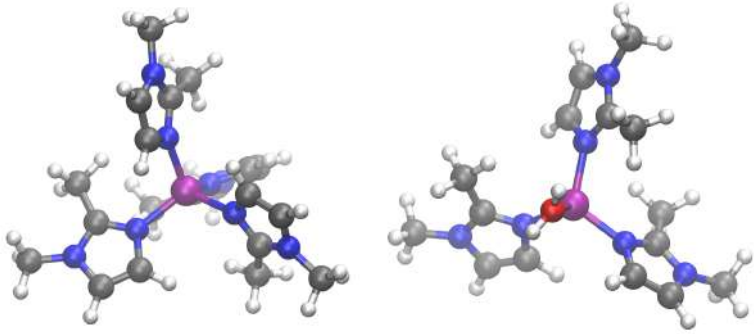

Figure 14: Visualization of the geometrical structure of $[Co(1,2\text{-dmIm})_4]^{2+}$ (left) and $[Co(1,2\text{-dmIm})_3(H_2O)]^{2+}$ (right). Carbon, cobalt, hydrogen, nitrogen, and oxygen are indicated in gray, purple, light gray, blue, and red, respectively.

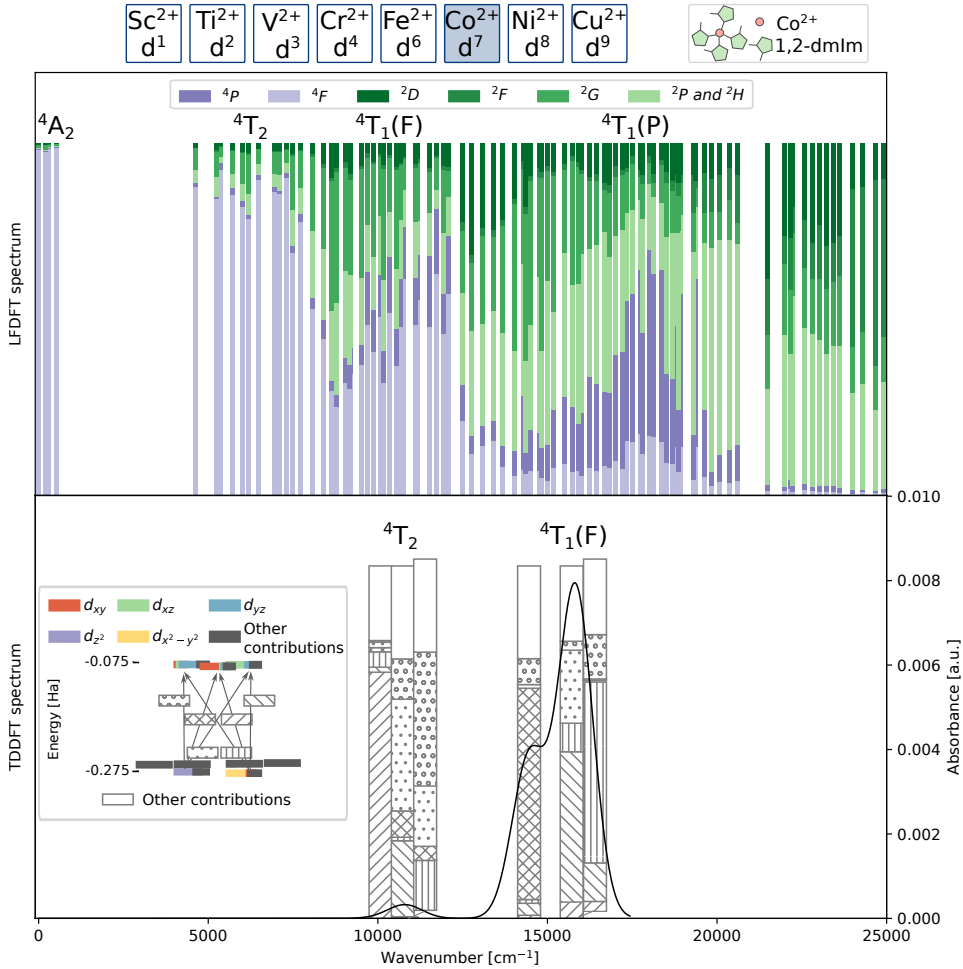

Figure 15: LFDFT (top) and TDDFT (bottom) spectrum of $[Co(1,2\text{-dmIm})_4]^{2+}$. The vertical bars in the LFDFT spectrum indicate the contribution of each micro-state. The degeneracy is not displayed. In the TDDFT spectrum, the vertical bars show the excitations with mainly d-d character, whereby the largest contributions are denoted. The legend for the different hatch types is given in the inset in which the β d-orbital splitting obtained via UDFT is presented. The black curve represents the convoluted absorption spectrum, for which the axis is presented on the right.

As the LFDFT spectrum of the tetrahedral complex with 1,2-dmIm ligands is rather diffuse, we performed AILFT(NEVPT2) calculations too. The results are shown in Figure 16. Contrary to the LFDFT spectra, shown in the top pane of Figure 15, the states are grouped together. Comparison to the TDDFT spectrum shown in the bottom pane of Figure 15 reveals that $^4T_2$ and $^4T_1(F)$ are situated at much smaller energies with a shift of more than 5000 cm^{-1}, which is

in good agreement with the findings of Banci *et al.* discussed in Section 3.1. The double excited $^4T_1(P)$ state is situated at larger energies compared to the experimental spectrum shown in Figure 13 and the results of Banci *et al*.

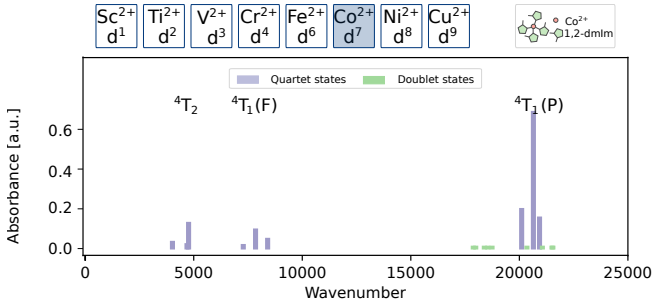

Figure 16: AILFT(NEVPT2) spectrum of $[Co(1,2\text{-dmIm})_4]^{2+}$. Quartet and doublet states are indicated in purple and green, respectively. The intensity of the transition is indicated by the height of the bar. Although the doublet states are spin-forbidden, their bars are given a small height in order to be visible.

3.2 $[Co(2\text{-mIm})_3(OR)]^{2+}$

The following d-d excitations are discerned in the spectrum of $[Co(2\text{-mIm})_3(OR)]^{2+}$ indicated in red in Figure 13. First, two doublet ESs are observed: $^2E(G)$ at 15408 cm^{-1} and $^2T_1(G)$ at 16155 cm^{-1}. These spin-forbidden bands are the most narrow ones in the spectrum, which is in line with our expectations. Because these states correspond to the $t_2^3e^4$ configuration, as shown in Figure 4, it is also possible that some broadening occurs due to JT distortions. At 17825 and 19268 cm^{-1}, the double excited $^4T_1(P)$ state is situated. This spectrum is clearly different from that of $[Co(2\text{-mIm})_4]^{2+}$.

The geometrical structure of $[Co(1,2\text{-dmIm})_3(H_2O)]^{2+}$ is shown in the right pane of Figure 14. The splitting of the d-orbitals is shown in Figure S27 and the LFDFT and TDDFT spectra in Figure 17. We do not observe large differences concerning the d-d transitions corresponding with single excitations obtained via TDDFT between $[Co(1,2\text{-dmIm})_3(H_2O)]^{2+}$ and $[Co(1,2\text{-dmIm})_4]^{2+}$. We only note that there is no shoulder in the second band for the former complex. The four ESs identified in the experimental spectrum are not reachable by TDDFT as they are SF or double excitations. The LFDFT spectrum is even more diffuse than for the previous complex, making it impossible to draw conclusions from it. As the large differences between the tetrahedral Co^{2+} complexes found by Filez *et al.* are not observed by TDDFT, we conclude that

more advanced techniques are needed, which are more precise and capable of determining d-d transitions corresponding with double excitations.

The AILFT(NEVPT2) spectrum of $[Co(1,2\text{-dmIm})_3(H_2O)]^{2+}$ is shown in Figure S29. There are no large differences between this spectrum and the one of $[Co(1,2\text{-dmIm})_4]^{2+}$. As such, we conclude that AILFT(NEVPT2) is more suited to study the tetrahedral complexes with 1,2-dmIm ligands than LFDFT. Nevertheless, the differences observed by Filez between tetrahedral complexes with three and four 1,2-dmIm ligands are not retrieved.

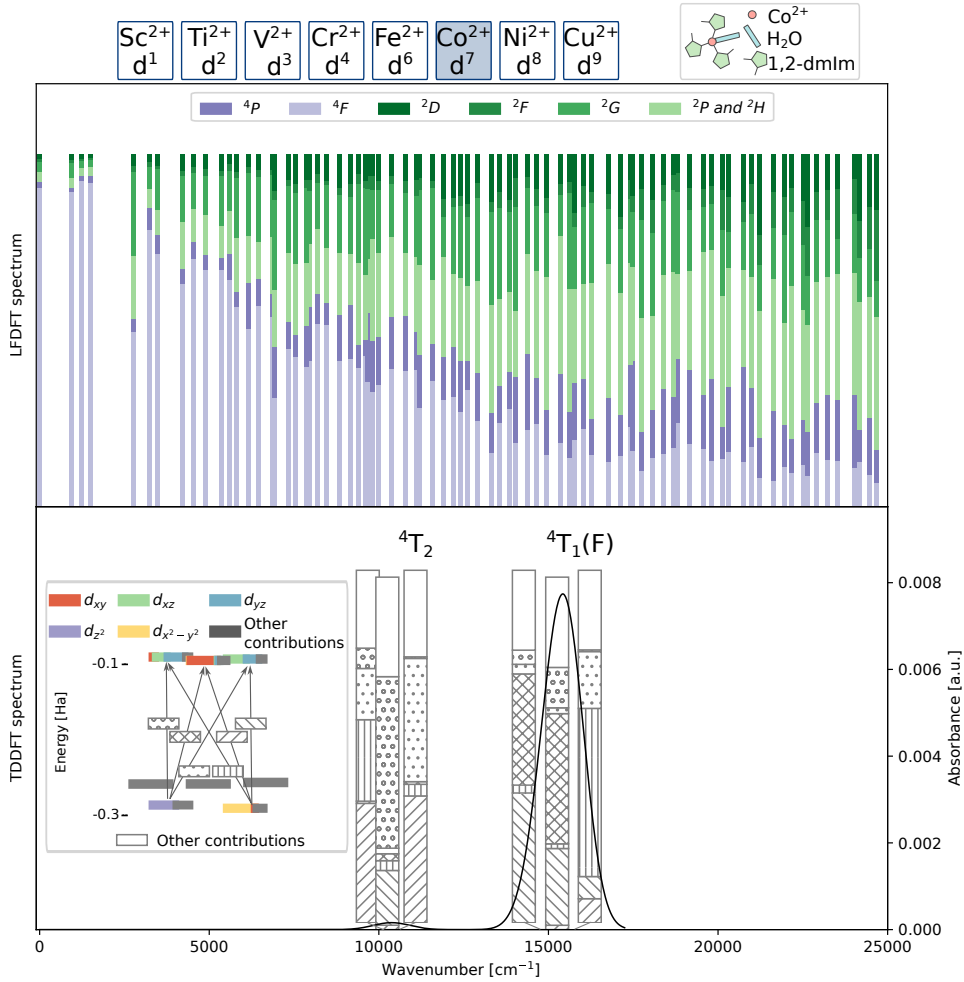

Figure 17: LFDFT (top) and TDDFT (bottom) spectrum of $[Co(1,2\text{-dmIm})_3(OR)]^{2+}$. The vertical bars in the LFDFT spectrum indicate the contribution of each micro-state. The degeneracy is not displayed. In the TDDFT spectrum, the vertical bars show the excitations with mainly d-d character, whereby the largest contributions are denoted. The legend for the different hatch types is given in the inset in which the β d-orbital splitting obtained via UDFT is presented. The black curve represents the convoluted absorption spectrum, for which the axis is presented on the right.

3.3 $[Co(OR)_6]^{2+}$

As indicated with yellow in Figure 13, $[Co(OR)_6]^{2+}$ complexes are characterized by their band maximum at 19531 cm^{-1}, corresponding to the $^4T_{1g}(P)$ state. It has a shoulder located at 21277 cm^{-1}, which also corresponds to the $^4T_{1g}(P)$ state. This is in agreement with the results of Banci

et al., who found that, in general, $^4T_{1g}(P)$ is situated in between 15500 and 22000 cm^{-1} for octahedral Co^{2+} complexes[10]. Furthermore, she found that $^4T_{2g}$ is situated in the band 6500-10500 cm^{-1}, but as this ES is situated below the experimentally measured range, it is not observed in Figure 13. Finally, octahedral Co^{2+} complexes have a double excited $^4A_{2g}$ state with a lower intensity which is therefore often hidden by $^4T_{1g}(P)$. The $^4A_{2g}$ state is experimentally observed as a small peak around 15400 cm^{-1} in the raw experimental absorption spectrum of Filez *et al.*, presented in Figure S28.

Good agreement is found between the spectrum shown in Figure 13 and experimental data of $[Co(H_2O)_6]^{2+}$ complexes in aqueous solution[38] too. Indeed, in Ref.[38], the spin-allowed single excitations to $^4T_{2g}$ and $^4T_{1g}(P)$ are situated at 8100 cm^{-1} and at 19400 and 21550 cm^{-1}, respectively and the spin-allowed double excitation to $^4A_{2g}$ is located at 16000 cm^{-1}. Finally, the lowest energy doublet state, *i.e.*, ^2E_g, is situated at 11300 cm^{-1}.

We now compare the experimental spectrum shown in Figure 13 to the LFDFT and TDDFT results presented in Figure 12. There is a good agreement with the LFDFT spectrum in which $^4T_{2g}$ and $^4T_{1g}(P)$ are situated at 8100-9400 cm^{-1} and 18400-21900 cm^{-1}, respectively. $^4A_{2g}$ is located at 17500 cm^{-1}. It is more difficult to determine the specific excitation energy of ^2E_g as contributions from doublet states are observed at 6600, 8400, and 13600-15700 cm^{-1}. The TDDFT results are also in good agreement: $^4T_{1g}(P)$ is located around 20000 cm^{-1}, whereas there is a slight shift observed for $^4T_{2g}$, which is located at 10000-11300 cm^{-1}.

The AILFT(NEVPT2) spectrum of $[Co(H_2O)_6]^{2+}$ is shown in Figure 18. When comparing with the LFDFT spectrum shown in Figure 12, we note that the spectra are similar but some differences need to be highlighted. First of all, $^4T_{2g}$ and $^4A_{2g}$ are shifted to smaller energies. Excitation energies of $[Co(H_2O)_6]^{2+}$ determined via the ab initio methods, both CASSCF and NEVPT2, and the LFT models derived from them, AILFT(CASSCF) and AILFT(NEVPT2), are listed in Table S1. The influence of dynamic correlation can be estimated by comparing the CASSCF and NEVPT2 on the one hand and the AILFT(CASSCF) and AILFT(NEVPT2) results on the other hand. These results reveal that the inclusion of dynamic correlation effects can not be omitted.

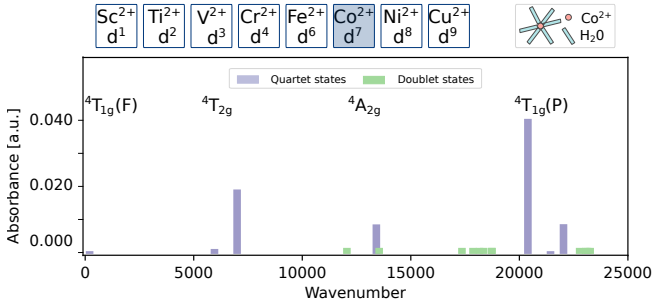

Figure 18: AILFT(NEVPT2) spectrum of $[Co(H_2O)_6]^{2+}$. Quartet and doublet states are indicated in purple and green, respectively. The intensity of the transition is indicated by the height of the bar. Although the doublet states are spin-forbidden, their bars are given a small height in order to be visible.

3.4 Spectroscopic fingerprint

We are now able to propose a spectroscopic fingerprint to follow the nucleation process of Co-ZIF-67. Therefore, we compare the TDDFT spectra, which are shown in Figures 12, 15, and 17 and summarized in Figure 19. Remark that the absorbance is shown on the right axis for $[Co(H_2O)_6]^{2+}$, whereas it is on the left axis for the other complexes. The LFDFT spectra are not considered as no conclusions can be drawn when the TMC possesses extended ligands. First of all, we note that the oscillator strength of the centrosymmetric octahedral complexes is much smaller than of tetrahedral TMCs, which accords with experiments. Based on the calculated absorbance shown in Figure 19 and the experimental data shown in Figure 13, the order of magnitude of the ratio of octahedral versus tetrahedral concentrations can be estimated. We found that the tetrahedral complexes which trigger the nucleation process are 10^{-7}-10^{-8} times less present than the octahedral structures. This indicates that there is only a limited number of tetrahedral complexes which trigger the nucleation process. Furthermore, the most intense peak of the octahedral Co^{2+} complexes is situated at larger energies compared to that of the tetrahedral structures, *i.e.*, 20000 versus 15000 cm^{-1}. Generally, these energies are in the correct ranges and strongly align with CFT, in which a smaller Δ is predicted for tetrahedral complexes than for octahedral ones. Besides the main absorption peak, both octahedral and tetrahedral complexes have additional, less intense, ESs around 10000 cm^{-1}. Finally, d-d excitations with very low energies are observed for the octahedral complexes and arise due to the degeneracy of the GS. As the tetrahedral systems have a non-degenerate GS, no d-d excitations are observed in this region. Unfortunately, on the basis of TDDFT calculations, we are not able to calculate

the characterizing d-d excitations of $[Co(1,2\text{-dmIm})_3(H_2O)]^{2+}$ and $[Co(2\text{-mIm})_4]^{2+}$ as proposed by Filez *et al.* as they are double or SF excitations. Therefore, we must emphasize that other techniques are needed which are able to calculate double excitations, in contrast to TDDFT, or which can handle TMCs with extended ligands, as opposed to LFDFT.

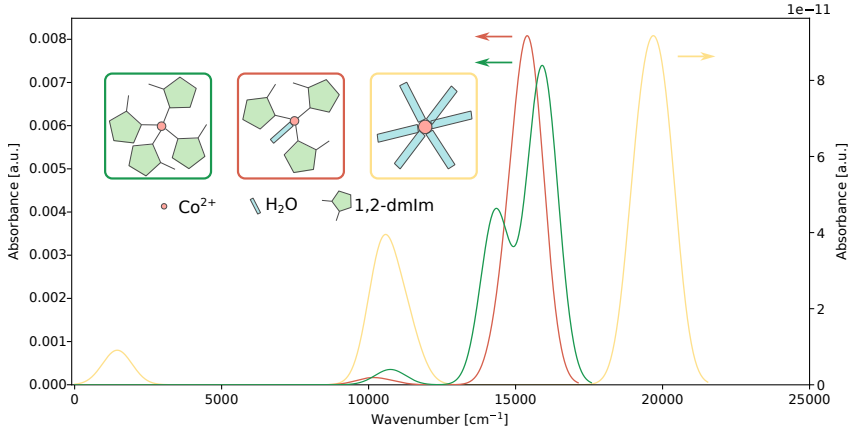

Figure 19: TDDFT spectra of $[Co(H_2O)_6]^{2+}$ (yellow), $[Co(1,2\text{-dmIm})_3(H_2O)]^{2+}$ (red), and $[Co(1,2\text{-dmIm})_4]^{2+}$ (green). The absorbance is on the right for $[Co(H_2O)_6]^{2+}$, whereas it is on the left for $[Co(1,2\text{-dmIm})_3(H_2O)]^{2+}$ and $[Co(1,2\text{-dmIm})_4]^{2+}$.

4 Conclusions

In this work, we studied the d-d excitations of Co^{2+} complexes relevant for the nucleation process of Co-ZIF-67 and compared them with experimental spectra in order to investigate in how far TDDFT or LFDFT are able to provide a spectroscopic fingerprint. As it is widely known that the calculation of ESs for TMCs is very challenging, we first focused on octahedral aqua-complexes in order to investigate the challenges encountered when calculating d-d excitations via LFDFT and TDDFT. In the former, one starts from an AOC reference with fractional occupation numbers whereas ESs are calculated from an UDFT GS in the latter. The octahedral aqua-complexes were divided in three categories based on the degeneracy of the GS and the presence of double excitations. The following conclusions have been made. Although the gap between occupied and unoccupied orbitals is overestimated by UDFT compared to AOC, the results of TDDFT and LFDFT are qualitatively in agreement. This even holds for challenging TMCs with a degenerate GS and double excitations. Furthermore, both techniques provide complementary information, double excitations can be studied via LFDFT whereas the oscil-

lator strength can only be retrieved from TDDFT. However, when one wants to make a quantitative comparison, one needs to take in mind that the energies of single ESs interacting with double ESs are overestimated by TDDFT in which double excitations are not included. In addition, the TDDFT spectra of tetrahedral complexes need a significant red-shift to match the LFDFT and experimental results. As we observed that the d-d excitations strongly depend on the chosen functional, the performance of additional functionals could be tested. Finally, care must be taken when TMCs with S_6 symmetry and a degenerate GS are studied.

In a second step, we reverted our attention to complexes which are relevant for the nucleation of Co-ZIF-67. These include octahedral Co^{2+} aqua-complexes and tetrahedral Co^{2+} complexes with 2-mIm and aqua ligands. The most prominent difference between the octahedral and tetrahedral Co^{2+} complexes is that the oscillator strengths of the former are much smaller as these systems posses a center of symmetry. A comparison of the ratio of the absorption peaks in experiment and theory allowed us to estimate the ratio of octahedral and tetrahedral complexes. It was found that the tetrahedral structures which trigger the nucleation process are 10^{-7}-10^{-8} times less present than the octahedral complexes. Another way in which the tetrahedral and octahedral TMCs can be distinguished is by the position of the main absorption peak, which is shifted to smaller wavelengths for the former, which is in agreement with CFT. Furthermore, additional ESs are observed at very small energies for the octahedral complex, whereas this is not the case for the tetrahedral structures. Neither TDDFT nor LFDFT were able to differentiate between the $[Co(1,2\text{-dmIm})_4]^{2+}$ and $[Co(1,2\text{-dmIm})_3(H_2O)]^{2+}$ complexes. We found that LFDFT can no longer be used for the tetrahedral complexes containing 2-mIm ligands because the obtained spectra are too spread-out. Therefore, we briefly investigated the performance of AILFT and found, just like for TDDFT, that no large differences are observed between the spectra of $[Co(1,2\text{-dmIm})_4]^{2+}$ and $[Co(1,2\text{-dmIm})_3(H_2O)]^{2+}$. Nevertheless, AILFT is a promising technique to study these complicated systems. As the experimentally proposed fingerprint by Filez *et al.* is situated in the UV-Vis region and contains mainly double and SF excitations, other techniques which are able to include double excitations and can handle TMCs with no symmetry are needed to distinguish between these tetrahedral complexes.

5 Supporting Information

Tanabe-Sugano diagrams for octahedral d^2 and d^8 complexes, *d*-orbital splittings obtained with AOC and AILFT, LFDFT, TDDFT, and raw experimental absorption spectra, and geometries of optimized structures (PDF).

6 Acknowledgements

The authors acknowledge the Research Board of Ghent University (BOF) for funding. The computational resources and services used in this work were provided by VSC (Flemish Supercomputer Center), funded by Ghent University, FWO, and the Flemish Government Department EWI. M.F. acknowledges the FWO for a senior postdoctoral research fellowship (1280621N).

References

[1] ADAMO, C., AND BARONE, V. Toward Reliable Density Functional Methods Without Adjustable Parameters: The PBE0 Model. *J. Chem. Phys. 110* (1999), 6158–6169.

[2] ALMEIDA, N. M. S., MCKINLAY, R. G., AND PATERSON, M. J. Computation of excited states of transition metal complexes. *Struct. Bonding 167* (2014), 107–138.

[3] ATANASOV, M., COMBA, P., DAUL, C., AND NEESE, F. The Ligand-Field Paradigm. In *Models, Mysteries and Magic of Molecules*, J. C. A. Boeyens and J. F. Ogilvie, Eds. Springer, 2008, pp. 411–445.

[4] ATANASOV, M., AND DAUL, C. Modeling Properties of Molecules with Open d-shells Using Density Functional Theory. *C. R. Chim. 8* (2005), 1421–1433.

[5] ATANASOV, M., DAUL, C., AND RAUZY, C. New Insights into the Effects of Covalency on the Ligand Field Parameters: a DFT Study. *Chem. Phys. Lett. 367* (2003), 737–746.

[6] ATANASOV, M., DAUL, C., AND RAUZY, C. A DFT Based Ligand Field Theory. *Struct Bond. 106* (2004), 97–125.

[7] ATKINS, P., OVERTON, T., WELLER, M., ARMSTRONG, F., AND HAGERMAN, M. *Shriver & Atkins' Inorganic Chemistry*. W. H. Freeman and Company, 2010.

[8] BAER, R. Prevalence of the Adiabatic Exchange-Correlation Potential Approximation in Time-Dependent Density Functional Theory. *J. Mol. Struct. Teochem. 914* (2009), 19–21.

[9] BAHERS, T. L., BRÉMOND, E., CIOFINI, I., AND ADAMO, C. The Nature of Vertical Excited States of Dyes Containing Metals for DSSC Applications: Insights from TD-DFT and Density Based Indexes. *Phys. Chem. Chem. Phys. 16* (2014), 14435–14444.

[10] BANCI, L., BENCINI, A., BENELLI, C., GATTESCHI, D., ZANCHINI, C., R. BOHRA, J.-M. D., JAIN, V., MEHROTRA, R., TRESSAUD, A., AND WOOLLEY, R. Spectral-Structural Correlations in High-Spin Cobalt(II) Complexes. *Struct. Bonding 52* (2007), 37–86.

[11] BARONE, V., AND COSSI, M. Quantum Calculation of Molecular Energies and Energy Gradients in Solution by a Conductor Solvent Model. *J. Phys. Chem. A 102* (1998), 1995.

[12] BAUERNSCHMITT, R., AND AHLRICHS, R. Stability Analysis for Solutions of the Closed Shell KohnSham Equation. *J. Chem. Phys. 104* (1996), 9047–9052.

[13] BAUERNSCHMITT, R., AND AHLRICHS, R. Treatment of Electronic Excitations Within the Adiabatic Approximation of Time Dependent Density Functional Theory. *Chem. Phys. Lett. 256* (1996), 454 – 464.

[14] BECKE, A. D. Density-Functional Thermochemistry. III. The Role of Exact Exchange. *J. Chem. Phys. 98* (1993), 5648.

[15] BRUECKER, L. D., EVERAERT, J., VOORT, P. V. D., STEVENS, C. V., WAROQUIER, M., AND SPEYBROECK, V. V. Structural and Photophysical Properties of Various Polypyridyl Ligands: A Combined Experimental and Computational Study. *ChemPhysChem 21* (2020), 2489.

[16] BRUECKER, L. D., AND SPEYBROECK, V. V. Influence of Number of Ligands and Point Group on the Electronic Structure of Co^{2+} Aqua-Complexes. *Inorg. Chem. 61* (2022), 20743.

[17] CASIDA, M. E. Time-Dependent Density Functional Response Theory for Molecules. In *Recent Advances in Density Functional Methods*, D. P. Chong, Ed. World Scientific, 1995, p. 155.

[18] CASIDA, M. E., JAMORSKI, C., CASIDA, K. C., AND SALAHUB, D. R. Molecular Excitation Energies to High-Lying Bound States from Time-Dependent Density-Functional Response Theory: Characterization and Correction of the Time-Dependent Local Density Approximation Ionization Threshold. *J. Chem. Phys. 108* (1998), 4439–4449.

[19] CHAN, B., GILL, P. M. W., AND KIMURA, M. Assessment of DFT Methods for Transition Metals with the TMC151 Compilation of Data Sets and Comparison with Accuracies for Main-Group Chemistry. *J. Chem. Theory Comput. 15* (2019), 3610–3622.

[20] CRAMER, C. J., AND TRUHLAR, D. G. Density Functional Theory for Transition Metals and Transition Metal Chemistry. *Phys. Chem. Chem. Phys. 11* (2009), 10757–10816.

[21] CULLEN, J., KRYKUNOV, M., AND ZIEGLER, T. The Formulation of a Self-Consistent Constricted Variational Density Functional Theory for the Description of Excited States. *Chem. Phys. 391* (2011), 11.

[22] DANIEL, C. *Density Functional Theories and Coordination Chemistry*. Elsevier, 2020.

[23] DANIEL, C., GONZÁLEZ, L., AND NEESE, F. Quantum Theory: The Challenge of Transition Metal Complexes. *Phys. Chem. Chem. Phys. 23* (2021), 2533–2534.

[24] DAUL, C. Density Functional Theory Applied to the Excited States of Coordination Compounds. *Int. J. Quantum Chem. 52* (1994), 867–877.

[25] DEETH, R. J. Ligand Field and Density Functional Descriptions of the d-States and Bonding in Transition Metal Complexes. *Faraday Discuss. 124* (2003), 379–391.

[26] DENNINGTON, R., KEITH, T. A., AND MILLAM, J. M. Gaussview Version 5, 2019. Semichem Inc. Shawnee Mission KS.

[27] FILEZ, M., CARATELLI, C., RIVERA-TORRENTE, M., MUNIZ-MIRANDA, F., HOEK, M., ALTELAAR, M., HECK, A. J. R., SPEYBROECK, V. V., AND WECKHUYSEN, B. M. Elucidation of the Pre-Nucleation Phase Directing Metal-Organic Framework Formation. *Cell Rep. Phys. Sci. 2* (2021), 100680.

[28] GISBERGEN, S. V., GROENEVELD, J., ROSA, A., SNIJDERS, J., AND BAERENDS, E. Excitation Energies for Transition Metal Compounds from Time-Dependent Density Functional Theory. Applications to MnO_4^-, $Ni(CO)_4$, and $Mn_2(CO)_{10}$. *J. Phys. Chem. A 103* (1999), 6835–6844.

[29] GONZÁLEZ, L., ESCUDERO, D., AND SERRANO-ANDRÉS, L. Progress and Challenges in the Calculation of Electronic Excited States. *ChemPhysChem 13* (2012), 28–51.

[30] GRIFFITH, J. S. *The theory of transition metal ions*. Cambridge university press, 1961.

[31] GRIMME, S., ANTONY, J., EHRLICH, S., AND KRIEG, H. A Consistent and Accurate Ab Initio Parametrization of Density Functional Dispersion Correction (DFT-D) for the 94 Elements H-Pu. *J. Chem. Phys. 132* (2010), 154104.

[32] GRIMME, S., EHRLICH, S., AND GOERIGK, L. Effect of The Damping Function in Dispersion Corrected Density Functional Theory. *J. Comp. Chem. 32* (2011), 1456–1465.

[33] HOLMES, O. G., AND MCCLURE, D. S. Optical Spectra of Hydrated Ions of the Transition Metals. *J. Chem. Phys. 26* (1957), 1686–1694.

[34] HU, Y., KAZEMIAN, H., ROHANI, S., HUANG, Y., AND SONG, Y. In Situ High Pressure Study of ZIF-8 by FTIR Spectroscopy. *Chem. Commun. 47* (2011), 12694–12696.

[35] JAHN, H. A., AND TELLER, E. Stability of Polyatomic Molecules in Degenerate Electronic States. I. Orbital Degeneracy. *Proc. R. Soc. London A 220-235* (1937), 161.

[36] JAMORSKI, C., CASIDA, M. E., AND SALAHUB, D. R. Dynamic Polarizabilities and Excitation Spectra from a Molecular Implementation of TimeDependent DensityFunctional Response Theory: N_2 as a Case Study. *J. Chem. Phys. 104* (1996), 5134.

[37] JÖRGENSEN, C. K. *Absorption Spectra and Chemical Bonding in Complexes*. Pergamon Press, 1962.

[38] JÖRGENSEN, C. K. *Spectroscopy of Transition-Group Complexes in Advances in Chemical Physics*. John Wiley and Sons, Inc., 1963.

[39] KRYKUNOV, M., AND ZIEGLER, T. Self-Consistent Formulation of Constricted Variational Density Functional Theory with Orbital Relaxation. Implementation and Applications. *J. Chem. Theory Comput. 9* (2013), 2761.

[40] LAURENT, A. D., ADAMO, C., AND JACQUEMIN, D. Dye Chemistry with Time-Dependent Density Functional Theory. *Phys. Chem. Chem. Phys. 16* (2014), 14334–14356.

[41] LAURENT, A. D., AND JACQUEMIN, D. TD-DFT Benchmarks: A Review. *Int. J. Quantum Chem. 113* (2013), 2019–2039.

[42] LEE, C., YANG, W., AND PARR, R. G. Development of the Colle-Salvetti Correlation-Energy Formula into a Functional of the Electron Density. *Phys. Rev. B 37* (1988), 785.

[43] LEJAEGHERE, K., BIHLMAYER, G., BJÖRKMAN, T., BLAHA, P., BLÜGEL, S., BLUM, V., CALISTE, D., CASTELLI, I. E., CLARK, S. J., CORSO, A. D., DE GIRONCOLI, S., DEUTSCH, T., DEWHURST, J. K., MARCO, I. D., DRAXL, C., DUŁAK, M., ERIKSSON, O., FLORES-LIVAS, J. A., GARRITY, K. F., GENOVESE, L., GIANNOZZI, P., GIANTOMASSI, M., GOEDECKER, S., GONZE, X., GRÅNÄS, O., GROSS, E. K. U., GULANS, A., GYGI, F., HAMANN, D. R., HASNIP, P. J., HOLZWARTH, N. A. W., IUŞAN, D., JOCHYM, D. B., JOLLET, F., JONES, D., KRESSE, G., KOEPERNIK, K., KÜŞÜKBENLI, E., KVASHNIN, Y. O., LOCHT, I. L. M., LUBECK, S., MARSMAN, M., MARZARI, N., NITZSCHE, U., NORDSTRÖM, L., OZAKI, T., PAULATTO, L., PICKARD, C. J., POELMANS, W., PROBERT, M. I. J., REFSON, K., RICHTER, M., RIGNANESE, G.-M., SAHA, S., SCHEFFLER, M., SCHLIPF, M., SCHWARZ, K., SHARMA, S., TAVAZZA, F., THUNSTRÖM, P., TKATCHENKO, A., TORRENT, M., VANDERBILT, D., VAN SETTEN, M. J., SPEYBROECK, V. V., WILLS, J. M., YATES, J. R., ZHANG, G.-X., AND COTTENIER, S. Reproducibility in Density Functional Theory Calculations of Solids. *Science 351* (2016), aad3000.

[44] LEVER, A. B. P. *Inorganic electronic spectroscopy (Second edition)*. Elsevier, 1984.

[45] MAITRA, N. T. Double and Charge-Transfer Excitations in Time-Dependent Density Functional Theory. *Ann. Rev. Phys. Chem. 73* (2022), 117–140.

[46] MIESSLER, G. L., FISCHER, P. J., AND TARR, D. A. *Inorganic Chemistry*. Pearson, 2014.

[47] MINGOS, D. M. P., DAY, P., AND DAHL, J. P. *Molecular Electronic Structures of Transition Metal Complexes II*. Springer Berlin Heidelberg, 2012.

[48] MORI, K., GOUMANS, T. P. M., VAN LENTHE, E., AND WANG, F. Predicting Phosphorescent Lifetimes and Zero-Field Splitting of Organometallic Complexes with Time-Dependent Density Functional Theory Including Spin-Orbit Coupling. *Phys. Chem. Chem. Phys. 16* (2014), 14523–14530.

[49] MUNIZ-MIRANDA, F., BRUECKER, L. D., VOS, A. D., BUSSCHE, F. V., STEVENS, C., DER VOORT, P. V., LEJAEGHERE, K., AND SPEYBROECK, V. V. Optical Properties of Isolated and Covalent Organic Framework-Embedded Ruthenium Complexes. *J. Phys. Chem. A 123* (2019), 6854.

[50] NEESE, F. Software Update: The ORCA Program System-Version 5.0. *WIREs Comput Mol Sci. 12* (2022), e1606.

[51] NEESE, F., PETRENKO, T., GANYUSHIN, D., AND OLBRICH, G. Advanced Aspects of Ab Initio Theoretical Optical Spectroscopy of Transition Metal Complexes: Multiplets, Spin-Orbit Coupling and Resonance Raman Intensities. *Coord. Chem. Rev. 251* (2007), 288–327.

[52] NEESE, F., WENNMOHS, F., BECKER, U., AND RIPLINGER, C. The ORCA Quantum Chemistry Program Package. *J. Chem. Phys. 152* (2020), 224108.

[53] PYE, C. C., AND ZIEGLER, T. An Implementation of the Conductor-Like Screening Model of Solvation Within the Amsterdam Density Functional Package. *Theor. Chem. Acc. 101* (1999), 396–408.

[54] RADOŃ, M., AND DRABIK, G. Spin States and Other Ligand-Field States of Aqua Complexes Revisited with Multireference ab Initio Calculations Including Solvation Effects. *J. Chem. Theory Comput. 14* (2018), 4010–4027.

[55] RINKEVICIUS, Z., VAHTRAS, O., AND AGREN, H. Spin-Flip Time Dependent Density Functional Theory Applied to Excited States with Single, Double, or Mixed Electron Excitation Character. *J. Chem. Phys. 113* (2010), 114104.

[56] ROSA, A., RICCIARDI, G., GRITSENKO, O., AND BAERENDS, E. Principles and Applications of Density Functional Theory in Inorganic Chemistry I. Springer, 2004, pp. 49–116.

[57] RUNGE, E., AND GROSS, E. K. U. Density-Functional Theory for Time-Dependent Systems. *Phys. Rev. Lett. 52* (1984), 997–1000.

[58] SEIDU, I., KRYKUNOV, M., AND ZIEGLER, T. The Formulation of a Constricted Variational Density Functional Theory for Double Excitations. *Mol. Phys. 112* (2014), 661–668.

[59] SHAO, Y., HEAD-GORDON, M., AND KRYLOV, A. I. The Spin-Flip Approach within Time-Dependent Density Functional Theory: Theory and Applications to Diradicals. *J. Chem. Phys. 118* (2003), 4807.

[60] SHEE, J., LOIPERSBERGER, M., HAIT, D., LEE, J., AND HEAD-GORDON, M. Revealing the Nature of Electron Correlation in Transition Metal Complexes with Symmetry-Breaking and Chemical Intuition. *J. Chem. Phys. 154* (2021), 194109.

[61] SINGH, S. K., ENG, J., ATANASOV, M., AND NEESE, F. Covalency and Chemical Bonding in Transition Metal Complexes: An Ab Initio Based Ligand Field Perspective. *Coor. Chem. Rev. 344* (2017), 2–25.

[62] SUN, Y., ROGGE, S. M. J., LAMAIRE, A., VANDENBRANDE, S., WIEME, J., SIVIOUR, C. R., SPEYBROECK, V. V., AND TAN, J.-C. High-Rate Nanofluidic Energy Absorption in Porous Zeolitic Frameworks. *Nat. Mater. 20* (2021), 1015–1023.

[63] TANABE, Y., AND SUGANO, S. On the Absorption Spectra of Complex Ions. I. *J. Phys. Soc. Japan 9* (1954), 753–766.

[64] TE VELDE, G., BICKELHAUPT, F. M., BAERENDS, E., GUERRA, C. F., VAN GISBERGEN, S., SNIJDERS, J., AND ZIEGLER, T. Chemistry with ADF. *J. Comp. Chem. 22* (2001), 931–967.

[65] VAN LENTHE, E., BAERENDS, E. J., AND SNIJDERS, J. G. Relativistic Regular Two-Component Hamiltonians. *J. Chem. Phys. 99* (1993), 4597.

[66] VAN LENTHE, E., BAERENDS, E. J., AND SNIJDERS, J. G. Relativistic Total Energy Using Regular Approximations. *J. Chem. Phys. 101* (1994), 9783–9792.

[67] VAN LENTHE, E., EHLERS, A., AND BAERENDS, E. J. Geometry Optimization in the Zero Order Regular Approximation for Relativistic Effects. *J. Chem. Phys. 110* (1999), 8943–8953.

[68] VLAHOVIC, F., PERIC, M., GRUDEN-PAVLOVIĆ, M., AND ZLATAR, M. Assessment of TD-DFT and LF-DFT for Study of d-d Transitions in First Row Transition Metal Hexaaqua Complexes. *J. Chem. Phys. 142* (2015), 214111.

[69] WEYMUTH, T., COUZIJN, E. P. A., CHEN, P., AND REIHER, M. New Benchmark Set of Transition-Metal Coordination Reactions for the Assessment of Density Functionals. *J. Chem. Theory Comput. 10* (2014), 3092–3103.

[70] YANG, Y., RATNER, M. A., AND SCHATZ, G. C. Multireference Ab Initio Study of Ligand Field d-d Transitions in Octahedral Transition-Metal Oxide Clusters. *J. Phys. Chem. C 118* (2014), 29196–29208.

[71] YAO, J., AND WANG, H. Zeolitic Imidazolate Framework Composite Membranes and Thin Films: Synthesis and Applications. *Chem. Soc. Rev. 43* (2014), 4470–4493.

[72] ZIEGLER, T., KRYKUNOV, M., SEIDU, I., AND PARK, Y. C. *Constricted Variational Density Functional Theory Approach to the Description of Excited States*. Springer International Publishing, 2016, pp. 61–95.

[73] ZIEGLER, T., RAUK, A., AND BAERENDS, E. J. On the Calculation of Multiplet Energies by the Hartree-Fock-Slater Method. *Theor. Chim. Acta. 43* (1977), 261–271.

[74] ZOBEL, J. P., AND GONZÁLEZ, L. The Quest to Simulate Excited-State Dynamics of Transition Metal Complexes. *JACS Au 1* (2021), 1116–1140.

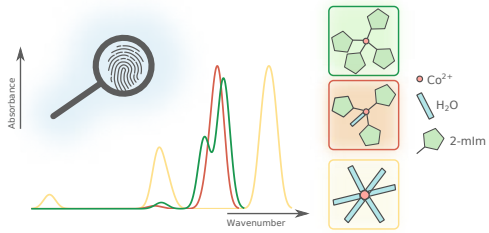

For Table of Contents Only

The number, intensity, and position of $d - d$ excitations of transition metal complexes relevant in the ZIF nucleation process have been investigated to propose a spectroscopic fingerprint. These excited states are characterized via computational techniques based on density functional theory. In general, the spectra obtained from time-dependent density functional theory and ligand field density functional theory are qualitatively similar and provide complementary information, but the latter is not suited for complexes with extended ligands.

B

Appendix

In this appendix, the proofs of the fundamental theorems of TDDFT and derivations for expressions encountered in Chapter 2 are given based on Ref. 88. Furthermore, the symmetry elements for five-coordinated trigonal bipyramidal and square pyramidal complexes are visualized. In addition, the character tables of point groups encountered in this work are given. Finally, the Tanabe-Sugano diagrams for various d-electron configurations are provided.

B.1 Proofs of the fundamental theorems and derivations of expressions encountered in the study of TDDFT

B.1.1 Proof of the Runge-Gross theorem

Before proving the Runge-Gross theorem, we elucidate what is meant by different potentials. Based on the TD Schrödinger equation given in Eq. (2.1), we can state that, if two potentials differ by an additive TD scalar function $c(t)$, the corresponding wavefunctions only differ by a TD phase factor:

$$\tilde{v}(\boldsymbol{r},t) = v(\boldsymbol{r},t) + c(t) \rightarrow \tilde{\Psi}(t) = e^{-i\alpha(t)}\Psi(t), \tag{B.1}$$

with $c(t) = \mathrm{d}\alpha(t)/\mathrm{d}t$. When there is no confusion, we drop the spatial and spin dependence of the TD wavefunction $\Psi(\boldsymbol{x}_1 \cdots \boldsymbol{x}_N, t)$ by writing it as

$\Psi(t)$. The resulting densities are identical since the phase factors cancel out:

$$\begin{aligned}\tilde{n}(\boldsymbol{r},t) =& \langle\tilde{\Psi}(t)|\hat{n}(\boldsymbol{r})|\tilde{\Psi}(t)\rangle \\ =& \langle\Psi(t)|e^{i\alpha(t)}\hat{n}(\boldsymbol{r})e^{-i\alpha(t)}|\Psi(t)\rangle \\ =& \langle\Psi(t)|\hat{n}(\boldsymbol{r})|\Psi(t)\rangle \\ =& n(\boldsymbol{r},t).\end{aligned} \tag{B.2}$$

Therefore, we say that two potentials are non-identical when they differ by more than an additive TD scalar function.

In order to prove the Runge-Gross theorem, it is required that the external potential is expandable in a Taylor series with respect to the time coordinate around the initial time t_0:

$$\begin{aligned}v(\boldsymbol{r},t) =& \sum_{k=0}^{\infty}\frac{1}{k!}\frac{\partial^k v(\boldsymbol{r},t)}{\partial t^k}|_{t=t_0}(t-t_0)^k \\ =& \sum_{k=0}^{\infty}\frac{1}{k!}v_0^{(k)}(\boldsymbol{r})(t-t_0)^k,\end{aligned} \tag{B.3}$$

and similar for $v'(\boldsymbol{r},t)$. In the second line, we introduced a shorthand notation for the k-th time-derivative at $t=t_0$.

We prove the Runge-Gross theorem by showing that two different potentials result in different densities. As the potentials are non-identical, a smallest integer l exists such that

$$v_0^{(l)}(\boldsymbol{r}) - v_0'^{(l)}(\boldsymbol{r}) \neq \text{constant}. \tag{B.4}$$

In the first part of the proof, we demonstrate that different potentials result in different currents. In the second part, we extend this to the densities by making use of the continuity equation.

Proof. In the first part, we show that a one-to-one correspondence exists between current densities and external potentials. Therefore, we start from the current density which is given by

$$\boldsymbol{j}(\boldsymbol{r},t) = \langle\Psi(t)|\hat{\boldsymbol{j}}(\boldsymbol{r})|\Psi(t)\rangle, \tag{B.5}$$

with the paramagnetic current-density operator defined as:

$$\hat{\boldsymbol{j}}(\boldsymbol{r}) = \frac{1}{2i}\sum_{l=1}^{N}\left[\nabla_l\delta(\boldsymbol{r}-\boldsymbol{r}_l) + \delta(\boldsymbol{r}-\boldsymbol{r}_l)\nabla_l\right]. \tag{B.6}$$

The equation of motion for the expectation value of a general operator $\hat{Q}(t)$ is given by

$$\frac{\partial}{\partial t}\langle\Psi(t)|\hat{Q}(t)|\Psi(t)\rangle = \langle\Psi(t)|\left(\frac{\partial\hat{Q}}{\partial t} - i\left[\hat{Q}(t),\hat{H}(t)\right]\right)|\Psi(t)\rangle, \tag{B.7}$$

which results in the following expression for the current density:

$$\frac{\partial}{\partial t}\boldsymbol{j}(\boldsymbol{r},t) = -i\langle\Psi(t)|\left[\hat{\boldsymbol{j}}(\boldsymbol{r}),\hat{H}(t)\right]|\Psi(t)\rangle. \tag{B.8}$$

We also consider a second system, indicated with a prime:

$$\frac{\partial}{\partial t}\boldsymbol{j}'(\boldsymbol{r},t) = -i\langle\Psi'(t)|\left[\hat{\boldsymbol{j}}(\boldsymbol{r}),\hat{H}'(t)\right]|\Psi'(t)\rangle. \tag{B.9}$$

When we evaluate Eq. (B.8) and (B.9) at $t = t_0$ and subtract the results, we obtain:

$$\frac{\partial}{\partial t}\left\{\boldsymbol{j}(\boldsymbol{r},t) - \boldsymbol{j}'(\boldsymbol{r},t)\right\}|_{t=t_0} = -i\langle\Psi_0|\left[\hat{\boldsymbol{j}}(\boldsymbol{r}),\hat{H}(t_0) - \hat{H}'(t_0)\right]|\Psi_0\rangle, \tag{B.10}$$

where both $\Psi(t)$ and $\Psi'(t)$ evolve from the same initial state Ψ_0. Hence, the kinetic and electron-electron interaction terms are identical at t_0 in both systems and the Hamiltonians only differ in their one-body external potentials:

$$\frac{\partial}{\partial t}\left\{\boldsymbol{j}(\boldsymbol{r},t) - \boldsymbol{j}'(\boldsymbol{r},t)\right\}|_{t=t_0} = -i\langle\Psi_0|\left[\hat{\boldsymbol{j}}(\boldsymbol{r}),\sum_{i=1}^{N}v(\boldsymbol{r}_i,t_0) - \sum_{i=1}^{N}v'(\boldsymbol{r}_i,t_0)\right]|\Psi_0\rangle. \tag{B.11}$$

We first focus on the un-primed terms in Eq. (B.11)

$$\frac{\partial}{\partial t}\boldsymbol{j}(\boldsymbol{r},t)|_{t=t_0} = -i\langle\Psi_0|\left[\hat{\boldsymbol{j}}(\boldsymbol{r}),\sum_{i=1}^{N}v(\boldsymbol{r}_i,t_0)\right]|\Psi_0\rangle. \tag{B.12}$$

When we pass to the coordinate representation, we introduce the following shorthand notations:

$$\begin{aligned}
&\bar{\boldsymbol{x}} \equiv \boldsymbol{x}_1\cdots\boldsymbol{x}_N\\
&\mathrm{d}\bar{\boldsymbol{x}} \equiv \mathrm{d}\boldsymbol{x}_1\cdots\mathrm{d}\boldsymbol{x}_{\boldsymbol{N}}\\
&\bar{\Psi} \equiv \Psi(\bar{\boldsymbol{x}},t)\\
&\bar{\Psi}_0 \equiv \Psi_0(\bar{\boldsymbol{x}}) \equiv \Psi(\bar{\boldsymbol{x}},t_0).
\end{aligned} \tag{B.13}$$

We obtain for the right-hand side of Eq. (B.12):

$$
\begin{aligned}
&-\frac{1}{2}\sum_{i,l=1}^{N}\int \mathrm{d}\bar{\boldsymbol{x}}\bar{\Psi}_0^*\left[\nabla_l\delta(\boldsymbol{r}-\boldsymbol{r}_l)+\delta(\boldsymbol{r}-\boldsymbol{r}_l)\nabla_l, v(\boldsymbol{r}_i,t_0)\right]\bar{\Psi}_0\\
&=-\frac{1}{2}\sum_{i,l=1}^{N}\int \mathrm{d}\bar{\boldsymbol{x}}\bar{\Psi}_0^*\Big\{\nabla_l\left[\delta(\boldsymbol{r}-\boldsymbol{r}_l)v(\boldsymbol{r}_i,t_0)\bar{\Psi}_0\right]+\delta(\boldsymbol{r}-\boldsymbol{r}_l)\nabla_l\left[v(\boldsymbol{r}_i,t_0)\bar{\Psi}_0\right]\\
&\qquad\qquad -v(\boldsymbol{r}_i,t_0)\nabla_l\left[\delta(\boldsymbol{r}-\boldsymbol{r}_l)\bar{\Psi}_0\right]-v(\boldsymbol{r}_i,t_0)\delta(\boldsymbol{r}-\boldsymbol{r}_l)\nabla_l[\bar{\Psi}_0]\Big\}.
\end{aligned}
\tag{B.14}
$$

On the first and third term in the integrand, an integration by parts is performed where the boundary terms cancel.

$$
\begin{aligned}
-\frac{1}{2}\sum_{i,l=1}^{N}\int \mathrm{d}\bar{\boldsymbol{x}}\Big\{&-\nabla_l[\bar{\Psi}_0^*]\delta(\boldsymbol{r}-\boldsymbol{r}_l)v(\boldsymbol{r}_i,t_0)\bar{\Psi}_0+\bar{\Psi}_0^*\delta(\boldsymbol{r}-\boldsymbol{r}_l)\nabla_l\left[v(\boldsymbol{r}_i,t_0)\bar{\Psi}_0\right]\\
&+\nabla_l[\bar{\Psi}_0^*v(\boldsymbol{r}_i,t_0)]\delta(\boldsymbol{r}-\boldsymbol{r}_l)\bar{\Psi}_0-\bar{\Psi}_0^*v(\boldsymbol{r}_i,t_0)\delta(\boldsymbol{r}-\boldsymbol{r}_l)\nabla_l[\bar{\Psi}_0]\Big\}.
\end{aligned}
\tag{B.15}
$$

The second and third term are calculated and part of them cancel with the first and fourth term. The resulting two terms are identical and the factor $1/2$ cancels

$$
\frac{\partial}{\partial t}\boldsymbol{j}(\boldsymbol{r},t)|_{t=t_0}=-\sum_{i,l=1}^{N}\int \mathrm{d}\bar{\boldsymbol{x}}\bar{\Psi}_0^*\delta(\boldsymbol{r}-\boldsymbol{r}_l)\bar{\Psi}_0\nabla_l v(\boldsymbol{r}_i,t_0).
\tag{B.16}
$$

∇_l is acting on $v(\boldsymbol{r}_i,t)$ and will only differ from zero when $i=l$. Furthermore, all terms in the summation are equal, therefore we chose $l=1$ and introduce a factor N

$$
\frac{\partial}{\partial t}\boldsymbol{j}(\boldsymbol{r},t)|_{t=t_0}=-N\int \mathrm{d}\bar{\boldsymbol{x}}\bar{\Psi}_0^*\delta(\boldsymbol{r}-\boldsymbol{r}_1)\bar{\Psi}_0\nabla_1 v(\boldsymbol{r}_1,t_0).
\tag{B.17}
$$

Working out the delta function, we obtain

$$
\begin{aligned}
\frac{\partial}{\partial t}\boldsymbol{j}(\boldsymbol{r},t)|_{t=t_0}=&-N\sum_{\sigma}\times\\
&\int \mathrm{d}\boldsymbol{x}_2\cdots\mathrm{d}\boldsymbol{x}_N\Psi_0^*(\boldsymbol{r},\boldsymbol{x}_2\cdots\boldsymbol{x}_N,t)\Psi_0(\boldsymbol{r},\boldsymbol{x}_2\cdots\boldsymbol{x}_N,t)\nabla v(\boldsymbol{r},t_0).
\end{aligned}
\tag{B.18}
$$

Finally, this can be rewritten using the density

$$
\frac{\partial}{\partial t}\boldsymbol{j}(\boldsymbol{r},t)|_{t=t_0}=-n(\boldsymbol{r},t_0)\nabla v(\boldsymbol{r},t_0).
\tag{B.19}
$$

The same holds for the primed-terms in Eq. (B.11). Inserting the obtained results in Eq. (B.11) results in

$$\frac{\partial}{\partial t}\left\{\boldsymbol{j}(\boldsymbol{r},t)-\boldsymbol{j}'(\boldsymbol{r},t)\right\}|_{t=t_0}=-n(\boldsymbol{r},t_0)\nabla\left[v(\boldsymbol{r},t_0)-v'(\boldsymbol{r},t_0)\right]. \tag{B.20}$$

If Eq. (B.4) is satisfied for $l=0$, the right-hand side cannot vanish identically and $\boldsymbol{j}$ and $\boldsymbol{j}'$ will become different infinitesimally later than $t=t_0$. If the smallest integer l for which the condition holds, is larger than zero, we repeatedly use the equation of motion given in Eq. (B.7) and evaluate at $t=t_0$ [129]:

$$\frac{\partial^{l+1}}{\partial t^{l+1}}\left[\boldsymbol{j}(\boldsymbol{r},t)-\boldsymbol{j}'(\boldsymbol{r},t)\right]|_{t=t_0}=-n(\boldsymbol{r},t_0)\nabla\left[v_0^{(l)}(\boldsymbol{r})-v_0'^{(l)}(\boldsymbol{r})\right]. \tag{B.21}$$

Again, as the right-hand side is not identically equal to zero, the left-hand side must be different from zero. From this we can conclude that a one-to-one correspondence exists between the current density and the external potential.

In the second part of the proof, we use the continuity equation, providing a relation between the current density and the density:

$$\frac{\partial n(\boldsymbol{r},t)}{\partial t}=-\nabla\cdot\boldsymbol{j}(\boldsymbol{r},t). \tag{B.22}$$

We take the divergence of Eq. (B.21) and use Eq. (B.22) to obtain:

$$\frac{\partial^{l+2}}{\partial t^{l+2}}\left[n(\boldsymbol{r},t)-n'(\boldsymbol{r},t)\right]|_{t=t_0}=\nabla\cdot\left[n(\boldsymbol{r},t_0)\nabla w_0^{(l)}(\boldsymbol{r})\right], \tag{B.23}$$

where $w_0^{(l)}(\boldsymbol{r})=v_0^{(l)}(\boldsymbol{r})-v_0'^{(l)}(\boldsymbol{r})$. After multiplying with $w_0^{(l)}(\boldsymbol{r})$, the right-hand side can be rewritten as follows:

$$\begin{aligned}w_0^{(l)}(\boldsymbol{r})\nabla\cdot\left[n(\boldsymbol{r},t_0)\nabla w_0^{(l)}(\boldsymbol{r})\right]&=\nabla\cdot\left[w_0^{(l)}(\boldsymbol{r})n(\boldsymbol{r},t_0)\nabla w_0^{(l)}(\boldsymbol{r})\right]-\\&\quad n(\boldsymbol{r},t_0)\left[\nabla w_0^{(l)}(\boldsymbol{r})\right]^2.\end{aligned} \tag{B.24}$$

When we integrate over a volume element, Green's theorem can be used for the first term on the right-hand side and Eq. (B.24) becomes:

$$\begin{aligned}\int \mathrm{d}\boldsymbol{r}\, w_0^{(l)}(\boldsymbol{r})\nabla\cdot\left[n(\boldsymbol{r},t_0)\nabla w_0^{(l)}(\boldsymbol{r})\right]&=\oint \mathrm{d}\boldsymbol{S}\cdot\left[n(\boldsymbol{r},t_0)w_0^{(l)}(\boldsymbol{r})\nabla w_0^{(l)}(\boldsymbol{r})\right]-\\&\quad\int \mathrm{d}\boldsymbol{r}\, n(\boldsymbol{r},t_0)\left[\nabla w_0^{(l)}(\boldsymbol{r})\right]^2.\end{aligned} \tag{B.25}$$

For physically reasonable potentials, the surface integral on the right-hand side vanishes when the surface is taken far enough. As we assumed that the two potentials are different, the right-hand side of Eq. (B.23) is strictly negative and thus

$$\frac{\partial^{l+2}}{\partial t^{l+2}} n(\boldsymbol{r},t)|_{t=t_0} \neq \frac{\partial^{l+2}}{\partial t^{l+2}} n'(\boldsymbol{r},t)|_{t=t_0}. \tag{B.26}$$

As such, we have shown that densities evolving from the same initial states under the influence of different potentials can not be identical. □

B.1.2 Proof of the van Leeuwen theorem

In order to proof the van Leeuwen theorem, we require that $n(\boldsymbol{r},t) = n'(\boldsymbol{r},t)$ and use the fact that therefore all derivatives of the density are equal. Consequently, in contrast to the Runge-Gross theorem, not only the potential must be time-analytic around the initial time, but also the density.

The proof proceeds in two steps. In the first part, an expression between the density and the external potential is derived. In the second step, the new external potential is explicitly constructed, with the only constraint being that $v'(\boldsymbol{r},t)$ vanishes at infinity.

Proof. In the first step, we derive a relation between the density and the external potential. In a similar way as for the Runge-Gross theorem, the following expression is obtained for Eq. (B.8):

$$\frac{\partial \boldsymbol{j}(\boldsymbol{r},t)}{\partial t} = \frac{N}{2} \int \mathrm{d}\bar{\boldsymbol{x}}\, \delta(\boldsymbol{r}-\boldsymbol{r}_1)\Big\{ H\bar{\Psi}^* \nabla[\bar{\Psi}] - \bar{\Psi}^* \nabla[H\bar{\Psi}] + \text{c.c.}\Big\}, \tag{B.27}$$

where c.c. indicates the complex conjugate. We start with the time evolution of the α component, being x, y, or z, of the probability current as given in Eq. (B.27):

$$\frac{\partial j_\alpha(\boldsymbol{r},t)}{\partial t} = \frac{N}{2} \int \mathrm{d}\bar{\boldsymbol{x}}\, \delta(\boldsymbol{r}-\boldsymbol{r}_1)\left\{ H\bar{\Psi}^* \frac{\partial \bar{\Psi}}{\partial r_\alpha} - \bar{\Psi}^* \frac{\partial H\bar{\Psi}}{\partial r_\alpha} + \text{c.c.}\right\}. \tag{B.28}$$

In the following, we treat each part of the Hamiltonian given in Eq. (2.10) separately.

kinetic term

The kinetic energy of the electrons is given by Eq. (2.3). The part of the integrand of Eq. (B.28) situated between the brackets, without considering

the complex conjugate, is given by:

$$\begin{aligned}
&\left(-\frac{1}{2}\sum_{i=1}^{N}\nabla_i^2\bar{\Psi}^*\right)\frac{\partial\bar{\Psi}}{\partial r_\alpha}+\frac{1}{2}\bar{\Psi}^*\frac{\partial}{\partial r_\alpha}\left(\sum_{i=1}^{N}\nabla_i^2\bar{\Psi}\right)\\
=&-\frac{1}{2}\sum_{i=1}^{N}\left(\nabla_i\cdot\left[\left(\nabla_i\bar{\Psi}^*\right)\frac{\partial\bar{\Psi}}{\partial r_\alpha}\right]-\nabla_i\bar{\Psi}^*\cdot\nabla_i\frac{\partial\bar{\Psi}}{\partial r_\alpha}\right)\\
&+\frac{1}{2}\sum_{i=1}^{N}\left(\nabla_i\cdot\left[\bar{\Psi}^*\nabla_i\frac{\partial\bar{\Psi}}{\partial r_\alpha}\right]-\nabla_i\bar{\Psi}^*\cdot\nabla_i\frac{\partial\bar{\Psi}}{\partial r_\alpha}\right)\\
=&-\frac{1}{2}\sum_{i=1}^{N}\nabla_i\cdot\left(\left(\nabla_i\bar{\Psi}^*\right)\frac{\partial\bar{\Psi}}{\partial r_\alpha}-\bar{\Psi}^*\nabla_i\frac{\partial\bar{\Psi}}{\partial r_\alpha}\right).
\end{aligned}\tag{B.29}$$

A similar expression holds for the complex conjugate. Like for the previous theorem, Green's theorem is used. Again, the integral yields a vanishing surface integral at infinity for $i\neq 1$ and only the term with $i=1$ remains. Eq. (B.28) then becomes:

$$\begin{aligned}
\frac{\partial j_\alpha(\boldsymbol{r},t)}{\partial t}=&-\nabla\cdot\frac{N}{4}\sum_{\sigma}\int \mathrm{d}\boldsymbol{x}_2\cdots\mathrm{d}\boldsymbol{x}_N\times\\
&\Big\{\nabla\Psi^*(\boldsymbol{r},\boldsymbol{x}_2\cdots\boldsymbol{x}_N,t)\frac{\partial}{\partial r_\alpha}\Psi(\boldsymbol{r},\boldsymbol{x}_2\cdots\boldsymbol{x}_N,t)-\\
&\Psi^*(\boldsymbol{r},\boldsymbol{x}_2\cdots\boldsymbol{x}_N,t)\nabla\frac{\partial}{\partial r_\alpha}\Psi(\boldsymbol{r},\boldsymbol{x}_2\cdots\boldsymbol{x}_N,t)+\text{c.c.}\Big\}.
\end{aligned}\tag{B.30}$$

Furthermore, we introduce a new short-hand notation

$$\begin{aligned}
\hat{\boldsymbol{x}}&\equiv\boldsymbol{r},\boldsymbol{x}_2\cdots\boldsymbol{x}_N\\
\hat{\Psi}&\equiv\Psi(\hat{\boldsymbol{x}},t).
\end{aligned}\tag{B.31}$$

Let us take a look at the β component of the divergence for which the integrand becomes:

$$\begin{aligned}
&\frac{\partial\hat{\Psi}^*}{\partial r_\beta}\frac{\partial\hat{\Psi}}{\partial r_\alpha}-\hat{\Psi}^*\frac{\partial^2\hat{\Psi}}{\partial r_\alpha\partial r_\beta}+\frac{\partial\hat{\Psi}}{\partial r_\beta}\frac{\partial\hat{\Psi}^*}{\partial r_\alpha}-\hat{\Psi}\frac{\partial^2\hat{\Psi}^*}{\partial r_\alpha\partial r_\beta}\\
=&2\frac{\partial\hat{\Psi}^*}{\partial r_\beta}\frac{\partial\hat{\Psi}}{\partial r_\alpha}+2\frac{\partial\hat{\Psi}}{\partial r_\beta}\frac{\partial\hat{\Psi}^*}{\partial r_\alpha}-\frac{\partial^2\hat{\Psi}\hat{\Psi}^*}{\partial r_\alpha\partial r_\beta}
\end{aligned}\tag{B.32}$$

With the momentum-stress tensor $T_{\beta\alpha}(\boldsymbol{r},t)$, which is part of the energy-momentum tensor, defined as:

$$T_{\beta\alpha}(\boldsymbol{r},t)\triangleq\frac{N}{2}\int\mathrm{d}\boldsymbol{x}_2\cdots\mathrm{d}\boldsymbol{x}_N\,\frac{\partial}{\partial r_\beta}\left\{\frac{\partial\hat{\Psi}^*}{\partial r_\beta}\frac{\partial\hat{\Psi}}{\partial r_\alpha}+\frac{\partial\hat{\Psi}}{\partial r_\beta}\frac{\partial\hat{\Psi}^*}{\partial r_\alpha}-\frac{1}{2}\frac{\partial^2\hat{\Psi}\hat{\Psi}^*}{\partial r_\alpha\partial r_\beta}\right\},\tag{B.33}$$

Eq. (B.30) becomes

$$\frac{\partial j_\alpha(\boldsymbol{r},t)}{\partial t} = -\sum_\beta \frac{\partial}{\partial r_\beta} T_{\beta\alpha}(\boldsymbol{r},t). \tag{B.34}$$

electron-electron interaction

The electron-electron repulsion is given by Eq. (2.4). The right-hand side of Eq. (B.28), without considering the complex conjugate, is then:

$$\begin{aligned}
&\frac{N}{2}\int \mathrm{d}\bar{\boldsymbol{x}}\,\delta(\boldsymbol{r}-\boldsymbol{r}_1)\left\{\left(\frac{1}{2}\sum_{i\neq j}^{N}\frac{1}{|\boldsymbol{r}_i-\boldsymbol{r}_j|}\bar{\Psi}^*\right)\frac{\partial\bar{\Psi}}{\partial r_\alpha} - \bar{\Psi}^*\frac{\partial}{\partial r_\alpha}\left(\frac{1}{2}\sum_{i\neq j}^{N}\frac{1}{|\boldsymbol{r}_i-\boldsymbol{r}_j|}\bar{\Psi}\right)\right\}\\
&= \frac{N}{2}\int \mathrm{d}\bar{\boldsymbol{x}}\,\delta(\boldsymbol{r}-\boldsymbol{r}_1)\left\{\frac{1}{2}\sum_{i\neq j}^{N}\frac{1}{|\boldsymbol{r}_i-\boldsymbol{r}_j|}\bar{\Psi}^*\frac{\partial\bar{\Psi}}{\partial r_\alpha} - \bar{\Psi}^*\frac{\partial\bar{\Psi}}{\partial r_\alpha}\left(\frac{1}{2}\sum_{i\neq j}^{N}\frac{1}{|\boldsymbol{r}_i-\boldsymbol{r}_j|}\right)\right.\\
&\qquad\qquad \left. - \frac{1}{2}\bar{\Psi}^*\bar{\Psi}\frac{\partial}{\partial r_\alpha}\sum_{i\neq j}^{N}\frac{1}{|\boldsymbol{r}_i-\boldsymbol{r}_j|}\right\}\\
&= -\frac{N}{4}\int \mathrm{d}\bar{\boldsymbol{x}}\,\delta(\boldsymbol{r}-\boldsymbol{r}_1)|\bar{\Psi}|^2\frac{\partial}{\partial r_\alpha}\sum_{i\neq j}^{N}\frac{1}{|\boldsymbol{r}_i-\boldsymbol{r}_j|},
\end{aligned} \tag{B.35}$$

where, in the first step, the derivative of the product in the second term is calculated. The complex conjugate results in an identical contribution.

In order for the integrand to be different from zero, either $\boldsymbol{r}_i = \boldsymbol{r}_\alpha$ or $\boldsymbol{r}_j = \boldsymbol{r}_\alpha$. In the first case, $j \in \{1,\cdots,\alpha-1,\alpha+1,\cdots N\}$, whereas in the second case $i \in \{1,\cdots,\alpha-1,\alpha+1,\cdots N\}$. Since all particles are indistinguishable , we put $\boldsymbol{r}_j = \boldsymbol{r}_2$ in the first case and $\boldsymbol{r}_i = \boldsymbol{r}_2$ in the second case. Furthermore, as $|\boldsymbol{r}_\alpha - \boldsymbol{r}_2| = |\boldsymbol{r}_2 - \boldsymbol{r}_\alpha|$, both cases yield the same result. As such, the following expression for the electron-electron interaction $V_{ee,\alpha}(\boldsymbol{r},t)$ is obtained:

$$-V_{ee,\alpha}(\boldsymbol{r},t) = -\frac{N(N-1)}{2}\int \mathrm{d}\bar{\boldsymbol{x}}\,\delta(\boldsymbol{r}-\boldsymbol{r}_1)|\bar{\Psi}|^2\frac{\partial}{\partial r_\alpha}\frac{1}{|\boldsymbol{r}_\alpha-\boldsymbol{r}_2|}. \tag{B.36}$$

external potential

The external potential is given by Eq. (2.27) and this part was already treated in the proof of the Runge-Gross theorem in Section B.1.1. The result is given in Eq. (B.19).

Putting all contributions together, we obtain:

$$\frac{\partial j_\alpha(\boldsymbol{r},t)}{\partial t} = -n(\boldsymbol{r},t)\frac{\partial v(\boldsymbol{r},t)}{\partial r_\alpha} - \sum_\beta \frac{\partial T_{\beta\alpha}(\boldsymbol{r},t)}{\partial r_\beta} - V_{ee,\alpha}(\boldsymbol{r},t), \tag{B.37}$$

which is a local quantum version of Newton's third law [255]. From now on, we drop the position- and time-dependence to ease the notation. We take the time-derivative of the continuity Eq. (B.22) and use Eq. (B.37), which results in:

$$\begin{aligned}\frac{\partial^2 n}{\partial t^2} &= \nabla\cdot(n\nabla v) + \sum_{\alpha,\beta}\frac{\partial^2 T_{\beta\alpha}}{\partial r_\beta \partial r_\alpha} + \sum_\alpha \frac{\partial V_{ee,\alpha}}{\partial r_\alpha} \\ &= \nabla\cdot(n\nabla v) + q.\end{aligned} \tag{B.38}$$

In the last equation, we introduced a new quantity q, encompassing the momentum-stress tensor and the electron-electron interaction. Eq. (B.38) is very useful as it defines a relation between the density and the external potential.

In the second step, we explicitly construct the new external potential. Consider a system with Hamiltonian given by Eq. (2.10). We define a new system evolving under a new external potential, denoted with a prime, with Hamiltonian: $H'(t) = T_e + V'_{ee} + V'_{en}(t)$. Both systems give the same density, *i.e.*, $n(\boldsymbol{r},t) = n'(\boldsymbol{r},t)$.

We start with determining the new initial state Ψ'_0. As Eq. (B.38) is a second order differential equation in time for $n(\boldsymbol{r},t)$, two conditions are imposed. First of all, at $t = t_0$, the density in the new system must be equal to the target probability density:

$$\begin{aligned}n'(\boldsymbol{r},t_0) &= \langle\Psi'_0|\hat{n}(\boldsymbol{r})|\Psi'_0\rangle \\ &= \langle\Psi_0|\hat{n}(\boldsymbol{r})|\Psi_0\rangle \\ &= n(\boldsymbol{r},t_0)\end{aligned} \tag{B.39}$$

The second condition that needs to be fulfilled is:

$$\frac{\partial}{\partial t}n'(\boldsymbol{r},t)|_{t=t_0} = \frac{\partial}{\partial t}n(\boldsymbol{r},t)|_{t=t_0}, \tag{B.40}$$

which can be rewritten by using the continuity equation given in Eq. (B.22):

$$\begin{aligned}\nabla\cdot\boldsymbol{j}'(\boldsymbol{r},t)|_{t=t_0} &= \langle\Psi'_0|\nabla\cdot\hat{\boldsymbol{j}}(\boldsymbol{r})|\Psi'_0\rangle \\ &= \langle\Psi_0|\nabla\cdot\hat{\boldsymbol{j}}(\boldsymbol{r})|\Psi_0\rangle \\ &= \nabla\cdot\boldsymbol{j}(\boldsymbol{r},t)|_{t=t_0}.\end{aligned} \tag{B.41}$$

Now, we construct the external potential $v'(\boldsymbol{r},t)$ in such a way that $n(\boldsymbol{r},t) = n'(\boldsymbol{r},t)$. Therefore, we impose $n_0'^{(k)} = n_0^{(k)}$ for all k. As $v'(\boldsymbol{r},t)$ is time-analytic, it can be written as shown in Eq. (B.3) and is completely defined when all $v_0'^{(k)}$ are specified. We evaluate Eq. (B.38) for the primed system at $t = t_0$:

$$n_0'^{(2)} = \nabla \cdot \left(n_0'^{(0)} \nabla v_0'^{(0)} \right) + q_0'^{(0)}. \tag{B.42}$$

Now, we impose $n_0'^{(2)} = n_0^{(2)}$. As the initial state $|\Psi_0'\rangle$ is chosen in such a way that $n_0'^{(0)} = n_0^{(0)}$, as shown in Eq. (B.39), this can be rewritten as follows:

$$\nabla \cdot \left(n_0^{(0)} \nabla v_0'^{(0)} \right) = n_0^{(2)} - q_0'^{(0)}. \tag{B.43}$$

This is a Sturm-Liouville equation which defines $v_0'^{(0)}$ as all other quantities are known. This equation has a unique solution provided the following boundary condition is specified: $v_0'^{(0)}(\boldsymbol{r}) \to 0$ for $\boldsymbol{r} \to \infty$.

As such, the total potential is defined recursively via its Taylor expansion coefficients $v_0'^{(k)}$. $v_0'^{(1)}$ is obtained by taking the derivative of Eq. (B.38) and evaluating the resulting expression in $t = t_0$:

$$n_0'^{(3)} = \nabla \cdot \left(n_0'^{(0)} \nabla v_0'^{(1)} \right) + \nabla \cdot \left(n_0'^{(1)} \nabla v_0'^{(0)} \right) + q_0'^{(1)}. \tag{B.44}$$

Again, we equate the derivatives of the probability densities $n_0'^{(3)} = n_0^{(3)}$ and obtain the following expression for $v_0'^{(1)}$:

$$\nabla \cdot \left(n_0^{(0)} \nabla v_0'^{(1)} \right) = n_0^{(3)} - \nabla \cdot \left(n_0'^{(1)} \nabla v_0'^{(0)} \right) - q_0'^{(1)}. \tag{B.45}$$

All quantities on the right-hand side are known as $v_0'^{(0)}$ has been determined from Eq. (B.43) and $q_0'^{(1)}$ can be calculated from

$$\begin{aligned} q_0'^{(1)} =& \frac{\partial}{\partial t} q'(\boldsymbol{r},t)|_{t=t_0} \\ =& -i\langle \Psi_0' | \left[\hat{\boldsymbol{q}}'(\boldsymbol{r}), \hat{H}'(t_0) \right] | \Psi_0' \rangle. \end{aligned} \tag{B.46}$$

From this we conclude that $q_0'^{(1)}$ can be determined from the knowledge of the initial state and the initial potential $v_0'^{(0)}$ occurring in $\hat{H}'(t_0)$.

Proceeding in the same fashion leads to:

$$n_0'^{(k+2)} = q_0'^{(k)} + \sum_{l=0}^{k} \binom{k}{l} \nabla \cdot \left(n_0'^{(k-l)}(\boldsymbol{r}) \nabla v_0'^{(l)} \right). \tag{B.47}$$

Imposing that $n_0'^{(k)} = n_0^{(k)}$ yields:

$$\nabla \cdot \left(n_0^{(0)} \nabla v_0'^{(k)} \right) = n_0^{(k+2)} - q_0'^{(k)} - \sum_{l=0}^{k-1} \binom{k}{l} \nabla \cdot \left(n_0^{(k-l)} \nabla v_0'^{(l)} \right), \quad \text{(B.48)}$$

from which $v_0'^{(k)}$ can be determined. Indeed, the right-hand side is completely known as the potentials $v_0'^{(l)}$ with $l \in \{0, 1, \cdots, k-1\}$ and the initial state are known. □

B.1.3 Derivation of expression for the Lehmann representation of the LR function

In this section, we prove that the Lehmann representation of the LR function is given by:

$$\chi_{\alpha\beta}(\boldsymbol{r}, \boldsymbol{r}', \omega) = \lim_{\eta \to 0^+} \sum_{n=1}^{\infty} \left\{ \frac{\langle \Psi_0 | \hat{\alpha} | \Psi_n \rangle \langle \Psi_n | \hat{\beta} | \Psi_0 \rangle}{\omega - \Omega_n + i\eta} - \frac{\langle \Psi_0 | \hat{\beta} | \Psi_n \rangle \langle \Psi_n | \hat{\alpha} | \Psi_0 \rangle}{\omega + \Omega_n + i\eta} \right\}. \quad \text{(B.49)}$$

Proof. First of all, we transform the LR function to the frequency domain by taking the Fourier transform of Eq. (2.40):

$$\chi_{\alpha\beta}(\omega) = -i \int_{-\infty}^{\infty} d\tau \theta(\tau) \langle \Psi_0 | \left[\hat{\alpha}^I(\tau), \hat{\beta} \right] | \Psi_0 \rangle e^{i\omega\tau}. \quad \text{(B.50)}$$

Then, a completeness relation, $\hat{1} = \sum_{n=0}^{\infty} |\Psi_n\rangle\langle\Psi_n|$, is inserted:

$$\begin{aligned} \chi_{\alpha\beta}(\omega) = -i \sum_{n=1}^{\infty} \int_{-\infty}^{\infty} \mathrm{d}\tau \, \theta(\tau) e^{i\omega\tau} \times \\ \left\{ \langle \Psi_0 | \hat{\alpha}^I(\tau) | \Psi_n \rangle \langle \Psi_n | \hat{\beta} | \Psi_0 \rangle - \langle \Psi_0 | \hat{\beta} | \Psi_n \rangle \langle \Psi_n | \hat{\alpha}^I(\tau) | \Psi_0 \rangle \right\}. \end{aligned} \quad \text{(B.51)}$$

Now, we use the explicit form of the operator $\hat{\alpha}$ in the interaction picture representation given in Eq. (2.35) and obtain:

$$\begin{aligned} \chi_{\alpha\beta}(\omega) = -i \sum_{n=1}^{\infty} \int_{-\infty}^{\infty} \mathrm{d}\tau \, \theta(\tau) e^{i\omega\tau} \times \\ \left\{ \langle \Psi_0 | \hat{\alpha} | \Psi_n \rangle \langle \Psi_n | \hat{\beta} | \Psi_0 \rangle e^{-i\Omega_n \tau} - \langle \Psi_0 | \hat{\beta} | \Psi_n \rangle \langle \Psi_n | \hat{\alpha} | \Psi_0 \rangle e^{i\Omega_n \tau} \right\}. \end{aligned} \quad \text{(B.52)}$$

By making use of the integral representation of the step function $\theta(\tau)$

$$\theta(\tau) = \lim_{\eta\to 0^+} \frac{i}{2\pi} \int_{-\infty}^{\infty} \mathrm{d}\omega' \, \frac{e^{-i\omega'\tau}}{\omega' + i\eta}, \tag{B.53}$$

the first term in Eq. (B.52) becomes:

$$\frac{1}{2\pi} \lim_{\eta\to 0^+} \sum_{n=1}^{\infty} \int_{-\infty}^{\infty} \mathrm{d}\tau \int_{-\infty}^{\infty} \mathrm{d}\omega' \, \frac{e^{-i\omega'\tau}}{\omega' + i\eta} e^{i(\omega-\Omega_n)\tau} \langle\Psi_0|\hat{\alpha}|\Psi_n\rangle\langle\Psi_n|\hat{\beta}|\Psi_0\rangle. \tag{B.54}$$

We make use of the general relation

$$\int_{-\infty}^{\infty} \mathrm{d}\tau \, e^{i\tau(\omega-\omega')} = 2\pi\delta(\omega - \omega') \tag{B.55}$$

to rewrite Eq. (B.54) as follows:

$$\begin{aligned} &\lim_{\eta\to 0^+} \sum_{n=1}^{\infty} \int_{-\infty}^{\infty} \mathrm{d}\omega' \, \frac{\delta(\omega' - \omega + \Omega_n)}{\omega' + i\eta} \langle\Psi_0|\hat{\alpha}|\Psi_n\rangle\langle\Psi_n|\hat{\beta}|\Psi_0\rangle \\ = &\lim_{\eta\to 0^+} \sum_{n=1}^{\infty} \frac{\langle\Psi_0|\hat{\alpha}|\Psi_n\rangle\langle\Psi_n|\hat{\beta}|\Psi_0\rangle}{\omega - \Omega_n + i\eta}. \end{aligned} \tag{B.56}$$

The second term in Eq. (B.52) is calculated similarly. By summing both parts, we obtain the Lehmann representation of the LR function $\chi_{\alpha\beta}(\omega)$ as shown in Eq. (B.49). □

B.1.4 Derivation of expression for the Lehmann representation of the KS response function

Here, we derive the following expression for the Lehmann representation of the KS response function:

$$\chi_s(\boldsymbol{r}, \boldsymbol{r}', \omega) = \lim_{\eta\to 0^+} \sum_{j,k=1}^{\infty} (a_k - a_j) \frac{\phi_k^*(\boldsymbol{r})\phi_k(\boldsymbol{r}')\phi_j^*(\boldsymbol{r}')\phi_j(\boldsymbol{r})}{\omega - \omega_{jk} + i\eta}. \tag{B.57}$$

Proof. For this proof, we work in the second quantization, where $|\Phi_n\rangle$ is written using creation- and annihilation operators:

$$|\Phi_n\rangle = \hat{a}_p^\dagger \hat{a}_h |\Phi_0\rangle, \tag{B.58}$$

where $\hat{a}_h$ annihilates a particle in orbital ϕ_h and $\hat{a}_p^\dagger$ creates a particle in orbital ϕ_p. In the GS, p denotes an empty orbital with occupation number

$a_p = 0$, whereas h denotes an occupied orbital with an occupation number $a_h = 1$. It is the other way around for the ES.

Since $\phi_\alpha(\boldsymbol{r}) = \langle \boldsymbol{r}|\alpha\rangle$ and $\phi^*_\alpha(\boldsymbol{r}) = \langle \alpha|\boldsymbol{r}\rangle$, relations for changing between the $\boldsymbol{r}$-basis and α-basis are the following:

$$\begin{aligned}\Phi^\dagger(\boldsymbol{r}) &= \sum_\alpha \langle \alpha|\boldsymbol{r}\rangle a^\dagger_\alpha \\ &= \sum_\alpha \phi^*_\alpha(\boldsymbol{r}) a^\dagger_\alpha\end{aligned} \tag{B.59}$$

and similarly

$$\begin{aligned}\Phi(\boldsymbol{r}) &= \sum_\alpha \langle \boldsymbol{r}|\alpha\rangle a_\alpha \\ &= \sum_\alpha \phi_\alpha(\boldsymbol{r}) a_\alpha.\end{aligned} \tag{B.60}$$

An expression for $\hat{n}(\boldsymbol{r})$ in second quantization is derived as follows:

$$\begin{aligned}\hat{n}(\boldsymbol{r}) &= \Phi^\dagger(\boldsymbol{r})\Phi(\boldsymbol{r}) \\ &= \sum_{\alpha,\beta} \phi^*_\alpha(\boldsymbol{r})\phi_\beta(\boldsymbol{r}) a^\dagger_\alpha a_\beta.\end{aligned} \tag{B.61}$$

First, we determine $\langle \Phi_0|\hat{n}(\boldsymbol{r})|\Phi_n\rangle$:

$$\begin{aligned}\langle \Phi_0|\hat{n}(\boldsymbol{r})|\Phi_n\rangle &= \langle \Phi_0|\hat{n}(\boldsymbol{r}) a^\dagger_p a_h|\Phi_0\rangle \\ &= \sum_{\alpha,\beta} \phi^*_\alpha(\boldsymbol{r})\phi_\beta(\boldsymbol{r}) \langle \Phi_0|a^\dagger_\alpha a_\beta a^\dagger_p a_h|\Phi_0\rangle.\end{aligned} \tag{B.62}$$

Note that, due to the orthonormality of Φ_0, this term only differs from zero when $\alpha = h$ and $\beta = p$. Therefore, we obtain the following:

$$\langle \Phi_0|\hat{n}(\boldsymbol{r})|\Phi_n\rangle = \phi^*_h(\boldsymbol{r})\phi_p(\boldsymbol{r}). \tag{B.63}$$

In a similar fashion, we get:

$$\langle \Phi_n|\hat{n}(\boldsymbol{r})|\Phi_0\rangle = \phi^*_p(\boldsymbol{r})\phi_h(\boldsymbol{r}). \tag{B.64}$$

Substituting these equations in Eq. (2.53) yields:

$$\chi_s(\boldsymbol{r},\boldsymbol{r}',\omega) = \lim_{\eta\to 0^+} \sum_{j,k=1}^{\infty} (a_k - a_j) \frac{\phi^*_k(\boldsymbol{r})\phi_k(\boldsymbol{r}')\phi^*_j(\boldsymbol{r}')\phi_j(\boldsymbol{r})}{\omega - \omega_{jk} + i\eta}, \tag{B.65}$$

where Ψ_0 and Ψ_n are replaced by Φ_0 and Φ_n, respectively. The excitation energies $\omega_{jk} = \epsilon_j - \epsilon_k$ are energy differences between KS orbital energies. □

B.1.5 Derivation of expression for the transition density

In this section, we prove that the transition density can be written as follows:

$$n_1(\boldsymbol{r},\Omega) = \sum_{j,k=1}^{\infty} \alpha_{kj}\Phi_{jk}(\boldsymbol{r})\beta_{jk}. \tag{B.66}$$

Proof. Eq. (2.69), evaluated at $\omega = \Omega$, is introduced in Eq. (2.74):

$$\beta_{jk} = \frac{\int \mathrm{d}\boldsymbol{r}' \int \mathrm{d}\boldsymbol{r}'' \Phi^*_{jk}(\boldsymbol{r}') f_{HXC}(\boldsymbol{r}',\boldsymbol{r}'',\Omega)\gamma(\boldsymbol{r}'',\Omega)}{\Omega - \omega_{jk}}. \tag{B.67}$$

We take the Fourier transform of Eq. (2.61) without an external perturbation and evaluate it at $\omega = \Omega$:

$$n_1(\boldsymbol{r},\Omega) = \int \mathrm{d}\boldsymbol{r}' \chi_s(\boldsymbol{r},\boldsymbol{r}',\Omega) \int \mathrm{d}\boldsymbol{x} f_{HXC}(\boldsymbol{r}',\boldsymbol{x},\Omega) n_1(\boldsymbol{x},\Omega). \tag{B.68}$$

Inserting Eq. (2.59) results in:

$$\begin{aligned} n_1(\boldsymbol{r},\Omega) = \sum_{j,k=1}^{\infty} (a_k - a_j) \int \mathrm{d}\boldsymbol{r}' \frac{\phi^*_k(\boldsymbol{r})\phi_k(\boldsymbol{r}')\phi^*_j(\boldsymbol{r}')\phi_j(\boldsymbol{r})}{\Omega - \omega_{jk}} \times \\ \int \mathrm{d}\boldsymbol{x} f_{HXC}(\boldsymbol{r}',\boldsymbol{x},\Omega) n_1(\boldsymbol{x},\Omega), \end{aligned} \tag{B.69}$$

where we dropped $\lim_{\eta\to 0^+}$ and $i\eta$ in the denominator to ease the notation. Now, we use the definitions given in Eq. (2.68) to obtain

$$n_1(\boldsymbol{r},\Omega) = \sum_{j,k=1}^{\infty} \alpha_{kj} \int \mathrm{d}\boldsymbol{r}' \frac{\Phi_{jk}(\boldsymbol{r})\Phi^*_{jk}(\boldsymbol{r}')}{\Omega - \omega_{jk}} \int \mathrm{d}\boldsymbol{x} f_{HXC}(\boldsymbol{r}',\boldsymbol{x},\Omega) n_1(\boldsymbol{x},\Omega). \tag{B.70}$$

By inserting Eq. (B.67), this simplifies to

$$n_1(\boldsymbol{r},\Omega) = \sum_{j,k=1}^{\infty} \alpha_{kj}\Phi_{jk}(\boldsymbol{r})\beta_{jk}. \tag{B.71}$$

□

B.1.6 Derivation of the alternative form of the Casida equation

It is proven in this section that, by assuming that f_{XC} is frequency-independent, so that the matrices **L** and **M** are real, the Casida equation can be cast into the alternative form:

$$\mathbf{C}\boldsymbol{Z} = \Omega^2 \boldsymbol{Z}, \tag{B.72}$$

with

$$\begin{aligned}\mathbf{C} =&(\mathbf{L}-\mathbf{M})^{1/2}(\mathbf{L}+\mathbf{M})(\mathbf{L}-\mathbf{M})^{1/2}\\ \boldsymbol{Z} =&(\mathbf{L}-\mathbf{M})^{1/2}(\boldsymbol{X}-\boldsymbol{Y}).\end{aligned} \tag{B.73}$$

Proof. The Casida equation given in Eq. (2.82) can be written as two coupled linear matrix equations:

$$\begin{aligned}\mathbf{L}\mathbf{X}+\mathbf{M}\mathbf{Y} =&-\Omega\mathbf{X}\\ \mathbf{M}\mathbf{X}+\mathbf{L}\mathbf{Y} =&\Omega\mathbf{Y}.\end{aligned} \tag{B.74}$$

Subtracting and summing these two equations results in

$$(\mathbf{L}-\mathbf{M})(\mathbf{X}-\mathbf{Y}) =-\Omega(\mathbf{X}+\mathbf{Y}) \tag{B.75}$$

$$(\mathbf{L}+\mathbf{M})(\mathbf{X}+\mathbf{Y}) =-\Omega(\mathbf{X}-\mathbf{Y}). \tag{B.76}$$

Multiplying both sides of Eq. (B.75) with $(\mathbf{L}+\mathbf{M})$ leads to

$$(\mathbf{L}+\mathbf{M})(\mathbf{L}-\mathbf{M})(\mathbf{X}-\mathbf{Y}) =-\Omega(\mathbf{L}+\mathbf{M})(\mathbf{X}+\mathbf{Y}), \tag{B.77}$$

in which Eq. (B.76) can be substituted:

$$(\mathbf{L}+\mathbf{M})(\mathbf{L}-\mathbf{M})(\mathbf{X}-\mathbf{Y}) =\Omega^2(\mathbf{X}-\mathbf{Y}). \tag{B.78}$$

In order to obtain a Hermitian eigenvalue problem, we multiply both sides by $(\mathbf{L}-\mathbf{M})^{1/2}$, where we assumed that $(\mathbf{L}-\mathbf{M})$ is positive definite:

$$(\mathbf{L}-\mathbf{M})^{1/2}(\mathbf{L}+\mathbf{M})(\mathbf{L}-\mathbf{M})^{1/2}(\mathbf{L}-\mathbf{M})^{1/2}(\mathbf{X}-\mathbf{Y}) =\Omega^2(\mathbf{L}-\mathbf{M})^{1/2}(\mathbf{X}-\mathbf{Y}). \tag{B.79}$$

This expression has the form described in Eq. (B.72) with

$$\begin{aligned}\mathbf{C} =&(\mathbf{L}-\mathbf{M})^{1/2}(\mathbf{L}+\mathbf{M})(\mathbf{L}-\mathbf{M})^{1/2}\\ \mathbf{Z} =&(\mathbf{L}-\mathbf{M})^{1/2}(\mathbf{X}-\mathbf{Y}).\end{aligned} \tag{B.80}$$

□

B.2 Symmetry elements of trigonal bipyramidal and square pyramidal structures

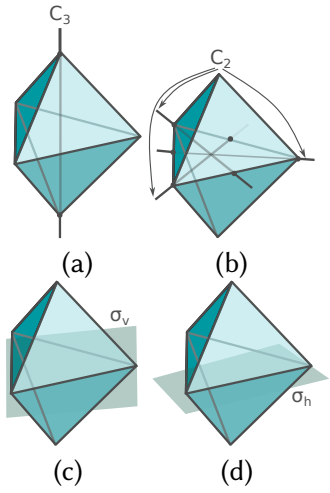

Figure B.1: Visualization of the symmetry elements of a TBP structure. The first line contains the rotational symmetry elements of a TBP structure (a): 1 C_3 axis. (b): 3 C_2 axes. The mirror planes are visualized in the second line (c): One of three σ_v mirror planes. (d) one σ_h mirror plane.

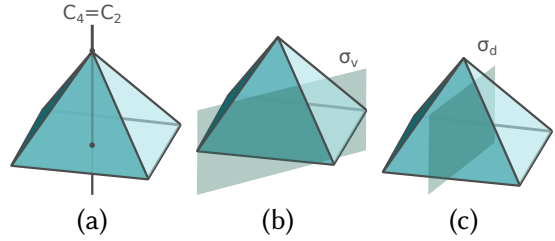

Figure B.2: Visualization of the symmetry elements of a SP structure. There is one rotational symmetry element (a): 1 C_4 axis and coincident C_2 axis. In addition, two mirror planes occur (b): One of two σ_v mirror planes. (c): one of two σ_d mirror planes.

B.3 Character tables

C_{4v}	E	$2C_4(z)$	C_2	$2\sigma_v$	$2\sigma_d$
A_1	1	1	1	1	1
A_2	1	1	1	-1	-1
B_1	1	-1	1	1	-1
B_2	1	-1	1	-1	1
E	2	0	-2	0	0

Table B.1: Character table of C_{4v}.[43]

D_{3h}	E	$2C_3(z)$	$3C_2'$	$\sigma_h(xy)$	$2S_3$	$3\sigma_v$
A_1'	1	1	1	1	1	1
A_2'	1	1	-1	1	1	-1
E'	2	-1	0	2	-1	0
$A"_1$	1	1	1	-1	-1	-1
$A"_2$	1	1	-1	-1	-1	1
$E"$	2	-1	0	-2	1	0

Table B.2: Character table of D_{3h}.[43]

The point group contains 4 complex-valued 1D irreducible representations that can be combined into E_g^* and E_u^* . These E representations are reducible, but have the advantage of real character values. They almost behave like true irreducible representations, however, their norm is twice the group order. Therefore, they are marked with an asterisk. Also, the 4 C_3 and 4 S_6 true classes, containing separate left and right rotations, are combined into 8 pseudo-classes.

T_h	E	$4C_3$	$4(C_3)^2$	$3C_2$	i	$4S_6$	$4(S_6)^5$	$3\sigma_h$
A_g	1	1	1	1	1	1	1	1
E_g	1	$+\epsilon$	$+\epsilon^*$	1	1	ϵ	ϵ^*	1
E_g	1	$+\epsilon^*$	$+\epsilon$	1	1	ϵ^*	ϵ	1
T_g	3	0	0	-1	3	0	0	-1
A_u	1	1	1	1	-1	-1	-1	-1
E_u	1	$+\epsilon$	$+\epsilon^*$	1	-1	$-\epsilon$	$-\epsilon^*$	- 1
E_u	1	$+\epsilon^*$	$+\epsilon$	1	-1	$-\epsilon^*$	$-\epsilon$	-1
T_u	3	0	0	-1	-3	0	0	1

Table B.3: Character table of T_h, $\epsilon = \frac{2\pi i}{3}$ (operator that rotates a vector by $\frac{2\pi}{3}$).[43]

D_{2h}	E	$C_2(z)$	$C_2(y)$	$C_2(x)$	i	$\sigma(xy)$	$\sigma(xz)$	$\sigma(yz)$
A_g	1	1	1	1	1	1	1	1
B_{1g}	1	1	-1	-1	1	1	-1	-1
B_{2g}	1	-1	1	-1	1	-1	1	-1
B_{3g}	1	-1	-1	1	1	-1	-1	1
A_u	1	1	1	1	-1	-1	-1	-1
B_{1u}	1	1	-1	-1	-1	-1	1	1
B_{2u}	1	-1	1	-1	-1	1	-1	1
B_{3u}	1	-1	-1	1	-1	1	1	-1

Table B.4: Character table of D_{2h}.[43] The naming of irreducible representations in this group as B_{1x}, B_{2x}, B_{3x} is a special convention used only for D_2 and D_{2h}.

D_{3d}	E	$2C_3$	$3C_2'$	i	$2S_6$	$3\sigma_d$
A_{1g}	1	1	1	1	1	1
A_{2g}	1	1	-1	1	1	-1
E_g	2	-1	0	2	-1	0
A_{1u}	1	1	1	-1	-1	-1
A_{2u}	1	1	-1	-1	-1	1
E_u	2	-1	0	-2	1	0

Table B.5: Character table of D_{3d}.[43]

S_6	E	$C_3(z)$	$(C_3)^2$	i	$(S_6)^5$	S_6
A_g	1	1	1	1	1	1
E_g	1	$+\epsilon$	$+\epsilon^*$	1	ϵ	ϵ^*
E_g	1	$+\epsilon^*$	$+\epsilon$	1	ϵ^*	ϵ
A_u	1	1	1	-1	-1	-1
E_u	1	$+\epsilon$	$+\epsilon^*$	-1	$-\epsilon$	$-\epsilon^*$
E_u	1	$+\epsilon^*$	$+\epsilon$	-1	$-\epsilon^*$	$-\epsilon$

Table B.6: Character table of S_6, $\epsilon = \frac{2\pi i}{3}$ (operator that rotates a vector by $\frac{2\pi}{3}$).[43]

C_{2v}	E	$C_2(z)$	$\sigma_v(xz)$	$\sigma_v(yz)$
A_1	1	1	1	1
A_2	1	1	-1	-1
B_1	1	-1	1	-1
B_2	1	-1	-1	1

Table B.7: Character table of C_{2v}.[43]

D_{2d}	$2S_4$	E	$C_2(z)$	$2C_2'$	$2\sigma_d$
A_1	1	1	1	1	1
A_2	1	1	1	-1	-1
B_1	1	-1	1	1	-1
B_2	1	-1	1	-1	1
E	2	0	-2	0	0

Table B.8: Character table of D_{2d}.[43]

B.4 Tanabe-Sugano diagrams

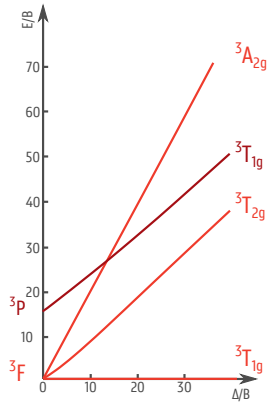

Figure B.3: Tanabe-Sugano diagram for octahedral d^2 complexes. Only spin-allowed transitions are included. Figure adapted from Ref. 165. Figure adapted from Ref. 165 with permission of Oxford Publishing Limited, copyright 2010.

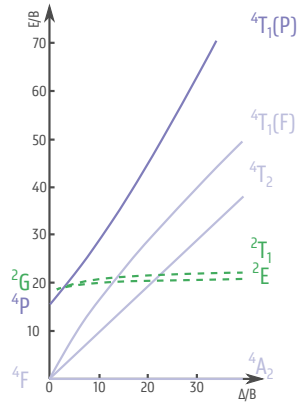

Figure B.4: Tanabe-Sugano diagram for octahedral d^3 and tetrahedral d^7 complexes. Spin-allowed and spin-forbidden transitions are indicated with full and dashed lines, respectively. Figure adapted from Ref. 165. Figure adapted from Ref. 165 with permission of Oxford Publishing Limited, copyright 2010.

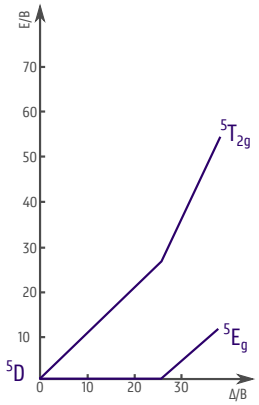

Figure B.5: Tanabe-Sugano diagram for octahedral d^4 complexes. Only spin-allowed transitions are included. Figure adapted from Ref. 165. Figure adapted from Ref. 165 with permission of Oxford Publishing Limited, copyright 2010.

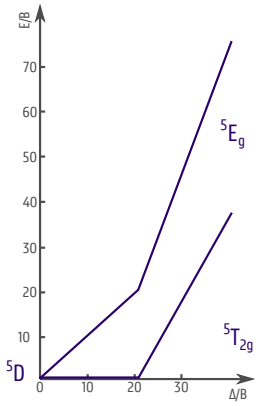

Figure B.6: Tanabe-Sugano diagram for octahedral d^6 complexes. Only spin-allowed transitions are included. Figure adapted from Ref. 165. Figure adapted from Ref. 165 with permission of Oxford Publishing Limited, copyright 2010.

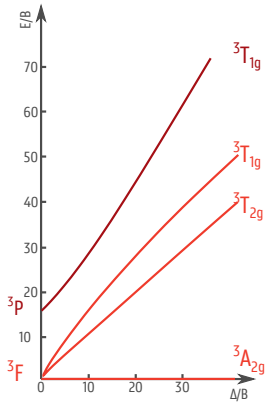

Figure B.7: Tanabe-Sugano diagram for octahedral d^8 complexes. Only spin-allowed transitions are included. Figure adapted from Ref. 165. Figure adapted from Ref. 165 with permission of Oxford Publishing Limited, copyright 2010.

C

List of Publications

Publications in international peer–reviewed journals

1. Optical Properties of Isolated and Covalent Organic Framework-Embedded Ruthenium Complexes, F. Muniz-Miranda[†], L. De Bruecker[†], A. De Vos, F. Vanden Bussche, C.V. Stevens, P. Van der Voort, K. Lejaeghere, V. Van Speybroeck, *J. Phys. Chem. A*, 123 (32), 6854-6867, 2019.

2. Structural and photophysical properties of various polypyridyl ligands: A combined experimental and computational study, L. De Bruecker, J. Everaert, P. Van Der Voort, C.V. Stevens, M. Waroquier, V. Van Speybroeck, *ChemPhysChem*, 21 (22), 2489-2505, 2020.

3. Influence of Number of Ligands and Point Group on the Electronic Structure of Co^{2+} Aqua-Complexes, L. De Bruecker and V. Van Speybroeck, *Inorg. Chem.*, 61 (51), 20743-20756, 2022.

4. Using DFT to examine the spectroscopic fingerprint of Co^{2+} complexes relevant for ZIF nucleation processes, L. De Bruecker and V. Van Speybroeck, *Inorg. Chem.*, *Submitted*, 2023.

[†] Authors contributed equally to this work.

Book chapter

1. Operando Methods in Catalysis and Material Science, A. E. J. Hoffman, P. Cnudde, L. De Bruecker, S.M.J. Rogge, and V. Van Speybroeck, Wiley-VCH, ISBN in press, 2022.

Conference contributions

Oral presentation

1. Zeolite-catalyzed benzene ethylation: New mechanistic insights from an old-school reaction class, M. Bocus, L. De Bruecker, L. Vanduyfhuys, V. Van Speybroeck, ACS Spring 2021, Online, 05/04/2021 to 30/04/2021.

Poster presentations

1. Nuclear quantum effects in metal-organic frameworks, A. Lamaire, J. Wieme, S.M.J. Rogge, L. De Bruecker, V. Van Speybroeck, Solvay New Horizons Lectures in Chemistry, Zwijnaarde, Belgium, 01/06/2018.

2. Nuclear quantum effects in metal-organic frameworks, A. Lamaire, J. Wieme, S.M.J. Rogge, L. De Bruecker, V. Van Speybroeck, Path Integral Quantum Mechanics: From the Basics to the Latest Developments, Lausanne, Switzerland, 27/06/2018.

3. Nuclear quantum effects in metal-organic frameworks, A. Lamaire, J. Wieme, S.M.J. Rogge, L. De Bruecker, V. Van Speybroeck, Ab initio Modeling in Solid State Chemistry, Torino, Italy, 05/09/2018.

4. Nuclear quantum effects in metal-organic frameworks, A. Lamaire, J. Wieme, S.M.J. Rogge, L. De Bruecker, V. Van Speybroeck, MOF-SIM2019, Ghent, Belgium, 10/04/2019 to 12/04/2019.

5. Optical Properties of Isolated and Covalent Organic Framework-Embedded Ruthenium Complexes, L. De Bruecker, F. Muniz-Miranda, A. De Vos, F. Vanden Bussche, C. V. Stevens, P. Van Der Voort, K. Lejaeghere, and V. Van Speybroeck, European Summer School of Quantum Chemistry, Palermo, Italy, 08/09/2019 to 21/09/2019.

6. Computational Study of the Electronic Structure of Co^{2+} Aqua-Complexes, L. De Bruecker, V. Van Speybroeck, DFT2022, Brussels, Belgium, 29/08/2022 to 02/09/2022.

Master's thesis

Including nuclear quantum effects via path integral techniques to accurately model breathing in metal-organic frameworks, L. De Bruecker, Supervisor: Prof. Dr. ir. Veronique Van Speybroeck, 2018.

D

List of Software Packages

In the context of this PhD dissertation, various software packages have been used extensively. Below, an overview of these software packages is provided.

ADF and AMS

Amsterdam Density Functional (ADF), version 2018.105, is a quantum chemistry software package based on DFT, for molecules, solids, and liquids.[256, 257] Amsterdam Modeling Suite (AMS), version 2020.103[258] and 2021.103[259], is the new driver program introduced in the 2018 release of AMS and handles all changes in the simulated geometry of the system. These programs were adopted in this PhD dissertation to perform AOC, LFDFT, UDFT, and unrestricted TDDFT calculations.

CP2K

CP2K is a quantum chemistry and solid state physics program package to perform atomistic simulations of solid state, liquid, molecular, periodic, material, crystal, and biological systems.[260] CP2K was adopted in this PhD dissertation to perform *ab initio* MD simulations.

Gaussian 16

Gaussian 16 is the latest in the Gaussian series of programs and provides

state–of–the–art capabilities for electronic structure modeling. Gaussian 16 was adopted in this PhD dissertation to perform geometry optimizations, rotational scans, frequency calculations, and TDDFT calculations. More information about this software is available under this link and in Ref. 261.

Bibliography

[1] J. M. Hollas, *Modern Spectroscopy*. John Wiley & Sons, 2004.

[2] J. A. Kim, D. J. Wales, and G.-Z. Yang, "Optical Spectroscopy for In Vivo Medical Diagnosis: A Review of the State of the Art and Future Perspectives," *Prog. Biomed. Eng.*, vol. 2, p. 042001, 2020.

[3] W. Querido, S. Kandel, and N. Pleshko, "Applications of Vibrational Spectroscopy for Analysis of Connective Tissues," *Molecules*, vol. 26, p. 922, 2021.

[4] X. Yang, X. Zhao, K. Yang, Y. Liu, Y. Liu, W. Fu, and Y. Luo, "Biomedical Applications of Terahertz Spectroscopy and Imaging," *Trends Biotechnol*, vol. 34, p. 810, 2016.

[5] J. Tennyson, *Astronomical Spectroscopy: An Introduction to the Atomic and Molecular Physics of Astronomical Spectra*. Imperial College Press, 2005.

[6] A. Van Yperen-De Deyne, *Development of Theoretical Tools to Accurately Determine Spectroscopic Properties Using Advanced Electronic Structure Methods*. PhD thesis, Ghent University, 2013-2014.

[7] V. P. Gupta, *Principles and Applications of Quantum Chemistry*. Academic Press, 2015.

[8] O. Virtanen, E. Constantinidou, and E. Tyystjärvi, "Chlorophyll Does Not Reflect Green Light: How to Correct a Misconception," *J. Biol. Educ.*, vol. 56, p. 552, 2020.

[9] G. Q. Lu and X. S. Zhao, *Nanoporous Materials Science and Engineering*. Imperial College Press, 2004.

[10] M. E. Davis, "Ordered Porous Materials for Emerging Applications," *Nature*, vol. 417, p. 813, 2002.

[11] C. Perego and R. Millini, "Porous Materials in Catalysis: Challenges for Mesoporous Materials," *Chem. Soc. Rev.*, vol. 42, p. 3956, 2013.

[12] J. Jiang, Y. Zhao, and O. M. Yaghi, "Covalent Chemistry beyond Molecules," *J. Am. Chem. Soc.*, vol. 138, p. 3255, 2016.

[13] A. Corma and H. García, "Lewis Acids: From Conventional Homogeneous to Green Homogeneous and Heterogeneous Catalysis," *Chem. Rev.*, vol. 103, p. 4307, 2003.

[14] S.-Y. Ding and W. Wang, "Covalent Organic Frameworks (COFs): From Design to Applications," *Chem. Soc. Rev.*, vol. 42, p. 548, 2013.

[15] P. Kuhn, M. Antonietti, and A. Thomas, "Porous, Covalent Triazine-Based Frameworks Prepared by Ionothermal Synthesis," *Angew. Chem. Int. Ed Engl.*, vol. 47, p. 3450, 2008.

[16] X. Feng, X. Ding, and D. Jiang, "Covalent Organic Frameworks," *Chem. Soc. Rev.*, vol. 41, p. 6010, 2012.

[17] D. Stewart, D. Antypov, M. S. Dyer, M. J. Pitcher, A. P. Katsoulidis, P. A. Chater, F. Blanc, and M. J. Rosseinsky, "Stable and Ordered Amide Frameworks Synthesised under Reversible Conditions Which Facilitate Error Checking," *Nat. Commun.*, vol. 8, p. 1102, 2017.

[18] A. Halder, S. Karak, M. Addicoat, S. Bera, A. Chakraborty, S. H. Kunjattu, P. Pachfule, T. Heine, and R. Banerjee, "Ultrastable Imine-Based Covalent Organic Frameworks for Sulfuric Acid Recovery: An Effect of Interlayer Hydrogen Bonding," *Angew. Chem. Int. Ed Engl.*, vol. 57, p. 5797, 2018.

[19] S.-Y. Ding, J. Gao, Q. Wang, Y. Zhang, W.-G. Song, C.-Y. Su, and W. Wang, "Construction of Covalent Organic Framework for Catalysis: Pd/COF-LZU1 in Suzuki-Miyaura Coupling Reaction," *J. Am. Chem. Soc.*, vol. 133, p. 19816, 2011.

[20] P. J. Waller, F. Gándara, and O. M. Yaghi, "Chemistry of Covalent Organic Frameworks," *Acc. Chem. Res.*, vol. 48, p. 3053, 2015.

[21] W. A. Maza and A. J. Morris, "Photophysical Characterization of a Ruthenium(II) Tris(2,2'-bipyridine)-Doped Zirconium UiO-67 Metal–Organic Framework," *J. Phys. Chem. C*, vol. 118, p. 8803, 2014.

[22] C.-C. Hou, T.-T. Li, S. Cao, Y. Chen, and W.-F. Fu, "Incorporation of a $[Ru(dcbpy)(bpy)_2]^{2+}$ Photosensitizer and a $Pt(dcbpy)Cl_2$ Catalyst into Metal-Organic Frameworks for Photocatalytic Hydrogen Evolution from Aqueous Solution," *J. Mater. Chem. A*, vol. 3, p. 10386, 2015.

[23] D. Yang, S. O. Odoh, T. C. Wang, O. K. Farha, J. T. Hupp, C. J. Cramer, L. Gagliardi, and B. C. Gates, "Metal–Organic Framework Nodes as Nearly Ideal Supports for Molecular Catalysts: NU-1000- and UiO-66-Supported Iridium Complexes," *J. Am. Chem. Soc.*, vol. 137, p. 7391, 2015.

[24] M. S. Lohse and T. Bein, "Covalent Organic Frameworks: Structures, Synthesis, and Applications," *Adv. Funct. Mater.*, vol. 28, p. 1705553, 2018.

[25] L. D. Bruecker, J. Everaert, P. V. D. Voort, C. V. Stevens, M. Waroquier, and V. V. Speybroeck, "Structural and Photophysical Properties of Various Polypyridyl Ligands: A Combined Experimental and Computational Study.," *Chem Phys Chem*, vol. 21, p. 2489, 2020.

[26] U. I. E. Agency *International Energy Outlook*, 2016.

[27] A. M. Beale, S. D. M. Jacques, and B. M. Weckhuysen, "Chemical Imaging of Catalytic Solids with Synchrotron Radiation," *Chem. Soc. Rev.*, vol. 39, p. 4656, 2010.

[28] A. Primo and H. Garcia, "Zeolites as Catalysts in Oil Refining," *Chem. Soc. Rev.*, vol. 43, p. 7548, 2014.

[29] B. M. Weckhuysen, "Recalcitrance of Nature: Chemocatalysis for the Production of Biomass-Based Building Blocks," *ChemSusChem*, vol. 6, p. 1559, 2013.

[30] P. A. Jacobs, M. Dusselier, and B. F. Sels, "Will Zeolite-Based Catalysis be as Relevant in Future Biorefineries as in Crude Oil Refineries?," *Angew. Chem. Int. Ed.*, vol. 53, p. 8621, 2014.

[31] K. Takanabe, "Photocatalytic Water Splitting: Quantitative Approaches toward Photocatalyst by Design," *ACS Catal.*, vol. 7, p. 8006, 2017.

[32] C. K. Prier, D. A. Rankic, and D. W. C. MacMillan, "Visible Light Photoredox Catalysis with Transition Metal Complexes: Applications in Organic Synthesis," *Chem. Rev.*, vol. 113, p. 5322, 2013.

[33] M. D. Kärkäs, and J. A. Porco Jr, and C. R. J. Stephenson, "Photochemical Approaches to Complex Chemotypes: Applications in Natural Product Synthesis," *Chem. Rev.*, vol. 116, p. 9683, 2016.

[34] D. M. Schultz and T. P. Yoon, "Solar Synthesis: Prospects in Visible Light Photocatalysis," *Science*, vol. 343, p. 1239176, 2014.

[35] J. M. R. Narayanam and C. R. J. Stephenson, "Visible Light Photoredox Catalysis: Applications in Organic Synthesis," *Chem. Soc. Rev.*, vol. 40, p. 102, 2011.

[36] A. G. Slater and A. I. Cooper, "Porous Materials. Function-Led Design of New Porous Materials," *Science*, vol. 348, p. aaa8075, 2015.

[37] S. M. J. Rogge, A. Bavykina, J. Hajek, H. Garcia, A. I. Olivos-Suarez, A. Sepúlveda-Escribano, A. Vimont, G. Clet, P. Bazin, F. Kapteijn, M. Daturi, E. V. Ramos-Fernandez, F. X. L. I. Xamena, V. V. Speybroeck, and J. Gascon, "Metal-Organic and Covalent Organic Frameworks as Single-Site Catalysts," *Chem. Soc. Rev.*, vol. 46, p. 3134, 2017.

[38] H. Takeda, M. Ohashi, Y. Goto, T. Ohsuna, T. Tani, and S. Inagaki, "A Versatile Solid Photosensitizer: Periodic Mesoporous Organosilicas with Ruthenium Tris(bipyridine) Complexes Embedded in the Pore Walls," *Adv. Funct. Mater.*, vol. 26, p. 5068, 2016.

[39] W. Tu, Y. Xu, S. Yin, and R. Xu, "Rational Design of Catalytic Centers in Crystalline Frameworks," *Adv. Mater.*, vol. 30, p. 1707582, 2018.

[40] V. S. Vyas, F. Haase, L. Stegbauer, G. Savasci, F. Podjaski, C. Ochsenfeld, and B. V. Lotsch, "A Tunable Azine Covalent Organic Framework Platform for Visible Light-Induced Hydrogen Generation," *Nat. Commun.*, vol. 6, p. 8508, 2015.

[41] L. Stegbauer, K. Schwinghammer, and B. V. Lotsch, "A Hydrazone-Based Covalent Organic Framework for Photocatalytic Hydrogen Production," *Chem. Sci.*, vol. 5, p. 2789, 2014.

[42] T. Banerjee and B. V. Lotsch, "COF Photocatalysts: The Wetter the Better," *Nat. Chem.*, vol. 10, p. 1175, 2018.

[43] G. L. Miessler, P. J. Fischer, and D. A. Tarr, *Inorganic Chemistry*. Pearson, 2013.

[44] K. S. Park, Z. Ni, A. P. Côté, J. Y. Choi, R. Huang, F. J. Uribe-Romo, H. K. Chae, M. O'Keeffe, and O. M. Yaghi, "Exceptional Chemical and Thermal Stability of Zeolitic Imidazolate Frameworks," *Proc. Natl. Acad. Sci. USA*, vol. 103, p. 10186, 2006.

[45] Z. Öztürk, J. P. Hofmann, M. Lutz, M. Mazaj, N. Z. Logar, and B. M. Weckhuysen, "Controlled Synthesis of Phase-Pure Zeolitic Imidazolate Framework Co-ZIF-9," *Eur. J. Inorg. Chem.*, vol. 2015, p. 1625, 2015.

[46] J. Cravillon, C. A. Schröder, H. Bux, A. Rothkirch, J. Caro, and M. Wiebcke, "Formate Modulated Solvothermal Synthesis of ZIF-8 Investigated using Time-Resolved in Situ X-Ray Diffraction and Scanning Electron Microscopy," *CrystEngComm*, vol. 14, p. 492, 2012.

[47] J. Cravillon, R. Nayuk, S. Springer, A. Feldhoff, K. Huber, and M. Wiebcke, "Controlling Zeolitic Imidazolate Framework Nano- and Microcrystal Formation: Insight into Crystal Growth by Time-Resolved In Situ Static Light Scattering," *Chem. Mater.*, vol. 23, p. 2130, 2011.

[48] J. Cravillon, S. Münzer, S.-J. Lohmeier, A. Feldhoff, K. Huber, and M. Wiebcke, "Rapid Room-Temperature Synthesis and Characterization of Nanocrystals of a Prototypical Zeolitic Imidazolate Framework," *Chem. Mater.*, vol. 21, p. 1410, 2009.

[49] J. Cravillon, C. A. Schröder, R. Nayuk, J. Gummel, K. Huber, and M. Wiebcke, "Fast Nucleation and Growth of ZIF-8 Nanocrystals Monitored by Time-Resolved In Situ Small-Angle and Wide-Angle X-Ray Scattering," *Angew. Chem. int. Ed. Engl.*, vol. 50, p. 8067, 2011.

[50] S. R. Venna, J. B. Jasinski, and M. A. Carreon, "Structural Evolution of Zeolitic Imidazolate Framework-8," *J. Am. Chem. Soc.*, vol. 132, p. 18030, 2010.

[51] A. Phan, C. J. Doonan, F. J. Uribe-Romo, C. B. Knobler, M. O'Keeffe, and O. M. Yaghi, "Synthesis, Structure, and Carbon Dioxide Capture Properties of Zeolitic Imidazolate Frameworks," *Acc. Chem. Res.*, vol. 43, p. 58, 2010.

[52] H. Hayashi, A. P. Côté, H. Furukawa, M. O'Keeffe, and O. M. Yaghi, "Zeolite A Imidazolate Frameworks," *Nat. Mater.*, vol. 6, p. 501, 2007.

[53] G. Kaur, R. K. Rai, D. Tyagi, X. Yao, P.-Z. Li, X.-C. Yang, Y. Zhao, Q. Xu, and S. K. Singh, "Room-Temperature Synthesis of Bimetallic Co–Zn Based Zeolitic Imidazolate Frameworks in Water for Enhanced CO_2 and H_2 Uptakes," *J. Mater. Chem. A*, vol. 4, p. 14932, 2016.

[54] H. T. Kwon, H.-K. Jeong, A. S. Lee, H. S. An, and J. S. Lee, "Heteroepitaxially Grown Zeolitic Imidazolate Framework Membranes with Unprecedented Propylene/Propane Separation Performances," *J. Am. Chem. Soc.*, vol. 137, p. 12304, 2015.

[55] C. Wang, F. Yang, L. Sheng, J. Yu, K. Yao, L. Zhang, and Y. Pan, "Zinc-Substituted ZIF-67 Nanocrystals and Polycrystalline Membranes for

Propylene/Propane Separation," *Chem. Commun.*, vol. 52, p. 12578, 2016.

[56] H. Yang, X.-W. He, F. Wang, Y. Kang, and J. Zhang, "Doping Copper into ZIF-67 for Enhancing Gas Uptake Capacity and Visible-Light-Driven Photocatalytic Degradation of Organic Dye," *J. Mater. Chem.*, vol. 22, p. 21849, 2012.

[57] C. Fedorchuk and T. Swaddle, "Comment on "Reinterpretation of the Spectra of Hydrated Co^{++}: An ab Initio Study" (J. Phys. Chem. A 1998, 102, 6525)," *J. Phys. Chem. A*, vol. 104, p. 5651, 2000.

[58] J. Yao and H. Wang, "Zeolitic Imidazolate Framework Composite Membranes and Thin Films: Synthesis and Applications.," *Chem. Soc. Rev.*, vol. 43, p. 4470, 2014.

[59] Y. Sun, S. M. J. Rogge, A. Lamaire, S. Vandenbrande, J. Wieme, C. R. Siviour, V. V. Speybroeck, and J.-C. Tan, "High-Rate Nanofluidic Energy Absorption in Porous Zeolitic Frameworks.," *Nat. Mater.*, vol. 20, p. 1015, 2021.

[60] Y.-R. Lee, M.-S. Jang, H.-Y. Cho, H.-J. Kwon, S. Kim, and W.-S. Ahn, "ZIF-8: A Comparison of Synthesis Methods," *Chem. Eng. J.*, vol. 271, p. 276, 2015.

[61] R. Banerjee, A. Phan, B. Wang, C. Knobler, H. Furkawa, M. O'Keeffe, and O. M. Yaghi, "High-Throughput Synthesis of Zeolitic Imidazolate Frameworks and Application to CO2 Capture," *Science*, vol. 319, p. 939, 2008.

[62] M. J. V. Vleet, T. Weng, X. Li, and J. R. Schmidt, "In Situ, Time-Resolved, and Mechanistic Studies of Metal-Organic Framework Nucleation and Growth," *Chem. Rev.*, vol. 118, p. 3681, 2018.

[63] J. D. Rimer and M. Tsapatsis, "Nucleation of Open Framework Materials: Navigating the Voids," *MRS Bull.*, vol. 41, p. 393, 2016.

[64] M. Filez, C. Caratelli, M. Rivera-Torrente, F. Muniz-Miranda, M. Hoek, M. Altelaar, A. J. R. Heck, V. V. Speybroeck, and B. M. Weckhuysen, "Elucidation of the Pre-Nucleation Phase Directing Metal-Organic Framework Formation," *Cell Rep. Phys. Sci.*, vol. 2, p. 100680, 2021.

[65] J. P. Zobel and L. González, "The Quest to Simulate Excited-State Dynamics of Transition Metal Complexes," *JACS Au*, vol. 1, p. 1116, 2021.

[66] C. Daniel, "Photochemistry and Photophysics of Transition Metal Complexes: Quantum Chemistry," *Coord. Chem. Rev.*, vol. 282-283, p. 19, 2015.

[67] C. Daniel, *Photochemistry of Transition Metal Complexes: Theory. Encyclopedia of Inorganic and Bioinorganic Chemistry.* John Wiley & Sons, 2006.

[68] D. Escudero, "Photodeactivation channels of transition metal complexes: A computational chemistry perspective," in *Transition Metals in Coordination Environments. Challenges and Advances in Computational Chemistry and Physics* (E. Broclawik, T. Borowski, and M. Radoń, eds.), p. 259, Springer, 2019.

[69] T. J. Penfold, E. Gindensperger, C. Daniel, and C. M. Marian, "Spin-Vibronic Mechanism for Intersystem Crossing," *Chem. Rev.*, vol. 118, p. 6975, 2018.

[70] C. Daniel, "Ultrafast Processes: Coordination Chemistry and Quantum Theory," *Phys. Chem. Chem. Phys.*, vol. 23, p. 43, 2021.

[71] J. Tomasi, B. Mennucci, and R. Cammi, "Quantum Mechanical Continuum Solvation Models," *Chem. Rev.*, vol. 105, p. 2999, 2005.

[72] C. C. Pye and T. Ziegler, "An Implementation of the Conductor-Like Screening Model of Solvation Within the Amsterdam Density Functional Package," *Ther. Chem. Acc.*, vol. 101, p. 396, 1999.

[73] K. Lejaeghere, G. Bihlmayer, T. Björkman, P. Blaha, S. Blügel, V. Blum, D. Caliste, I. E. Castelli, S. J. Clark, A. D. Corso, S. de Gironcoli, T. Deutsch, J. K. Dewhurst, I. D. Marco, C. Draxl, M. Dułak, O. Eriksson, J. A. Flores-Livas, K. F. Garrity, L. Genovese, P. Giannozzi, M. Giantomassi, S. Goedecker, X. Gonze, O. Grånäs, E. K. U. Gross, A. Gulans, F. Gygi, D. R. Hamann, P. J. Hasnip, N. A. W. Holzwarth, D. Iuşan, D. B. Jochym, F. Jollet, D. Jones, G. Kresse, K. Koepernik, E. Küşükbenli, Y. O. Kvashnin, I. L. M. Locht, S. Lubeck, M. Marsman, N. Marzari, U. Nitzsche, L. Nordström, T. Ozaki, L. Paulatto, C. J. Pickard, W. Poelmans, M. I. J. Probert, K. Refson, M. Richter, G.-M. Rignanese, S. Saha, M. Scheffler, M. Schlipf, K. Schwarz, S. Sharma, F. Tavazza, P. Thunström, A. Tkatchenko, M. Torrent, D. Vanderbilt, M. J. van Setten, V. V. Speybroeck, J. M. Wills, J. R. Yates, G.-X. Zhang, and S. Cottenier, "Reproducibility in Density Functional Theory Calculations of Solids," *Science*, vol. 351, p. aad3000, 2016.

[74] R. G. Parr and W. Yang, *Density-Functional Theory of Atom and Molecules*. Oxford University Press, 1989.

[75] D. Frenkel and B. Smit, *Understanding Molecular Simulation: From Algorithms to Applications*. Elsevier Science, 2002.

[76] E. Schrödinger, "An Undulatory Theory of the Mechanics of Atoms and Molecules," *Phys. Rev.*, vol. 28, p. 1049, 1926.

[77] M. Born and R. oppenheimer, "Zur Quantentheorie der Molekeln," *Annal. Phys.*, vol. 389, p. 457, 1927.

[78] M. Born and K. Huang, *Dynamical theory of crystal lattices*. Oxford, Clarendon Press, 1954.

[79] P. Hohenberg and W. Kohn, "Inhomogeneous Electron Gas," *Phys. Rev.*, vol. 136, p. B864, 1964.

[80] W. Kohn and L. J. Sham, "Self-Consistent Equations Including Exchange and Correlation Effects," *Phys. Rev.*, vol. 140, p. A1133, 1965.

[81] S. Lehtola, "A Review on Non-Relativistic, Fully Numerical Electronic Structure Calculations on Atoms and Diatomic Molecules," *Int. J. Quantum Chem.*, vol. 119, p. e25968, 2019.

[82] J. P. Perdew, A. Ruzsinszky, J. Tao, V. N. Staroverov, G. E. Scuseria, and G. I. Csonka, "Prescription for the Design and Selection of Density Functional Approximations: More Constraint Satisfaction with Fewer Fits," *J. Chem. Phys.*, vol. 123, p. 062201, 2005.

[83] T. Ziegler, A. Rauk, and E. J. Baerends, "On the Calculation of Multiplet Energies by the Hartree-Fock-Slater Method," *Theor. Chim. Acta.*, vol. 43, p. 261, 1977.

[84] R. O. Jones and O. Gunnarsson, "The Density Functional Formalism, its Applications and Prospects," *Rev. Mod. Phys.*, vol. 61, p. 689, 1989.

[85] A. Hellman, B. Razaznejad, and B. I. Lundqvist, "Potential-Energy Surfaces for Excited States in Extended Systems," *J. Chem. Phys.*, vol. 120, p. 4593, 2004.

[86] E. Runge and E. K. U. Gross, "Density-Functional Theory for Time-Dependent Systems.," *Phys. Rev. Lett.*, vol. 52, p. 997, 1984.

[87] M. E. Casida, C. Jamorski, K. C. Casida, and D. R. Salahub, "Molecular Excitation Energies to High-Lying Bound States from Time-Dependent

Density-Functional Response Theory: Characterization and Correction of the Time-Dependent Local Density Approximation Ionization Threshold.," *J. Chem. Phys.*, vol. 108, p. 4439, 1998.

[88] C. A. Ullrich, *Time-Dependent Density-Functional Theory: Concepts and Applications.* Oxford University Press, 2012.

[89] R. van Leeuwen, "Mapping from Densities to Potentials in Time-Dependent Denisty-Functional Theory," *Phys. Rev. Lett.*, vol. 82, p. 3863, 1999.

[90] A. Gonis, "Is an Interacting Ground State (Pure State) v-Representable Density also Non-Interacting Ground State v-Representable by a Slater Determinant? In the Absence of Degeneracy, Yes!," *Phys. Lett. A*, vol. 383, p. 2772, 2019.

[91] G. Mazur and R. Wlodarczyk, "Application of the Dressed Time-Dependent Density Functional Theory for the Excited States of Linear Polynes," *J. Comput. Chem*, vol. 30, p. 811, 2009.

[92] F. Furche and R. Ahlrichs, "Adiabatic Time-Dependent Density Functional Methods for Excited State Properties," *J. Chem. Phys.*, vol. 117, p. 7433, 2002.

[93] F. Furche and R. Ahlrichs, "Erratum: "Time-Dependent Density Functional Methods for Excited State Properties" [J. Chem. Phys. 117, 7433 (2002)]," *J. Chem. Phys.*, vol. 121, p. 12772, 2004.

[94] M. E. Casida in *Recent Advances in Density Functional Methods* (D. P. Chong, ed.), World Scientific, 1995.

[95] M. E. Casida, "Time-Dependent Density-Functional Theory for Molecules and Molecular Solids," *J. Mol. Struct.: THEOCHEM*, vol. 914, p. 3, 2009.

[96] X. F. J. Liang, D. Hait, and M. Head-Gordon, "Revisiting the Performance of Time-Dependent Density Functional Theory for Electronic Excitations: Assessment of 43 Popular and Recently Developed Functionals from Rungs One to Four," *J. Chem. Theory Comput.*, vol. 18, p. 3460, 2022.

[97] E. R. Davidson, "The Iterative Calculation of a Few of the Lowest Eigenvalues and Corresponding Eigenvectors of Large Real-Symmetric Matrices," *J. Comput. Phys.*, vol. 17, p. 87, 1975.

[98] R. E. Stratmann, G. E. Scuseria, and M. J. Frisch, "An Efficient Implementation of Time-Dependent Density-Functional Theory for the Calculation of Excitation Energies of Large Molecules," *J. Chem. Phys.*, vol. 109, p. 8218, 1998.

[99] U. von Barth and L. Hedin, "A Local Exchange-Correlation Potential for the Spin Polarized Case. I," *J. Phys. C*, vol. 5, p. 1629, 1972.

[100] O. Gunnarsson and B. I. Lundqvist, "Exchange and Correlation in Atoms, Molecules, and Solids by the Spin-Density-Functional Formalism," *Phys. Rev. B*, vol. 13, p. 4274, 1976.

[101] R. M. Dreizler and E. K. U. Gross, *Density Functional Theory*. Springer, 1990.

[102] K. L. Liu and S. H. Vosko, "A Time-Dependent Spin Density Functional Theory for the Dynamical Spin Susceptibility," *Can. J. Phys.*, vol. 67, p. 1015, 1989.

[103] N. Mardirossian and M. Head-Gordon, "Thirty Years of Density Functional Theory in Computational Chemistry: An Overview and Extensive Assessment of 200 Density Functionals," *Mol. Phys.*, vol. 115, p. 2315, 2017.

[104] C. Lee, W. Yang, and R. G. Parr, "Development of the Colle-Salvetti Correlation-Energy Formula into a Functional of the Electron Density," *Phys. Rev. B*, vol. 37, p. 785, 1988.

[105] A. D. Becke, "Density-Functional Exchange-Energy Approximation with Correct Asymptotic Behavior," *Phys. Rev. A*, vol. 38, p. 3098, 1988.

[106] C. Adamo and V. Barone, "Toward Reliable Density Functional Methods Without Adjustable Parameters: The PBE0 Model," *J. Chem. Phys.*, vol. 110, p. 6158, 1999.

[107] H. S. Yu, X. He, and D. G. Truhlar, "MN15-L: A New Local Exchange-Correlation Functional for Kohn–Sham Density Functional Theory with Broad Accuracy for Atoms, Molecules, and Solids," *J. Chem. Theory Comput.*, vol. 12, p. 1280, 2016.

[108] Y. Zhao and D. G. Truhlar, "A New Local Density Functional for Main-Group Thermochemistry, Transition Metal Bonding, Thermochemical Kinetics, and Noncovalent Interactions," *J. Chem. Phys.*, vol. 125, p. 194101, 2006.

[109] A. D. Becke, "Density-Functional Thermochemistry. III. The Role of Exact Exchange," *J. Chem. Phys.*, vol. 98, p. 5648, 1993.

[110] A. J. Cohen and N. C. Handy, "Dynamic Correlation," *Mol. Phys.*, vol. 99, p. 607, 2001.

[111] X. Xu and W. A. Goddard, "The X3LYP Extended Density Functional for Accurate Descriptions of Nonbond Interactions, Spin States, and Thermochemical Properties," *Proc. Natl. Acad. Sci. USA*, vol. 101, p. 2673, 2004.

[112] Y. Zhao and D. G. Truhlar, "The M06 Suite of Density Functionals for Main Group Thermochemistry, Thermochemical Kinetics, Noncovalent Interactions, Excited States, and Transition Elements: Two New Functionals and Systematic Testing of Four M06-Class Functionals and 12 other Functionals," *Theor. Chem. Acc.*, vol. 120, p. 215, 2008.

[113] V. N. Staroverov, G. E. Scuseria, J. Tao, and J. P. Perdew, "Comparative Assessment of a New Nonempirical Density Functional: Molecules and Hydrogen-Bonded Complexes," *J. Chem. Phys.*, vol. 119, p. 12129, 2003.

[114] J. Tao, J. P. Perdew, V. N. Staroverov, and G. E. Scuseria, "Climbing the Density Functional Ladder: Nonempirical Meta-Generalized Gradient Approximation Designed for Molecules and Solids," *Phys. Rev. Lett.*, vol. 91, p. 146401, 2003.

[115] H. S. Yu, X. He, S. L. Li, and D. G. Truhlar, "MN15: A Kohn-Sham Global-Hybrid Exchange-Correlation Density Functional with Broad Accuracy for Multi-Reference and Single-Reference Systems and Noncovalent Interactions," *Chem. Sci.*, vol. 7, p. 5032, 2016.

[116] T. Yanai, D. P. Tew, and N. C. Handy, "A New Hybrid Exchange-Correlation Functional using the Coulomb-Attenuating Method (CAM-B3LYP)," *Chem. Phys. Lett.*, vol. 393, p. 51, 2004.

[117] J.-D. Chai and M. Head-Gordon, "Long-Range Corrected Hybrid Density Functionals with Damped Atom–Atom Dispersion Corrections," *Phys. Chem. Chem. Phys.*, vol. 10, p. 6615, 2008.

[118] T. M. Henderson, A. F. Izmaylov, G. Scalmani, and G. E. Scuseria, "Can Short-Range Hybrids Describe Long-Range-Dependent Properties?," *J. Chem. Phys.*, vol. 131, p. 044108, 2009.

[119] R. Bauernschmitt and R. Ahlrichs, "Treatment of Electronic Excitations Within the Adiabatic Approximation of Time Dependent Density Functional Theory.," *Chem. Phys. Lett.*, vol. 256, p. 454, 1996.

[120] M. E. Casida and M. Huix-Rotllant, "Progress in Time-Dependent Density-Functional Theory," *Annu. Rev. Phys.*, vol. 63, p. 287, 2012.

[121] N. T. Maitra, "Perspective: Fundamental Aspects of Time-Dependent Density Functional Theory.," *J. Chem. Phys.*, vol. 144, p. 220901, 2016.

[122] G. Wu, H. Stewart, F. D. Lemon, H. Cox, and A. J. Stace, "The UV Photofragmentation Spectroscopy of the Metal Dication Complex $[Mn(pyridine)_4]^{2+}$," *Mol. Phys.*, vol. 108, p. 1199, 2010.

[123] A. Dreuw, J. L. Weisman, and M. Head-Gordon, "Long-Range Charge-Transfer Excited States in Time-Dependent Density Functional Theory Require Non-Local Exchange," *J. Chem. Phys.*, vol. 119, p. 2943, 2003.

[124] M. Campetella, F. Maschietto, M. J.Frisch, G. Scalmani, I. Ciofini, and C. Adamo, "Charge Transfer Excitations in TDDFT: A Ghost-Hunter Index," *J. Comput. Chem.*, vol. 38, p. 2151, 2017.

[125] F. Zhang and K. Burke, "Adiabatic Connection for Near Degenerate Excited States," *Phys. Rev. A*, vol. 69, p. 052510, 2004.

[126] J. G. Brandenburg, K. Burke, E. Fromager, M. Gatti, S. Giarrusso, N. I. Gidopoulos, P. Gori-Giorgi, D. Gowland, T. Helgaker, M. J. P. Hodgson, L. Lacombe, G. Levi, P.-F. Loos, N. T. Maitra, E. M. Morais, N. Mehta, F. Monti, M. R. Mulay, K. Pernal, L. Reining, P. Romaniello, M. R. Ryder, A. Savin, D. Sirbu, A. M. Teale, A. J. W. Thom, D. G. Truhlar, J. Wetherell, and W. Yang, "New Approaches to Study Excited States in Density Functional Theory: General Discussion," *Faraday Discuss.*, vol. 224, p. 483, 2020.

[127] N. T. Maitra, "Double and Charge-Transfer Excitations in Time-Dependent Density Functional Theory.," *Ann. Rev. Phys. Chem.*, vol. 73, p. 117, 2022.

[128] N. T. Maitra, F. Zhang, R. J. Cave, and K. Burke, "Double Excitations within Time-Dependent Density Functional Theory Linear Response," *J. Chem. Phys.*, vol. 120, p. 5932, 2004.

[129] M. Marques, N. Maitra, F. Nogueira, E. Gross, and A. Rubio, *Fundamentals of Time-Dependent Density Functional Theory*. Springer, 2012.

[130] Y. Shao, M. Head-Gordon, and A. I. Krylov, "The Spin-Flip Approach within Time-Dependent Density Functional Theory: Theory and Applications to Diradicals," *J. Chem. Phys.*, vol. 118, p. 4807, 2003.

[131] F. Wang and T. Ziegler, "Time-Dependent Density Functional Theory Based on a Noncollinear Formulation of the Exchange-Correlation Potential," *J. Chem. Phys.*, vol. 121, p. 12191, 2004.

[132] F. Wang and T. Ziegler, "The Performance of Time-Dependent Density Functional Theory Based on a Noncollinear Exchange-Correlation Potential in the Calculations of Excitation Energies," *J. Chem. Phys.*, vol. 122, p. 074109, 2005.

[133] F. Wang and T. Ziegler, "Use of Noncollinear Exchange-Correlation Potential in Multiplet Resolutions by Time-Dependent Density Functional Theory," *Int. J. Quantum Chem.*, vol. 106, p. 2545, 2006.

[134] X. Xu, K. R. Yang, and D. G. Truhlar, "Testing Noncollinear Spin-Flip, Collinear Spin-Flip, and Conventional Time-Dependent Density Functional Theory for Predicting Electronic Excitation Energies of Closed-Shell Atoms," *J. Chem. Theory Comput.*, vol. 10, p. 2070, 2014.

[135] F. Vlahović, M. Perić, M. Gruden-Pavlović, and M. Zlatar, "Assessment of TD-DFT and LF-DFT for Study of d-d Transitions in First Row Transition Metal Hexaaqua Complexes," *J. Chem. Phys.*, vol. 142, p. 214111, 2015.

[136] I. Seidu, M. Krykunov, and T. Ziegler, "Applications of Time-Dependent and Time-Independent Density Functional Theory to Rydberg Transitions," *J. Phys. Chem. A*, vol. 119, p. 5107, 2015.

[137] I. Seidu, M. Krykunov, and T. Ziegler, "The Formulation of a Constricted Variational Density Functional Theory for Double Excitations," *Mol. Phys.*, vol. 112, p. 661, 2014.

[138] E. C. Constable and C. E. Housecroft, "Coordination Chemistry: The Scientific Legacy of Alfred Werner," *Chem. Soc. Rev.*, vol. 42, p. 1429, 2013.

[139] B. N. Figgis and M. A. Hitchman, *Ligand Field Theory and its applications*. Wiley, 1999.

[140] S. Sugano, Y. Tanabe, and H. Kamimura, *Multiplets of Transition-Metal Ions in Crystals*. Academic Press, 1970.

[141] S. Reine and T. Saue, *European Summerschool in Quantum Chemistry*. 2019.

[142] C. Daniel, *Photochemistry of Transition Metal Complexes: Theory Based in part on the article Photochemistry of Transition Metal Complexes:*

Theory by Jeffrey I. Zink which appeared in the Encyclopedia of Inorganic Chemistry, First Edition. John Wiley & Sons, Ltd, 2011.

[143] J. N. Harvey, "On the Accuracy of Density Functional Theory in Transition Metal Chemistry," *Annu. Rep. Prog. Chem., Sect. C: Phys. Chem.*, vol. 102, p. 203, 2006.

[144] C. K. Jorgensen, *Structure and Bonding.* Springer, 1966.

[145] R. Tsuchida, "Absorption Spectra of Coordination Compounds. I," *Bull. Chem. Soc. Jpn.*, vol. 13, p. 388, 1938.

[146] S. Stepanović, M. Zlatar, M. Swart, and M. Gruden, "The Irony of Manganocene: An Interplay between the Jahn–Teller Effect and Close-Lying Electronic and Spin States," *J. Chem. Inf. Model.*, vol. 59, p. 1806, 2019.

[147] B. M. Flöser, Y. Guo, C. Riplinger, F. Tuczek, and F. Neese, "Detailed Pair Natural Orbital-Based Coupled Cluster Studies of Spin Crossover Energetics," *J. Chem. Theory Comput.*, vol. 16, p. 2224, 2020.

[148] A. Nandy, C. Duan, M. G. Taylor, F. Liu, A. H. Steeves, and H. J. Kulik, "Computational Discovery of Transition-metal Complexes: From High-throughput Screening to Machine Learning," *Chem. Rev.*, vol. 121, p. 9927, 2021.

[149] M. A. Palacios, E. M. Pineda, S. Sanz, R. Inglis, M. B. Pitak, S. J. Coles, M. Evangelisti, H. Nojiri, C. Heesing, E. K. Brechin, J. Schnack, and R. E. P. Winpenny, "Copper Keplerates: High-Symmetry Magnetic Molecules," *ChemPhysChem*, vol. 17, p. 55, 2016.

[150] S. F. A. Kettle, *Symmetry and Structure: Readable Group Theory for Chemists.* Wiley, 2007.

[151] F. A. Cotton and F. R. S. G. Wilkinson, *Advanced Inorganic Chemistry*. John Wiley & Sons, 1972.

[152] I. Hargittai, "Book Review: Fuzzy Definitions: Concepts in Chemistry—A Contemporary Challenge. Edited by D. H. Rouvray," *Angew. Chem. Int. Ed.*, vol. 36, p. 2525, 1997.

[153] H. Zabrodsky, S. Peleg, and D. Avnir, "Continuous Symmetry Measures," *J. Am. Chem. Soc.*, vol. 114, p. 7843, 1992.

[154] M. Pinsky and D. Avnir, "Continuous Symmetry Measures. 5. The Classical Polyhedra," *Inorg. Chem.*, vol. 37, p. 5575, 1998.

[155] S. Alvarez and M. Llunell, "Continuous Symmetry Measures of Penta-Coordinate Molecules: Berry and non-Berry Distortions of the Trigonal Bipyramid," *J. Chem. Soc., Dalton Trans.*, p. 3288, 2000.

[156] E. Larsen and G. N. L. Mar, "The Angular Overlap Model: How to use it and why," *J. Chem. Educ.*, vol. 51, p. 633, 1974.

[157] G. Racah, "Theory of Complex Spectra. III," *Phys. Rev.*, vol. 63, p. 367, 1943.

[158] J. S. Griffith, *The theory of transition metal ions.* Cambridge university press, 1961.

[159] H. A. O. Hill and P. Day, *Physical Methods in Advanced Inorganic Chemistry.* John Wiley & Sons, Inc., 1968.

[160] I. B. Bersuker, *Electronic structure and properties of transition metal compounds: introduction to the theory.* John Wiley & Sons, 2010.

[161] C. J. Ballhausen, *Introduction to ligand field theory.* McGraw-Hill Book Company, Inc., 1962.

[162] J. von Neumann and E. P. Wigner, "Uber Merkwürdige Diskrete Eigenwerte. Uber das Verhalten von Eigenwerten bei Adiabatischen Prozessen," *Z. Physik*, vol. 30, p. 467, 1929.

[163] B. H. Bransden and C. J. Joachain, *Physics of Atoms and Molecules.* Longman Scientific & Technical, New York, 1983.

[164] Y. Tanabe and S. Sugano, "On the Absorption Spectra of Complex Ions. I," *J. Phys. Soc. Japan*, vol. 9, p. 753, 1954.

[165] P. Atkins, T. Overton, M. Weller, F. Armstrong, and M. Hagerman, *Shriver & Atkins' Inorganic Chemistry.* W. H. Freeman and Company, 2010.

[166] H. Bethe, "Termaufspaltung in Kristallen," *Ann. Phys.*, vol. 395, p. 133, 1929.

[167] J. H. V. Vleck, "Theory of the Variations in Paramagnetic Anisotropy Among Different Salts of the Iron Group," *Phys. Rev.*, vol. 41, p. 208, 1932.

[168] J. H. V. Vleck, "Valence Strength and the Magnetism of Complex Salts," *J. Chem. Phys.*, vol. 3, p. 807, 1935.

[169] F. Neese, L. Lang, and V. G. Chilkuri, "Effective Hamiltonians in Chemistry," in *Topology, Entanglement, and Strong Correlations. Modeling and Simulation* (E. Pavarini and E. Koch, eds.), ch. 4, Jülich, Germany: Forschungszentrum Jülich, 2020.

[170] E. U. Condon and G. H. Shortley, *The Theory of Atomic Spectra*. Cambridge University Press, 1959.

[171] J. J. Sakurai and J. J. Napolitano, *Modern Quantum Mechanics*. Pearson, 2014.

[172] J. A. Gaunt, "IV. The Triplets of Helium," *Phil. Trans. A*, vol. 228, p. 151, 1929.

[173] J. S. Griffith and L. E. Orgel, "Ligand-Field Theory," *Q. Rev. Chem. Soc.*, vol. 11, p. 381, 1957.

[174] C. J. Ballhausen and C. K. Jorgensen, "Studies of Absorption Spectra: IX. The Spectra of Cobalt (II) Complexes," *Acta.chem. scand.*, vol. 9, p. 397, 1955.

[175] J. K. Burdett, *Molecular Shapes: Theoretical Models of Inorganic Stereochemistry*. J. Wiley, 1980.

[176] E. I. Solomon, E. G. Pavel, K. E. Loeb, and C. Campochiaro, "Magnetic Circular Dichroism Spectroscopy as a Probe of the Geometric and Electronic Structure of Non-Heme Ferrous Enzymes," *Coord. Chem. Rev.*, vol. 144, p. 369, 1995.

[177] C. Daul, "Density Functional Theory Applied to the Excited States of Coordination Compounds," *Int. J. Quantum Chem.*, vol. 52, p. 867, 1994.

[178] M. Atanasov, C. Daul, and C. Rauzy, "New Insights into the Effects of Covalency on the Ligand Field Parameters: a DFT Study," *Chem. Phys. Lett.*, vol. 367, p. 737, 2003.

[179] M. Atanasov, C. Daul, and C. Rauzy, "A DFT Based Ligand Field Theory," *Struct Bond.*, vol. 106, p. 97, 2004.

[180] M. Atanasov and C. Daul, "Modeling Properties of Molecules with Open d-shells Using Density Functional Theory," *C. R. Chim.*, vol. 8, p. 1421, 2005.

[181] M. Atanasov, P. Comba, C. Daul, and F. Neese, "The Ligand-Field Paradigm," in *Models, Mysteries and Magic of Molecules* (J. C. A. Boeyens and J. F. Ogilvie, eds.), p. 411, Springer, 2008.

[182] J. C. Slater, *The Self-consistent Field for Molecules and Solids.* McGraw-Hill Book Company, Inc., 1974.

[183] M. Atanasov, C. Rauzy, P. Baettig, and C. Daul, "Calculation of Spin-Orbit Coupling Within the LFDFT: Applications to $[NiX_4]$ (X=F^-, Cl^-, Br^-, I^-)," *Int. J. Quantum Chem.*, vol. 102, p. 119, 2005.

[184] M. Atanasov, E. J. Baerends, P. Baettig, R. Bruyndonckx, C. Daul, C. Rauzy, and M. Zbiri, "The Calculation of ESR Parameters by Density Functional Theory: The g- and A-Tensors of Co(acacen)," *Chem. Phys. Lett.*, vol. 399, p. 433, 2004.

[185] M. Atanasov and C. Daul, "Theoretical Studies on the Electronic Properties and the Chemical Bonding of Transition Metal Complexes using DFT and Ligand Field Theory," *Chimia*, vol. 59, p. 504, 2005.

[186] M. Atanasov, C. Daul, H. U. Güdel, T. A. Wesolowski, and M. Zbiri, "Ground States, Excited States, and Metal-Ligand Bonding in Rare Earth Hexachloro Complexes: A DFT-Based Ligand Field Study," *Inorg. Chem.*, vol. 44, p. 2954, 2005.

[187] M. Atanasov, C. Daul, M.-M. Rohmer, and T. Venkatachalam, "A DFT based ligand field study of the EPR spectra of Co(II) and Cu(II) porphyrins," *Chem. Phys. Lett.*, vol. 427, p. 449, 2006.

[188] F. Senn and C. Daul, "Calculation of ^{59}Co Shielding Tensor σ using LF-DFT," *J. Mol. Struct.: THEOCHEM*, vol. 954, p. 105, 2010.

[189] F. Senn, M. Zlatar, M. Gruden-Pavlović, and C. Daul, "Computational Analysis of tris(1,2-ethanediamine) Cobalt(III) Complex Ion: Calculation of the ^{59}Co Shielding Tensor using LF-DFT," *Monatsh. Chem.*, vol. 142, p. 593, 2011.

[190] F. Senn, L. Helm, A. Borel, and C. Daul, "Electronic Fine Structure Calculation of $[Gd(DOTA)(H2O)]^-$ using LF-DFT: The Zero Field Splitting," *C. R. Chim.*, vol. 15, p. 250, 2012.

[191] Z. D. Matović, M. S. Jeremić, R. M. Jelić, M. Zlatar, and I. Z. Jakovljević, "Configurational, LFDFT and NBO Analysis of Chromium(III) Complexes of Edta-Type Ligands," *Polyhedron*, vol. 55, p. 131, 2013.

[192] H. Ramanantoanina and C. Daul, "A Non-Empirical Calculation of 2p Core-electron Excitation in Compounds with 3d Transition Metal Ions using Ligand-Field and Density Functional Theory (LFDFT)," *Phys. Chem. Chem. Phys.*, vol. 19, p. 20919, 2017.

[193] H. Ramanantoanina, W. Urland, F. Cimpoesu, and C. Daul, "Ligand Field Density Functional Theory Calculation of the $4f^2 \rightarrow 4f^1 5d^1$ Transitions in the Quantum Cutter $Cs_2KYF_6:Pr^{3+}$," *Phys. Chem. Chem. Phys.*, vol. 15, p. 13902, 2013.

[194] H. Ramanantoanina, W. Urland, A. Garcia-Fuente, F. Cimpoesu, and C. Daul, "Ligand Field Density Functional Theory for the Prediction of Future Domestic Lighting," *Phys. Chem. Chem. Phys.*, vol. 16, p. 14625, 2014.

[195] H. Ramanantoanina, M. Sahnoun, A. Barbiero, M. Ferbinteanu, and F. Cimpoesu, "Development and Applications of the LFDFT: The Non-Empirical Account of Ligand Field and the Simulation of the f–d Transitions by Density Functional Theory," *Phys. Chem. Chem. Phys.*, vol. 17, p. 18547, 2015.

[196] H. Ramanantoanina, G. Kuri, C. Daul, and J. Bertsch, "Core Electron Excitations in U^{4+}: Modelling of the $nd^{10}5f^2 \rightarrow nd^9 5f^3$ Transitions with n = 3, 4 and 5 by Ligand Field Tools and Density Functional Theory," *Phys. Chem. Chem. Phys.*, vol. 18, p. 19020, 2016.

[197] H. Ramanantoanina, "On the Calculation of Multiplet Energies of Three-Open-Shell $4f^{13}5f^n6d^1$ Electron Configuration by LFDFT: Modeling the Optical Spectra of 4f Core-Electron Excitation in Actinide Compounds," *Phys. Chem. Chem. Phys.*, vol. 19, p. 32481, 2017.

[198] H. Ramanantoanina, G. Kuri, M. Martin, and J. Bertsch, "Study of Electronic Structure in the L-edge Spectroscopy of Actinide Materials: UO_2 as an Example," *Phys. Chem. Chem. Phys.*, vol. 21, p. 7789, 2019.

[199] H. Ramanantoanina, "LFDFT-A Practical Tool for Coordination Chemistry," *Comput.*, vol. 10, p. 70, 2022.

[200] H. Ramanantoanina, L. Merzoud, J. T. Muya, H. Chermette, and C. Daul, "Electronic Structure and Photoluminescence Properties of $Eu(\eta^9\text{-}C_9H_9)_2$," *J. Phys. Chem. A*, vol. 124, p. 152, 2020.

[201] C. Daul, M. Zlatar, M. Gruden-Pavlović, and M. Swart, *Application of Density Functional and Density Functional Based Ligand Field Theory to Spin States in Spin States in Biochemistry and Inorganic Chemistry*. 2015.

[202] C. Daul, "Modelling Properties of Molecules with Open d- or f-Shells Using Density Functional Theory," *Chimia*, vol. 58, p. 316, 2004.

[203] C. Daul, "Ligand Field Theory: An Ever-Modern Theory," *JPCS*, vol. 428, p. 012023, 2013.

[204] C. E. Schäffer, C. Anthon, and J. Bendix, "Kohn-Sham DFT Results Projected on Ligand-Field Models: Using DFT to Supplement Ligand-Field Descriptions and to Supply Ligand-Field Parameters," *Coord. Chem. Rev.*, vol. 253, p. 575, 2009.

[205] M. Atanasov, D. Ganyushin, K. Sivalingam, and F. Neese, "Molecular Electronic Structures of Transition Metal Complexes II," p. 149, Springer, 2011.

[206] A. De Vos, and K. Lejaeghere, and F. Muniz-Miranda, and C. V. Stevens, and P. Van Der Voort, and V. Van Speybroeck, "Electronic Properties of Heterogenized Ru(II) Polypyridyl Photoredox Complexes on Covalent Triazine Frameworks," *J. Mater.Chem.A*, vol. 7, p. 8433, 2019.

[207] S. Hug, M. E. Tauchert, S. Li, U. E. Pachmayr, and B. V. Lotsch, "A Functional Triazine Framework Based on N-Heterocyclic Building Blocks," *J. Mater. Chem.*, vol. 22, p. 13956, 2012.

[208] S. Grimme, J. Antony, S. Ehrlich, and H. Krieg, "A Consistent and Accurate Ab Initio Parametrization of Density Functional Dispersion Correction (DFT-D) for the 94 Elements H-Pu.," *J. Chem. Phys.*, vol. 132, p. 154104, 2010.

[209] S. Cogan, S. Zilberg, and Y. Haas, "The Electronic Origin of the Dual Fluorescence in Donor-Acceptor Substituted Benzene Derivatives," *J. Am. Chem. Soc.*, vol. 128, p. 3335, 2006.

[210] C. L. Cheng, D. S. N. Murthy, and G. L. D. Ritchie, "Molecular Conformations from Magnetic Anisotropies," *J. Chem. Soc. Faraday Trans. 2*, vol. 68, p. 1679, 1972.

[211] H. Suzuki, "Relations between Electronic Absorption Spectra and Spatial Configurations of Conjugated Systems. I. Biphenyl," *Bull. Chem. Soc. Jpn.*, vol. 32, p. 1340, 1959.

[212] R. Olivares-Amaya, W. Hu, N. Nakatani, S. Sharma, J. Yang, and G. K.-L. Chan, "The Ab-Initio Density Matrix Renormalization Group in Practice," *J. Chem. Phys.*, vol. 142, p. 034102, 2015.

[213] J. Ho, E. Kish, D. D. Mendez-Hernández, K. WongCarter, S. Pillai, G. Kodis, J. Niklas, O. G. Poluektov, D. Gust, T. A. Moore, A. L. Moore, V. S. Batista, and B. Robert, "Triplet-Triplet Energy Transfer in Artificial and Natural Photosynthetic Antennas," *Proc. Natl. Acad. Sci. U. S. A.*, vol. 114, p. E5513, 2017.

[214] K. Kalyanasundaram, "Photophysics, Photochemistry and Solar Energy Conversion with tris(bipyridyl)ruthenium(II) and its Analogues," *Coord. Chem. Rev.*, vol. 46, p. 159, 1982.

[215] M. H. Shaw, J. Twilton, and D. W. C. MacMillan, "Photoredox Catalysis in Organic Chemistry," *J. Org. Chem.*, vol. 81, p. 6898, 2016.

[216] P. Pyykko, "Relativistic Effects in Structural Chemistry," *Chem. Rev.*, vol. 88, p. 563, 1988.

[217] A. Nandy, D. B. K. Chu, D. R. Harper, C. Duan, N. Arunachalam, Y. Cytter, and H. J. Kulik, "Large-Scale Comparison of 3d and 4d Transition Metal Complexes Illuminates the Reduced Effect of Exchange on Second-Row Spin-State Energetics," *Phys. Chem. Chem. Phys.*, vol. 22, p. 19326, 2020.

[218] F. Muniz-Miranda, L. D. Bruecker, A. D. Vos, F. V. Bussche, C. V. Stevens, P. V. der Voort, K. Lejaeghere, and V. V. Speybroeck, "Optical Properties of Isolated and Covalent Organic Framework-Embedded Ruthenium Complexes.," *J. Phys. Chem. A*, vol. 123, p. 6854, 2019.

[219] T. A. Word, C. L. Whittington, A. Karolak, M. T. Kemp, H. L. Woodcock, A. van der Vaart, and R. W. Larsen, "Photoacoustic Calorimetry Study of Ligand Photorelease from the Ru(II)Bis(2,2'-Bipyridine)(6,6'-Dimethyl-2,2'-Bipyridine) Complex in Aqueous Solution," *Chem. Phys. Lett.*, vol. 619, p. 214, 2015.

[220] R. Kobayashi and R. D. Amos, "Erratum to 'The Application of CAM-B3LYP to the Charge-Transfer Band Problem of the Zincbacteriochlorin–Bacteriochlorin Complex' [Chem. Phys. Lett. 420 (2006) 106–109]," *Chem. Phys. Lett.*, vol. 424, p. 225, 2006.

[221] J.-L. Bredas, "Mind the Gap!," *Mater. Horiz.*, vol. 1, p. 17, 2014.

[222] F. Alary, M. Boggio-Pasqua, J.-L. Heully, C. J. Marsden, and P. Vicendo, "Theoretical Characterization of the Lowest Triplet Excited States of the Tris-(1,4,5,8-Tetraazaphenanthrene) Ruthenium Dication Complex," *Inorg. Chem.*, vol. 47, p. 5259, 2008.

[223] F. Alary, J.-L. Heully, L. Bijeire, and P. Vicendo, "Is the ^{3}MLCT the Only Photoreactive State of Polypyridyl Complexes?," *Inorg. Chem.*, vol. 46, p. 3154, 2007.

[224] L. Zhang, W. Wang, S. Sun, and D. Jiang, "Near-Infrared Light Photocatalysis with Metallic/Semiconducting HxWO3/WO3

Nanoheterostructure In Situ Formed in Mesoporous Template," *Applied Catalysis, B: Environmental*, vol. 168, p. 9, 2015.

[225] W.-X. Liu, X.-L. Zhu, S.-Q. Liu, Q.-Q. Gu, and Z.-D. Meng, "Near-Infrared-Driven Selective Photocatalytic Removal of Ammonia Based on Valence Band Recognition of an α-MnO2/N-Doped Graphene Hybrid Catalyst," *ACS Omega*, vol. 3, p. 5537, 2018.

[226] H. A. Jahn and E. Teller, "Stability of Polyatomic Molecules in Degenerate Electronic States. I. Orbital Degeneracy," *Proc. R. Soc. London A*, vol. 161, p. 220, 1937.

[227] L. D. Bruecker and V. V. Speybroeck, "Influence of Number of Ligands and Point Group on the Electronic Structure of Co^{2+} Aqua-Complexes," *Inorg. Chem.*, vol. 61, p. 20743, 2022.

[228] D. F. Schriver, P. W. Atkins, and C. H. Langford, *Inorganic Chemistry*. Oxfor University Press, 1994.

[229] A. M. Schmiedekamp, M. D. Ryan, and R. J. Deeth, "Six-Coordinate Co^{2+} with H_2O and NH_3 Ligands: Which Spin State Is More Stable?," *Inorg. Chem.*, vol. 41, p. 5733, 2002.

[230] L. Sacconi, "Five-Coordination in 3d Complexes," *Pure and Applied Chemistry*, vol. 17, p. 95, 1968.

[231] L. Sacconi, "Some Factors Governing the Spin-Multiplicity of 5-Coordinate Complexes of Cobalt(II) and Nickel(II)," *J. Chem. Soc. (A)*, p. 248, 1970.

[232] J. Shee, M. Loipersberger, D. Hait, J. Lee, and M. Head-Gordon, "Revealing the Nature of Electron Correlation in Transition Metal Complexes with Symmetry-Breaking and Chemical Intuition," *J. Chem. Phys.*, vol. 154, p. 194109, 2021.

[233] F. Neese, W. Ames, G. Christian, M. Kampa, D. G. Liakos, D. A. Pantazis, M. Roemelt, P. Surawatanawong, and Y. E. Shengfa, *Dealing with Complexity in Open-shell Transition Metal Chemistry from a Theoretical Perspective: Reaction Pathways, Bonding, Spectroscopy, and Magnetic Properties*. Academic Press, 2010.

[234] P. R. Varadwaj and H. M. Marques, "The Physical Chemistry of Coordinated Aqua-, Ammine-, and Mixed-Ligand Co^{2+} Complexes: DFT Studies on the Structure, Energetics, and Topological Properties of the Electron Density," *Phys. Chem. Chem. Phys.*, vol. 12, p. 2126, 2010.

[235] D. A. Johnson and P. G. Nelson, "Factors Determining the Ligand Field Stabilization Energies of the Hexaaqua 2+ Complexes of the First Transition Series and the Irving-Williams Order," *Inorg. Chem.*, vol. 34, p. 5666, 1995.

[236] R. J. Deeth, "Ligand Field and Density Functional Descriptions of the d-States and Bonding in Transition Metal Complexes," *Faraday Discuss.*, vol. 124, p. 379, 2003.

[237] L. Banci, and A. Bencini, and C. Benelli, and D. Gatteschi, and C. Zanchini, and R. Bohra, J.-M. Dance, and V. K. Jain, and R. C. Mehrotra, and A. Tressaud, and R. G. Woolley, "Spectral-Structural Correlations in High-Spin Cobalt(II) Complexes.," *Struct. Bonding*, vol. 52, p. 37, 2007.

[238] C. K. Jörgensen, *Spectroscopy of Transition-Group Complexes in Advances in Chemical Physics*. John Wiley and Sons, Inc., 1963.

[239] R. M. Bullock, J. G. Chen, L. Gagliardi, P. J. Chirik, O. K. Farha, C. H. Hendon, C. W. Jones, J. A. Keith, J. Klosin, S. D. Minteer, R. H. Morris, A. T. Radosevich, T. B. Rauchfuss, N. A. Strotman, A. Vojvodic, T. R. Ward, J. Y. Yang, and Y. Surendranath, "Using Nature's Blueprint to Expand Catalysis with Earth-Abundant Metals," *Science*, vol. 369, p. eabc3183, 2020.

[240] P. Nuss and M. J. Eckelman, "Life Cycle Assessment of Metals: A Scientific Synthesis," *PLOS ONE*, vol. 9, p. e101298, 2014.

[241] D. C. Ashley and E. Jakubikova, "Ironing out the Photochemical and Spin-Crossover Behavior of Fe(ii) Coordination Compounds with Computational Chemistry," *Coord. Chem. Rev.*, vol. 337, p. 97, 2017.

[242] J. A. Pople, P. M. W. Gill, and N. C. Handy, "Spin-Unrestricted Character of Kohn-Sham Orbitals for Open-Shell Systems," *Int. J. Quantum Chem.*, vol. 56, p. 303, 1995.

[243] A. Ipatov, F. Cordova, L. J. Doriol, and M. E. Casida, "Excited-State Spin-Contamination in Time-Dependent Density-Functional Theory for Molecules with Open-Shell Ground States," *J. Mol. Struct. THEOCHEM*, vol. 914, p. 60, 2009.

[244] H. J. Kulik, "Making Machine Learning a Useful Tool in the Accelerated Discovery of Transition Metal Complexes," *WIREs Comput Mol Sci.*, vol. 10, p. e1439, 2019.

[245] H. J. Kulik, T. Hammerschmidt, J. Schmidt, S. Botti, M. A. L. Marques, M. Boley, M. Scheffler, M. Todorović, P. Rinke, C. Oses, A. Smolyanyuk, S. Curtarolo, A. Tkatchenko, A. P. Bartók, S. Manzhos, M. Ihara, T. Carrington, J. Behler, O. Isayev, M. Veit, A. Grisafi, J. Nigam, M. Ceriotti, K. T. Schütt, J. Westermayr, M. Gastegger, R. J. Maurer, B. Kalita, K. Burke, R. Nagai, R. Akashi, O. Sugino, J. Hermann, F. Noé, S. Pilati, C. Draxl, M. Kuban, S. Rigamonti, M. Scheidgen, M. Esters, D. Hicks, C. Toher, P. V. Balachandran, I. Tamblyn, S. Whitelam, C. Bellinger, and L. M. Ghiringhelli, "Roadmap on Machine Learning in Electronic Structure," *Electron. Struct.*, vol. 4, p. 023004, 2022.

[246] M. G. Taylor, T. Yang, S. Lin, A. Nandy, J. P. Janet, C. Duan, and H. J. Kulik, "Seeing Is Believing: Experimental Spin States from Machine Learning Model Structure Predictions," *J. Phys. Chem. A*, vol. 124, p. 3286, 2020.

[247] G. G. Terrones, C. Duan, A. Nandy, and H. J. Kulik, "Low-Cost Machine Learning Prediction of Excited State Properties of Iridium-Centered Phosphors," *Chem. Sci.*, vol. 14, p. 1419, 2023.

[248] J. P. Janet and H. J. Kulik, "Predicting Electronic Structure Properties of Transition Metal Complexes with Neural Networks," *Chem. Sci.*, vol. 8, p. 5137, 2017.

[249] C. Duan, J. P. Janet, F. Liu, A. Nandy, and H. J. Kulik, "Learning from Failure: Predicting Electronic Structure Calculation Outcomes with Machine Learning Models," *J. Chem. Theory Comput.*, vol. 15, p. 2331, 2019.

[250] J. P. Janet, F. Liu, A. Nandy, C. Duan, T. Yang, S. Lin, and H. J. Kulik, "Designing in the Face of Uncertainty: Exploiting Electronic Structure and Machine Learning Models for Discovery in Inorganic Chemistry," *Inorg. Chem.*, vol. 58, p. 10592, 2019.

[251] R. Orús, "Tensor Networks for Complex Quantum Systems," *Nat. Rev. Phys.*, vol. 1, p. 538, 2019.

[252] S. Wouters, T. Bogaerts, P. V. D. Voort, V. V. Speybroeck, and D. V. Neck, "DMRG-SCF Study of the Singlet, Triplet, and Quintet States of oxo-Mn(Salen)," *J. Chem. Phys.*, vol. 140, p. 241103, 2014.

[253] L. Vanderstraeten, J. Haegeman, P. Corboz, and F. Verstraete, "Gradient Methods for Variational Optimization of Projected Entangled-Pair States," *Phys. Rev. B*, vol. 94, p. 155123, 2016.

[254] L. Vanderstraeten, M. Mariën, F. Verstraete, and J. Haegeman, "Excitations and the Tangent Space of Projected Entangled-Pair States," *Phys. Rev. B*, vol. 92, p. 201111, 2015.

[255] R. van Leeuwen, "Key Concepts in Time-Dependent Density-Functional Theory," *Int. J. Mod. Phys. B*, vol. 15, p. 1969, 2001.

[256] G. te Velde, and F. M. Bickelhaupt, and E. J. Baerends, and C. Fonseca Guerra, and S.J.A. van Gisbergen, and J.G. Snijders, and T. Ziegler, "Chemistry with ADF," *J. Comp. Chem.*, vol. 22, p. 931, 2001.

[257] ADF 2018.105, SCM, Theoretical Chemistry, Vrije Universiteit, Amsterdam, The Netherlands, http://www.scm.com

[258] AMS 2020.103, SCM, Theoretical Chemistry, Vrije Universiteit, Amsterdam, The Netherlands, http://www.scm.com

[259] AMS 2021.103, SCM, Theoretical Chemistry, Vrije Universiteit, Amsterdam, The Netherlands, http://www.scm.com

[260] T. D. Kühne, M. Iannuzzi, M. D. Ben, V. V. Rybkin, P. Seewald, F. Stein, T. Laino, R. Z. Khaliullin, O. Schütt, F. Schiffmann, D. Golze, J. Wilhelm, S. Chulkov, M. H. Bani-Hashemian, V. Weber, U. Borštnik, M. Taillefumier, A. S. Jakobovits, A. Lazzaro, H. Pabst, T. Müller, R. Schade, M. Guidon, S. Andermatt, N. Holmberg, G. K. Schenter, A. Hehn, A. Bussy, F. Belleflamme, G. Tabacchi, A. Glöß, M. Lass, I. Bethune, C. J. Mundy, C. Plessl, M. Watkins, J. VandeVondele, M. Krack, and J. Hutter, "CP2K: An Electronic Structure and Molecular Dynamics Software Package - Quickstep: Efficient and Accurate Electronic Structure Calculations," *J. Chem. Phys.*, vol. 152, p. 194103, 2020.

[261] M. J. Frisch, G. W. Trucks, H. B. Schlegel, G. E. Scuseria, M. A. Robb, J. R. Cheeseman, G. Scalmani, V. Barone, G. A. Petersson, H. Nakatsuji, M. C. X. Li, A. V. Marenich, J. Bloino, B. G. Janesko, R. Gomperts, B. Mennucci, H. P. Hratchian, J. V. Ortiz, A. F. Izmaylov, J. L. Sonnenberg, D. Williams-Young, F. Ding, F. Lipparini, F. Egidi, J. Goings, B. Peng, A. Petrone, T. Henderson, D. Ranasinghe, V. G. Zakrzewski, J. Gao, N. Rega, G. Zheng, W. Liang, M. Hada, M. Ehara, K. Toyota, R. Fukuda, J. Hasegawa, M. Ishida, T. Nakajima, Y. Honda, O. Kitao, H. Nakai, T. Vreven, K. Throssell, J. A. Montgomery, J. E. P. Jr., F. Ogliaro, M. J. Bearpark, J. J. Heyd, E. N. Brothers, K. N. Kudin, V. N. Staroverov, T. A. Keith, R. Kobayashi, J. Normand, K. Raghavachari, A. P. Rendell, J. C. Burant, S. S. Iyengar, J. Tomasi, M. Cossi, J. M. Millam, M. Klene, C. Adamo, R. Cammi, J. W. Ochterski, R. L. Martin,

K. Morokuma, O. Farkas, J. B. Foresman, and D. J. Fox, *Gaussian 16 Revision B.01.* Gaussian Inc. Wallingford CT, 2016.

This research was performed within the Excellence of Science (EOS) project BioFact (EOS ID 30902231), founded by the Research Foundation Flanders (FWO). Funding was also received from the Research Board of Ghent University (BOF) through a Concerted Research Action (GOA) and the European Union's Horizon 2020 research and innovation program under the European Research Council consolidator grant agreement no. 647755 (project acronym: DYNPOR).

The computational resources (Stevin Supercomputer Infrastructure) and services used in this work were provided by the VSC (Flemish Supercomputer Center), funded by Ghent University, FWO and the Flemish Government-department EWI.